OCS Study
MMS 2006-074

Exploratory Study of Deepwater Currents in the Gulf of Mexico

Volume II: Technical Report

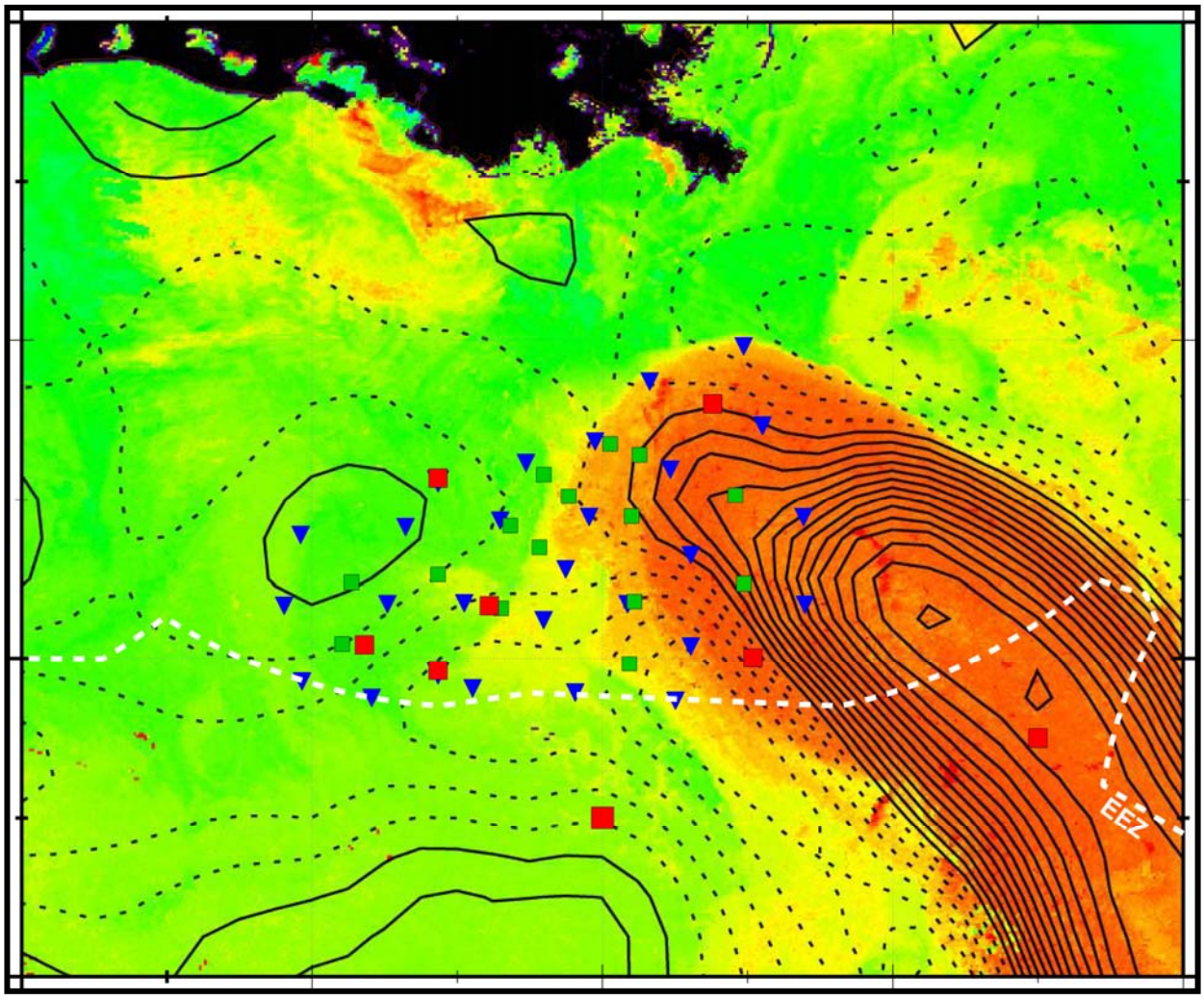

MMS U.S. Department of the Interior
Minerals Management Service
Gulf of Mexico OCS Region

OCS Study
MMS 2006-074

Exploratory Study of Deepwater Currents in the Gulf of Mexico

Volume II: Technical Report

Authors

Kathleen Donohue
Peter Hamilton
Kevin Leaman
Robert Leben
Mark Prater
Evans Waddell
Randolph Watts

Prepared under MMS Contract
1435-01-02-CT-31152
by
Science Applications International Corporation
615 Oberlin Road, Suite 100
Raleigh, North Carolina 27605

Published by

U.S. Department of the Interior
Minerals Management Service
Gulf of Mexico OCS Region

New Orleans
December 2006

DISCLAIMER

This report was prepared under contract between the Minerals Management Service (MMS) and Science Applications International Corporation. This report has been technically reviewed by the MMS, and it has been approved for publication. Approval does not signify that the contents necessarily reflect the views and policies of the MMS, nor does mention of trade names or commercial products constitute endorsement or recommendation for use. It is, however, exempt from review and compliance with the MMS editorial standards.

REPORT AVAILABILITY

Extra copies of this report may be obtained from the Public Information Office (Mail Stop 5034) at the following address:

U.S. Department of the Interior
Minerals Management Service
Gulf of Mexico OCS Region
Public Information Office (MS 5034)
1201 Elmwood Park Blvd.
New Orleans, LA 70123-2394

Telephone: (504) 736-2519 or
1-800-200-GULF

CITATION

Donohue, K., P. Hamilton, K. Leaman, R. Leben, M. Prater, D.R.Watts, and E. Waddell. 2006. Exploratory study of deepwater currents in the Gulf of Mexico. Volume II: Technical report. U.S. Dept. of the Interior, Minerals Management Service, Gulf of Mexico OCS Region, New Orleans, LA. OCS Study MMS 2006-074. 430 pp.

ABOUT THE COVER

Shows that portion of the northern Gulf of Mexico in which field measurements were made overlaid on a sea surface temperature image near the beginning of the field study. At that time, the warm (orange) Loop Current waters extended well into the measurement array. In this presentation, inverted triangles show the locations of PIES, green squares the locations of short or near bottom moorings and red squares are full depth mooring locations.

ACKNOWLEDGEMENT

The support and encouragement of Dr. Alexis Lugo-Fernandez, the MMS COTR, from project inception through completion has been fundamental to the program success and resulting oceanographic insights. Valuable suggestions and support from the Science Review Group (Dr. J. Bane [UNC], Dr. A. Kirwan [U. of Delaware] and Mr. D. Driver, [BP]), during the course of the study, were positive, constructive and are greatly appreciated. SAIC program personnel, Paul Blankinship (Data Management) and James Singer (Field Operations and Logistics), were crucial to the smooth data support and the outstanding data return and field activities. Mr. G. Chaplin (URI) very successfully conducted all aspects of the PIES instrumentation and field operations. GEOS provided the equipment and field personnel for deployment, rotation and recovery of most of the near-bottom moorings deployed for the study. Many additional people, too numerous to identify individually, were important to the program success, e.g., the captains and crews of the *R/V Longhorn* and the *R/V Pelican*. The patience, diligence and expertise of Mrs. Carol Harris in the production of reports is greatly appreciated by the Program Manager.

TABLE OF CONTENTS

Page

TABLE OF CONTENTS (continued)

Page

TABLE OF CONTENTS (continued)

TABLE OF CONTENTS (continued)

LIST OF FIGURES

LIST OF FIGURES (continued)

LIST OF FIGURES (continued)

LIST OF FIGURES (continued)

LIST OF FIGURES (continued)

LIST OF FIGURES (continued)

LIST OF FIGURES (continued)

LIST OF FIGURES (continued)

LIST OF FIGURES (continued)

LIST OF FIGURES (continued)

LIST OF FIGURES (continued)

LIST OF FIGURES (continued)

LIST OF FIGURES (continued)

LIST OF FIGURES (continued)

LIST OF FIGURES (continued)

LIST OF TABLES

LIST OF TABLES (continued)

LIST OF ABBREVIATIONS AND ACRONYMS

ADCP	Acoustic Doppler Current Profiler
ALS	Autonomous Listening Station
APEX	Autonomous Profiling Explorer
AR	Autoregressive
ARGOS	Advanced Research Global Observation Satellite (no longer an acronym)
AVHRR	Advanced Very High Resolution Radiometer
BP	British Petroleum
BC	Baroclinic Streamfunction
BT	Barotropic Streamfunction
CCAR	Colorado Center for Astrodynamics Research
CEOF	Complex EOF
CERSAT	Centre ERS d'Archivage et de Traitement
CICESE	Centro de Investigacion Cientifica y de Educacion Superior de Ensenada
CNES	Centre National d'Etudes Spatiales, France
CPD	Cycles per Day
CPIES	PIES with an attached Doppler current sensor suspended 50 m above the PIES
CTD	Conductivity/Temperature/Depth
C/T/D	Conductivity/Temperature/Depth
CUPOM	University of Colorado – Princeton Ocean Model
DOF	Degrees of Freedom
EEZ	Exclusive Economic Zone
EKE	Eddy Kinetic Energy
EOF	Empirical Orthogonal Function
ERM	Exact Repeat Mission
ERS-2	Earth Resources Satellite – 2
ESA	European Space Agency
GDR	Geophysical Data Record
GEM	Gravest Empirical Mode
GEOS	Fugro Global Environmental and Ocean Services
GEOSAT	Geodetic Satellite
GFO	Geosat Follow-On
GMT	Greenwich Mean Time or UTC
GOES	Geostationary Operational Environmental Satellite
GOM	Gulf of Mexico
GSFC	Goddard Space Flight Center
IES	Inverted Echo Sounder
HHP	Hour High Pass
HLP	Hour Low Pass
HMI	Horizon Marine, Inc.
JHU/APL	Johns Hopkins University/Applied Physics Laboratory
JIP	Joint Industry Program
KE	Kinetic Energy
LC	Loop Current

LIST OF ABBREVIATIONS AND ACRONYMS (continued)

LCE	Loop Current Eddy
LCFE	Loop Current Frontal Eddy
LH	Left Hand
LSU	Louisiana State University
MAB	Meters Above Bottom
MICOM	Miami Isopycnic Coordinate Ocean Model
MMS	Minerals Management Service
MODIS	Moderate Resolution Imaging Spectroradiometer
NASA	National Aeronautics and Space Administration
NDBC	National Data Buoy Center
NESDIS	National Environmental Satellite, Data, and Information Service
NOAA	National Oceanic and Atmospheric Administration
N-Sigs	North of Sigsbee Escarpment
OA	Objective Analysis
OISSH	Optimally Interpolated Sea Surface Height
PALACE	Profiling Autonomous Lagrangian Circulation Explorer
PALFOS	PALACE float with Sound Fixing and Ranging
PI	Principal Investigator
PIES	Inverted Echo Sounder with Pressure
PNG	Portable Network Graphics
PO	Physical Oceanography
PODAAC	Physical Oceanography Distributed Active Archive Center
PSU	Practical Salinity Unit
PV	Potential Vorticity
RAFOS	Ranging and Fixing of Sound (SOFAR spelled backwards)
RFP	Request for Proposal
RH	Right Hand
SAIC	Science Applications International Corporation
SEBCEP	Sigsbee Escarpment Bottom Current Enhancement Project
SNR	Signal-to-Noise Ratio
SOFAR	Sound Fixing and Ranging
SSH	Sea Surface Height
SSHA	Sea Surface Height Anomaly
S-Sigs	South of Sigsbee Escarpment
SST	Sea Surface Temperature
SUW	Subtropical Underwater
Sv	Sverdrups
T	Temperature
T/C/P	Temperature/Conductivity/Pressure
TOPEX/Poseidon	Ocean Topography Experiment
TOP/POS	Abbreviation for TOPEX/Poseidon
T/P	Abbreviation for Temperature/Pressure
TRW	Topographic Rossby Wave
T/S	Abbreviation for Temperature/Salinity

LIST OF ABBREVIATIONS AND ACRONYMS (continued)

T/S/P	Temperature/Salinity/Pressure (or T/P/S: Temperature/Pressure/Salinity)
UNC	University of North Carolina, Chapel Hill
UTC	Coordinated Universal Time or GMT
URI	University of Rhode Island
WKB	Wentzel-Kramers-Brillouim
XBT	Expendable Bathythermograph

1.0 INTRODUCTION

1.1 Background

The Minerals Management Service (MMS) awarded a contract to Science Applications International Corporation (SAIC) to conduct a four-year study titled: Exploratory Study of Deepwater Currents in the Gulf of Mexico (often referred to as simply the Exploratory Study). Generally, this project had been in the MMS planning phases for several years, however, the specifics were substantially affected by two years of field measurements (August 1999 – August 2001) made in the vicinity of Green Knoll (Figure 1.1-1) by SAIC (Hamilton et al., 2003). The objectives and background leading to the present study also incorporated the substantial insights developed as part of the MMS-funded Deepwater Physical Oceanography Reanalysis and Synthesis of Historical Data conducted by Texas A&M University (Nowlin et al., 2001). In addition to the Exploratory Study, the MMS is presently funding two additional field measurement programs with the goal of an improved documentation and understanding of physical oceanographic conditions in the deepwater of the northern Gulf of Mexico (GOM). The Survey of Deepwater Currents in the Western Gulf of Mexico and the Survey of Deepwater Currents in the Eastern Gulf of Mexico, while not concurrent with the Exploratory Study, will provide valuable insights to conditions in these areas of the US Exclusive Economic Zone (EEZ) that bracket the present study area. Note that the Western GOM Survey has two coordinated components producing measurements within the American and the Mexican EEZs.

The specified domain for field measurements for the Exploratory Study is shown in Figure 1.1-1. The east-west extent was from 88°W to 94°W, and the north-south extent was defined by the 1,000 m isobath to the north and the EEZ boundary to the south. The field measurement program designed and implemented by SAIC and its team of scientists fully supported the goal and requirements specified in the Request for Proposal (RFP).

The Exploratory Study field measurement program as called for in the RFP and designed by SAIC's team had three primary objectives:

A. Increase the deepwater current database and knowledge of deep circulation in the GOM,

B. Collect measurements sufficient to estimate parameters needed to design full-scale PO studies in deepwater regions of the GOM, and

C. Collect current data sufficient to test and/or evaluate the hypotheses listed below:

- **H1**: Currents shallower than 800 m are dynamically uncoupled from currents at depths greater than about 1,000 m.
- **H2**: Rare mid-water jets occur in areas of eddy-eddy interactions.
- **H3**: Currents in water depths greater than 1,000 m never show a large vertical gradient of velocity.

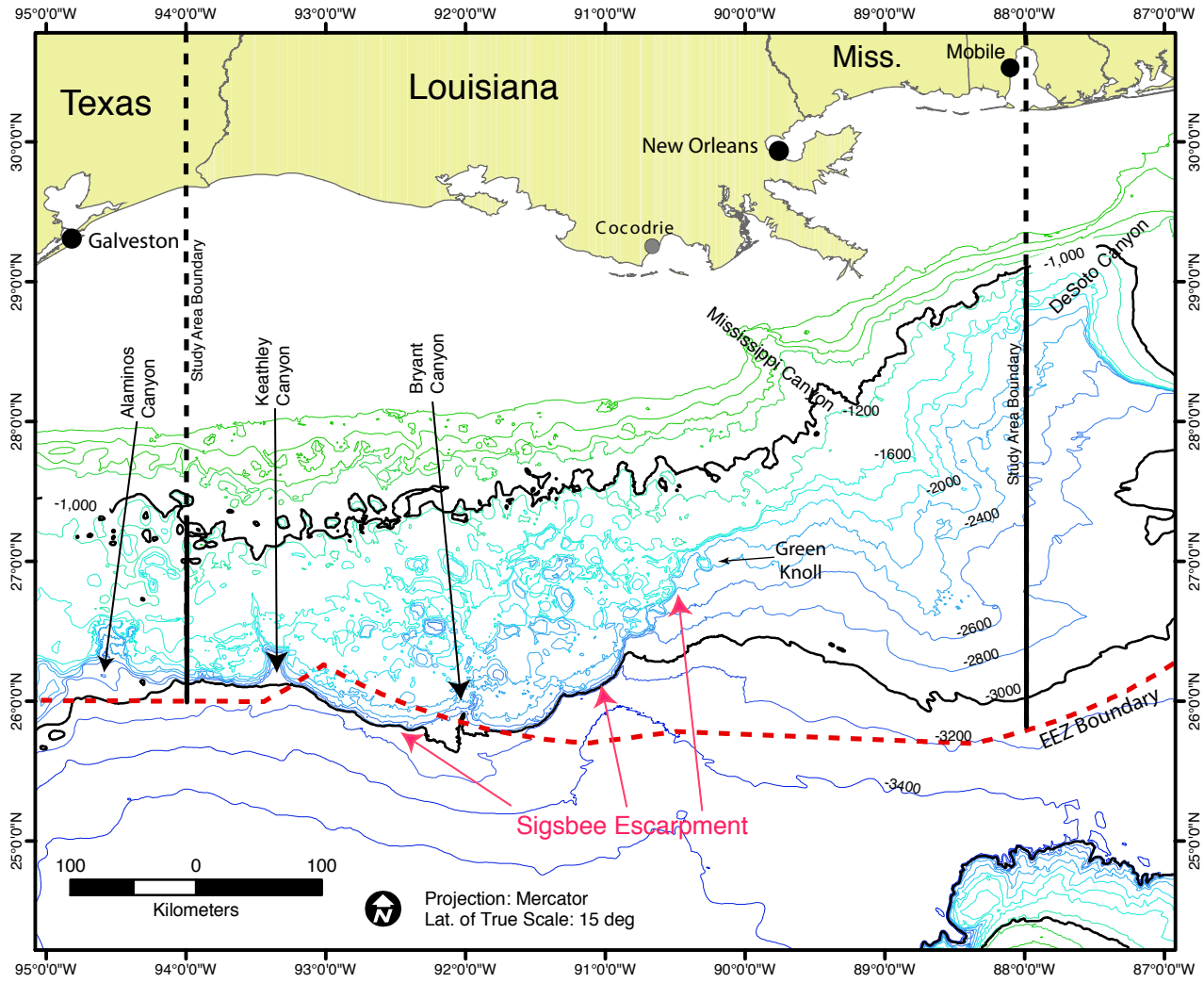

Figure 1.1-1. Map showing locations of key bathymetric features and several place names to orient the reader to the extent of the study area and bottom features that may be important to discussions of deep water currents.

H4: Deepwater parameters measured in areas dominated by cyclones/anticyclones of scales of 50-100 km are not different from areas not dominated by cyclones/anticyclones of 50-100 km.

H5: There are no differences in the occurrence and/or intensity of near bottom currents near steep bathymetric gradients and areas of small bathymetric gradients**.**

H6: The characteristics of topographic Rossby waves (TRWs) change from east to west in the Gulf of Mexico because of changes in bottom slopes and frictional dissipation that causes the TRWs to reflect, trap and dissipate by wave breaking**.**

H7: Circulation below 1,000 m in the Gulf of Mexico is dominated by cyclone/anticyclone pairs and is fundamentally cyclonic.

H8: Storm generated inertial oscillations trigger resonant phenomena that propagate into deepwater.

1.2 Proposed Approach

The SAIC team of scientists and engineers designed an innovative, data rich, and observationally integrated field measurement program that supported all of the program objectives. This was done using: Inverted Echo Sounders with Pressure (PIES), direct and acoustic current velocity measurements with related hydrographic variables, Lagrangian drifters and remote sensing. As proposed, PIES in conjunction with conventional current meter moorings provided the following key cost-effective design advantages:

- Full-depth current profiles at sixteen sites over the study area (See PIES locations relative to Tall and Short Mooring locations in Figure 1.2-1).

- Substantially broader and better resolved time varying, 3-D coverage of the temperature and salinity structure than was possible with 15 conventional moorings.

- Bottom pressure measurements at 25 PIES sites to map deep eddies and distinguish between deep eddies and TRWs.

- An analytical method for determining the baroclinic and barotropic bottom pressure contributions to altimeter measurements of sea surface height (SSH).

Proposed Study Area

As presented in Figure 1.1-1, the Sigsbee Escarpment is a major bathymetric feature affecting conditions and processes in the study area. As shown, the Escarpment is oriented approximately NE to SW from approximately 89°W to 92°W. Generally, the relative elevation change across the Escarpment (top to base) is on the order of 500 m. However, the Escarpment is inclined such that the top of the Escarpment is approximately 1500 m below the surface at the NE end and approximately 2500 m at the SW end as shown in Figure 1.1-1. On the eastern end of the study area a more gently sloping bottom occurs between the 2,000 and 3,000 m isobaths. The location and presence of this latter area may be of importance in discussions of the characteristics and behavior of TRWs.

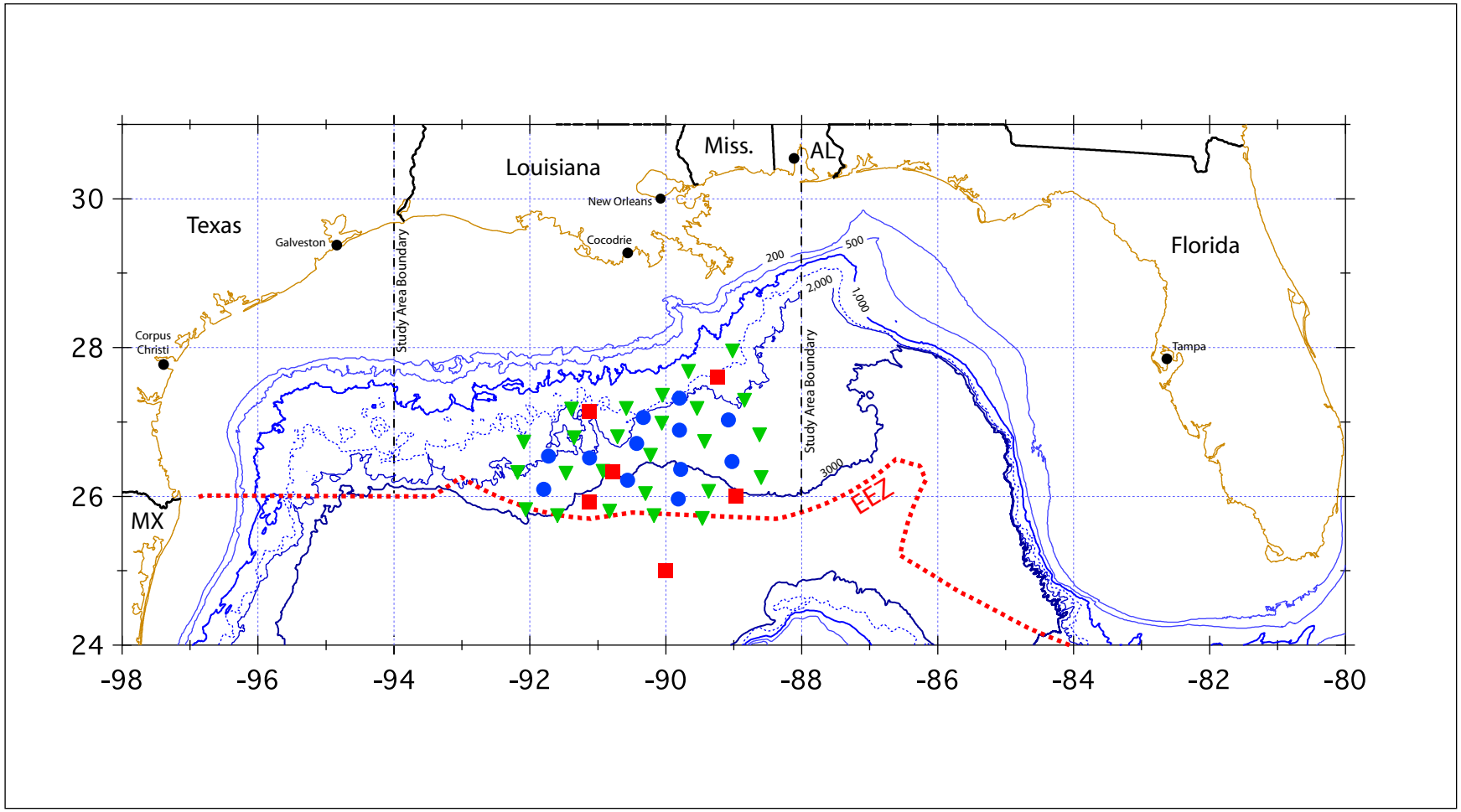

Figure 1.2-1. Map showing the regional bathymetry of the northern GOM, the east-west and north-sourth extent of the study area. In the above map, the locations of PIES are indicated by inverted triangles, the near-bottom or short moorings by blue solid circles and the full depth moorings (Exploratory, LSU and CICESE) are shown by red solid squares.

By coordinating other programs that were completely or partially funded by the MMS, the Exploratory Study had access to measurements taken over an area larger than the spatial extent defined in Section 1.1. Particularly, Louisiana State University deployed a well-instrumented, full-depth mooring within the Exploratory Study domain. Additionally, the MMS supported CICESE to instrument and deploy a full-depth mooring south of the Exploratory Study area and within the Mexican EEZ. Data sharing among the various entities responsible for acquiring the field measurements was such that each participant (LSU, CICESE and the Exploratory Study) had access to the complete set of observations regardless of the origin. This sharing arrangement has been well defined by the MMS data-sharing protocols.

Team Participants

Presented below are Science Team/Principal Investigators (PIs) who contributed to the analyses and subsequent writing of this report. Also shown are the primary SAIC personnel that supported the project. Note that each PI was supported in their various activities by scientists and engineers at their home institutions. These additional support personnel were essential to the success of all aspects of the study from observations to analyses to graphics production.

Science Team and associated measurement responsibility:

PIES

Dr. Kathleen Donohue, University of Rhode Island
Dr. Randolph Watts, University of Rhode Island

Lagrangian

Dr. Kevin Leaman, University of Miami
Dr. Mark Prater, University of Rhode Island

Remote Sensing

Dr. Robert Leben, University of Colorado

In-situ Current Measurements

Dr. Peter Hamilton, SAIC

It is important to note that the complete and comprehensive data set was available to each of the members of the Science Team, thus, a multivariate approach was used by each scientist. In conjunction with this approach, there was considerable collegial interaction so that combined expertise was brought to bear on the complex processes occurring in the upper and lower layers of the water column in the study area.

The Science Team was supported by the Management and Logistics personnel as follows:

Dr. Evans Waddell, Program Manager
Mr. James Singer, Logistics Manager and Cruise Chief Scientist
Mr. Paul Blankinship, Data Manager

Twelve of the near-bottom moorings were built, deployed and recovered by GEOS. Mr. David Szabo was the primary point of contact for most of the study in support of this component of the field measurements. All other moored current meter arrays were the responsibility of SAIC. URI was responsible for all aspect of the PIES instrumentation, including building, preparation, deployment and recovery.

The MMS and the project team has been supported by a Science Review Group (SRG) composed of:

Dr. John Bane, University of North Carolina
Dr. Albert Kirwan, University of Delaware
Mr. David Driver, British Petroleum (BP)

Report Organization

This report provides a dynamic characterization of processes occurring in the upper and lower layers of the north central GOM. In support of this goal, report sections include:

Section 1: Introduction that describes the general context and content of the study;

Section 2: Experimental Design and Methodology that briefly describes measurements made and associated aspects of the study.

Section 3: Gulfwide and Historical Perspective that provides information to the reader on some of the work done previously as well as metrics and descriptions of dynamic features that affect the study area directly or indirectly.

Section 4: Basic Description in the Study Area provides a general characterization of the basic conditions and processes occurring in the study area.

Section 5: Interpretation and Analyses provides a more in-depth presentation of the results of analyses in both the upper and lower layer of the water column.

Section 6: Upper and Lower Layer Interactions describes possible linkages that may relate conditions in the upper and lower layers of the water column.

Section 7: High-frequency Oscillations describes the measured current variations that occurred at or above the tidal or inertial frequency with a tentative explanation for some of the episodes documented.

Section 8: Summary and Recommendation provides a brief review of key understandings developed during this study in conjunction with suggestions for future studies.

The appendices to Volume II contain information that the reader may find of use, but if it had been included in the main body of the report would have tended to detract from a focus on the insights to conditions and processes resulting to date from the measurements and analyses associated with the Exploratory Study.

2.0 EXPERIMENT DESIGN AND METHODOLOGY

The Exploratory Study involves development and use of comprehensive multivariate database to support study objectives. This database consists of an extensive array of:

- Fixed-level current measurements and current profilers,
- RAFOS and PALACE lagrangian drifters,
- Inverted Echo Sounders with Pressure (PIES), site specific CTD profiles,
- Fixed level C/T sensors, and
- Remotely sensed observations information with particular emphasis on sea surface height and temperatures.

2.1 Current Meters

A major component of the Exploratory Study involved taking and using current observations measured with both single-level and profiling instruments. Deployment of Exploratory Study moorings that provided current velocity time series began at the end of February 2003 and ended in the middle of April 2004. These observations were made over a mooring array that was tailored to resolve particular scales of motion and to provide essential reference level velocities for use in conjunction with geostrophic current profiles developed from PIES observations. As proposed and implemented, two types of mooring were deployed: Tall or full-depth moorings and short or near-bottom moorings (see Figure 2.1-1). The general characteristics of measurements on these moorings are discussed below.

As originally proposed, the Exploratory Study short/near-bottom moorings all had the same configuration. These moorings were all approximately 500 m tall with current meters placed 100 m and 500 m above the local bottom. During continued evaluation of the ability of PIES to be well referenced to a velocity, given the scales of motion that might be expected in the vicinity of the Sigsbee Escarpment, it was determined that three additional short moorings (M3-M5) would be useful and appropriate. These moorings had only one current meter placed 100 m above the bottom. As a consequence, a total of 15 short moorings were deployed. Four tall or full-depth moorings (designated L1 – L4) were used in this study. There was consistent instrument placement on these moorings relative to the water surface. A 75-kHz ADCP was at 400-m depth. Fixed-level current meters were placed at 750 and 1,000-m depths. Below 1,000 m, current meters were placed at approximately 500-m intervals to the bottom. In each case, one current meter was always placed 100 m above the local bottom. As designed, this placement of current meters on tall and short moorings was appropriate for conditions as measured in prior studies, as well as to provide appropriate reference velocities at consistent local heights for use in process definition and in the PIES analyses.

In addition to current meters, the tall moorings also had a variety of sensors measuring and recording time series of temperature, salinity and pressure (T/S/P). The placement of these instruments and the current meters are summarized in Table 2.1-1. The overall data return for the Exploratory Study instrumentation was 97.5%. This computation assumed that multilevel ADCP current records only counted as one time series. This is a very good data return. A timeline of observations from moored arrays is shown in Figure 2.1-2a through Figure 2.1-2d.

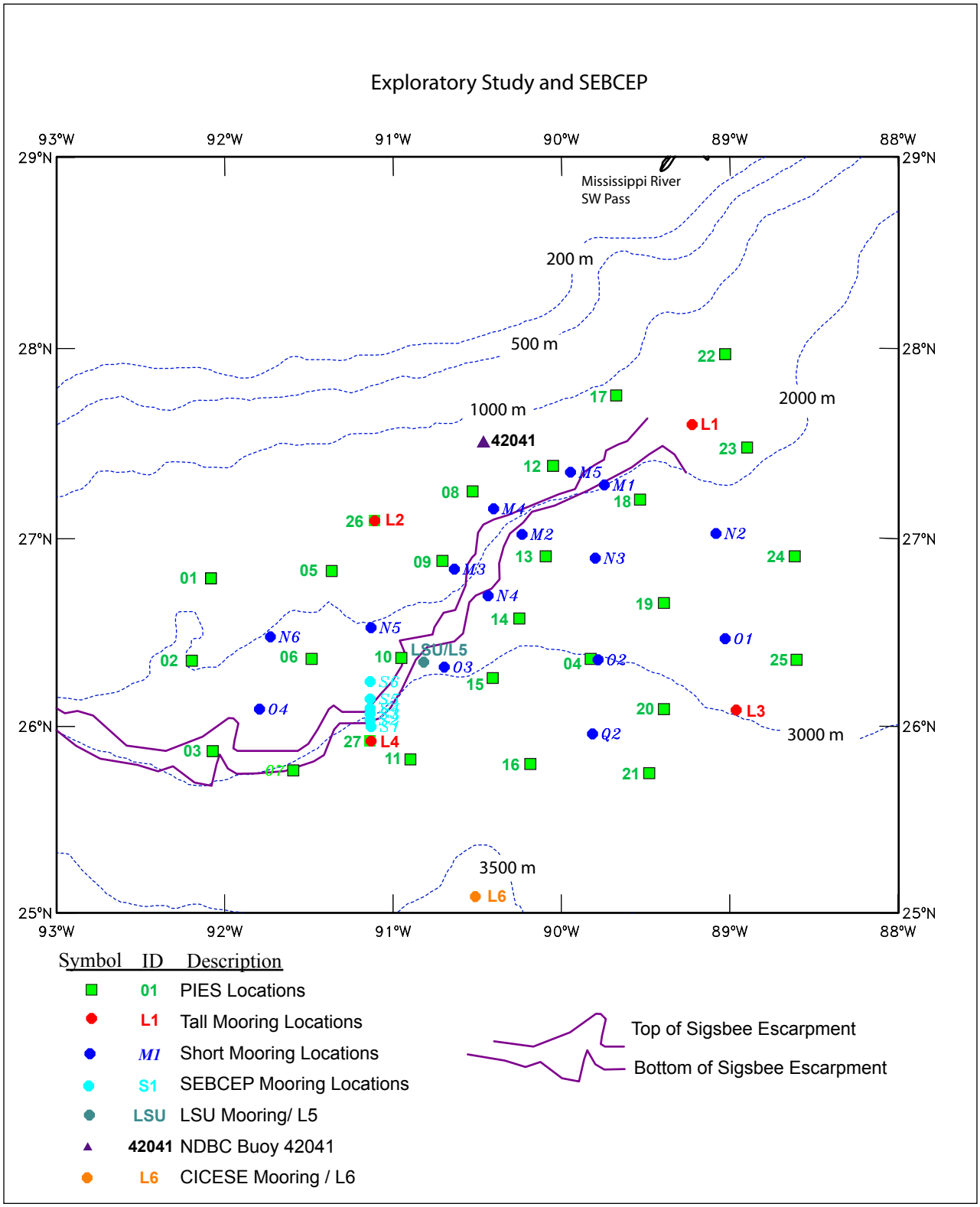

Figure 2.1-1. General bathymetric map showing the location of various instrument sites used during the Exploratory Study. The legend at the bottom indicates the relation of map symbols to the types of measurements made.

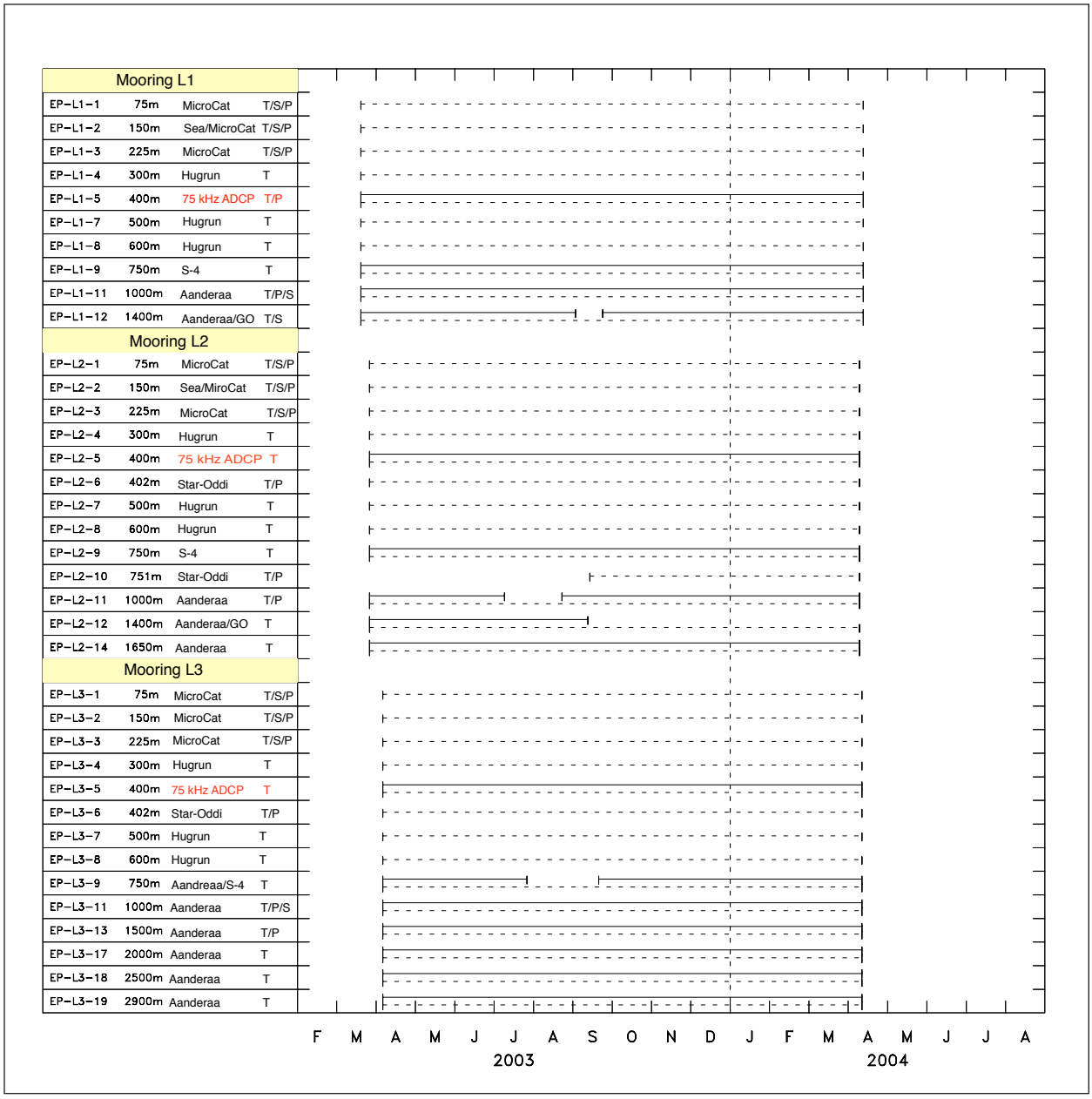

Figure 2.1-2a. Timelines of observations made by fixed position (Eulerian) instruments. On this page are listed full-depth moorings L1, L2, and L3. Each has an upward directed 75 kHz ADCP to profile the upper 400 m of the water column. As shown, a number of fixed level current meters as well as T/S/P and T sensors were attached to these moorings. In the above figure, solid lines indicate measurement of a vector quantity; dashed lines a scalar quantity.

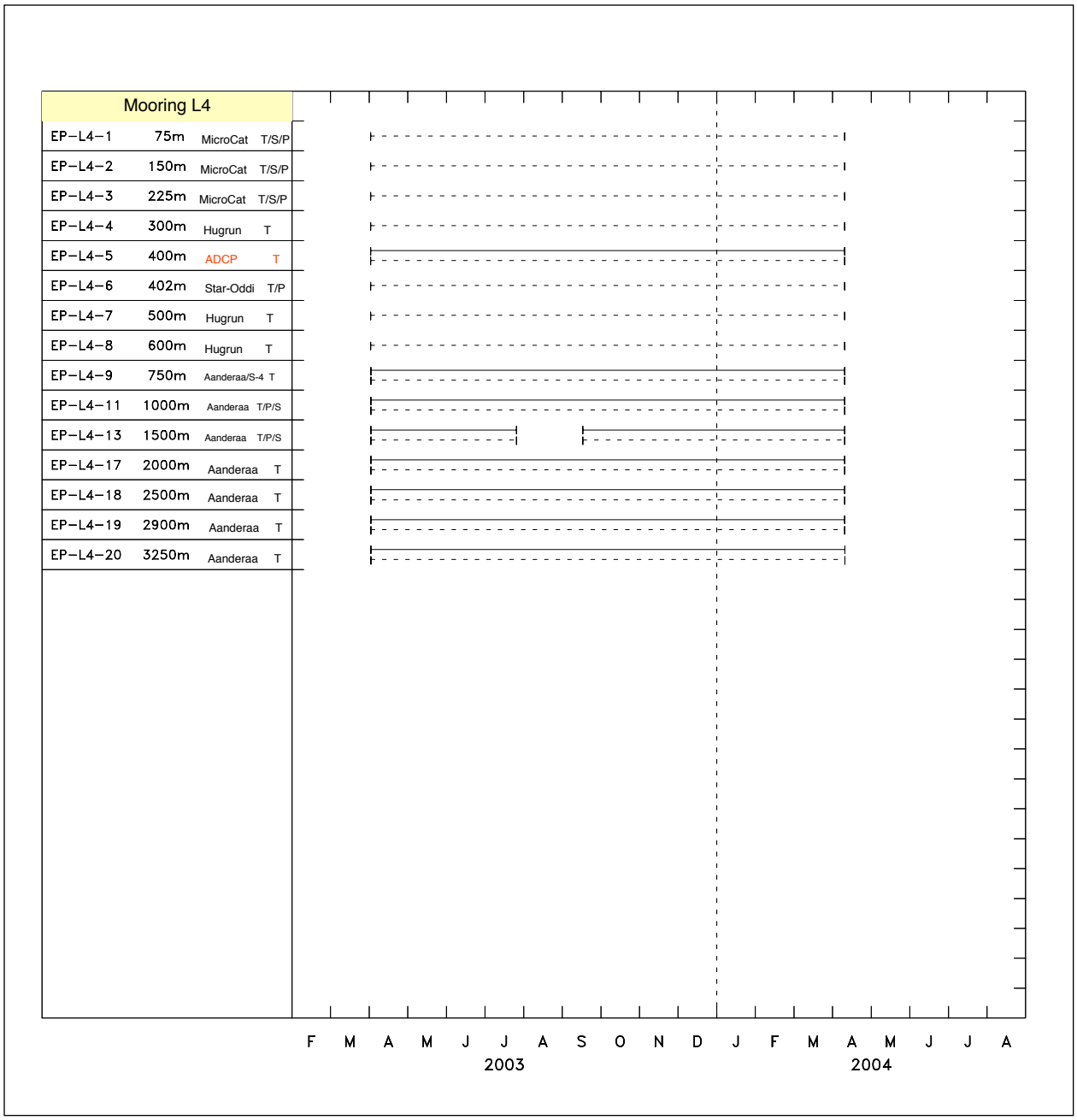

Figure 2.1-2b. Timeline of observations made by fixed position (Eulerian) instruments. On this page is listed the full-depth mooring L4. This mooring had an upward directed 75-kHz ADCP to profile the upper 400 m of the water column. As shown, a number of fixed level current meters as well as T/S/P and T sensors were attached to the mooring. In the above figure, solid lines indicate measurement of a vector quantity; dashed lines a scalar quantity.

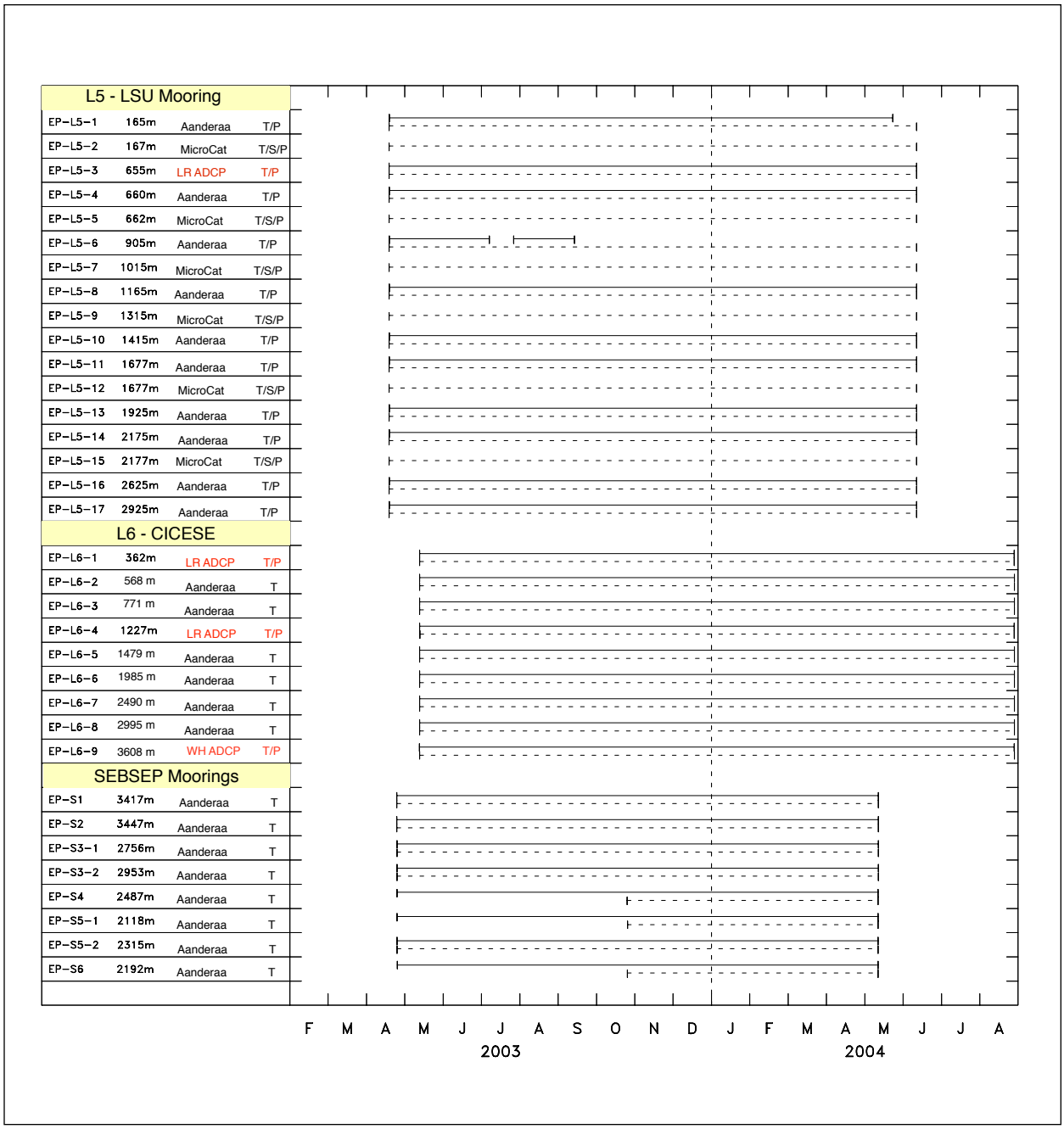

Figure 2.1-2c. Timelines of observations made by fixed position (Eulerian) instruments. On this page are listed full-depth moorings L5 and L6 which were deployed and maintained by LSU and CICESE respectively. Also shown are a series of near bottom moorings (SEBSEP) funded by the Deepstar Consortium (see Figure 2.1-1 for locations). In the above figure, solid lines indicate measurement of a vector quantity; dashed lines a scalar quantity.

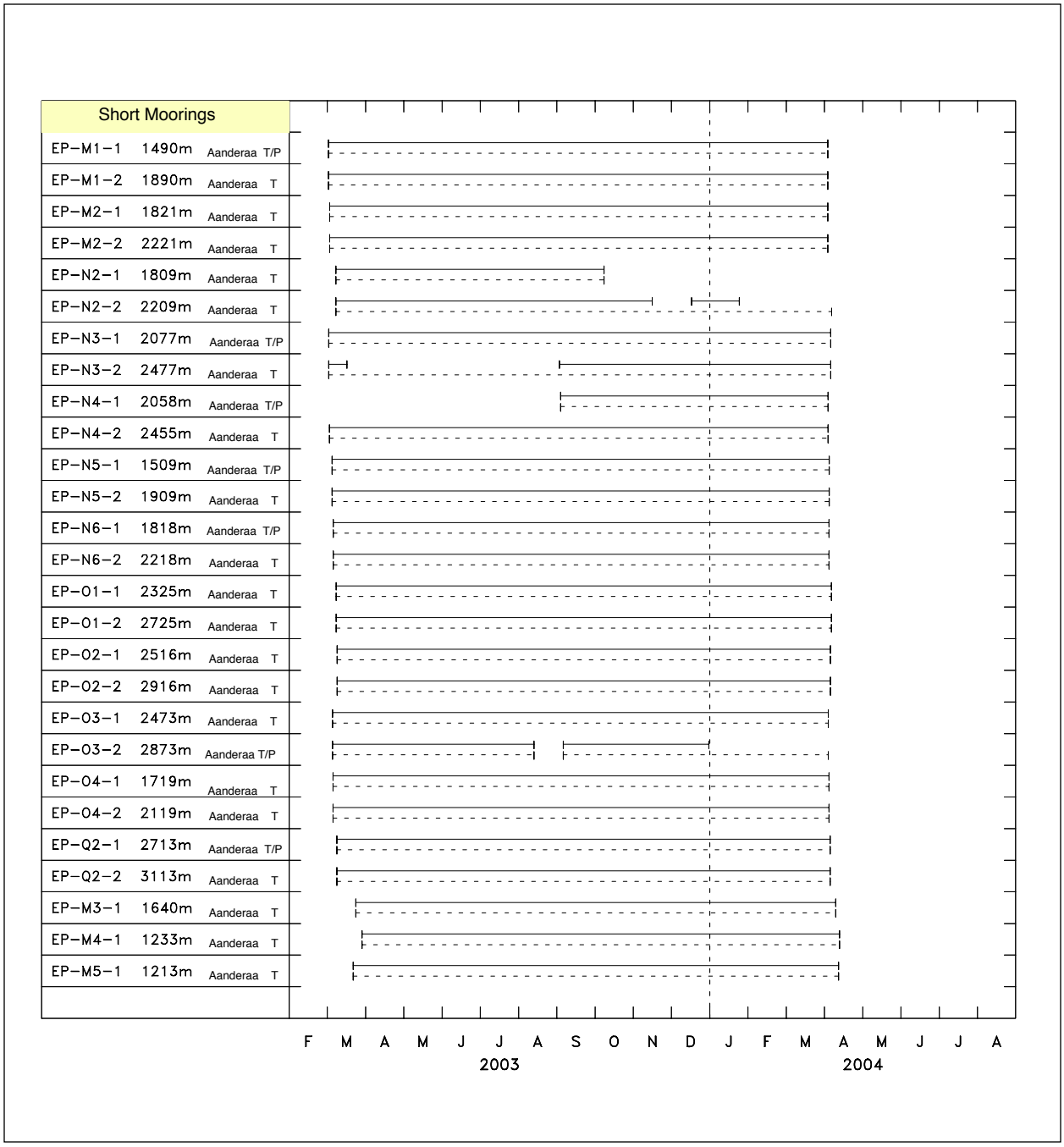

Figure 2.1-2d. Timelines of observations made by fixed position (Eulerian) instruments. On this page are listed Exploratory near-bottom moorings. The first 12 moorings shown had two instruments each, one at 100 m above bottom and one 500 m above bottom. The last three short moorings shown each had one current meter 100 m above bottom. These latter three moorings were added to the array to help resolve spatial scales across the Sigsbee Escarpment when defining reference velocities for PIES-based geostrophic computations.

The observations made for the Exploratory Study were supplemented with measurements made on full-depth moorings deployed by LSU (Mooring L5 in Figure 2.1-1) and CICESE (Mooring L6 in Figure 2.1-1). Both of these measurement activities were all (CICESE) or partially (LSU) funded by the MMS. Additionally, the MMS and the Deepstar Consortium agreed on a data exchange by which current observations made on near-bottom moorings would be available for use in the analysis and interpretation phase of the Exploratory Study. Each of these six (S1-S6 on Figure 2.1-1) moorings had current meters 3 m above the local bottom at locations across the Sigsbee Escarpment on 91°W starting just north of full-depth mooring L4. Two of the mid-slope moorings (S3 and S5) had an additional current meter at 100 m above the bottom. For the present study these are collectively referred to as SEBSEP moorings.

The LSU mooring contained two upward looking ADCPs: a 150 kHz at 150 m depth, and a 75 kHz at 655 m depth. Below the deeper ADCP, Aanderaa current meters were placed at approximately 250 m intervals to a depth of 2175 m. Below this, current meters were placed at separations of 300 to 450 m to a depth of 2925 m in a water depth of 2960 m. The CICESE mooring, deployed in 3620 m of water, consisted of two ADCPs at 362 m and 1227 m depth. Between these two instruments, Aanderaa current meters were placed at 200 to 550 m below 1227 m, Aandera current meters were placed at 500 m and at 1479 m separations to a depth of 2995 m. Also, an upward looking 300 KHz ADCP was placed at 3608 m, or 12 meter above the local bottom.

As shown in Table 2.1-1 and Figure 2.1-2, additional physically pertinent variables were measured at selected locations over the water column. These observations provided information on water mass characteristics (T/S) and mooring dynamics (P). These data were also in conjunction with and as separate validation checks of PIES data processing as described in Section 2.4.

Table 2.1-1

Moored instrument measurement levels for the Exploratory Study
(initial deployment with nominal instrument depths).

Mooring	Water Depth (M)	Instrument Depth (M) (MAB)	Instrument Type (SN)
L1	1512	75	T/S/P (0057)
		150	T/S/P (1719) (2702)
		225	T/S/P (2693) (2703)
		300	TEMP (C919)
		400	ADCP (75 KHz) – up (924)
		500	TEMP (C937)
		600	TEMP (C929)
		750	S4 (07801745)
		1000 (500)	RCM-7/8(6922) (7528)
		1400 (100)	RCM-7 (9948)/MK2 (457)

Table 2.1-1. Moored instrument measurement levels for the Exploratory Study (initial deployment with nominal instrument depths)(continued).

Mooring	Water Depth (M)	Instrument Depth (M) (MAB)	Instrument Type (SN)
L2	1762	75	T/S/P (0059)
		150	T/S/P (1720) (2701)
		225	T/S/P (2694)
		300	TEMP (C933)
		400	ADCP (75 KHz) – up (1495)
		402	T/P (4660)
		500	TEMP (C940)
		600	TEMP (C959)
		750	S4 (08161753)
		751	T/P (Deployment 2 only) (4663)
		1000	RCM-8 (7582) (12788)
		1400 (350)	RCM-7 (9949)/MK2 (453)
		1650 (100)	RCM-8 (12803)
L3	2998	75	T/S/P (2695)
		150	T/S/P (2696)
		225	T/S/P (2697)
		300	TEMP (C939)
		400	ADCP (75 KHz) – up (1607)
		402	T/P (4662)
		500	TEMP (C960)
		600	TEMP (C947)
		750	RCM-7 (10350)/S4 (08161757)
		1000	RCM-7 (6892) (9525)
		1500	RCM-8 (7528) (12789)
		2000	RCM-8 (12808)
		2500 (500)	RCM-8 (12809)
		2900 (100)	RCM-8 (12810)
L4	3350	75	T/S/P (2698)
		150	T/S/P (2699)
		225	T/S/P (2700)
		300	TEMP (C944)
		400	ADCP (75 KHz) – up (1536)
		402	T/P (4661)
		500	TEMP (C946)
		600	TEMP (C943)
		750	RCM-7 (9524)/S4 (08161755)
		1000	RCM-7 (10881)
		1500	RCM-8 (10533) (9524)
		2000	RCM-8 (12804)

Table 2.1-1. Moored instrument measurement levels for the Exploratory Study (initial deployment with nominal instrument depths)(continued).

Mooring	Water Depth (M)	Instrument Depth (M) (MAB)	Instrument Type (SN)
L4	3350	2500	RCM-8 (12805)
		2900 (450)	RCM-8 (12806)
		3250 (100)	RCM-8 (12807)
M1	1990	1490 (500)	RCM-7 (12391)
		1890 (100)	RCM-7 (12415)
M2	2321	1821 (500)	RCM-7 (12403)
		2221 (100)	RCM-8 (12480)
M3	1740	1640 (100)	RCM-8 (7356)
M4	1333	1233 (100)	RCM-8 (7357)
M5	1313	1213 (100)	RCM-8 (9268)
N2	2309	1809 (500)	RCM-7 (12134) (10621)
		2209 (100)	RCM-8 (5721)
N3	2577	2077 (500)	RCM-8 (12477)
		2477 (100)	RCM-8 (12110)
N4	2558	2058 (500)	RCM-8 (12475) (12473)
	2555	2455 (100)	RCM-8 (6238)
N5	2009	1509 (500)	RCM-7 (12398)
		1909 (100)	RCM-7 (12429)
N6	2318	1818 (500)	RCM-7 (12278)
		2218 (100)	RCM-8 (12050)
O1	2825	2325 (500)	RCM-8 (11574)
		2725 (100)	RCM-8 (11258)
O2	3016	2516 (500)	RCM-8 (11263)
		2916 (100)	RCM-8 (11257)
O3	2973	2473 (500)	RCM-8 (12049)
		2873 (100)	RCM-8 (11492) (11512)
O4	2219	1719 (500)	RCM-7 (12414)
		2119 (100)	RCM-8 (11577)
Q2	3213	2713 (500)	RCM-8 (12474)
		3113 (100)	RCM-8 (12111)

2.2 LaGrangian Measurements

2.2.1 RAFOS Float Methodology

RAFOS floats (Rossby et al., 1986) are neutrally buoyant glass-tube floats that can be ballasted in the laboratory to drift with the currents below the surface at a user-selected pressure (roughly, depth) or density for extended periods. The floats are equipped with temperature and pressure sensors and with an acoustic hydrophone that listens to the arrival times of acoustic signals sent

from sound sources (below, and Appendix E) deployed in the ocean. Floats were programmed to record acoustic travel time and the other data every eight hours. At the end of the deployment (one year for the initial 30 floats) the floats dropped a ballast weight, surfaced, and transmitted all their accumulated data to shore via satellite (Service Argos). Since our focus was on deep (below 1000 m) currents, all floats were ballasted to follow pressure as opposed to density surfaces.

2.2.2 PALFOS Float Methodology

PALFOS floats are PALACE- or APEX-type profiling floats (Davis et al., 2001) with the added capability to be tracked acoustically in much the same manner as RAFOS floats. The six PALFOS floats in this experiment were ballasted to drift at a "rest depth" of 1000 m between profiles. Every ten days these floats were programmed to surface and transmit the acoustic tracking data (arrival times of acoustic signals from the sources) to shore via Service Argos. When the floats surfaced they would also obtain a CTD (conductivity/temperature/depth) profile using a SeaBird CTD sensor. These data would also be transmitted to shore via Argos and would allow the determination of important hydrographic quantities, such as potential density. When on the surface (typically a float would spend about 10 hours on the surface), float drifts could be tracked via the Argos system. The trajectories that will be presented in Section 3 are combined acoustic and satellite tracking (except for PALFOS float pfl, which did not receive travel times).

Of the PALFOS floats, pf3 and pf4 were still active in August 2005 and providing autonomous profiles in the Gulf of Mexico. Profiler pf1 provided 18 profiles (180 days) but did not track acoustically. Profiler pf2 provided 21 profiles (210 days). Profiler pf6 escaped the Gulf of Mexico via the Straits of Florida (by essentially "hopping along the bottom" as it cycled vertically) and ultimately disappeared off eastern Florida, possibly picked up by a local fisherman. Parameters for all PALFOS and RAFOS floats are given in Table 2.2-1. Maps showing deployment sites are shown in Figure 2.2-1.

Table 2.2-1

Parameters for all RAFOS and PALFOS floats.

SN	ARGOS ID	Date & Time of Deployment (GMT)	Deployment Lat (deg min)	Deployment Long (deg min)	Intended Depth (m)	Water Depth (m)	RAFOS/ PALFOS	Obtained/ Total # Messages
456	40228	10/29/03 01:14	26 25.94	90 31.85	1500	2814	RAFOS	215/215
457	40211	04/13/03 02:49	27 37.85	88 59.59	1500	1710	RAFOS	366/366
458	40214	04/14/03 15:00	27 02.86	90 28.93	1500	1780	RAFOS	366/366
459	40213	04/14/03 11:29	27 27.69	90 30.16	1000	1286	RAFOS	366/366
460	40240	04/12/03 22:45	28 15.07	89 00.12	1000	1215	RAFOS	0/366
461	40215	04/14/03 19:01	26 29.75	90 30.01	1500	2745	RAFOS	365/366
462	40216	04/14/03 17:10	26 46.83	90 30.33	1500	2175	RAFOS	366/366
463	40217	04/13/03 18:??	25 45.00	89 00.00	1500	3230	RAFOS	0/366
464	40218	04/14/03 00:30	25 51.01	89 45.01	1500	3240	RAFOS	366/366
465	40219	10/29/03 03:13	26 38.99	90 31.98	1500	2575	RAFOS	215/215
466	40220	04/15/03 04:20	27 06.42	89 44.90	1500	2198	RAFOS	329/366
467	40221	04/13/03 07:35	27 03.61	88 59.06	1500	2295	RAFOS	366/366
468	40222	04/14/03 05:15	26 40.00	89 45.00	1500	2760	RAFOS	366/366
469	40223	10/29/03 04:20	26 46.98	90 32.00	1500	1780	RAFOS	215/215
470	40224	04/15/03 06:54	27 30.17	89 45.15	1000	1290	RAFOS	365/366

Table 2.2-1. Parameters for all RAFOS and PALFOS floats (continued).

SN	ARGOS ID	Date & Time of Deployment (GMT)	Deployment Lat (deg min)	Deployment Long (deg min)	Intended Depth (m)	Water Depth (m)	RAFOS/ PALFOS	Obtained/ Total # Messages
472	40226	04/14/03 21:20	26 06.79	90 30.04	1500	3250	RAFOS	365/366
473	40227	04/15/03 06:05	27 22.58	89 45.17	1500	1795	RAFOS	366/366
474	40210	04/14/03 19:01	26 29.75	90 30.01	2500	2745	RAFOS	366/366
475	40229	04/13/03 07:35	27 03.61	88 59.06	2000	2295	RAFOS	333/366
476	40230	10/29/03 01:14	26 25.94	90 31.85	2500	2814	RAFOS	215/215
477	40231	04/14/03 21:20	26 06.79	90 30.04	3000	3250	RAFOS	366/366
478	40232	04/13/03 18:??	25 45.00	89 00.00	3000	3230	RAFOS	143/366
479	40233	04/14/03 00:30	25 51.01	89 45.01	3000	3200	RAFOS	0/366
480	40234	04/14/03 17:10	26 46.83	90 30.33	2000	2175	RAFOS	366/366
481	40235	04/13/03 11:50	26 35.00	89 00.57	2500	2692	RAFOS	285/366
482	40236	04/14/03 21:20	26 06.79	90 30.04	2000	3250	RAFOS	366/366
483	40237	04/13/03 11:50	26 35.00	89 00.57	2000	2692	RAFOS	366/366
484	40238	10/28/03 23:35	26 13.96	90 31.89	2500	3100	RAFOS	215/215
485	40239	04/14/03 19:01	26 29.75	90 30.01	2000	2745	RAFOS	366/366
486	40212	04/14/03 05:15	26 40.00	89 45.00	2500	2760	RAFOS	366/366
487	40241	04/14/03 00:30	25 51.01	89 45.01	2000	3240	RAFOS	161/366
488	40242	04/14/03 05:15	26 40.00	89 45.00	2000	2760	RAFOS	366/366
489	40243	04/15/03 04:20	27 06.42	89 44.90	2000	2198	RAFOS	357/366
490	40244	04/13/03 18:??	25 45.00	89 00.00	2000	3230	RAFOS	366/366
491	40245	10/28/03 22:23	26 05.04	90 31.94	2500	3250	RAFOS	215/215
pf1	28445	04/13/03 04:34	27 23.12	88 59.83	1000	1900	PALFOS	
pf2	28446	04/13/03 15:45	26 10.58	88 59.83	1000	2950	PALFOS	
pf3	28447	03/14/03 16:54	27 15.10	89 25.54	1000	2200	PALFOS	
pf4	28448	04/14/03 00:30	25 51.01	89 45.01	1000	3200	PALFOS	
pf5	28449	04/14/03 17:10	26 46.83	90 30.33	1000	2175	PALFOS	
pf6	28450	04/14/03 21:20	26 06.79	90 30.04	1000	3250	PALFOS	
On surface ~04/14/04 for the RAFOS floats deployed in April 2003 ~05/30/04 for the ones deployed in October 2003								

Sound sources were deployed at three locations (in the eastern, central and western GOM) to provide navigating triangulation for all floats. These sources provided three float positions per day. In addition, an acoustic monitor or ALS was deployed on a full-depth mooring to track possible changes in the clocks aboard the sound sources. A more detailed discussion of the tracking methodology is given in Appendix E. Unfortunately, two of the sources (SoSo2, SoSo3) failed approximately two months after the start of the experiment in April 2003 and were replaced in October 2003 by sources kindly loaned to the project by the Institut fur Meereskunde in Germany (Drs. Walter Zenk and Fritz Schott). These gaps in the tracking are indicated in subsequent figures by the straight lines (Figures 3.2-2b through 3.2-2g). These sound sources were part of a production run by Webb Engineering that had a high failure rate. The only source from the larger group that was recovered indicated a leak in the pressure switch that "shorted" the electronics.

Parameters for source deployments are given in Table 2.2-2.

Table 2.2-2
Parameters for source deployments.

ID	Latitude	Longitude	Date & Time	Comments
SoSo1	At 27° 00.0054' N	93° 41.0144' W	03/13/03 02:42 (GMT)	
SoSo2	At 25° 46.0007' N	90° 44.0481' W	03/14/03 02:51 (GMT)	Failed 06/10/03
SoSo2bis	At 25° 46.020 N'	90° 56.280' W	10/28/03 16:25 (GMT)	Recovered 05/26/04
SoSo3	At 28° 12.9947' N	89° 03.9514' W	03/15/03 02:43 (GMT)	Failed 05/01/03
SoSo3bis	At 28° 12.840' N	89° 03.940' W	10/27/03 13:55 (GMT)	Recovered 05/25/04

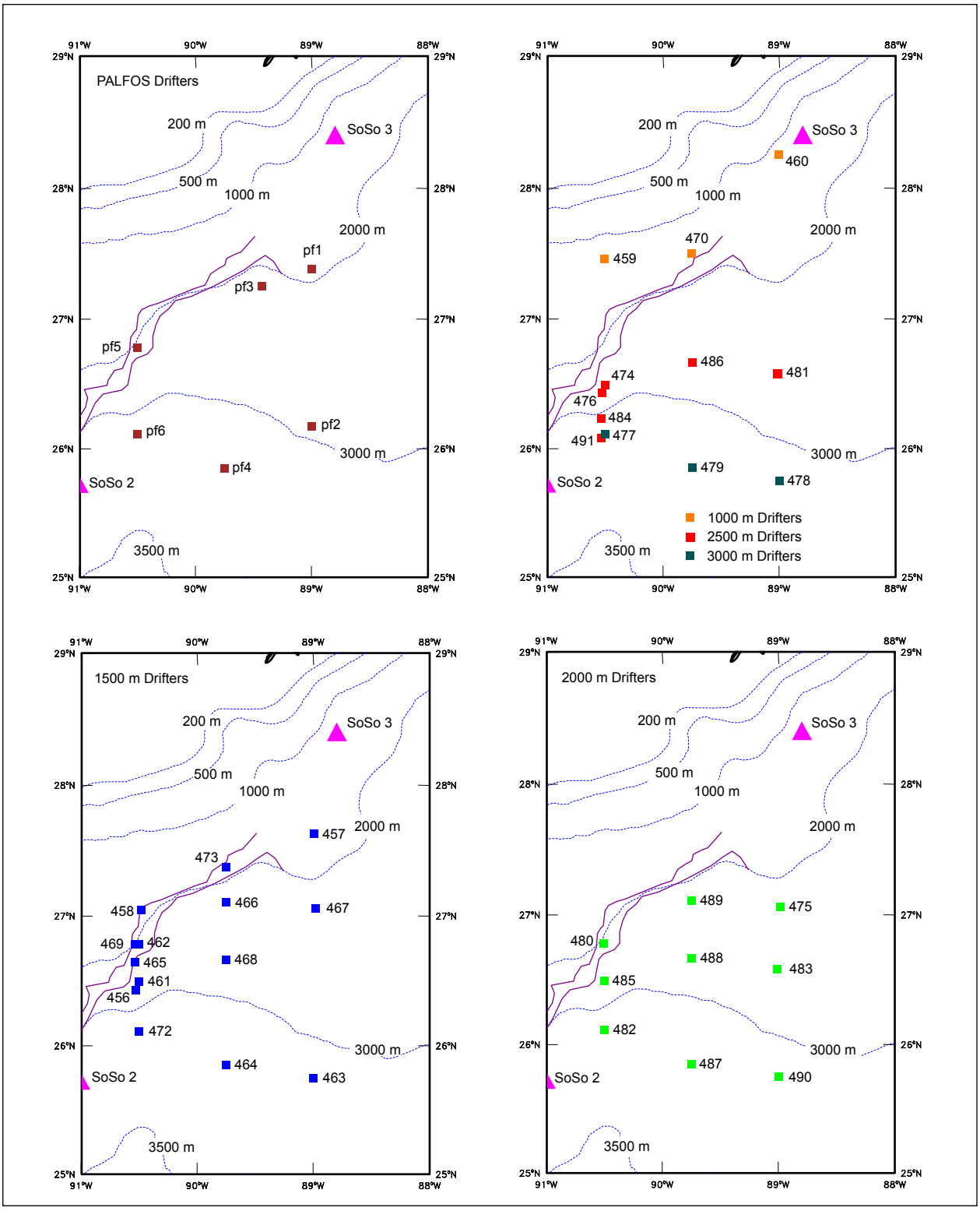

Figure 2.2-1. Deployment sites of PALFOS and RAFOS drifters relative to bathymetry and the Sigsbee Escarpment. Upper left panel shows PALFOS deployment sites. Upper right panel shows deployment sites of RAFOS drifters ballasted for nominal depths of 1000 m, 2500 m and 3000 m. Lower left shows deployment sites of 1500-m RAFOS floats. Lower right panel shows locations of 2000-m RAFOS deployments.

2.3 PIES

A mesoscale-resolving array of twenty-seven inverted echo sounders with pressure gauges (PIES) were deployed in March 2003 and recovered in April 2004 as a key part of the Exploratory Study with the intent to identify key circulation processes in a deep-water region in the Gulf of Mexico (Figure 2.1-1). The PIES is a bottom-mounted instrument that emits 12 kHz sound pulses and measures the round trip travel times or τ (tau) of these acoustic pulses from sea floor to sea surface and back. The PIES, equipped with a pressure gauge, also measures bottom pressure. A detailed description of the instrument and initial processing may be found in Hamilton et al. (2003), with key steps being discussed in this section. Data return from the Exploratory PIES was excellent (Figures 2.3-1 and 2.3-2); full deployment records are available from all PIES with three exceptions. PIES 11 was determined 'lost' after it failed to respond to interrogation during the mid-experiment mooring turnaround in September 2003. This instrument was replaced at that time. PIES 27 did not return useful round-trip travel times. We suspect that PIES 27 was placed beneath tall mooring L4 in such a way that the acoustic pulses reflected off the mooring rather than the sea surface. PIES 17 has no round-trip travel time measurements after September 28, 2003 when the transducer failed. Time series of travel time were filtered with a 72-hour, 4^{th}-order Butterworth filter and subsampled at 6-hour intervals.

The broad extent of the array, nominally 92°W to 88°W, 26°N to 28°N enabled a quantitative mapping of the regional circulation. Round-trip acoustic travel time measured by the inverted echo sounder, allowed estimates of vertical profiles of temperature, salinity, and density, utilizing empirical relationships established from historical hydrography. Pressure was leveled via geostrophy using mean current measurements. Deep pressure records combined with estimated horizontal density gradients yielded referenced geostrophic velocities. With this array we produced 4-D maps (x,y,z,t) of temperature, salinity, density, and velocity. Figure 2.3-3 illustrates the various views of current and temperature structure provided by the PIES and deep current meter mooring array for August 31, 2003.

2.3.1 Gravest Empirical Mode Method

For this experiment PIES measurements of total travel time of the acoustic signal (τ) were converted into profiles of temperature, salinity, and specific volume anomaly through the use of a look-up table. A relationship has been established between a τ index and vertical profiles of temperature, salinity, and specific volume anomaly using historical hydrography. This is the so-called Gravest Empirical Mode (GEM) representation (e.g., Meinen and Watts, 2000). The procedure consists of two branches. First the empirical relationship is established. Second the measured τ is converted to the τ index of the look-up table.

2.3.1.1 Determine τ Index

Round trip travel time between the 150 and 1000 dbar surfaces, τ(150-1000) was used as the τ index. The 150-dbar upper limit of the τ integration avoids the influence of the seasonal cycle, particularly of temperature. Further refinements discussed below detail a seasonal correction. The 1000-dbar lower limit of the τ integration balances two needs: extend the integration below the thermocline and retain as many of the acquired historical hydrocasts as possible.

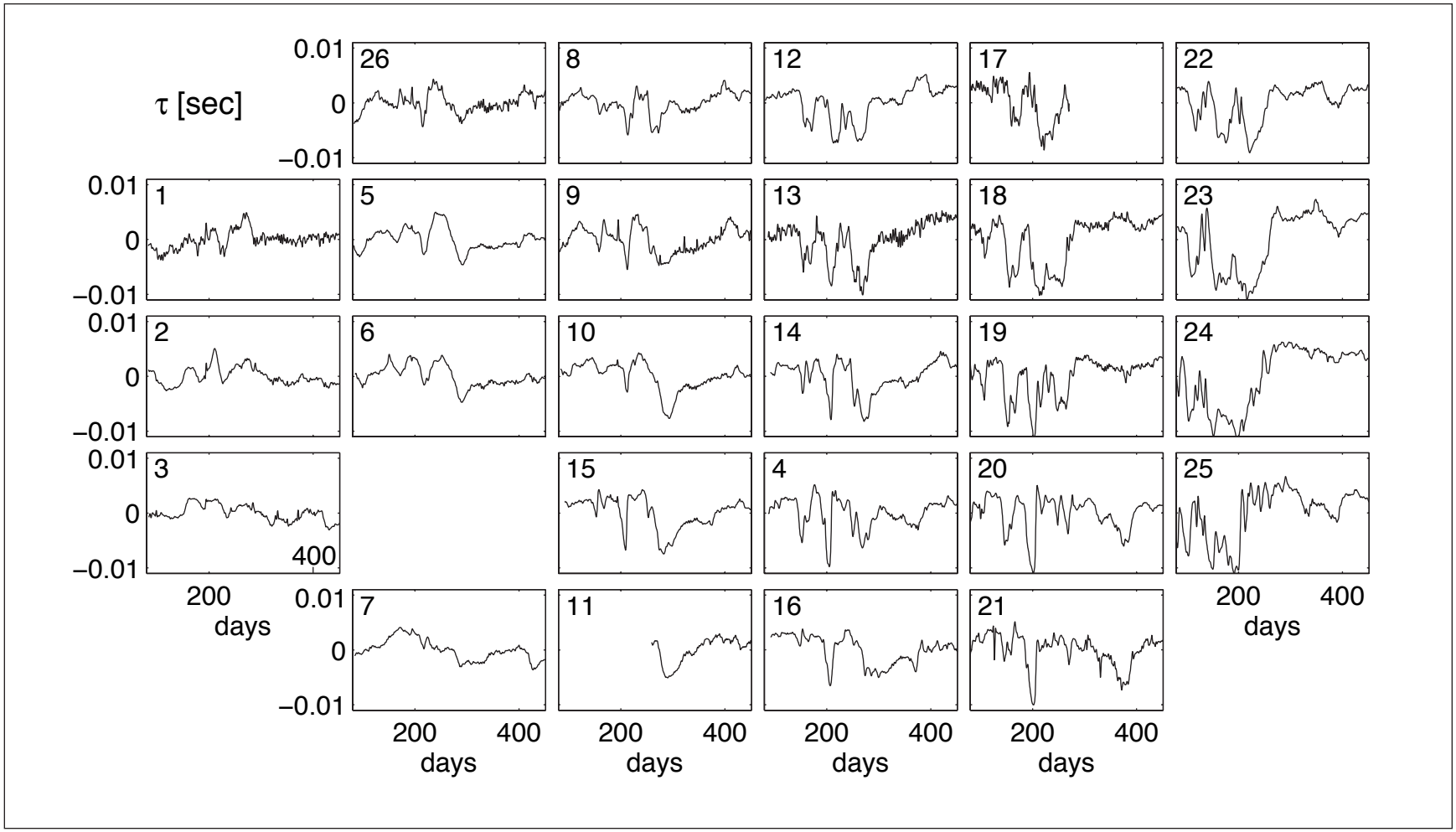

Figure 2.3-1. Time series of τ anomaly in seconds plotted according to approximate geographic location. Instrument number is noted in the upper left corner of each subplot.

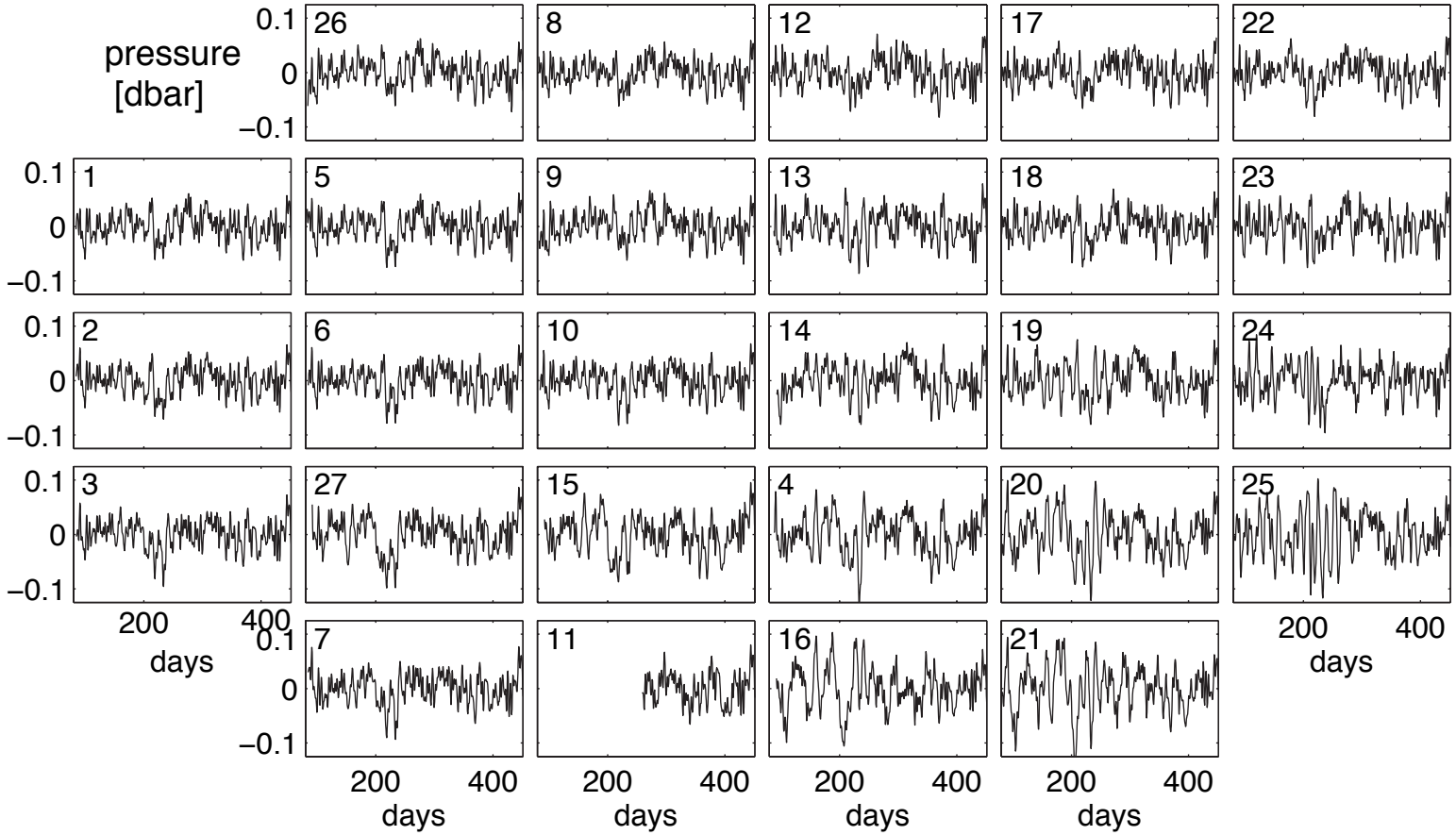

Figure 2.3-2. Time series of bottom pressure anomaly in dbar plotted according to approximate geographic location. Instrument number noted in the upper left corner of each subplot.

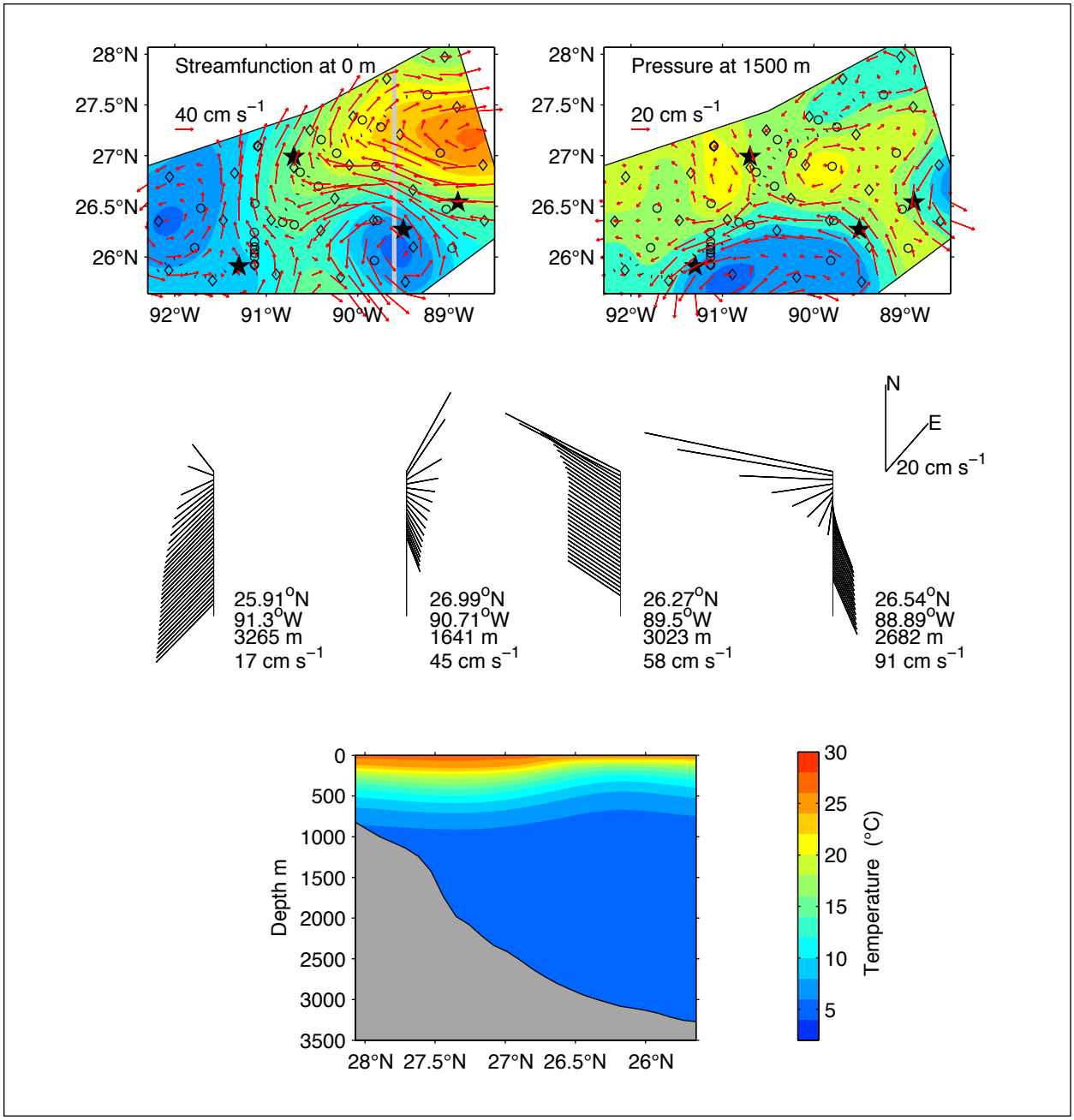

Figure 2.3-3. Several views of current and temperature structure in the region for August 31, 2003 provided by the PIES and deep current measurements. Top panels: Streamfunction at the sea surface (left) and pressure at 1500 m (right) in plan view. Contour intervals are 5 km m s^{-1} and 0.02 dbar, respectively. Anticyclonic circulations are shown by reddish hues; cyclonic circulations by bluish hues. Currents vectors plotted at 20 km spacing. PIES sites denoted by the diamonds; current meter moorings indicated by the circles. A dotted line marks the center of the Sigsbee escarpment. Middle panels: Vector profiles of absolute velocity every 100 m from the surface to the bottom at 4 locations indicated by the solid black stars in top panels. Latitude, longitude, bottom depth, and surface speed at each location are noted. Bottom panel: Cross-section of temperature in °C along the gray line in the top left panel.

2.3.1.2 Assemble Regional Hydrographic Data Set

The hydrographic data set derived from historical hydrography was supplemented by CTD hydrocasts taken during field operations and hydrocasts from profiling floats (Figure 2.3-4). Due to the integral nature of τ we used only high vertical resolution CTD hydrocasts. The historical database contains 498 hydrographic stations from the GOM HYDRO Database compiled by TAMU as part of the MMS-funded Deepwater Reanalysis as well as additional stations provided by SAIC. The northwestern GOM is well sampled; hydrocasts represent about 20 years of sampling; hydrocasts sample most of the annual cycle except in October and December; the bulk of casts extend to 1000 to 2000-dbar with relatively few casts below 2000 dbar. We also included 242 hydrocasts taken by the Exploratory PALFOS floats. They substantially increased the spatial and temporal sampling. These casts reached maximum pressures of 1000 dbar.

2.3.1.3 Sort Hydrographic Data by τ Index

Hydrocasts were linearly interpolated to a uniform 10-dbar grid and sorted by τ(150-1000) (Figure 2.3-5). In this figure are shown the results for temperature. The same methodology was applied to salinity and specific volume, and their associated GEM fields are in Appendix B. Every 10 dbar, a cubic smoothing spline was fitted to temperature as a function of τ(150-1000) (Figure 2.3-6). Root-mean-square residual, rms, for each curve provides an indication of the departure any individual profile might have from the GEM curve. The rms values are the standard deviation of the error variance where the error is the difference between the GEM based estimates and the cubic spline fitted to the data. The rms values for temperature were small; 0.25°C within the thermocline and decreased with increasing pressure.

The curves show that a functional relationship exists between the integrated variable, τ(150-1000) and vertical profiles of temperature. The two-dimensional GEM fields are shown in Figure 2.3-7. Note that there was little structure in the fields below 1000 dbar and this reflects the more uniform deep-water properties in the GOM.

An example of how the GEM look-up table works is illustrated in Figure 2.3-8. PE04-12.012 was a hydrocast taken near PIES 4 on the telemetery/mooring turnaround cruise. τ(150-1000) calculated from the profile is plotted as the vertical line in the GEM field. We ‘look up’ the temperature and salinity profiles (blue lines) given the calculated τ(150-1000). GEM-determined profiles agree well with the measured profiles. Note that for this illustration the GEM fields did not include cast PE04-12.012.

2.3.1.4 Seasonal Correction

Finally, the upper 150 dbar of the temperature GEM field (Figures 2.3-9 and 2.3-10) was corrected for seasonal affects. The procedure, which utilized all available data, is as follows. Fit a cubic spline under tension every 10 dbar from the surface to 150 dbar. Determine the residual from the cubic spline curve. Sort residuals by time of year and create a smoothed empirical relationship for the residual as a function of time of year. This becomes the 'correction' to the profile determined by the GEM field. No seasonal correction has been applied to salinity because

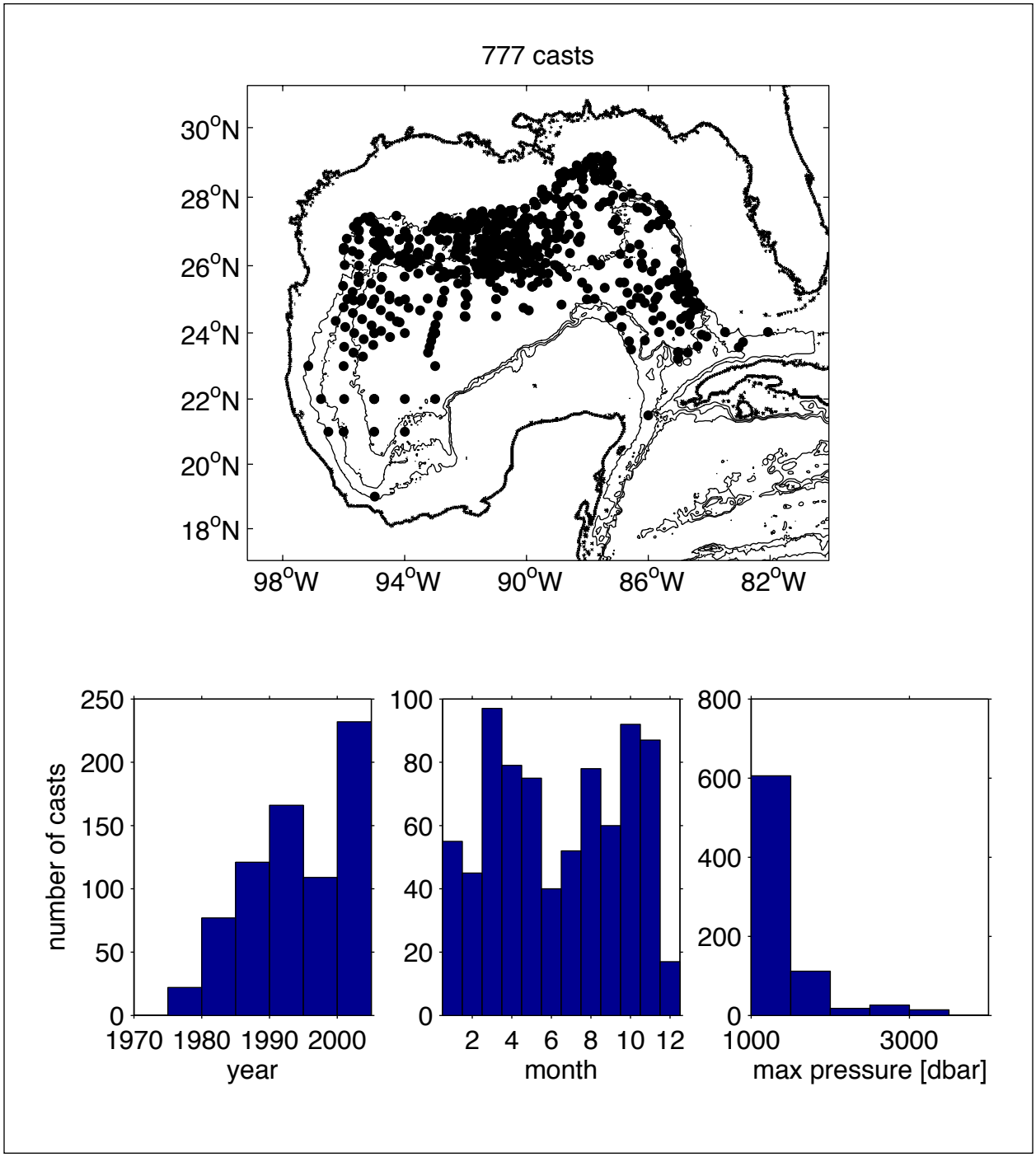

Figure 2.3-4. Spatial and temporal distribution of hydrocasts used to construct the Gravest Empirical Mode. Data provided by the Gulf of Mexico HYDRO Database compiled by TAMU as part of the MMS-funded Deepwater Reanalysis and additional stations provided by SAIC, hydrocasts taken during the experiment, and profiling float hydrocasts. Top panel: Spatial distribution of the hydrocasts with bathymetry contoured every 1000 m. Bottom panels: Histograms of the maximum hydrocast pressure (bottom right), year of hydrocast (left), and month of hydrocast (middle).

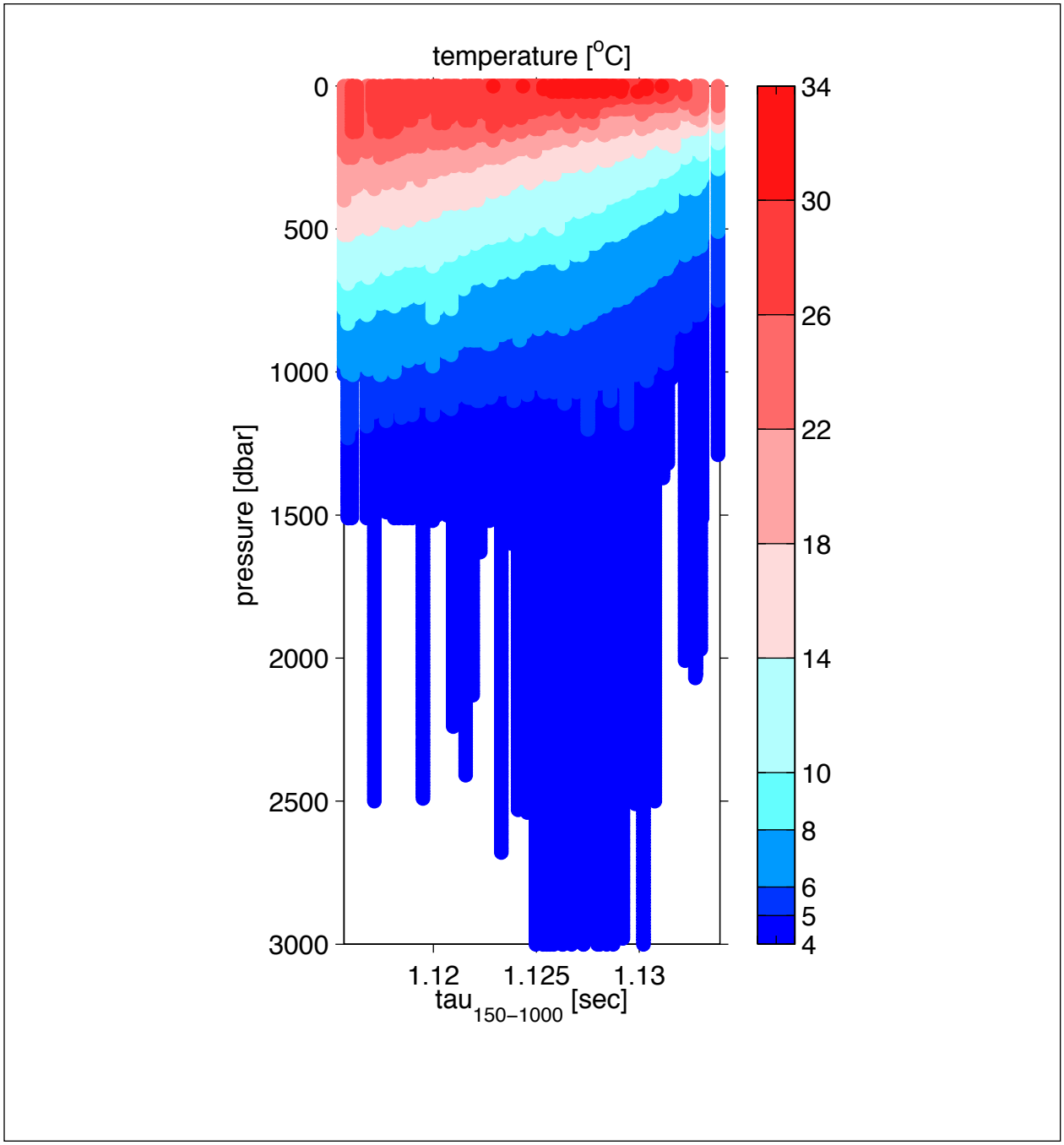

Figure 2.3-5. Temperature profiles interpolated every 10 dbar and sorted by τ(150-1000).

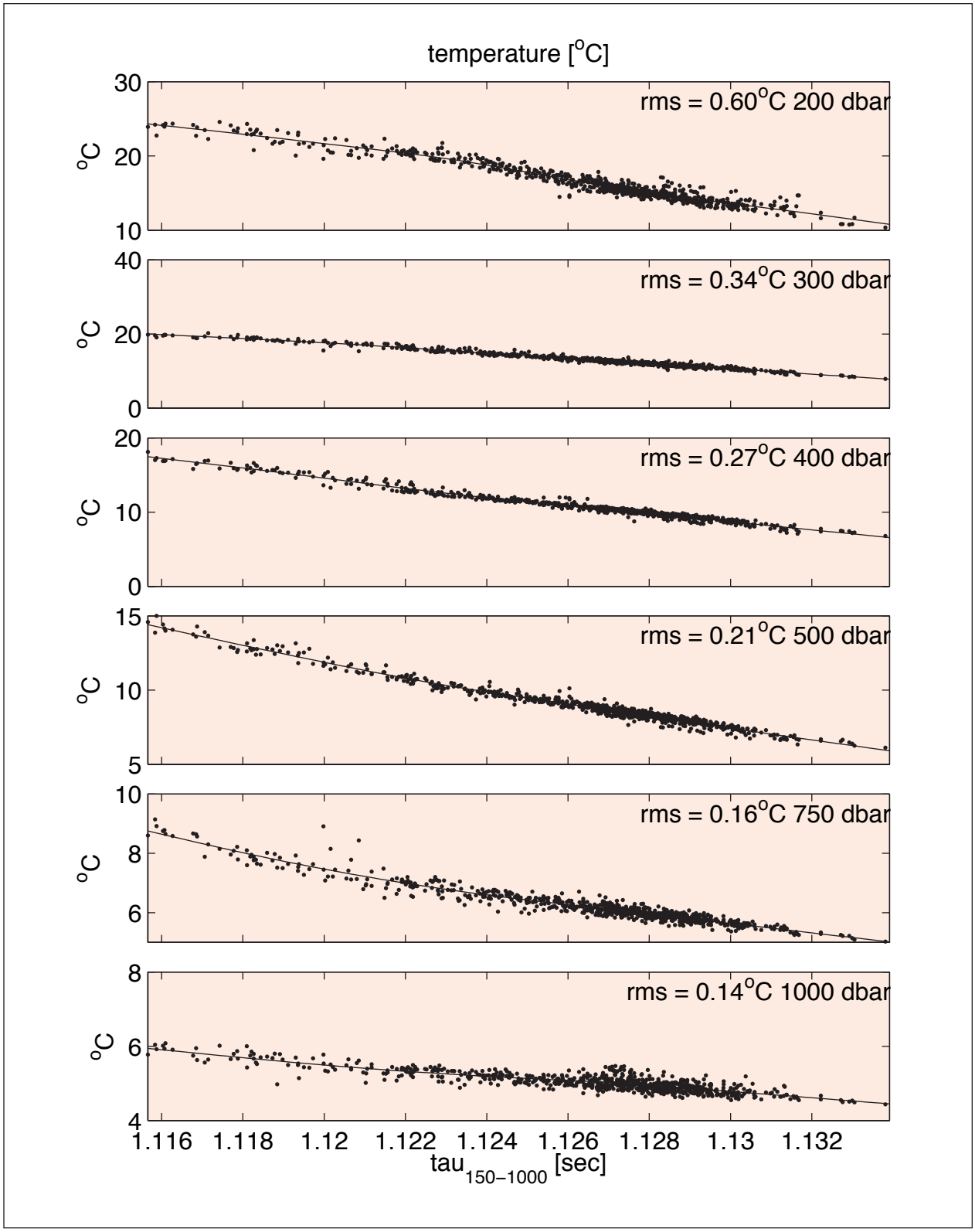

Figure 2.3-6. Scatter plots of temperature versus τ (150 - 1000) for six representative pressure levels. At each pressure, the temperature versus τ (150 - 1000) data were fitted by a cubic smoothing spline (solid line).

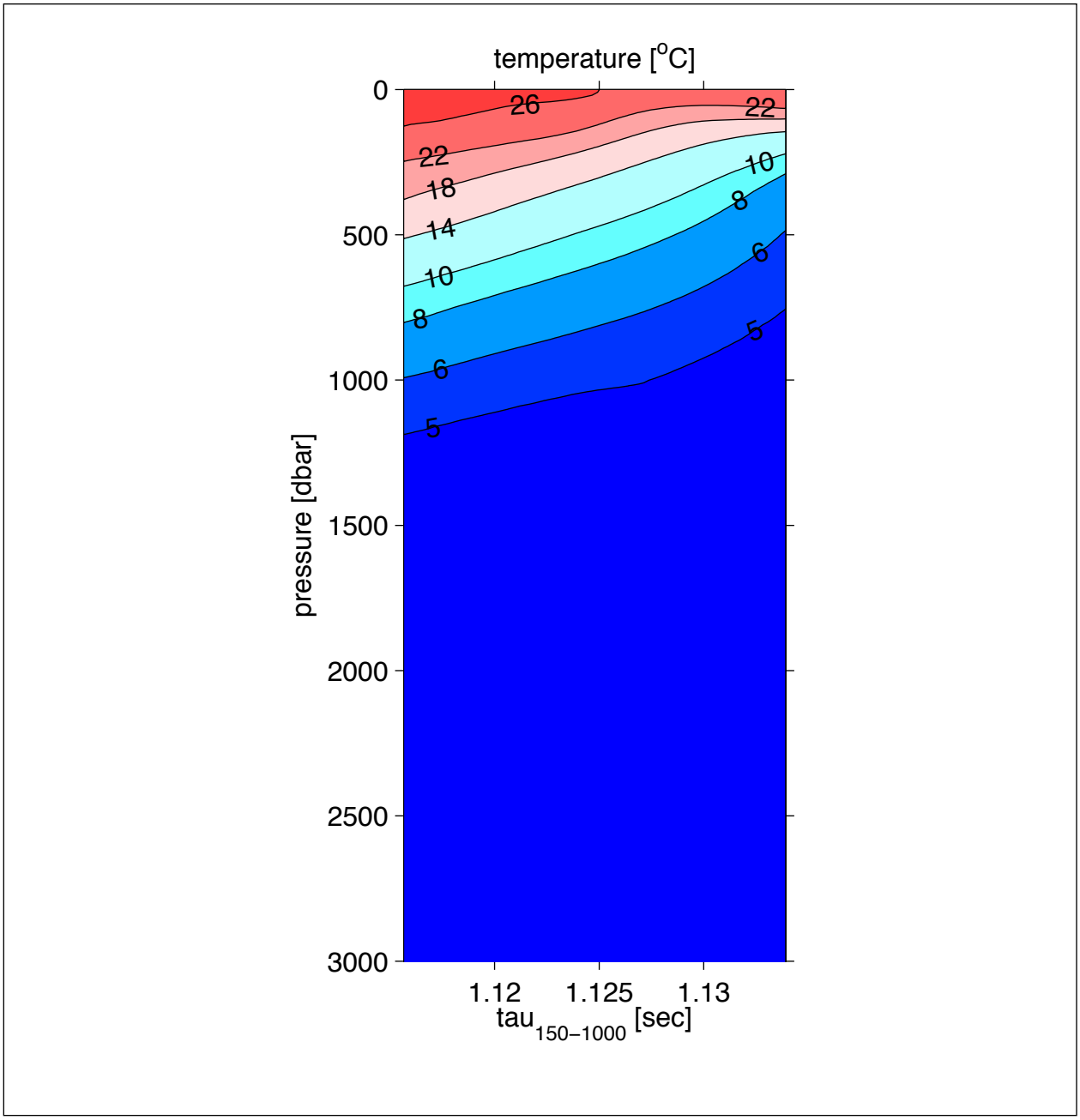

Figure 2.3-7. Contour plot of the cubic smoothing spline fits for the GEM temperature field.

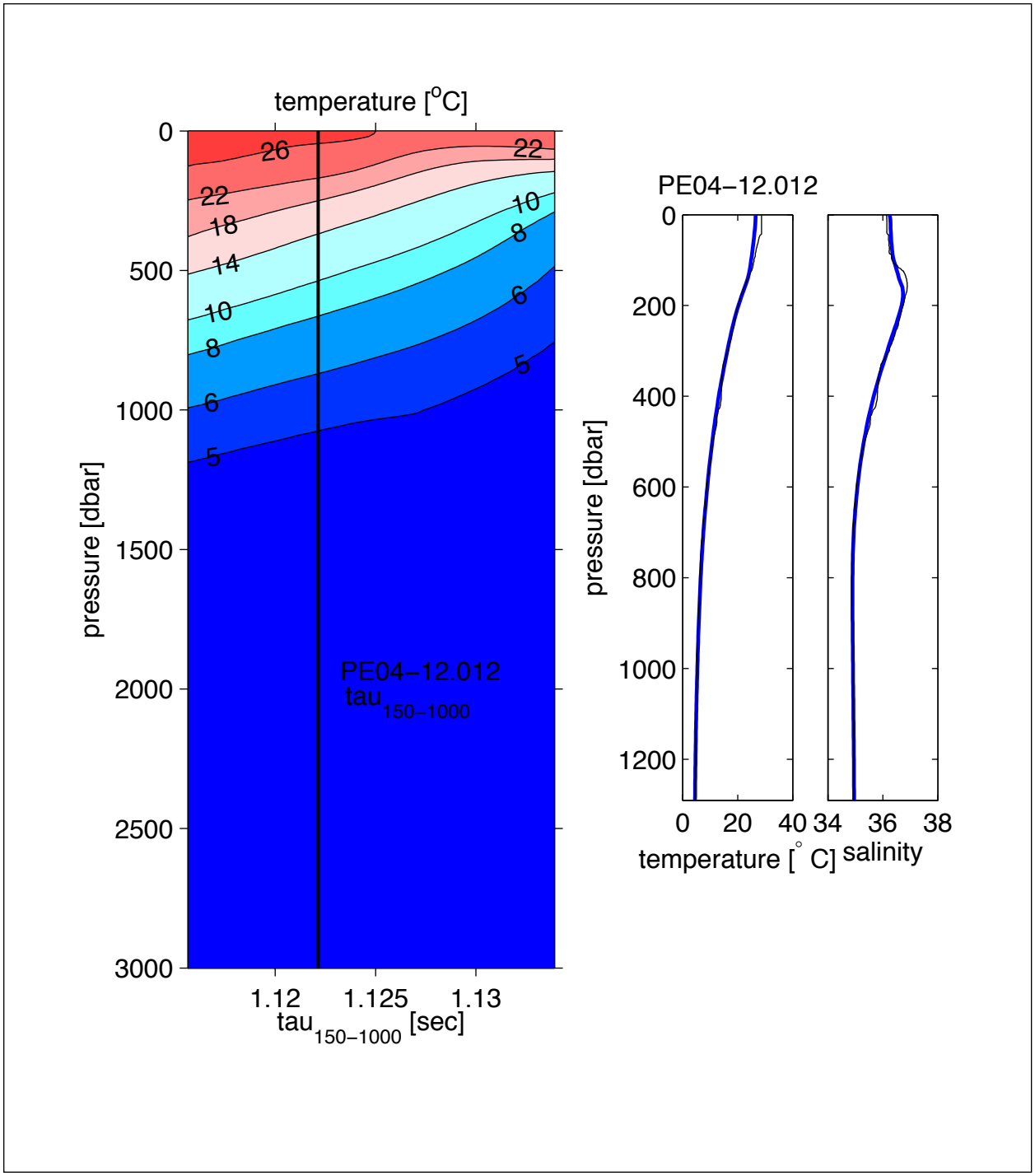

Figure 2.3-8. GEM-determined temperature and salinity profiles agree well with measured profiles. τ(150-1000) determined from CTD PE04-12.012, a hydrocast taken near PIES 4 on the telemetery/mooring turnaround cruise, is plotted as a vertical line in the temperature GEM field (left panel). Middle and right panels show the temperature and salinity profiles from the hydrocast (black). We 'look up' the temperature and salinity profiles given the calculated τ(150-1000) and produced estimates shown with the blue line.

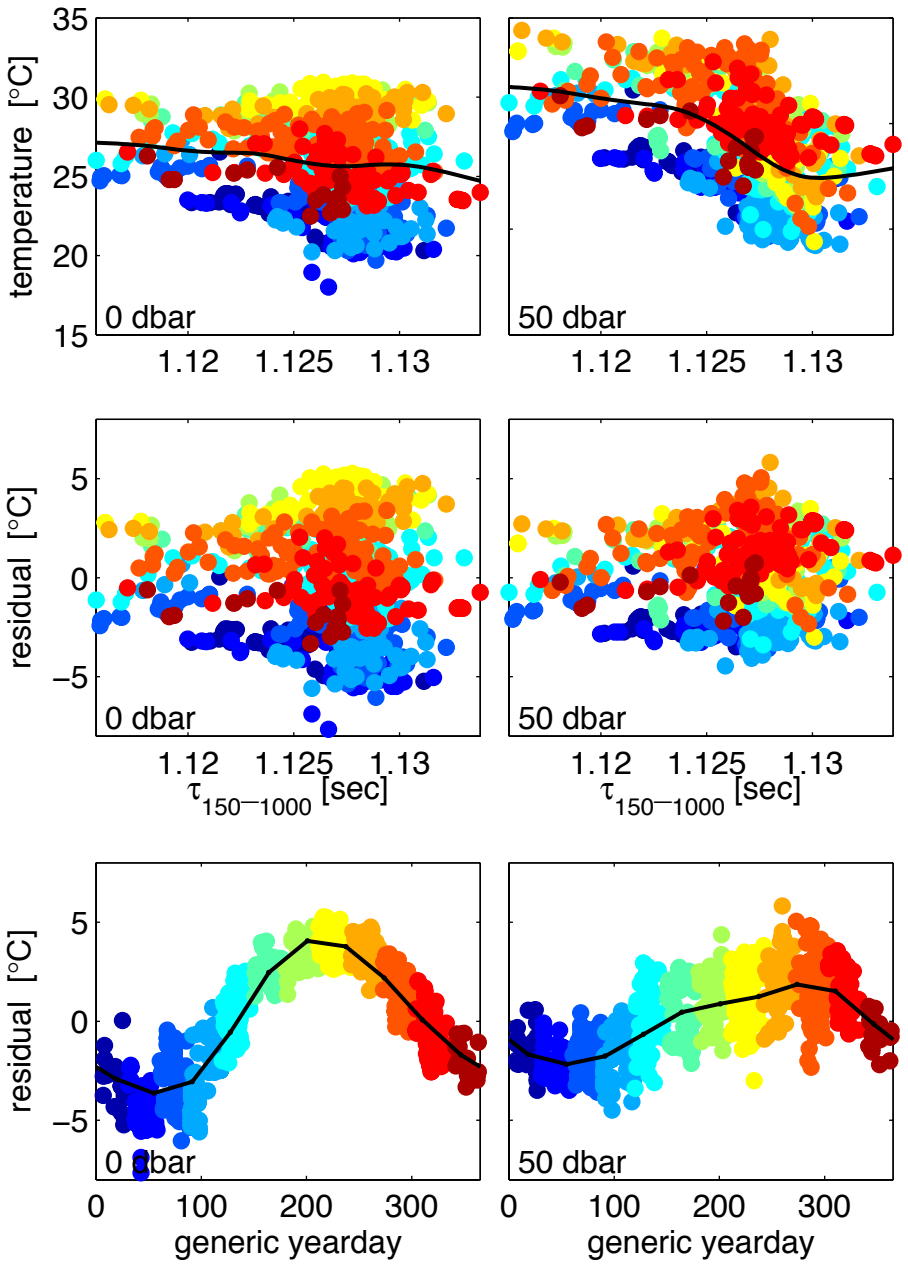

Figure 2.3-9. Upper panels: Scatter plots of temperature versus τ(150-1000) for surface (left) and 50 dbar (right) with the cubic spline fit shown as a solid dark line. All samples in all panels are color coded by generic yearday transitioning from blue in January to red in December. Middle panels show the residual from the cubic spline fit. Lower panels: A clear seasonal signal in temperature emerges when the residual is sorted by time of year.

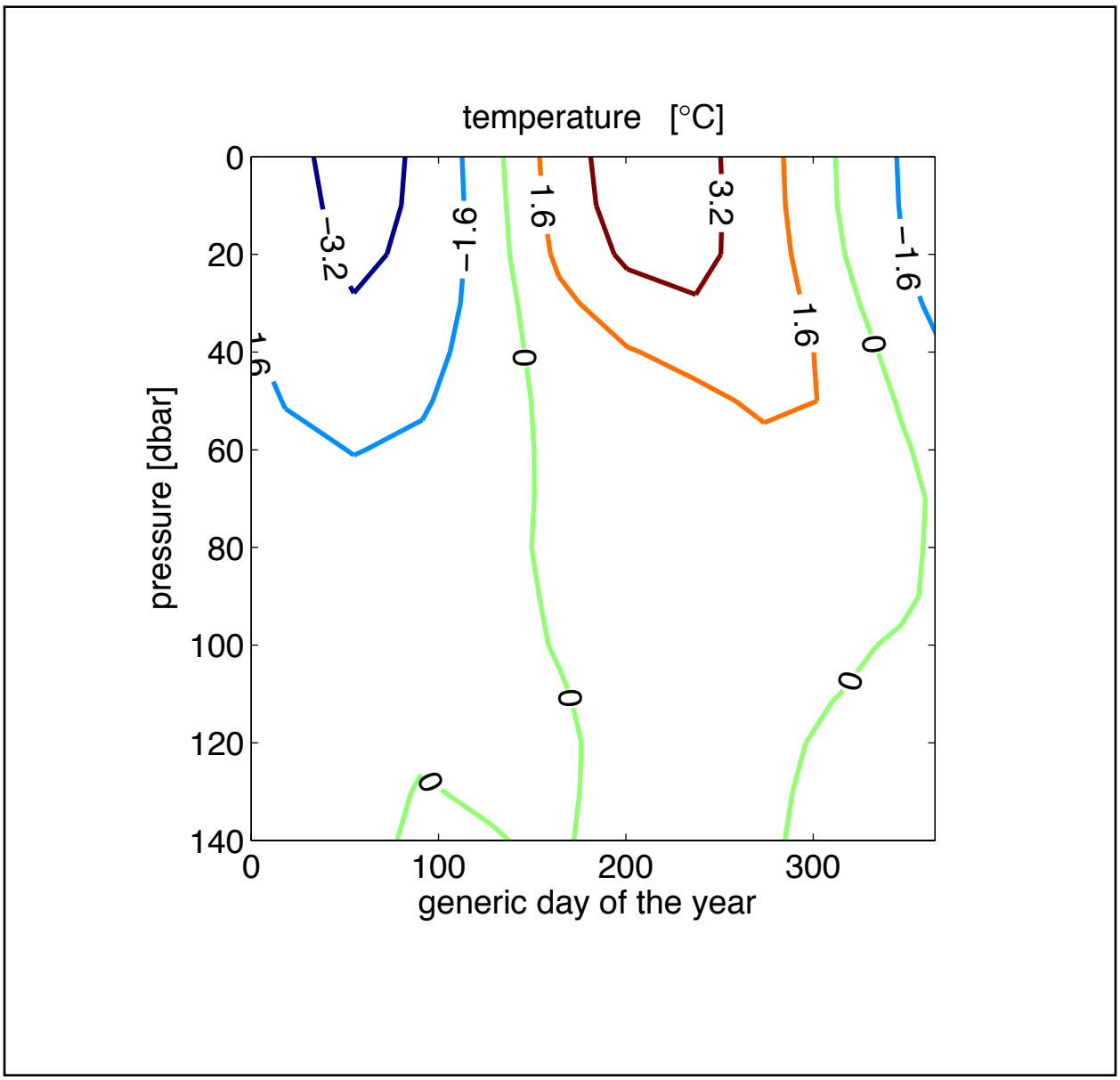

Figure 2.3-10. Seasonal temperature correction/amplitude contoured as function of day of year and pressure. The amplitude of the temperature seasonal correction is about 3°C at the surface and decays to less than 0.5°C by 90 dbar.

variability in the surface layer does not appear to have been seasonal. The amplitude of the temperature seasonal correction was about 3°C at the surface and decreased to less than 0.5°C by 90 dbar.

2.3.1.5 Conversion of Measured τ to τ (150-1000)

To use the GEM fields with the PIES τ measurements, measured τ was converted to τ(150-1000). We took advantage of the fact that τ at any deep pressure is linearly related to τ at any other deep pressure, $\tau(150\text{-}1000) = A \cdot \tau_{p1} + B$. Historical hydrography establishes the slope of this relationship and hydrocasts taken during the telemetery/mooring turnaround cruise determine B for each time series. The mean pressure of each instrument was determined from the recorded average pressure adjusted for the vertical offset between the pressure sensor and the transducer (0.6 dbar) and mean atmospheric pressure (10.16 dbar). The final τ(150-1000) records are shown in Figure 2.3-11.

Before measured τ records were converted to τ(150-1000), a seasonal τ signal was subtracted from the τ records. This seasonal signal was determined from the historical hydrography in a manner similar to the seasonal temperature adjustment. Here we considered the influence of the seasonal cycle in τ between the surface and 150 dbar because the hydrography showed that historically there was little seasonal signal below 150 dbar. The scatter plot of τ(0-150) versus τ(150-1000) is largely due to the seasonal cycle and we determined the amplitude of the residual to be 0.3320 milliseconds (Figure 2.3-12). The correction is small, about 2% of the total range in τ(150-1000).

2.3.2 Bottom Pressure

Several bottom-pressure processing details are noteworthy. First, experience indicates that sensor preconditioning greatly reduces pressure drift. Sensors were subjected to pressures near 3000 dbar for 1-2 months in the lab prior to their first deployment. Second, pressure data were detided. Tidal response analysis (Munk and Cartwright, 1966) determined the eight major tidal constituents for each instrument. Tidal amplitudes are generally small. The largest tidal amplitudes are near 15 cm for O_1 and K_1, near 5 cm for P_1, and less than 5 cm for the remaining five constituents. Appendix D details the amplitudes and phases determined for each site. Estimated tides and phases vary smoothly across the array. Finally, pressure drift was removed using techniques found in Watts and Kontoyiannis (1990), an exponential-plus-linear drift curve determined by a least-squares fit was removed from the measurements. The PIES used during the Exploratory Study experienced small drifts. The maximum drift was 0.25 dbar and 19 (12) instruments had drift less than 0.1 (.05) dbar.

Bottom-pressure measurements must be leveled to produce spatially consistent maps since each dedrifted pressure record has an arbitrary constant (level) relative to the other records. 'Leveled bottom pressures' refers to bottom pressures that have been adjusted to the same geopotential surface; mean near-bottom currents and bottom pressures are dynamically constrained to be in geostrophic balance. Watts et al. (2001) provides a detailed description of the leveling procedure. Within the Exploratory instrument array, currents and bottom pressure were measured at a variety of depths. We scaled these records to a common level, 1500 dbar, under the assumption

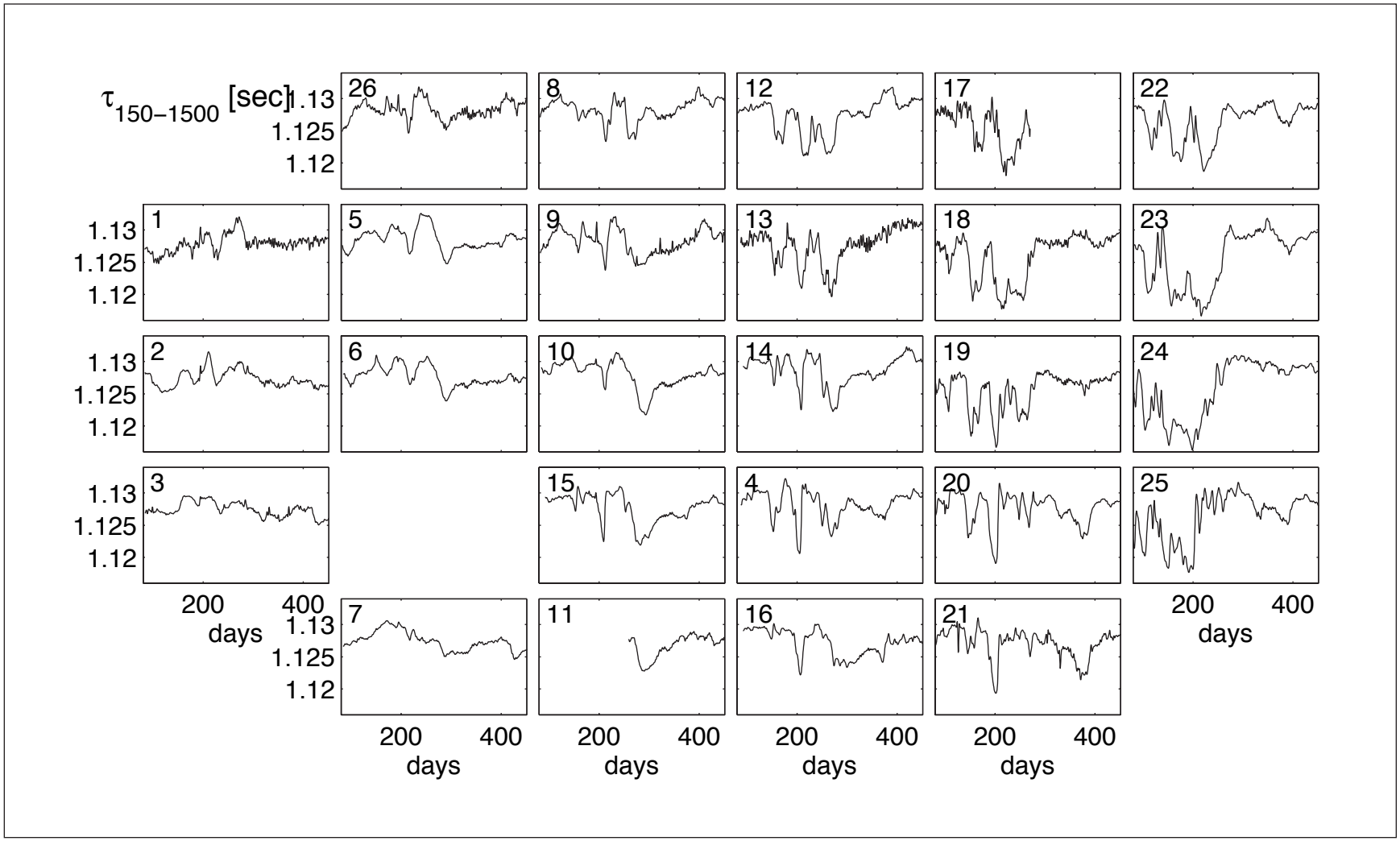

Figure 2.3-11. τ(150-1000) for each time series. The time series are shown in approximate geographic location. Instrument number in the upper left corner of each subplot.

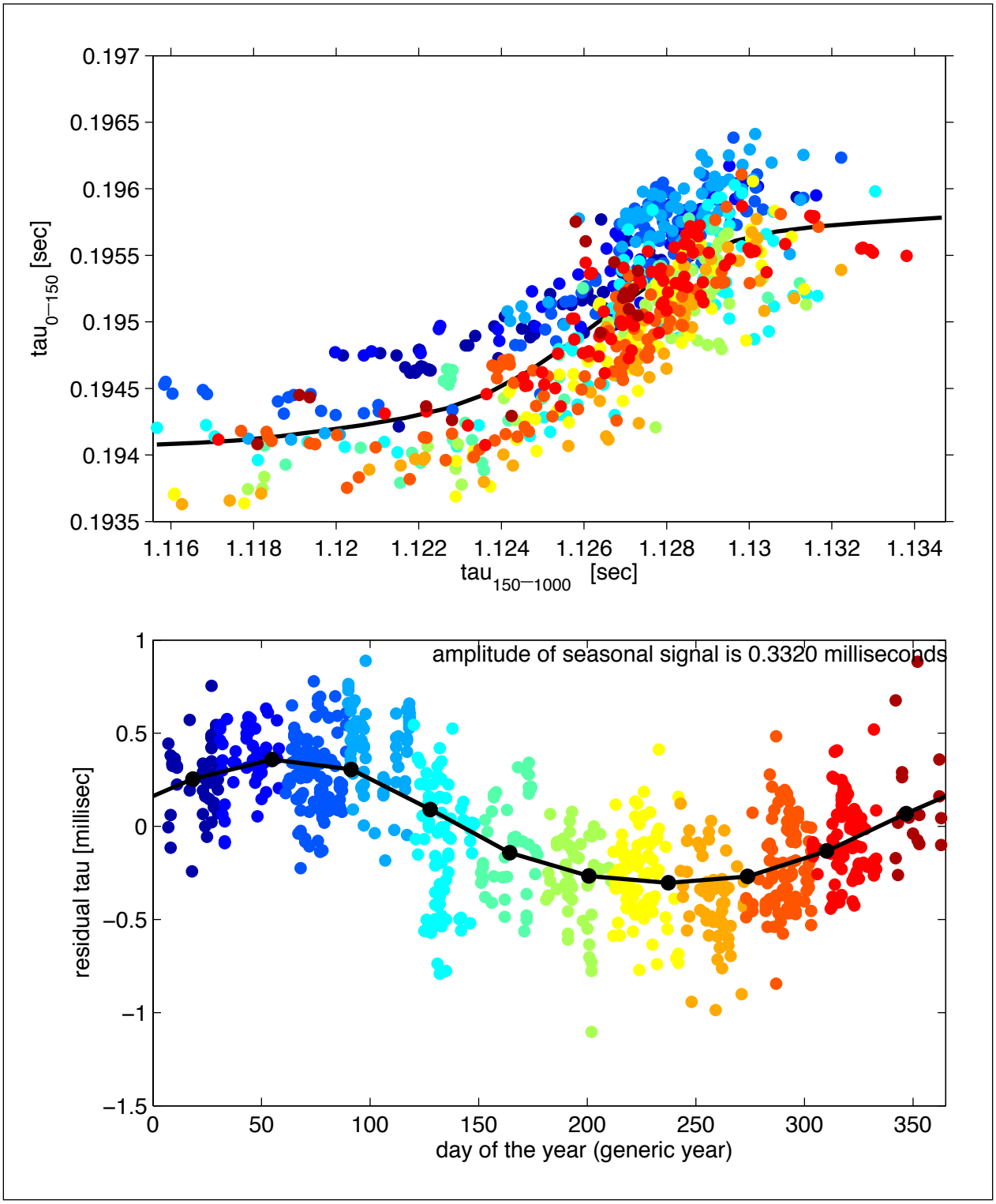

Figure 2.3-12. Upper panel: Scatter plots of τ(0-150) versus τ(150-1000). Each point is color coded by generic yearday transitioning from blue in January to red in December. The scatter about the spline fit (solid dark line) is largely due to the seasonal cycle. Lower panel: The residual from the cubic spline fit shown in the upper panel sorted by generic yearday shows a clear annual signal.

that the vertical structure was given by the linear topographic Rossby wave vertical structure, U,P ~ cosh(γz/H). Here the scaling parameter is defined as γ=NH/f |k|, where z is the vertical coordinate and is positive up, H is the water depth, N is the Brunt-Vaisala frequency, f is the Coriolis parameter and |k| is magnitude of the wavenumber (Rhines, 1970). Note that we have assumed that the topographic beta is much larger than planetary beta. The scaling parameter, γ, was determined by fitting the cosh function to deep current meter mean speeds (Figure 2.3-13). The scaling parameter was then interpolated onto an even grid within the array. The scale factor ranges from 0 to 1.3. A spatial structure emerges. South of the Escarpment γ tends to be small and near zero which is indicative of barotropic structure while north and northeast of the Escarpment γ tends to be larger indicative of a bottom-intensification. Additionally since γ is proportional to wavenumber, a larger γ suggests larger wavenumber. In this report, we refer to the common level of 1500 dbar as 1500 m, for convenience.

2.3.3 Maps

Maps were produced with optimal interpolation techniques adapted from Bretherton et al. (1976) and outlined in Watts et al. (1989, 2001). Optimal interpolation requires that the input fields have zero mean and uniform variance. To meet this requirement, a mean field must be subtracted from the fields before mapping and then added back to produce maps of the total field. We have removed the mean in such a way that the mapped fields "behaved" well at locations away from the measurement sites. Additionally, the cross-correlations among the measurements determined the correlation function and length scales used to map anomalies with the optimal interpolation scheme. We employed a Gaussian correlation function to construct upper- and lower-layer maps. Multivariate optimal interpolation mapped pressure and velocity, constrained to be geostrophic.

Maps of upper-ocean fields such as temperature and velocity were calculated by subtracting a 110-day running-mean mapped with a long correlation length scale of 180 km which produced smooth features at map edges. The anomaly field was then mapped with a short correlation length scale of 80 km determined by the correlation functions of the measurement anomalies (Figure 2.3-14). The measurement correlation function is isotropic indicating that the use of an isotropic Gaussian correlation function for the objective analysis was appropriate. We experimented with several different mean fields by varying the length of the running mean and ultimately chose the running-mean length which produced the best agreement with the directly-measured temperature, salinity, and velocity from the tall moorings.

Lower-ocean mappings were comparable to the upper-ocean procedure. Before mapping, a common mode or array-averaged pressure was subtracted from the 1500-dbar pressures. The common mode is discussed in Section 4.2.3. Retention of the common mode in the deep maps simply adds a spatially constant, time varying function that has no dynamical significance for the mesoscale circulation. The mean field was derived from fitting a plane to the mean of the 1500-dbar pressures. A 60-km correlation length scale determined from the near-bottom pressure correlations was used to map anomaly fields (Figure 2.3-15). Similar to the τ time series, the near-bottom pressure autocorrelations are nearly isotropic. Streamfunction maps were created using inputs from both pressure and current-meter data. The inclusion of the current-meter data

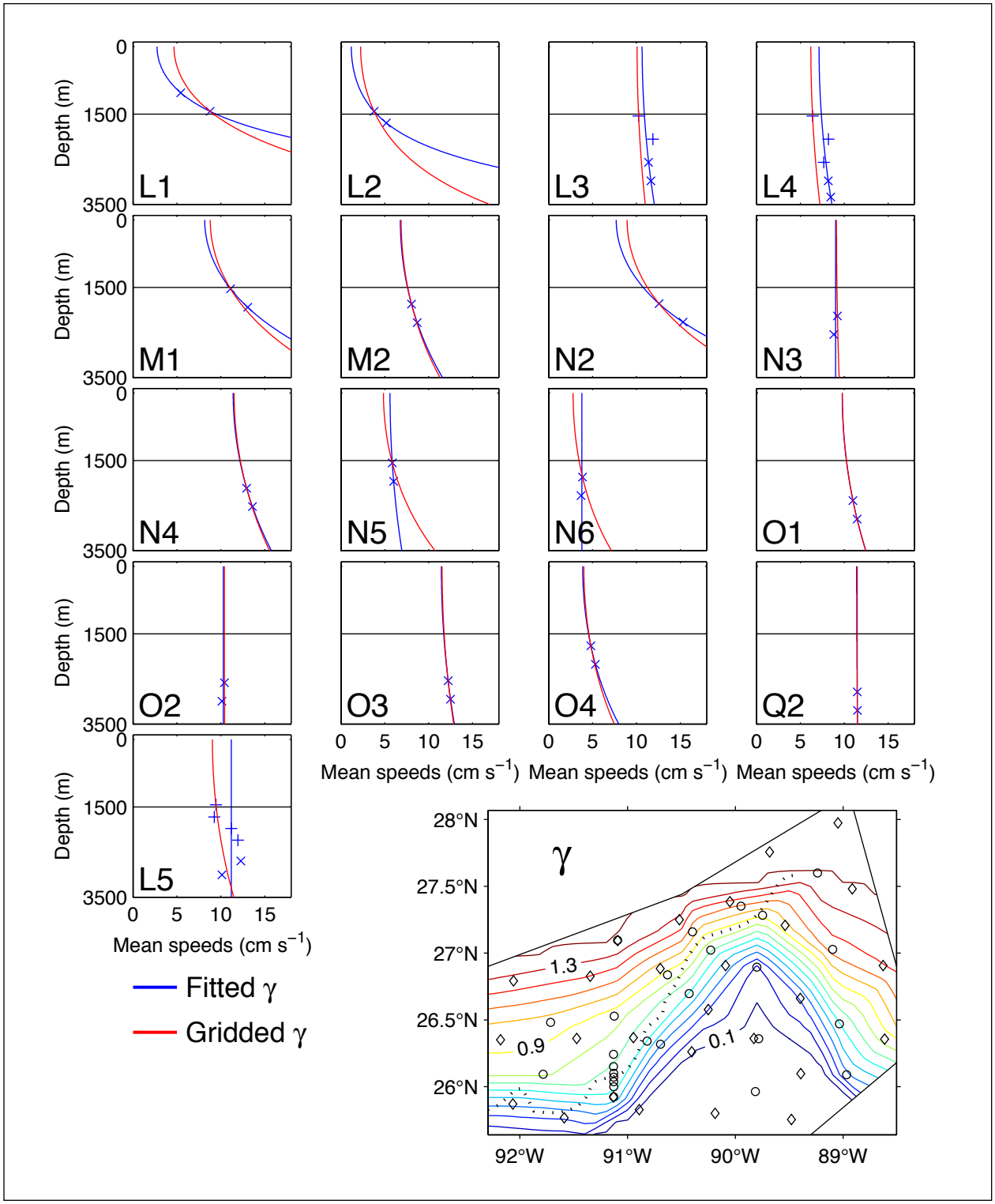

Figure 2.3-13. Deep current and pressure scaling parameter. Small panels: A cosh fit (blue line) applied to the deep current meter mean speeds (blue crosses). Gridded scaling parameter contoured for the array (bottom right panel) and plotted for each current meter (red lines in small panels). The dashed line is the mean position of the Escarpment. PIES shown as diamonds. deep current meters shown as circles.

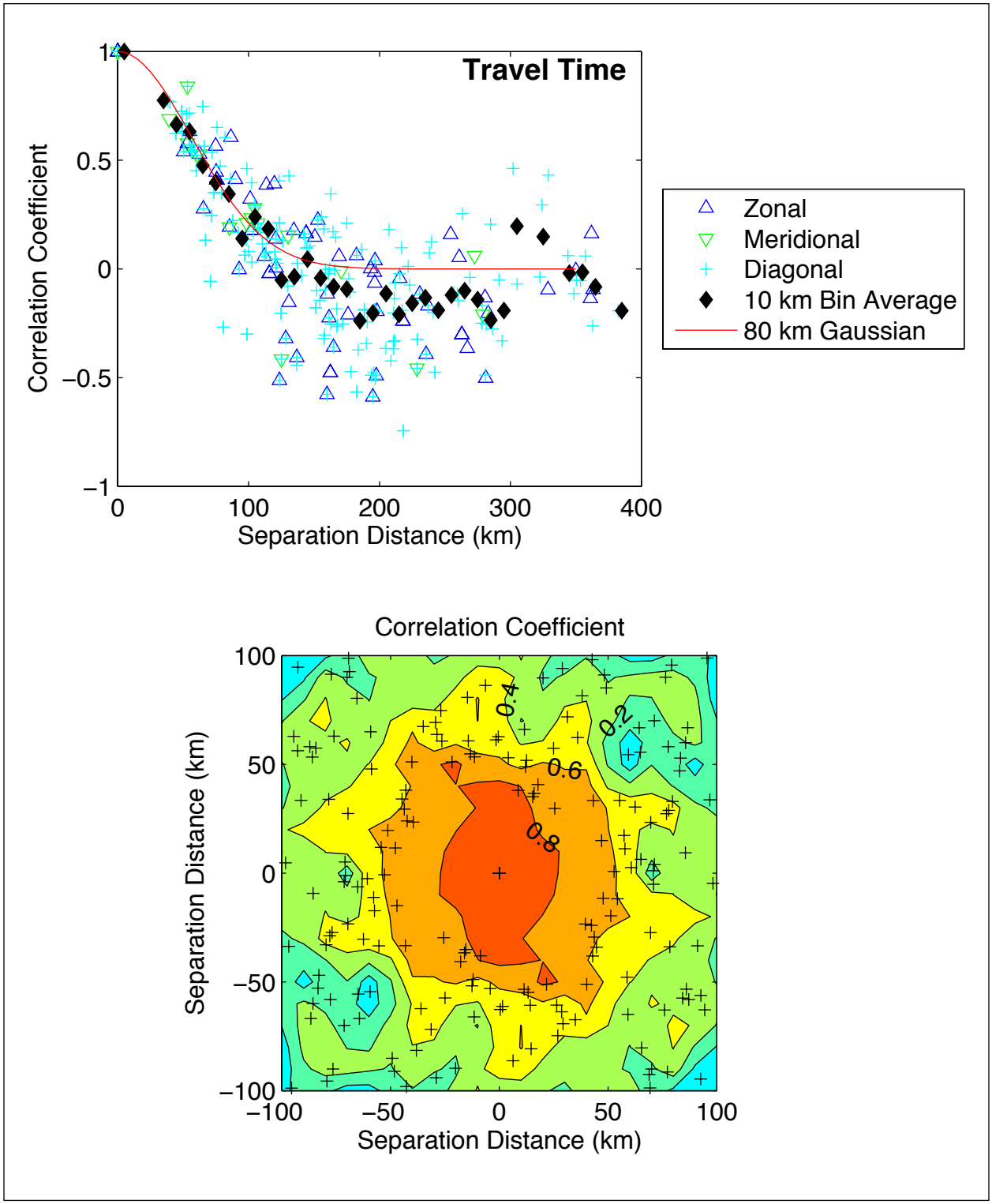

Figure 2.3-14. Correlation coefficients between pairs of PIES τ records. Upper panel: Correlations coefficients as a function of separation distance and binned every 10 km (black triangles). Pairs have also been classified by zonal (blue triangle), meridional (green triangle), and diagonal (cyan cross). An 80-km Gaussian function is plotted with red line. Lower panel: correlation coefficients contoured vs. distance.

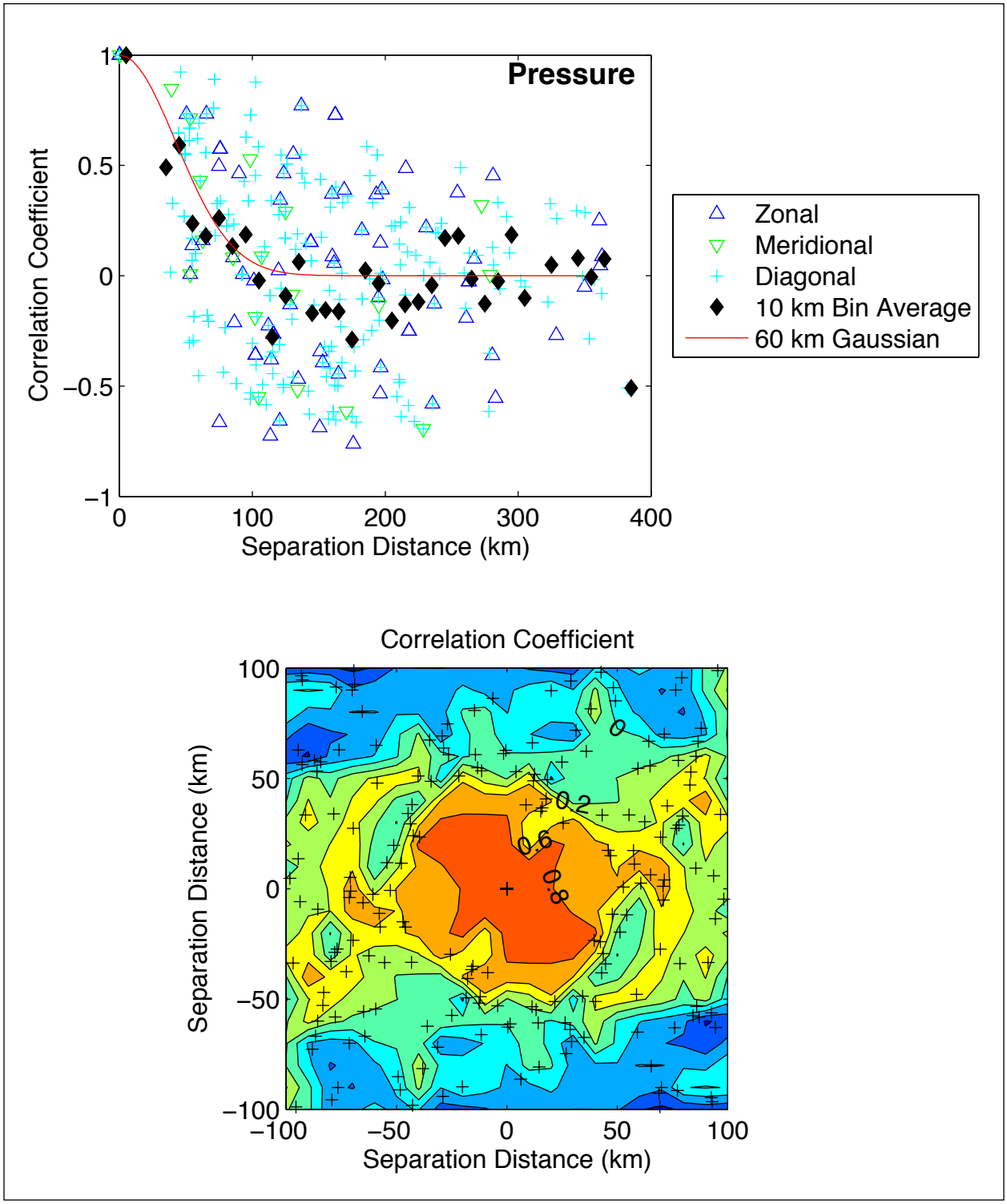

Figure 2.3-15. Correlation coefficients between pairs of pressure records. Upper panel: Correlations coefficients plotted as a function of separation distance and binned every 10 km (black triangles). Pairs have also been classified by zonal (blue triangle), meridional (green triangle), and diagonal (cyan cross). A 60-km Gaussian function is plotted with red line. Lower panel: Correlation coefficients contoured as a function of distance.

better resolves the local gradients. Below 1500 dbar, pressure and currents are adjusted by the scaling parameter discussed in Section 2.3.2.

Combining upper- and lower-ocean maps produced absolute velocities throughout the water column. Upper-ocean relative velocities were created by mapping velocities referenced to zero at 1500 dbar. The 1500-dbar velocities created with the bottom pressure and current meter records then referenced these upper-ocean relative velocities. Absolute SSH was also determined. First, 1500-dbar pressures were converted to their height equivalent (pressure divided by gravity and density). Second, surface geopotentials referenced to 1500 dbar were converted to their height equivalent (geopotential divided by g). The 1500-dbar referenced and 1500-dbar fields were combined to yield absolute SSH.

2.3.4 Mooring Comparisons

Instruments on tall moorings provided independent measurements to evaluate our PIES-derived fields of temperature, salinity, and velocity. Five moorings were available, four from the Exploratory Study and one from the LSU mooring. The comparisons were excellent (Table 2.4-1), highlighted here, and detailed in Appendix C. Note that the tall moorings experienced some vertical motion when ocean currents caused the moorings to 'blow over' or "draw down." The proper comparison was thus between measured and estimated T(t,p(t)), S(t,p(t)), u(t,p(t)),v(t,p(t)). PIES and tall moorings were collocated only at PIES 26 so we compared moored time series against mapped time series. Differences derive from instrument errors (both mooring and PIES), the GEM parameterization, and from mapping. Figures 2.3-16 and 2.3-17 show the comparison from the L1 mooring. The PIES-estimated series track the measured series. Typically the statistics are slightly more favorable below the influence of the seasonally varying upper layer. In terms of variance explained, the PIES derived temperatures (salinities) explain 85.3 (74.4) percent of the variance in the mooring series between 150 dbar and 1000 dbar.

Table 2.4-1

Percent of variance from moored instruments that were explained by PIES-based estimates.

Depth Range	Average Variance Explained
Temperature	
0-150 m	76.63 %
150-1000	85.33 %
Salinity	
0-150 m	58.75 %
150-1000	74.42%

A more stringent test of the GEM/PIES/mapping methodology is the comparison with measured velocities since the PIES velocities are 2nd-order quantities determined via differentiation. Again, the agreement between measured and PIES-estimated series was excellent. Figure 2.3-18 shows a comparison with observations made on L1. Note that four of the tall moorings are located at the

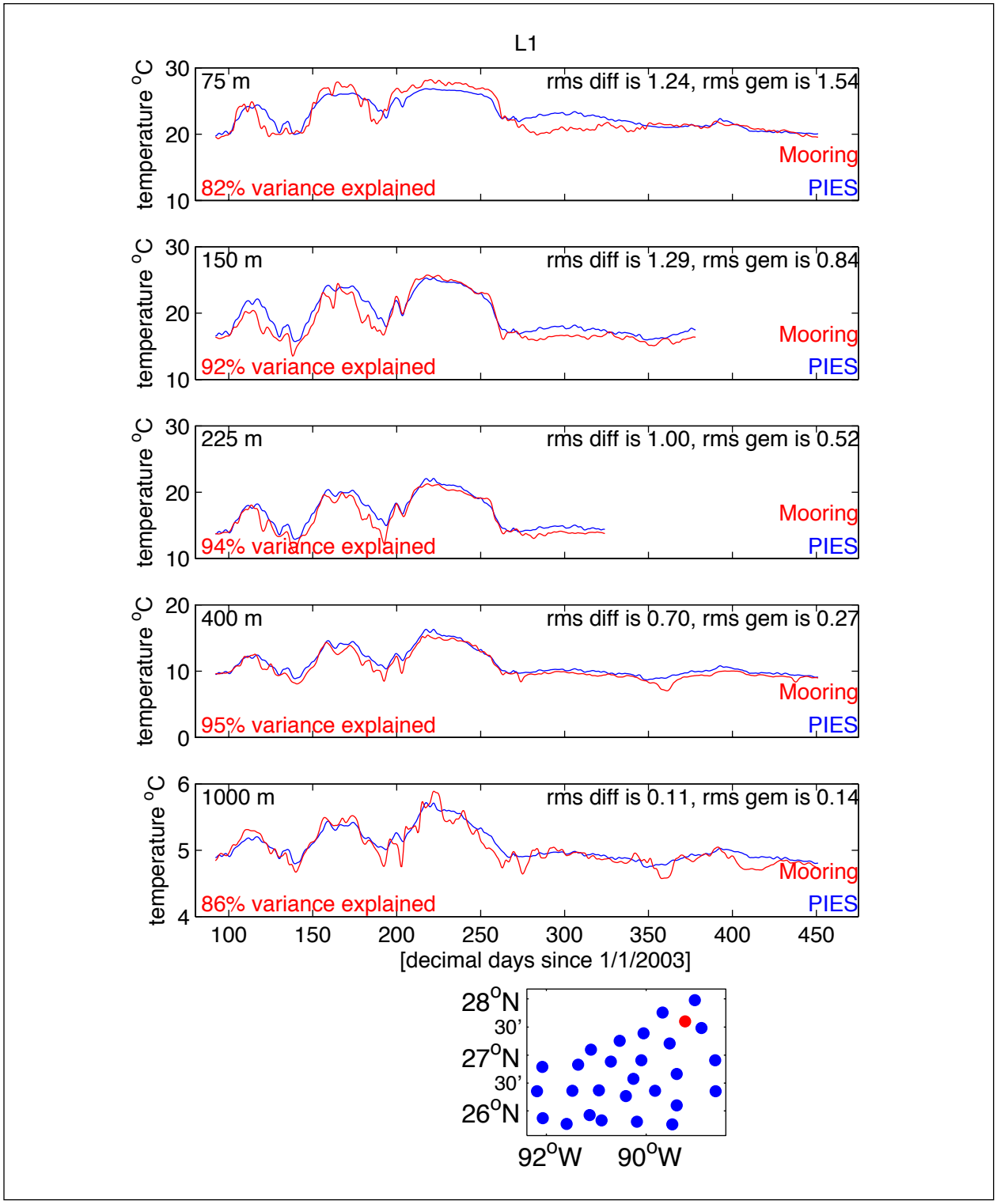

Figure 2.3-16. Comparison between L1 mooring (red) and PIES-derived (blue) temperature. The variance explained is noted in red in the bottom left corner of each panel. The rms difference between the series and the rms in the GEM is noted in the upper right corner. The bottom panel shows the location of the PIES (blue) and the mooring (red).

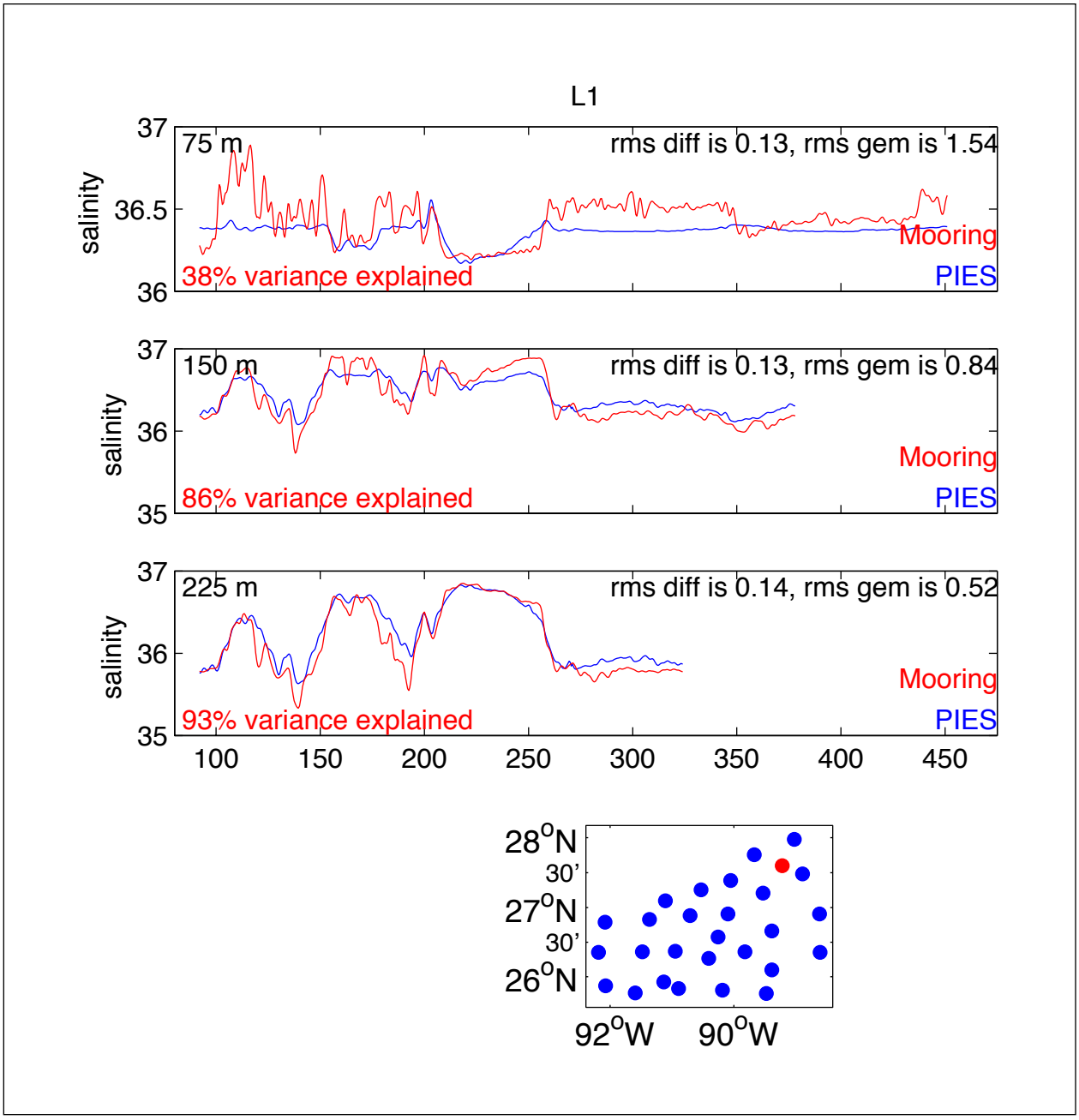

Figure 2.3-17. Comparison between L1 mooring (red) and PIES-derived (blue) salinity. The variance explained is noted in red in the bottom left corner of each panel. The rms difference between the series and the rms in the GEM is noted in the upper right corner. The bottom panel shows the location of the PIES (blue) and the mooring (red).

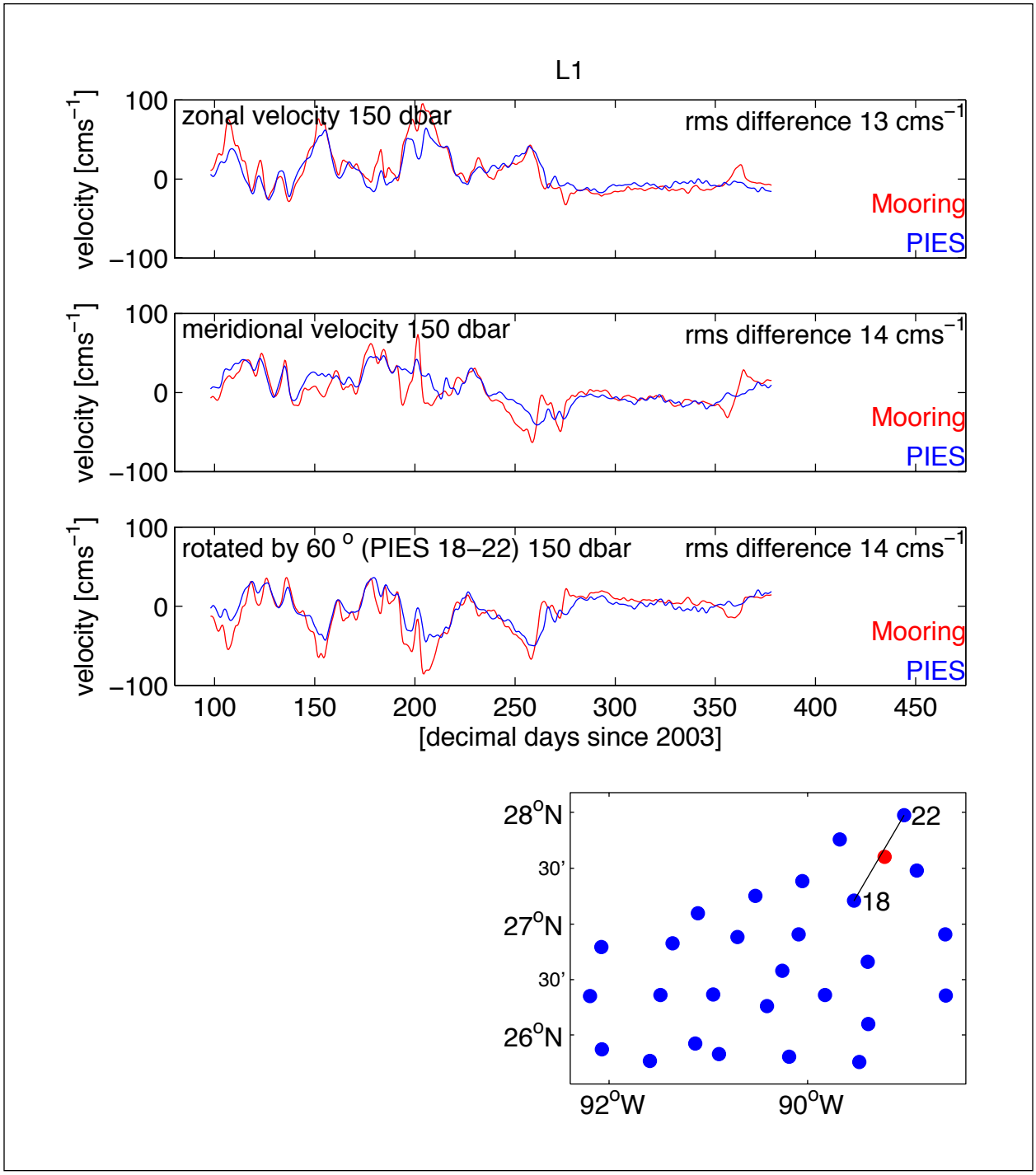

Figure 2.3-18. Comparison between L1 mooring (red) and PIES-derived (blue) velocity for zonal, meridional, and rotated meridional velocity components for the 150 m level. The rms difference between the two series is noted in the upper right corner. The bottom panel shows the location of the PIES (blue) and the mooring (red)

periphery of our mapping grid which means that the most direct comparison is not necessary between zonal or meridional velocity but between cross-PIES velocities. We term this 'meridional rotated velocity.' The average variance explained by the meridional rotated velocity for all available moorings is 70.7%.

2.4 Remote Sensing

The remote sensing component of the Exploratory Study was designed to acquire remotely sensed (satellite) data to aid in the interpretation of mesoscale features and physical data in the study area. A combination of a variety of satellite platforms have been used.

To carry out this task, CCAR collected and processed a complementary suite of satellite observations from satellite altimeter and radiometer remote sensing data systems. This suite incorporated sea surface height (SSH) data with high-resolution sea surface temperature (SST) and ocean color imagery. Satellite altimetry provided the all-weather multi-satellite monitoring capability required to map mesoscale circulation variability in the GOM. During cloud free conditions, multi-channel radiometry was used to supplement the altimetric sampling by providing high-resolution synoptic imagery for monitoring the Loop Current front and rapidly evolving small-scale eddies in and around the study region.

2.4.1 Altimetry

Altimeter data used during the Exploratory Study were the near real-time and archival data streams available from TOPEX/Poseidon (TOP/POS), ERS-2, Geosat Follow-on, Jason-1 and Envisat satellite missions. Processing of the SSH data was based on near real-time mesoscale analysis techniques designed to exploit the multi-satellite altimetric sampling (Leben et al., 2002). This method has been used to monitor the GOM operationally since November 1995. Altimeter data from a total of five satellites were available during the program time period. Basic information on each of the missions is given in Table 2.4-2. The groundtrack coverage provided by these satellites in the study region is shown in Figure 2.4-1.

Table 2.4-2.

Satellite altimeter missions during Exploratory Study.

Satellite	Launch Date	Agency	Repeat Period (days)	Crosstrack Spacing	
				Degrees of Longitude	km*
TOPEX/Poseidon	10 Sep 1992	NASA/CNES	10	2.83	282
ERS-2	21 Apr 1995	ESA	35	0.72	71
Geosat Follow-On	10 Feb 1998	U. S. Navy	17	1.47	147
Jason-1	18 Dec 1999	NASA/CNES	10	2.83	285
Envisat	1 Mar 2002	ESA	35	0.72	71
					*at 26.5°N
Tandem/Interleaved Mission: 20 Sep 2000 to present.					
TOPEX/Poseidon/Jason-1 Interleaved			10	1.42	141

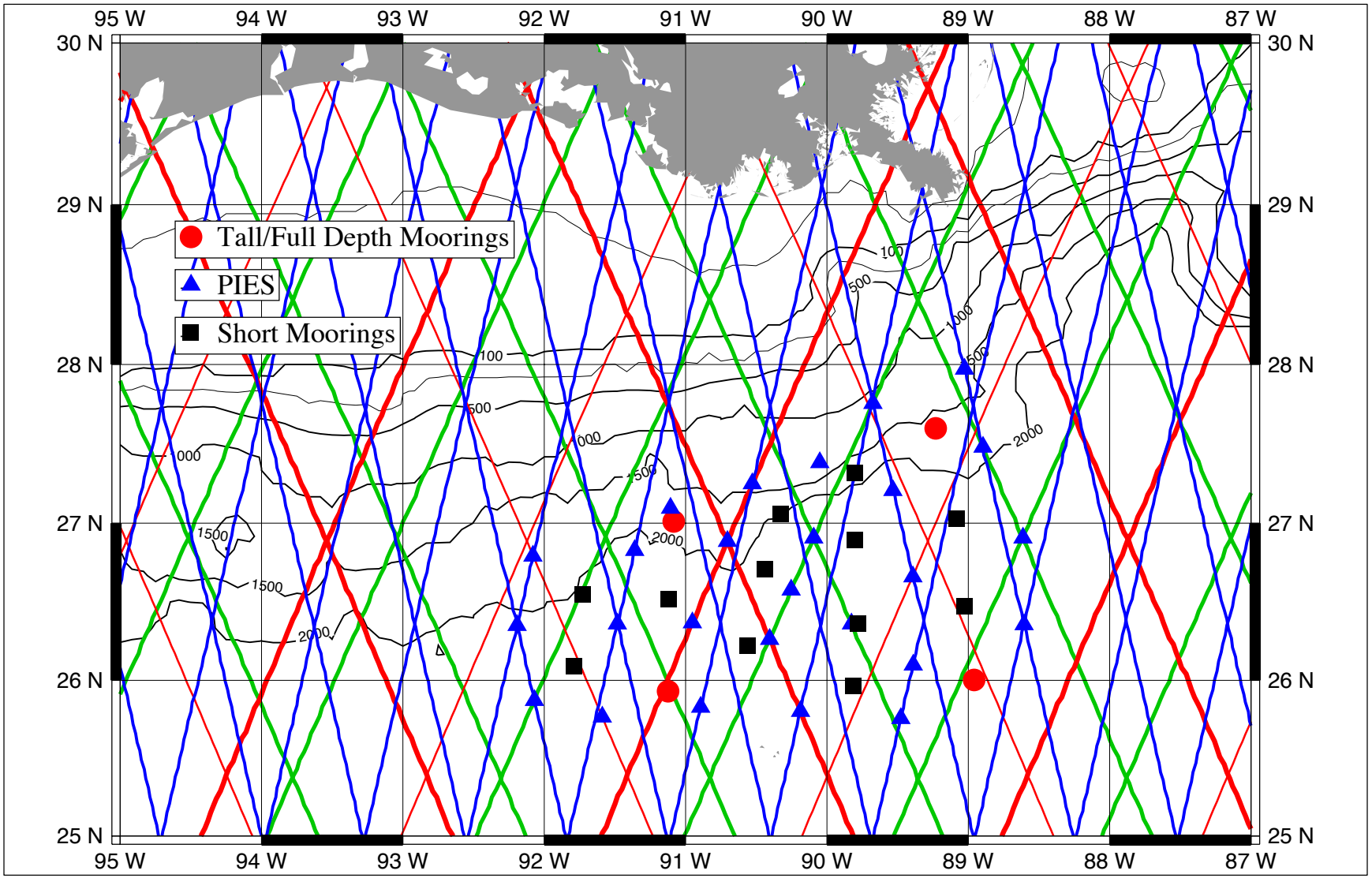

Figure 2.4-1 Satellite altimeter groundtrack coverage in study region. TOP/POS (thin red), Jason-1(thick read), GFO(green) and ERS-2/Envisat (blue) are shown with a schematic of the instrument array.

Note that during the study the TOP/POS and Jason-1 satellites were in tandem orbits with interleaved groundtracks. NASA/CNES scientists selected this configuration to improve the sampling of mesoscale ocean circulation by precision altimeters (Fu et al., 2003). The space/time sampling provided from the 10-day repeat orbit of the TOP/POS satellite, which was selected to map the ocean topography associated with large-scale variations in SSH, is not sufficient for monitoring mesoscale variability because of the large distance between neighboring ascending or descending tracks. In the GOM, this spacing is 2.83° of longitude or about 282 km at 26.5°N, which is also the distance between crossover points between ascending and descending tracks. Moving TOP/POS onto a parallel groundtrack that is midway between two adjacent ground tracks of the original TOP/POS orbit, which Jason-1 now occupies, reduced this distance by half – a spacing of 141 km cross track at 26.5°N. At latitudes midway between intra- and inter-satellite crossover points the ascending/descending groundtrack sampling improves by another factor of two giving a cross track spacing of just 72 km. Thus, the average crosstrack sampling in the study region from the tandem mission data alone was 70 to 140 km within the study region. The addition of GFO and ERS/Envisat data augments this spatial sampling, but at more irregular sampling times.

Intuitively, sampling should improve by combining data from multiple altimeters; however, SSH fields produced by combining multi-mission altimetry may not be better than those constructed from TOP/POS or Jason data alone if uniform errors and wavelength/frequency resolution satisfying the Nyquist criteria are required of the space/time gridded product as has been proposed by Greenslade et al. (1997). While these metrics may be reasonable for theoretical sampling studies or mission design, the constraints are too limiting for mesoscale mapping. Operational multiple satellite objective mapping of the mesoscale circulation must therefore rely on suboptimal smoothing to resolve eddy-scale wavelength albeit with the commensurate errors caused by non-uniform sampling and aliasing. This is true of both formal “optimal” interpolation and suboptimal objective analysis schemes. The efficacy of the final product, however, can be evaluated by comparing with coincident data to assess quantitatively the processing and gridding strategies. PIES data are an ideal in-situ measurement type for these comparisons, and during the design of the field measurements selected instrument sites were placed along altimeter groundtracks where possible to allow accurate assessment of not only the space/time gridded products, but the along-track data as well.

2.4.1.1 Along-track Data

Along-track data were collected from the agencies providing archival altimeter geophysical data records (GDRs). The TOP/POS and Jason-1 data were from the Physical Oceanography Distributed Active Archive Center (PO.DAAC) at the Jet Propulsion Laboratory. ERS-2 and Envisat data were from the "Centre ERS d'Archivage et de Traitement" (CERSAT), the French Processing and Archiving Facility for ERS-1, ERS-2 and Envisat data. GFO data were from the NOAA/NESDIS Laboratory for Satellite Altimetry.

All of the altimeter data sets were processed in as consistent a fashion as possible to produce accurate analysis maps based on the blended altimetric observations. Standard corrections were applied to the along-track data including inverted barometer, electromagnetic bias, ionosphere and wet/dry troposphere corrections. Ocean tides were removed using the tide model supplied

on the GDRs for TOP/POS, Jason and Envisat . GFO and ERS-2 ocean tides were removed using the tide solution derived from the CCAR tide model (Tierney et al., 1998).

Each cycle of corrected 10-day repeat TOP/POS and Jason, 17-day repeat of GFO, and 35-day repeat of ERS-2 and Envisat data was linearly interpolated to reference ground tracks based on precision orbit determination ephemerides for each satellite at 1 s^{-1} along-track spacing. The TOP/POS and Jason reference track used the computed ground track for TOP/POS cycle 18. The TOP/POS interleaved mission reference ground track was the same ground track with an offset in longitude corresponding to the nominal interleaved orbit. The ERS-2 and Envisat 35-day reference ground tracks were based on repeat cycle 6 of the ERS-1 Multidisciplinary 1 mission. The GFO reference ground track was based on the cycle 2 from the GEOSAT ERM.

2.4.1.2 Mesoscale Analysis

Processing of altimeter data was designed to retain mesoscale signals while filtering out longer wavelength altimetric errors. This filtering, however, also removes long wavelength oceanographic signals. A detailed description of this processing and its implementation and validation in the GOM can be found in Leben et al. (2002). The procedure incorporates data from all of the available satellites, treating each data set in a consistent fashion as follows:

1. All sub-satellite data are referenced to an independent gridded mean sea surface by subtracting the mean sea surface value at the sub-satellite point from each observation.

2. Along-track loess filtering is used to remove residual orbit and environmental correction errors. The loess filter removes a running least squares fit of a tilt plus bias within a sliding window from the along-track data. The window width is approximately 15 degrees of latitude (200 seconds along track).

3. A multigrid preconditioned Cressman analysis with temporal weighing is used to objectively interpolate the along-track data to a 1/4° grid.

4. A model mean SSH field is added to the mapped SSH anomaly field to provide an estimate of the total SSH in the GOM.

2.4.1.3 Mean Reference Surface and Model Mean SSH

All along-track data were referenced to an existing altimetric mean sea surface. The data were treated as non-repeating ground tracks and referenced directly to the mean sea surface by interpolating the mean sea-surface value to the sub-satellite point and subtracting it from the sea-surface height. This applied an implicit cross-track geoid gradient correction to the along-track data before interpolation to the reference ground tracks.

The GSFC00.1_MSS, which was computed by Y. M. Wang of Raytheon ITSS (Wang, 2001), was used as the reference surface. This mean sea surface is based on 6-years of TOP/POS data (Cycles 11 to 232), multi-years of ERS-1&2 35-day exact repeat data (ERS-1 Phase C: Cycles 1 to 18; Phase G: Cycles 1 to 13; ERS-2: Cycles 1 to 29), Geosat 17-day exact repeat data (Cycles

1 to 41), Geosat Geodetic Mission data and both cycles of the ERS-1 168-day repeat data. All the altimeter data used to calculate the mean sea surface came from the GSFC's Altimeter Pathfinder products (Koblinsky et al., 1999).

To calculate the synthetic SSH estimates, we selected a model mean sea-surface height computed for the time period 1993 through 1999 from a data assimilation hindcast performed by Drs. Lakshmi Kantha and Jei Choi for the MMS Deepwater Physical Oceanography Reanalysis and Synthesis Program (Nowlin et al., 2001) using the University of Colorado-Princeton Ocean Model (CUPOM). Along-track TOPEX and ERS-1&2 sea-surface height anomalies were assimilated into CUPOM on a track-by-track basis as subsurface temperature anomalies (Kantha et al., 2005). Before adding the model mean to the gridded SSH anomaly fields we averaged the 1993 through 1999 SSH anomaly fields and removed the residual anomalous altimetric mean. This references the SSH anomaly fields to a mean spanning the same time period as determined from the model hindcast data assimilation experiment. The anomalous altimetric mean reflects the difference between the mean circulation contained in the GSFC mean sea surface and the 1993-1999 model mean. More discussion of these differences is found in Leben et al. (2002).

2.4.1.4 Objective Mapping

Daily analysis maps of height anomaly relative to the mean sea surface were estimated using an objective analysis procedure (Cressman, 1959) to interpolate the along-track data to a 1/4° spatial grid. The method uses an iterative difference-correction scheme to update an initial guess field and converges to a final gridded map. A multi-grid procedure provided the initial guess. Five iterations were used with radii of influences of 200, 175, 150, 125 and 100 km, while employing a 100-km spatial decorrelation length scale in the isotropic Cressman weighting function. The data were weighted in time using a 12-day decorrelation time-scale, relative to the analysis date, using a ±10 day window for the TOP/POS and Jason data and a ±17 day window for the ERS-2, Envisat and GFO data. The details of the space and time weighted version of the multigrid preconditioned Cressman analysis is described below and was based on the space weighting only technique described in Hendricks et al. (1996).

2.4.1.4.1 Objective Analysis Procedure

An objective analysis (OA) procedure was used to interpolate the along-track SSH anomalies onto a regularly spaced 1/4° global grid. The OA algorithm is based on the iterative difference-correction scheme of Cressman (1959). The initial guess field for the Cressman algorithm is supplied by an efficient multigrid procedure.

A rough estimate of the 1/4° field was created by collecting the along-track SSH anomaly data into 1/4°grid cells. In grid cells where at least one SSH measurement is available, the average of all measurements within the cell is computed. Some of the grid cells may not have contained data depending on the spacing of ground tracks. The OA procedure is designed to fill in these data gaps by creating a SSH anomaly field that is consistent with the along-track measurements.

The 1/4°-binned data can be used as an initial guess in the Cressman algorithm, however, the efficiency of the iteration procedure can be enhanced by having initial values in the empty grid

cells. A simple multigrid procedure was used to estimate values in cells where no altimeter measurements were available. Multigrid methods (Briggs, 1987) rapidly solve a set of equations by working at several grid resolutions. In this case, if the along-track data are binned into 1° or 2° grid cells there would be fewer or even no empty ocean grid cells. Using a multigrid interpolation strategy to compute the means efficiently, a set of progressively coarser grids (1/2°, 1°, 2°, …) was created from the global 1/4° grid and the average SSH was computed at all coarser grid resolutions in each cell containing data. The mean values were transferred back to the original 1/4° grid from the finest-scale grid containing a mean value coincident with that location. Finally, a fast red-black smoothing operator (e.g., see Press et al., 1992) was used on the 1/4° initial guess field to smooth high-frequency noise introduced by the multigrid interpolation.

The Cressman objective analysis routine is an iterative-difference corrections scheme in which a new estimate of the SSH value for a given grid cell is equal to the sum of the previously estimated SSH at that location and a correction term. The correction term is forced by the difference between the estimated heights and the original data values over all grid cells within a specified radius of influence. A weight based on the number of original measurements within a grid cell is included in the correction term, as is a weight based on the distance of a grid cell from the point being updated.

The *n*th iteration for the SSH at grid cell *i* is computed using:

$$h_i^n = h_i^{n-1} + \frac{\sum w_m n_m^* \left(h_m^* - h_m^{n-1} \right)}{\sum w_m n_m^*}, \qquad (1)$$

where the sums are taken over all *m* grid cells within the specified radius of influence *R* from the grid cell *i* being updated. The variables in (Eq. 1) are defined as:

h_i^n the *n*th iteration of SSH at grid cell *i*;

h_i^{n-1} the *(n-1)*th iteration of SSH at grid cell *i*;

h_m^* the average height at grid cell *m* based on the original data;

h_m^{n-1} the *(n-1)*th iteration of SSH at grid cell *m*.

n_m^* the number of original measurements within grid cell *m*.

The weights in the correction term are defined by:

$$w_m = \exp(-a r_m^2 / R^2) \quad \text{for } r \le R;$$
$$w_m = 0 \quad \text{for } r > R;$$

where r_m is the distance between grid cell m and the grid cell being updated and R is the maximum radius of influence. The parameter a is an adjustable weighting factor that scales the exponential spatial weighting of the data.

To incorporate weighting of the data in time, the data and the number of original measurements within a grid cell are each scaled by the weighting function:

$$w_t = \exp(-b\Delta t_m^2 / T^2) \quad \text{for } \Delta t \le T;$$
$$w_t = 0 \quad \text{for } \Delta t > T;$$

where Δt_m is the difference between the measurement time and the time corresponding to the analyzed field, b is the time weighting factor, and T is the maximum time window of influence.

The empirical weighting parameters, a and b, were selected to map the mesoscale structure within the limitation of the scales resolvable by the cross-track altimeter sampling. The mesoscale analysis used a = 4 and b = 2, which corresponds to decorrelation space and time scales of 100 km and 12 days, respectively, for R = 200 km and T = 17 days. The maximum radius of influence, R, was decreased between the Cressman iterations to allow smaller scales to converge more quickly and to increase resolution when along-track sampling is available. For this study, R was decreased from 200 to 100 km over five iterations giving a decorrelation length scale of 50 km on the final Cressman iteration.

2.4.2 Ocean Color Imagery

Daily ocean color imagery at 4-km resolution was downloaded from the OceanColor group web and ftp sites (http://oceancolor.gsfc.nasa.gov/) at the NASA Goddard Space Flight Center (GSFC). These images are from the Moderate Resolution Imaging Spectroradiometer (MODIS) instrument onboard the Aqua satellite. Chlorophyll concentration provided in these images is estimated by the GSFC OceanColor group using the OC3M empirical chlorophyll algorithm using the measured radiances (O'Reilly et al., 1998). A variety of multi-day composites were made to help with the detection and tracking of oceanographic features in and around the study region as shown in Sections 3 and 4.

2.4.3 SST Imagery

Two SST products were acquired for remote sensing and in-situ data synthesis activities. First, we obtained Advanced Very High Resolution Radiometer (AVHRR) imagery from the Johns Hopkins University/Applied Physics Laboratory (JHU/APL) Ocean Remote Sensing Group. Three-day warmest pixel composite images in Portable Network Graphics (PNG) format were downloaded from the JHU/APL Ocean Remote Sensing Group website. These images are 1-km resolution with image values (0-255) corresponding the rounded integer SST values. The full precision values before rounding were calculated by the multi-channel algorithm used in the TerraScan software that converts raw antenna brightness temperatures to SST values in the APL ground station. Although the rounding limits the accuracy to only 0.5°C, which is less than required for most scientific work, the capability to detect spatial features was not compromised

and the data were sufficiently accurate for data synthesis activities. The images collected for the Exploratory Study were once-per-day 3-day composite images from 1 January 2003 through 30 June 2004.

We also acquired Geostationary Operational Environmental Satellite (GOES-8 & 12) SST images from Dr. Nan Walker at the Louisiana State University Earth Scan Laboratory. A major advantage of GOES data is the frequent repeat coverage (48 images/day) that enables removal of cloud cover, improving feature detection and SST accuracy (Walker et al., 2003). The images collected for the Exploratory Study were once-per-day nighttime composite images from 1 April 2003 through 31 March 2004.

2.5 PIES/Altimeter Comparisons

PIES and satellite altimetry are complementary data types. Although the two measurement systems measure completely different physical quantities, they both yield an estimate of the height of the ocean surface relative to some datum, which is commonly referred to as the sea-surface height (SSH). In this section, we present a brief overview of the PIES SSH calculation and show several preliminary comparisons of the PIES SSH to the coincident altimeter-derived SSH collected during the study program.

This is the first opportunity for this type of comparison and analysis in the GOM. These studies have the potential to identify problems and test improvements in the altimeter data processing and products for the region. This will facilitate the synthesis of altimetry data and PIES data from the study array, and from other PIES arrays deployed in the deep GOM, to improve observing and understanding of deepwater circulation patterns and dynamics throughout the water column.

2.5.1 PIES Sea Surface Height

The PIES measurements were converted to sea-surface-height anomaly (SSHA) and the baroclinic and barotropic SSHA components determined. For each instrument the calculations below were made:

$$SSHA = p'(t)/(\rho g) + \Phi'(t)/g \qquad (2.6.1a)$$

$$SSHA = \text{barotropic} + \text{baroclinic} \qquad (2.6.1b)$$

Here the prime indicates anomaly from the record mean. The barotropic component, the first term on the right-hand side of equation 2.6.1a is the bottom pressure anomaly, p'(t) divided by gravity, g, and density, ρ, and represents the mass contribution to SSHA. The baroclinic component, the second term on the right-hand side of equation 2.6.1a, is the geopotential, Φ, divided by gravity and represents the steric-height contribution to SSHA. Time series of τ(150-1000) were converted to specific-volume via the GEM look-up and integrated vertically to yield the geopotential.

The baroclinic component dominates SSHA variance (Figure 2.5-1, Table 2.5-1) while the barotropic component typically contributes less than 10% to the signal and only exceeds 10% at instruments in the northwest corner where total SSHA variance is low. Low covariances between baroclinic and barotropic SSHA indicate weak correlations between the two components. A tendency exists for positive correlations above the Escarpment and negative correlations below the Escarpment and the northeastern portion of the array. Barotropic variance is strongest south of the Escarpment where deep ocean variability is greatest and is noticeably weak above the Escarpment. The total variance reflects the variance in the baroclinic variance and high values in the northeast corner are associated with the meandering of the LC during the first six months of the experiment. A slight ridge of increased variance just south of the Escarpment traces the translation of Eddy Sargassum through the array.

Skewness and kurtosis indicate deviations from a normal distribution and have been computed for each time series (Figure 2.5-2, Table 2.5-2). Skewness indicates the symmetry or lack of symmetry around the mean: a normal distribution has skewness of 0 with positive (negative) values associated with a spread to the right (left). Kurtosis provides a measure of scatter about a normal distribution with a value of 3 for a normal distribution and values greater (less) than three indicating larger (smaller) scatter about the mean. Barotropic skewness and kurtosis are close to values appropriate for a normal distribution. In contrast, the baroclinic component has a larger range in values away from those expected for a normal distribution but close to normal distribution where the signal variance is high.

Section 2.3 details the calculation of SSH, stream function and velocity. A brief review is provided. We assumed that the current and pressure fields were in geostrophic balance $u = (-1/f\rho)\partial p/\partial y$, $v = (1/f\rho)\partial p/\partial x$, where f is the Coriolis parameter and ρ is density or equivalently in terms of geopotential, Φ, $u = (-1/f)\partial\Phi/\partial y$, $v = (1/f)\partial\Phi/\partial x$. Since the velocities are nondivergent, a stream function, Ψ, exists, $u = \partial\Psi/\partial y$, $v = -\partial\Psi/\partial x$. Pressure is then proportional to stream function by a factor ($f\rho$); geopotential is proportional to stream function by a factor (f). Note from equation (2.6.1a) that pressure is proportional to height by ($1/\rho g$); geopotential is proportional to height by ($1/g$). Velocities were determined by optimal interpolation with the specification that cross-covariance functions between velocity and stream function/pressure/geopotential are nondivergent and geostrophic. First, we mapped the surface geopotential and velocities referenced to 1500 dbar with inputs from the GEM-derived geopotential at each site. The 1500-dbar-referenced geopotential were converted to height and stream function. Second, 1500-dbar pressure and currents were mapped with inputs from scaled bottom pressure and current data. The 1500-dbar pressure was converted to its equivalent height and stream function values. Finally, the 1500-dbar level and 1500-dbar-referenced fields were added together to determine absolute SSH, sea-surface velocity, and stream function.

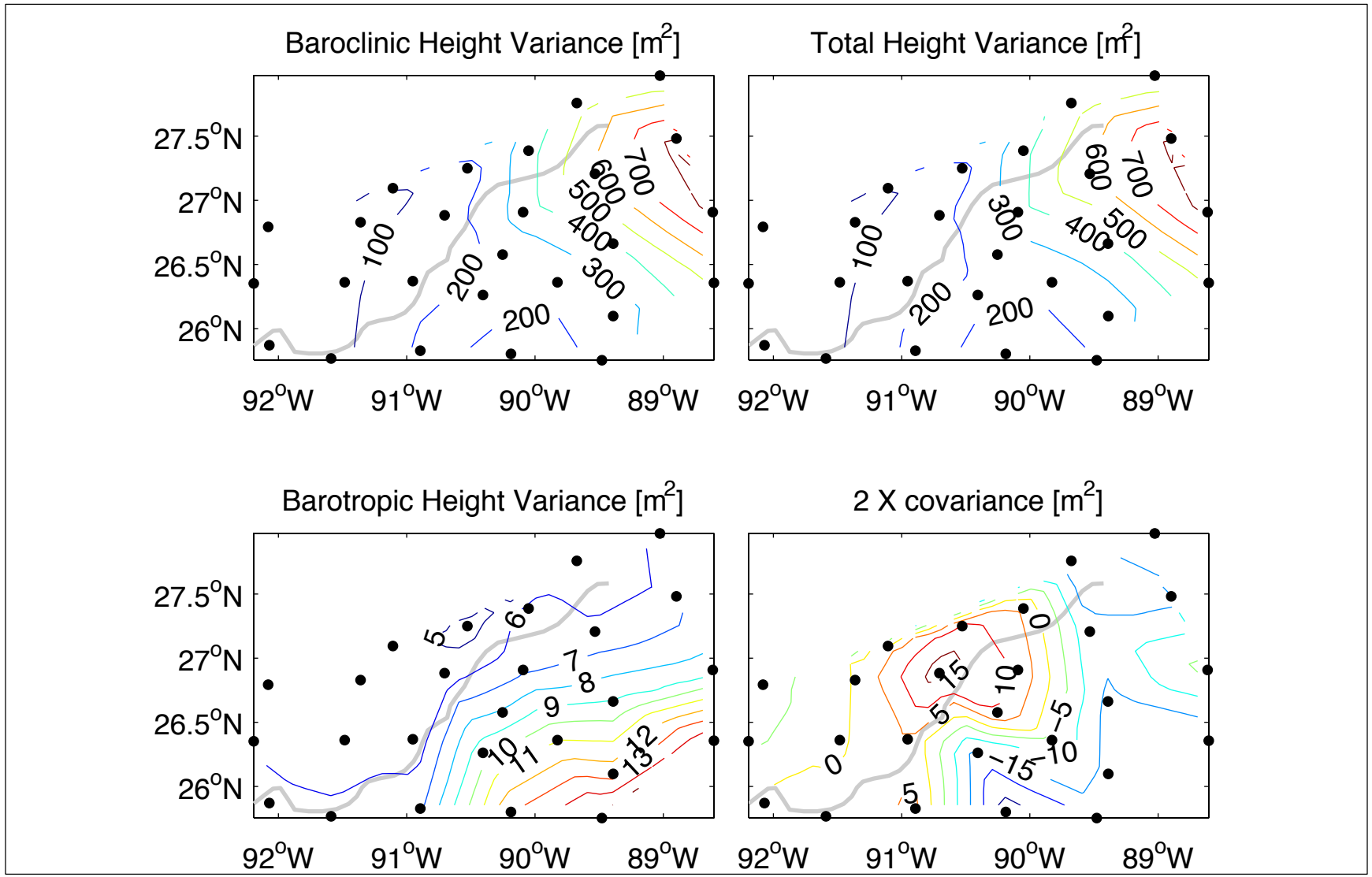

Figure 2.5-1. Variance in SSH anomaly fields determined from each PIES. Upper left: Baroclinic height variance. Upper right: Total height variance. Lower left. Barotropic height variance. Lower right. Twice the covariance between the barotropic and baroclinic height fields. Instrument locations shown with black dots. Thick grey line indicates the Sigsbee escarpment.

Table 2.5-1.

Tabulation of the baroclinic, barotropic, and total SSH variance, and covariance between baroclinic and barotropic SSH signals.

PIES Site	Baroclinic Variance (m^2)	Baroclinic % of total	Barotropic Variance (m^2)	Barotropic % of total	2*Covariance Variance (m^2)	2*Covariance % of total	Total Variance (m^2)
1	0.0051	103.5	0.0006	11.6	-0.0007	-15.1	0.0049
2	0.0033	100.7	0.0006	18.1	-0.0006	-18.7	0.0033
3	0.0026	77.5	0.0006	18.6	0.0001	3.9	0.0034
4	0.0205	97.0	0.0011	5.2	-0.0005	-2.2	0.0211
5	0.0069	92.4	0.0005	7.1	0.0000	0.5	0.0075
6	0.0071	94.0	0.0005	7.1	-0.0001	-1.1	0.0075
7	0.0061	89.2	0.0006	9.1	0.0001	1.7	0.0069
8	0.0152	90.0	0.0005	2.7	0.0012	7.3	0.0168
9	0.0147	86.2	0.0005	3.2	0.0018	10.7	0.0171
10	0.0173	94.4	0.0005	2.8	0.0005	2.8	0.0184
11	0.0216	94.4	0.0007	3.0	0.0006	2.7	0.0229
12	0.0364	97.1	0.0006	1.7	0.0005	1.2	0.0375
13	0.0348	95.6	0.0007	1.9	0.0009	2.6	0.0364
14	0.0232	92.6	0.0008	3.2	0.0010	4.2	0.0250
15	0.0217	104.0	0.0010	4.6	-0.0018	-8.6	0.0209
16	0.0183	109.2	0.0013	7.7	-0.0028	-16.9	0.0168
17	0.0468	102.8	0.0005	1.2	-0.0018	-4.0	0.0455
18	0.0619	101.3	0.0006	1.0	-0.0014	-2.3	0.0612
19	0.0389	102.0	0.0009	2.4	-0.0017	-4.3	0.0382
20	0.0226	101.9	0.0013	5.7	-0.0017	-7.6	0.0222
21	0.0204	102.1	0.0015	7.7	-0.0020	-9.8	0.0200
22	0.0405	101.0	0.0006	1.5	-0.0010	-2.5	0.0401
23	0.0834	101.3	0.0006	0.8	-0.0017	-2.0	0.0824
24	0.0823	99.3	0.0009	1.0	-0.0003	-0.4	0.0828
25	0.0510	101.0	0.0015	3.0	-0.0020	-4.0	0.0505
26	0.0074	89.6	0.0005	6.5	0.0003	3.9	0.0082

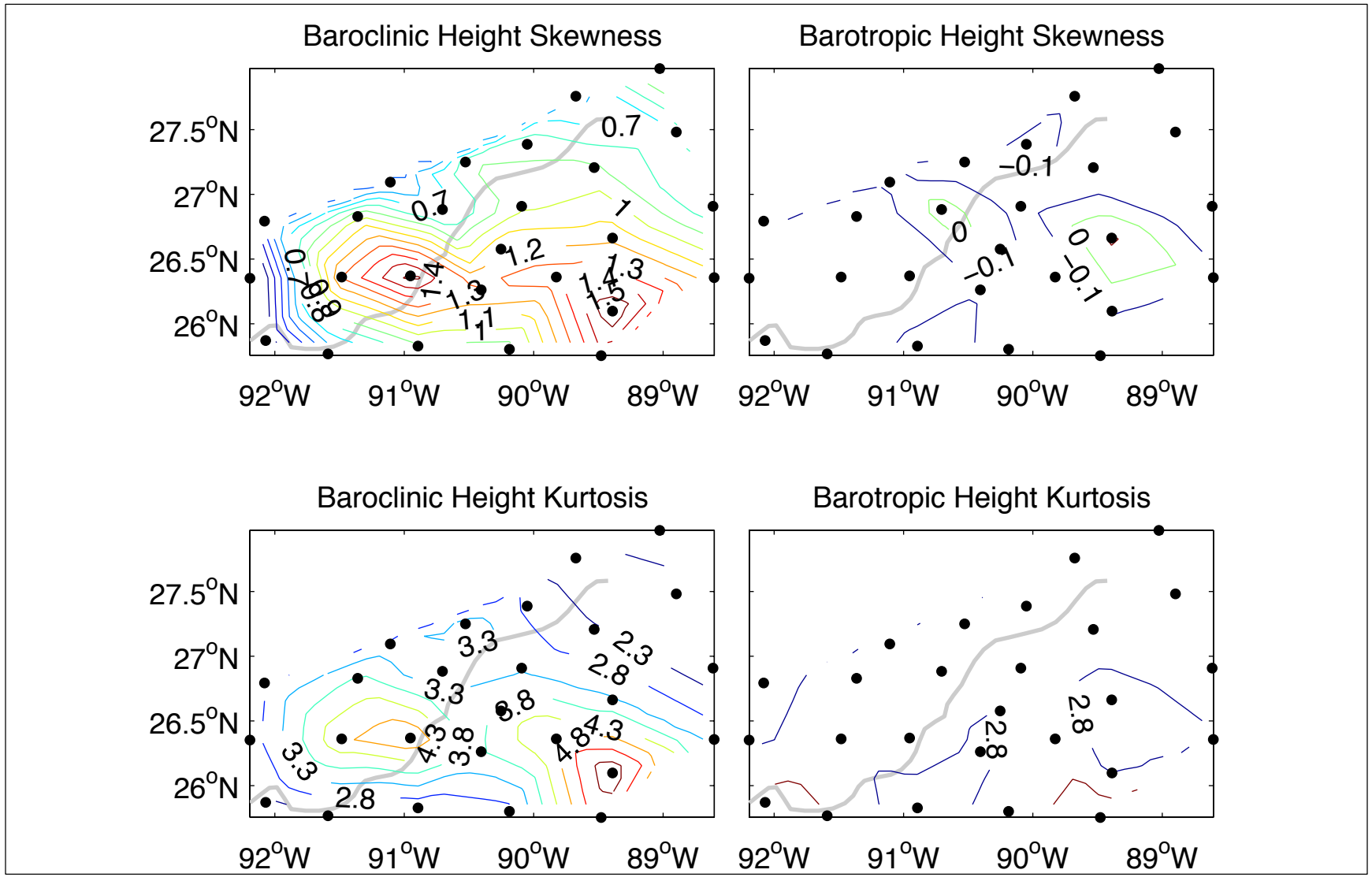

Figure 2.5-2. Skewness (top panels) and kurtosis (bottom panels) for the baroclinic (left panels) and barotopic (right panels) components of sea surface height anomaly. Instrument locations shown with black dots. Thick grey line indicates the Sigsbee Escarpment.

Table 2.5-2.

Sea-surface height, baroclinic and barotropic height statistics determined from Exploratory Study PIES time series.

PIES	Signal	Length (days)	Std (m)	Minimum (m)	Maximum (m)	Skewness	Kurtosis
1	SSH	368	0.070	1.421	1.781	0.325	2.709
	Baroclinic		0.071	1.423	1.778	0.446	2.759
	Barotropic		0.024	-0.062	0.060	-0.067	2.663
2	SSH	369	0.057	1.587	1.858	0.014	2.285
	Baroclinic		0.057	1.581	1.851	-0.072	2.531
	Barotropic		0.024	-0.070	0.065	-0.192	2.709
3	SSH	369	0.058	2.146	2.432	0.130	2.418
	Baroclinic		0.051	2.185	2.405	0.131	2.195
	Barotropic		0.025	-0.095	0.072	-0.461	3.465
4	SSH	368	0.145	2.114	2.838	1.206	4.236
	Baroclinic		0.143	2.160	2.871	1.368	4.862
	Barotropic		0.033	-0.121	0.078	-0.191	3.008
5	SSH	369	0.087	1.579	1.997	0.821	3.470
	Baroclinic		0.083	1.609	1.993	1.008	3.908
	Barotropic		0.023	-0.079	0.063	-0.236	3.007
6	SSH	368	0.087	1.711	2.163	1.254	4.446
	Baroclinic		0.084	1.700	2.135	1.315	4.743
	Barotropic		0.023	-0.082	0.058	-0.393	3.040
7	SSH	368	0.083	2.241	2.598	0.552	2.271
	Baroclinic		0.078	2.254	2.576	0.504	2.275
	Barotropic		0.025	-0.084	0.063	-0.297	3.308
8	SSH	369	0.130	1.148	1.766	0.862	3.596
	Baroclinic		0.123	1.164	1.742	0.893	3.629
	Barotropic		0.021	-0.082	0.050	-0.200	3.030
9	SSH	371	0.131	1.379	1.968	0.625	2.761
	Baroclinic		0.121	1.397	1.953	0.630	2.760
	Barotropic		0.023	-0.086	0.065	0.052	3.062
10	SSH	369	0.136	1.643	2.250	1.501	4.674
	Baroclinic		0.132	1.672	2.240	1.652	5.264
	Barotropic		0.023	-0.077	0.056	-0.294	3.226
11	SSH	194	0.151	2.230	2.772	0.879	2.537
	Baroclinic		0.147	2.259	2.736	0.879	2.446
	Barotropic		0.026	-0.063	0.067	-0.030	2.447
12	SSH	369	0.194	1.120	1.879	0.833	2.718
	Baroclinic		0.191	1.142	1.848	0.871	2.681
	Barotropic		0.025	-0.070	0.073	-0.003	2.927
13	SSH	367	0.191	1.790	2.612	0.964	3.324
	Baroclinic		0.186	1.846	2.614	0.971	3.198
	Barotropic		0.026	-0.085	0.075	-0.143	3.103

Table 2.5-2. Sea-surface height, baroclinic and barotropic height statistics determined from Exploratory Study PIES time series (continued).

PIES	Signal	Length (days)	Std (m)	Minimum (m)	Maximum (m)	Skewness	Kurtosis
14	SSH	361	0.158	1.955	2.682	1.026	3.712
	Baroclinic		0.152	1.988	2.663	1.191	4.033
	Barotropic		0.028	-0.075	0.080	-0.045	2.784
15	SSH	362	0.145	2.181	2.780	1.194	3.513
	Baroclinic		0.147	2.200	2.782	1.316	3.757
	Barotropic		0.031	-0.082	0.080	-0.103	2.690
16	SSH	362	0.130	2.130	2.697	0.566	2.462
	Baroclinic		0.135	2.224	2.778	0.837	2.618
	Barotropic		0.036	-0.105	0.090	-0.142	3.059
17	SSH	194	0.213	1.150	1.926	0.467	1.858
	Baroclinic		0.216	1.176	1.954	0.546	1.972
	Barotropic		0.024	-0.066	0.064	-0.086	2.836
18	SSH	375	0.247	1.689	2.600	0.870	2.296
	Baroclinic		0.249	1.728	2.583	0.917	2.319
	Barotropic		0.025	-0.074	0.068	-0.229	3.080
19	SSH	376	0.195	2.137	2.973	1.099	3.170
	Baroclinic		0.197	2.141	2.999	1.164	3.338
	Barotropic		0.030	-0.080	0.074	0.119	2.541
20	SSH	377	0.149	2.168	2.941	1.669	5.921
	Baroclinic		0.150	2.186	2.967	1.707	6.239
	Barotropic		0.035	-0.106	0.085	-0.072	2.745
21	SSH	377	0.141	2.151	2.927	1.181	4.717
	Baroclinic		0.143	2.205	2.951	1.488	5.690
	Barotropic		0.039	-0.139	0.107	-0.320	3.644
22	SSH	374	0.200	1.232	1.973	0.979	2.750
	Baroclinic		0.201	1.252	2.018	1.042	2.896
	Barotropic		0.025	-0.080	0.065	-0.216	3.163
23	SSH	379	0.287	1.486	2.395	0.666	1.820
	Baroclinic		0.289	1.487	2.466	0.694	1.872
	Barotropic		0.025	-0.082	0.070	-0.191	3.135
24	SSH	378	0.288	1.740	2.695	0.718	1.965
	Baroclinic		0.287	1.779	2.722	0.704	1.931
	Barotropic		0.029	-0.095	0.083	-0.251	3.130
25	SSH	378	0.225	1.973	2.883	1.126	3.158
	Baroclinic		0.226	1.996	2.852	1.145	3.107
	Barotropic		0.039	-0.120	0.095	-0.062	2.743
26	SSH	368	0.091	1.396	1.880	0.401	2.859
	Baroclinic		0.086	1.414	1.862	0.490	3.120
	Barotropic		0.023	-0.088	0.066	-0.097	3.021

2.5.2 Altimeter Sampling Issues

Satellite altimeters provide discrete measurements of SSH along sub-satellite points spaced approximately 5–7 km along groundtracks which repeat every 10, 17 or 35 days for the satellites used during this study (Table 2.5-3). Orbital dynamics determine the space/time sampling pattern achieved on orbit, and there is a trade-off between spatial and temporal resolution when selecting an orbit during the mission design phase of a satellite program [see Parke et al. (1987)]. For single satellite sampling, high spatial resolution is achieved only at the expense of less frequent sampling of the sea surface in time, and vice versa. Unlike ground-based instruments where the sampling rate can be selected to satisfy a specific Nyquist criteria, satellite-based measurement systems in non-geosynchronous orbits have a temporal sampling rate imposed by the orbit selected for the spacecraft. To increase the temporal sampling rate, therefore, either requires the addition of more satellites in the same orbit or a loss of spatial sampling density. Neither option is usually justified from an economic, scientific or operational perspective. Anecdotally, when additional sampling became available from the TOP/POS after the commissioning phase of the TOP/POS and Jason-1 tandem mission, the decision was made to increase the spatial sampling density (Fu et al., 2003), and, by default, accept the existing level of temporal aliasing of the 10-day repeat sampling.

Table 2.5-3.

Current satellite altimeter mission exact-repeat periods and periods associated with the Nyquist sampling frequency.

Satellite	Approximate Repeat	Repeat Period (days)	Nyquist Sampling Period (days)
TOPEX/Poseidon	10-day	9.9156	19.8313
ERS-2	35-day	35	70
Geosat Follow-On	17-day	17.0505	34,1010
Jason-1	10-day	9.9156	19.8313
Envisat	35-day	35	70

The temporal aliasing of ocean signals by satellite altimeter sampling can be addressed using the high-rate, in-situ SSH data provided by PIES measurements. Hendry et al. (2002) performed the first study along these lines using PIES data collected within the North Atlantic Current in the Newfoundland Basin. They found that the time scales of motion in this region are such that 86-95% of the subinertial period SSH variability is not aliased by the approximately 10-day TOP/POS repeat period sampling. An earlier study using only bottom pressure records was performed by Gille and Hughes (2001), but would not be appropriate in the Newfoundland basin or the GOM where the time scales associated with the bottom pressure variability is not representative of the time scales of the SSH variability.

Following the methodology of Hendry et al. (2002), a similar assessment was made of the SSH signal in the Exploratory Study region for the approximately 10-day, 17-day and 35-day repeat period sampling available from the ongoing satellite altimeter missions. We derived power spectra for each of the SSH time series, barotropic, baroclinic and combined, and calculated the

percentage of cumulative power in the spectra with the Nyquist frequency associated with the 10-day, 17-day and 35-day repeat periods. These periods are tabulated in Table 2.5-3. At the same time, we calculated the half-power period, $T_{0.5}$, defined as the 50% point of the cumulative power spectra, which will be discussed in more detail in Section 5.2 when we consider the time scales of the SSH signals within the study region.

Figures 2.5-3, 2.5-4 and 2.5-5 show maps of the unaliased variance associated with 10-day, 17-day and 35-day sampling periods in the study region for the present altimeter missions from the barotropic, baroclinic and combined SSH signals, respectively. Summary statistics are tabulated in Table 2.5-4**.** Tabulated values for each PIES sites are listed in Table 2.5-5.

Table 2.5-4.

Unaliased variance statistics for 10-day, 17-day and 35-day exact repeat sampling of the barotopric, baroclinic and combined SSH signals.

Location	**Barotropic Signal Mean (%)**			**Baroclinic Signal Mean (%)**			**Total SSH Signal Mean (%)**		
Repeat:	**10-day**	**17-day**	**35-day**	**10-day**	**17-day**	**35-day**	**10-day**	**17-day**	**35-day**
all stations	59	47	37	97	93	78	95	92	78
above Escarpment	56	45	39	96	93	75	94	91	75
below Escarpment	61	49	36	97	93	80	96	93	79
	Maximum (%)			**Maximum (%)**			**Maximum (%)**		
Repeat:	**10-day**	**17-day**	**35-day**	**10-day**	**17-day**	**35-day**	**10-day**	**17-day**	**35-day**
all stations	77	60	45	99	98	93	99	98	93
above Escarpment	60	50	42	99	98	90	97	96	90
below Escarpment	77	60	45	99	98	93	99	98	93
	Minimum (%)			**Minimum (%)**			**Minimum (%)**		
Repeat:	**10-day**	**17-day**	**35-day**	**10-day**	**17-day**	**35-day**	**10-day**	**17-day**	**35-day**
all stations	44	38	29	92	86	54	87	82	54
above Escarpment	51	42	36	92	86	54	87	82	54
below Escarpment	44	38	29	93	87	56	92	85	56

Note: PIES stations above the Escarpment are 1, 2, 3, 5, 6, 8, 9, 10, 26, 12, and 17. The stations below are 4, 7, 11, 13, 15, 16, 14, 18, 19, 20, 21, 22, 23, 24, and 25.

As expected, the aliasing of the barotropic SSH signal was the most severe because of the shorter time scales associated with this signal. The 10-day period unaliased variance mean value over the array was 59% and ranged from a minimum of 44% at PIES 10 & 25 to a maximum of 77% at PIES 16. With 35-day sampling, the mean value decreased to 37% and ranged from a minimum of 29% at PIES 25 to a maximum of 45% at PIES 14. The change in the spatial structure of the aliased signal is dramatic in going from 10-day or 17-day sampling to only every 35-day sampling. This change was associated with aliasing of the TRW signal in the 34 to 70 day period band. The overall low mean values at each of these sampling frequencies are attributable to the array-wide common mode in the bottom pressure signal that exhibits frequencies of about 14 to 16 days.

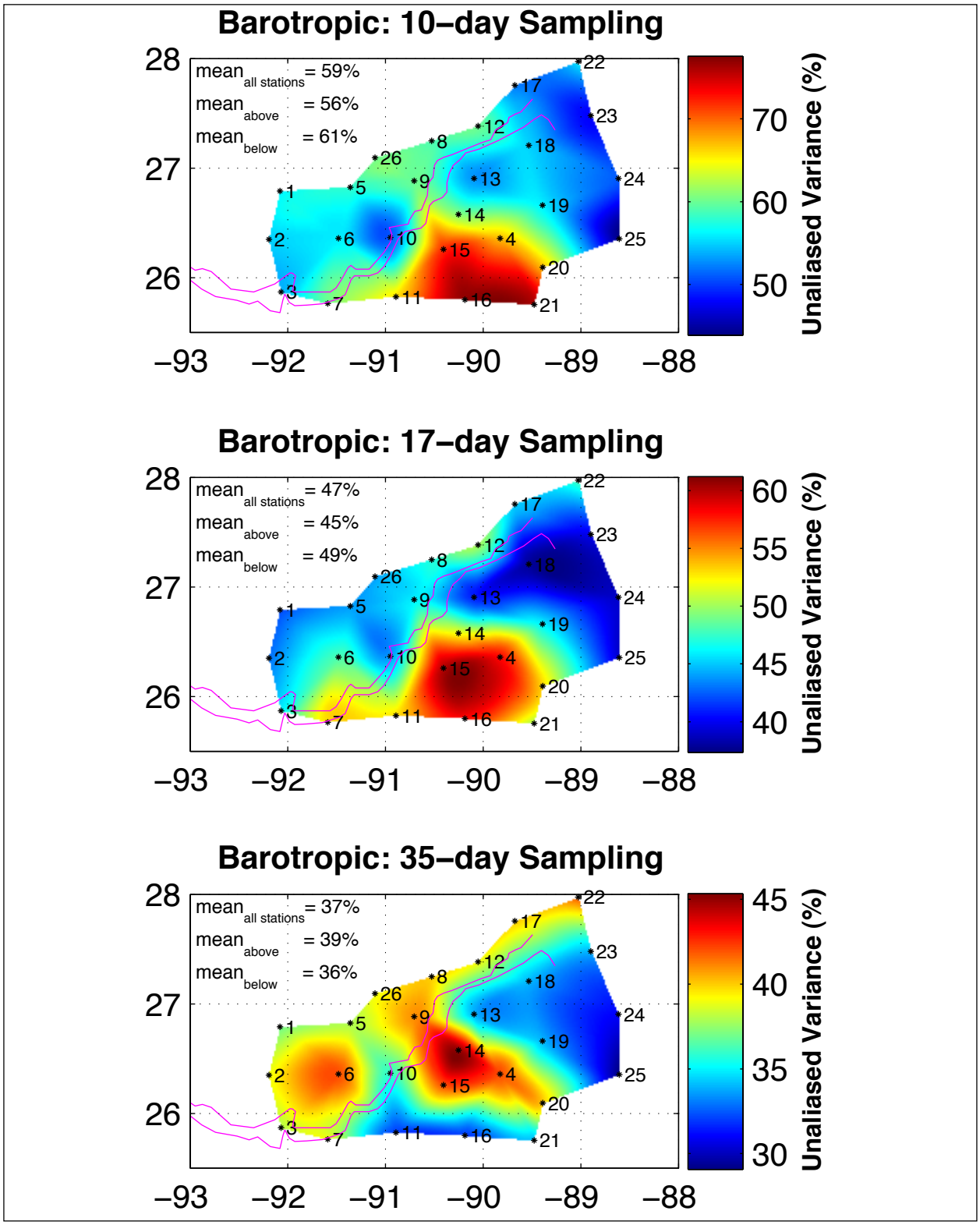

Figure 2.5-3. Maps of PIES barotropic SSH unaliased variance for 10-day, 17-day and 35-day sampling.

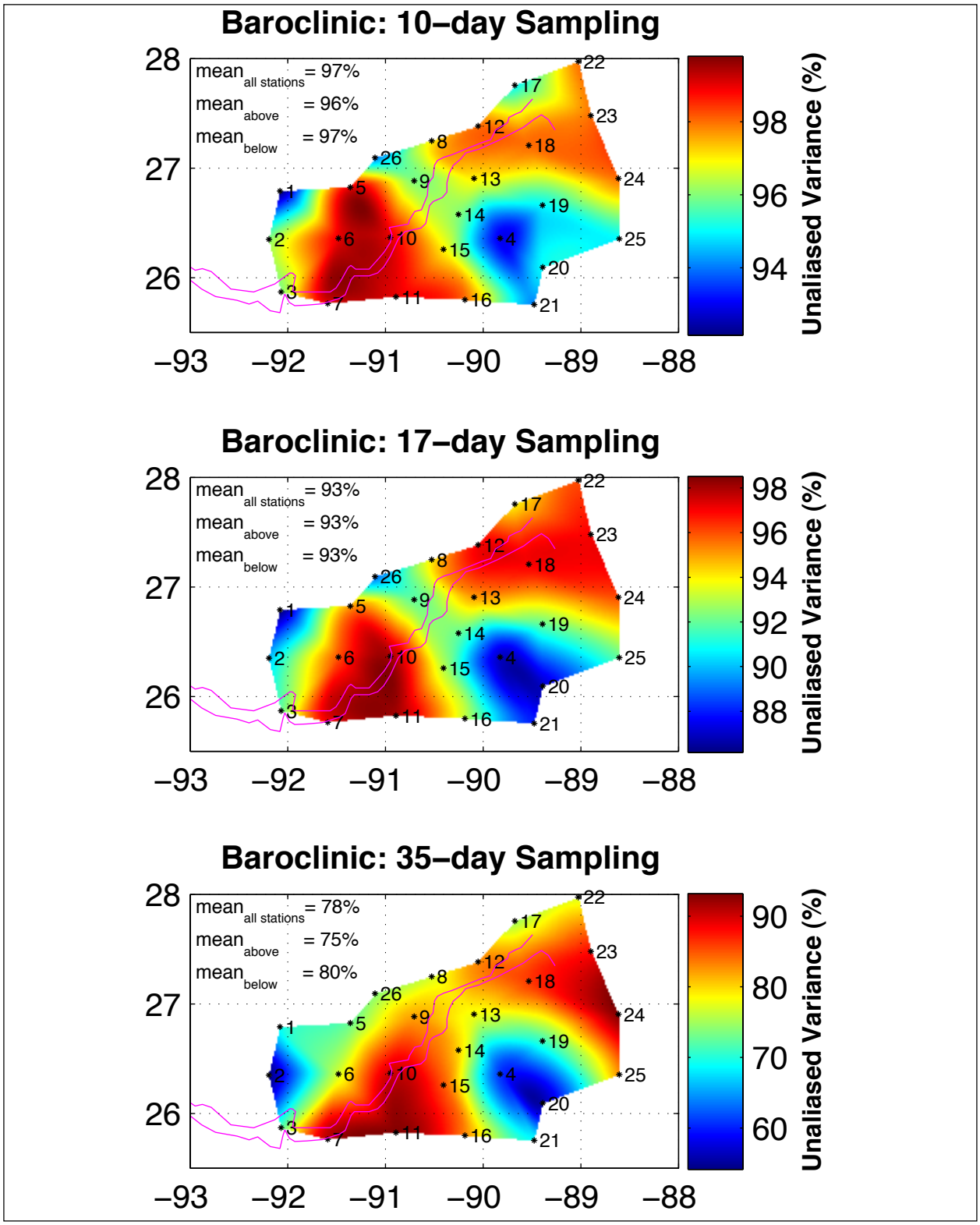

Figure 2.5-4. Maps of PIES baroclinic SSH unaliased variance for 10-day, 17-day and 35-day sampling.

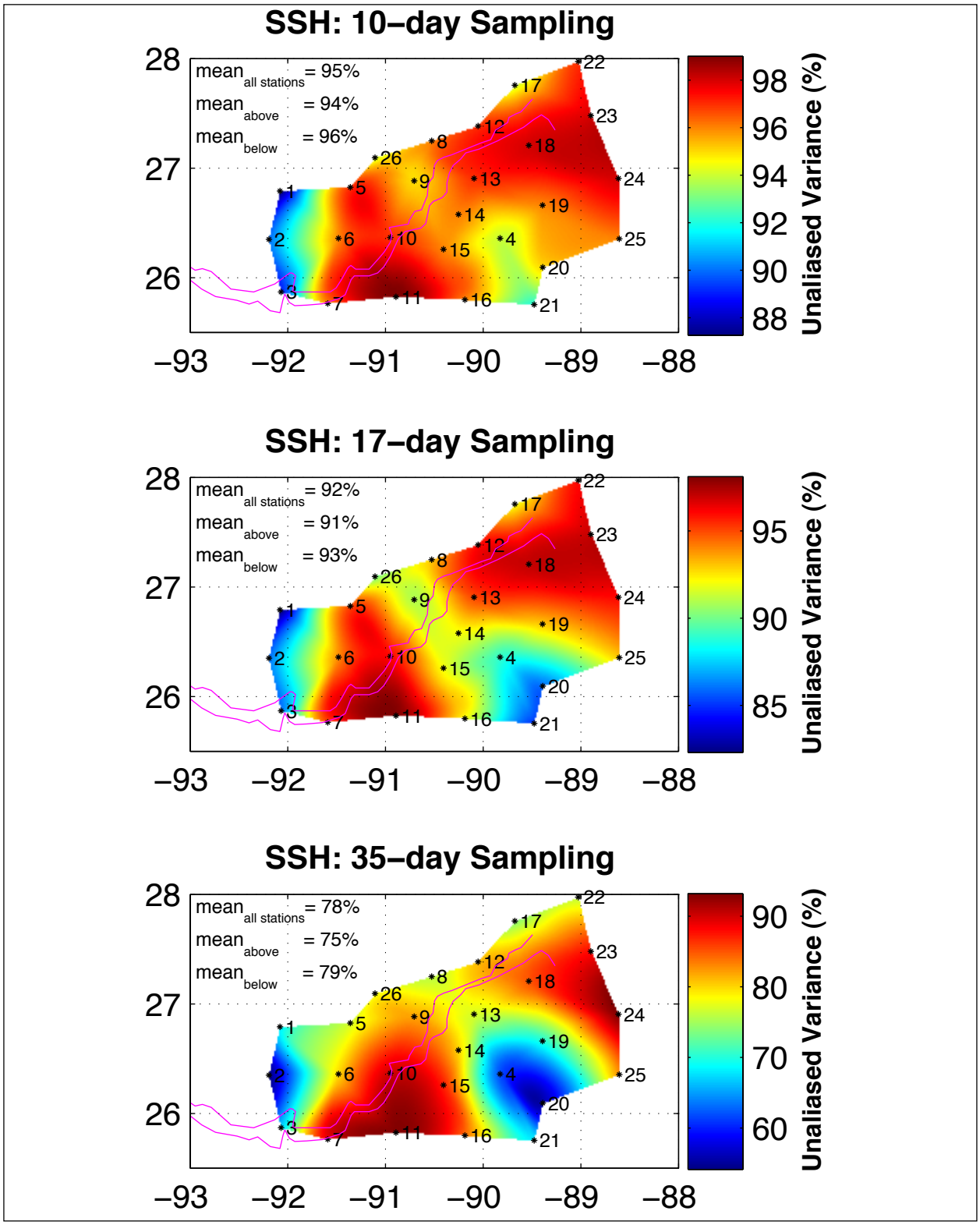

Figure 2.5-5. Maps of PIES SSH unaliased variance for 10-day, 17-day and 35-day sampling.

Table 2.5-5.

PIES SSH, baroclinic and barotropic statistics and percent of unaliased variance measured by satellites in 10-day, 17-day and 35-day exact repeat orbits.

PIES	Signal	Length (days)	Std (m)	$T_{0.5}$ (days)	Unaliased Variance (%)		
					10-day	17-day	35-day
1	SSH	368	0.070	146	87	82	68
	Baroclinic		0.071	120	92	86	69
	Barotropic		0.024	15.4	56	42	37
2	SSH	369	0.057	64	90	86	54
	Baroclinic		0.057	64	96	90	54
	Barotropic		0.024	15.1	55	43	39
3	SSH	369	0.058	102	89	86	67
	Baroclinic		0.051	108	96	92	72
	Barotropic		0.025	14.9	54	46	38
4	SSH	368	0.145	81.9	94	89	62
	Baroclinic		0.143	73.1	93	87	61
	Barotropic		0.033	30.1	67	58	42
5	SSH	369	0.087	114	97	95	77
	Baroclinic		0.083	102	99	95	73
	Barotropic		0.023	16.9	58	44	38
6	SSH	368	0.087	186	96	94	80
	Baroclinic		0.084	171	99	96	77
	Barotropic		0.023	16.8	56	48	42
7	SSH	368	0.083	228	96	95	89
	Baroclinic		0.078	256	99	97	91
	Barotropic		0.025	17.4	60	53	39
8	SSH	369	0.130	293	96	93	76
	Baroclinic		0.123	293	97	94	77
	Barotropic		0.021	16.4	59	47	40
9	SSH	371	0.131	256	95	91	82
	Baroclinic		0.121	256	96	92	82
	Barotropic		0.023	16.9	60	46	41
10	SSH	369	0.136	256	97	96	90
	Baroclinic		0.132	256	99	98	90
	Barotropic		0.023	15.2	51	44	36
11	SSH	194	0.151	256	99	98	93
	Baroclinic		0.147	256	99	98	93
	Barotropic		0.026	26.3	66	53	32
12	SSH	369	0.194	341	97	96	81
	Baroclinic		0.191	341	98	97	83
	Barotropic		0.025	17.5	60	50	39
13	SSH	367	0.191	293	97	95	77
	Baroclinic		0.186	341	97	95	78
	Barotropic		0.026	16.3	53	41	34

Table 2.5-5. PIES SSH, baroclinic and barotropic statistics and percent of unaliased variance measured by satellites in 10-day, 17-day and 35-day exact repeat orbits (continued).

PIES	Signal	Length (days)	Std (m)	$T_{0.5}$ (days)	Unaliased Variance (%)		
					10-day	17-day	35-day
14	SSH	361	0.158	256	96	92	80
	Baroclinic		0.152	256	96	92	80
	Barotropic		0.028	19.7	61	52	45
15	SSH	362	0.145	256	96	92	87
	Baroclinic		0.147	256	97	93	85
	Barotropic		0.031	33	72	60	42
16	SSH	362	0.130	293	96	92	84
	Baroclinic		0.135	256	98	93	83
	Barotropic		0.036	33.6	77	58	32
17	SSH	194	0.213	228	94	92	74
	Baroclinic		0.216	228	95	94	75
	Barotropic		0.024	13.8	52	45	40
18	SSH	375	0.247	341	98	97	85
	Baroclinic		0.249	341	98	97	86
	Barotropic		0.025	14.9	55	38	34
19	SSH	376	0.195	256	96	93	70
	Baroclinic		0.197	256	95	92	71
	Barotropic		0.030	16.9	56	46	34
20	SSH	377	0.149	60.2	95	86	56
	Baroclinic		0.150	60.2	95	87	56
	Barotropic		0.035	24.4	67	53	40
21	SSH	377	0.141	108	92	85	68
	Baroclinic		0.143	102	94	88	69
	Barotropic		0.039	32	76	50	34
22	SSH	374	0.200	293	97	96	76
	Baroclinic		0.201	293	98	96	77
	Barotropic		0.025	15.1	56	48	42
23	SSH	379	0.287	410	98	97	88
	Baroclinic		0.289	410	98	97	88
	Barotropic		0.025	12.3	48	40	34
24	SSH	378	0.288	512	98	96	93
	Baroclinic		0.287	512	98	96	93
	Barotropic		0.029	13.5	51	39	31
25	SSH	378	0.225	256	96	93	83
	Baroclinic		0.226	256	95	92	83
	Barotropic		0.039	14.2	44	39	29
26	SSH	368	0.091	158	94	90	78
	Baroclinic		0.086	128	94	89	74
	Barotropic		0.023	16.8	60	44	39

The unaliased variance of the baroclinic and total SSH signal was much higher than the barotropic only case because of the dominance of the longer period baroclinic signals in the study region, and because the baroclinic component of the SSH was much more energetic than the barotropic. Still, there were large differences between the 10-day and 35-day patterns, while the 10-day and 17-day patterns were more similar. The baroclinic 10-day period unaliased variance mean value over the array was 97% and ranged from a minimum of 92% at PIES 1 to a maximum of 99% at PIES 5, 6, 7 10 & 11. The 35-day sampling mean value decreased to 78% and ranged from a minimum of 54% at PIES 2 to a maximum of 93% at PIES 11 & 24. The combined baroclinic and barotropic SSH signal shows similar patterns. The SSH 10-day period unaliased variance mean value over the array was 95% and ranged from a minimum of 87% at PIES 1 to a maximum of 99% at PIES 5, 6, 7 10 &11. The 35-day sampling mean value decreased to 78% and ranged from a minimum of 54% at PIES 2 to a maximum of 93% at PIES 11 & 24.

In summary, 87% to 99% of the subinertial period SSH variability in the Exploratory Study region was unaliased by the approximately 10-day TOP/POS repeat period sampling, which is comparable to the 86-95% estimated from the Newfoundland Basin array by Hendry et al. (2002). These results show, however, that there can be significant aliasing of the GOM SSH signal in satellite altimetery even with the dominance of the longer period baroclinic signals in the deepwater of the Gulf. The degree to which this affected the space/time interpolated maps of SSH needs to be investigated in more detail. It is also unclear whether the weak surface signature of TRWs could be mapped effectively using satellite altimetry given the presence of the strong baroclinic SSH and the difficulties associated with aliasing of the signal.

More useful for the evaluation of an altimeter-derived estimate of SSH is the ratio of the unaliased variance to the aliased variance of the SSH signal, which is an estimate of the signal-to-noise (SNR) ratio of a perfect on-orbit measurement system (Figure 2.5-6). Note that we do not consider the barotropic and baroclinic components separately because they cannot be distinguished from on-orbit measurements alone. Also, the “noise” in the unaliased to aliased SNR is colored noise that is associated with undersampled geophysical signals that are very difficult to remove without excessive smoothing or filtering of the along-track data before interpolation. This is the primary reason that the requirement of uniform errors and wavelength/frequency resolution satisfying the Nyquist criteria as proposed by Greenslade et al. (1997) for gridded altimeter products is unrealistic in practice.

The SNR in the study region was very good for 10-day and 17-day altimetric sampling. The 35-day sampling is more problematic showing SNR ratios consistently as low as 2 over much of the array, which would make it difficult to distinguish between signal and aliased signals at that sampling frequency. Quantifying the SNR for combined sampling by multiple altimeters will be reported in future work.

2.5.3 Comparison of SSH and SSH Slope Anomalies

The CCAR mesoscale SSH gridded altimeter data product that was distributed and used for data synthesis activities in this report was evaluated by comparison with the coincident PIES SSH.

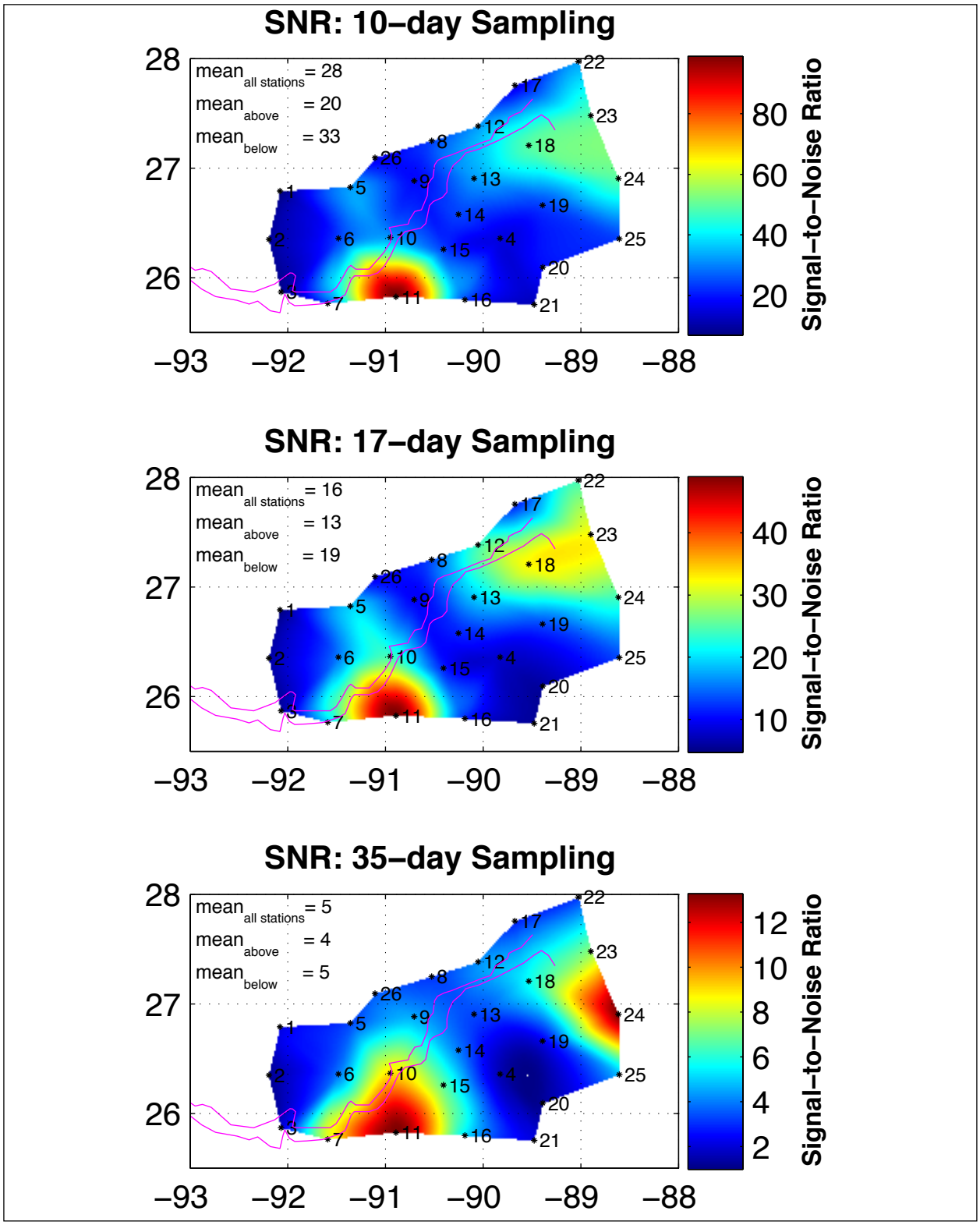

Figure 2.5-6. Maps of PIES SSH signal-to-noise ratio (SNR) for 10-day, 17-day and 35-day sampling. SNR is estimated from the ratio of unaliased to aliased variance.

The spatial map of the CCAR/PIES correlation is shown in Figure 2.5-7. Correlations were good with an overall mean correlation of 82%. Lowest correlations were found above the Escarpment and along the western edge of the study array. SSH slopes between PIES stations were also compared to the coincident slopes calculated from the CCAR mesoscale product. The overall mean correlation was 80%.

We also compared the along-track detrended SSH data for the altimeters to the coincident PIES SSH collected along the respective groundtracks. Figure 2.5-8 shows scatterplots and correlation values of PIES time series points with the collocated altimeter along-track data values. All five satellites coincident with the study program are shown: Envisat, ERS-2, GFO, Jason and TOP/POS. The correlations ranged from 56% (TOP/POS) to 81% (GFO), with four satellites in the range of correlation values from 72% to 81%. Note that these values are very sensitive to the along-track smoothing/gridding employed to interpolate the raw sub-satellite measurement points to a reference ground track. The CCAR gridding technique employs no smoothing of the along-track data and linear interpolation between sub-satellite points, which was consistently applied to all of the along-track data from each satellite. The objective analysis employed to interpolate the data to a regular space/time gird smoothed the along-track data, which is why the gridded product correlations with the PIES time series was much higher than the along-track correlations. The low correlation found between the TOP/POS along-track and PIES SSH data may be residual geoid error caused by referencing the along-track data to the GSFC mean sea surface, which contains no along-track sampling along the interleaved TOP/POS orbit. The coincident PIES data will be very useful for identifying, isolating and fixing such problems in the altimetry processing.

Our ongoing work is directed toward improving the CCAR SSH product by using optimal interpolation techniques and space/time correlation functions tuned to the SSH variability in the GOM. The ultimate goal is to combine altimeter and PIES SSH in a single data product exploiting the full sampling capabilities of both systems.

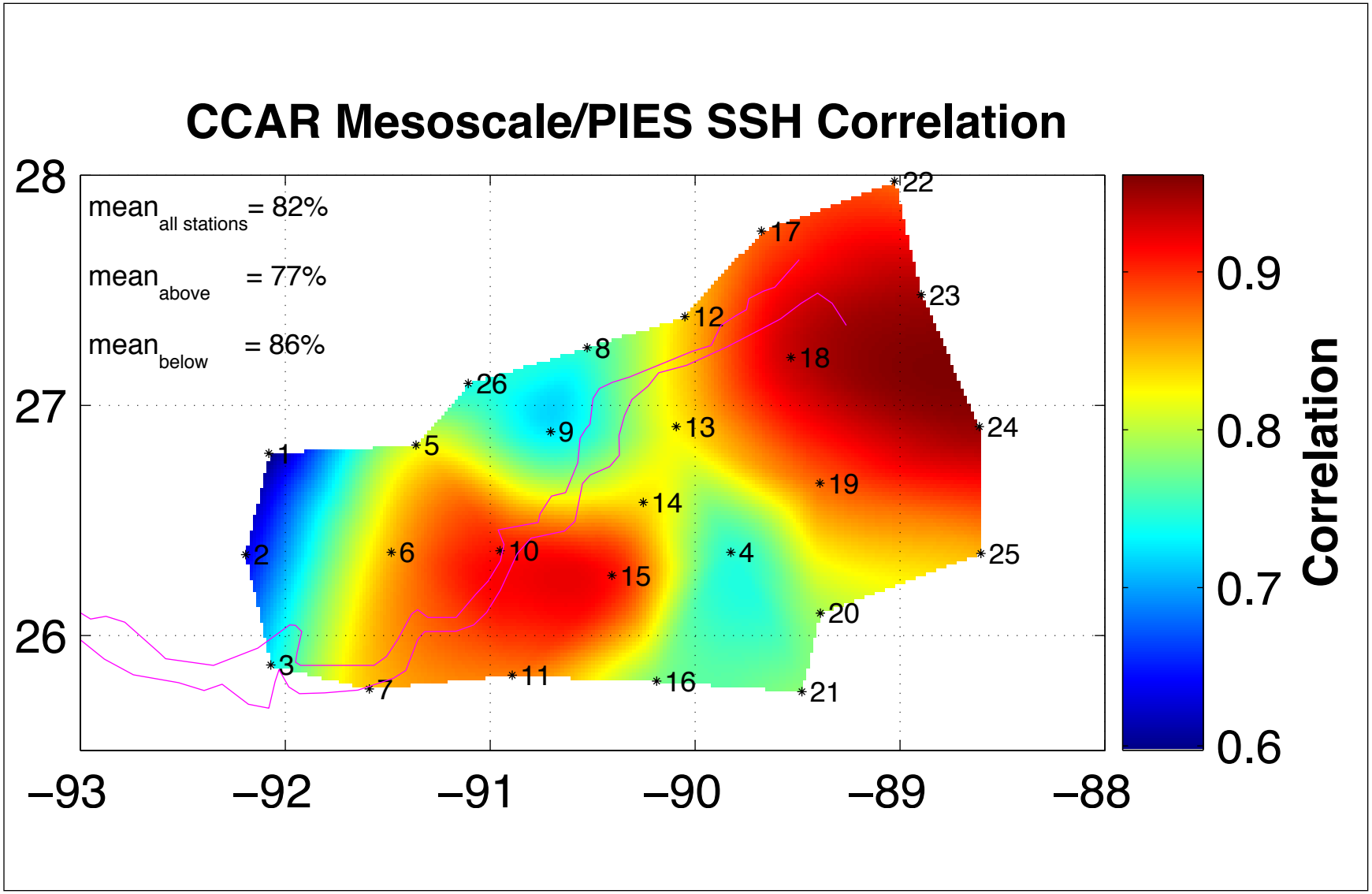

Figure 2.5-7. Spatial map of the CCAR/PIES SSH correlation. Average correlation of CCAR gridded mesoscale SSH data product at PIES station 1 with collocated PIES time series is 82%.

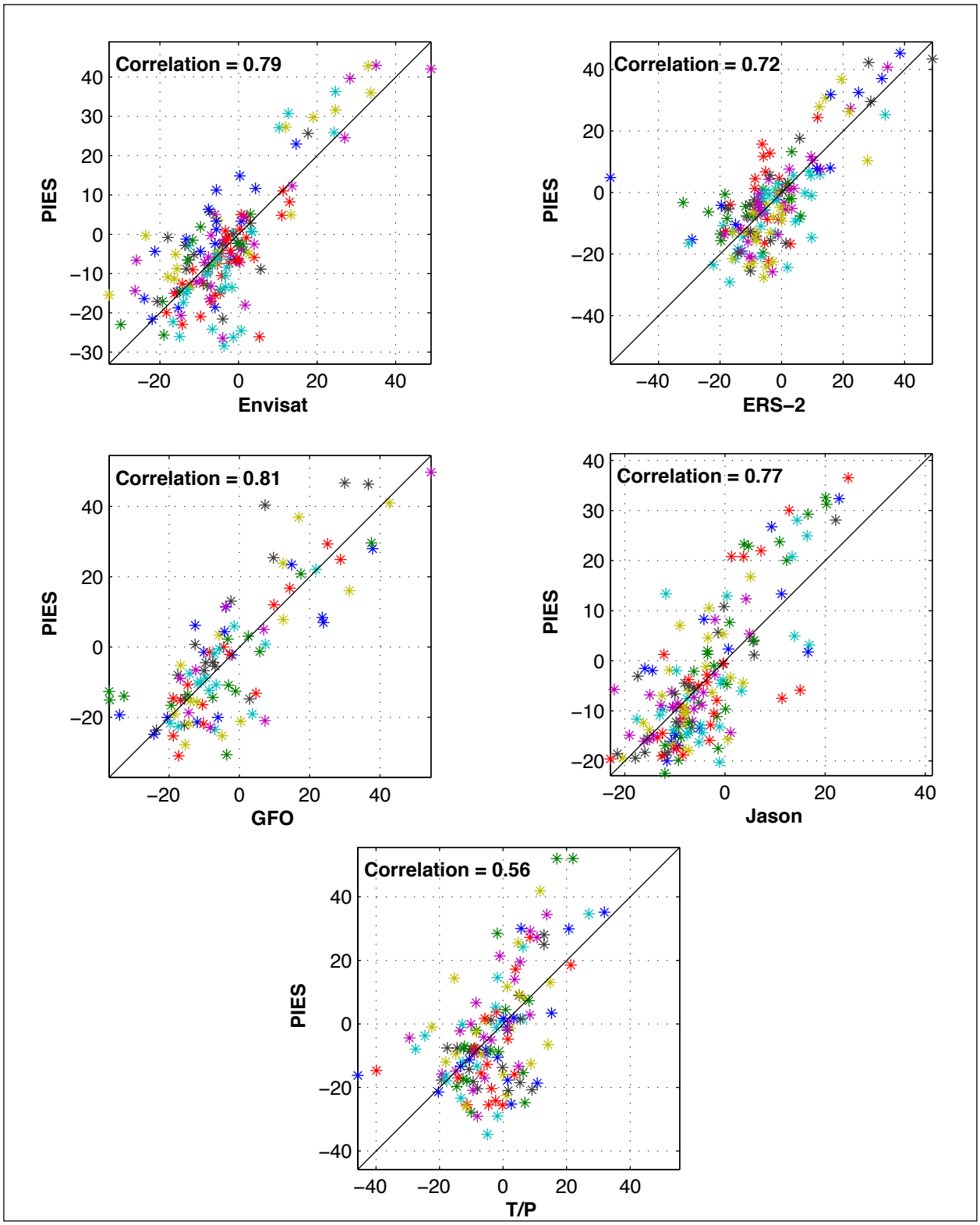

Figure 2.5-8. Scatterplot and correlation values of PIES time series points located on altimeter groundtracks with the coincident points from the along-track detrended altimeter data. Results derived from all five satellites coincident with the study program are shown: Envisat, ERS-2, GFO, Jason and T/P.

3.0 GULFWIDE AND HISTORICAL PERSPECTIVE

This study provides a broad base characterization of conditions and dynamic processes that occur in the present north-central slope study area. To put the present data and insights in a longer time and larger spatial context, Section 3 material provides a basin-wide and historical perspective with in which the study data can be viewed and evaluated.

3.1 Upper Ocean Circulation

The Loop Current (LC) dominates upper ocean circulation in the eastern and central Gulf of Mexico (GOM), therefore, no description of observations in the Exploratory Study region is complete without accounting for the position and movement of the LC and associated eddies. In this section, an historical perspective is used to place Gulfwide, upper ocean circulation documented during the Exploratory Study in the context of expected or "typical" conditions in the study area. Continuous altimeter mapping of the sea-surface height (SSH) in the GOM since 1993 provides the basis for such an historical perspective. Using available time series, the position of the LC and individual LC eddies from 1 January 1993 through 1 July 2004 for comparison with similar estimates made during the Exploratory Study interval, 1 April 2003 through 31 March 2004.

3.1.1 Remote Sensing Overview

Sea-Surface Temperature (SST) and ocean color images overlaid with SSH contours provide a synoptic view of the Gulf of Mexico ocean surface thermal and color patterns associated with the altimeter-inferred circulation during the Exploratory Study. We highlight two satellite images with SSH overlaid to give a basic overview of the LC eddy separation events that occurred during the study time period. Figures 3.1-1 and 3.1-2, respectively, show Eddies Sargassum and Titanic just after separating from the LC. Separation is defined as the final detachment of an eddy from the LC with no later reattachment. Eddy Sargassum separated from the LC on 5 August 2003, 17 months after the prior eddy separation event, and was followed five months later by the separation of Eddy Titanic on 31 December 2003. Eddy Sargassum separated during the summer so the surface circulation pattern is best observed in ocean color. Figure 3.1-1 shows the 8-day composite MODIS image overlaid with SSH contours from 9 August 2003, which is near the midpoint of the composite interval and just a few days after separation of the eddy. Eddy Sargassum, an unnamed anticyclone and the LC are identified in the image. Eddy Titanic separated from the LC during winter so SST imagery provides the best contrast for identifying upper ocean features at that time. Figure 3.1-2 shows a 3-day composite SST image overlaid with the SSH contour plot from the midpoint date of the composite, 3 January 2004, which was a few days after eddy separation.

Eddy separation events are identified by the breaking of the 17-cm SSH contour that closely tracks the edge of the high-velocity core of the LC. This is an objective method for tracking the LC and detecting LC-eddy separation events that gives separation periods comparable to those determined by subjective tracking methods (Leben, 2005). We quote an exact day of separation determined by the breaking of the tracking contour; however, estimated uncertainties in separation period may be as great as one month. Although eddies may detach from and reattach

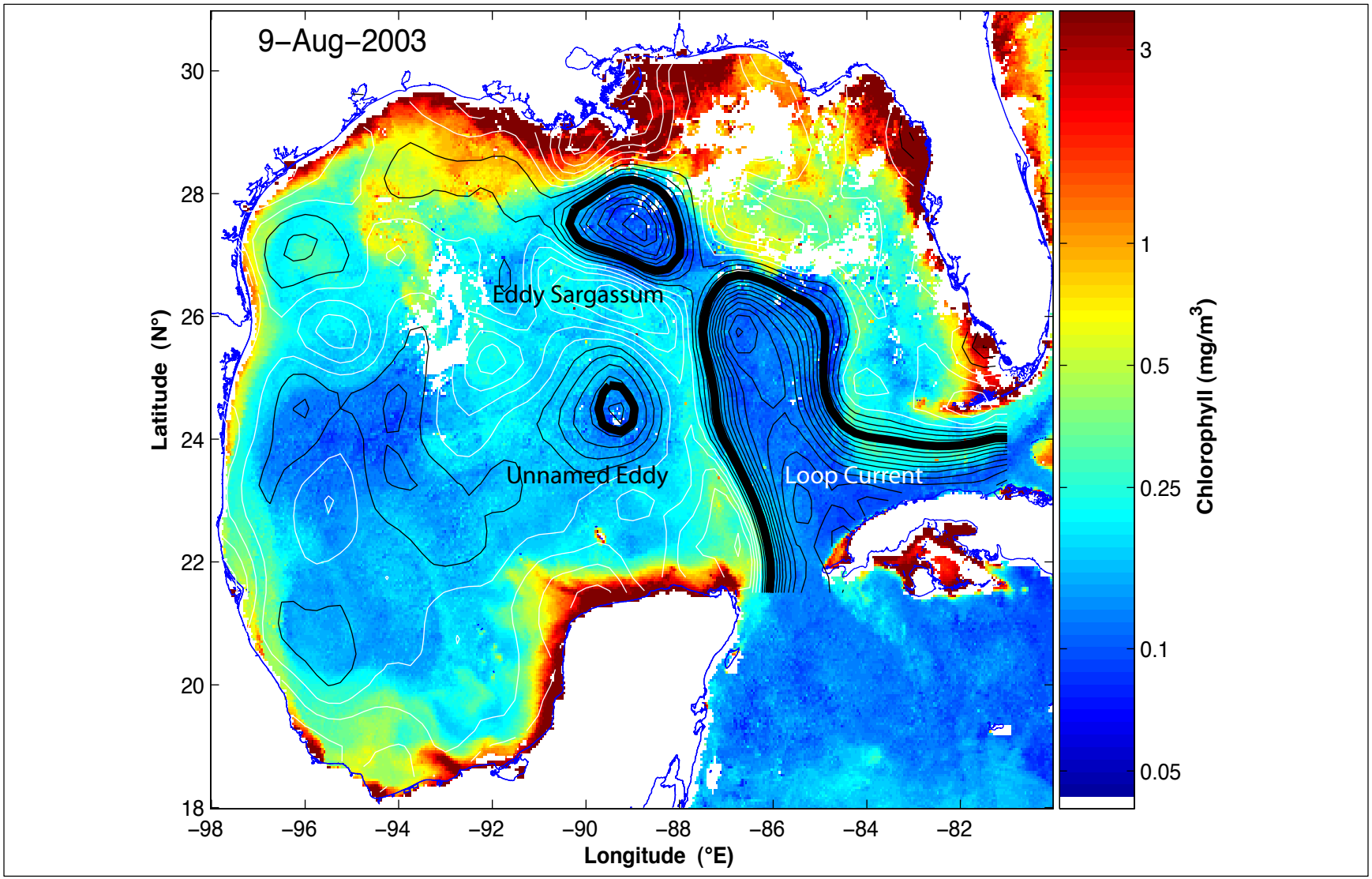

Figure 3.1-1. Eight-day composite image of chlorophyll concentration overlaid with SSH contour map from 9 August 2003 showing recent separation of Eddy Sargassum from the Loop Current. The SSH contour increment is 5 cm. Black contours are positive and white contours are negative. The 17-cm Loop Current and eddy tracking contour is shown by the thick black line.

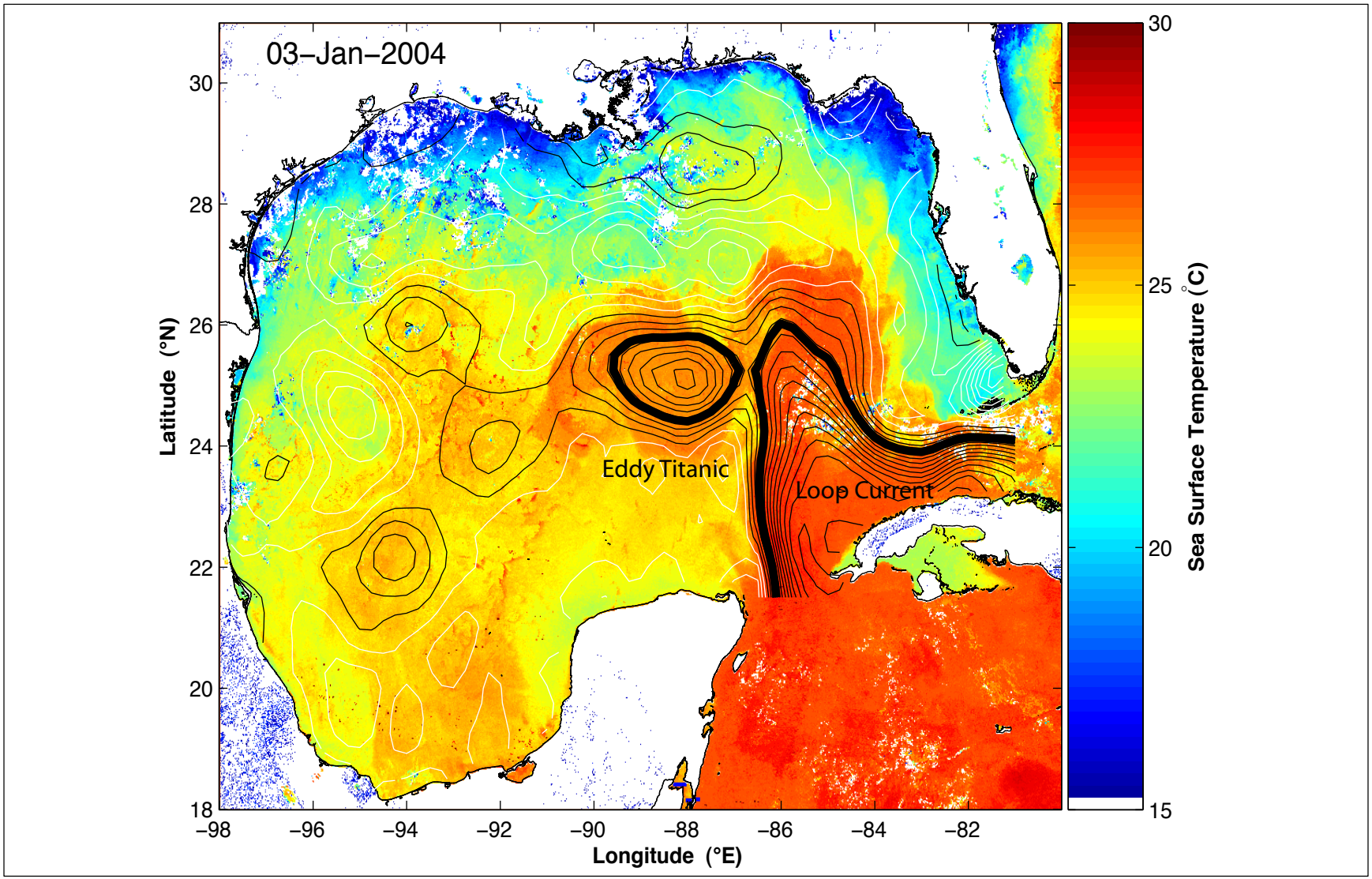

Figure 3.1-2. Three-day composite SST image overlaid with SSH contour map from 3 January 2004 showing recent separation of Eddy Titanic from the Loop Current. The SSH contour increment is 5cm. Black contours are positive and white contours are negative. The 17-cm Loop Current and eddy tracking countour is shown by the thick black line.

to the LC during intrusion, the ultimate detachment or separation occurs most frequently at intervals of about 6, 9 and 11.5 months based on the available historical measurements (Sturges and Leben, 2000). These two LC eddy separation events were the dominant upper ocean events affecting the study array during the field measurements. In the following sections, these events are compared and contrasted with those observed in the historical record to place the Exploratory Study in its historical context.

3.1.2 Loop Current Metrics and Statistics

The objective tracking of the LC using the 17-cm SSH contour also allows detailed monitoring of LC metrics such as extent, boundary length, enclosed area, volume and circulation. In previous studies (Hamilton et al., 2000; Leben et al., 2002; Leben, 2005), this objective tracking technique was developed and validated through qualitative and quantitative comparisons with satellite imagery and by direct comparisons with published subjective tracking results. The 11.5-year altimetry time series (1 January 1993 through 1 July 2004) of altimeter-derived LC metrics and statistics will be used to examine typical conditions and extreme events during the Exploratory Study.

The altimeter data set and objective tracking technique used to estimate the altimeter-derived LC metrics is described in detail in Leben (2005). The data set used in this study is similar to that used for the revised estimates of the frequency of LC eddy-shedding events published in Sturges and Leben (2000), with two notable improvements. First, we have reprocessed the historical altimeter data using a new mean surface as described in Leben et al. (2002). Second, to improve sampling during intervals when data were available, altimeter observations from Jason-l, Geosat Follow-on (GFO) and TOPEX/POSEIDON (TOP/POS) tandem mission have been incorporated in the analysis.

The procedure for computing the metrics from the SSH fields has been automated by a MATLAB® program that accesses a GOM-altimeter data archive and computes the values. Daily values for each metric are computed using the following algorithm:

1. Load the 0.25° gridded SSH field and generate the coordinates of the 17-cm contours within the Gulf (Leben, 2005).

2. Identify the LC core, which is defined as the continuous 17-cm contour that enters the GOM through the Yucatan Channel and exits through the Florida Straits.

3. Find the maximum west longitude and north latitude coordinates to determine the extent of westward and northward penetration of the LC.

4. Compute the length of the LC by summing the distances between the coordinates on the 17-cm contour.

5. Identify all 0.25° grid cells bounded by the 17-cm contour and compute the total LC area by summing the areas of the individual cells.

6. Estimate the LC volume, assuming a one and a half-layer ocean and a reduced gravity approximation, by evaluating the following area integral over the region bounded by the 17-cm contour:

$$\iint \frac{g}{g'} h dx dy$$

where h is the sea-surface height; g is the acceleration of gravity; and g' the reduced gravity. (A value of 0.03 $m \cdot s^{-2}$ was used for g'.)

7. Estimate the LC circulation by the line integral of the geostrophic velocity along the 17-cm contour:

$$\oint \vec{V} \cdot ds = \int u dx + \int v dy$$

where u and v are the geostrophic velocity components and dx and dy are the coordinate spacing in the east/west and north/south directions, respectively. The geostrophic velocity components at the midpoint locations were found by bilinear interpolation from the gridded geostrophic velocity components computed from the height field. (The sign convention employed here is such that the anticyclonic vorticity associated with the LC is positive and therefore in positive correlation to the other metrics.)

The 11.5-year time series of LC maximum latitude/longitude extension and length are shown in Figure 3.1-3 and area, volume, and circulation in Figure 3.1-4 with the time period spanning the Exploratory Study highlighted in black. Separate time-series plots of the respective metrics during the program field measurements (1 April 2003 through 31 March 2004) are shown in Figures 3.1-5 and 3.1-6. Histograms of each metric are shown in the lower panels of each of the figures.

Histograms calculated for the interval are overlaid on the histograms from the historical record (Figure 3.1-7) to allow direct comparison of the distribution of the LC metrics during the project and historical time periods. In general, the distributions are quite different, which is expected given the relatively short time interval of the observational program and the energetic LC events that occurred therein. More surprising, however, is how similar the mean LC metric values are for the two disparate time periods. The spatial structure of the mean LC position as determined by the 17-cm tracking contour is also nearly identical in the mean SSH height fields computed by averaging the daily SSH maps over the 1-year program time period and by averaging over the entire 11.5-year altimeter record (Figure 3.1-8). This similarity may also be a coincidence since the statistical independence from differing sampling intervals has not been examined further. The summary statistics for the altimeter-derived LC metrics are shown in Table 3.1-1 for each of the LC metrics and both time periods. This possible stationarity presumably was caused by the topographic confinement of the current and the fundamental physical control of the dominant eddy-shedding cycles on its mean dynamics.

The stationarity of the LC is further supported by the good agreement between altimeter-derived LC statistics and those based on earlier in-situ and satellite radiometry estimates. These comparisons were reported in Hamilton et al. (2000) and Leben (2005). The prealtimetry in-situ

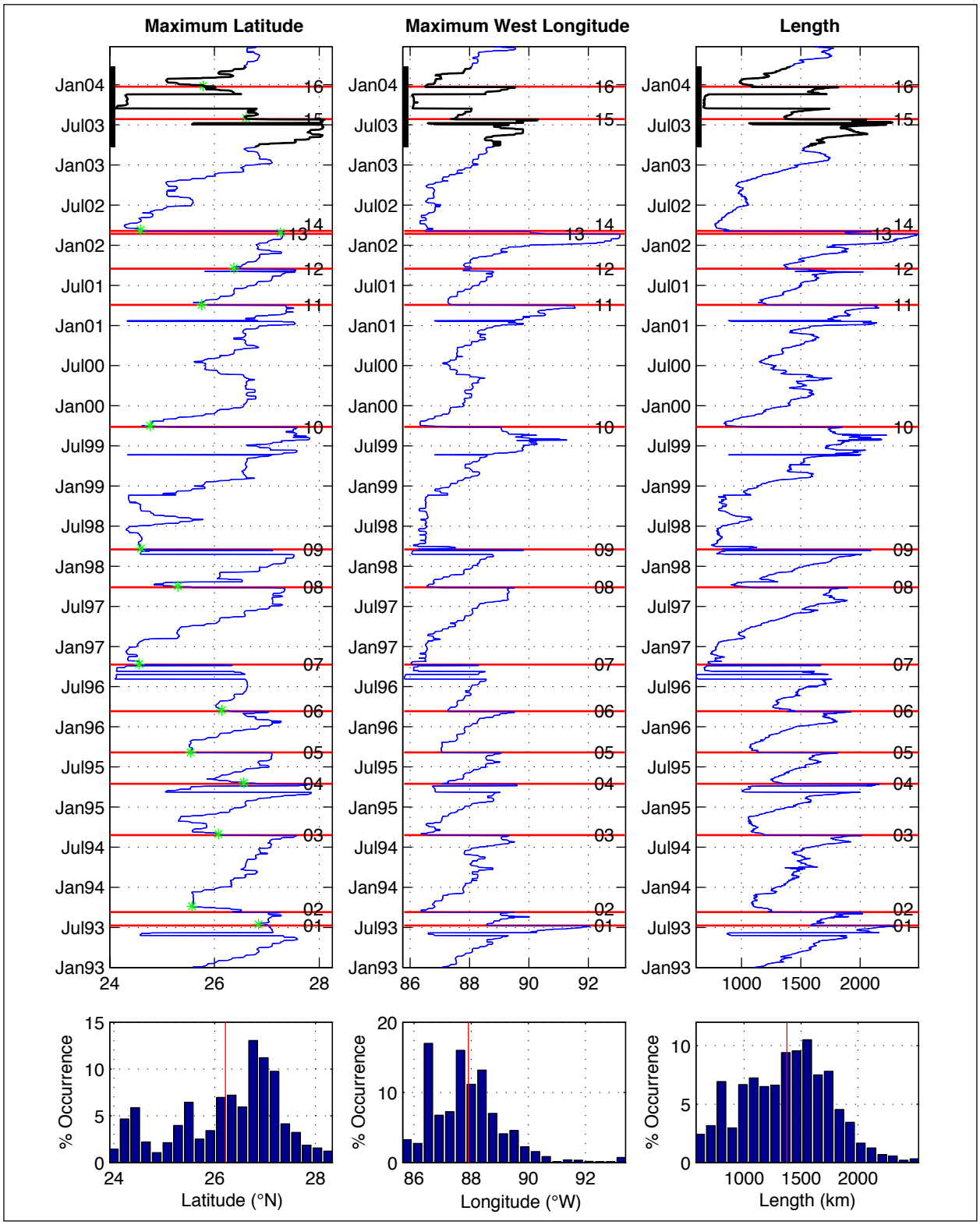

Figure 3.1-3. Loop Current maximum northern/western extension and length time series with percent occurrence histograms. The horizontal red lines identify the 16 LC eddy separation events and vertical red lines are the mean of the time series. Green stars identify the LC maximum latitude just after separation.

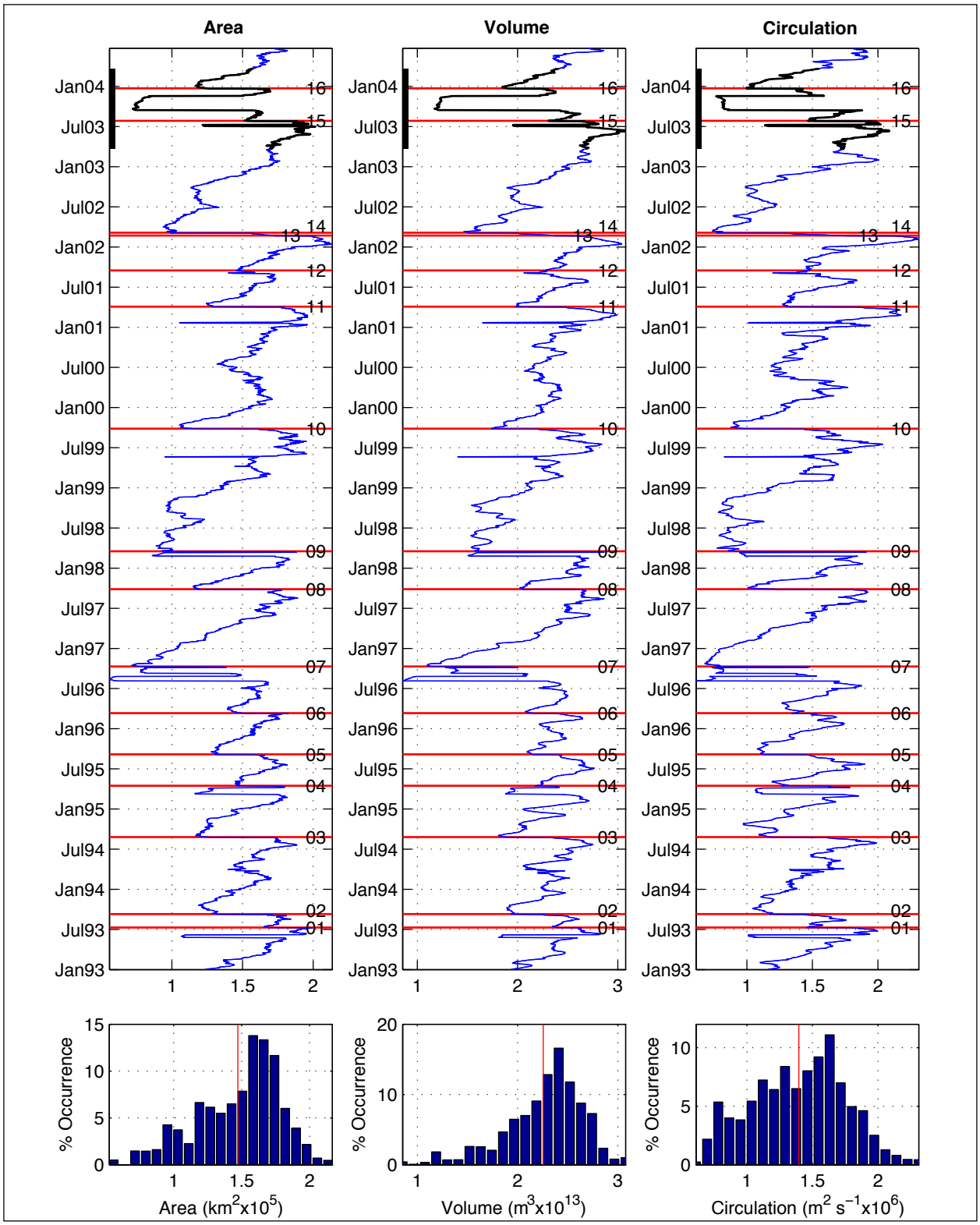

Figure 3.1-4. Loop Current area, volume and circulation time series with percent occurrence histograms. The horizontal red lines identify the 16 LC eddy separation events and vertical red lines are the mean of the time series. The Exploratory Study time period is highlighted in both Figures 3.1-3 & 3.1-4.

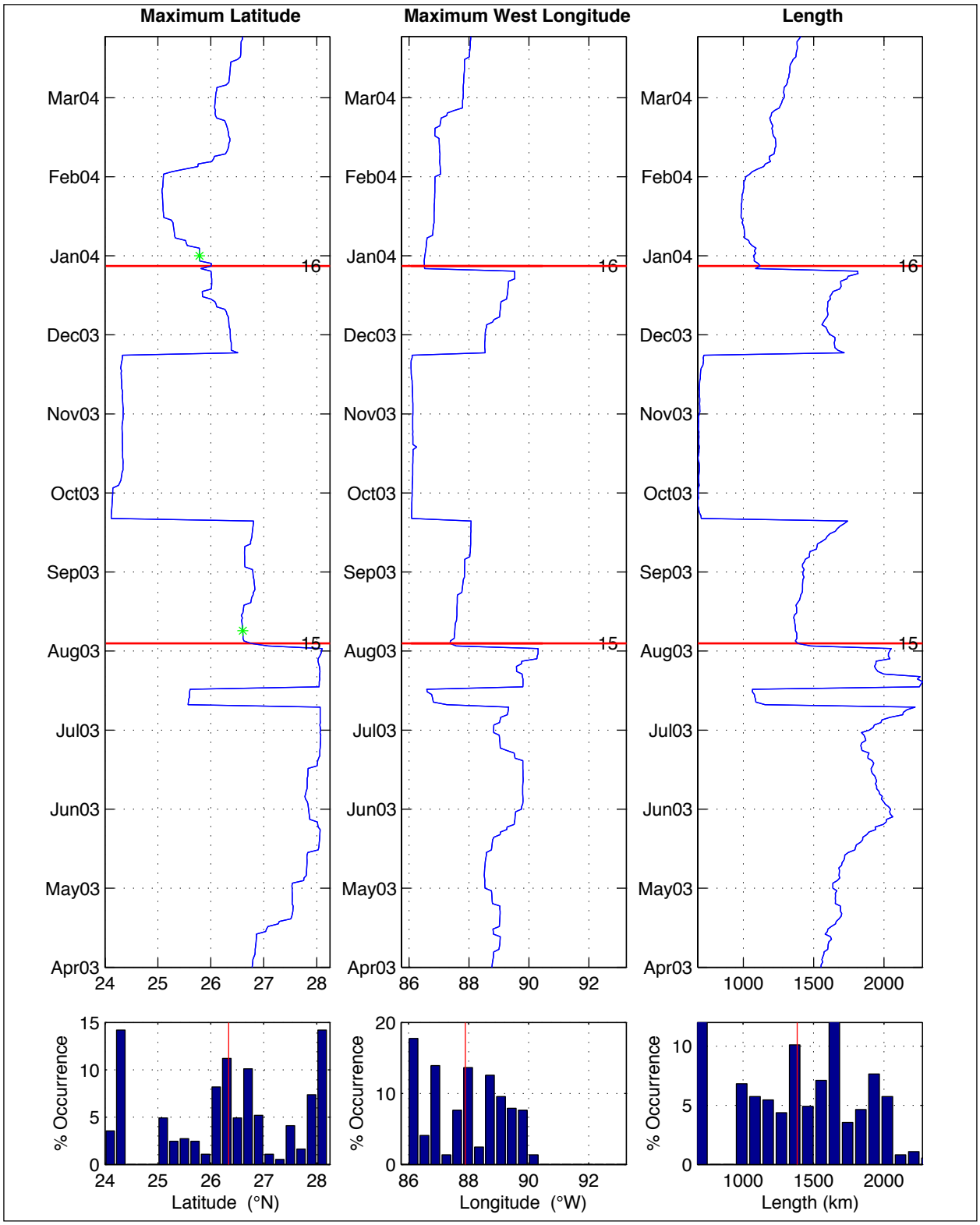

Figure 3.1-5. Loop Current maximum northern/western extension and length time series with percent occurrence histograms during the Exploratory Study. The horizontal red lines identify Eddies Sargassum (Eddy 15) and Titanic (Eddy 16) separation events and vertical red lines on the histograms are the mean values of the time series.

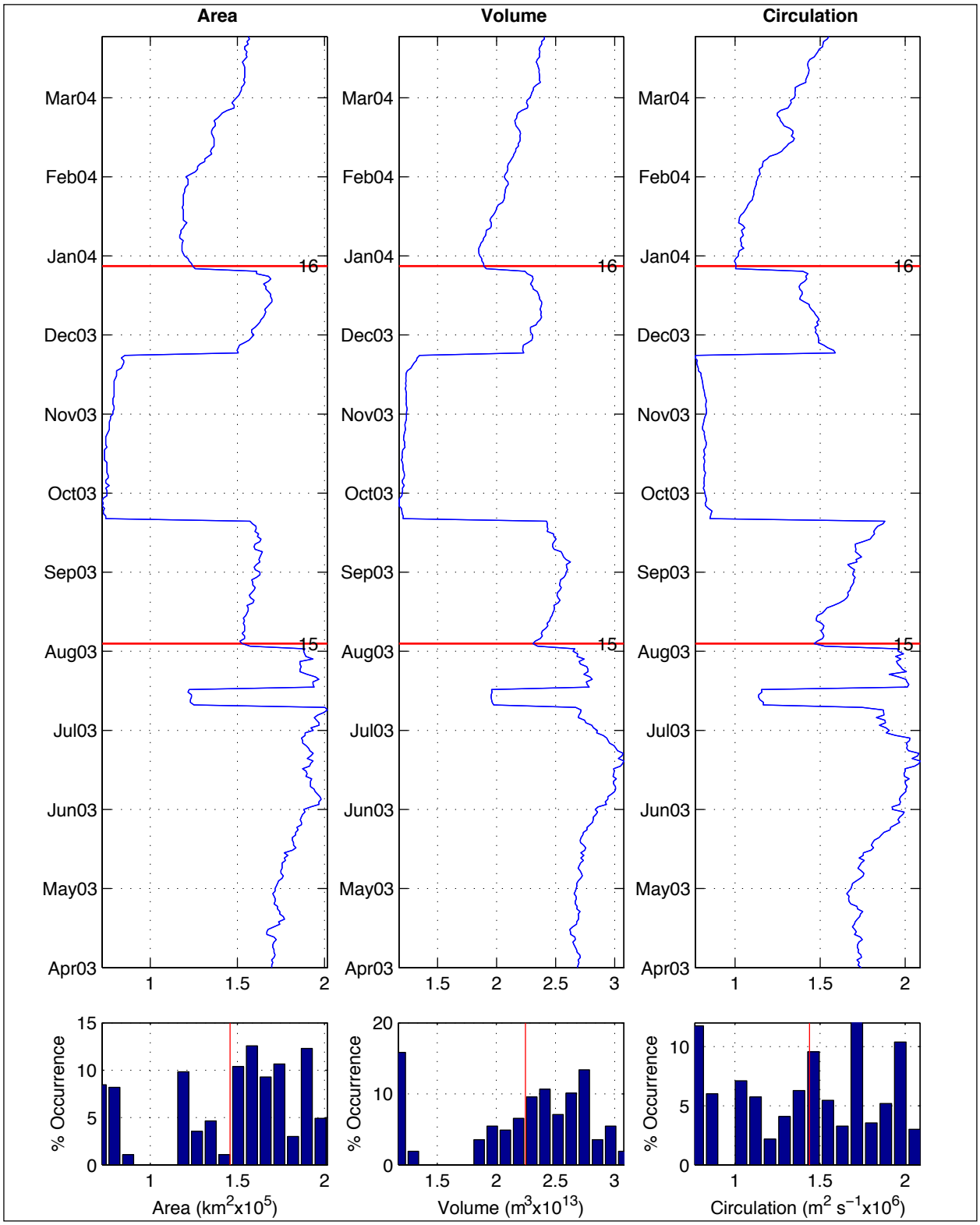

Figure 3.1-6. Loop Current area, volume and circulation time series with percent occurrence histograms during the Exploratory Study. The horizontal red lines identify Eddies Sargassum (Eddy 15) and Titanic (Eddy 16) separation events and the vertical red lines on the histograms are the mean values of the time series.

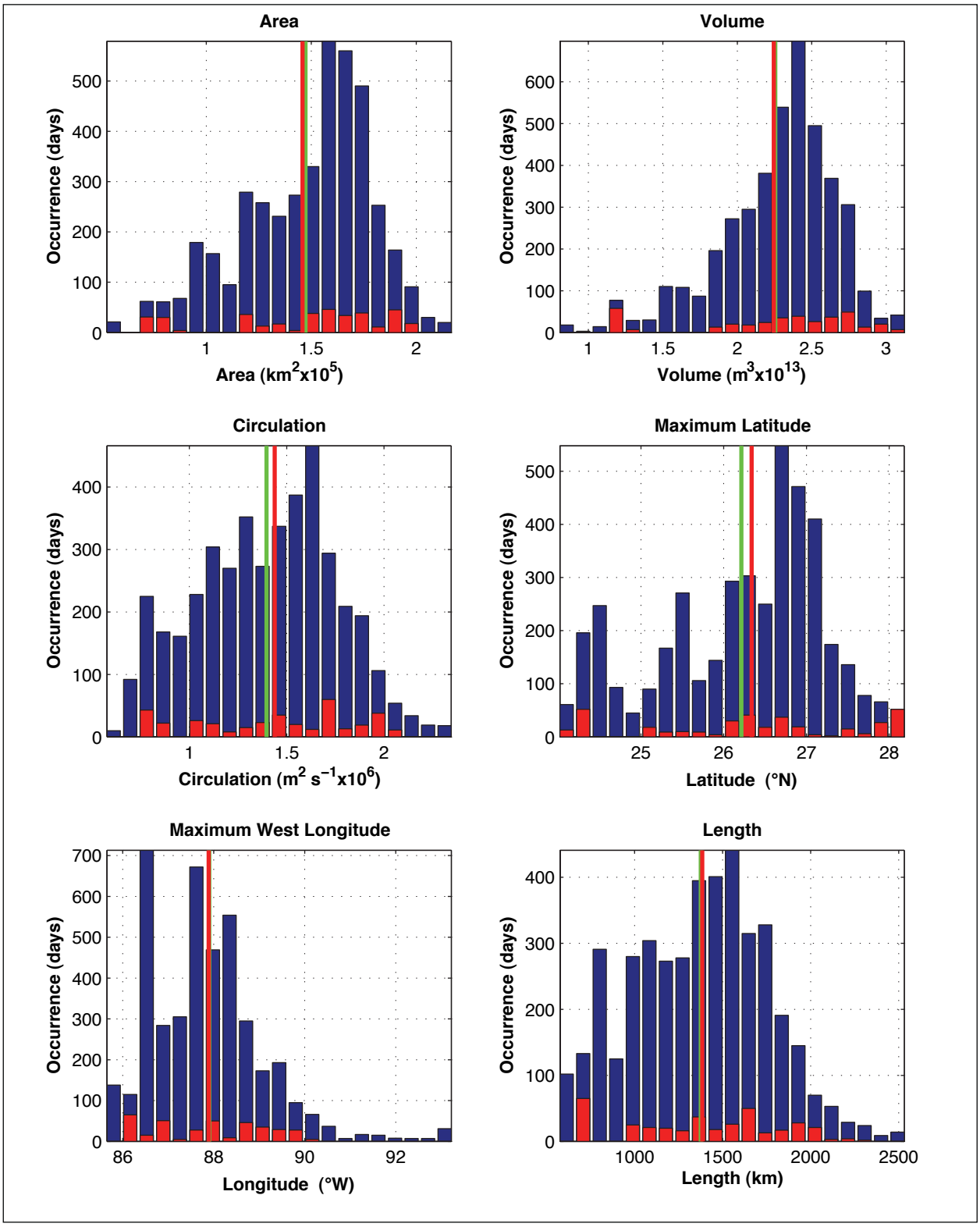

Figure 3.1-7. Histograms of Loop Current metrics during the Exploratory Study (red bars) versus historical time period (blue bars). Mean values from the program time period and the historical time period are shown by the vertical red and green lines, respectively. See Table 3.1-1 for tabulated values.

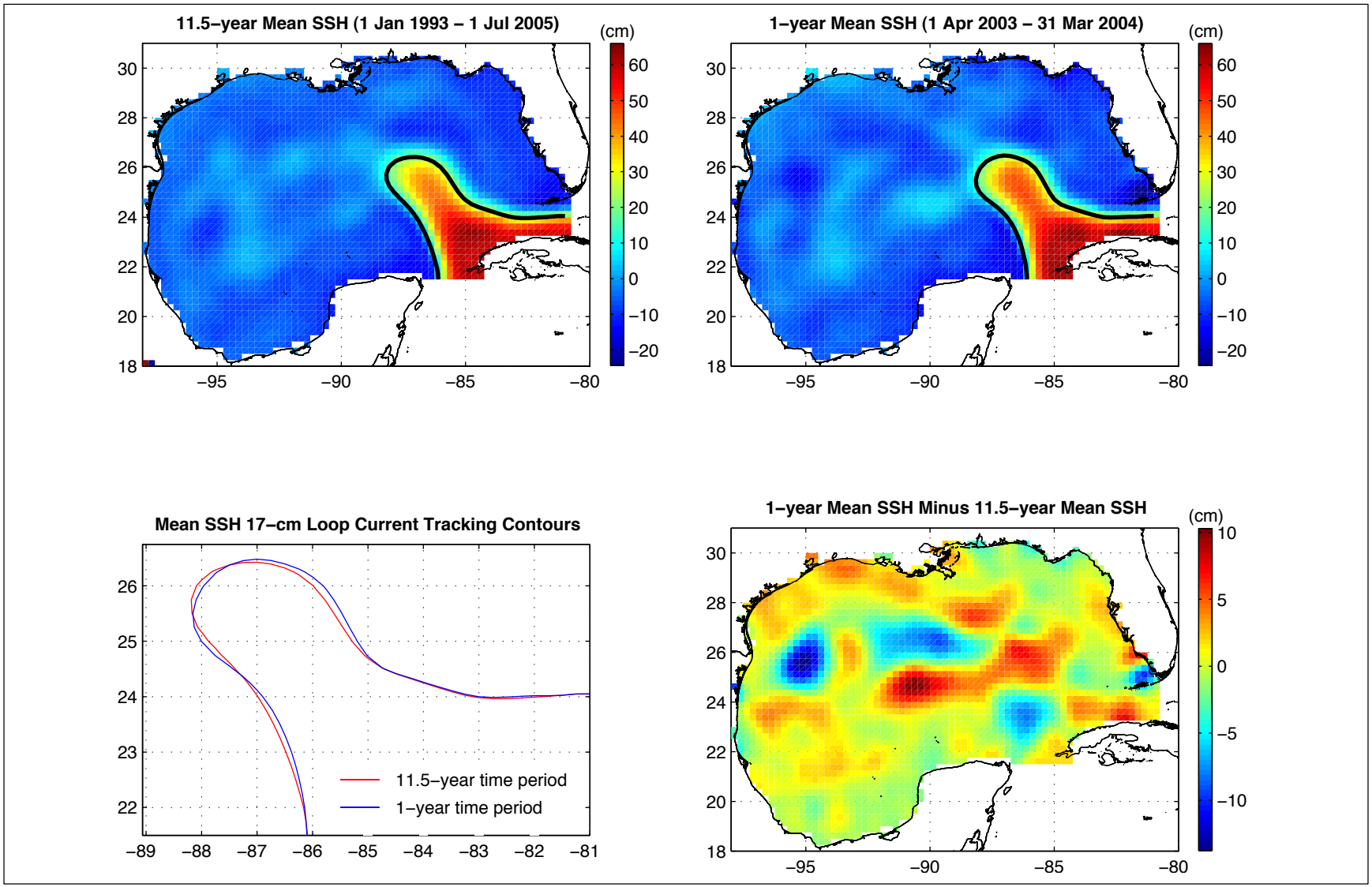

Figure 3.1-8. Mean SSH fields from the 11.5-year historical record and the 1-year Exploratory Study record are shown in the upper two panels. The mean LC position as determined from the 17-cm LC tracking contour is shown in the lower left panel. The difference of the two mean SSH fields is shown on the lower right panel.

and radiometry estimates span time periods comparable to the 11.5-year altimetric record with little or no overlap in time and support the conjecture that the fundamental LC behavior is statistically nearly stationary.

Table 3.1-1

Summary statistics for altimeter-derived Loop Current metrics computed from the historical and Exploratory Study records.

	Maximum West Longitude	Maximum North Latitude	Length (km)	Area (km^2)	Volume (m^3)	Circulation (m^2sec^{-1})
Historical Record: 1 January 1993 through 1 July 2004						
Mean	87.90°W	26.21°N	1376	147,240	$2.26x10^{13}$	1,396,200
Std. Dev.	1.18°	0.95°	365	29,295	$0.37x10^{13}$	338,960
Maximum	93.07°W	28.10°N	2494	213,540	$3.08x10^{13}$	2,311,200
Minimum	85.80°W	24.10°N	614	55,840	$0.85x10^{13}$	611,420
Exploratory Study Record: 1 April 2003 through 31 March 2004						
Mean	87.89°W	26.34°N	1384	145,820	$2.25x10^{13}$	1,438,200
Std. Dev.	1.24°	1.26°	440	38,583	$0.55x10^{13}$	400,960
Maximum	90.31°W	28.10°N	2274	201,640	$3.08x10^{13}$	2,087,300
Minimum	86.07°W	24.12°N	675	72,422	$1.17x10^{13}$	765,130

3.1.3 Loop Current Eddies

The primary goal of the objective LC tracking technique is to monitor the time-dependent behavior of the LC and its associated anticyclonic eddies commonly referred to as Loop Current eddies (LCEs). Timing of LC eddy separation events was identified using the LC-length time series, since the breaking of the 17-cm tracking contour between the LC and a detaching LCE into separate contours causes a discrete change in the LC length equal to the approximate circumference of the separating eddy. The day that this event occurs is identified as the "time" of eddy separation. Occasionally a detached eddy will reattach to the LC. In those cases the time associated with the final detachment of the eddy is referred to as the eddy separation time. The exact timing of a separation event, therefore, is dependent on the criteria selected to define separation and is complicated by the ambiguity of associating an exact time with what is clearly a continuous and complicated process. The tracking contour also impacts LC and LCE statistics, such as areal extent, that are estimated using the tracking contour. Nevertheless, an objective definition of separation provides a useful benchmark for comparing LC eddy events that occurred during the Exploratory Study with those observed in the prior ten-year altimeter record.

Sixteen LC eddy separation events were identified in the 11.5-year altimeter record, which includes the Exploratory Study. The LC-length time series and SSH maps of each of these events at the time of separation are shown in Figure 3.1-9. The separation date, separation period, eddy name and eddy area at the time of separation are tabulated for each of the 16 observed events in Table 3.1-2. Horizon Marine, Inc. (HMI) names the eddies in alphabetical order as anticyclones shed from the LC and/or impact offshore operations in the northern GOM.

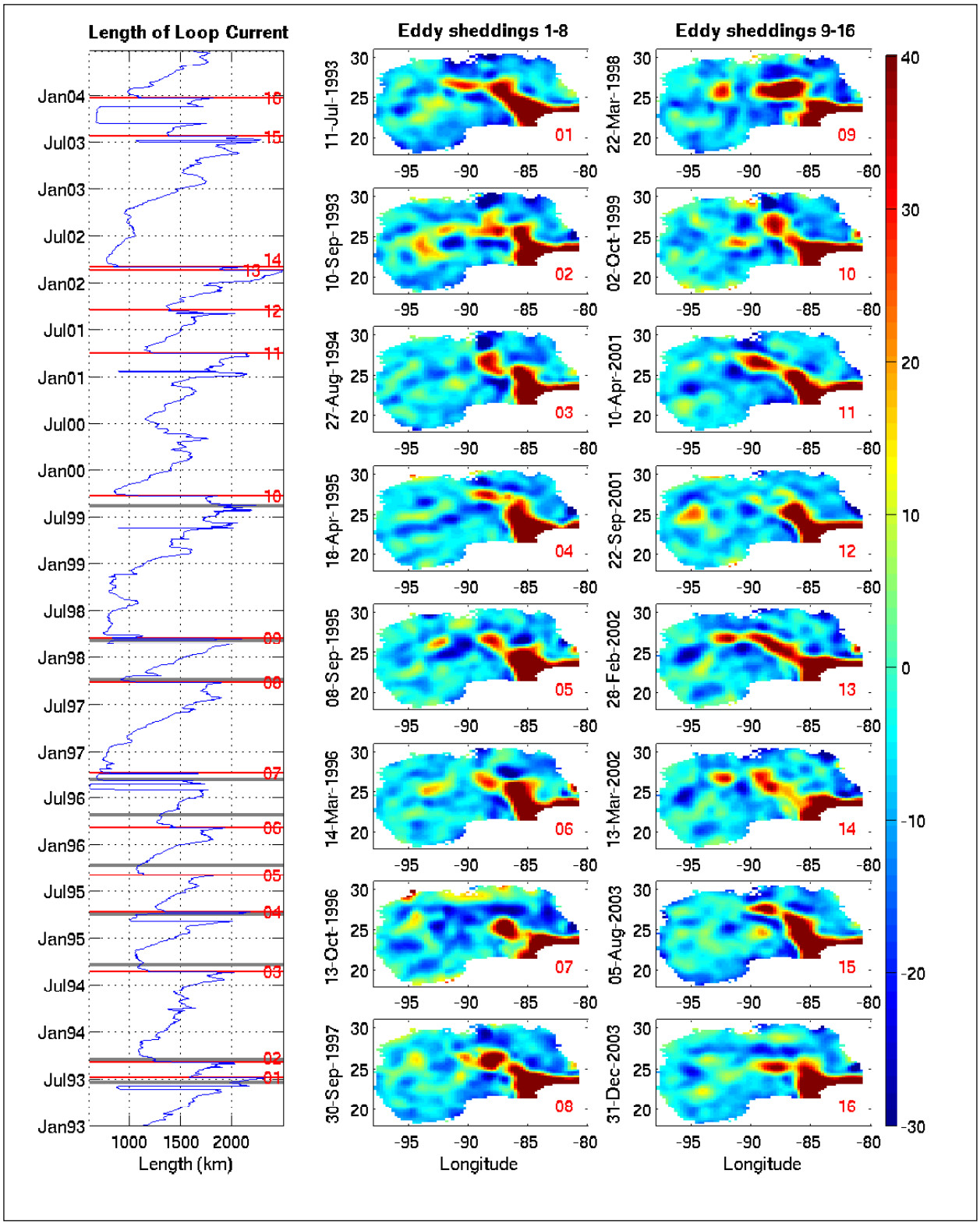

Figure 3.1-9. 16 LC eddy separation events identified in the altimeter record. SSH maps on the separation dates are shown in the panels to the right (values above 40 cm and below -30 cm have been clipped). The LC length time series is overlaid with red lines corresponding to the separation dates.

A complete list is published on the web at http://horizonmarine.com/namedlces.html. The names appear in the weekly EddyWatch™ reports provided to the GOM offshore oil and gas industry by subscription from HMI. All separation events identified using the SSH 17-cm tracking contour were monitored by the EddyWatch™ program, although a number of smaller anticyclonic eddies (seven total) were also named, causing the breaks in the alphabetical sequence. Only one marginal eddy separation event was identified by the objective tracking procedure (Eddy Odessa/Nansen, Eddy 12), which dissipated so quickly that an estimate of the eddy area could not be made. These smaller eddies are of LC origin, but form on the outer edge of the LC through the interaction of frontal cyclones with the current. This type of small anticyclonic eddy was observed in the northeast GOM during the DeSoto Canyon Eddy Intrusion Study (Hamilton et al., 2000). Other small named eddies originate as primary LCEs split and/or form smaller anticyclonic eddies after separation. An example of this type of event is the unnamed anticyclonic eddy that split off from the southwest quadrant of Eddy Sargassum during the final detachment of Eddy Sargassum from the LC (see Figure 3.1-1).

Table 3.1-2

Ring separation events from the altimetric record: 1 January 1993 through 31 March 2004.

Eddy Number	Separation Date	Separation Period (months)	Industry Eddy Name	Area (km^2)	Eddy Maximum SSH (cm)
1	11 Jul 1993	11.5	Whopper	24,183	33
2	10 Sep 1993	2.0	Xtra	38,481	39
3	27 Aug 1994	11.5	Yucatan	43,022	39
4	18 Apr 1995	7.5	Zapp	21,337	36
5	8 Sep 1995	4.5	Aggie	24,899	36
6	14 Mar 1996	6	Biloxi	24,912	32
7	13 Oct 1996	7	Creole	49,644	69
8	30 Sep 1997	11.5	El Dorado	49,229	56
9	22 Mar 1998	5.5	Fourchon	89,143	72
10	2 Oct 1999	18.5	Juggernaut	40,325	39
11	10 Apr 2001	18.5	Millennium	45,705	44
12	22 Sep 2001	5.5	Odessa/Nansen	?	12
13	28 Feb 2002	5.5	Pelagic	22,119	41
14	13 Mar 2002	0.5	Quick	49,936	41
15	5 Aug 2003	17	Sargassum	25,302	49
16	31 Dec 2003	5	Titanic	33,278	43

3.1.4 Loop Current Frontal Eddies (LCFE) and other Cyclonic Eddies

Cyclonic perturbations and eddies are common along the outer edge of the LC. Several observational studies have noted that these peripheral features, including LC frontal eddies (Vukovich and Maul, 1985), Tortugas eddies (Lee et al., 1995; Fratantoni et al., 1998) and

Campeche Bank eddies (Zavala-Hidalgo et al., 2003), are often associated with eddy separation events and therefore are thought to play a role in the detachment and/or separation of a LCE.

The combination of SSH maps and SST imagery has proven to be useful for detecting and tracking cyclonic features, which was demonstrated during the Desoto Canyon Eddy Intrusion Study when 12 LC frontal eddies were detected and tracked, 11 of which influenced the study region (Hamilton et al., 2000). In general, SST images are useful for tracking LCFEs because synoptic sampling is often required to map the rapid evolution of the features as they propagate around the LC at translation velocities of up to nearly 25 $km \cdot day^{-1}$. Ocean color imagery is also useful for detecting and tracking cyclones because of the higher chlorophyll concentrations typically associated with upwelling within the eddy.

Continuous monitoring using SST or color radiometric imagery, however, is not possible because of the frequent clouds over the Gulf and the seasonal degradation of the surface thermal gradients and biological signals. Even under good observing conditions, the surface temperature or color signature of an eddy in imagery can be difficult to interpret because the surface cyclonic circulation associated with a cyclonic eddy may advect filaments of warm chlorophyll-poor waters that mask the cold nutrient–rich conditions typical of cyclones. The cyclonic spiral of a warm filament within the eddy, therefore, frequently identifies the presence of a cyclone. On the other hand, satellite altimetry can unambiguously detect cyclones by their lower SSH; however, the relatively small size of the eddies and their often rapid evolution can make detecting and tracking of these features difficult because of the non-synoptic sampling of the ocean surface by satellite-borne radar altimeters. Therefore, no systematic census of cyclones in the GOM, such as those performed for LCEs, has been attempted given the imaging and sampling limitations of the current operational satellite systems, although some topographically isolated features such as the Campeche Bank (Zavala-Hidalgo et al., 2003) and Tortugas Eddies (Fratantoni et al., 1998) have been studied in detail. Systematic comparisons of the cyclones observed during this project with those in the historical record, therefore, may be difficult.

Cyclones, nevertheless, are an important dynamical component of the general circulation of the GOM and significantly impacted the study region during the Exploratory Study. They also are quite common along the boundary of the LC during intrusions into the north-central GOM, as was the case during nearly the entire program study period. As an example, we identify a number of cyclones on the 13 April 2003 nighttime composite SST image from GOES-12, courtesy of Nan Walker of Louisiana State University (Figure 3.1-9).

3.1.5 Study Time Period in the Context of the Historical Record

The altimeter-derived LC metrics and eddy statistics provide a useful benchmark to compare Gulfwide conditions during the program's field measurements to those observed during the historical record. We begin with a discussion of the LC intrusion and LCE separation events.

LC eddy separation events have been monitored over a 31-year time period from July 1973 through June 2004 (Leben, 2005). A total of 40 consecutive events have been identified (Table 3.1-3) of which the last two, Eddies Sargassum and Titanic, occurred during the program time period. A histogram of the separation periods is shown in Figure 3.1-10, with the 17-month

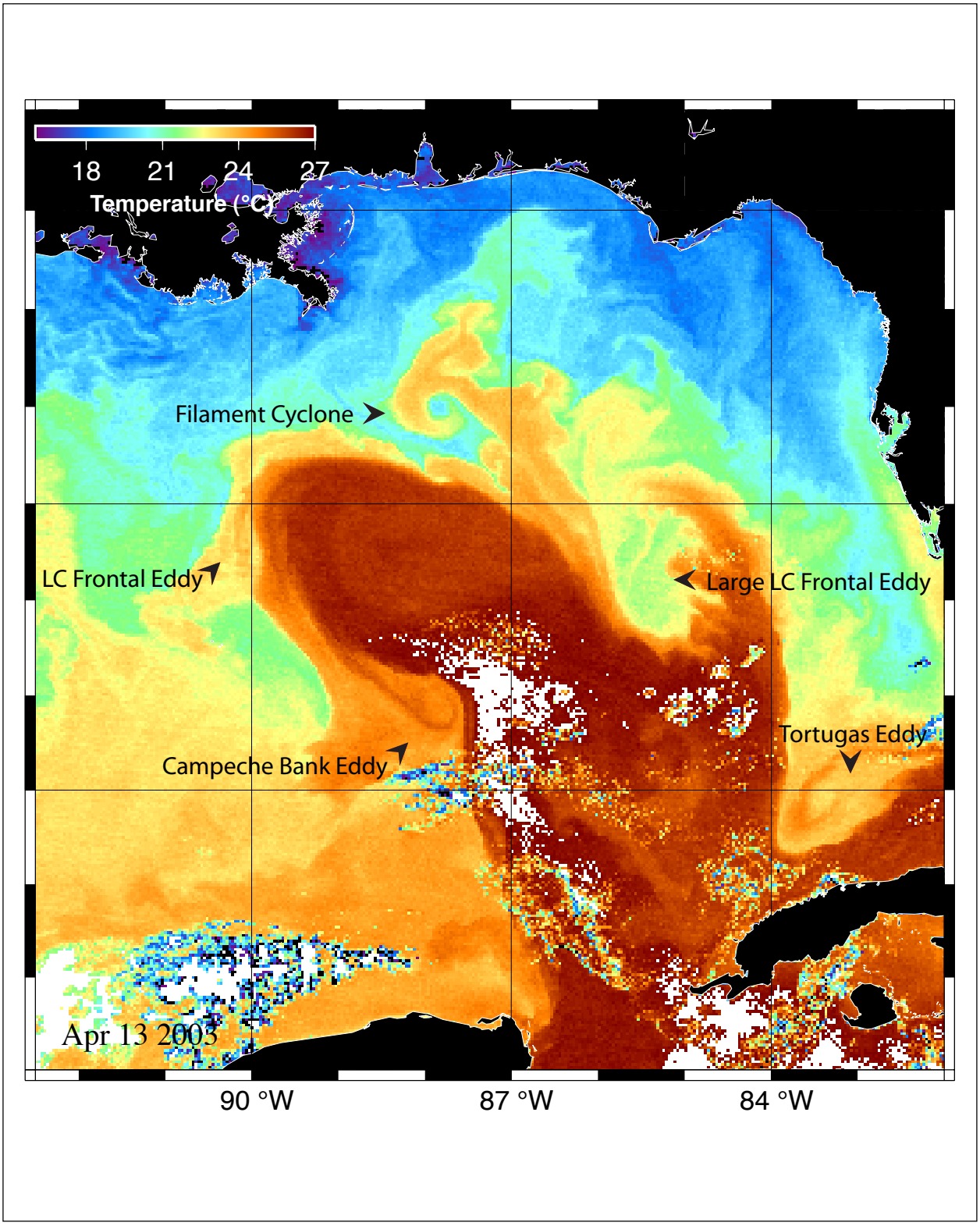

Figure 3.1-10. A single AVHRR pass from the NOAA 16 satellite on 13 April 2003 collected this nearly cloudfree SST image of the LC and its associated cyclonic features. Image courtesy of Dr. Nan Walker, Louisianna State University.

Sargassum and 5-month Titanic LC intrusion and LCE separation periods identified. SSH maps of the LC and LCE positions at the time of separation are also shown.

Table 3.1-3

Compilation of the 31-year record of separation periods for LC eddies from July 1973 through June 2004. A total of 40 consecutive events are listed. Entries through October 1986 are from Vukovich (1988); other entries prior to July 1992 are from Sturges (1994) using corrections based on Berger (1993). The separation event in July 1992 is from Sturges and Leben (2000). Data beginning in 1993 are based on objective tracking of the LC using satellite altimeter data (Leben, 2005).

Date	Separation Period (months)	Date	Separation Period (months)	Date	Separation Period (months)
July 1973		August 1984	6	8 Sep 1995	4.5
April 1974	9	July 1985	11	14 Mar 1996	6
January 1975	9	January 1986	6	13 Oct 1996	7
July 1975	6	October 1986	9	30 Sep 1997	11.5
August 1976	13	September 1987	11	22 Mar 1998	5.5
March 1977	7	May 1988	8	2 Oct 1999	18.5
June 1978	15	May-June(?) 1989	12.5	10 Apr 2001	18.5
April 1979	10	August 1990	14.5	22 Sep 2001	5.5
January 1980	9	Aug- Sep 1991	12.5	28 Feb 2002	5
March 1981	14	19 July 1992	11.5	13 Mar 2002	0.5
November 1981	8	11 Jul 1993	11.5	5 Aug 2003	17
May 1982	6	10 Sep 1993	2	31 Dec 2003	5
March 1983	10	27 Aug 1994	11.5		
February 1984	11	18 Apr 1995	7.5		

The 17-month interval associated with the Eddy Sargassum separation event was the third longest on record and followed the nearly simultaneous separation of two large LCEs, Pelagic and Quick (Eddies 13 and 14), in February and March 2002. The LC prior to separation of Eddy Saragassum was the most northerly intrusion event observed with the LC reaching 28.10°N, based on the 17-cm tracking contour. Immediately after eddy separation, the LC retreated to below 26.6°N and five months later Eddy Titanic separated. During this 5-month long intrusion event, Eddy Titanic was detached from the LC for a 2-month interval in the Fall of 2003. Time periods when an eddy detaches and later reattaches to the LC are common even with the stringent definition of detachment based on the breaking of the 17-cm SSH contour. Seven of the sixteen eddies (1,4,7,9,11,15 & 16) in the altimeter record detached and reattached before final separation based on this definition of detachment, including Eddies Sargassum and Titanic. Most of these events were short lived like the Eddy Sargassum detachment, which was only about one week in duration. The 2-month long detachment of Eddy Titanic was the longest observed in the altimeter record.

Eddy Sargassum ranked 10th in areal extent and 4th in maximum SSH on the date of separation relative to all 16 LCEs observed in the altimetric record (see values in Table 3.1-2). Eddy Titanic ranked 9th in areal extent and 6th in maximum SSH. These rankings show that the LCEs that separated during the Exploratory Study were relatively compact and yet more energetic on average than other LCEs observed. Composite plots of the locations (Figure 3.1-11) and zoomed maps of the SSH height fields, including maximum eddy SSH values and 17-cm tracking contour (Figures 3.1-12 & 3.1-13), are shown for all of the LCEs observed with altimetry.

The eddy locations at the time of separation (Figure 3.1-11) clearly show that Eddy Sargassum was the most northern separation event on record, while Eddy Titanic was one of the most southern. One LCE-separation event in the altimeter record was similar to Eddy Sargussum – Eddy Zapp (Eddy 5), which separated from the LC in April 1995. The general configurations of the LC and the LCEs at the time the Zapp and Sargassum separation intrusion events were very similar, although Eddy Zapp was clearly less energetic with a maximum SSH of 36 cm compared with the 49 cm maximum within Eddy Sargassum. The LC maximum north latitude after the separation of these eddies was also nearly equal, retreating to below 26.56°N and 26.6°N respectively, just after Zapp and Sargassum separated, (see green stars plotted on LC maximum north latitude time series in Figure 3.1-3). Because of a linear relationship between LC retreat and the period of the following eddy separation cycle (Leben, 2005), the subsequent LCE separation periods were nearly the same with Eddy Aggie (Eddy 6) separating 143 days after Eddy Zapp and Eddy Titanic separating 148 days after Eddy Sargassum. There was little similarity, however, between Eddies Aggie and Titanic other than their shedding period. In fact, there were no LCEs observed during the altimeter record that were comparable to Eddy Titanic. This was because Titanic was the only LCE-separation event where the entire 17-cm eddy tracking contour was south of the maximum north latitude of the LC at the time of separation, which caused no significant change in the maximum LC latitude associated with a separation event for the first time in the altimeter record. One may argue that the separation of Eddy Pelagic also showed little retreat of the LC; however, within a few weeks Eddy Quick separated and the LC retreated by nearly three degrees of latitude. Thus, the far southern separation and the direct westward separation of Eddy Titanic from the LC made the Titanic event relatively unique in the observational record.

The overall intensity of the Sargassum and Titanic intrusion events can be put into historical context by comparing the areal extent within the 17-cm tracking contour and maximum SSH for each eddy at the time of initial detachment from the LC to the same metrics calculated for other LCEs at the time of their separation (Table 3.1-2). At the time of its initial detachment on 13 July 2003, Eddy Sargassum covered an area of 63,635 km^2 and had a SSH maximum of 54 cm. Eddy Titanic at the time of its initial detachment on 25 September 2003 had an area of 80,034 km^2 and a maximum height of 73 cm. These metrics would have ranked both Sargassum and Titanic near the top of all LCEs in terms of eddy size and intensity if the eddies had not reattached to the LC. Typically, large detached LCEs reattach to the LC, as was the case for both Sargassum and Titanic. The one exception in the altimeter record was Eddy Fourchon, which exceeded both of the Sargassum and Titanic initial detachments in areal extent and SSH maximum and yet remained separated from the LC after its initial detachment. The overall intensity difference of the gulfwide mean circulation during the program time period relative to the long-term average is shown by the 1-year mean minus the 11.5 year mean SSH field in the

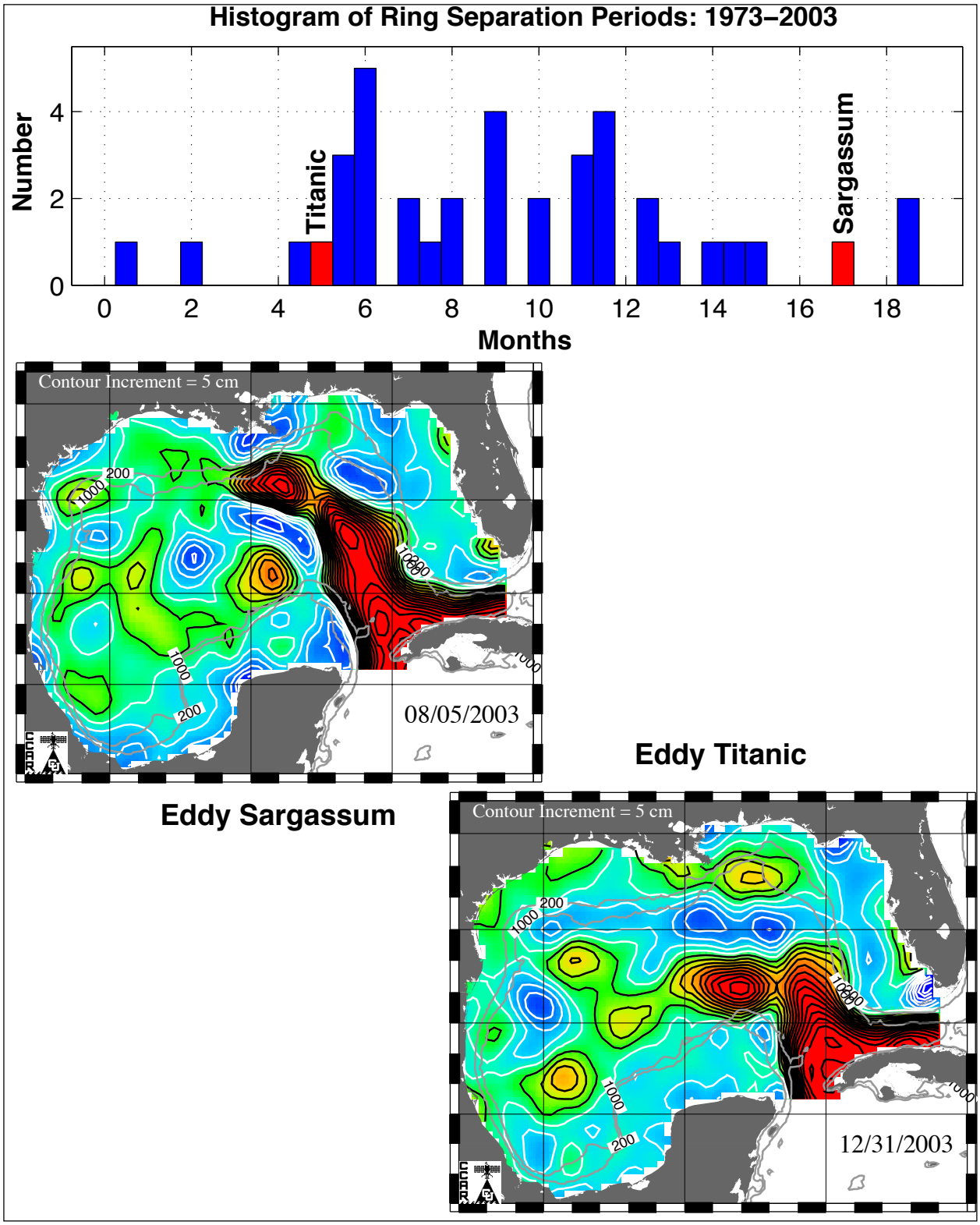

Figure 3.1-11. Histogram of ring separation periods from the entire observational record, 1973 through 2003. Separation periods associated with the Eddies Sargassum and Titanic intursion events are highlighted in red. SSH map on the date of separation are shown in the lower panels.

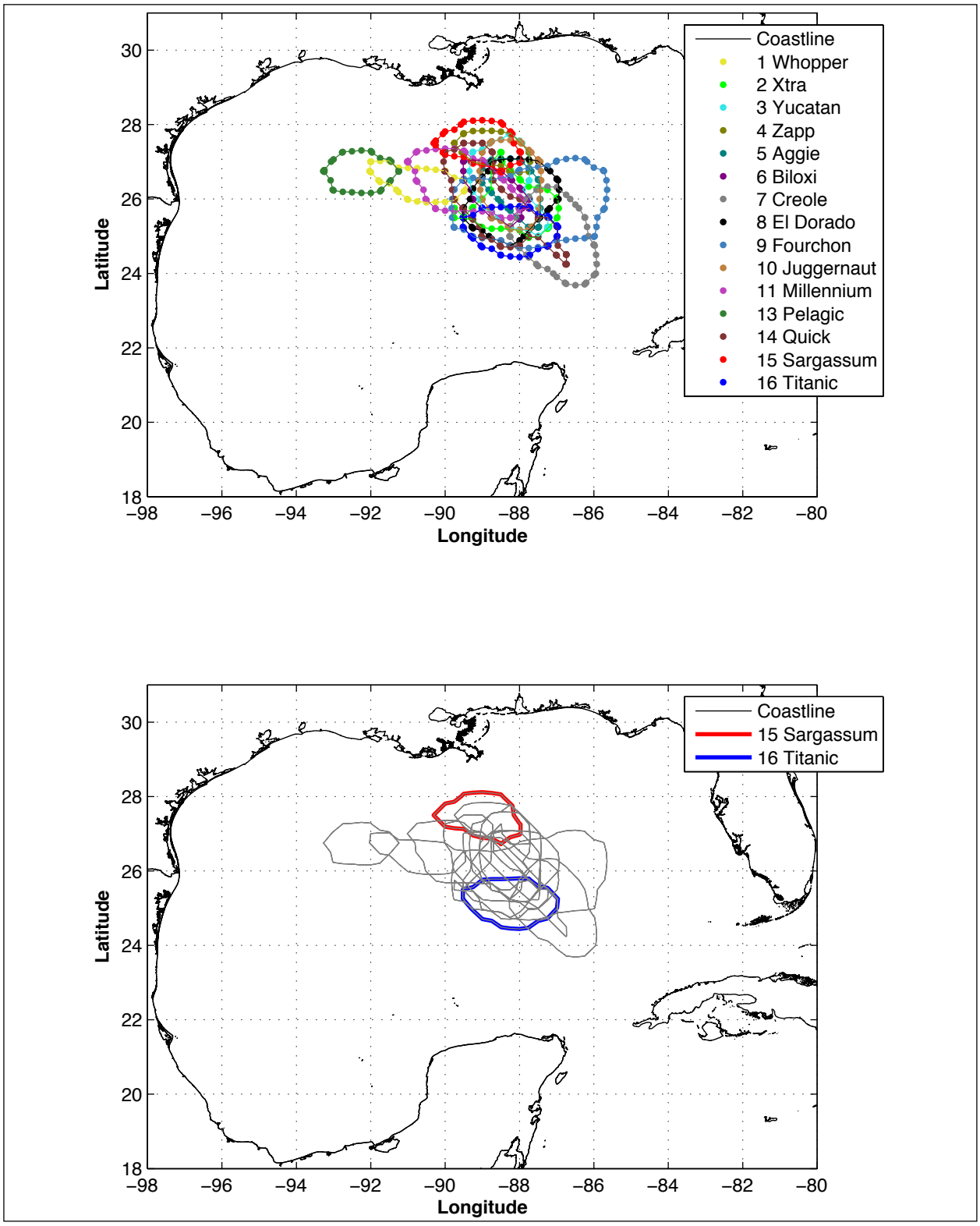

Figure 3.1-12. The 17-cm tracking contours at the time of separation for all 16 LC eddies observed from 1993-2003. The eddies that separated during the Exploratory Study, Sargassum and Titanic, are highlighted in the bottom panel

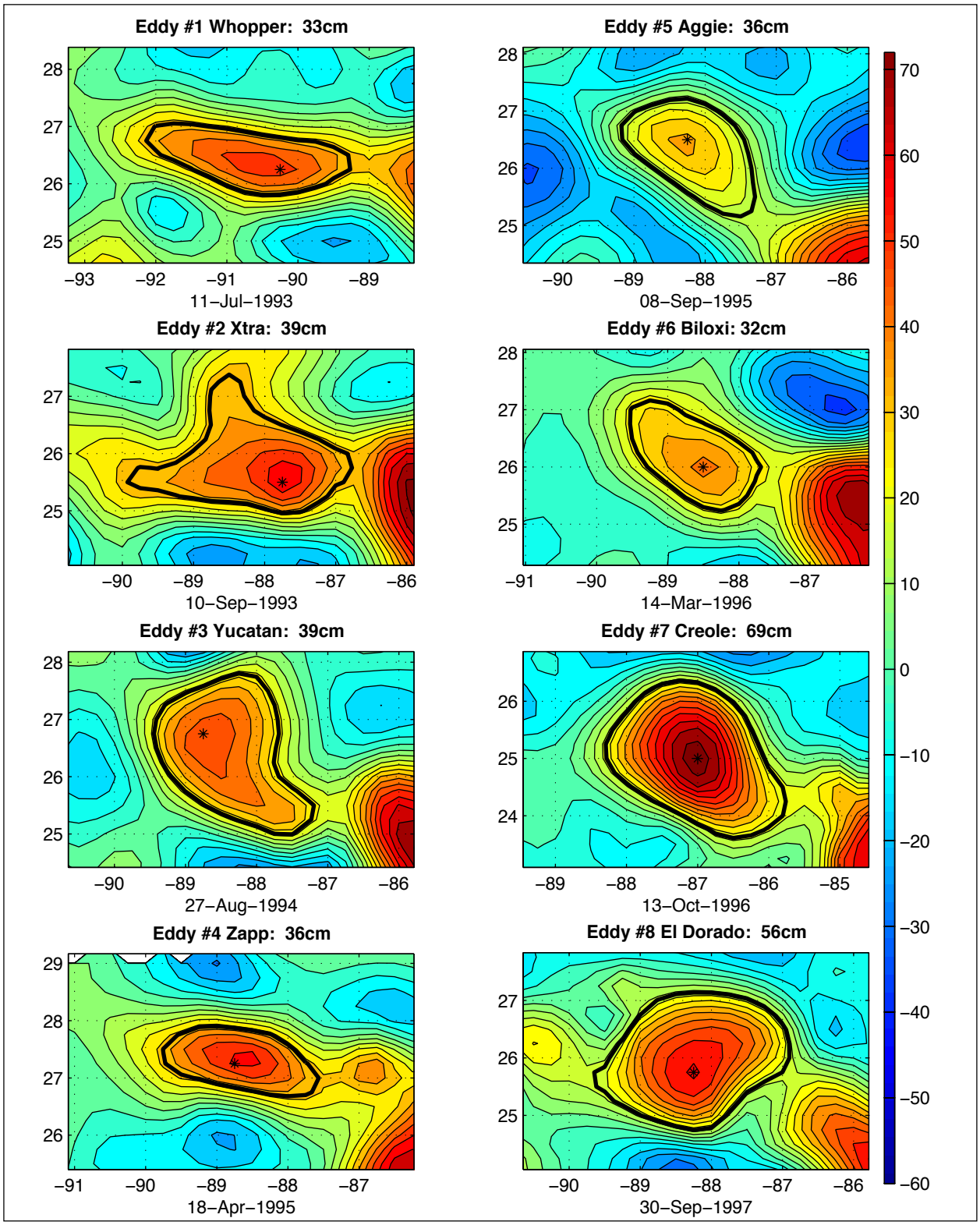

Figure 3.1-13a. Zoomed SSH maps of LC eddies 1-8 at the time of separation from the LC. The 17-cm tracking contour and maximum SSH are shown for each eddy. Plots are equal area.

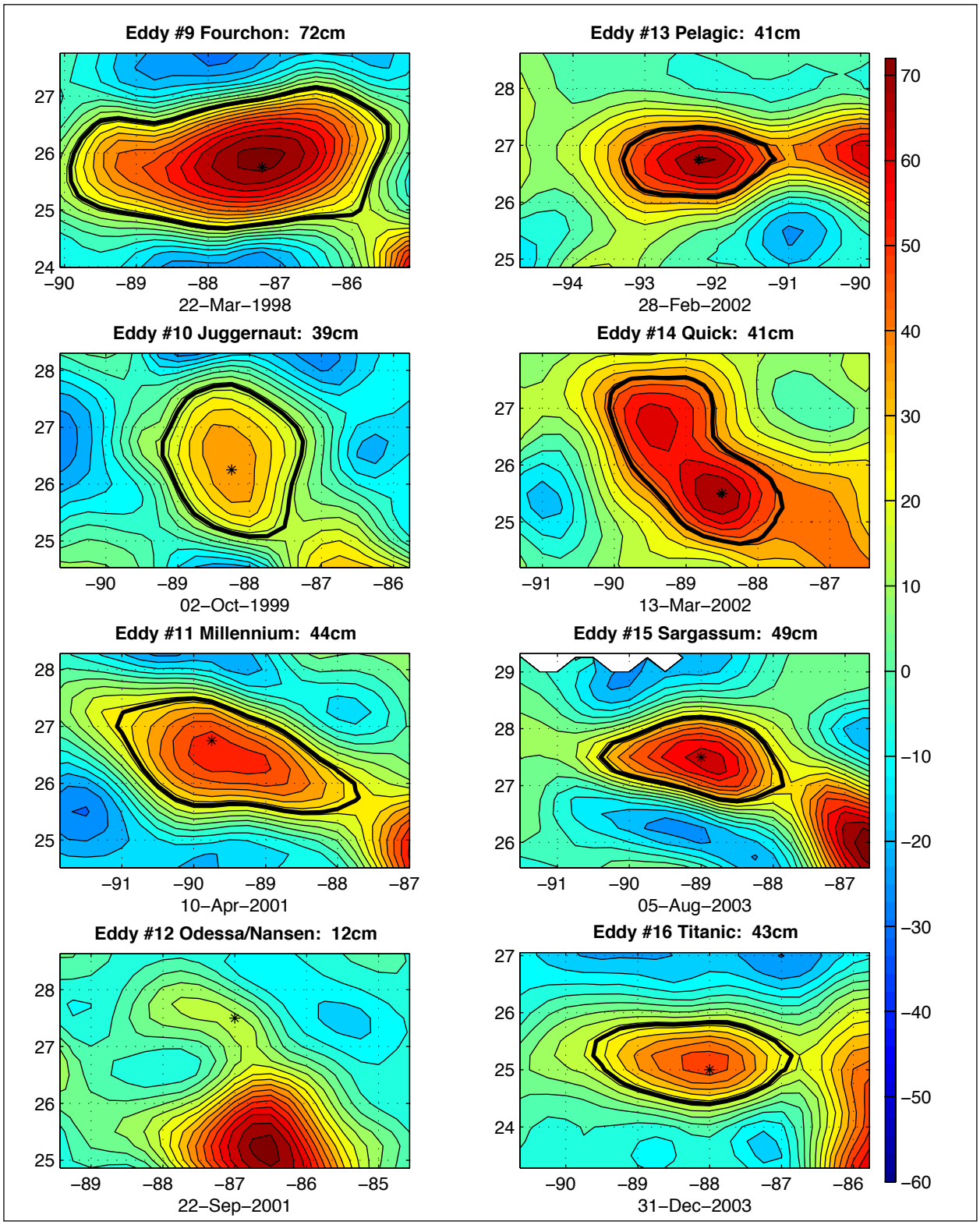

Figure 3.1-13b. Zoomed SSH maps of LC eddies 9-16 at the time of separation from the LC. The 17-cm tracking contour and maximum SSH are shown for each eddy. Plots are equal area. Eddy #12 (Odessa/Nansen) dissipated rapidly and contained no tracking contour at the time of separation.

lower right hand panel of Figure 3.1-8. The higher than average mean anticyclonic circulation during the program time period in the eastern GOM reflects the strength of the Sargassum and Titanic intrusion events.

Two energetic cyclonic events that impacted the Exploratory Study area during the field measurement program merit further consideration in the context of the historical record. The first event began in late May 2003 when a small LC frontal eddy formed within the observational array and grew rapidly as it propagated downstream, moving clockwise around the LC and in mid-July 2003 cleaving the LC and detaching Eddy Sargassum on 13 July 2003. This cyclone later interacted with Eddy Sargassum to split a small anticyclone from the southwestern flank of the detached Eddy Sargassum. Detailed observations of large eddy splitting or cleaving events are relatively rare. Only one other event has been observed in the GOM. In April 1992, Eddy Triton was cleaved in two by a deepwater cyclone in the deep central western Gulf as reported by Biggs et al. (1996).

The second notable cyclonic event was the companion cyclone to Eddy Titanic, which was located directly north of Titanic during its detachment from the LC from 25 September through 28 November 2003. It is likely that this 2-month-long detachment was caused by the interaction of the detached anticyclone with this strong cyclone to the north. This interaction arrested the westward β-induced drift that affects isolated eddies by causing an eastward self-induced velocity of the dipole pair formed by the cyclone to the north and the detached anticyclone to the south, allowing Eddy Titanic to remain nearly stationary until it eventually was recaptured by the LC. Such cyclonic "blocking" events have been identified as a possible mechanism for delaying LCE separation and may occur quite frequently, often involving more than a single cyclone. Schmitz et al., (2005) identified 15 cyclonic blocking events in the altimetric record during 12 of the LC intrusions separation intervals. The companion cyclone north of Eddy Titanic was one of the strongest single-eddy blocking events observed. The areal extent of the cyclone was 44,750 km^2, based on the area within the -17 cm SSH contour, and the minimum SSH was -40 cm.

The above characterizations during the Exploratory Study indicate that patterns were dominated by two strong LC events that resulted in LC and LCE activity in and around the study region. Cyclonic circulation that is typically associated with strong LC intrusions and eddy separation events was also present. It is simplistic to characterize the gulfwide oceanographic conditions impacting the study region as unique during the Exploratory Study, however, in this yearlong study the strong LC variability resulted in oceanographic conditions that would not be typically observed in a one-year time interval. Nevertheless, the conditions were not so atypical that the average LC behavior over the one-year time interval, as measured by the mean LC metric statistics, differed remarkable from the long-term average.

3.1.6 T/S Characteristics Based on PALFOS Profiles

The profiling capability of the PALFOS floats provided an opportunity to obtain an extensive set of salinity and temperature profiles at 10-day intervals. The locations of these profiles (Figure 3.1-14) were dependent on the cumulative horizontal displacement resulting from transport at the surface over the profiling depth and at the residence depth (1,000 m). At the end of the field measurement interval, it was apparent that these drifters spent a large percentage of time

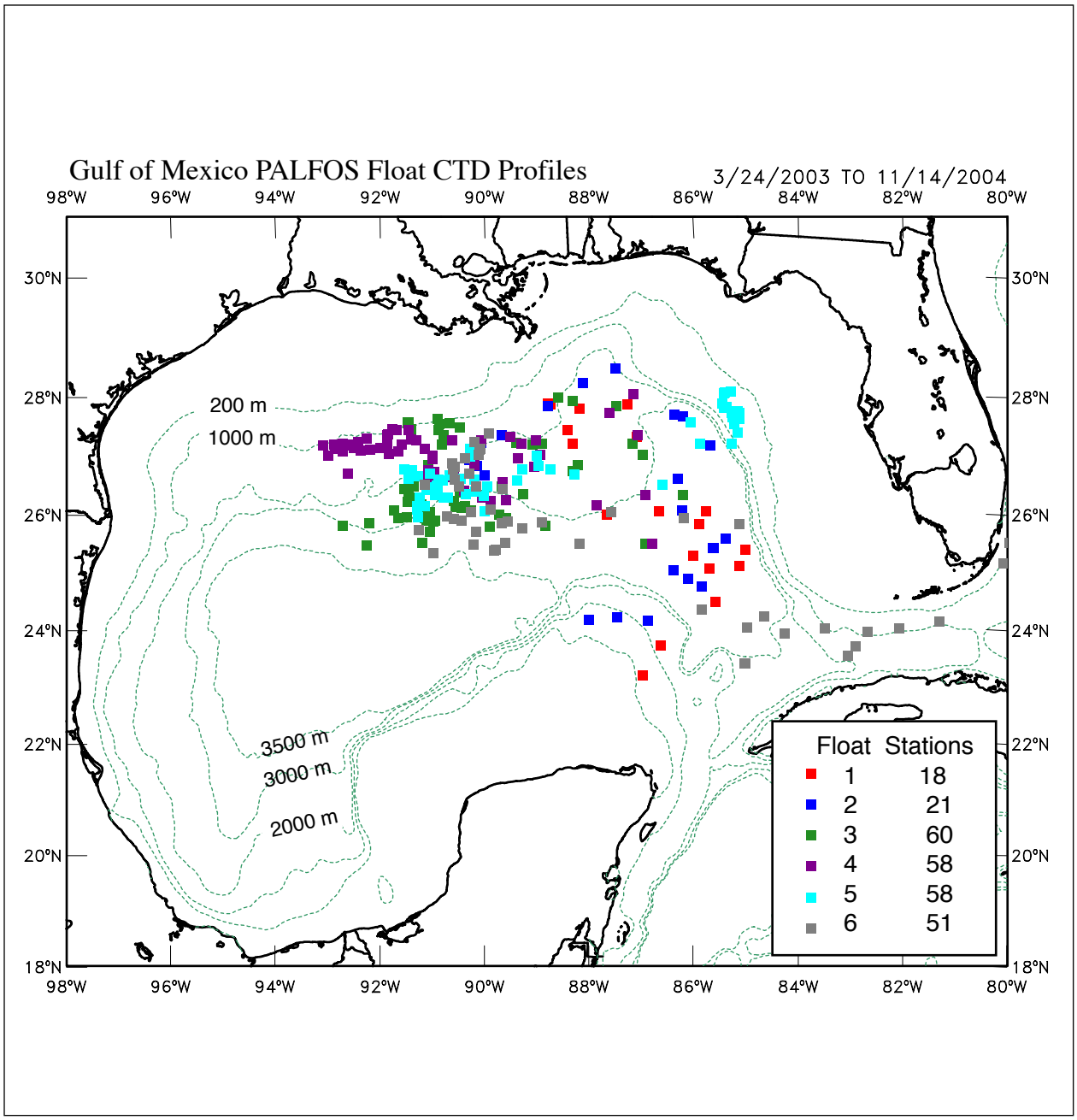

Figure 3.1-14. Locations at which the indicated PALFOS drifters measured vertical profiles of temperature and conductivity. This illustrates well that these drifters tended to spend much of the field program in the general study area. Some PALFOS drifters moved into the eastern Gulf, while no PALFOS drifters moved very far into the western Gulf over the one year measurement interval.

generally within or close to the boundaries of the study area. Given the presence of the LC, LCE and cyclonic features that were located in and near the study area, the PALFOS drifters profiled through many of the hydrographic conditions that occurred in the upper layer during the study. Note also that these profiles were incorporated into the GEM methodology for estimating T/S fields based on PIES observations.

To put the PALFOS-based temperature, salinity and density observations in an historical (Gulfwide) context, results from other surveys are used for comparison. A T/S plot of deepwater profiles taken during an MMS-funded physical oceanographic study (SAIC, 1986) is shown in Figure 3.1-15. Of note are the salinity maxima and minima. Salinity maximums that occur at sigma·t = 25.5 are associated with Subtropical Underwater that enters the Gulf via the Yucatan Channel at a nominal depth of 150 m. The salinity minimum is associated with Antarctic Intermediate water that also enters via the Yucatan Channel. Given that LCEs result from the separation of an anticyclonic rotating mass of LC water, LCEs should and do initially have characteristics of the original LC water mass properties. The Subtropical Underwater can and does erode and is modified as the LCE moves westward across the GOM. Using CTD profiles taken in Fast Eddy in October 1985 (Figure 3.1-16) many of the same characteristics of LC water were retained well into the western Gulf. Near the LCE boundaries, erosion and mixing occurred, which explains the fact that T/S observations had a comparable temperature range, but salinities were approximately 0.35 psu less than the Subtropical Underwater salinity maximum. A very comprehensive hydrographic survey of Fast Eddy, that occurred at the end of January 1986 shows continued erosion with loss of water with temperatures greater than approximately 22.5°C (Figure 3.1-17). While mixing was still occurring, the limb of the T/S curve leading to the Subtropical Underwater salinity maximum is still evident.

The historical observations point to the persistence of many LC-water characteristics as a LCE traverses westward across the GOM. Of general utility is recognition of the fact that GOM water with temperatures less than 16°C are consistently associated with the same salinities, such that knowledge of the temperature profile, in conjunction with a functional relationship of S to T for T≤16°C, allows computation of salinity and hence density.

A cumulative plot of all T/S profile data taken by PALFOS floats is shown in Figure 3.1-18. The distribution of T/S points is consistent with features seen in results from prior ship-based CTD surveys. Above approximately 18°C, the point scatter seems somewhat greater than results of tethered profiling instruments. The component T/S plots for each PALFOS drifter that contributed to the cumulative plot are shown in the six-panel presentation of Figure 3.1-19. PALFOS float 2 shows a well-defined Subtropical Underwater maximum that is similar to that expected for profiling in the LC or well within a LCE. There were few observations away from such a curve. In contrast, PALFOS floats 4 and 5 had little evidence of the presence of Subtropical Underwater, but showed the expected consistent T/S relationship for T≤16°C.

Selected profiles of temperature, salinity and sigma-t are shown in Figure 3.1-20. These were chosen from the database of PALFOS-based profiles to illustrate several features that contributed to the T/S plots and hence water mass characteristics shown in Figure 3.1-18. Readily discernable is the presence of a surface mixed layer for the winter profiles (Figure 3.1-20d and

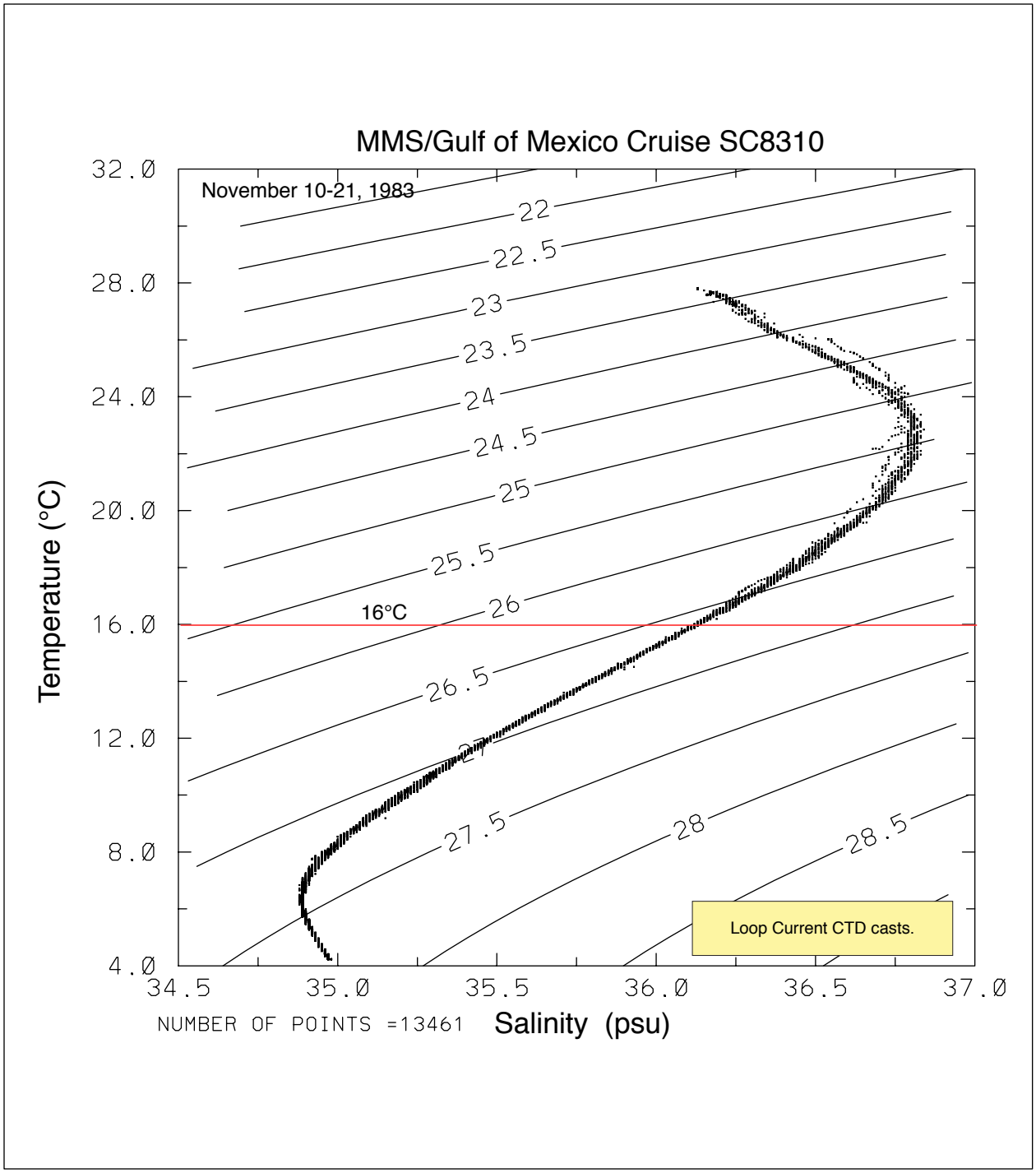

Figure 3.1-15. T/S diagram for CTD profiles taken within the central and eastern LC during a fall cruise. Profiles at the edge of the LC were not included in the summary plot.

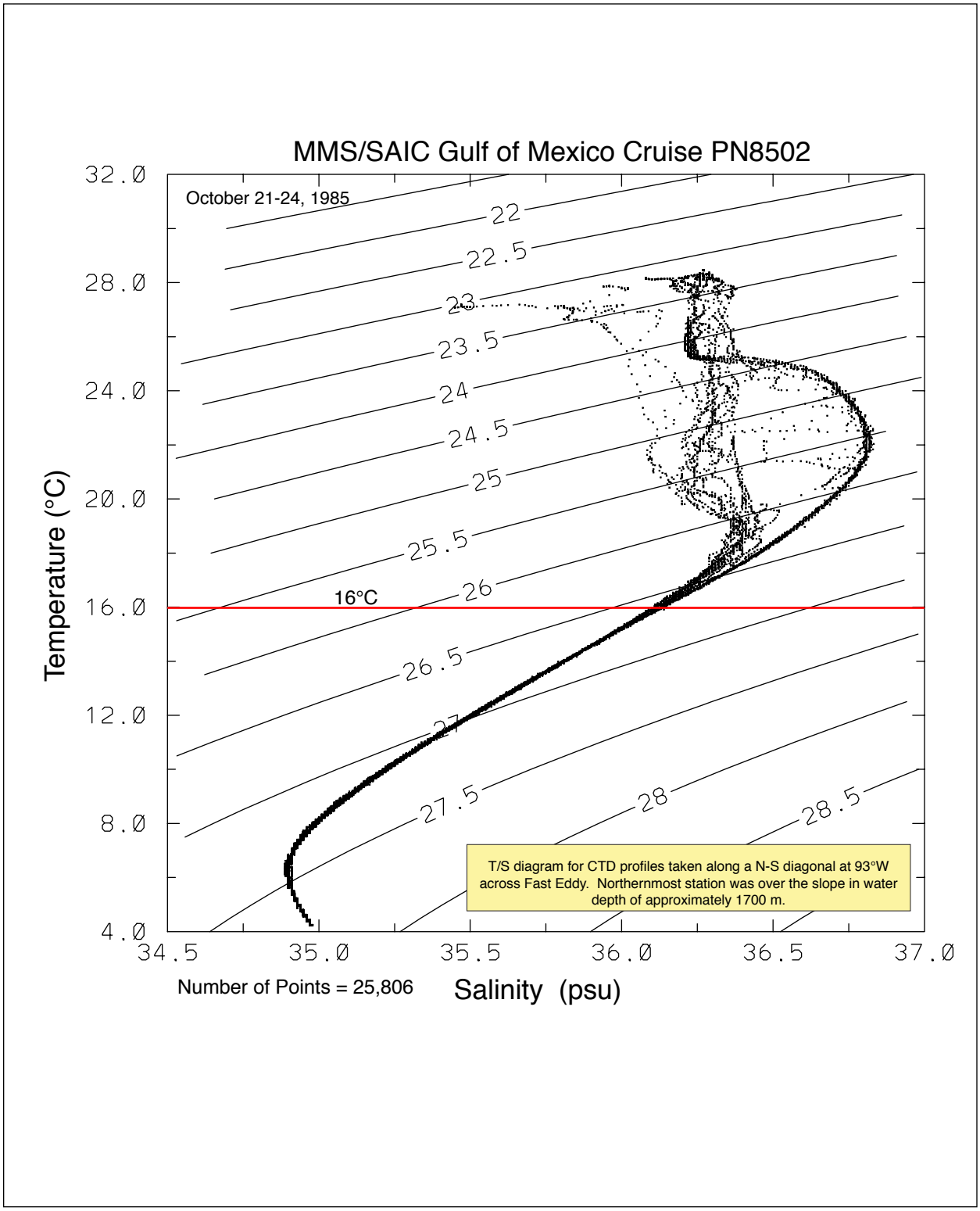

Figure 3.1-16. T/S diagram for CTD profiles taken in October 1985 on a transect through the center of this major LCE (Fast Eddy) prior to it interacting significantly with the western basin boundary.

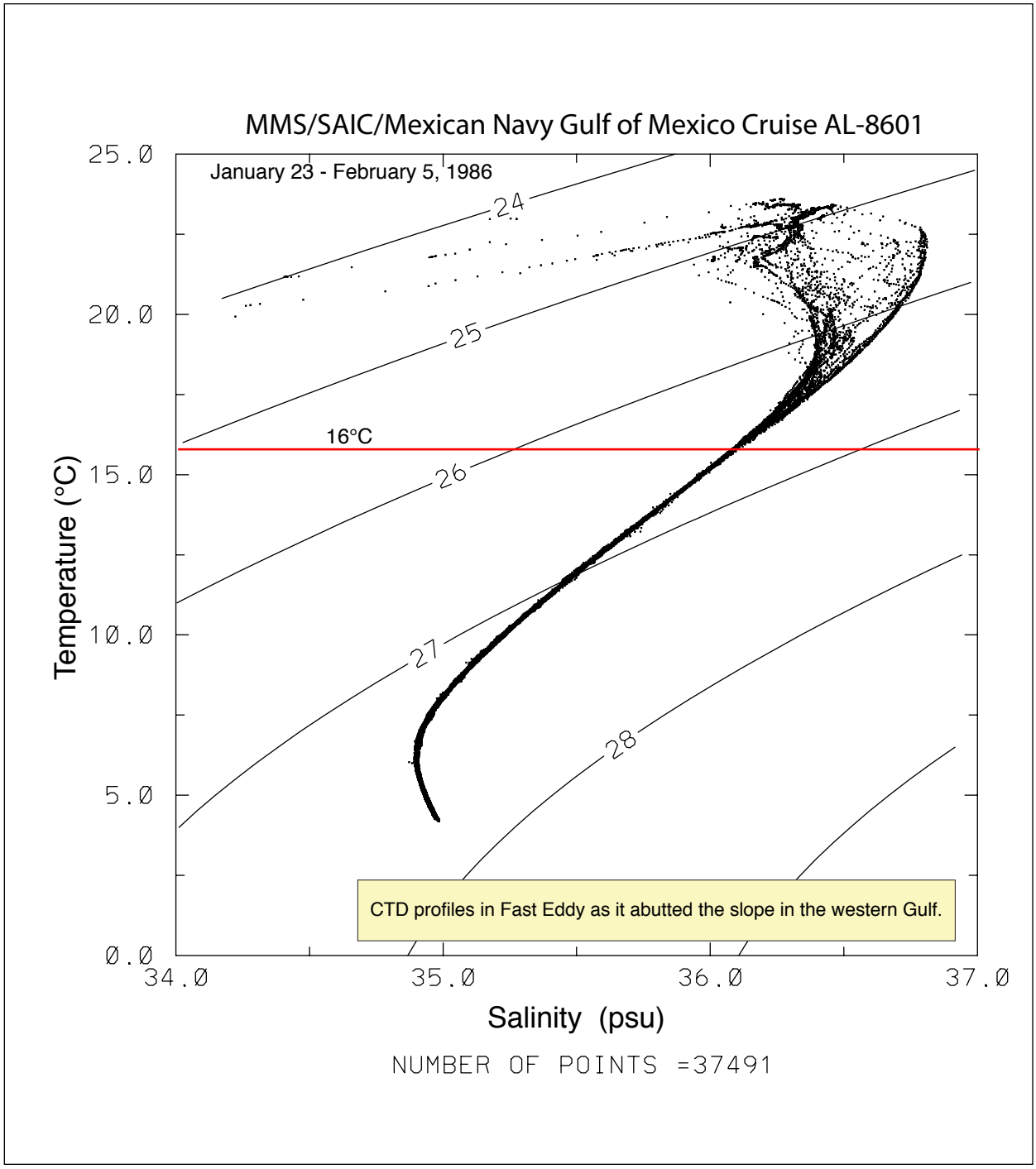

Figure 3.1-17. T/S diagram for CTD profiles taken in Fast Eddy after it had interacted significantly with the basin western boundary. Note also, this cruise occurred during winter with most of the profiles taken south of 26°N.

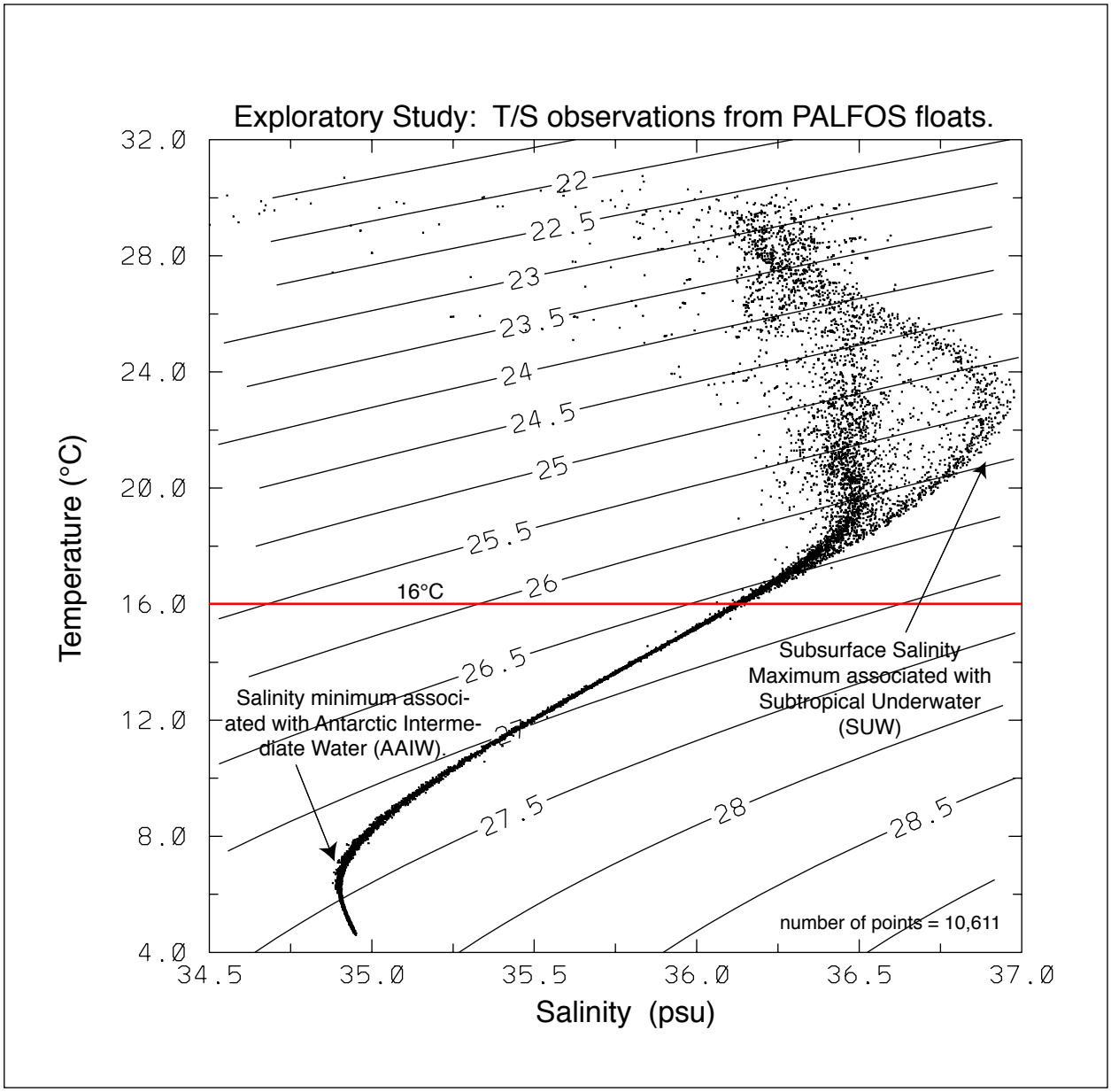

Figure 3.1-18. Plot of T/S values (small dots) measured by all PALFOS floats deployed for the Exploratory Study. Profiles were sampled at Δz=10 m above 300 m depth and at Δz=50 m below 300 m to the residence depth of 1000 m.

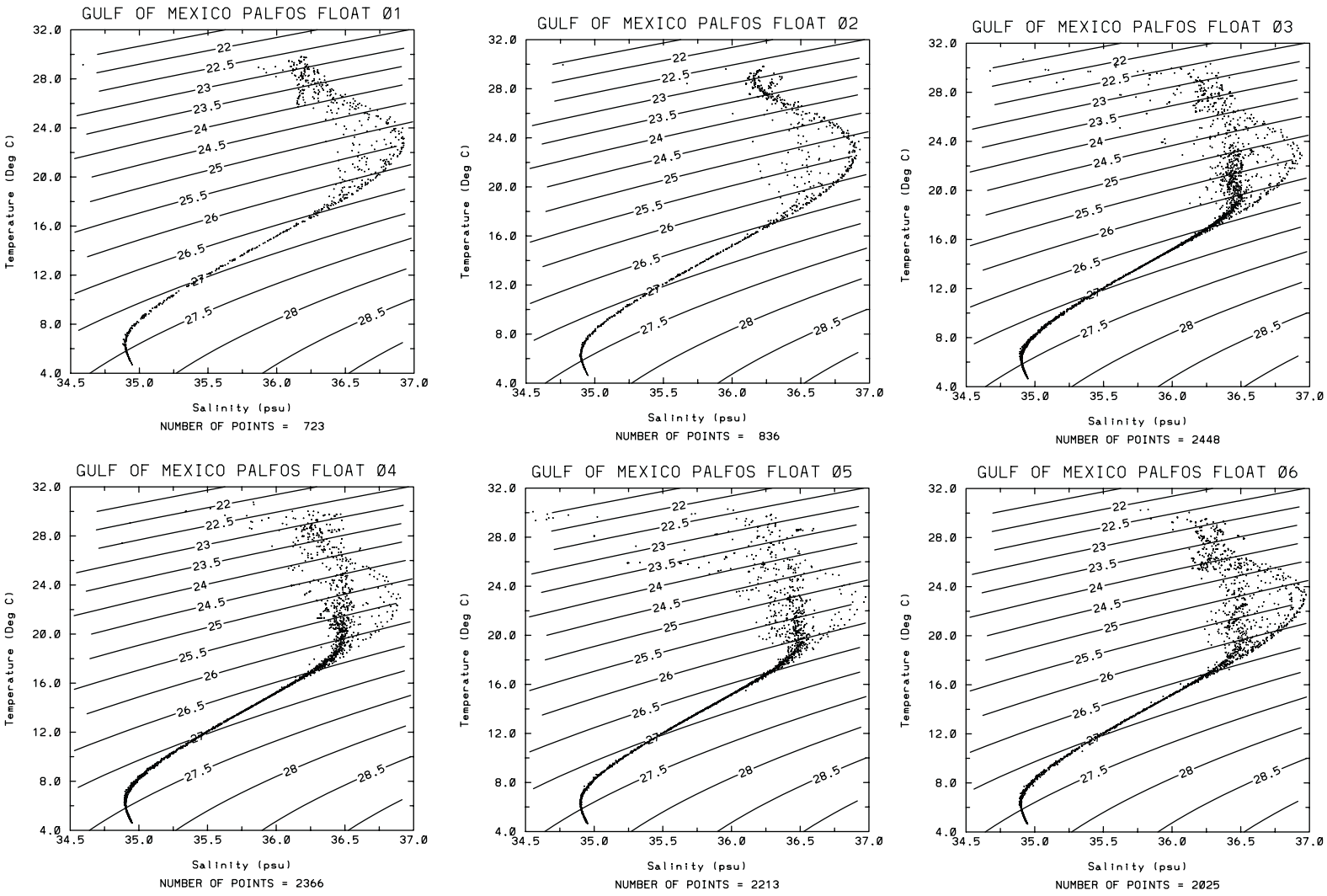

Figure 3.1-19. Separate cumulative T/S diagrams for each indicated PALFOS float. The float number corresponds to that in Figures 3.1-14 and 3.1-20.

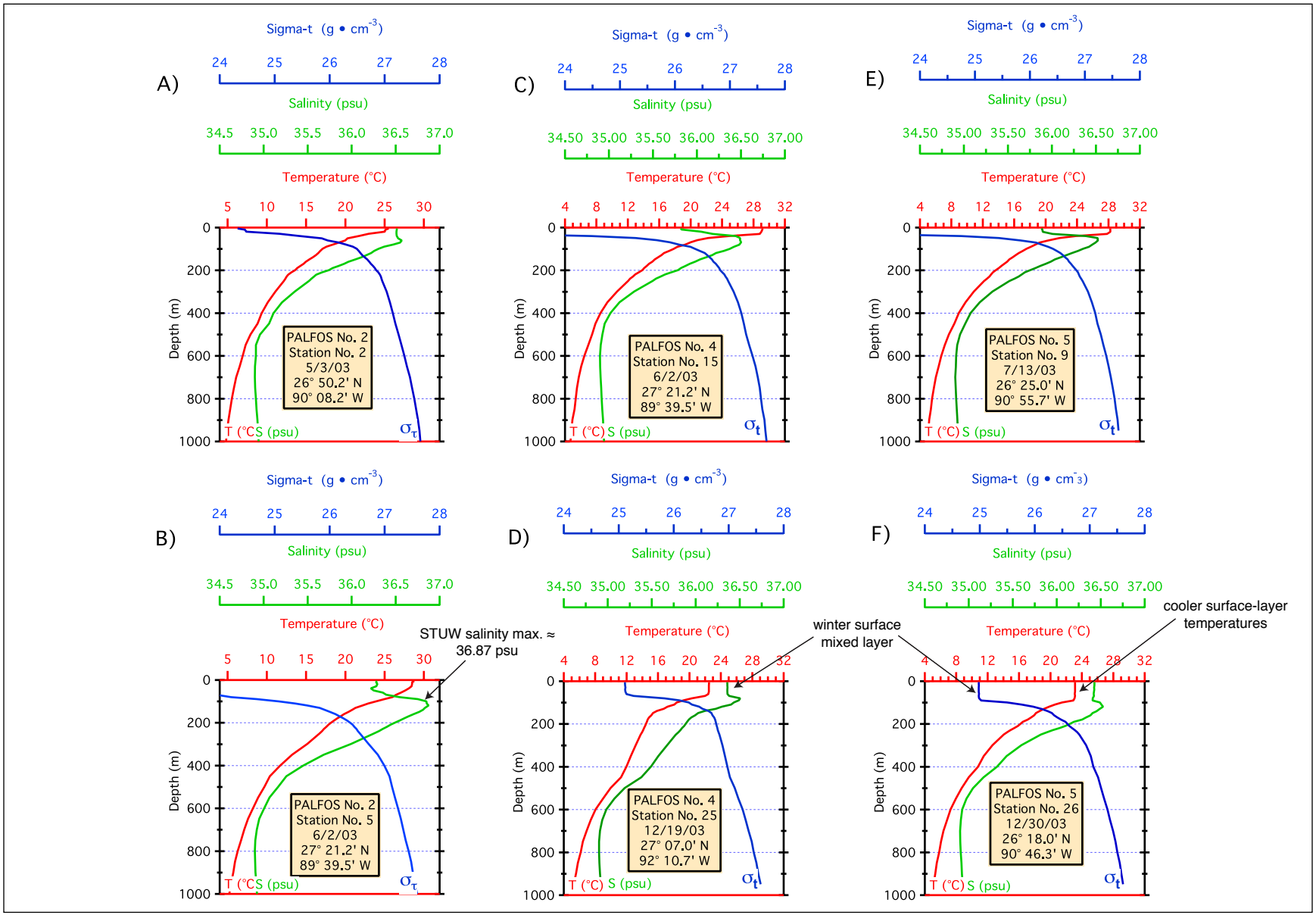

Figure 3.1-20. Series (Panels A-F) of PALFOS profiles illustrating upper layer conditions and processes. Description in the report is supplemented by profile features documented at the various locations and times.

20f). Additionally, the surface waters were substantially cooler than that occurring in the warmer months (e.g., 3.1-20c). In one of these example profiles (but also occurring in other profiles) the Subtropical Underwater was clearly present (Figure 3.1-20b) with a salinity maximum of 36.87 psu. These profiles vary only slightly from casts done with a tethered, calibrated CTD. Note the PALFOS profiles were sampled at Δz=10 m above 300 m and at Δz=50 m below 300 m. All CTD and PALFOS profiles also accurately measured the presence of a salinity minimum associated with Antarctic Intermediate water.

3.1.7 Salinity Changes in Subtropical Underwater

Secular salinity changes in the Subtropical Underwater appear in the core of the LC. Contemporary salinity values in Subtropical Underwater have become higher than the historial hydrography during the last two decades at low τ(150-500) in the GOM (Figure 3.1-21). Salinity between potential density 25.5 and 26.0 kg m^{-3}, Subtropical Underwater, for τ(150-500) < 0.459 seconds was freshest in the mid-1980's and increased by nearly 0.1 psu over the next two decades. Here we use τ from 150 to 500 to utilize as many historical profiles as possible. Recall that low τ is comparable to high dynamic height and represents the core of the LC. Subtropical Underwater refers to the shallow salinity maximum near 150 m and is formed when Tropical Surface Water subducts within the subtropical gyre. The LC, the western boundary current extension of the subtropical gyre, advects Subtropical Underwater into the GOM. During the past 20 years, evaporation-precipitation in the tropical Atlantic has increased and Tropical Surface Water salinities have accordingly increased (Curry et al., 2004). Salinity is nearly conserved beneath the surface. The trend of increasing Subtropical Underwater salinities over the last 20 years at low τ (high dynamic height) indicates that the LC carries this tropical signal into the GOM and ultimately into the Florida Straits and the Gulf Stream (Figure 3.1-21).

3.2 Lower Layer

3.2.1 Historical Floats

Few deep float measurements had been made in the GOM prior to this experiment. In fact, the only earlier experiment of any magnitude was a series of (temperature only) profiling floats launched into the GOM between April 1998 and February 2002 in two groups by Dr. G. Weatherly and his colleagues (Weatherly et al., 2005). These floats were set to drift at a rest depth of 900 m and cycle every seven days. Floats were launched between 83°W and 94°W in the northern Gulf in water depths between 900 m and 3000 m. Although a number of failures were experienced, these floats provided interesting data on the overall circulation patterns. In particular, it was observed that:

- There appeared to be little communication between the eastern and western basins; floats launched in the east stayed in the east, whereas floats launched in the west stayed in the west;

- The circulation in the western and southwestern Gulf of Mexico was typically cyclonic, whereas the circulation in the eastern Gulf was less steady and not clearly cyclonic;

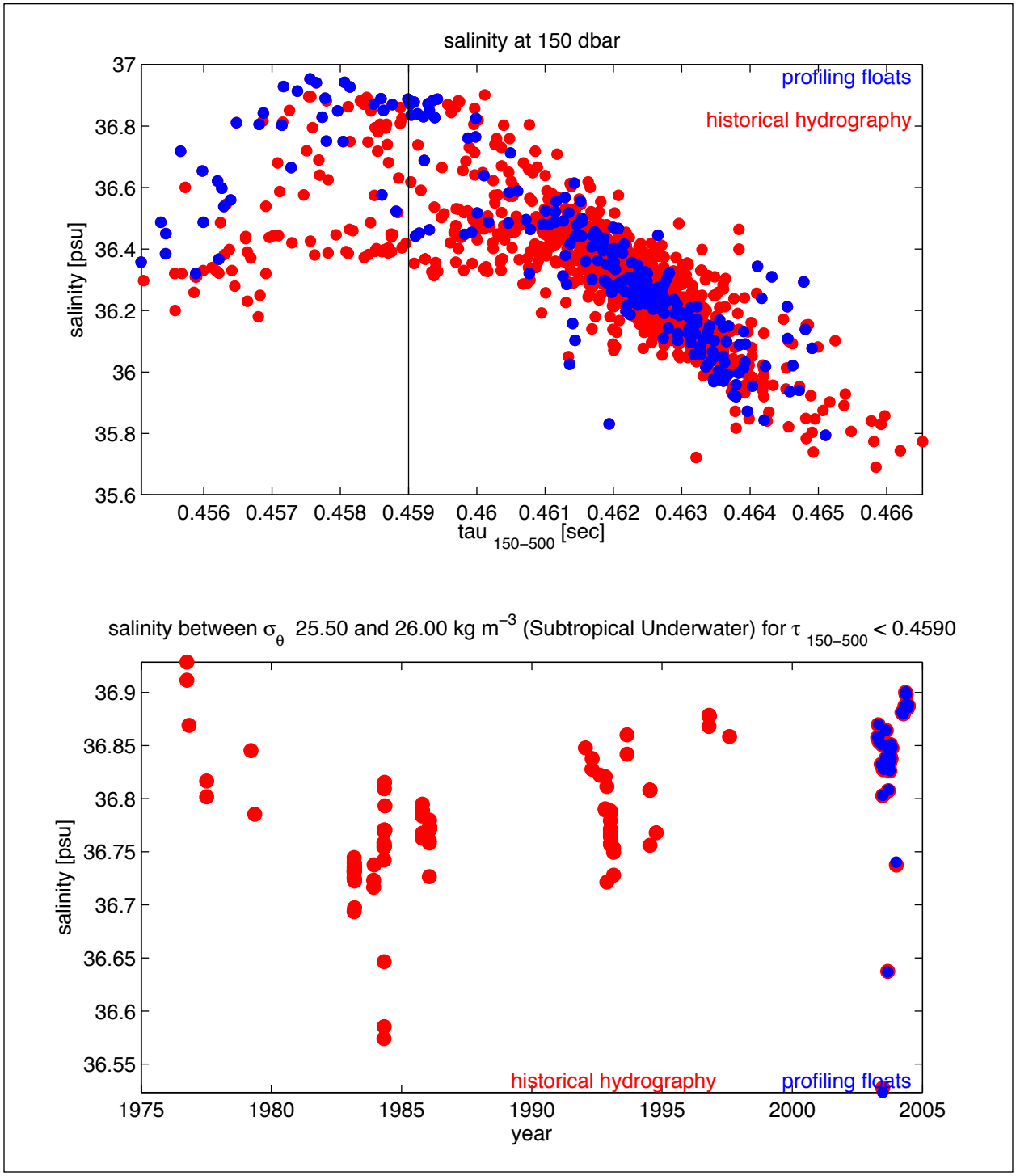

Figure 3.1-21. Secular signal exists in the salinity of the Subtropical Underwater. Upper panel: Salinity values from the most recent hydrocasts (float profiles and Exploratory CTDs) within the Subtropical Underwater layer, 150 dbar, at low tau (τ) are higher than salinity values from the historical hydrography. Lower panel: Salinity between potential density 25.5 and 26.0 kg m^{-3}, Subtropical Underwater, for τ(150-500) < 0.459 seconds is freshest mid-1980 and increases by nearly 0.1 psu over the next two decades.

- There was no clear connection observed between the flow patterns at 900 m and superimposed satellite-derived SSH patterns.

These observations, some of which are shown in Figure 3.2-1, should be kept in mind when the results from the present experiment are discussed.

3.2.2 Float Trajectories at Several Levels

Trajectories of all RAFOS and PALFOS floats are shown in Figures 3.2-2. An overall "spaghetti diagram" of all RAFOS floats is shown in Figure 3.2-2a. RAFOS float tracks at depths of 1000, 1500, 2000, 2500 and 3000 m are shown in Figures 3.2-2b-f. It should be noted that in several cases (e.g., RAFOS floats 475, 489) floats deployed near the bottom actually ran aground, suggesting significant upslope, cross-isobath flow during those times. The largest fraction of floats were deployed in the 1500 m and 2500 m layers, whereas fewer float tracks are available from 1000 m, 2500 m and 3000 m.

Although much of the current meter and PIES analysis is concentrated in the main study area, these tracks allow a better perspective on the larger-scale circulation in the GOM. In particular, it can be seen that floats originally deployed in a relatively small area rapidly spread throughout much of the northern basin.

The PALFOS floats which resided at 1000 m between vertical profiles tend to stay in the central basin for a relatively long time, although these finally "wander away" as well. If and when PALFOS floats moved out of the general deployment area, these profiling drifters moved toward the east. None were seen to move into the western basin of the GOM. This preferential movement appears to have similarities to the larger number of PALACE floats deployed and documented by Weatherly (2004) and shown in Figure 3.2-1. The reader is reminded that trajectories of PALFOS drifters reflect the currents at the residence depth, current profiles during rising and descending, and the time spent on the surface. Consequently, total trajectory plots of PALFOS drifters reflect integrated influences rather than movement at a depth as seen in RAFOS trajectories.

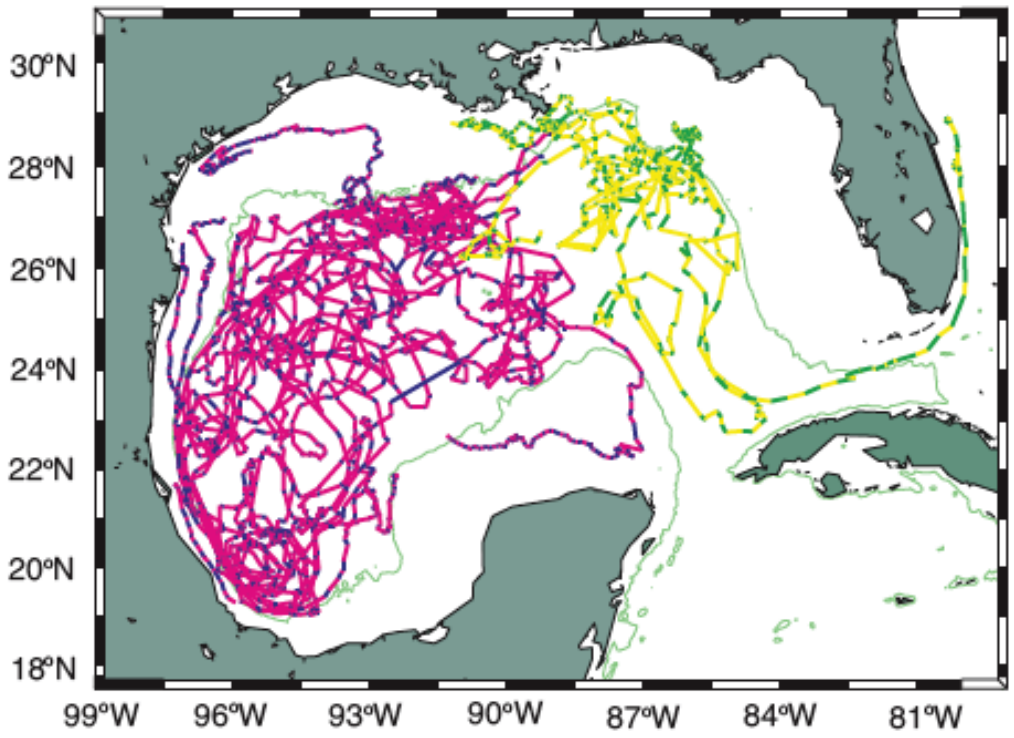

Figure 3.2-1. Map showing the various paths of PALACE floats as deployed, tracked and reported on by Dr. George Weatherly (2004). The red/blue lines show movement of the floats deployed in the western Gulf while the yellow/green lines show movement of floats deployed in the eastern Gulf. The continuous green line is the 900 m isobath.

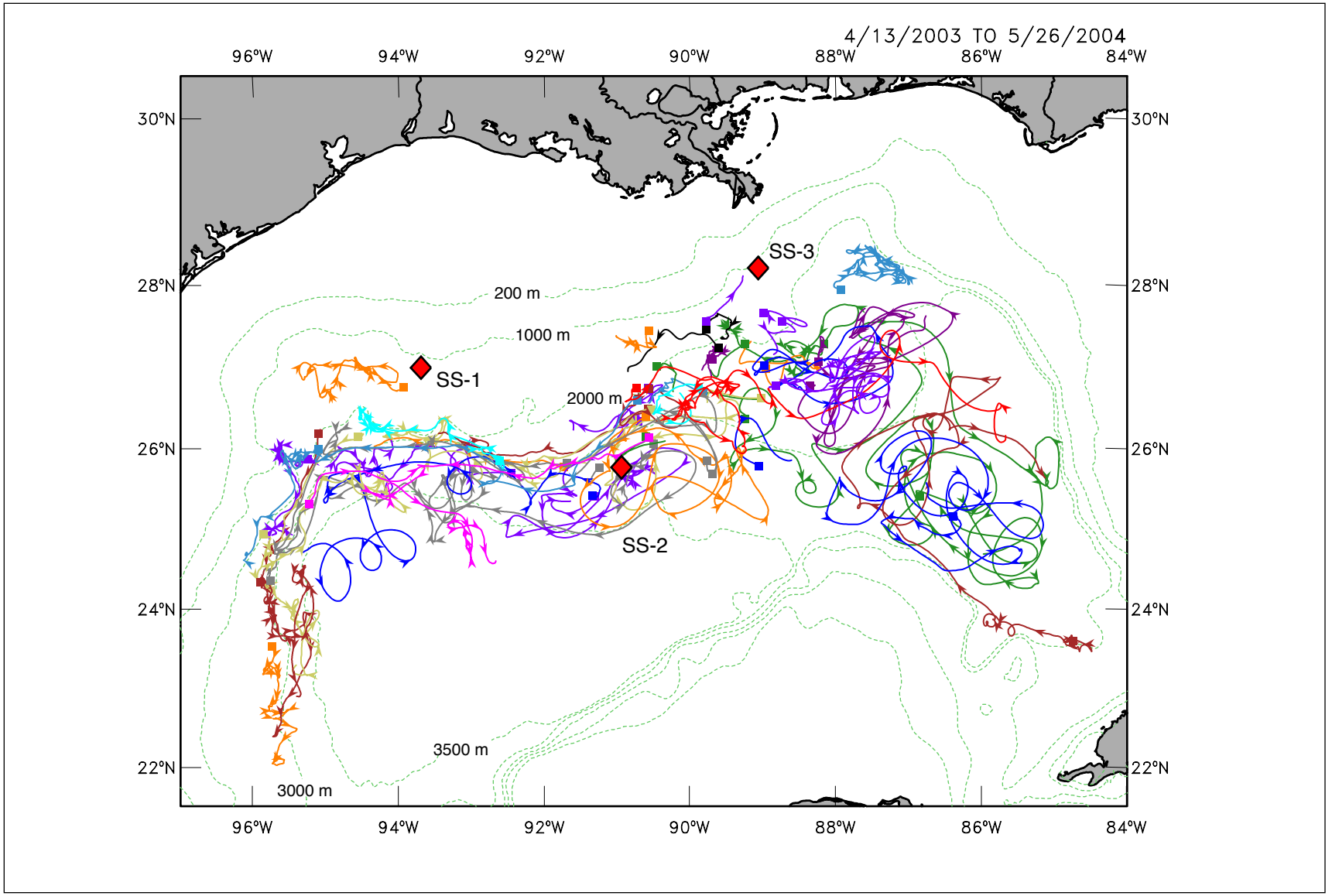

Figure 3.2-2a. Spaghetti plot of all RAFOS float trajectories at all depths in the Exploratory Study. Sound sources in this and following figures are SS-1, SS-2 and SS-3. Track beginning is indicated by a square. Tracks before and after sound source replacement are both shown in this color-coded presentation.

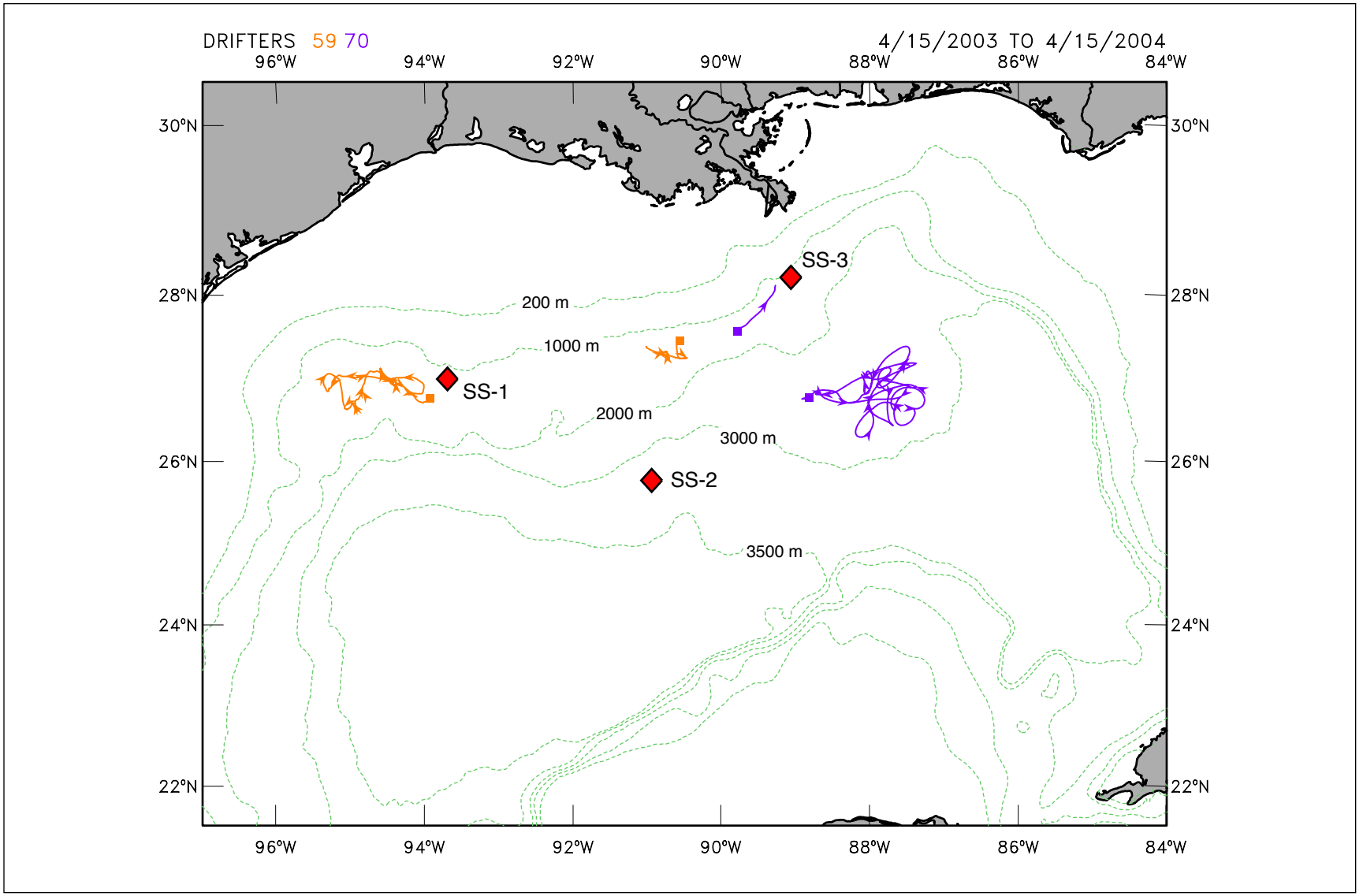

Figure 3.2-2b. RAFOS float trajectories at 1000 m. Drifter numbers in text are 400+nn, where nn is the drifter identification number. Track beginning is indicated above by a square. Portions of trajectory before and after sound source replacement are both shown in this color-coded presentation.

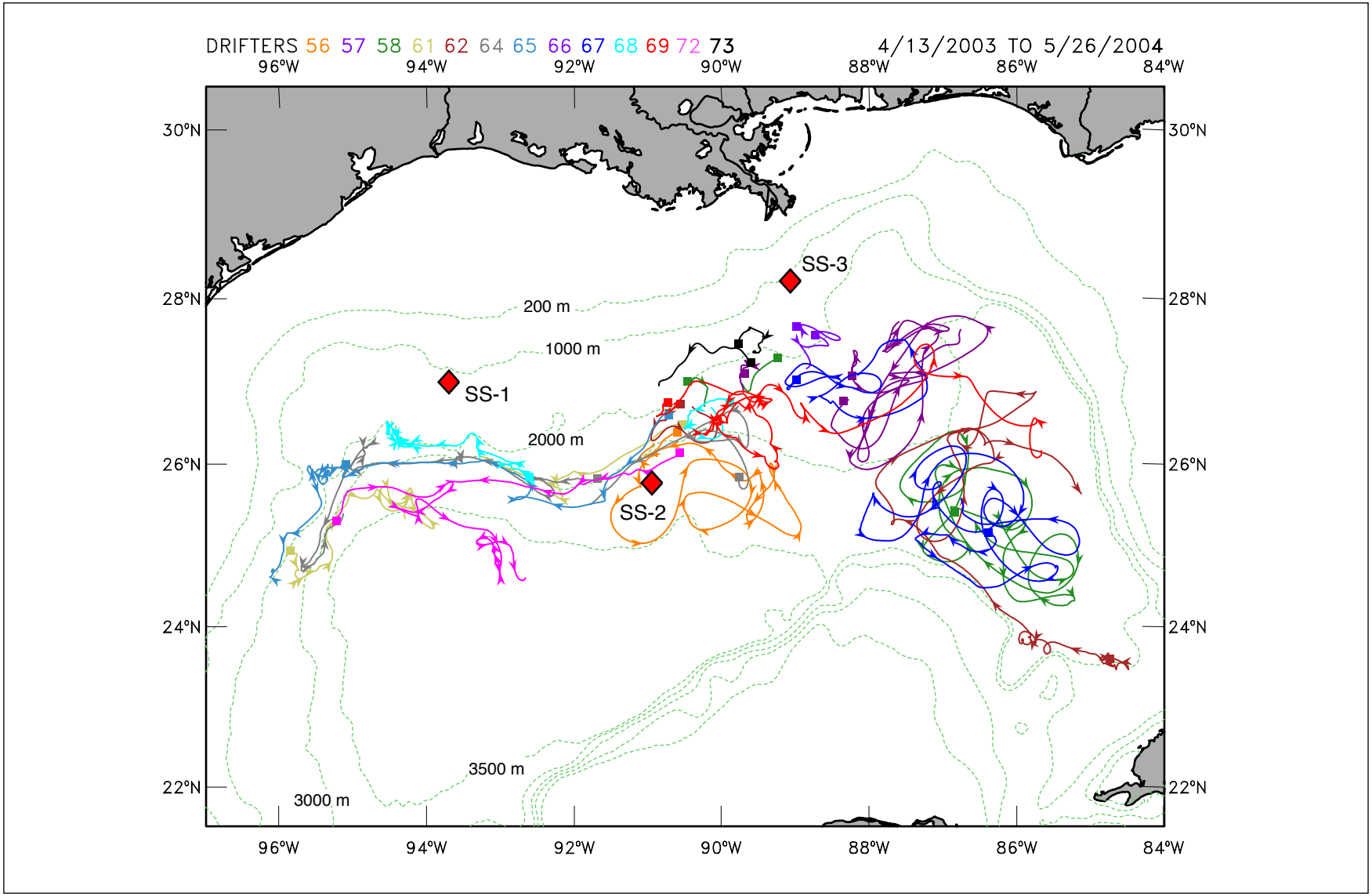

Figure 3.2-2c. RAFOS float trajectories at 1500 m. Drifter numbers in text are 400+nn, where nn is the drifter identification number. Track beginning is indicated above by a square. Portions of trajectory before and after sound source replacement are both shown in this color-coded presentation.

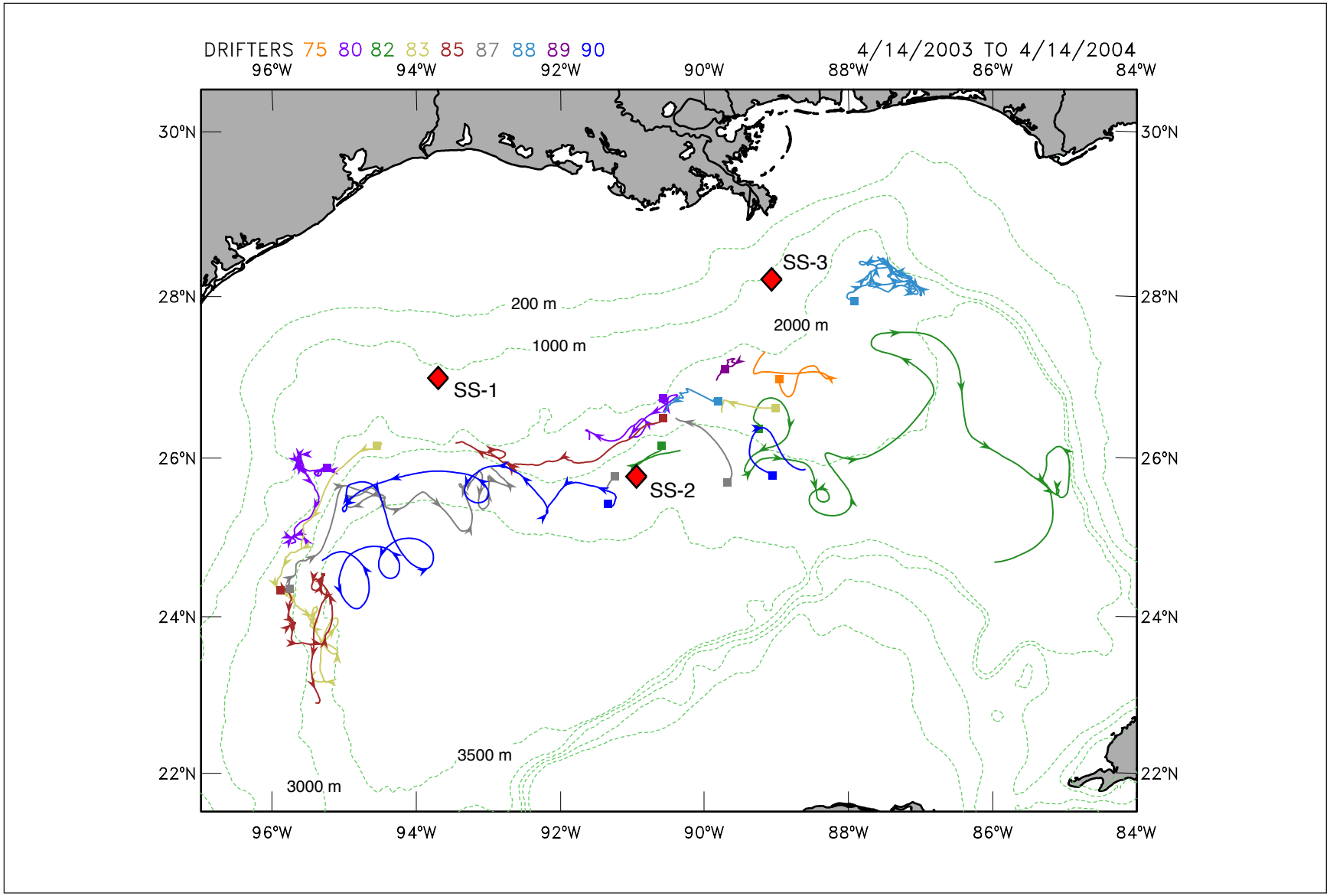

Figure 3.2-2d. RAFOS float trajectories at 2000 m. Drifter numbers in text are 400+nn, where nn is the drifter identification number. Track beginning is indicated above by a square. Portions of trajectory before and after sound source replacement are both shown in this color-coded presentation.

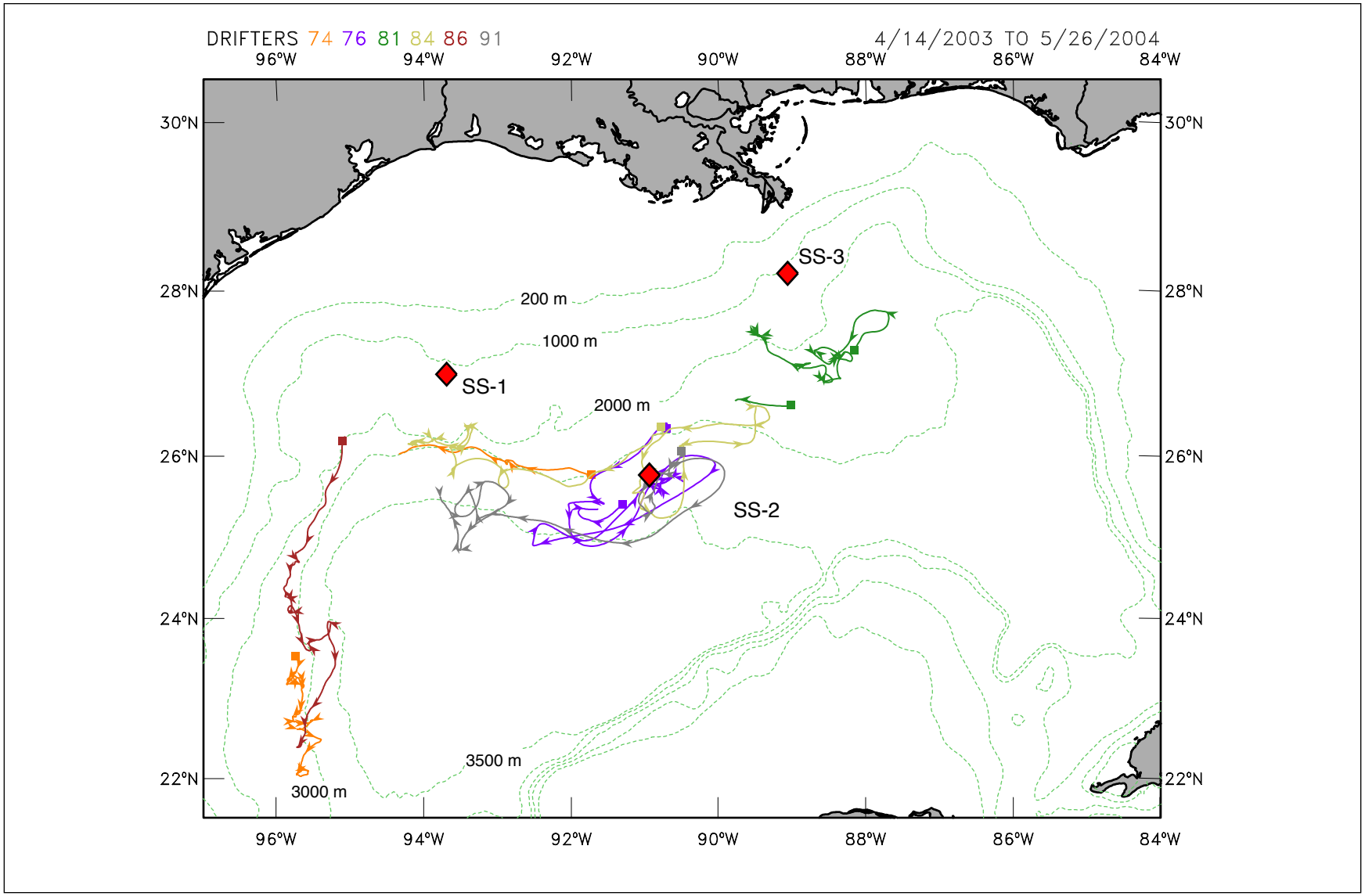

Figure 3.2-2e. RAFOS float trajectories at 2500 m. Drifter numbers in text are 400+nn, where nn is the drifter identification number. Track beginning is indicated above by a square. Portions of trajectory before and after sound source replacement are both shown in this color-coded presentation.

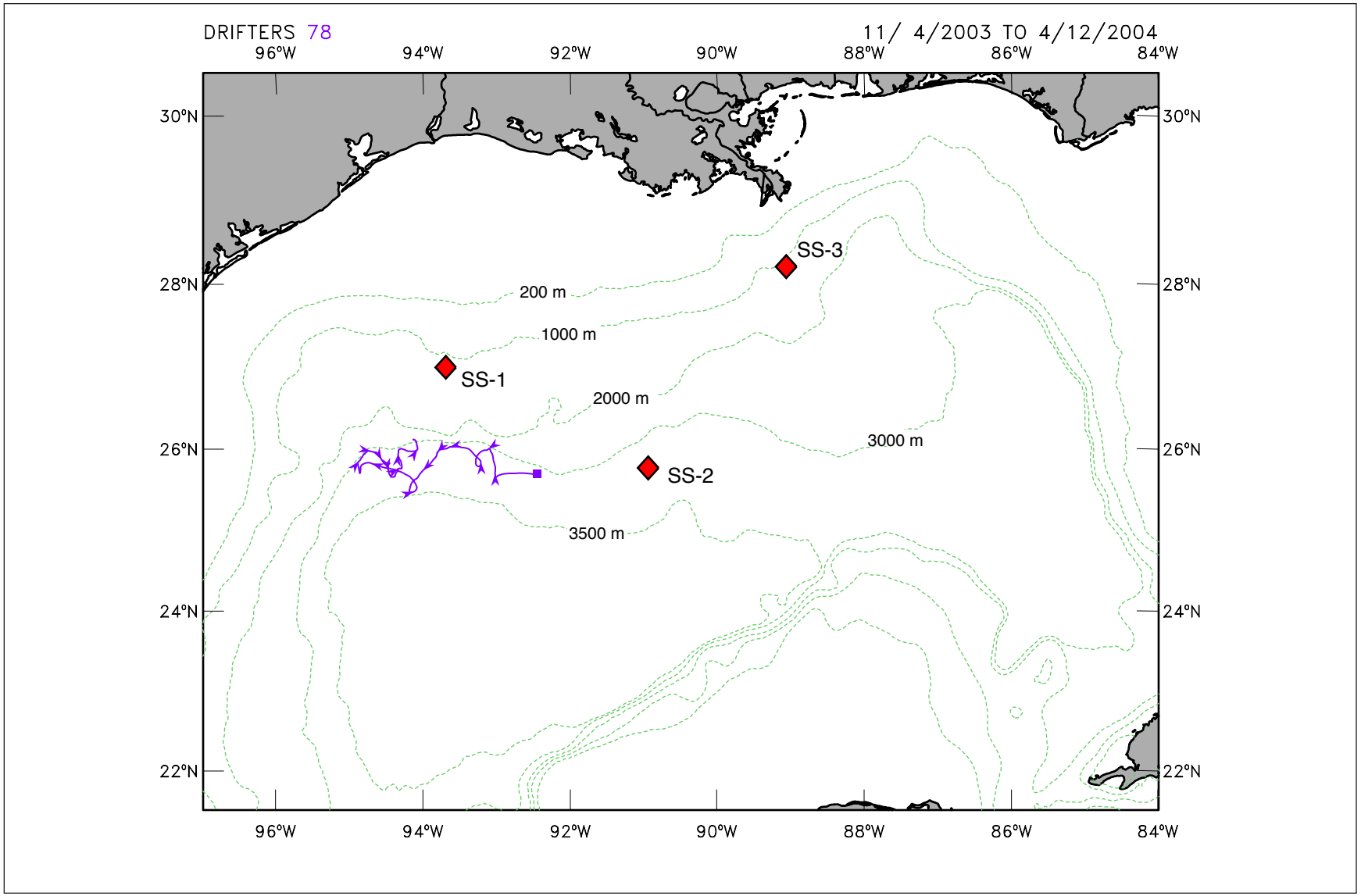

Figure 3.2-2f. RAFOS float trajectories at 3000 m. Drifter numbers in text are 400+nn, where nn is the drifter identification number. Track beginning is indicated above by a square. Any portion of trajectory before and after sound source replacement are shown in this color-coded presentation.

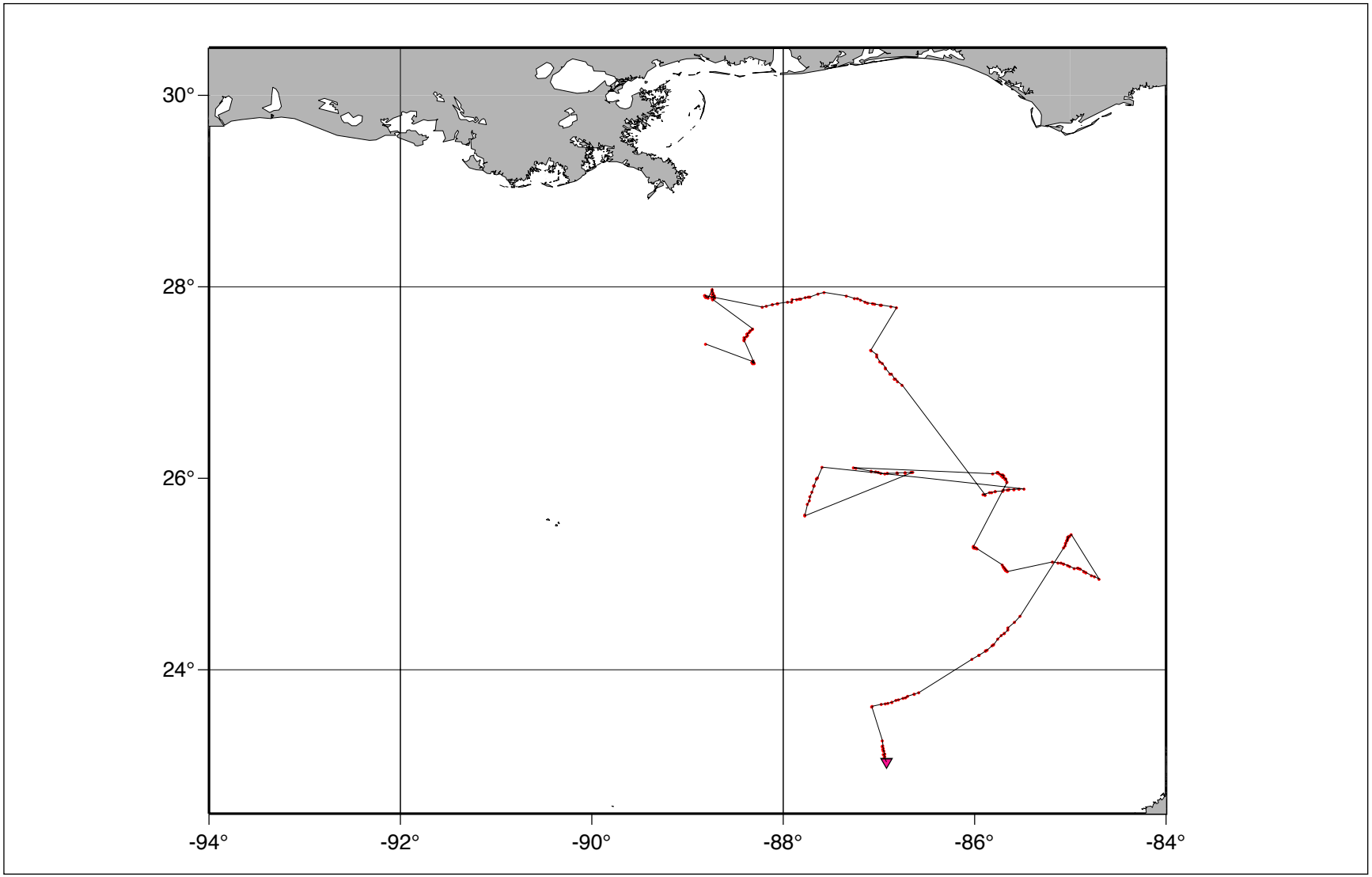

Figure 3.2-2g. Track of PALFOS float pf1. Acoustic tracking at 1000 m indicated by blue dots; Argos surface positions are red dots. During interval of source failures only red dots are available. Triangle shows final position.

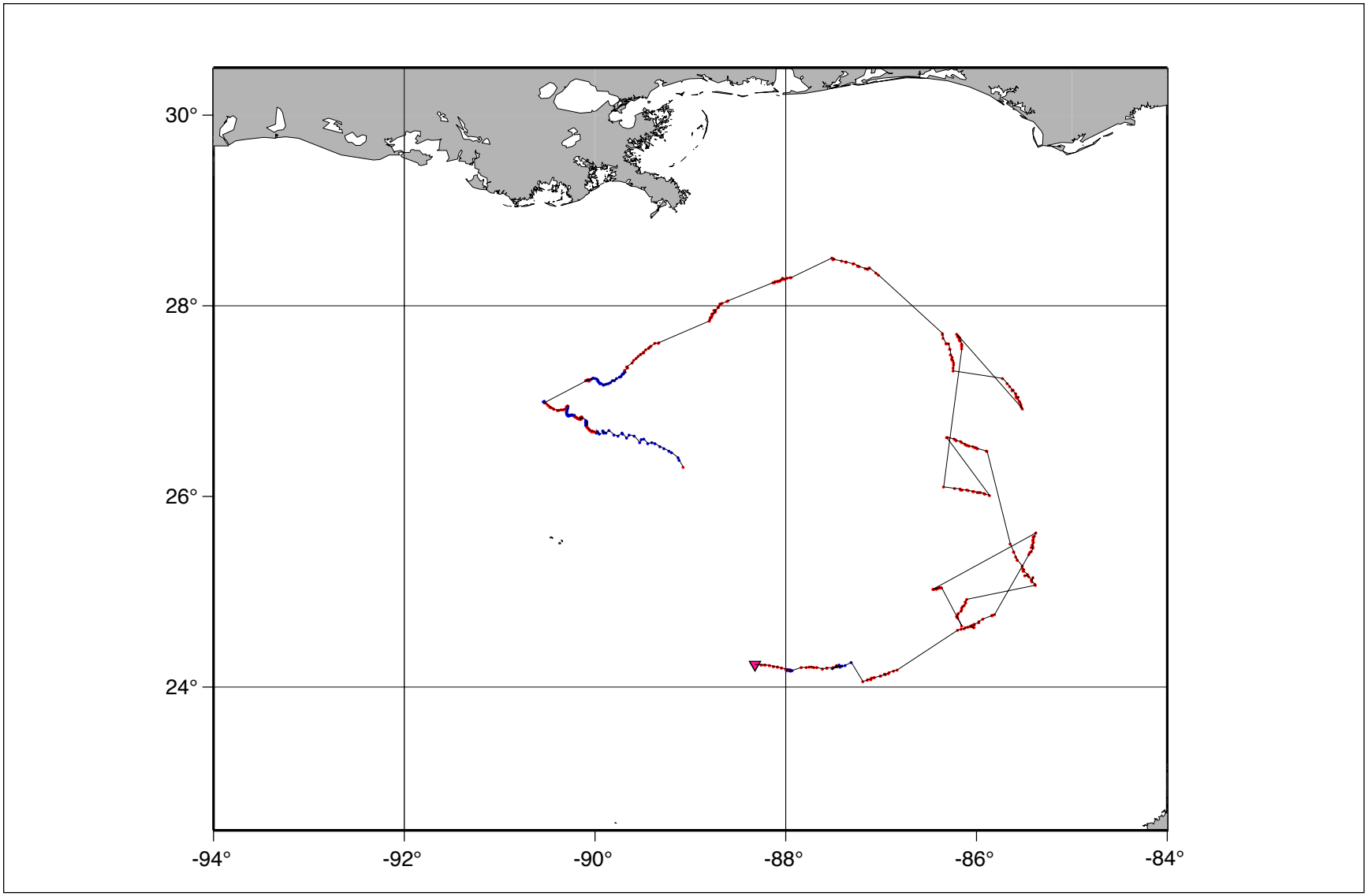

Figure 3.2-2h. Track of PALFOS float pf2. Acoustic tracking at 1000 m indicated by blue dots; Argos surface positions are red dots. During interval of source failures only red dots are available. Final position is shown by a triangle.

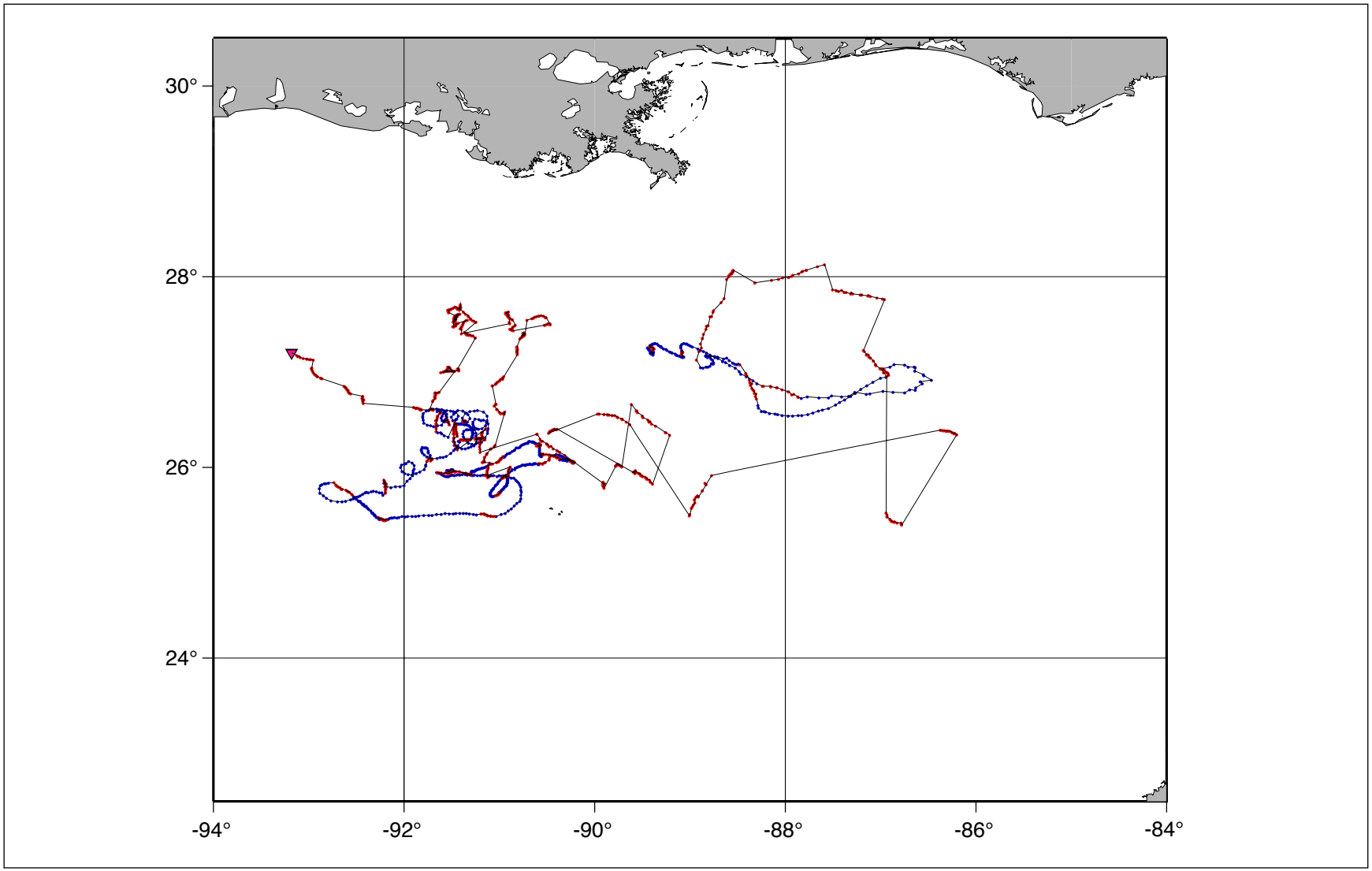

Figure 3.2-2i. Track of PALFOS float pf3. Acoustic tracking at 1000 m indicated by blue dots; Argos surface positions are red dots. During interval of source failures only red dots are available. Final position is shown by a triangle.

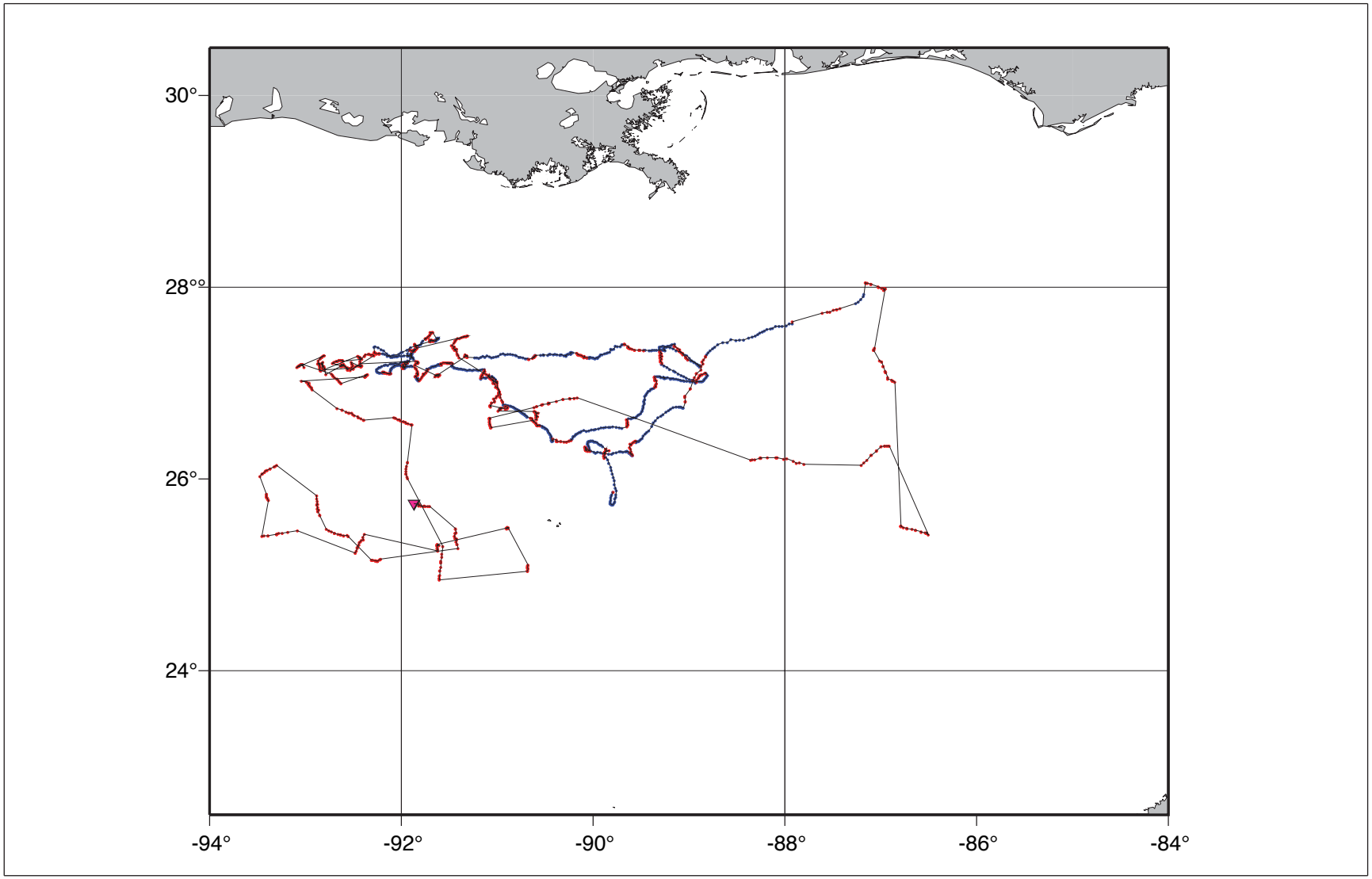

Figure 3.2-2j. Track of PALFOS float pf4. Acoustic tracking at 1000 m indicated by blue dots; Argos surface positions are red dots. During interval of source failures only red dots are available. Final position indicated by a triangle.

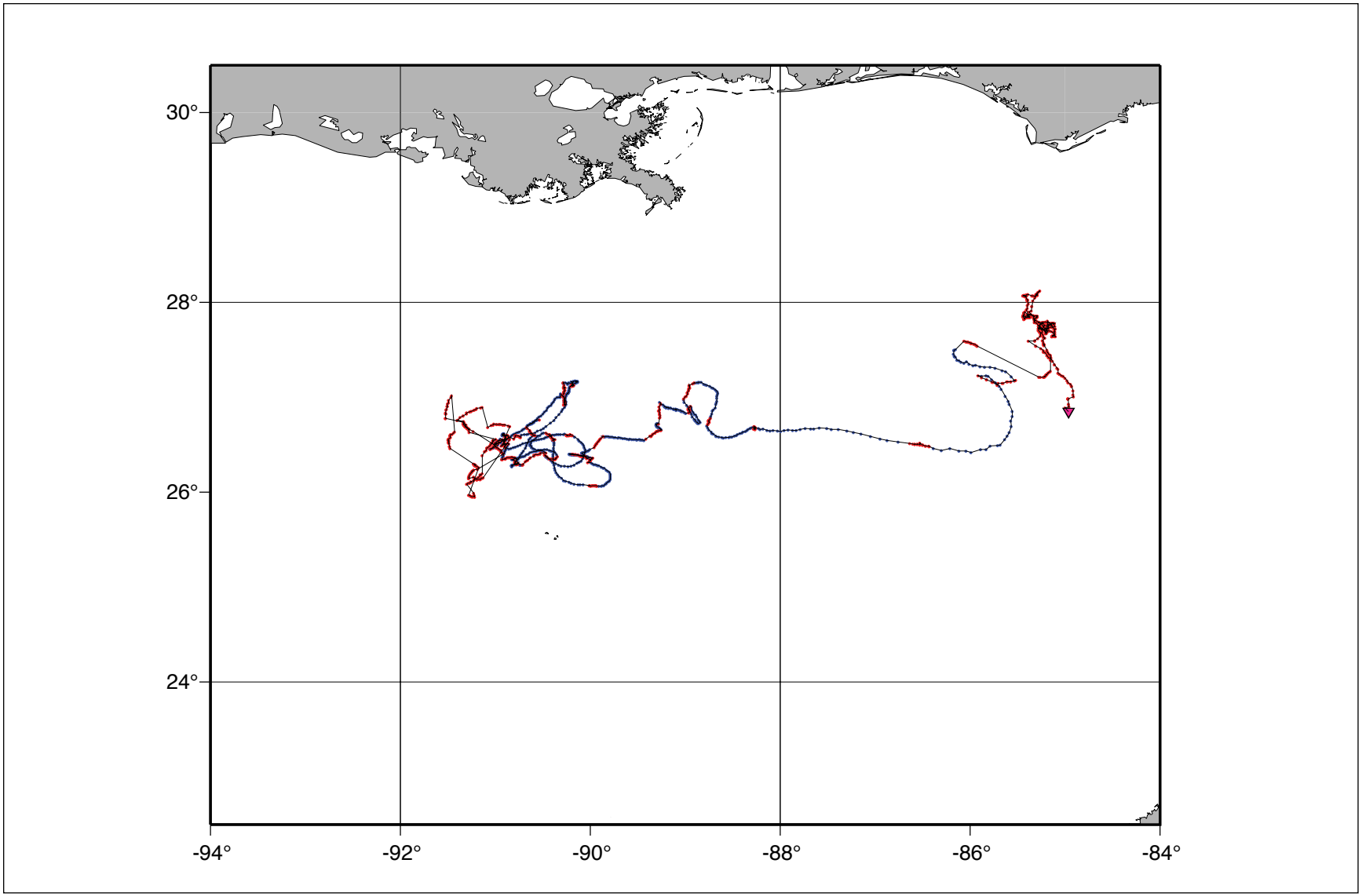

Figure 3.2-2k. Track of PALFOS float pf5. Acoustic tracking at 1000 m indicated by blue dots; Argos surface positions are red dots. During interval of source failures only red dots are available. Triangle shows final position.

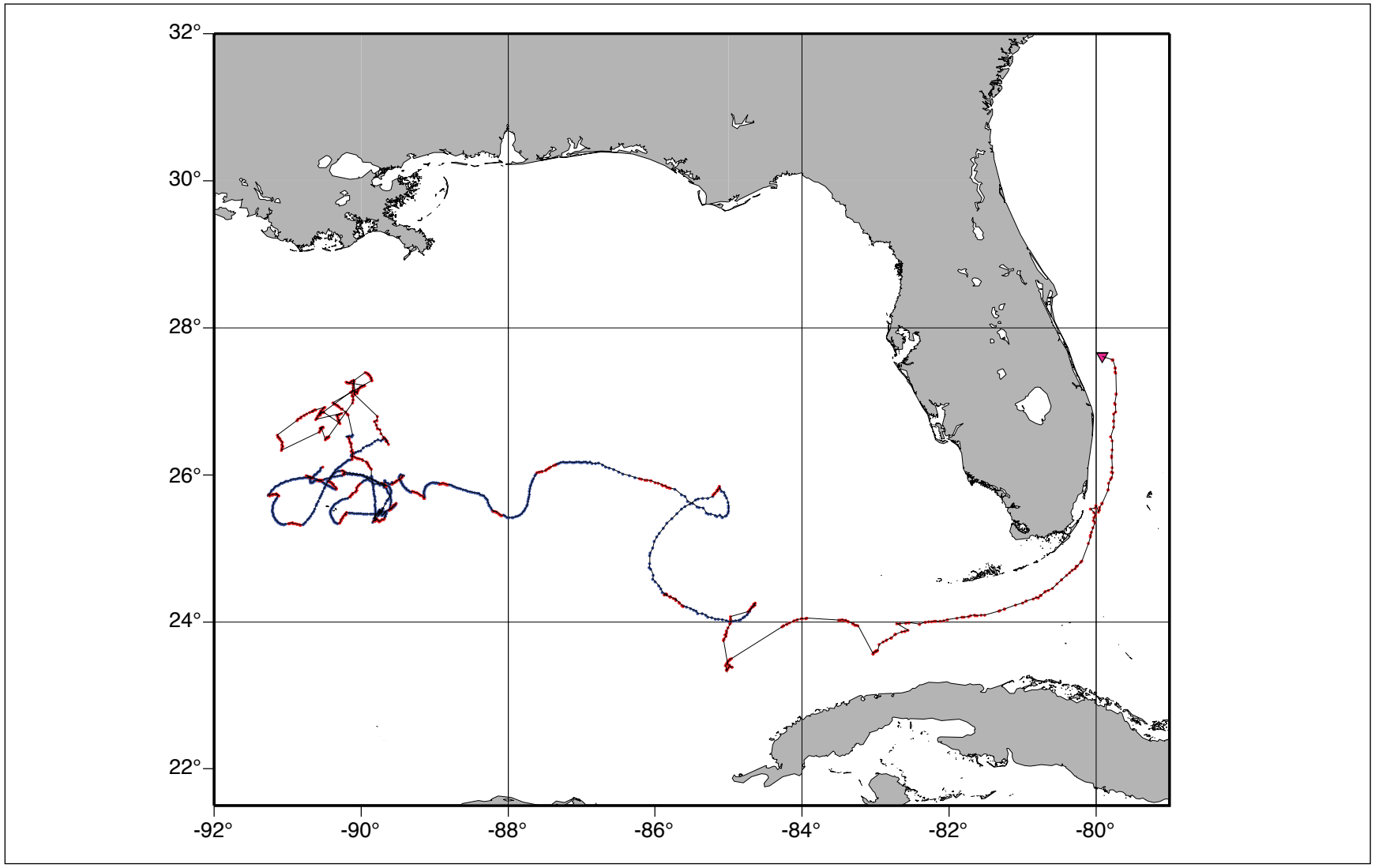

Figure 3.2-2l. Track of PALFOS float pf6. Acoustic tracking at 1000 m indicated by blue dots; Argos surface positions are red dots. During interval of source failures only red dots are available. Final position shown by a triangle.

4.0 BASIC DESCRIPTION IN THE STUDY AREA

4.1 Description of Upper-Layer Currents and Events in the Study Area

4.1.1 Vertical Structure of Upper-Ocean Features

The PIES array enables 'surveys' of the horizontal and vertical structure of ocean features. Here we provide a general overview of the vertical structure of temperature and velocity for six snapshots (Figures 4.1-1 through 4.1-6) which represent the four types upper-ocean features present in the Exploratory array: LC (Figures 4.1-1, 4.1-2, and 4.1-3), LCEs Sargassum (Figures 4.1-4 and 4.1-5) and Titanic (Figure 4.1-6), cyclones (Figures 4.1-1 through 4.1-5), and broad cyclonic flow characteristic of the circulation from December 2003 through March 2004. Each figure shows the surface velocity field with one or more sea-surface height contours meant to represent the perimeter of an anticyclonic or cyclonic feature. This contour was chosen as the sea-surface height value that most closely coincided with the velocity maxima of each feature. This definition worked best for strong anticyclonic LC and LCEs. Cyclones were often asymmetric and adjacent to the LC and LCE and so the definition of eddy boundary was somewhat subjective. A vertical temperature section is provided with each snapshot as well as the average speed around the perimeter. We include two parameters to quantify our description: mean radius and the ratio of relative to planetary vorticity. The Rossby number is one half the ratio of relative to planetary vorticity. Figures 4.1-1 through 4.1-6 provide values for the LC radius. We intend this radius to be interpreted as a measure of curvature rather than eddy radii since the LC is not strictly a closed feature. We include the vertical profile of mean speed around the periphery of each feature. The lower depth limit has been chosen as 1500 dbar to highlight the upper ocean structure. Beneath 1500 dbar, deep eddies and topographic Rossby waves dominate the current structure.

The strongest feature is the LC: surface speeds near 80 $cm \cdot s^{-1}$, radii near 100 km and a Rossby number near 0.1. In contrast to the cyclones, both the LC and the LCE have strong vertical shears and decrease rapidly with depth. Typically speeds decrease by 85 percent from surface to 1500 dbar. Eddy Sargassum has comparable vertical shears to the LC consistent with the fact that we sampled Sargassum soon after detachment. In contrast, we observed Eddy Titantic to have much weaker speeds and shears compared to Sargassum but that could be due to Titantic's presence at the edge of our PIES array.

Similar to the findings by Hamilton et al. (2002), cyclones have very little vertical shear. Typically the strongest cyclones are found in the southeast corner of the array adjacent to the LC. Surface speeds range from 20 to 60 $cm \cdot s^{-1}$ and typically decrease by only 70 percent from surface to 1500 dbar. Radii are small and between 35 and 70 km. Note that this lower value is close to the limit of what we resolve with the array: upper-ocean anomalies have been mapped with a correlation length scale of 80 km. Cyclone Rossby numbers approach values for the anticyclones. We note that the cyclone observed 16 June 2003 has a Rossby number of 0.25. Weak cyclonic flow dominates the array from December 2003 through March 2004. Surface speeds are near 20 $cm \cdot s^{-1}$. Strong velocities exist between the cyclonic flow and eddy Titantic, however.

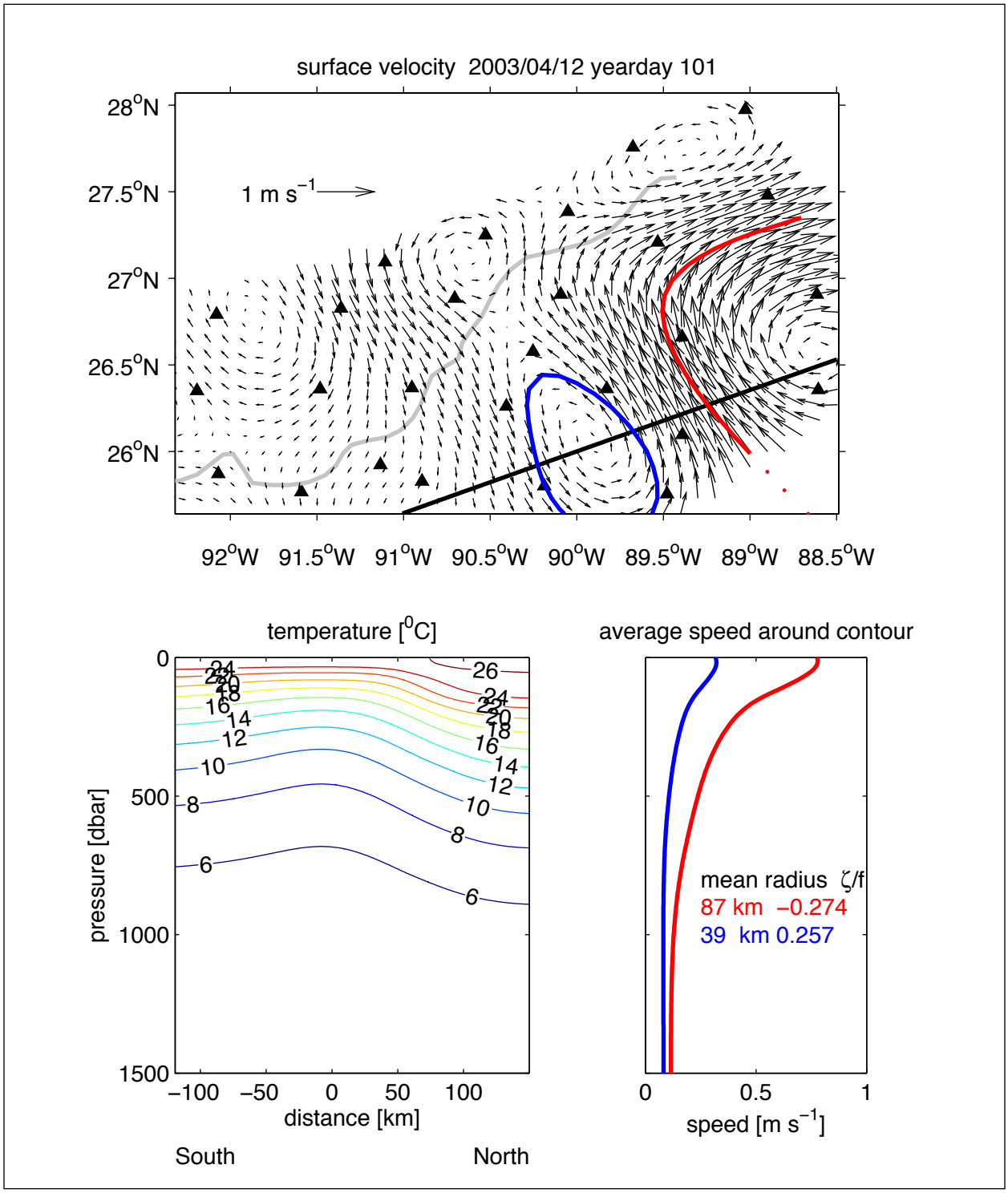

Figure 4.1-1. Top panel: Surface velocity vectors for 12 April 2003. PIES locations shown with triangles. Sigsbee Escarpment indicated with thick gray line. SSH contours are those that most closely coincided with the maximum surface speeds of LC (red) and adjacent cyclone (blue). Bottom left: Temperature contoured as a function of pressure and distance along the black line in the top panel. Bottom right: Average speed around the SSH contours shown in the top panel.

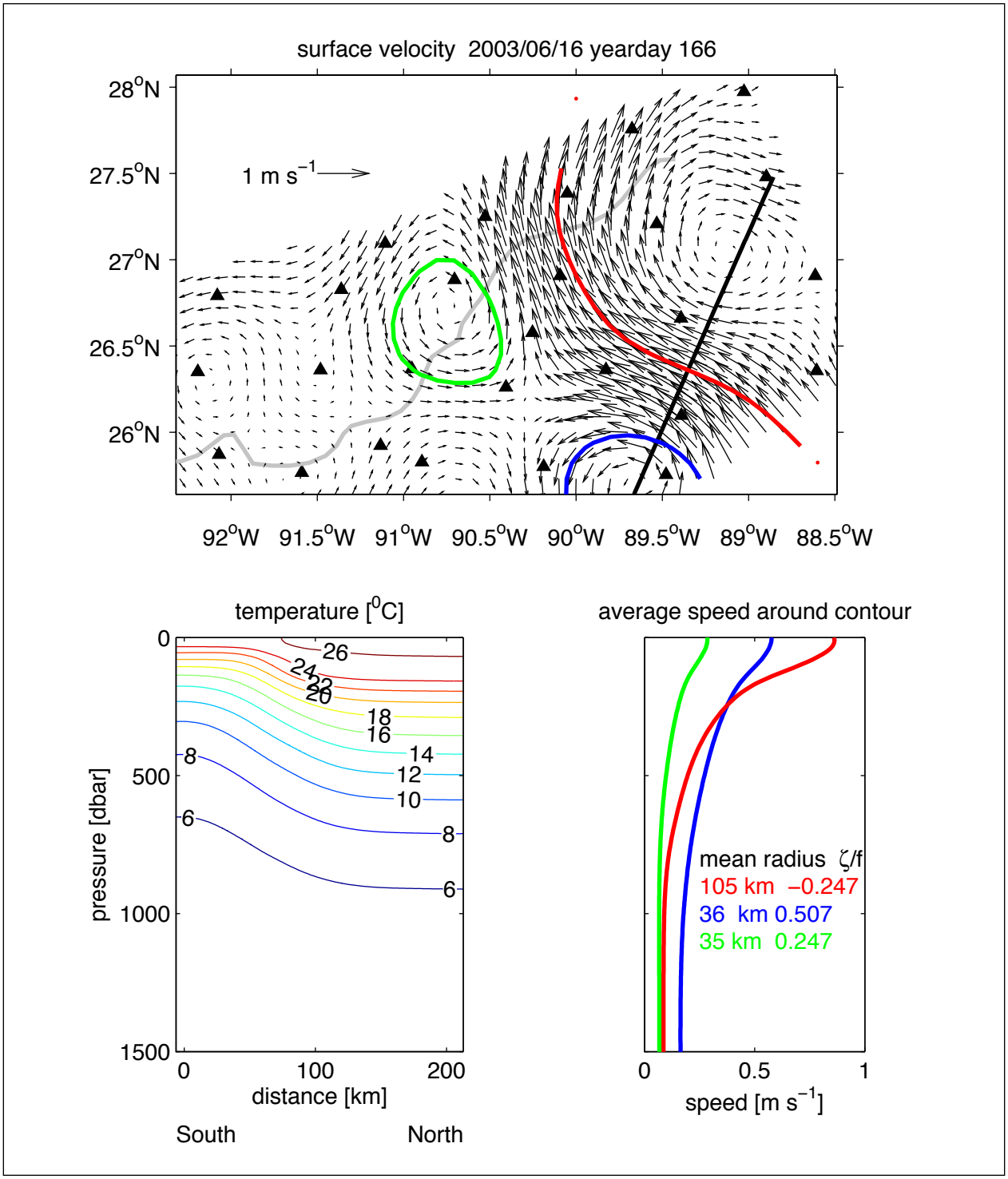

Figure 4.1-2. Top panel: Surface velocity vectors for 16 June 2003. PIES locations shown with triangles. Sigsbee Escarpment indicated with a gray line. SSH contours are those that most closely coincide with the maximum surface speeds of LC (red) and two adjacent cyclones (blue and green). Bottom left panel: Temperature contoured as a function of pressure and distance along the black line in the top panel. Bottom right panel: Average speed around the SSH contours shown in the top panel

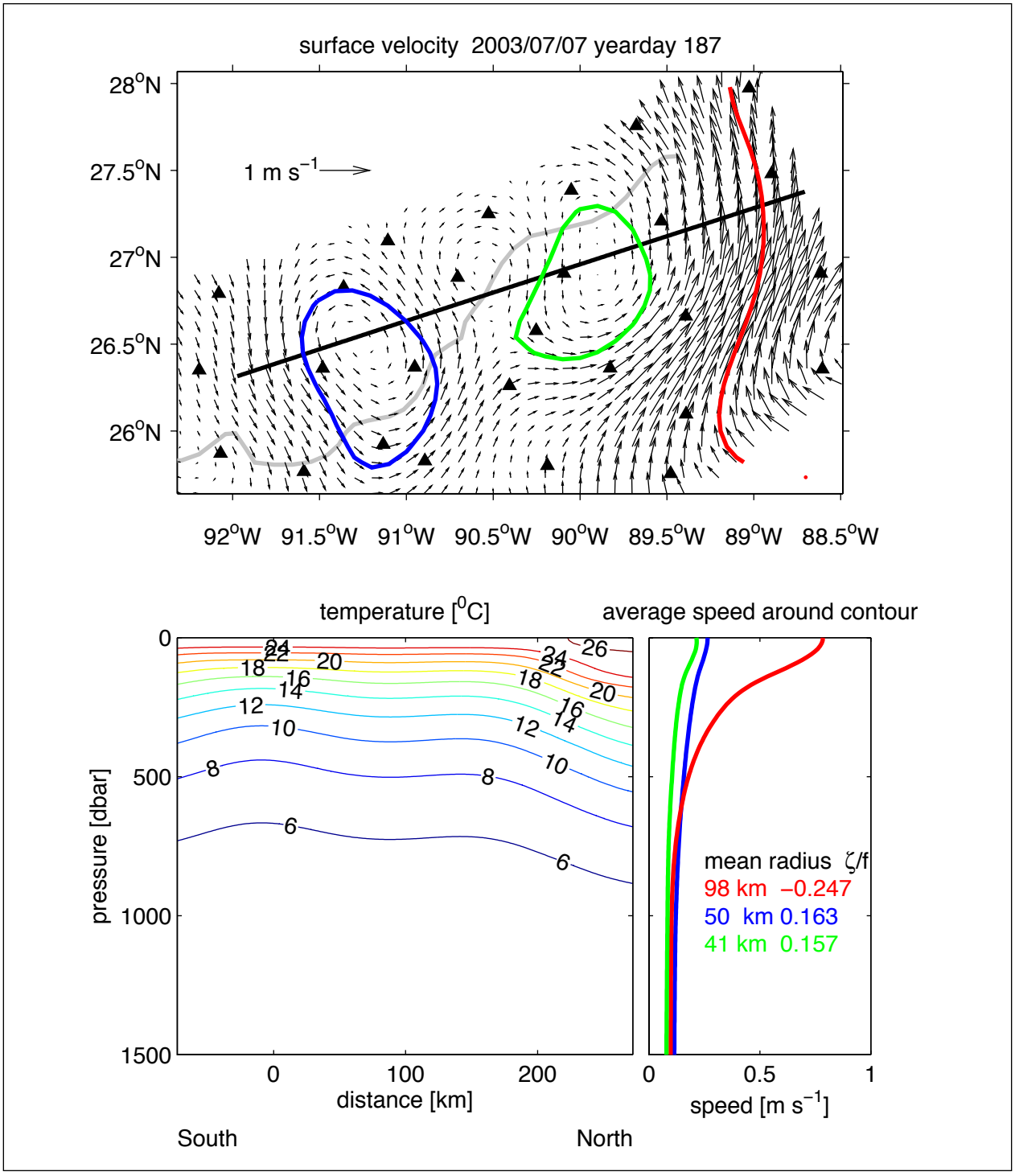

Figure 4.1-3. Top panel: Surface velocity vectors for 7 July 2003. PIES locations shown with triangles. Sigsbee Escarpment indicated with a gray line. SSH contours are those that most closely coincide with the maximum surface speeds of LC (red) and two adjacent cyclones (blue and green). Bottom left panel: Temperature contoured as a function of pressure and distance along the black line in the top panel. Bottom right panel: Average speed around the SSH contours shown in the top panel.

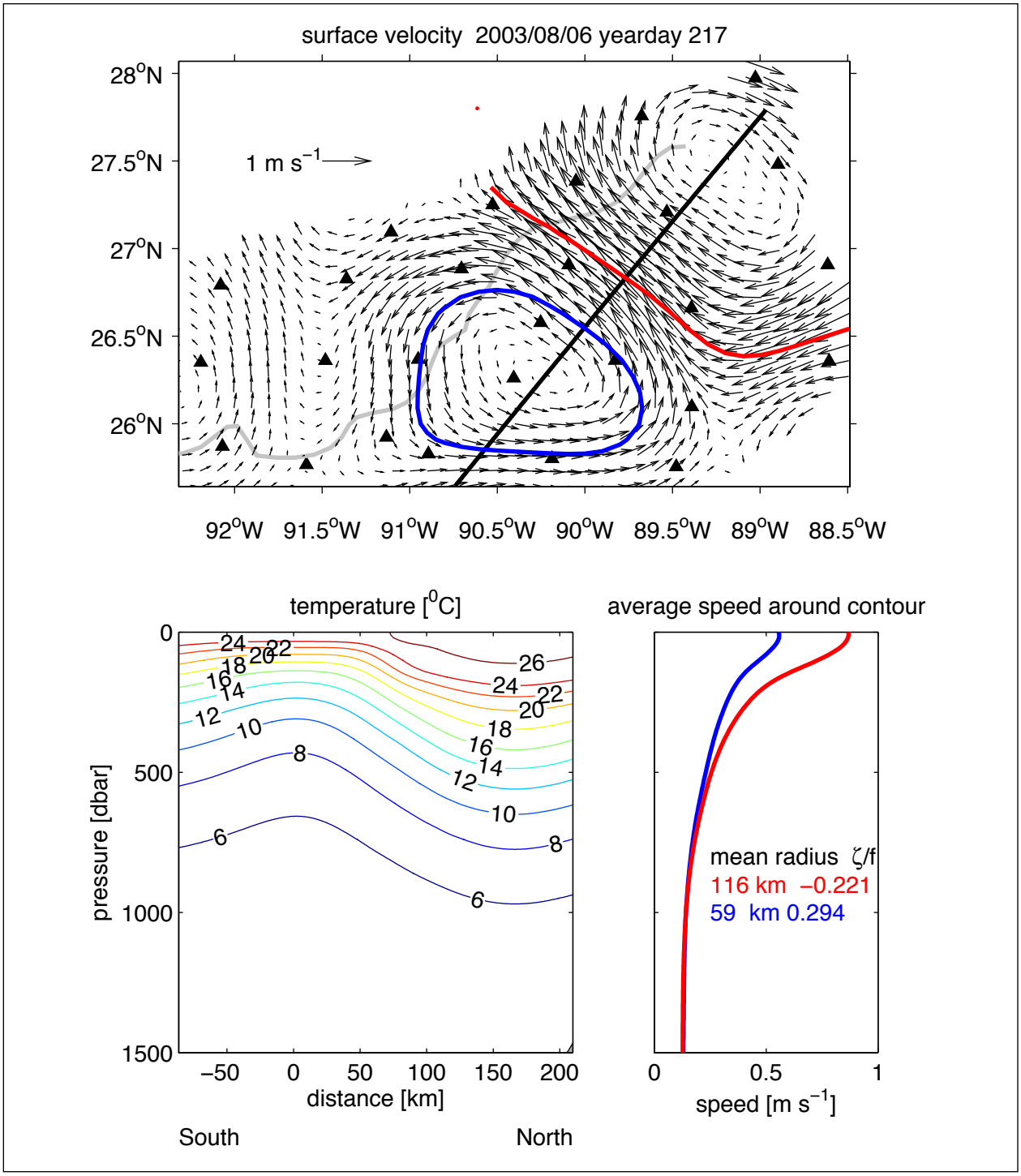

Figure 4.1-4. Top panel: Surface velocity vectors for 8 August 2003. PIES locations shown with triangles. Sigsbee escarpment indicated with a gray line. SSH contours are those that most closely coincide with the maximum surface speeds of Eddy Sargassum (red) and adjacent cyclone (blue). Bottom left panel: Temperature contoured as a function of pressure and distance along the thick black line in the top panel. Bottom right panel: Average speed around the SSH contours shown in the top panel.

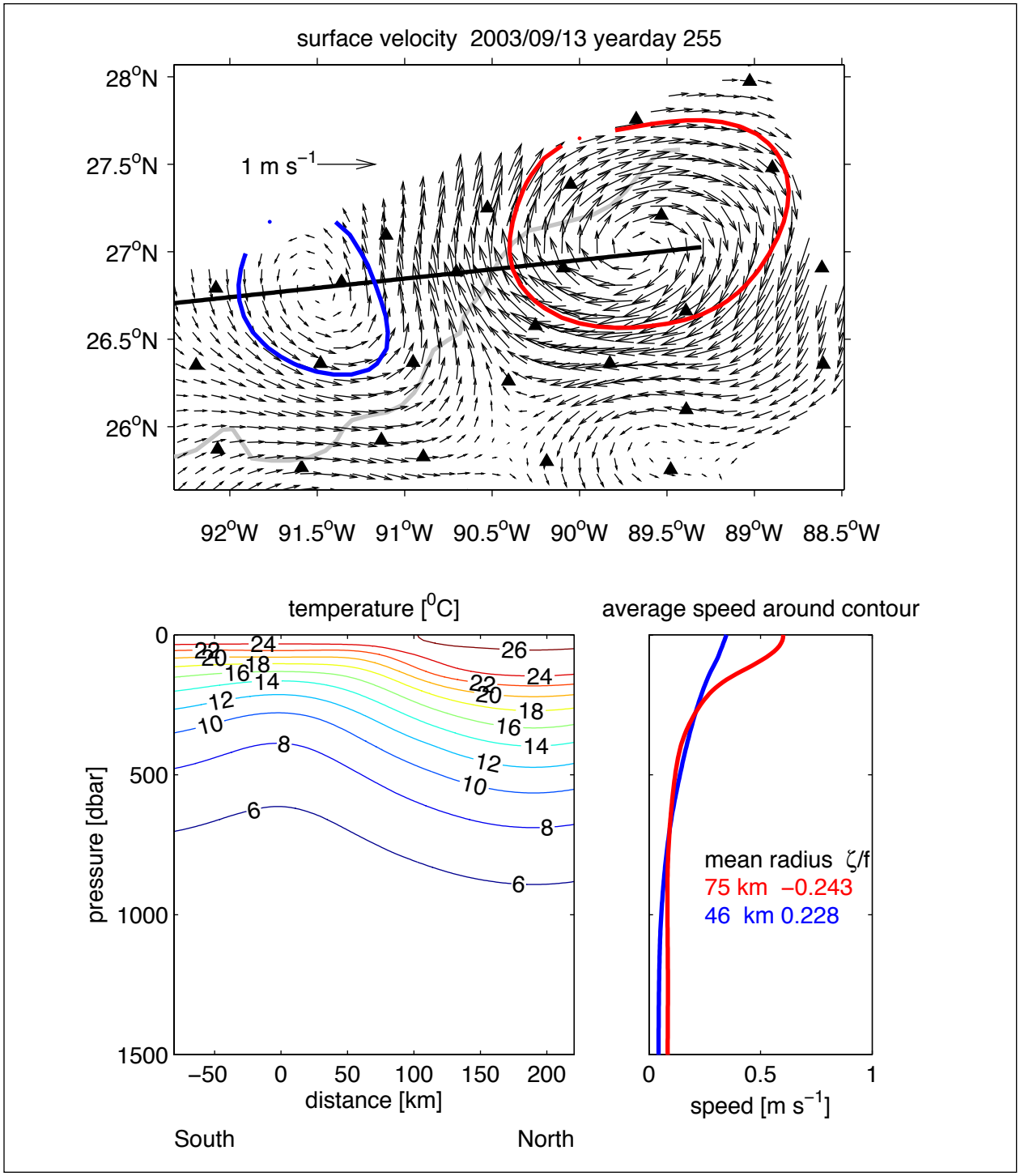

Figure 4.1-5. Top panel: Surface velocity vectors for 13 September 2003. PIES locations shown with triangles. Sigsbee Escarpment indicated with a gray line. SSH contours are those that most closely coincide with the maximum surface speeds of Eddy Sargassum (red) and adjacent cyclone (blue). Bottom left panel: Temperature contoured as a function of pressure and distance along the black line in the top panel. Bottom right panel: Average speed around the SSH contours shown in the top panel.

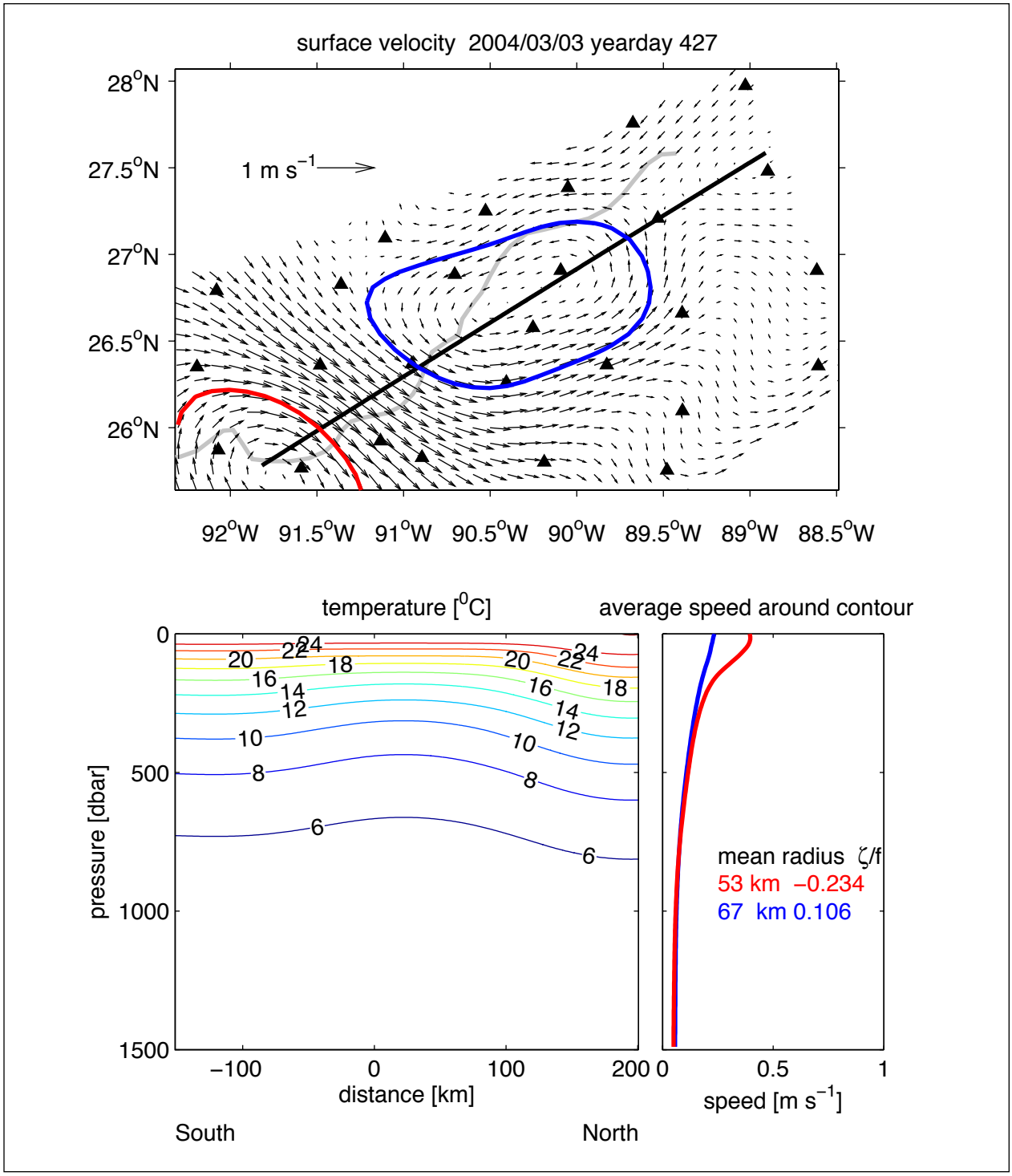

Figure 4.1-6. Top panel: Surface velocity vectors for 3 March 2004. PIES locations shown with triangles. Sigsbee Escarpment indicated with a gray line. SSH contours are those that most closely coincide with the maximum surface speeds of Eddy Titantic (red) and weak cyclonic flow (blue). Bottom left panel: Temperature contoured as a function of pressure and distance along the black line in the top panel. Bottom right panel: Average speed around the contours shown in the top panel.

4.1.2 Loop Current/Loop Current Eddies/Cyclones

The material below gives a brief description of the sequence of oceanographic conditions in the upper ocean during the Exploratory Study including the influence of the LC, LCE, LCFEs, and other cyclonic and anticyclonic eddy events that affected or occurred within the study region. The key events during the program are tabulated in Table 4.1-1 and will be described in the time order they occurred from a descriptive physical oceanographic perspective. Dynamical interpretation of these events will be considered in more detail in subsequent chapters.

LC Intrusion and LCFEs (26 March to 21 May 2003). At the beginning of the Exploratory Study the LC had already extended into the study region along the eastern margin of the array. This configuration allowed detailed mapping (with the PIES array) of the western and northwestern flank of the LC along which LCFEs are frequently observed. Throughout April and May the LC intruded to the north without extending much further westward into the array.

Two distinct LCFEs were identified propagating northward along the western LC boundary in the study region during this interval. To highlight these features, a region along the western LC boundary is enlarged and shown by the rectangle in Figure 4.1-7. Two consecutive 12-day sequences of PIES optimally interpolated sea-surface height (OISSH) contours in the enlarged region are shown overlaid on the coincident GOES nighttime composite SST images (Figures 4.1-8 and 4.1-9) showing the two LCFEs observed. The first LCFE, observed from 30 April 2003 through 12 May 2003, was weak enough or propagated fast enough to appear only as a cyclonic perturbation of the SSH streamlines along the LC front (Figure 4.1-8). This feature likely propagated northward along the LC front into the study array, as can be seen by the continuous trough of low SSH spanning the PIES OISSH time-latitude plot along 89°W as shown in Figure 4.1-10. The propagation speed was approximately 20 $km \cdot day^{-1}$. The second LCFE appeared to have formed within the study array or at least to have intensified significantly at about 27°N. This LCFE was much stronger than the previous event, forming closed SSH streamlines that clearly locate the eddy on the northwest flank of the LC front from 19-22 May 2003. There doesn't appear to be a strong SST signal associated with either of these LCFEs; however, the observing conditions at this time were difficult as is typical of late Spring conditions in the GOM. Nevertheless, the impact of the LCFEs on the LC frontal boundary in the SST imagery can be seen.

Other cyclonic eddies occurred in the study array during this time period; however, they could not be identified as canonical LCFEs, which typically propagate along the western intruded LC front. Although these eddies were influenced by the LC, they did not interact energetically with the current. For example, in April a cyclone paired with an anticyclone in the western part of the study array, just to the west of the intruded LC, advected shelf water south into the study area between the eddy pair.

Near-Detachment of Eddy Sargassum (29 May 2003). In Section 3 we defined LCE detachments based on the breaking of the 17-cm LC tracking contour in the altimeter-derived SSH maps. Brief energetic LCE detachments events can occur, however, that are missed by the

Table 4.1-1

Timeline of oceanographic events during the Exploratory Study.

Event	Date	Comments
LC intrusion reaching array	26 Mar 2003	
LCFE Events #1 and #2	30 April - 21 May 2003	LCFE detected by PIES
Detachment and Reattachment of Eddy Sargassum	25 May 2003	Brief surface flow detachment seen in ocean color imagery.
LCFE intensification and Eddy Sargassum/Unnamed Eddy splitting event	19 May – 1 Aug 2003	Cyclone originated on western flank of LC.
Separation of Unnamed Eddy (anticyclone)	25 Jul 2003	Defined by breaking of 17-cm SSH contour
Detachment and Reattachment of Eddy Sargassum	13 Jul – 19 Jul 2003	Observed in MODIS color imagery.
Separation of Eddy Sargassum	29 Aug 2003	Observed in MODIS color imagery.
Eddy Sargassum center within study array	5 Aug – 1 Nov 2003	Center tracked with PIES SSH.
Eddy Sargassum exits study array	20 Nov 2003	Eddy surface signature tracked in satellite imagery.
Detachment and Reattachment of Eddy Titanic	25 Sep - 28 Nov 2003	Defined 17-cm SSH contour, in good agreement with imagery.
Merging of Eddy Unnamed and Eddy Sargassum	17 Oct – 17 Nov 2003	Merging identified in SST and color imagery and change in SSH signatures.
Separation of Eddy Titanic	31 Dec 2003	Defined by breaking of 17-cm SSH contour with no subsequent reattachment.
Eddy Titanic northern flank propagates eastward within SE corner of PIES array	2 Jan 2004 – 30 Jan 2004	Eddy Titanic was an elliptical eddy at this time and rotating clockwise.
Cyclone-dominated flow within study array	1 Feb 2004 – 29 Feb 2004	-15 cm amplitude cyclone observed by PIES in center of array.
Eddy Titanic northern flank in SW corner of array	1 Mar 2004 – Mar 30 2004	Elongation and rotation once again brought northern edge of eddy into array.

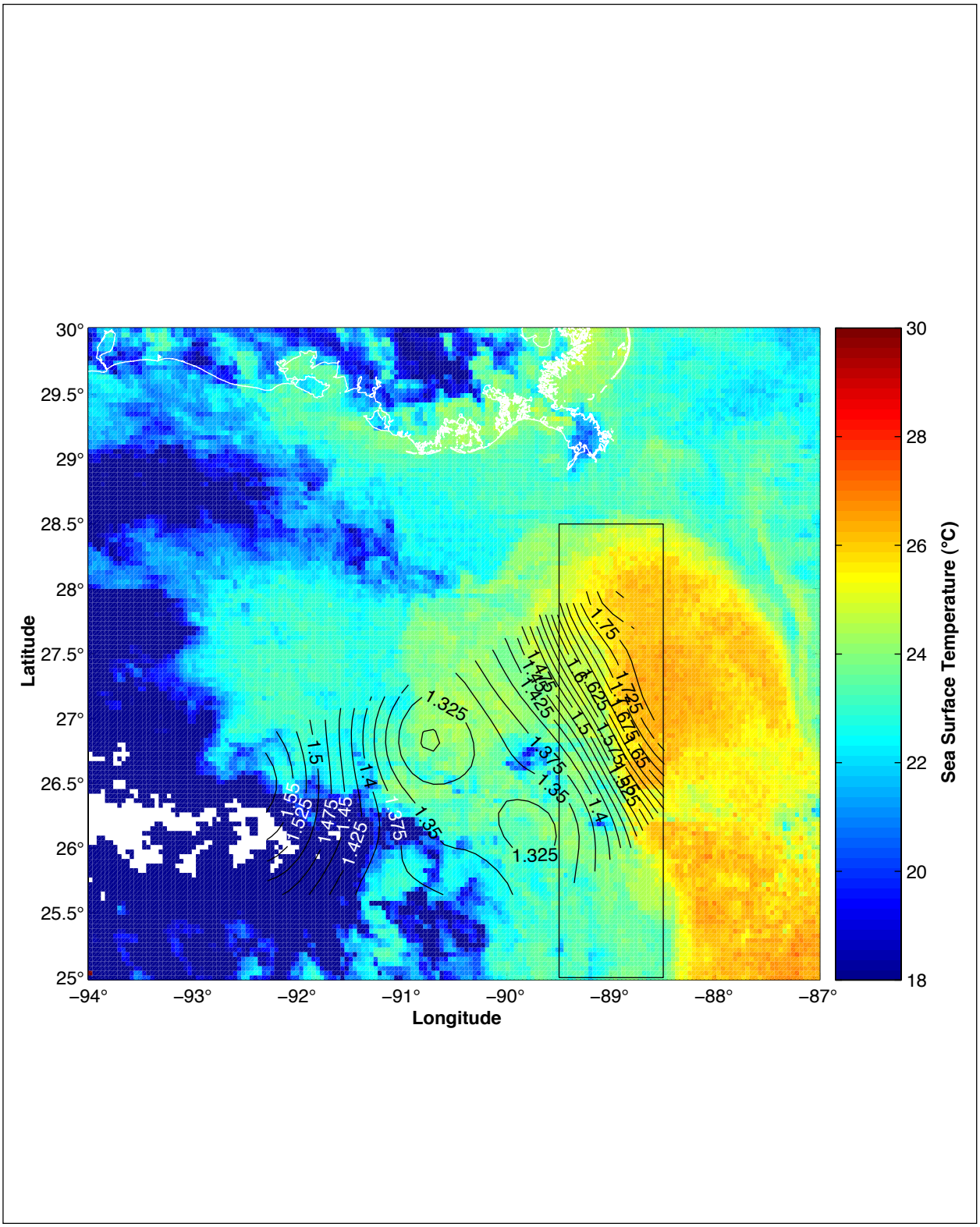

Figure 4.1-7. Overview of subregion shown in Figures 4.1-8 and 4.1-9. The rectangular subregion along the western LC front is shown overlaid on a GOES nighttime composite SST image from 30 April 2003 with the coincident PIES OISSH contours overlaid. Contour increment is 2.5 cm.

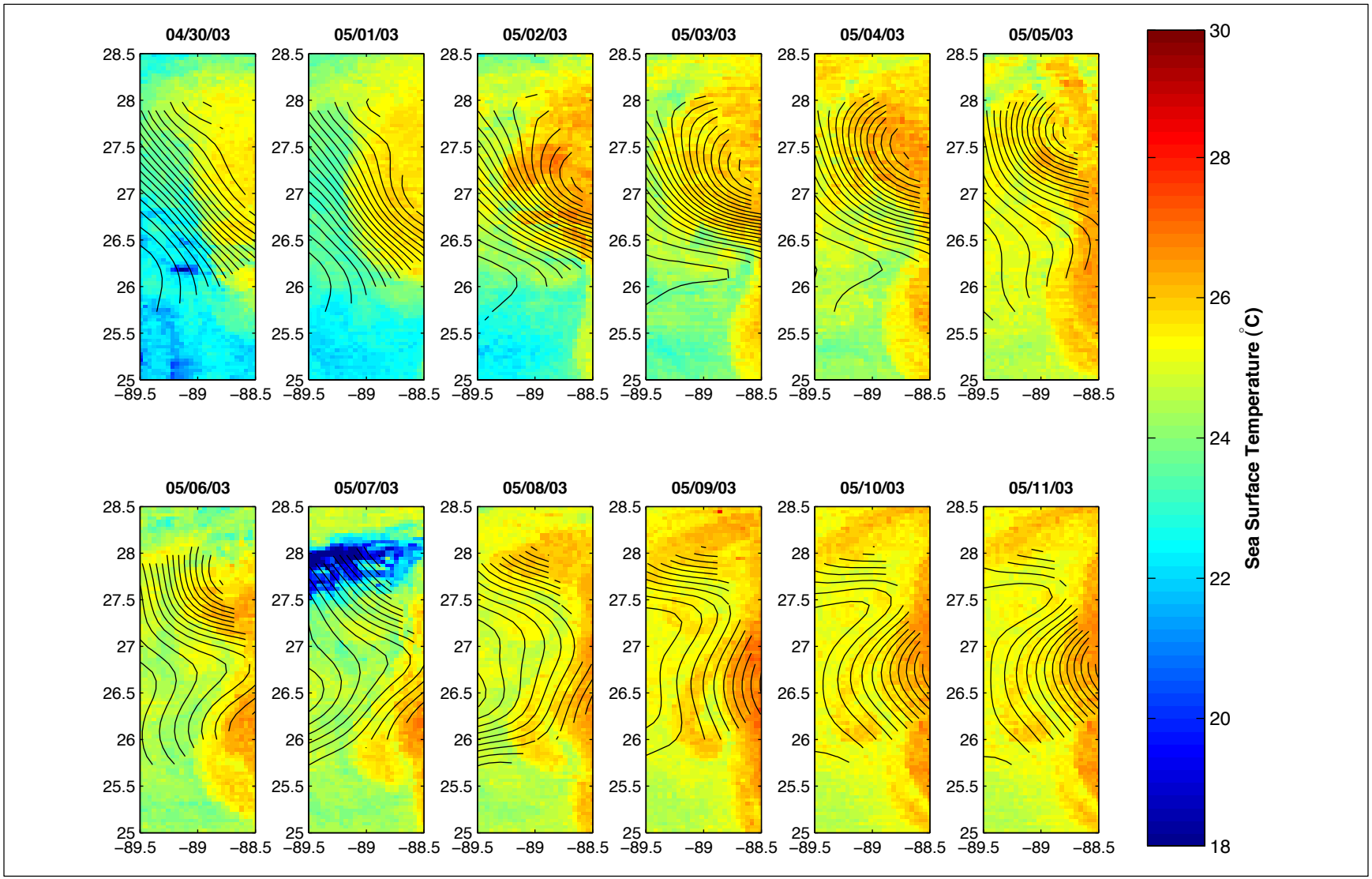

Figure 4.1-8. Loop Current Frontal Eddy (LCFE) events: 30 April through 11 May 2003. PIES OISSH contours are shown overlaid on GOES nighttime composite SST images. Contour increment is 2.5 cm.

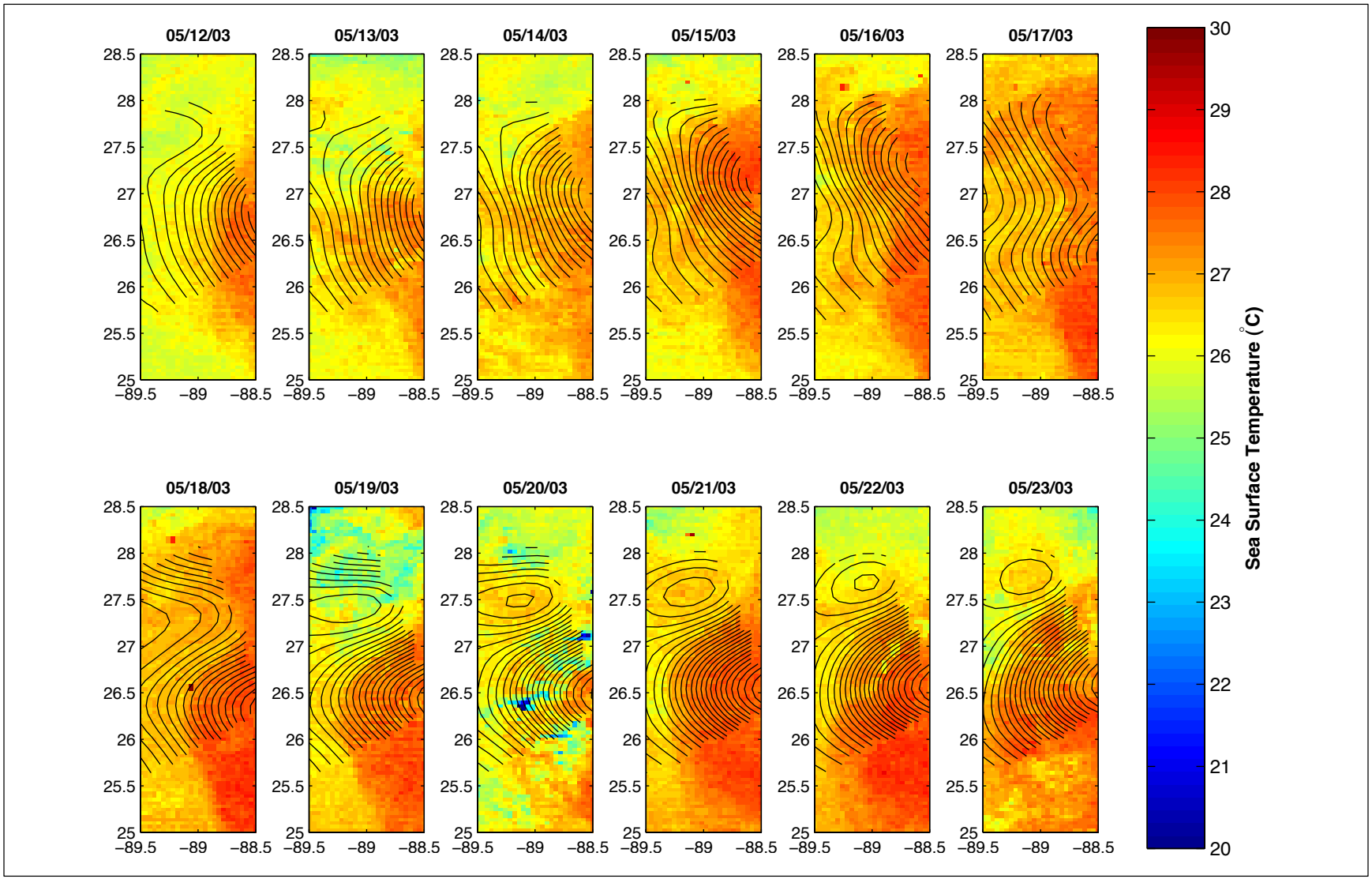

Figure 4.1-9. Loop Current frontal eddy (LCFE) event: 12 May through 23 May 2003. PIES OISSH contours are shown overlaid on GOES nighttime composite SST images. Contour increment is 2.5 cm.

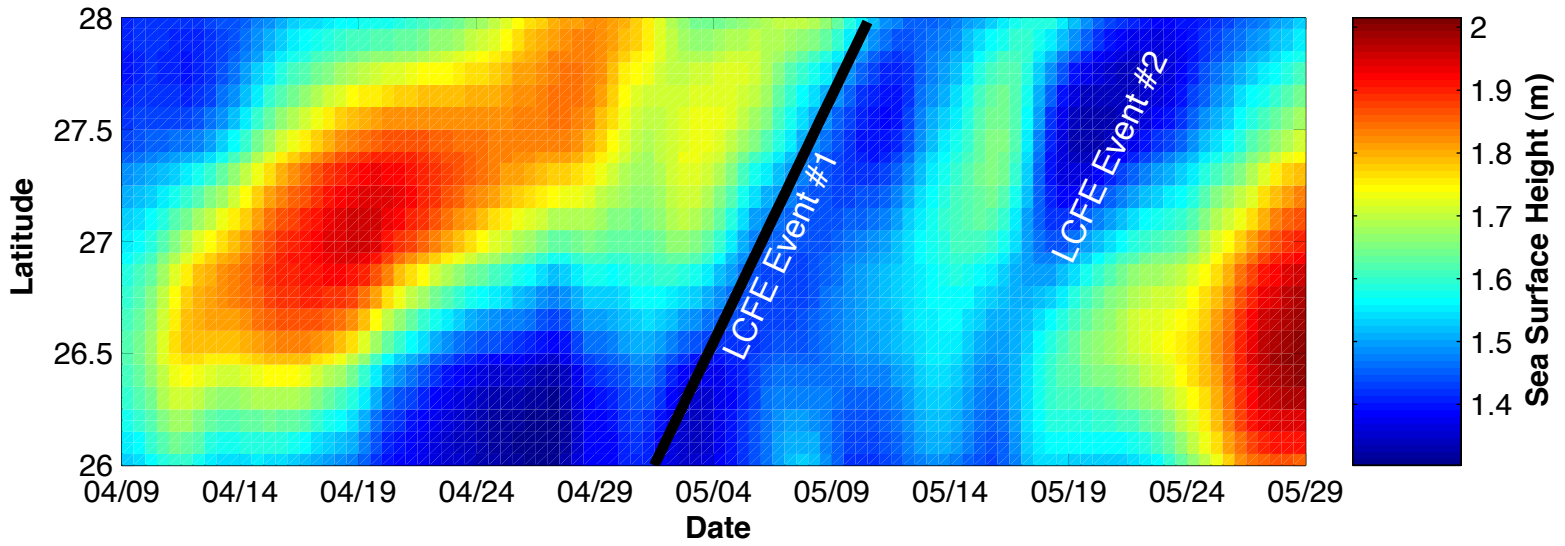

Figure 4.1-10. Latitude/time plot along 89°W longitude of PIES OISSH showing LCFE events in May 2003. Black line is a northward propagation speed of 20 km day^{-1}.

non-synoptic sampling of the altimeter data but which are clearly visible in satellite imagery. Although this type of "near" detachment detected in imagery may be confined to the near-surface circulation, the evolution of the LC and the associated LCE can be quite dynamic during these events and may impact the deeper-ocean circulation and therefore should be identified.

One such detachment occurred around 29 May 2003, which is seen in the 8-day composite ocean-color image centered on that date shown in Figure 4.1-11. The composite image shows a stream of chlorophyll-enhanced water cutting across the LC, briefly isolating the surface color signature of Eddy Sargassum from the LC through the combined interaction of the two LCFEs shown in the lower panel of Figure 4.1-11. This was the only image in the 8-day composite sequence that showed a detachment in the LC surface color signal, which was neither strong enough nor of sufficient duration to break the 17-cm LC tracking contour. The event was energetic enough, however, to exhibit PIES SSH measurements exceeding 2 m along the eastern margin of the array.

LCFE Propagation, Intensification and Interaction with the LC (17 May 2003 to 28 August 2003). An event that was observed during the Exploratory Study was the formation, propagation, and intensification of a LCFE along the periphery of the LC that ultimately contributed to the detachment and final separation of a LCE, Eddy Sargassum, and the splitting of a small anticyclone off the southwestern flank of the eddy. Portions of this complex event occurred within the study region, giving unprecedented and detailed observations of a dynamic LC event.

The genesis of this event was the second LCFE detected along the western margin of the LC that was observed in the study array in mid-May, as discussed previously. The locations of the eddy-center minimum SSH locations from the PIES OISSH and altimetry are overlaid on the 8-day color-composite images shown in Figures 4.1-12 and 4.1-13. The LCFE propagation around the LC is clearly seen in the composite color imagery sequence. Eddy center locations determined for each day from the PIES SSH and every 8 days from the altimetry overlaid on the composite color images are shown in Figure 4.1-14. The complete circuit around the periphery of the Sargassum LC detachment of the LCFE took approximately 70 days from the initial formation of the eddy within the study array near 27°N on 19 May 2003 to its eventual return to the study area on 29 July 2003. The eddy traveled a total of 1060 km over the 70-day time period, giving an average propagation speed of 15 $km \cdot day^{-1}$, that was only slightly slower than the propagation speed of the LCFEs observed within the array in May.

The LCFE increased in both size and amplitude by about a factor of four over the 10-week time period between leaving and returning to the study region. The size at the time it was observed within the array from 19-22 May 2003 was about 6000 km^2 and the amplitude -6 cm based on the closed SSH contours in the PIES OISSH. On 23 July 2003, just prior to returning to the study area, the cyclone was approximately 16,000 km^2 with a center SSH amplitude of -25 cm determined from the altimetry as shown in Figure 4.1-15**.** Upon returning to the study region, the amplitude was about -11 cm based on the PIES OISSH closed contours on 1 August 2003, which was only a portion of the total cyclonic circulation that had reformed west of the LC after the detachment of Eddy Sargassum on 13 July 2003. Figure 4.1-16 shows a composite of the PIES OISSH, altimeter SSH and the ocean color imagery mapping the total extent of the cyclone

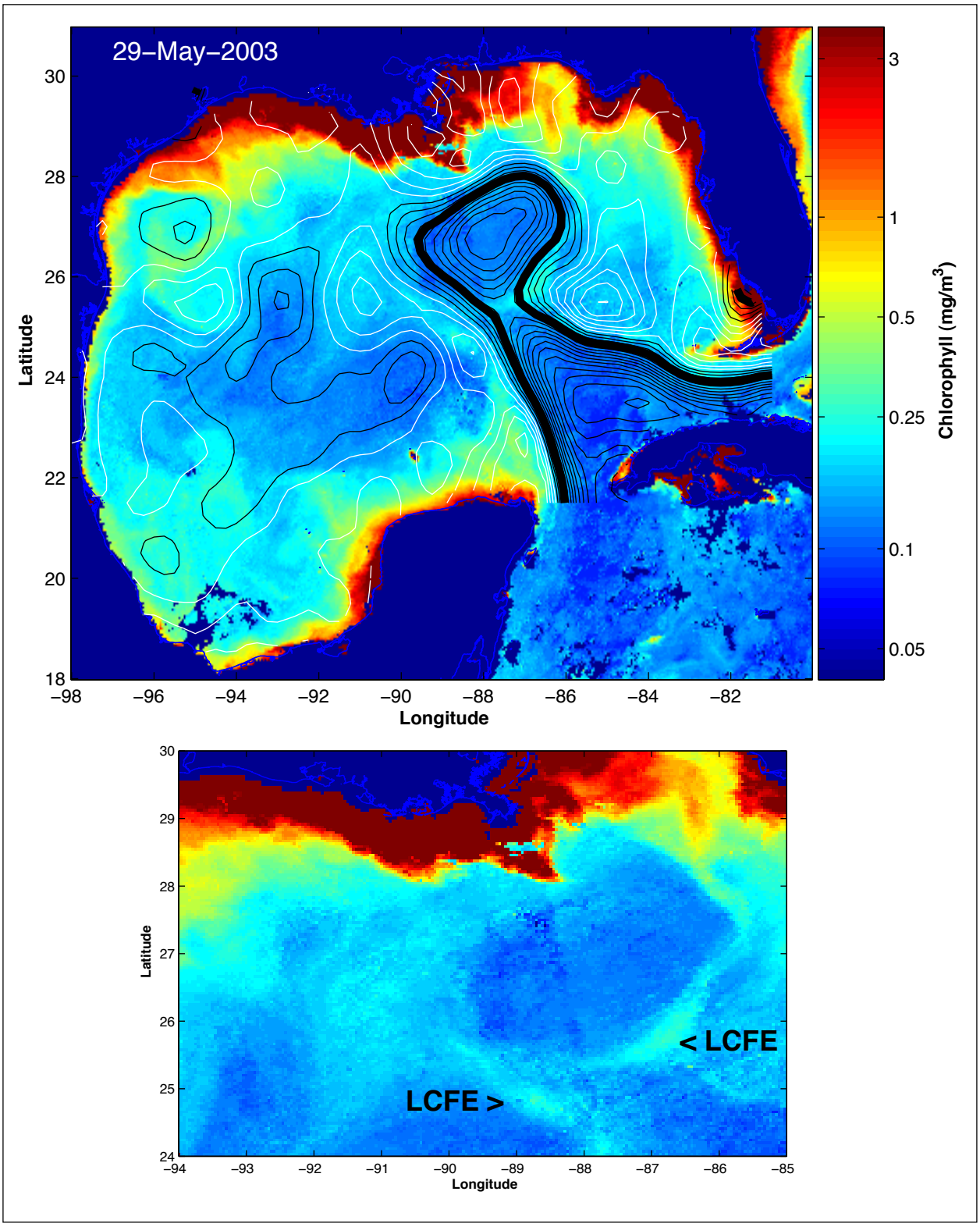

Figure 4.1-11. Brief detachment of Eddy Sargassum from the LC around 29 May 2003. Upper panel shows 8-day composite ocean color image overlaid with altimeter-derived SSH contours (white contours are negative, black contours are positive, contour increment is 5 cm). Lower panel shows a zoom of image with LCFEs identified.

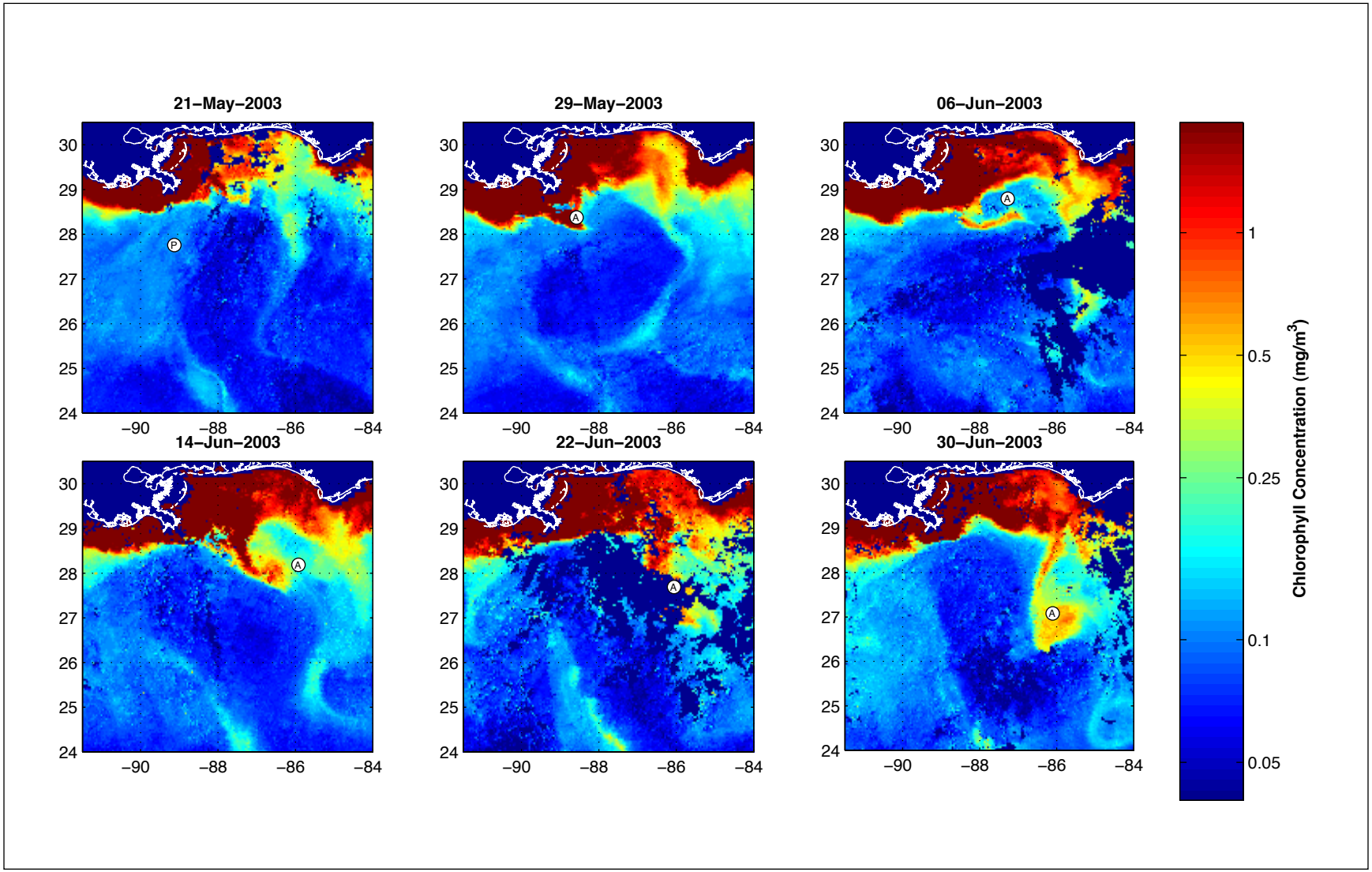

Figure 4.1-12. Loop Current Frontal Eddy (LCFE) positions 21 May through 30 Jun 2003. LCFE center positions determined from PIES OISSH (P) and altimetry (A) are overlaid on 8-day composite ocean color images.

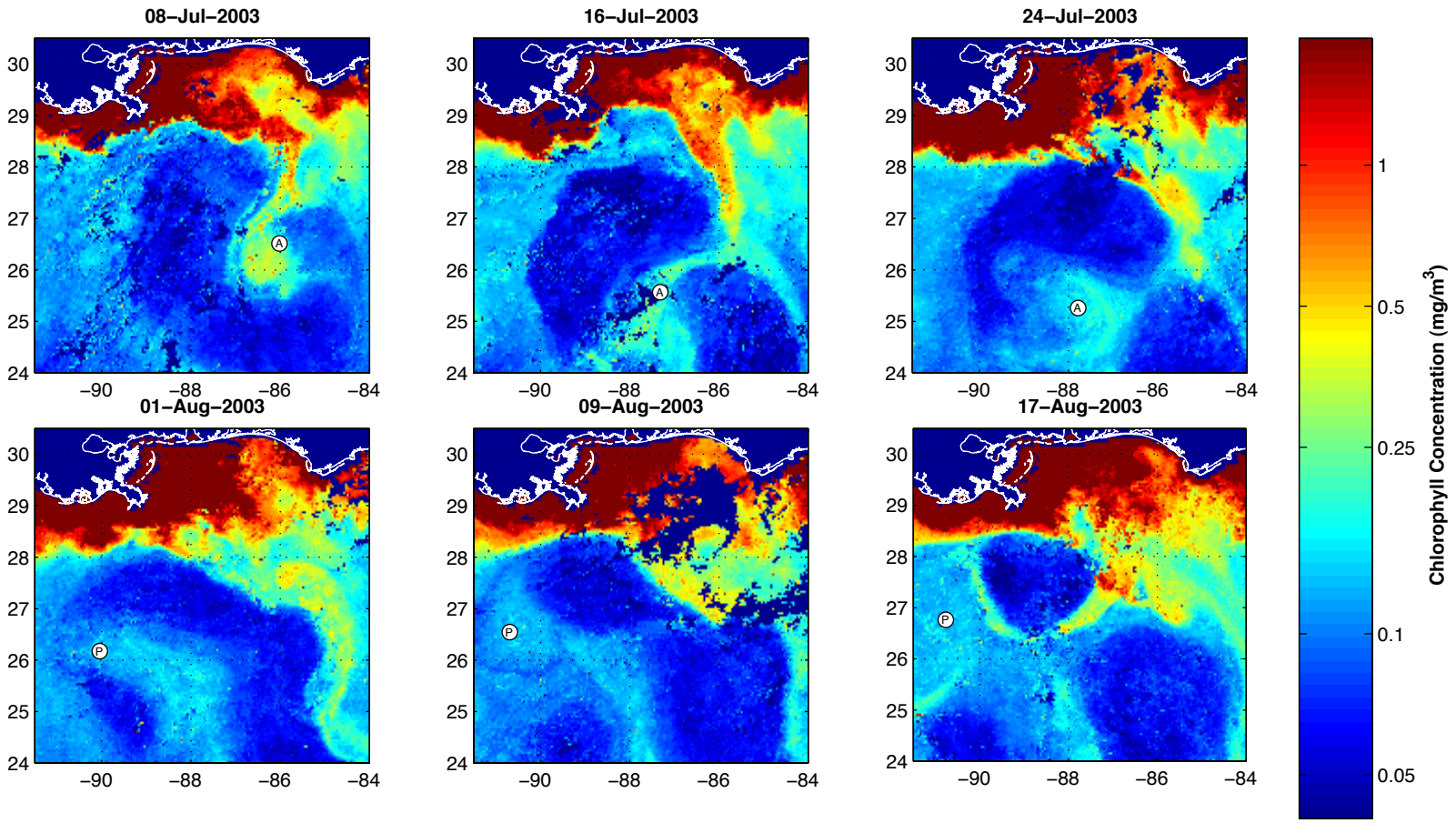

Figure 4.1-13. Loop Current Frontal Eddy (LCFE) positions 8 July through 17 August 2003. LCFE center positions determined from PIES OISSH (P) and altimetry (A) are overlaid on 8-day composite ocean color images.

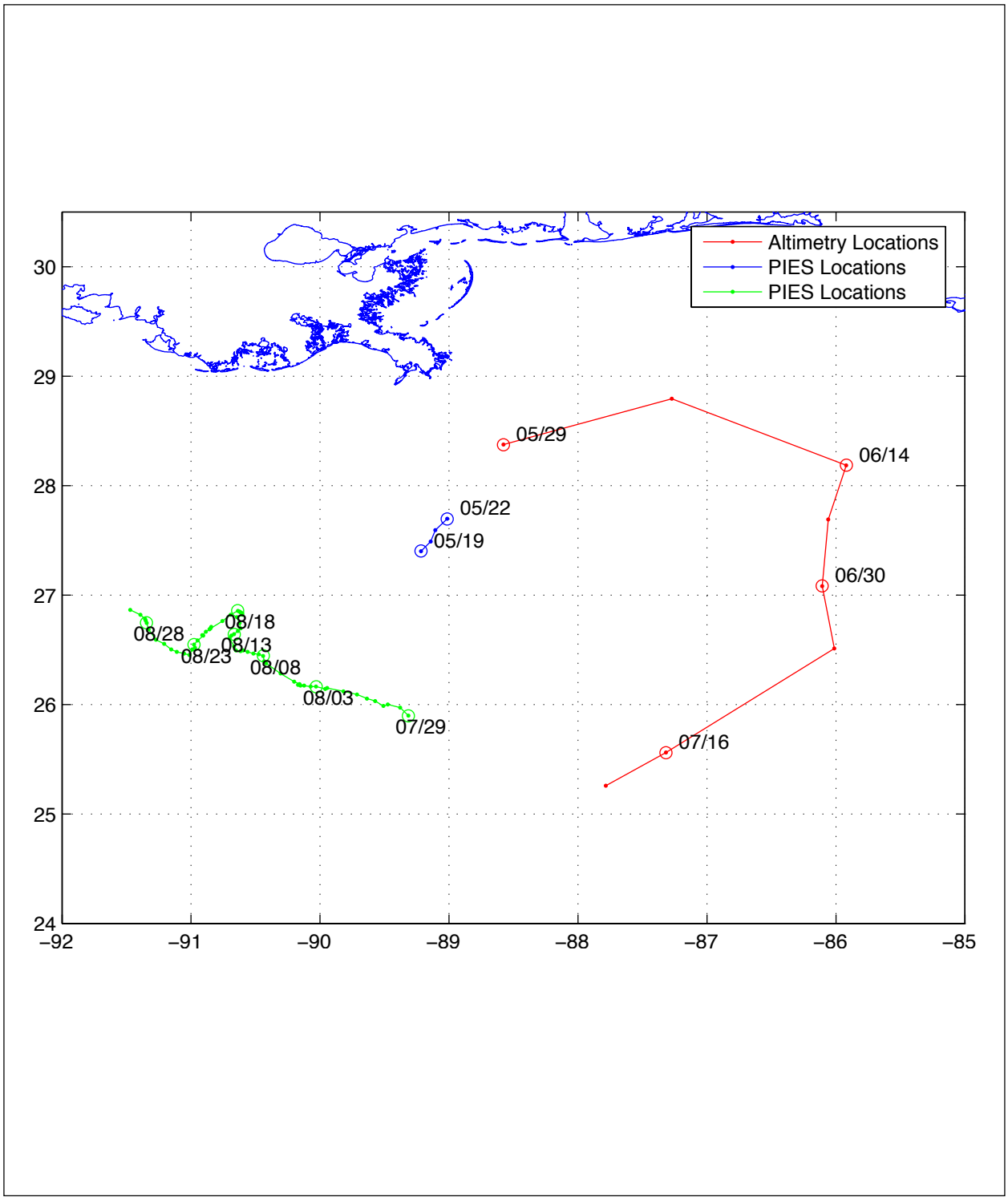

Figure 4.1-14. LCFE center locations during circuit of Eddy Sargassum from 19 May through 28 August 2003. Eddy center locations determined from daily PIES OISSH maps and 8-day color composite images overlaid with altimetry are shown.

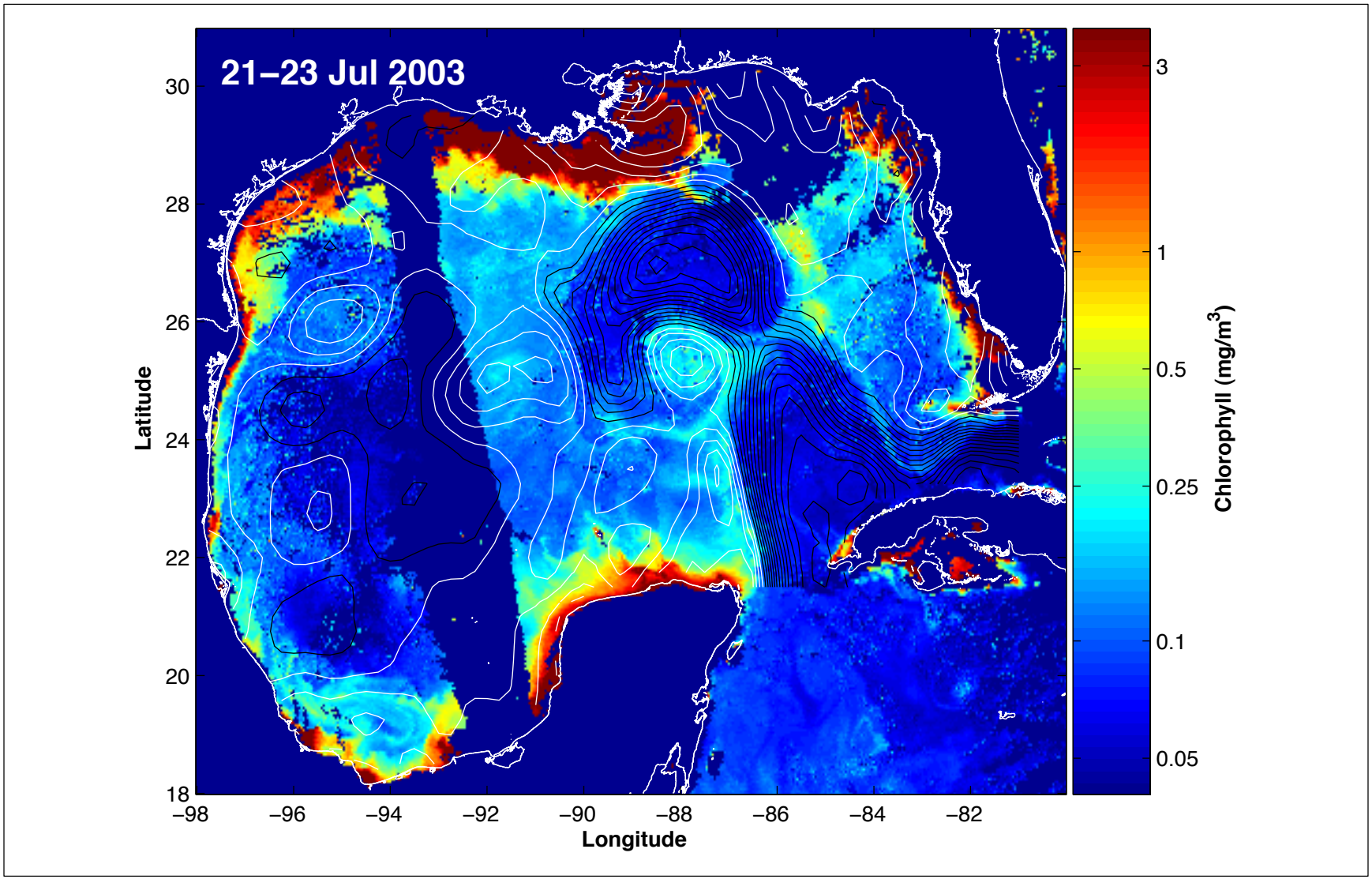

Figure 4.1-15. MODIS 3-day ocean color composite image from 21-23 July 2003 overlaid with altimeter-derived SSH contours.

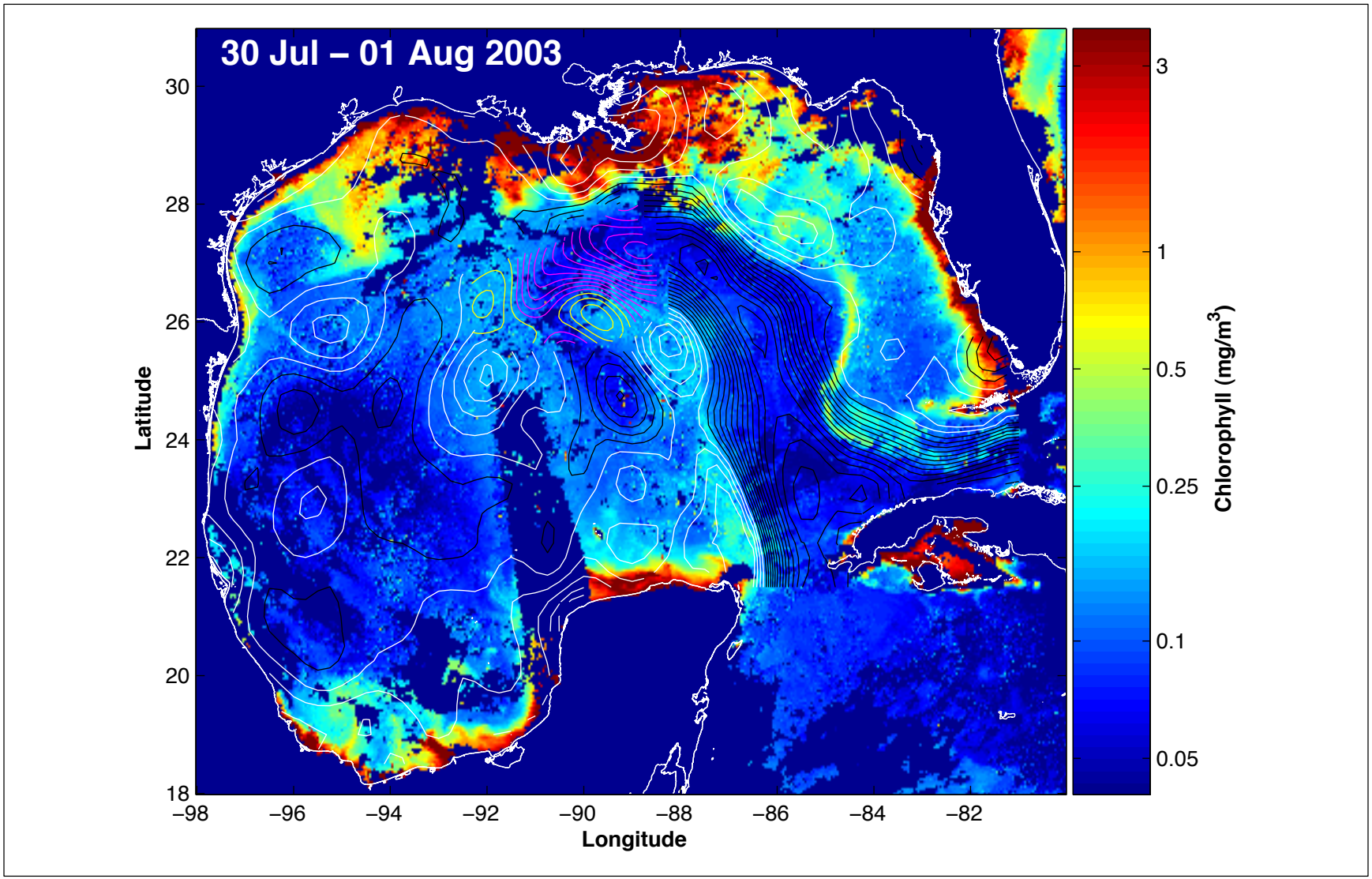

Figure 4.1-16. MODIS 3-day ocean color composite image from 30 July through 1 August 2003 overlaid with PIES OISSH and altimeter-derived SSH contours. Contour increment is 5 cm. PIES contours are shown in yellow and magenta to correspond to the white (negative) and black (positive) altimetry contours.

on 1 August 2003 at about 25,000 km^2. The eddy had elongated into a peanut shape with two separate local minimums, one within the PIES array at –15 cm and the stronger minimum to the southeast estimated from the altimetry at -21 cm. The energetic interaction of the eddy with the LC and Eddy Sargassum, which caused the splitting off of Unnamed Eddy, also caused the LCFE to split in two. The northwestern piece of the cyclone, which had returned to the study region, remained within the PIES array throughout September. The cyclone eventually moved directly westward out of the array in early October as Eddy Sargassum pushed southwest through the region.

Detachment and Reattachment of Eddy Sargassum (13 July 2003 through 19 July 2003). The primary effect on the LC of the LCFE cyclonic intensification discussed above was the detachment of Eddy Sargassum from the LC on 13 July 2003. Unlike the brief detachment in late May, this detachment was energetic enough to break the 17-cm SSH tracking contour while also showing a clear detachment of the eddy from the LC in the surface circulation patterns visible in the coincident color imagery on 16 July 2003. A MODIS satellite pass on 16 July was the only cloud-free image over that region of the GOM available during the detachment period identified by the altimetry. Daily color images from 20-23 July 2003 show the exchange of surface waters between the LC and Eddy Sargassum and the complete reattachment of the eddy to the LC in the 28-30 July 2003 images. A center of anticyclonic circulation exceeding 2.2 m dynamic height was measured by the PIES array within the detached eddy.

Separation of Unnamed Eddy (25 July 2003). Based on the 17-cm tracking contour, the interaction of the intensified LCFE and the detached Eddy Sargassum within the study region split Unnamed Eddy from the southwest flank of Eddy Sargassum to the south of the study region on 25 July 2003. Estimates from ocean-color imagery of the areal extent of Eddy Sargassum before the splitting event (110,220 km^2) and Unnamed Eddy after the splitting event (17,010 km^2) showed that approximately 15% of Eddy Sargassum split off to form Unnamed Eddy. The proximity of a cyclone to the west of Unnamed Eddy may have played a role in the event by pinning a piece of Eddy Sargassum between two energetic cyclones until the interaction of the LCFE and Eddy Sargassum effected the split (see Figure 4.1-15). The sequence of 5-day median filtered images in Figure 4.1-17 shows the surface color-signature of the splitting event**.** In Figure 4.1-18, PIES OISSH and altimeter SSH, respectively, inside and outside the study region are overlaid on the color images (Figure 4.1-17) to show the surface circulation patterns in detail.

Separation of Eddy Sargassum (5 August 2003 – altimetry, 29 August 2003 – color imagery). Unlike the detachment of Eddy Sargassum and the separation of Unnamed Eddy, the separation date determined from the break in the altimeter-derived, 17-cm tracking contour (5 August 2003) is not in good agreement with the separation date conservatively estimated from the available imagery (29 August 2003). Good coverage from MODIS during this interval allowed a closer examination of this event using 3-day composite images. The image from 4-6 August 2003 (Figure 4.1-19) clearly shows the surface color signature of the eddy was still attached to the LC and then detached in the image from 17-19 August 2003 (Figure 4.1-20). A brief reattachment is seen in the image from 22-24 August 2003 (Figure 4.1-21), which shows advection of surface water from Eddy Sargassum back into the LC along the northeast boundary of the current. By 26-28 August this flow was decreasing as Eddy Sargassum started to detach

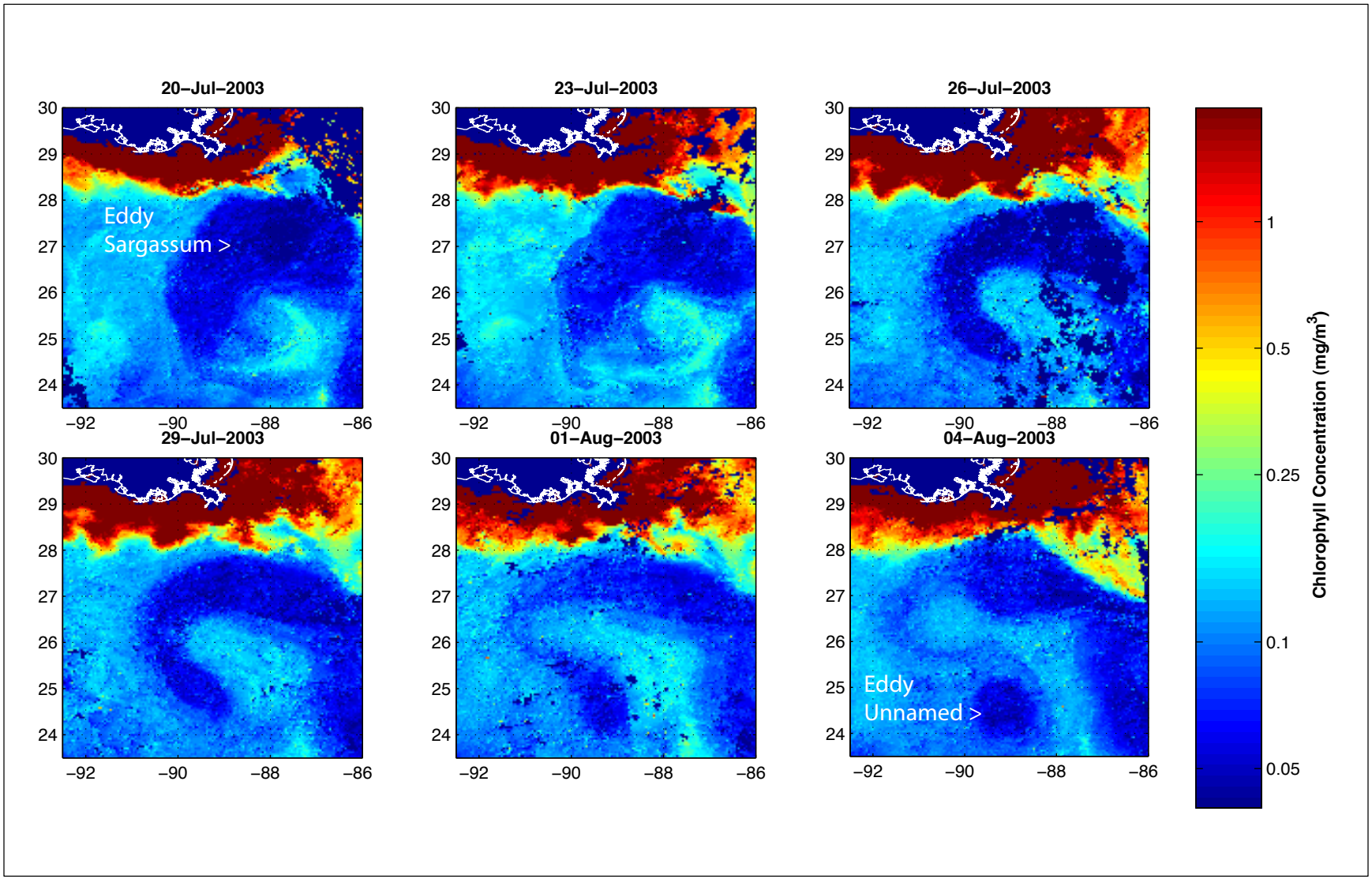

Figure 4.1-17. Sequence of 5-day median filtered ocean color images from 20 July through 4 August 2003 showing formation of Eddy Unnamed.

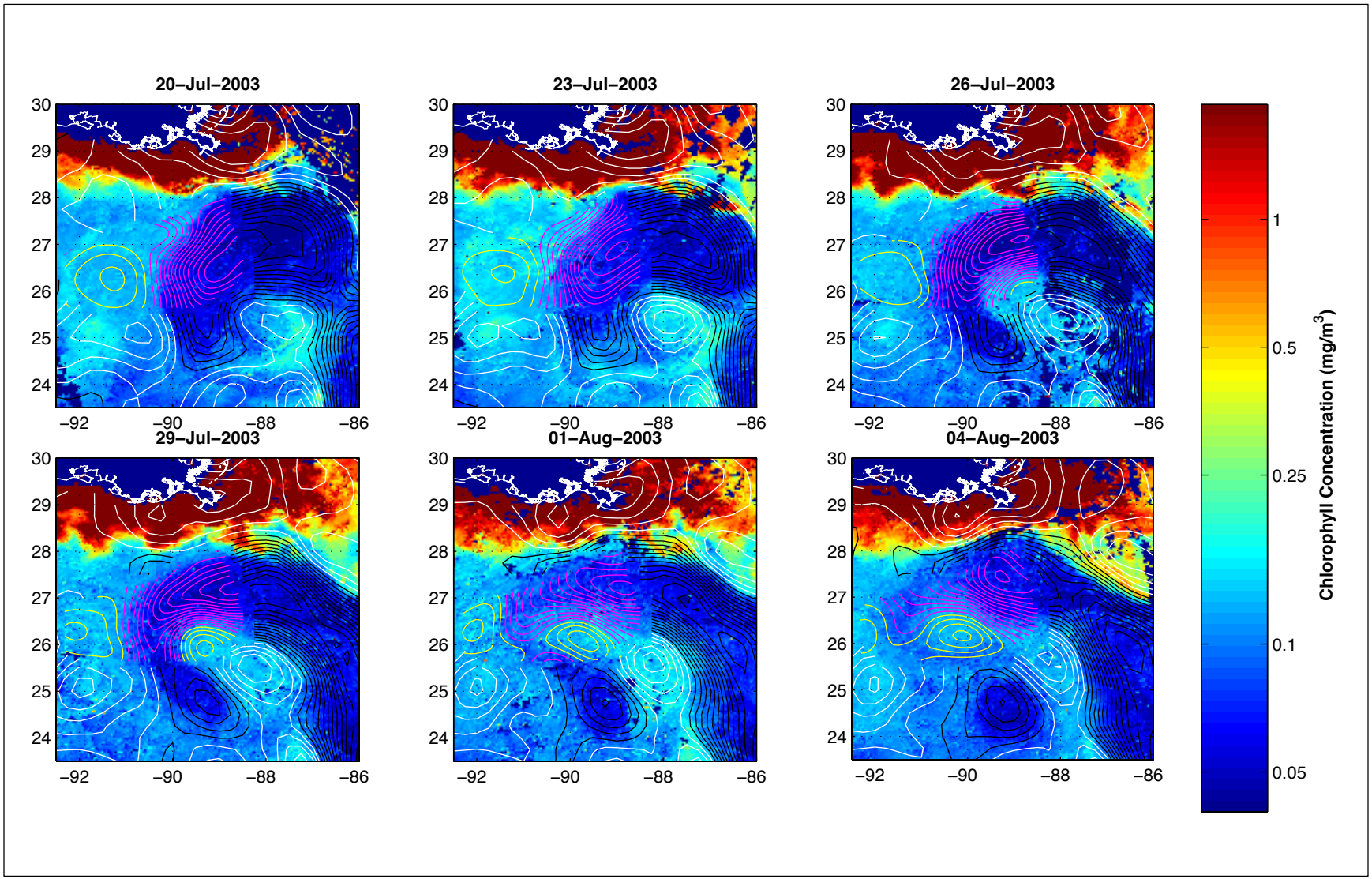

Figure 4.1-18. Same as Figure 4.1-17 overlaid with PIES OISSH and altimeter-derived SSH contours. Contour increment is 5 cm. PIES contours are shown in yellow and magenta to correspond to the white (negative) and black (positive) altimetry contours.

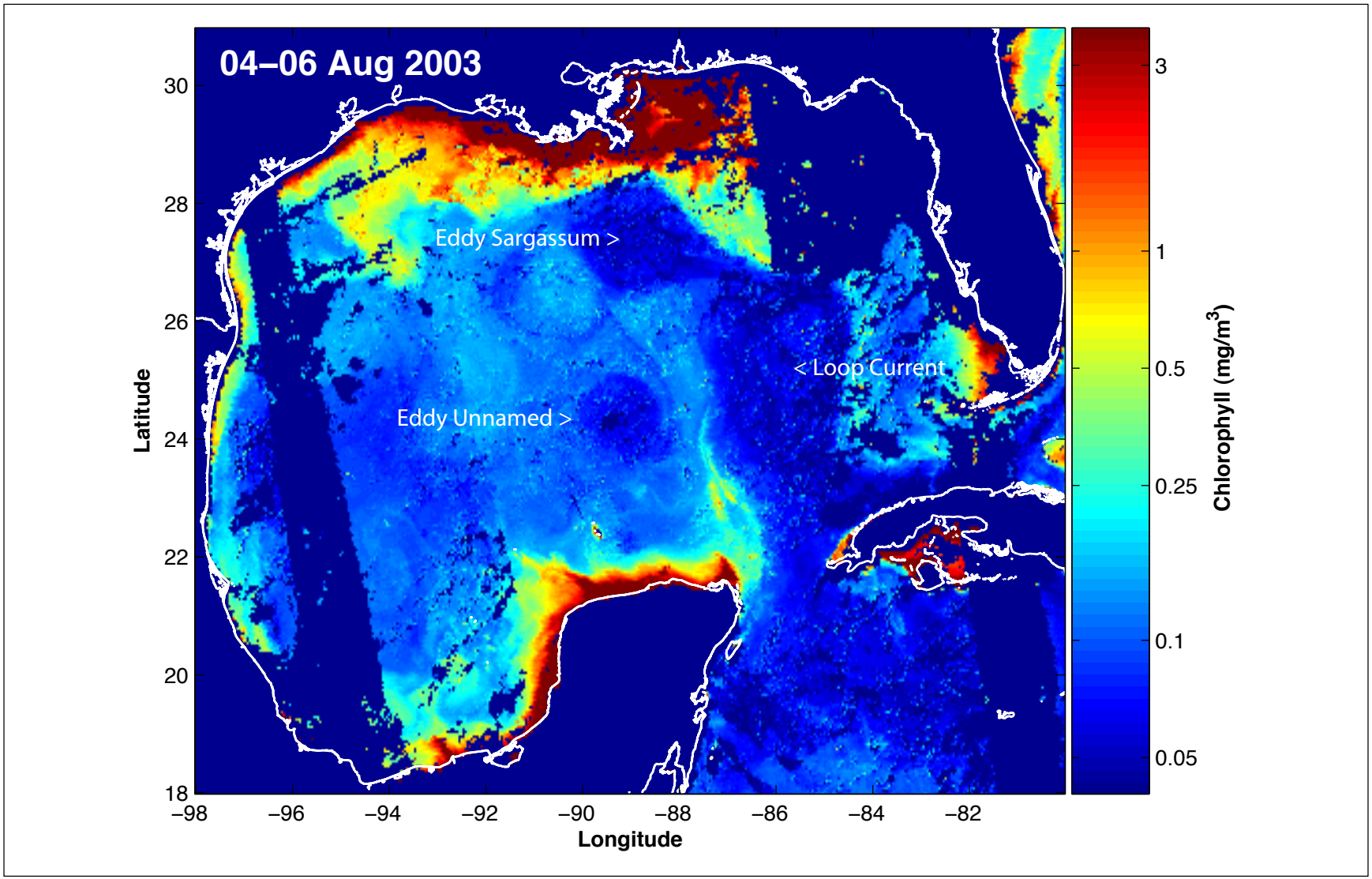

Figure 4.1-19. MODIS ocean color 3-day composite image from 4-6 August 2003 showing Eddy Sargassum still attached to LC.

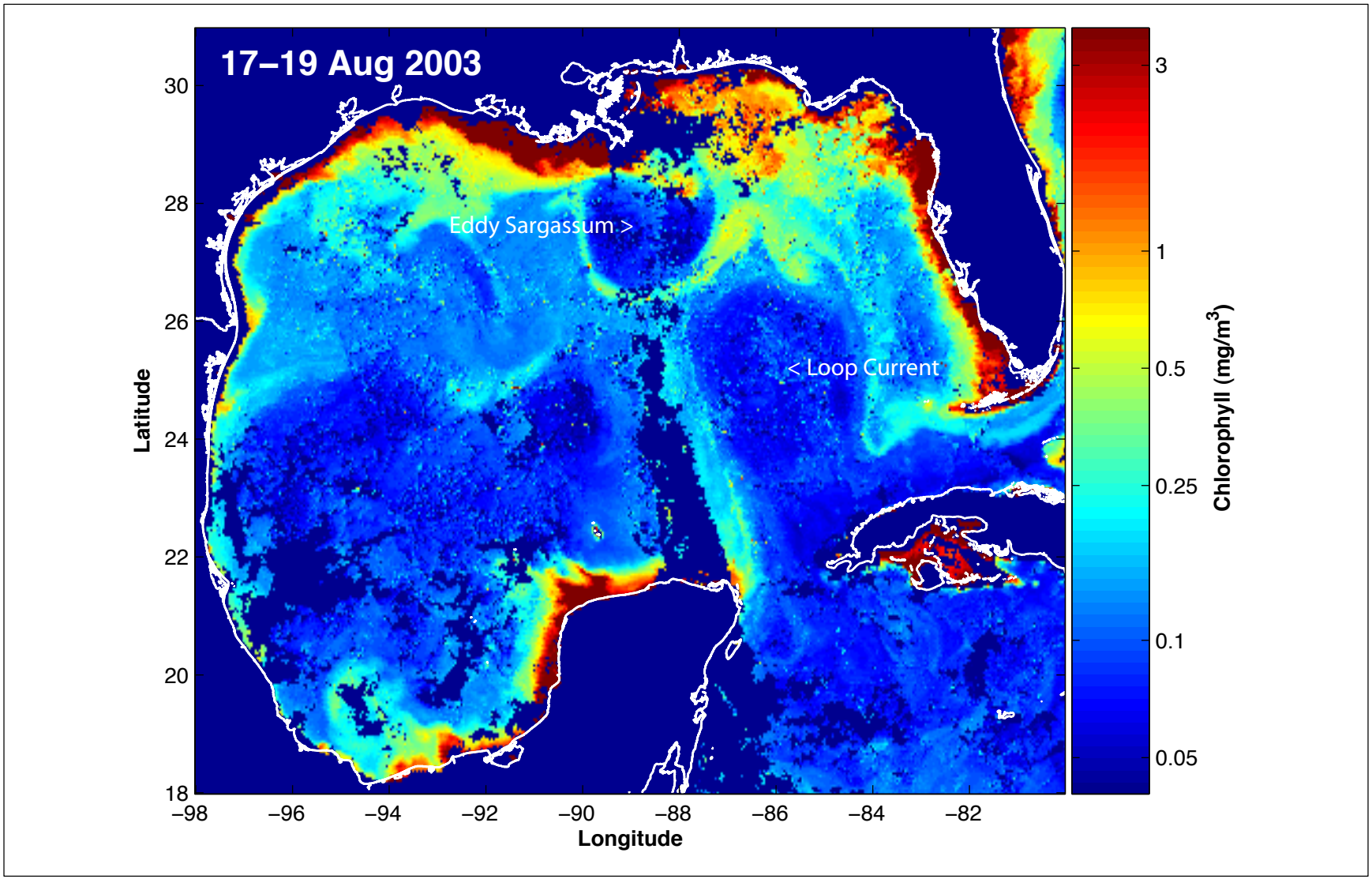

Figure 4.1-20. MODIS ocean color 3-day composite image from 17-19 August 2003 showing detachment of Eddy Sargassum from the LC.

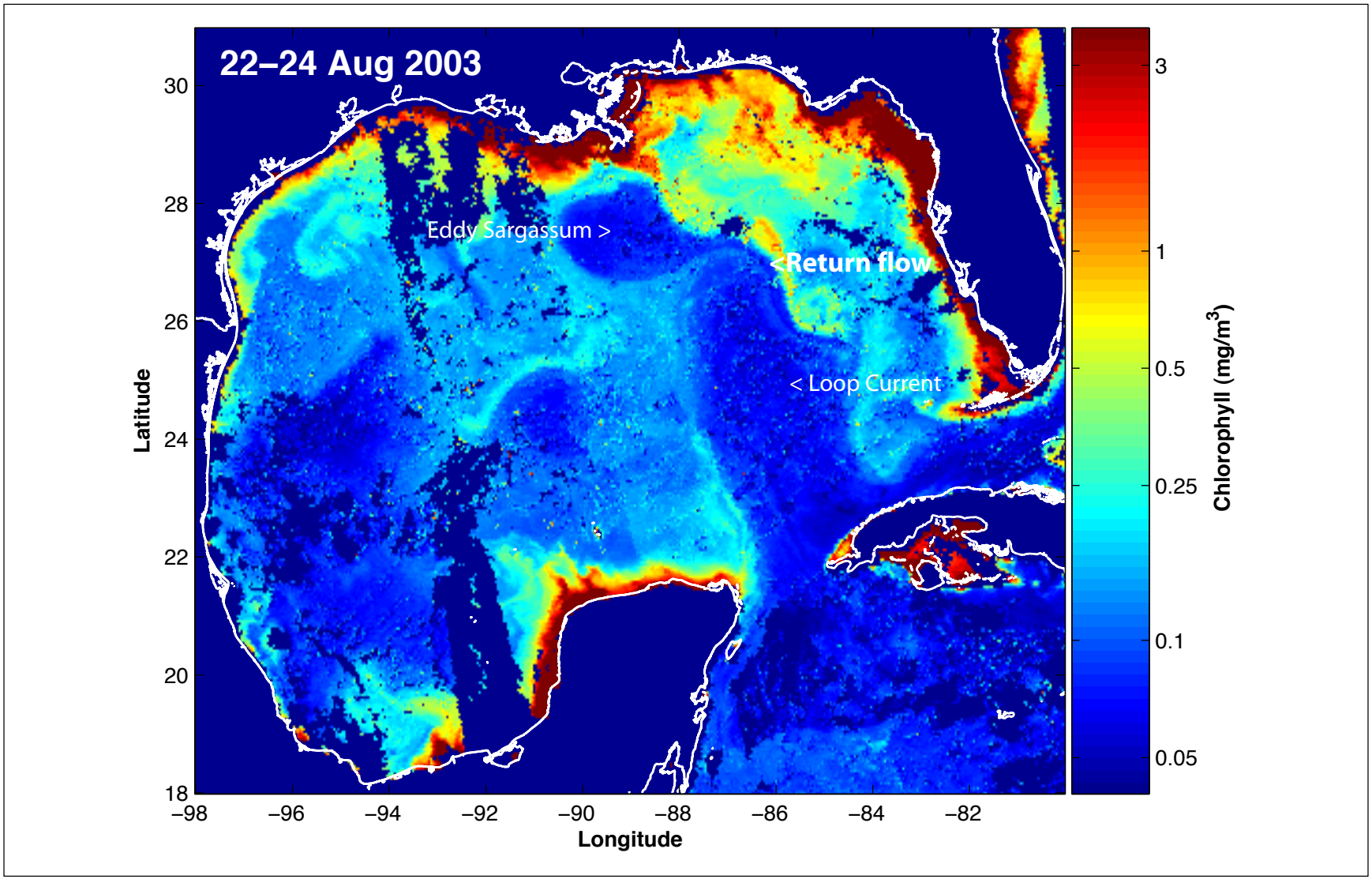

Figure 4.1-21. MODIS ocean color 3-day composite image from 22-24 August 2003 showing reattachment of Eddy Sargassum to LC. Note that the reattachment produced a return flow of surface water from Eddy Sargassum back into the LC along the northeast boundary of the current.

again and the final detachment or separation was observed in the 5-day median filtered image on 29 August 2003 (Figure 4.1-22).

Propagation of Eddy Sargassum through Study Array (5 August 2003 through 20 November 2003). During the final stages of the separation of Eddy Sargassum from the LC the eddy center was within the study region and was tracked with the PIES array through late October 2003**.** Values of the maximum SSH within the eddy center, the location of the eddy center, and the SSH value that coincides with the maximum speed within the eddy were determined from the PIES OISSH for the time interval from 7 August through 15 Oct 2004. The time series of SSH, SSHA (SSH at center minus the SSH at maximum velocity), and the eddy center latitudes and longitudes are shown in Figure 4.1-23. Coincident images at selected times are overlaid with the eddy-center track throughout this time period with the coincident locations of the eddy center and periphery on the date of the image (Figure 4.1-24.)

The maximum eddy-center SSH measured by the PIES array was 2.23 m on 9 August 2003, the highest SSH value observed within the study region during the entire field program. A significant decrease in the eddy-center maximum SSH and SSHA occurred from 24-29 August 2003 associated with the brief reattachment of Eddy Sargassum to the LC, as discussed above. This is consistent with a loss of mass associated with the observed surface flow from Eddy Sargassum back into the LC as seen in the color imagery. Another marked decrease occurred when Eddy Sargassum abruptly moved to the south around 28 September 2003. At this time the eddy went from a nearly circular shape to an elongated and clockwise rotating elliptical shape. This was also about the same time as the detachment of Eddy Sargassum from the LC and the transit of a strong atmospheric system through the GOM observed in satellite scatterometer winds. The center of Eddy Sargassum exited the array on 1 November 2003 and the entire eddy was outside of the array by 10 November 2003. As Eddy Sargassum exited the study region it merged with Unnamed Eddy and propagated west-southwest through the western GOM.

The MODIS ocean-color 3-day composite image from 20-22 October with the eddy center locations for Sargassum, Unnamed, and Titanic eddies, and the companion cyclone to Titanic Eddy is shown in Figure 4.1-25. The time series of the eddy-center SSH extrema are plotted in Figure 4.1-26. Altimeter and PIES estimates for the change in Eddy Sargassum's eddy-center maximum SSH during the time period that Sargassum was within the array are in good agreement, and show that the eddy amplitude had decayed by about 35 cm. The fine temporal sampling of the PIES, however, show that the change in eddy amplitude was more episodic than would be expected from the altimeter record alone. Note that the absolute bias between the PIES and altimeter SSH values were removed by setting the PIES time-series mean equal to the altimeter-mean SSH value over the same interval.

Detachment (25 September 2003) and Reattachment (28 November 2003) of Eddy Titanic. The detachment and reattachment of Eddy Titanic was remote from the study region; however, there were potential teleconnections of these events to the study area because of Titanic's large size and the energetic companion cyclone to the north of Titanic. The best estimate of the detachment time from imagery was the 25-27 September 2003 time period, which agrees well with the altimeter estimate of 25 September 2003. The combined influence of a Campeche Bank eddy and a Tortugas eddy acted to create strong regions of cyclonic circulation that cut across the

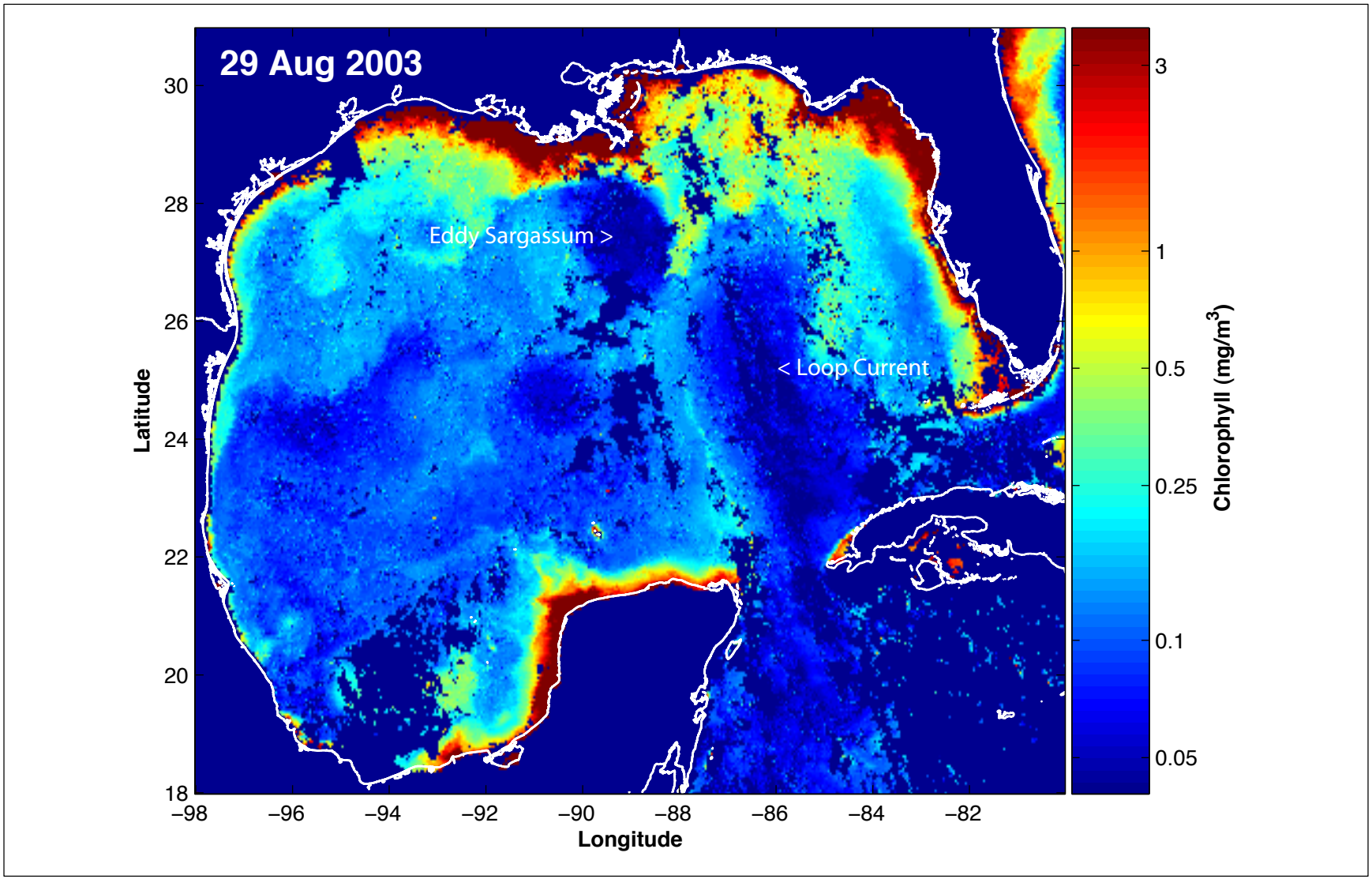

Figure 4.1-22. MODIS 5-day median filtered ocean color image for 29 August 2003 showing the separation (final detachment) of Eddy Sargassum from the LC.

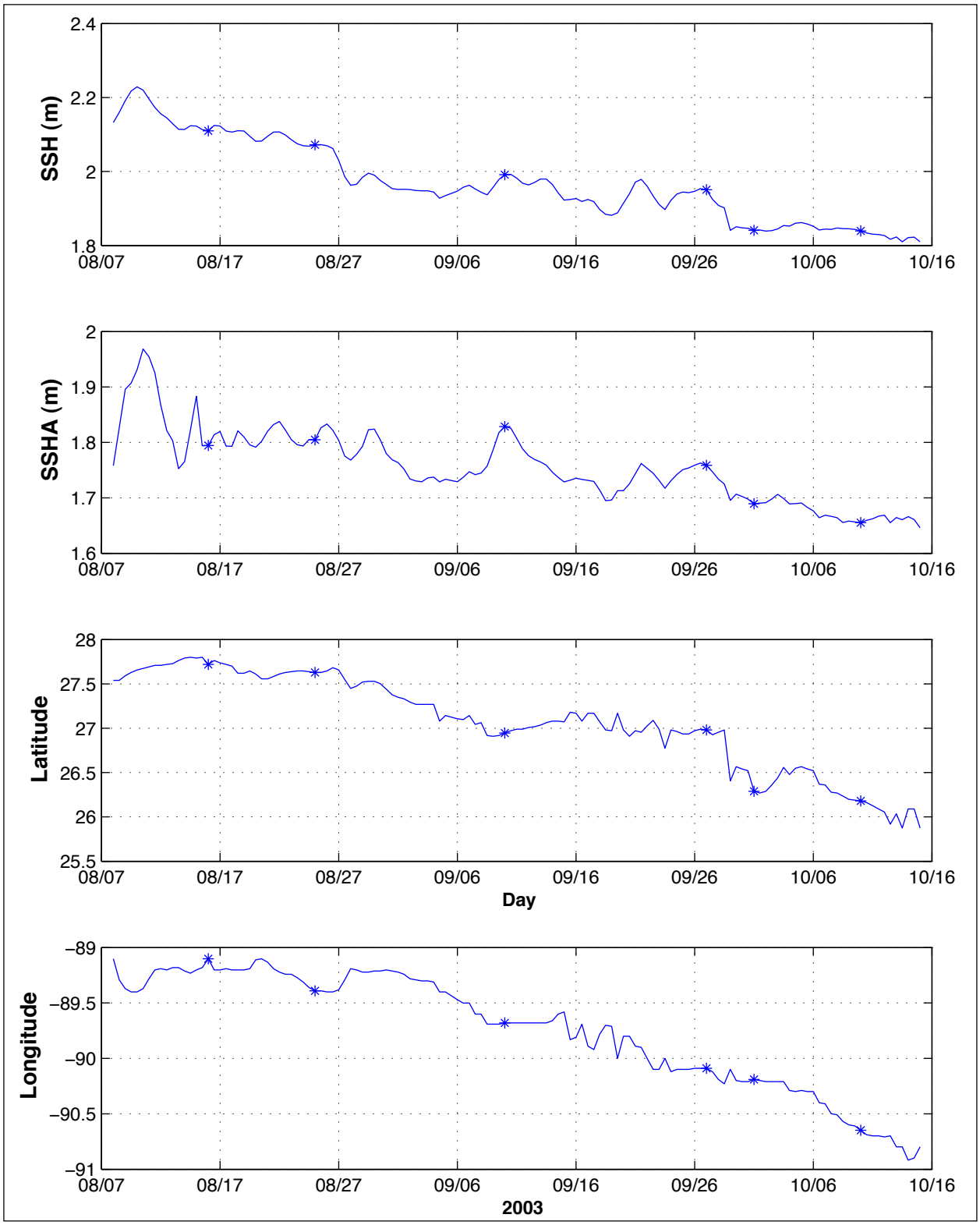

Figure 4.1-23. Time series of PIES SSH, SSHA (SSH at center minus the SSH at maximum velocity), and the eddy center latitudes and longitudes for Eddy Sargassum from 7 August through 15 October 2003. Selected times are highlighted corresponding to images in Figure 4.1-24.

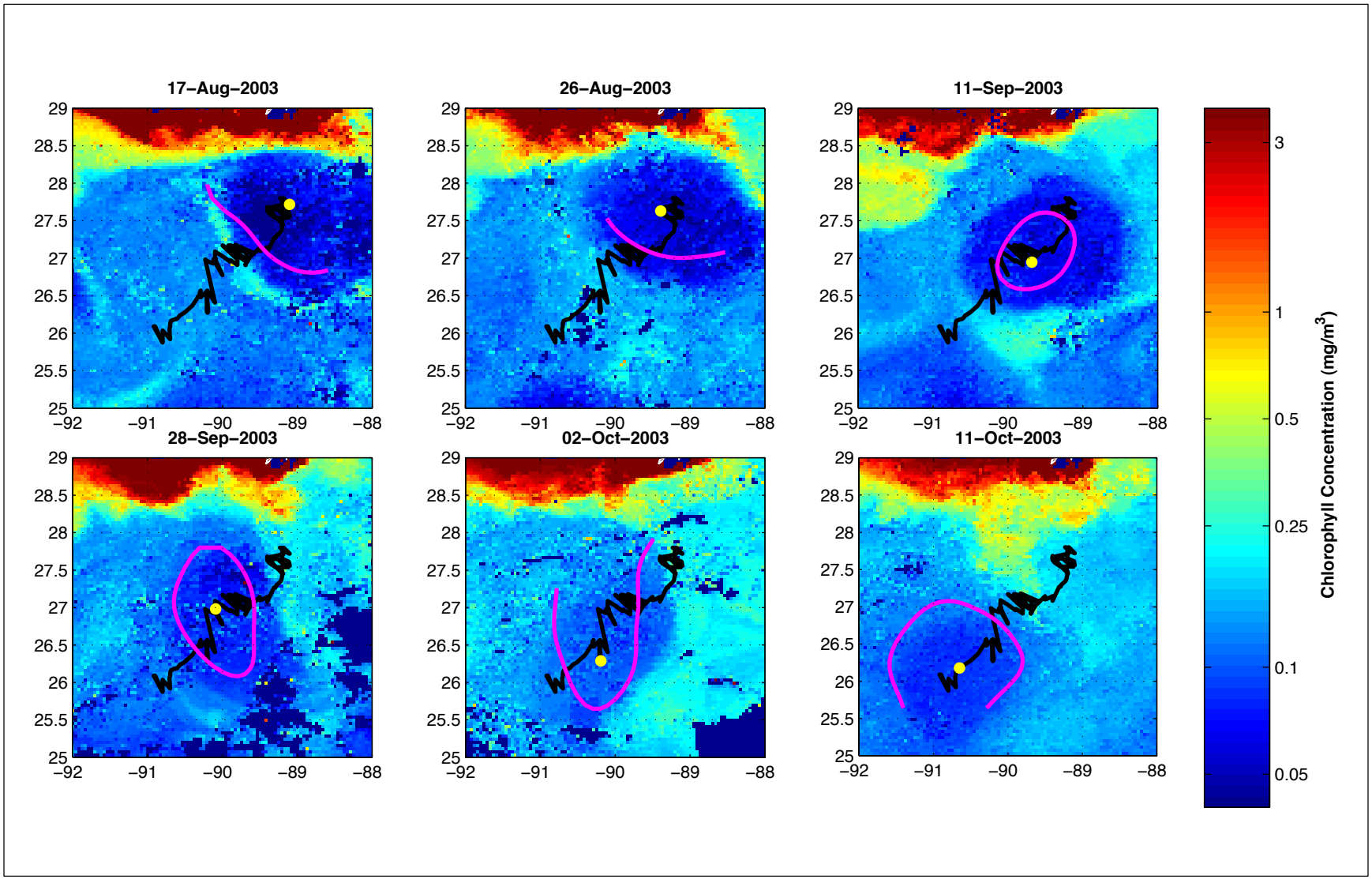

Figure 4.1-24. Coincident 5-day median filtered images at the selected times shown in Figure 4.1-23. Images are overlaid with the Sargassum eddy center track estimated from PIES OISSH . Eddy center locations (yellow dot) and the eddy periphery (magenta line) on the date of the images are also shown.

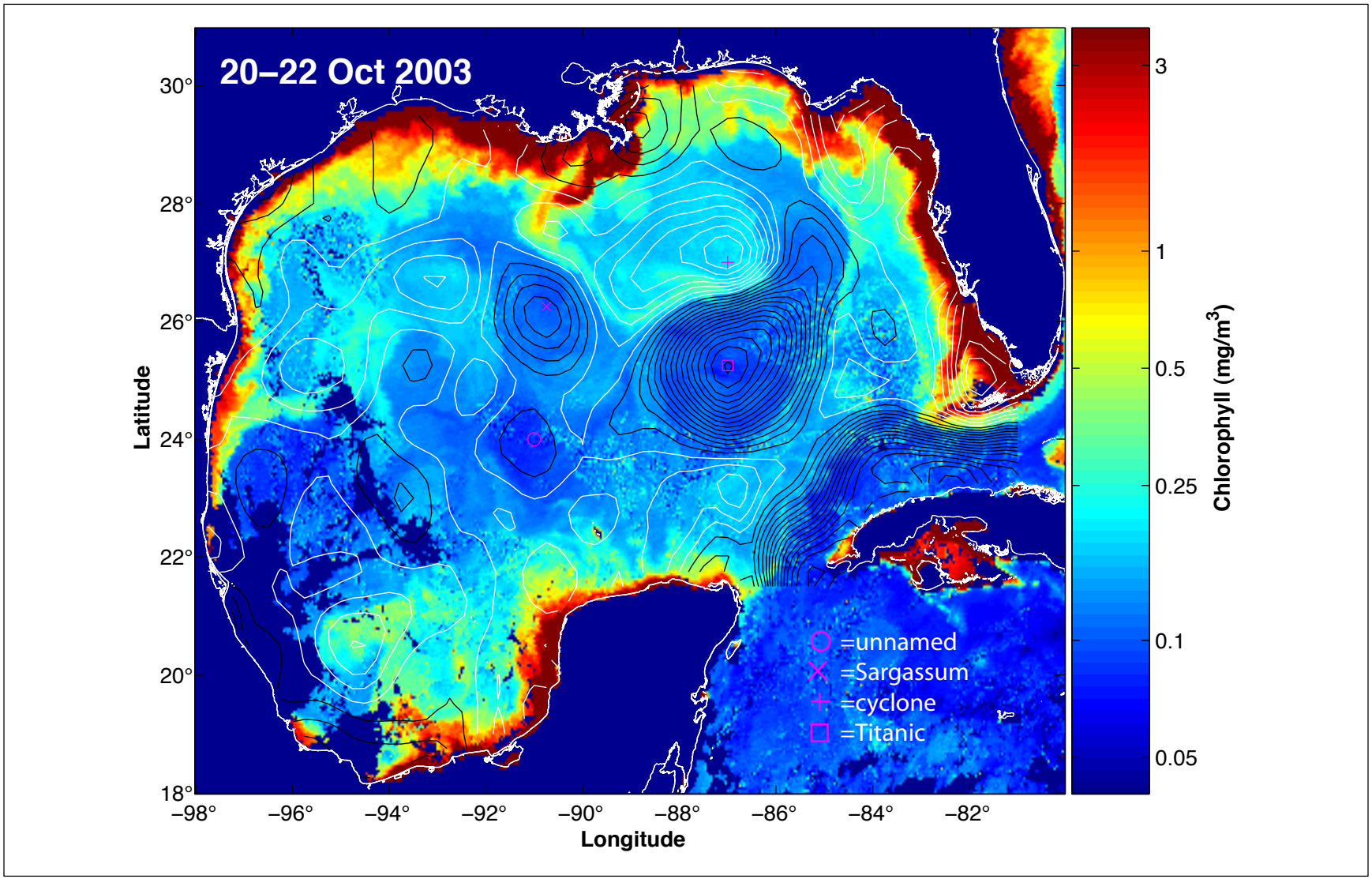

Figure 4.1-25. MODIS ocean color 3-day composite image from 20-22 October 2003 with overlaid altimeter-derived SSH. The eddy center SSH extrema for Sargassum, Unnamed, Titanic, and the companion cyclone to Titanic are identified with magenta symbols.

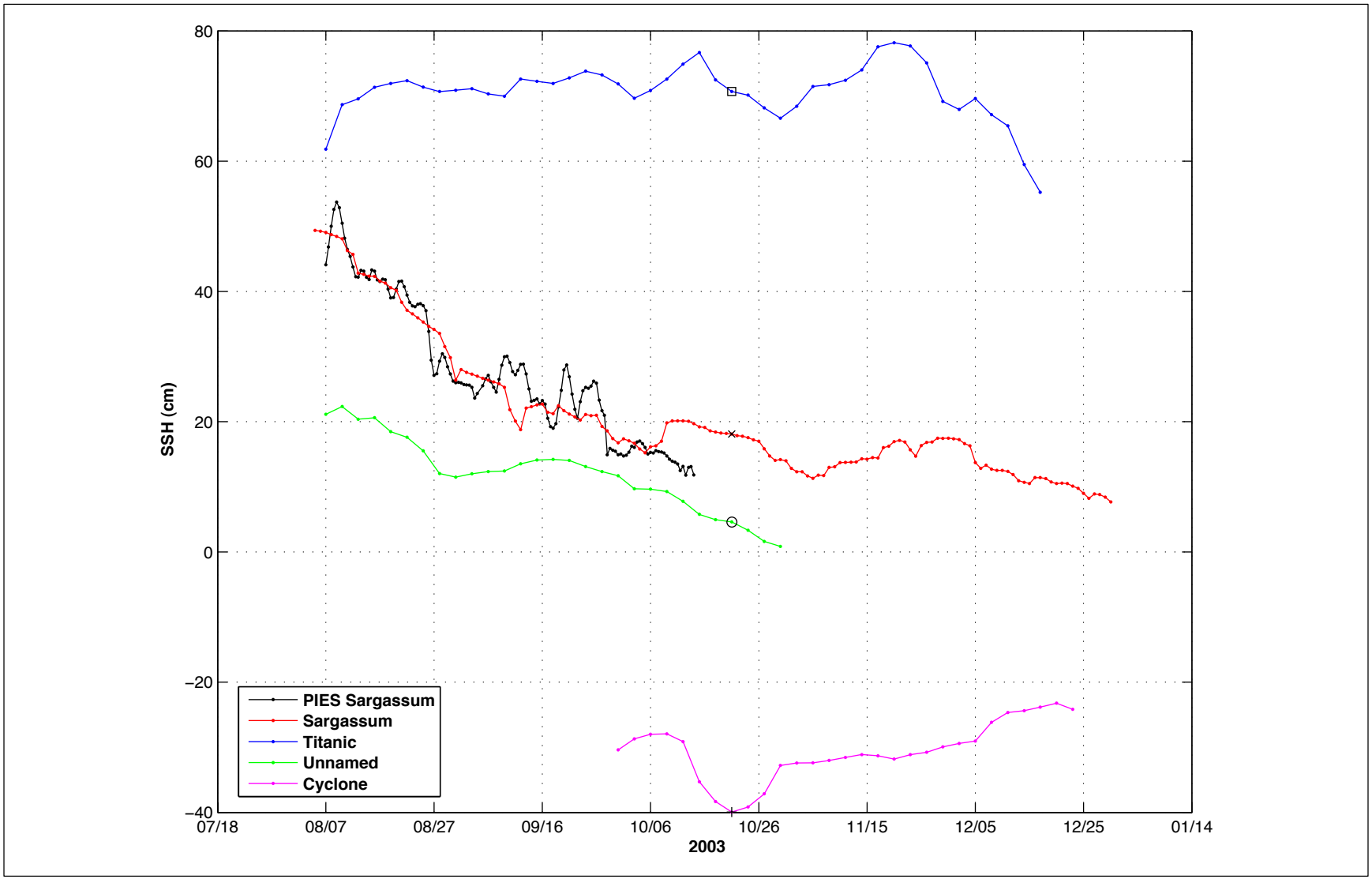

Figure 4.1-26. Time series of eddy center SSH extrema for Sargassum, Unnamed, Titanic, and the companion cyclone to Titanic. The points in the time series corresponding to the midpoint date of 3-day composite image in Figure 4.1-25 are shown by symbols. Both PIES and altimeter values are shown for Sargassum.

LC to complete the detachment. After the detachment of Eddy Titanic from the LC, the Campeche Bank eddy intensified and the LC remained in a port-to-port mode with the northern-most latitude of the LC remaining south of 24.5°N for over two months. North of Eddy Titanic a strong cyclonic eddy formed, which likely arrested westward propagation of the detached eddy (Figure 4.1-27). In late November, the cyclonic eddy had decayed sufficiently so that the east-west-elongated Eddy Titanic was able to rotate clockwise and reattach to the LC on 28 November 2003. This reattachment was confirmed by SST imagery that showed a warm filament from the LC advecting around the reattached eddy on 1 December 2003. After reattachment, the SSH extrema of the now reattached Eddy Titanic and the companion cyclone decayed substantially (see Figure 4.1-26).

The large companion cyclone north of Eddy Titanic had a significant influence on the study region. As Eddy Sargassum propagated through the study region, the western margin of the cyclone moved into the eastern part of the array from October through November 2003, behind Eddy Sargassum. The cross-shelfbreak flow induced between Eddy Sargassum and the cyclone is very visible in ocean-color images during that period, clearly showing the large amount of shelf water from near the Mississippi River outflow that advected across the shelfbreak between the two eddies within the array.

Separation of Eddy Titanic (31 December 2003) and Propagation South of the Study Array (1 January through 30 March 2004). The separation of Eddy Titanic, based on the breaking of the 17-cm LC contour, occurred on 31 December 2003, in good agreement with the available SST imagery (see Figure 3.1-2). The eddy propagated directly westward after separating from the LC with the majority of the eddy remaining south of the study region. In January 2004, the eddy elongated into an elliptical shape and rotated clockwise, passing the northern flank of the eddy eastward through the southeast corner of the array. Throughout February 2004, the eddy appeared to be entirely south of the array. The surface flowfield within the array was generally cyclonic with a large -15 cm amplitude cyclone of unknown origin positioned near the center of the array. In March, the elongation and rotation of Eddy Titanic again brought the northern edge of this LCE into the array, this time in the southwest corner.

4.1.3 Basic Statistics in the Study Array – Upper Layer

The basic statistics for the upper-layer currents and their variability observed in the Exploratory Study array are illustrated by the moored current observations at several levels in the upper water column, and summarized in this section by maps and tables for three levels, the sea surface (0 m), the base of the seasonal thermocline (150 m), and within the main thermocline (500 m). The PIES data can map absolute currents daily on these depths and on any other desired depths at a grid of locations within the study area. For comparison with these mapped currents, the directly measured currents are first reported for the current-meter moored observations at five tall moorings within the array. We report in this section the mean currents $(U, V) = (\langle u \rangle, \langle v \rangle)$ and the eddy kinetic energy, $EKE = (1/2) [(u')^2 + (v')^2]$, where $\langle\ \rangle$ indicates the average over the 1-year observation period, and $u' = (u - U)$, $v' = (v - V)$. We examine how the EKE varied with time as the strong LC and eddy features passed through the study region. We also report the time and length scales of correlations associated with these currents and their associated SSH and geostrophic pressure fields.

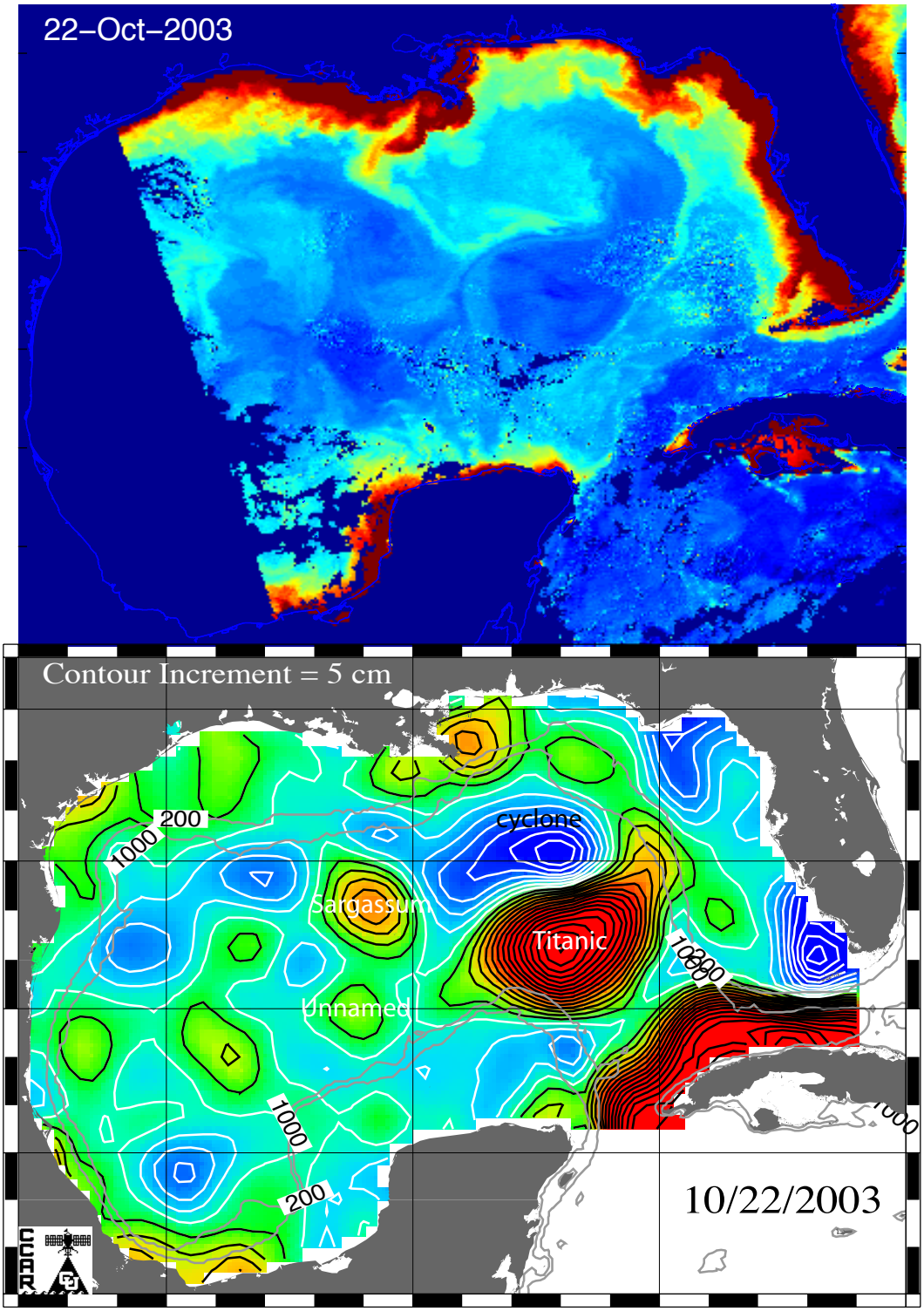

Figure 4.1-27. MODIS ocean color image (upper panel) and altimeter-derived SSH map (lower panel) on 22 October 2003. The anticyclonic eddies, Sargassum, Unnamed and Titanic, and the companion cyclone to Titanic are identified.

4.1.3.1 Upper-Layer Statistics from Moored Current Meters

Upper-layer 40-HLP currents, temperatures and salinities for selected depths are given in Figures 4.1-28 through 4.1-32, for moorings L1 through L5, respectively. The presence of the LC and LCE core water is generally shown by: high temperatures greater than 25, 20 and 17°C for the 75, 150 and 225 m instruments, respectively; strong currents in the upper 400 m that decrease with increasing depth; and salinities at 150 and 225 m that were greater than 36.5 PSU and also exceeded the salinities at 75 m. The later is the signature of subtropical underwater (SUW) that enters the Gulf around 100 to 200 m depth with the LC through the Yucatan Channel (see Section 3.1.6). LCEs often have a slightly fresher surface layer and this is reflected by the decrease in salinity at the 75-m level by about 0.2 PSU when an eddy is present. These features of eddy circulations are clearly seen in the L1 records (Figure 4.1-28), during June through September 2003, for Eddy Sargassum. At L1, the first half of the record was dominated by the passage of Eddy Sargassum and its associated cyclones. Cyclonic signatures are usually vigorous rotary currents over relatively short intervals, accompanied by cooler and fresher water at the deeper instruments (150 and 225 m), but with little or no signature in the temperature and salinity at 75 m (and above). After the eddy departed in October 2003, the upper-layer circulation at L1 became fairly quiescent. These figures also include deeper currents at 750 m, 1000 m and selected lower-layer instruments below 1000 m. Note that the direction of the V-component coordinate axis relative to north differs for each of the moorings and was determined from an analysis of the lower-layer flows and the topography. Upper-layer currents are much less polarized along a given direction than the lower layer flows, as will be described below.

The deeper current records are included to show there is little visual correlation between flows below 1000 m and the surface layer. However, the apparent influence of the lower-layer flows on flows above 1000 m varied by location and water depth. The 1000-m levels at L1 and L2 (Figures 4.1-28 and 29) mainly resemble the upper layers except for occasional lower-layer events (e.g. December 2003 at L1 where the lower-layer event penetrated through to the 750 m level). L2 had the most complex depth dependence of the currents and the usual notion of strictly two-layer flows dominating the deep-waters of the Gulf seems to have broken down to some degree. In the upper 400 m, flows were clearly coherent and similar though much weaker than the eddy flows at the other moorings. The warm event in October was caused by the periphery of Eddy Sargassum. For most of the record, L2 was influenced by cyclones, which accounts for the relatively cool temperatures in the upper layer. The 750-m level had a number of events with relatively stronger flows than at 400 or 1000 m. For example, the southward event in October and the short event at the beginning of December were only weakly reflected in the record at 1000 m and have little or no relationship to the records at 400 and 1650 m (Figure 4.1-29). This mooring was the furthest from the Escarpment and had very weak lower layer (below 1000 m) TRW activity (discussed in detail in the following sections). The lack of strong circulation processes in both the surface and bottom layers apparently allowed more complex mid-depth flows to develop.

The moorings in deeper water, below the Escarpment (i.e., L3, L4 and L5; Figures 4.1-30, 31 and 32, respectively) show the deep lower-layer bottom intensified fluctuations penetrating up to the 750-m level most of the time. At L5, the 660-m level was more of a mixture than the 750-m

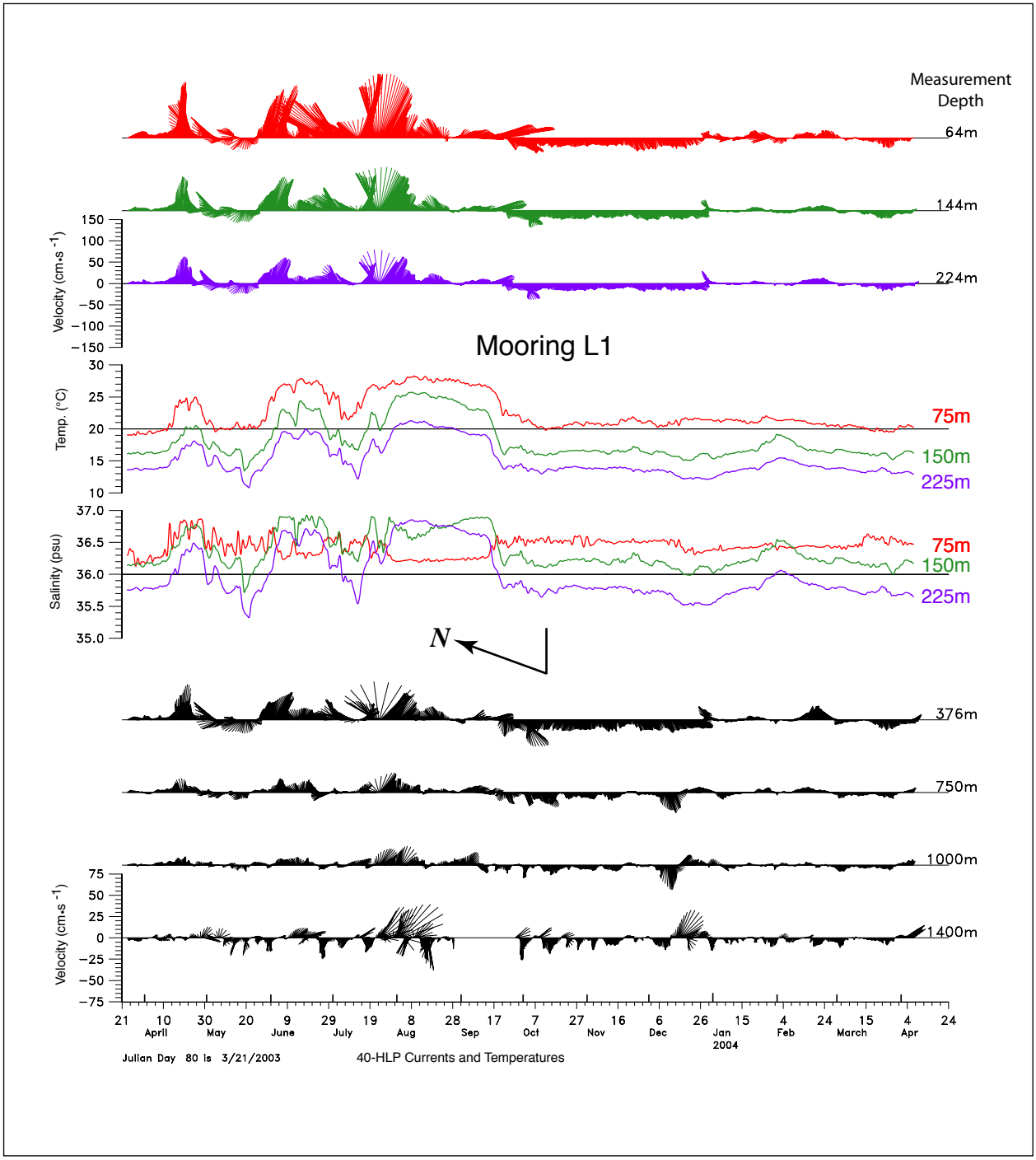

Figure 4.1-28. 40-HLP current vectors, temperature and salinities for the indicated depths at L1.

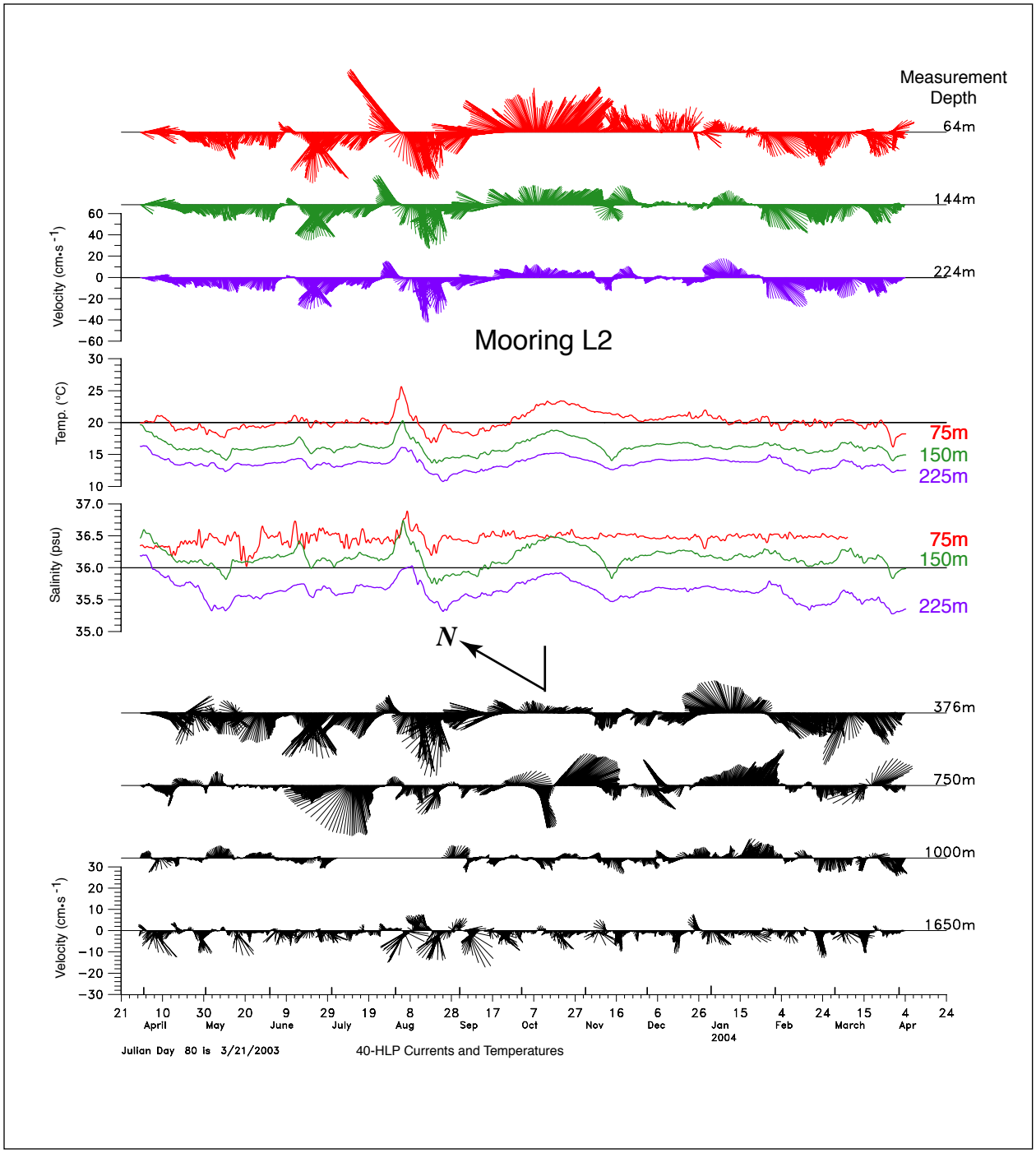

Figure 4.1-29. 40-HLP current vectors, temperature and salinities for the indicated depths at L2.

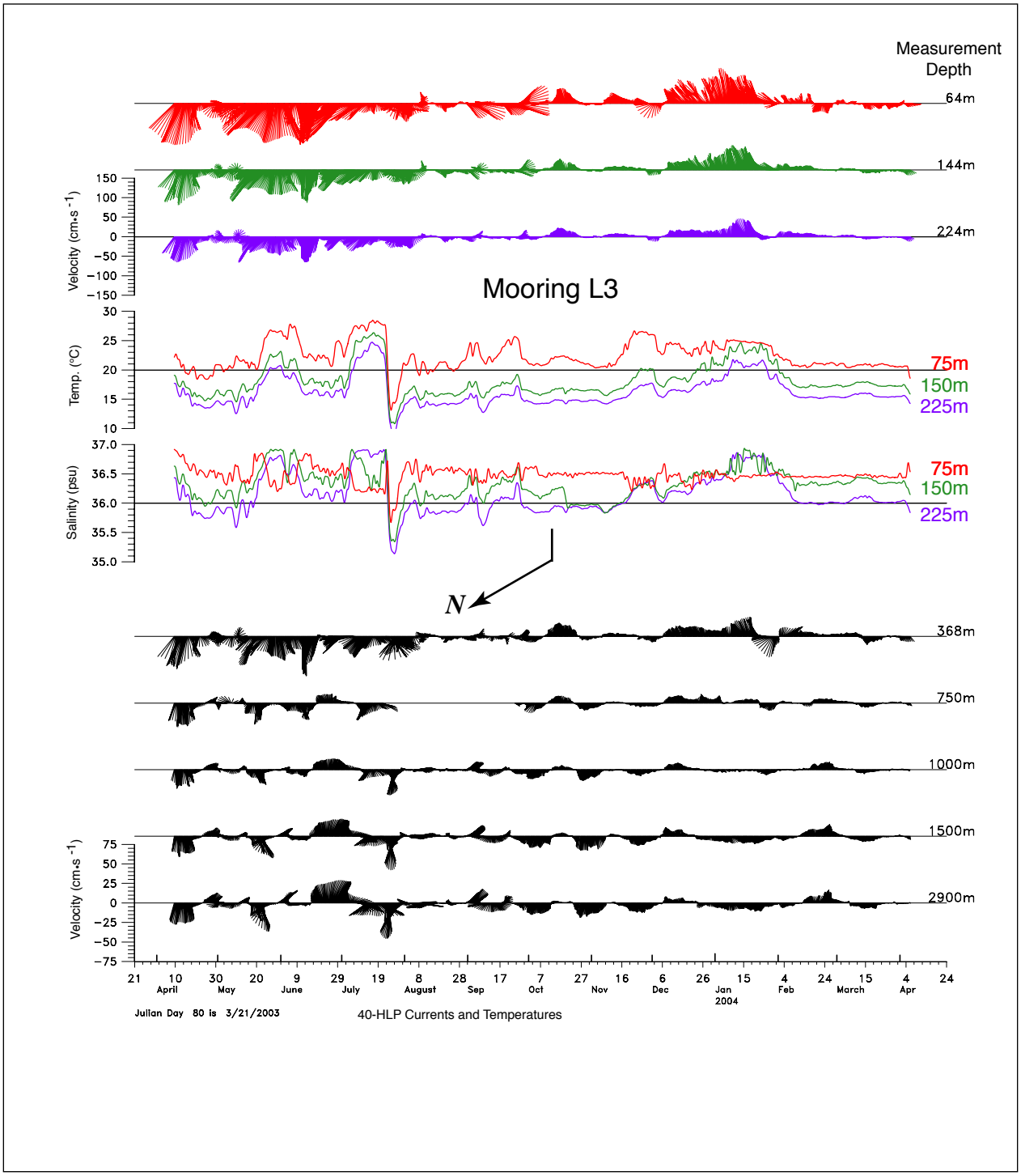

Figure 4.1-30. 40-HLP current vectors, temperature and salinities for the indicated depths at L3.

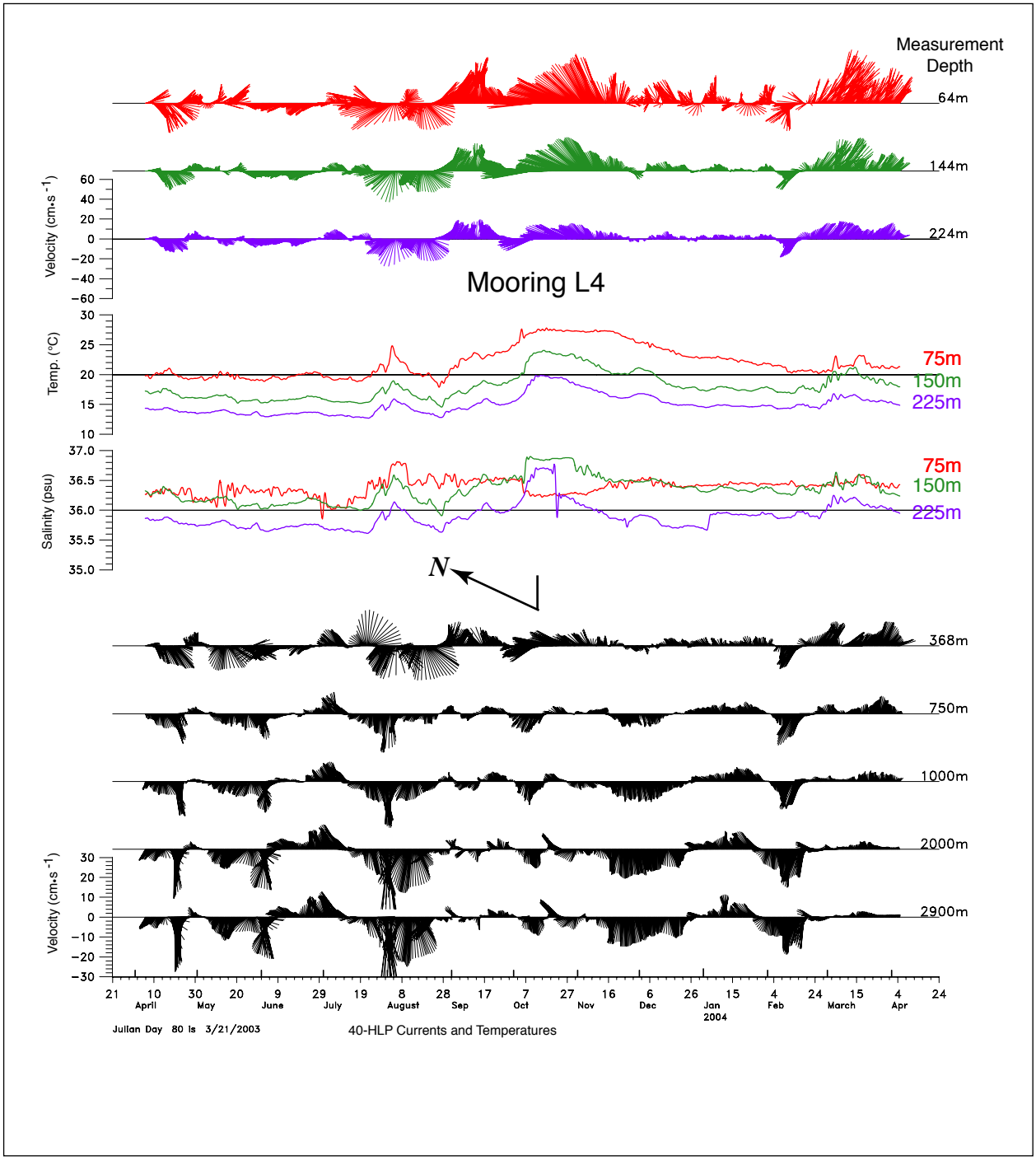

Figure 4.1-31. 40-HLP current vectors, temperature and salinities for the indicated depths at L4.

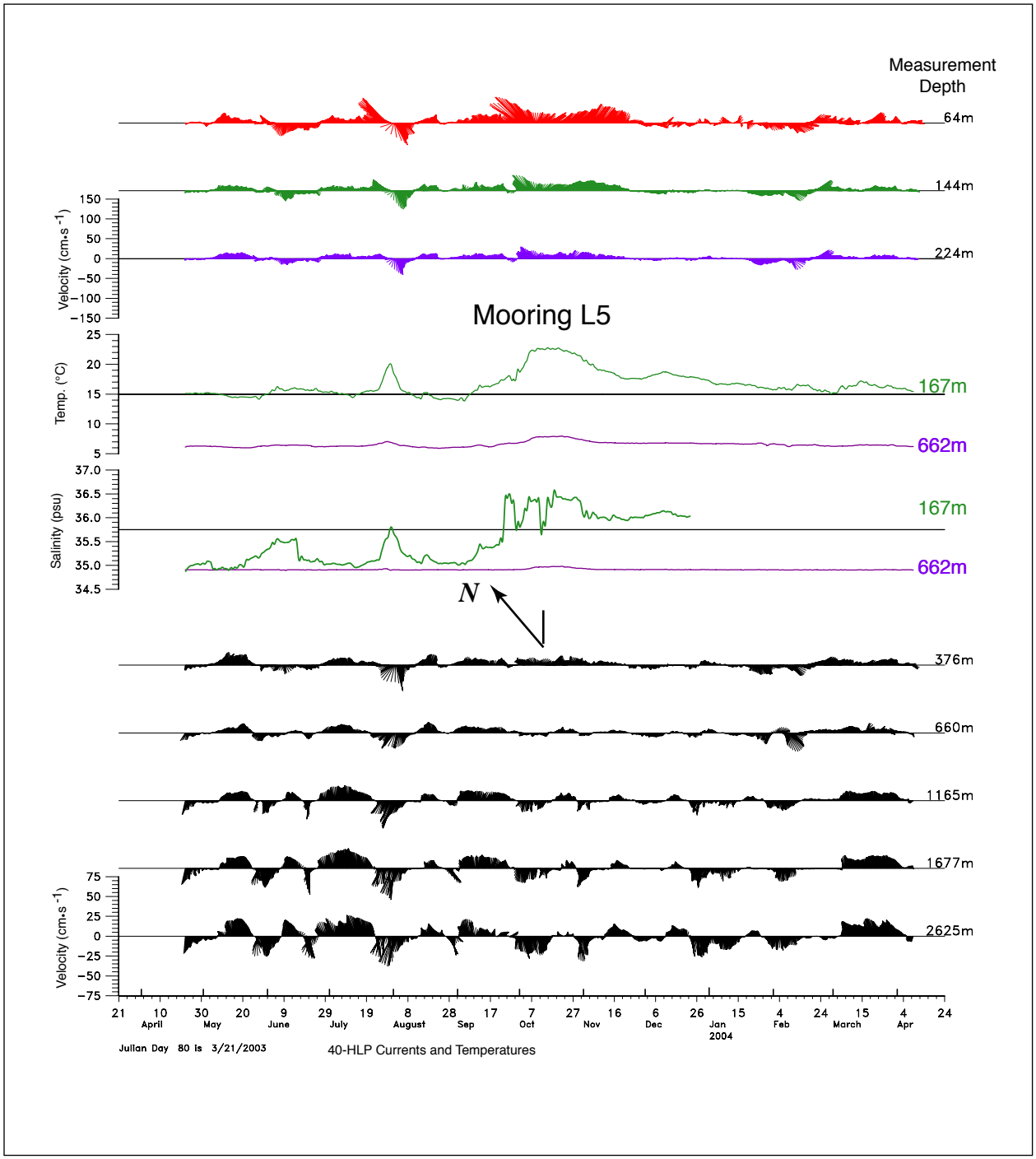

Figure 4.1-32. 40-HLP current vectors, temperature and salinities for the indicated depths at L5.

level at the other two moorings. The upper-layers at L3 had strong currents from LC intrusions in the first part of the record through August 2003 and then the northern edges of Eddy Titanic, which passed to the south of the array in January and February, 2004. Note that the dramatic cold event in the upper layer temperatures that occurred around July 25, 2003 was exaggerated by a large draw down of the mooring caused by strong (~ 40 to 50 $cm \cdot s^{-1}$) currents in the lower 2000 m of the water column. At L4 in the southwest corner of the array, the upper-layer flows were weaker as Eddy Sargassum became less vigorous by October 2003 and the mooring was mostly on the periphery of the eddy.

All three moorings below the Sigsbee Escarpment had a small number of events of 1 to 2 weeks in duration that appear to be visually coherent through most of the water column. At L3 (Figure 4.1-30), the beginning of the record ~ 10 August 2003 and ~ 15 October 2003 had similar northwest and southeast flows, respectively, at all depth levels with some indication of surface intensification. At L4 (Figure 4.1-31), ~ 12 February 2004, a westward event, and at L5 (Figure 4.1-32), ~ 4 August 2003, a southwestward event appeared to have similar currents at all levels throughout the water column. It is difficult to determine if these apparent whole-water-column events were significant connections or just coincidences between separate upper- and lower-layer flow regimes.

Mean flows for selected depth levels in the upper layer (750 m and above) are shown in Figure 4.1-33. The means were calculated for the same 11 1/2 month interval (22 April 2003 to 4 April 2004). The larger, near-surface means were on the east side of the array (L1 and L3) and all moorings, except L2, had similar decreases in magnitude with increasing depth. The directions reflect the dominant eddy influence at each station: LC intrusions for the northward means at L3, and Eddy Sargassum for the east or northeast mean flows at L1, L5 and L4. It is noted that stations that were more on the peripheries of anticyclonic eddies (L3 and L4) had a small anticlockwise turning with depth, and stations more influenced by the core (L1 and L5) had clockwise turning with depth. L2 was mainly influenced by cyclonic eddies and the means have little shear in the upper 400 m. Maximum mean currents were at 225 m towards the west. The standard deviation ellipses for the same records are given in Figure 4.1-34. The ellipses show the $\langle u'^2 \rangle^{1/2}$ and $\langle v'^2 \rangle^{1/2}$ along the directions of the principal axes (major and minor axes of the ellipse), where the major principal axis is defined as the direction where $\langle u'v' \rangle = 0$. The highest variances were near the surface. The eastern side of the array was more energetic than the western. All the records are only slightly polarized so that $\langle u'^2 \rangle^{1/2}$ has similar magnitudes to $\langle v'^2 \rangle^{1/2}$. The eastern stations had major axes that were similar at all depths down to 750 m and were approximately aligned with the general trend of the isobaths. Magnitudes decreased uniformly with increasing depth. On the western side, there were similar decreases in the magnitudes of the fluctuations with depth, but at L4 and L5, the major principal axes were more directed across the general trend of the slope isobaths. The directions of the L2 major axes were indeterminate. However, at the lowest levels (750 m at L2 and L4, 660 m at L5), the major axes differed from those at shallower depths, being more aligned with the isobaths. This change in direction was a consequence of the deeper lower-layer motions having some influence at this depth at these stations. The change in direction at 750 m at L2, was more a consequence of the special nature of the record at this depth than the influence of deeper motions as discussed above.

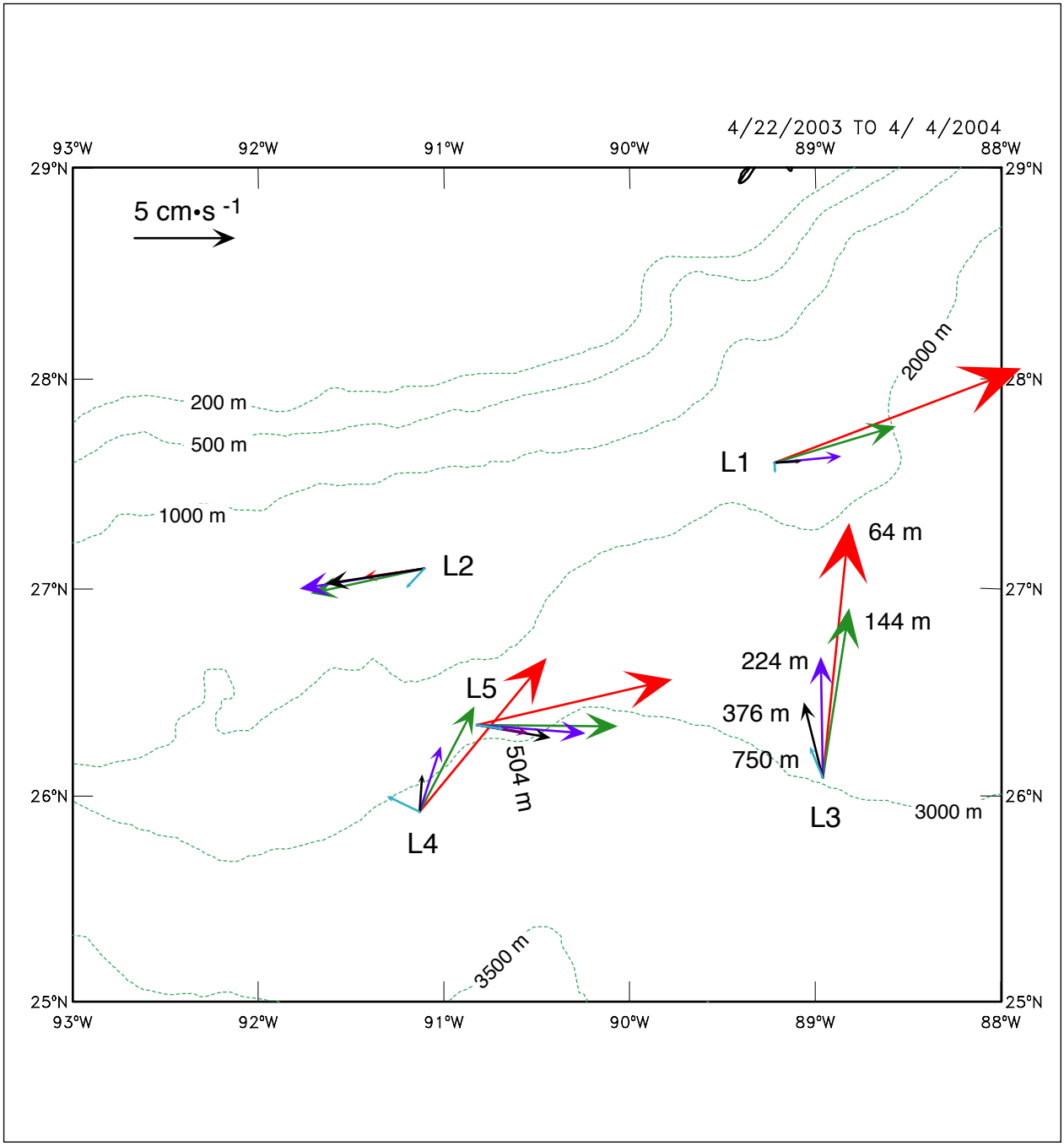

Figure 4.1-33. Annual mean 40-HLP currents at indicated depth levels in the upper layer. Depth levels are color coded. At L5, 504 m is purple and the deepest level (pale blue) is 660 m instead of 750 m.

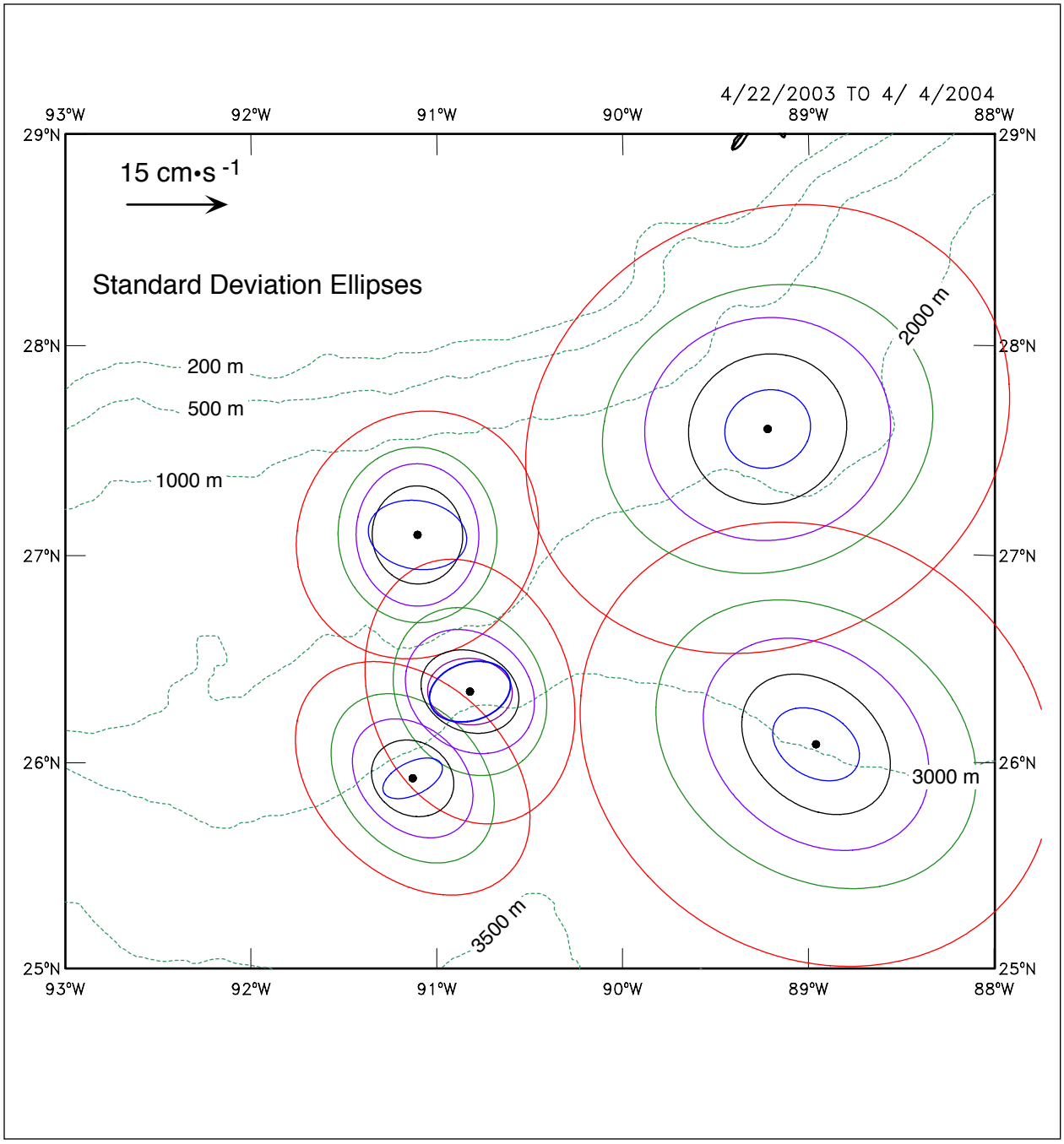

Figure 4.1-34. Annual mean 40-HLP current velocity standard deviation ellipses. Depth levels are color coded as in Figure 4.1-33.

4.1.3.2 Mapped Current Statistics at 0, 150, and 500 m

The time-average mapped currents and streamfunction for this 1-year observational period at three representative upper layer depths are shown in Figures 4.1-35, 36, and 37. The absolute currents for each of these representative levels were generated as the sum of the baroclinic profiles plus the deep reference currents. Those methods, described in Section 2.3, produced time series and mean currents that agreed well with all directly-measured currents, at levels within the upper layer on five tall moorings, and in the deep layer at these same sites plus 15 deep moorings for a total of twenty sites of deep current observations.

During the year of field measurements, the LC intruded into the eastern portion of the study array. Near 89°W and 90°W strong LC currents dominated the time-averages to generate anticyclonic flow centered near 89.3°W with time-average speeds typically near 15 $cm \cdot s^{-1}$ at the surface (0 m, Figure 4.1-35). In the rest of the array, the time-average currents were strongly influenced by the passage of the two LCEs. Eddy Sargassum passed westward through the array tracking south of Sigsbee Escarpment, and Eddy Titanic skirted along the southern border of the array. Their strong anticyclonic currents, which extended outward about 100 km from the eddy center, and which were to the east in the northern part of the LCEs, generated mean eastward currents up to 18 $cm \cdot s^{-1}$ at the surface (0 m) all along the southern half of the array west of 90°W. At 150 m and 500 m, the time-average currents exhibited similar patterns except that currents were smaller, with peak mean values respectively of 15 $cm \cdot s^{-1}$ and 10 $cm \cdot s^{-1}$. At 500 m moreover, because the baroclinic upper-layer component was weaker, the absolute currents were more influenced by the reference-level currents at 1500 m, which themselves had peak mean speeds near 15 $cm \cdot s^{-1}$, as will be discussed in Section 4.2.

It is important to recognize that the time-average currents were dominated by a few strong events for this year of observations. The maps for one year should not be interpreted to represent the long-term mean currents. The event-domination of the currents is emphasized by the 3-month mean fields illustrated in Figures 4.1-38 through 4.1-41. Each quarterly-mean figure includes three panels, (a) the baroclinic streamfunction at 0 m relative to 1500 m, (b) the 1500 m reference streamfunction (= geostrophic pressure field at 1500 m), and (c) their sum which gives the absolute streamfunction and currents at the sea surface. These figures illustrate the event-domination noted in the preceding paragraph. The upper currents in the first two quarters (Figures 4.1-38 and 4.1-39) were strongly dominated by the LC and the initial separation of Eddy Sargassum. The third quarter currents (Figure 4.1-40) were dominated by the west-southwestward passage of Eddy Sargassum, and the fourth quarter currents (Figure 4.1-41) were most influenced by the westward passage of Eddy Titanic. The point is that even the 1-year mean currents were event dominated, i.e., the average of only a few big events – accounting for the mean eastward currents all along the southern half of the array west of 90°W.

The current variability was much greater than were the mean currents in this region. The traditional measure of current variability is mean eddy kinetic energy,

$$<EKE> = (1/2) <(u')^2 + (v')^2>$$

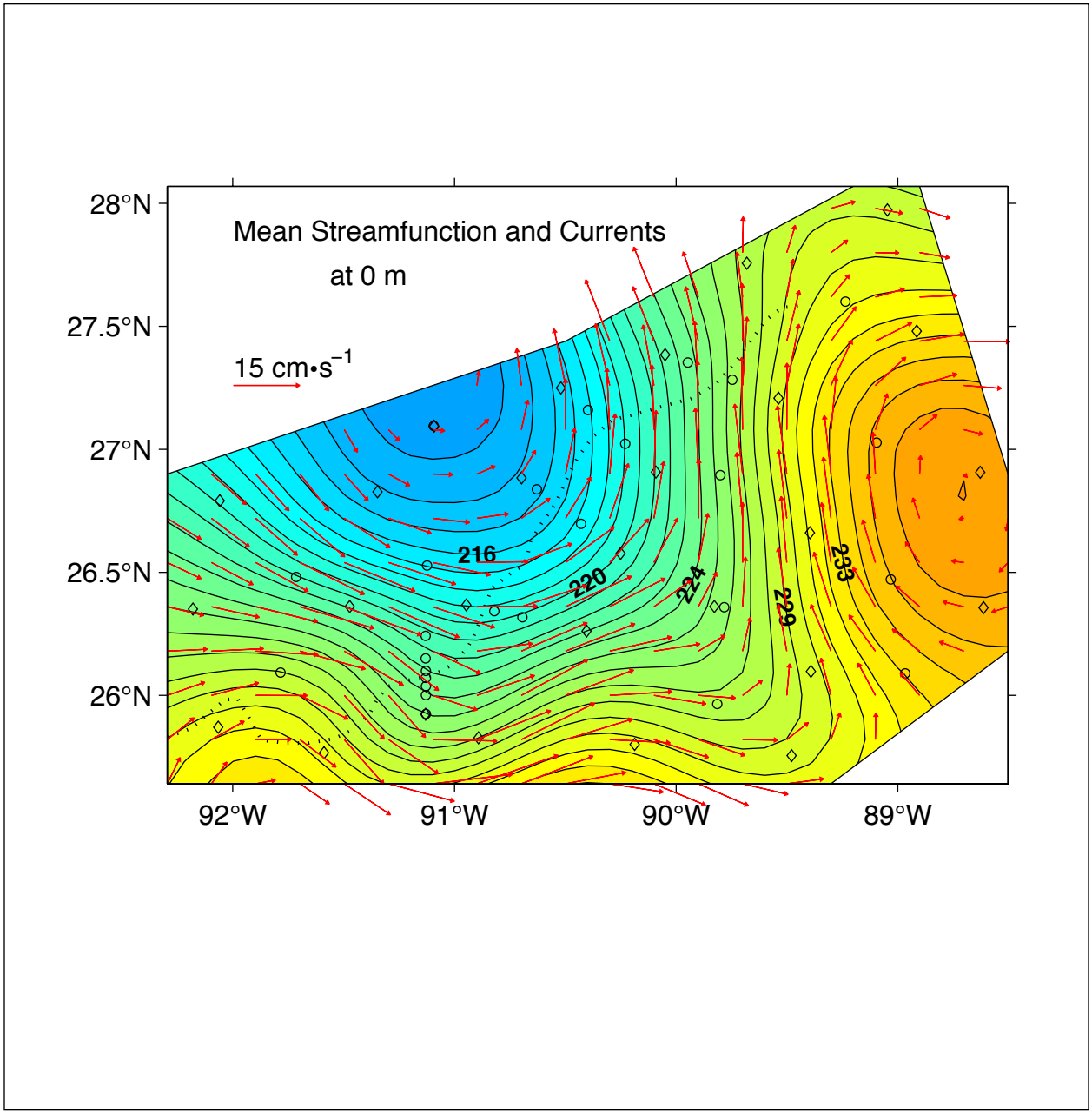

Figure 4.1-35. Time-average mean streamfunction (contours) and currents (red vectors) at 0 m depth. Dotted line denotes the center of the Sigsbee Escarpment. Streamfunction contoured every 1 km m•s^{-1} with low (high) values shown with blue (red) hues. Current vectors plotted at 20-km spacing. PIES sites indicated by diamonds; current meters by circles.

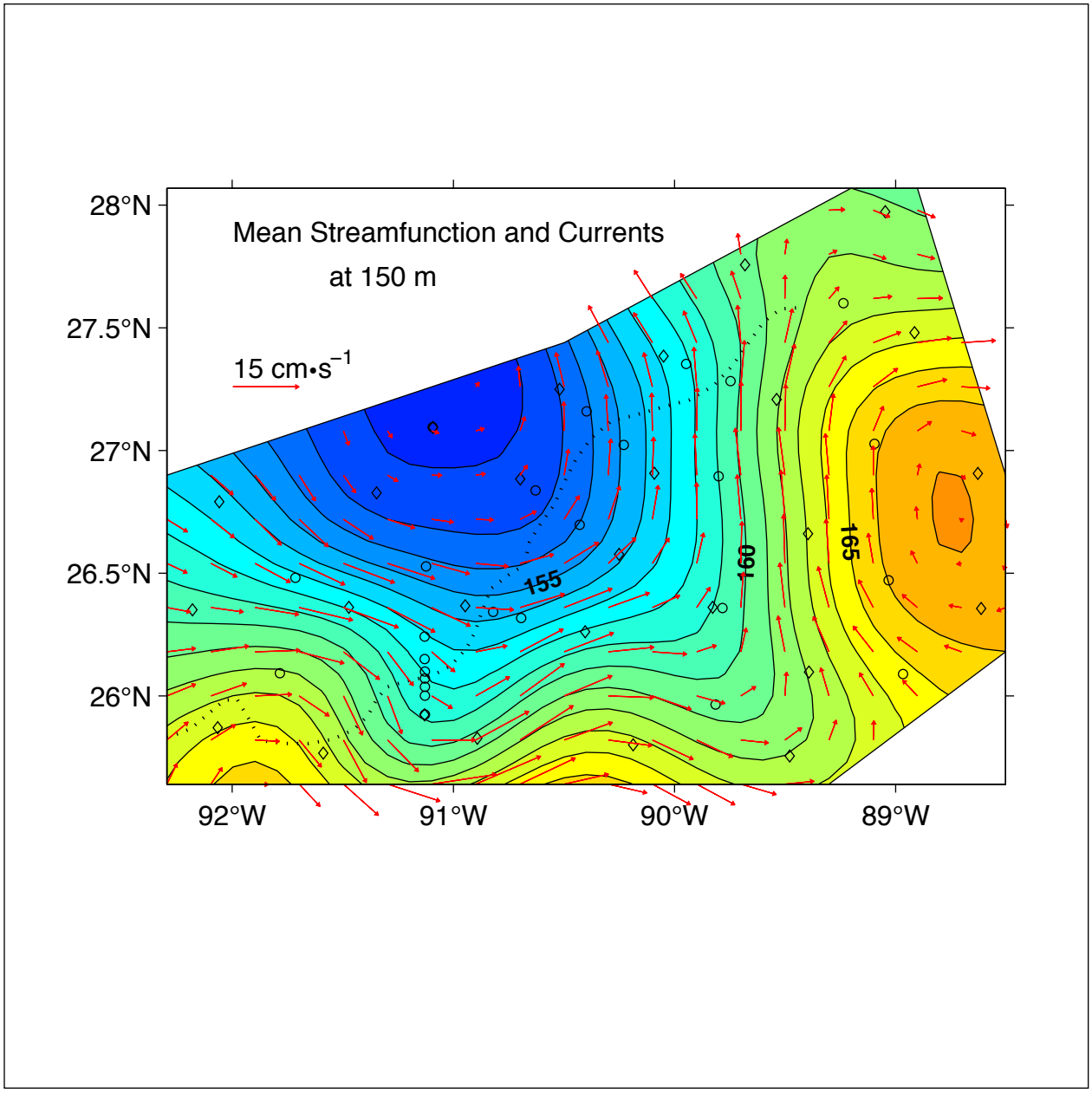

Figure 4.1-36. Time-average mean streamfunction (contours) and currents (red vectors) at 150-m depth. Dotted line denotes the center of the Sigsbee Escarpment. Streamfunction contoured every 1 km m•s^{-1} with low (high) values shown with blue (red) hues. Current vectors plotted at 20-km spacing. PIES sites indicated by diamonds; current meters by circles.

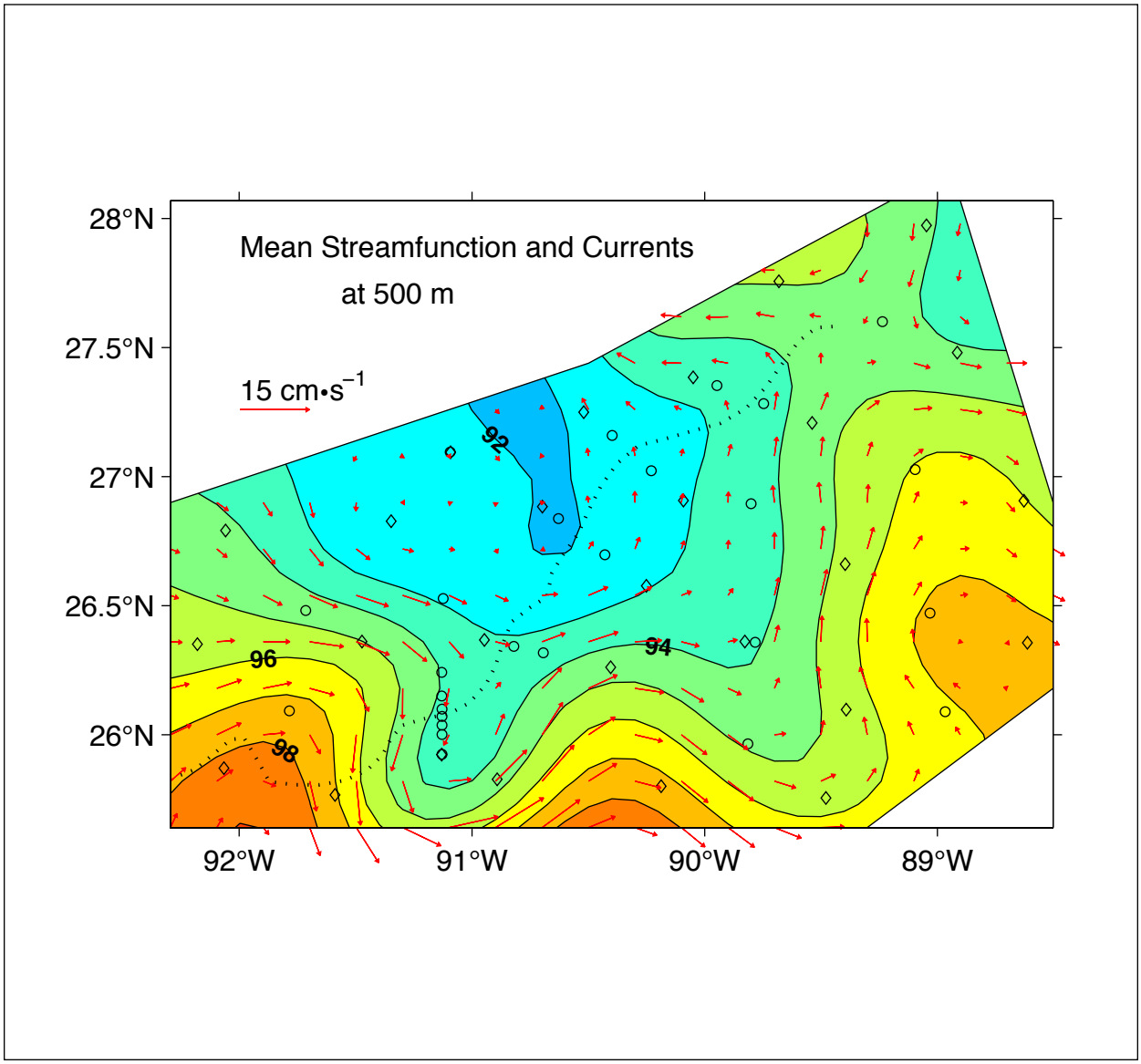

Figure 4.1-37. Time-average mean streamfunction (contours) and currents (red vectors) at 500-m depth. Dotted line denotes the center of the Sigsbee Escarpment. Streamfunction contoured every 1 km m•s^{-1} with low (high) values shown with blue (red) hues. Currents vectors plotted at 20-km spacing. PIES sites indicated by diamonds; current meters by circles.

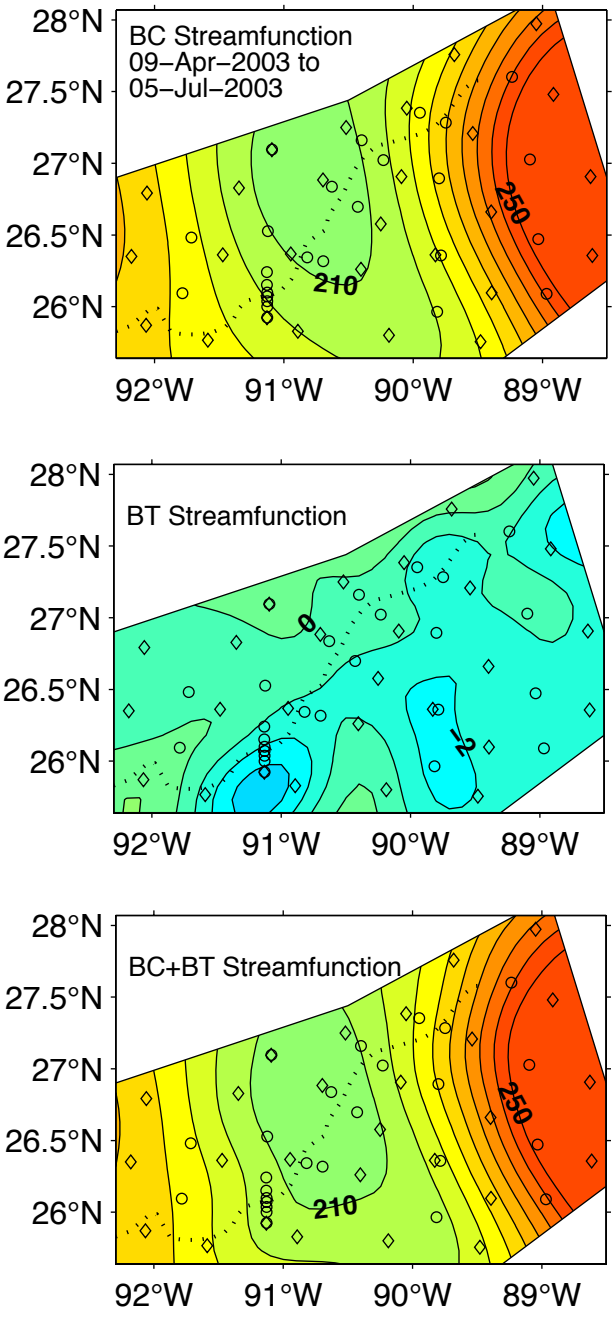

Figure 4.1-38. Quarterly mean surface streamfunction averaged from April 9, 2003 through July 5, 2003. Top panel: Streamfunction at 0-m depth relative to 1500 m, the baroclinic streamfunction (BC). Middle panel: 1500-m depth geostrophic pressure field, barotropic streamfunction (BT). Bottom panel: Sum of BC (top panel) and BT (middle) is the absolute surface streamfunction. Dotted line denotes the center of the Sigsbee Escarpment. Streamfunction contoured every 1 km m•s^{-1}. Low (high) values shown with blue (red) hues. PIES sites indicated by diamonds; current meters by circles.

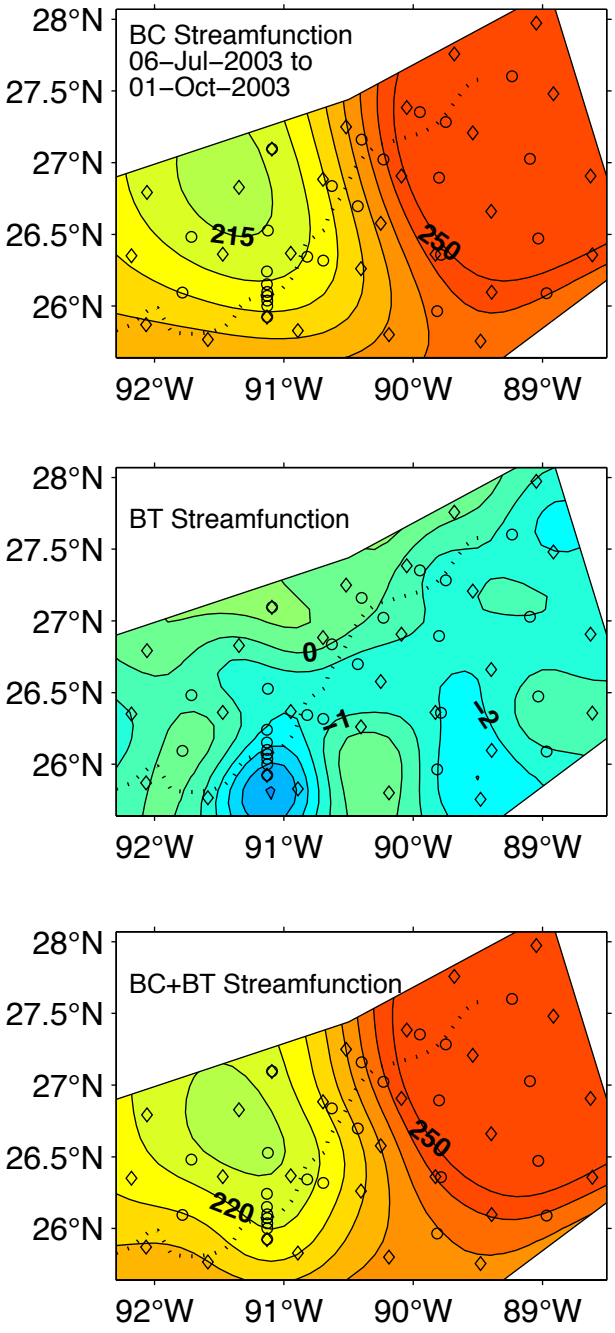

Figure 4.1-39. Quarterly mean surface streamfunction averaged from July 6, 2003 through October 1, 2003. Top panel: Streamfunction at 0-m depth relative to 1500 m, the baroclinic streamfunction (BC). Middle panel: 1500-m depth geostrophic pressure field, the barotropic streamfunction (BT). Bottom panel: Sum of the BC (top panel) and BT (middle) is the absolute surface streamfunction. Dotted line denotes the center of the Sigsbee Escarpment. Streamfunction contoured every 1 km m•s^{-1}. Low (high) values shown with blue (red) hues. PIES sites indicated by diamonds; current meters by circles.

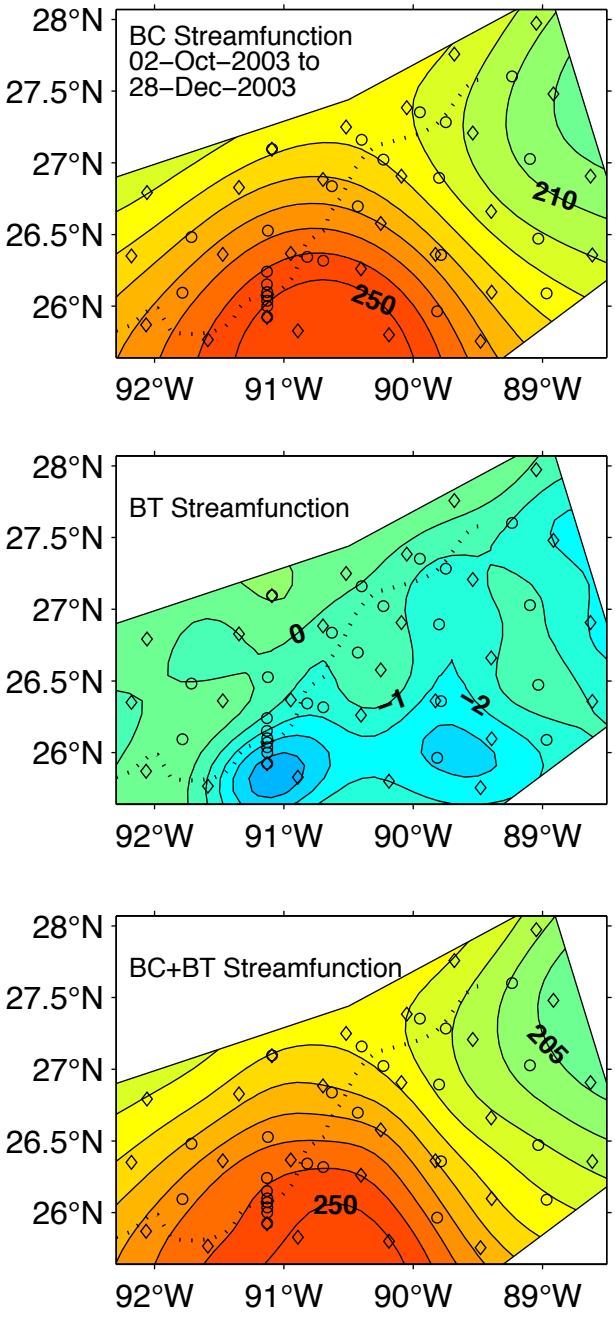

Figure 4.1-40. Quarterly mean surface streamfunction averaged from October 2, 2003 through December 28, 2003. Top panel: Streamfunction at 0-m depth relative to 1500 m, the baroclinic streamfunction (BC). Middle panel: 1500-m depth geostrophic pressure field, the barotropic streamfunction (BT). Bottom panel: Sum of the BC (top panel) and BT (middle) is the absolute surface streamfunction. Dotted line denotes the center of the Sigsbee Escarpment. Streamfunction contoured every 1 km m•s^{-1}. Low (high) values shown with blue (red) hues. PIES sites indicated by diamonds; current meters by circles.

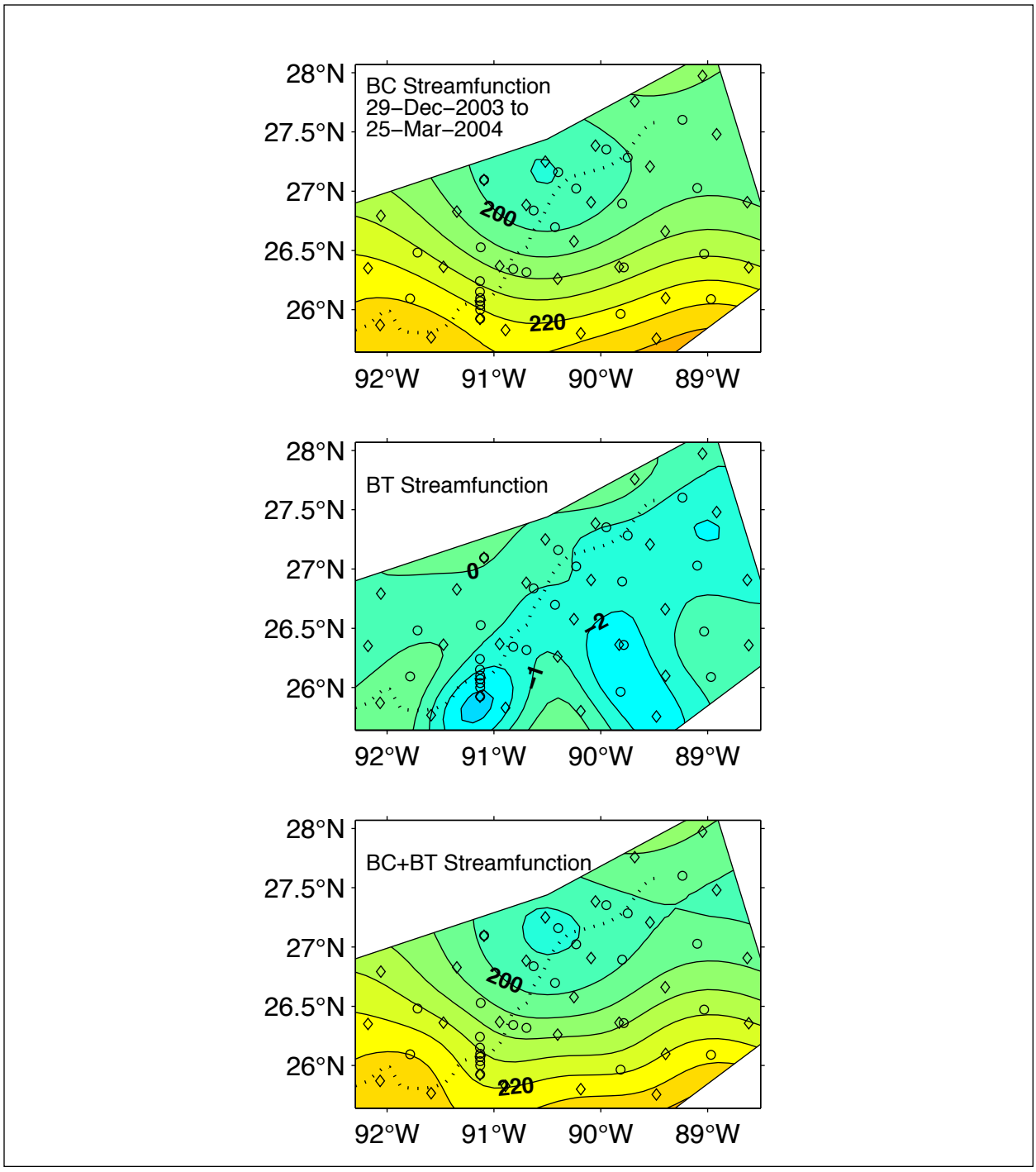

Figure 4.1-41. Quarterly mean surface streamfunction averaged from December 29, 2003 through March 25, 2004. Top panel: Streamfunction at 0-m depth relative to 1500 m, the baroclinic streamfunction (BC). Middle panel: 1500-m depth geostrophic pressure field, the barotropic streamfunction (BT). Bottom panel: Sum of the BC (top panel) and BT (middle) is the absolute surface streamfunction. Dotted line denotes the center of the Sigsbee Escarpment. Streamfunction contoured every 1 km m•s^{-1}. Low (high) values shown with blue (red) hues. PIES sites indicated by diamonds; current meters by circles.

where < > is the mean over the 1-year measurement period as defined above. Figures 4.1-42, 4.1-43, and 4.1-44 show <EKE> for the representative three upper levels, 0 m, 150 m, and 500 m. The highest values occurred along the edge of the LC where it swept into and out of the study array near 26°N to 27.5°N and 89°W to 90°W. For example, at 0 m within the large region encompassed by the 800 $cm^2 \cdot s^{-2}$ contour, the eddy current speeds exceeded 40 $cm \cdot s^{-1}$ on average, and the speeds within the 1400 $cm^2 \cdot s^{-2}$ contour exceeded 53 $cm \cdot s^{-1}$ on average. At 150 m, the <EKE> values were about half as great, with mean eddy speeds correspondingly about 70% as large as at the surface. At 500 m, the locations of high <EKE> were more broadly distributed, not only under the peak surface variability, but also associated with heightened deep eddy variability to the west, as will be discussed in Section 4.2. The 500-m <EKE> values were only about 10% as large as those at 0 m, and eddy speeds were therefore about one-third as great. The locations at 500 m where <EKE> values exceeded 70 $cm^2 \cdot s^{-2}$ and eddy current speeds exceeded about 12 $cm \cdot s^{-1}$ were mainly confined south of Sigsbee Escarpment (designated S-Sigs within the study array). At all three upper levels shown, the <EKE> was much higher south than north of the Sigsbee Escarpment (N-Sigs). For the two uppermost levels this was because the variability associated with the LC and LCEs was confined to south of the Escarpment, and for the 500-m level, on which deep-eddy variability contributes significantly, the Sigsbee Escarpment further constrained most deep current variability to its south.

Figures 4.1-45, 46, and 4.1-47 distinguish between the regions north and south of the Sigsbee Escarpment and illustrate the time history of spatially-averaged EKE at the three upper levels, 0 m, 150 m, and 500 m. The vertical scales for EKE are set equal for the N-Sigs and S-Sigs regions, but the scales differ between figures and depths to accommodate the wide range of EKE with depth. The EKE records at 0 m and 150 m illustrate essentially the same features, with the vertical scales simply differing by a factor of two. During days 100 to 220 (approximately April through July 2003), the repeated northward and westward incursion and retreat of the LC and preliminary separations of Eddy Sargassum accounted for the large range of EKE. The spike at day 220 for the S-Sigs region corresponds to the final separation of Eddy Sargassum. During days 220 to 300 the observed EKE varied depending upon how much of Eddy Sargassum was captured within the array; the two peaks near days 250 and 270 corresponding to capturing most of the eddy, and the subsequent decay of EKE until day 300 corresponds to a decreasing fraction of the eddy found within the array as it translates west-southwestward. Eddy Titanic skirted along the southern edge of the array and was responsible for the peak EKE at days 365-385 (January 2004) at 0 m and 150 m in the S-Sigs region. The upper-level EKE records for the N-Sigs region (upper panels) roughly mirror those for the S-Sigs region, but with reduced amounts of energy penetrating from events associated with the LC and Eddy Sargassum, and no evidence of Eddy Titanic.

The EKE records at 500 m (Figure 4.1-47) differ significantly from the 0-m and 150-m records for both the N-Sigs and S-Sigs regions. Except for one major event, the 500-m level was approximately equally influenced by the baroclinic and deep reference currents. The big event, from days 205 to 220 (mid-to-late July 2003) was a precursor to the final separation of Eddy Sargassum. This was associated with a highly energetic sequence of deep eddies, both cyclonic and anticyclonic, that entered the region from the east and southeast while Eddy Sargassum detached and reattached with intensified cyclones and anticyclones around its periphery (as described in Section 4.1.1). Those upper-layer LCE-formation processes occurred on the eastern

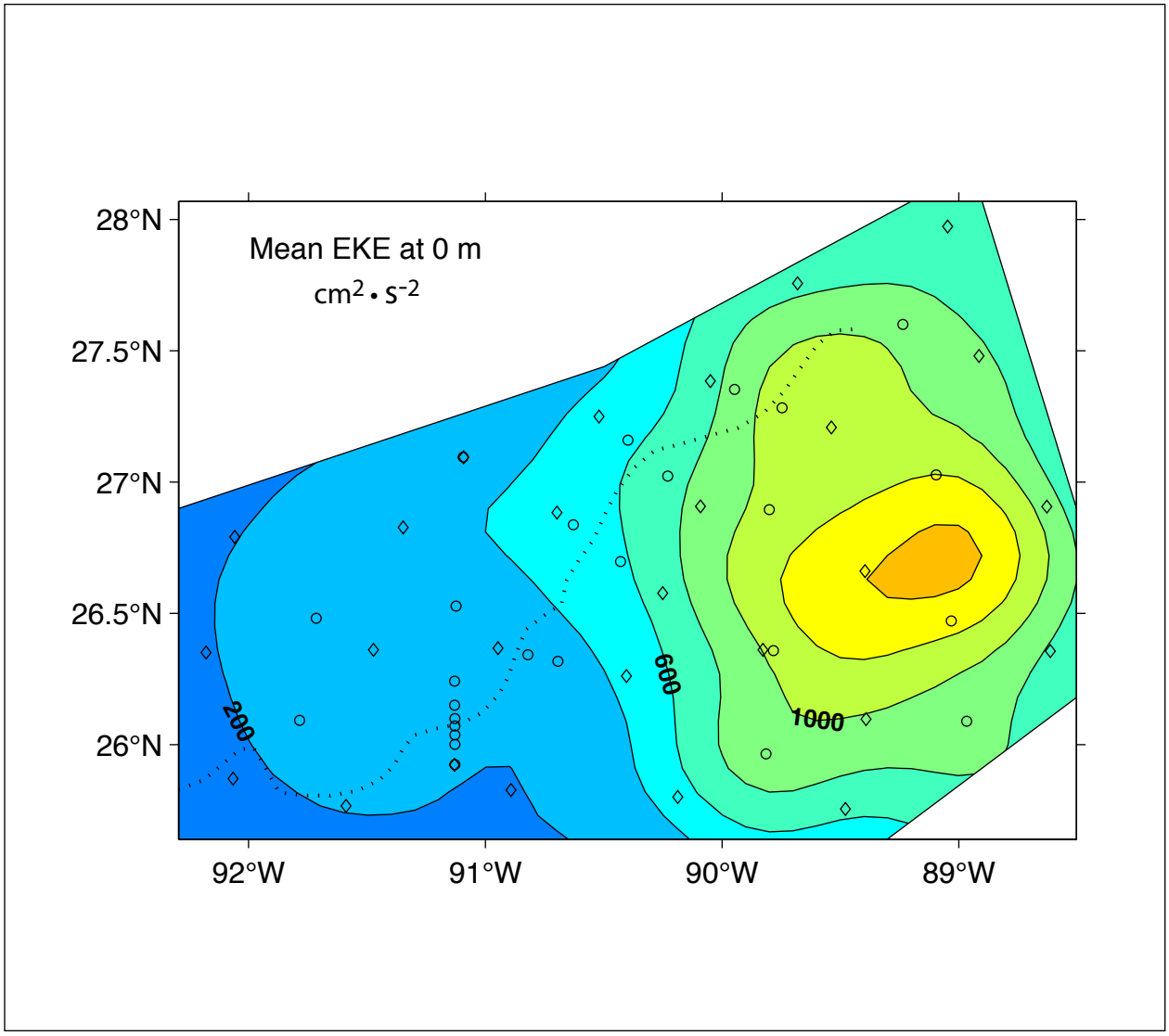

Figure 4.1-42. Mean eddy kinetic energy at 0-m depth. Mean eddy kinetic energy is defined as $\langle EKE \rangle = (1/2) \langle (u')^2 + (v')^2 \rangle$, where $\langle\ \rangle$ is the mean and the prime,', is the anomaly/deviation from the mean. The mean has been taken over the 1-year measurement period.

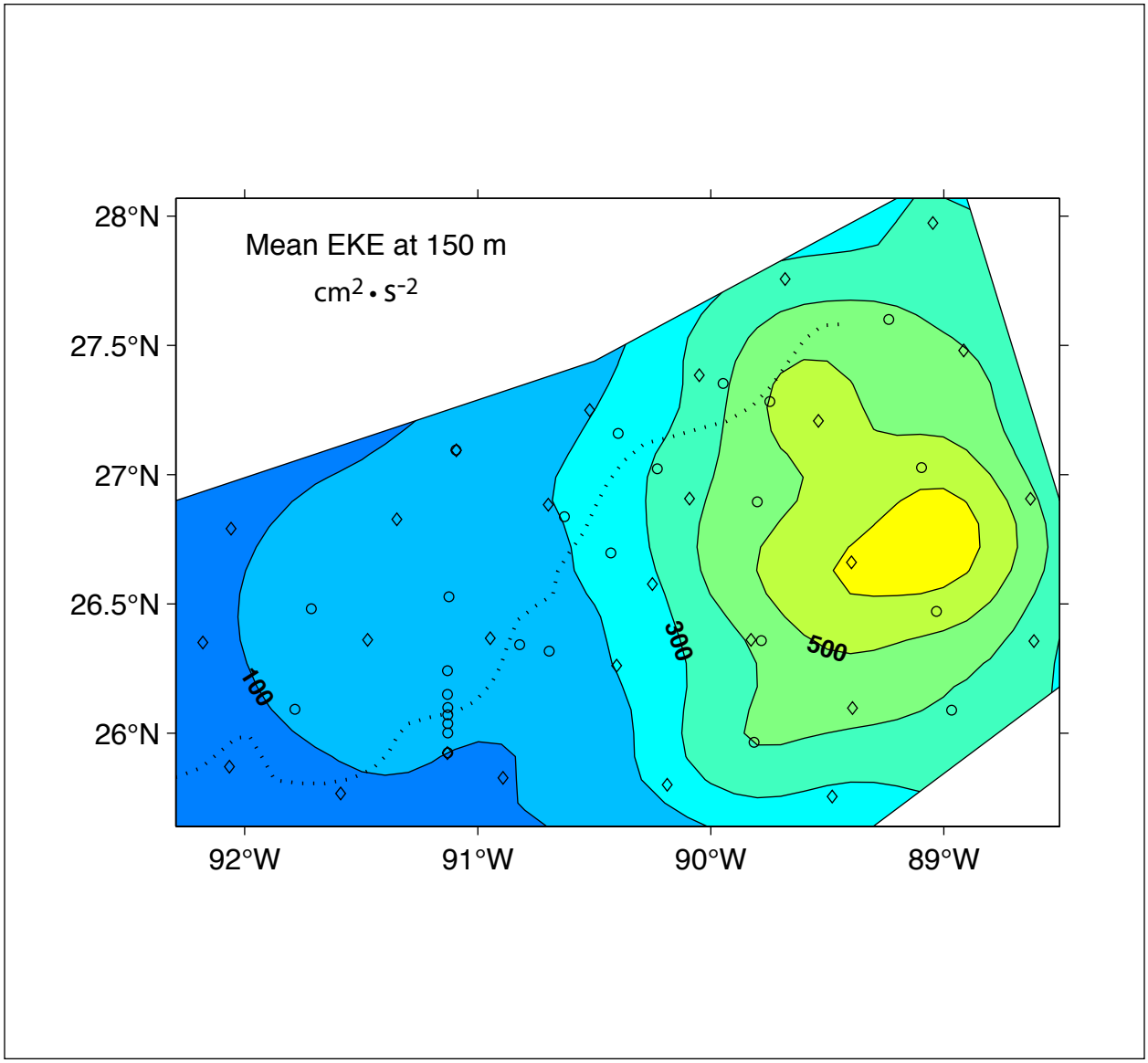

Figure 4.1-43. Mean eddy kinetic energy at 150-m depth. The mean has been taken over the 1-year measurement period.

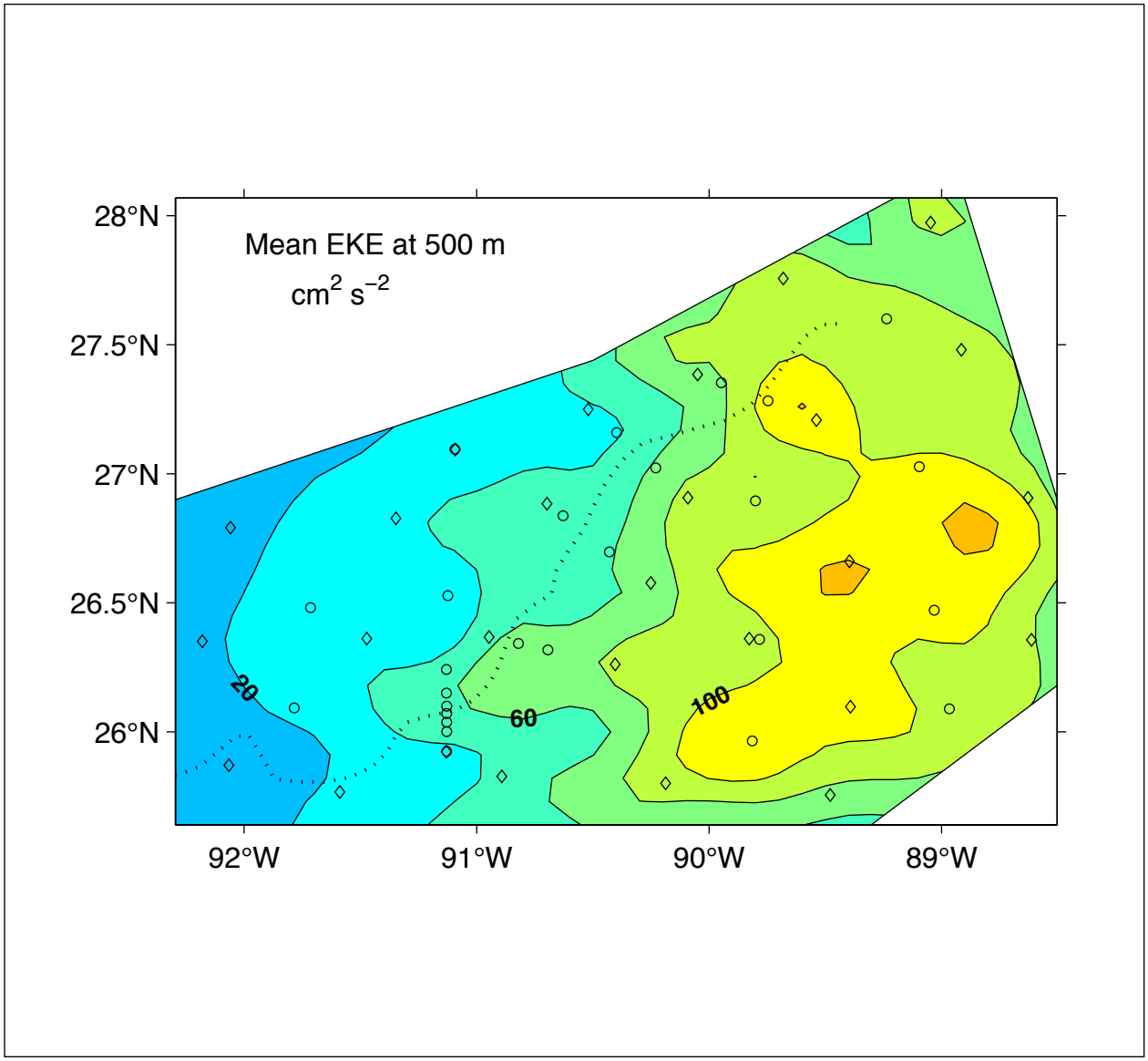

Figure 4.1-44. Mean eddy kinetic energy at 500-m depth. The mean has been taken over the 1-year measurement period.

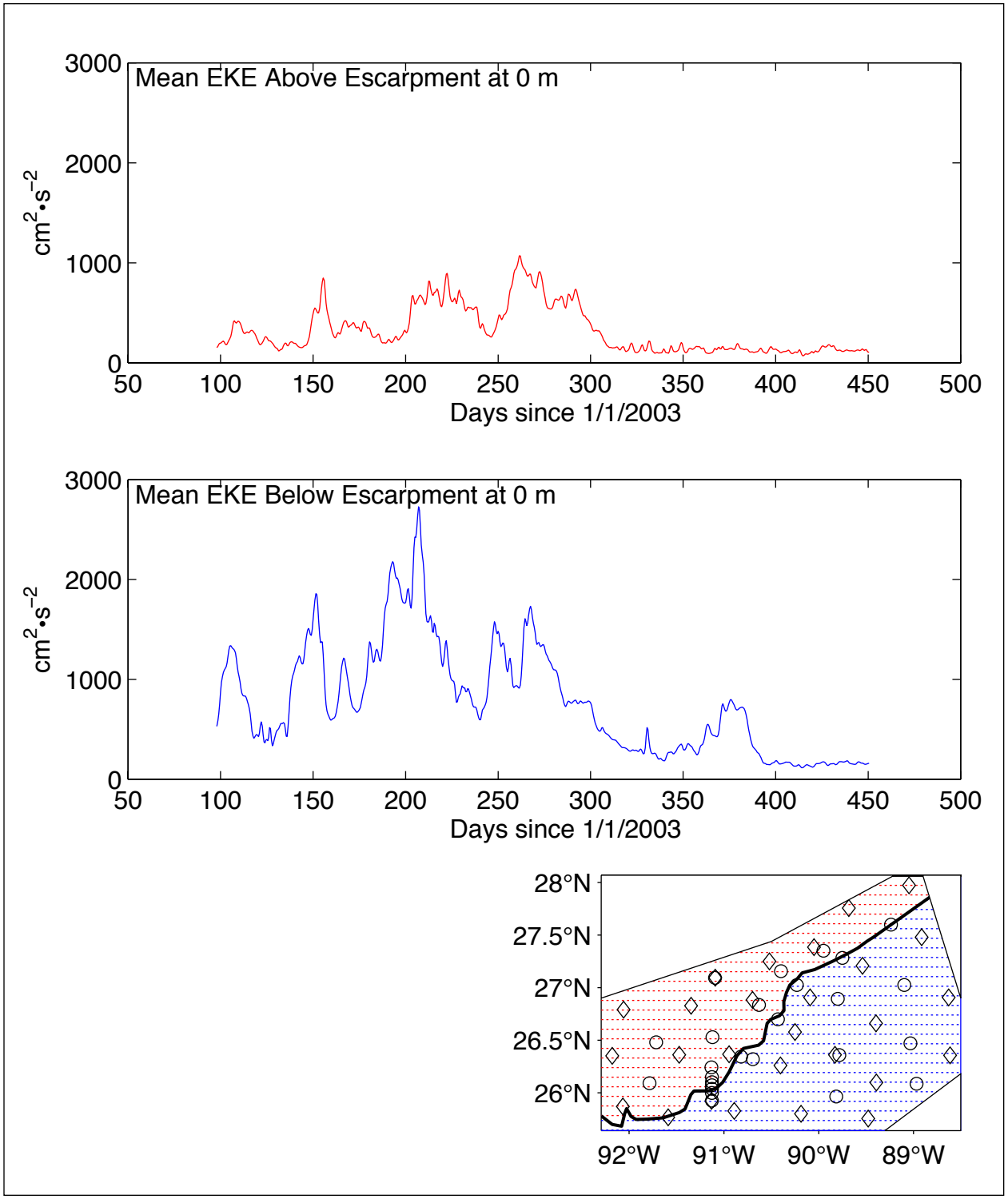

Figure 4.1-45. Mean eddy kinetic energy at the surface spatially averaged above (top panel) and below (middle panel) the Sigsbee Escarpment. The bottom panel shows the spatial area each mean encompasses, red hatching denotes above escarpment; blue hatching indicates below the escarpment.

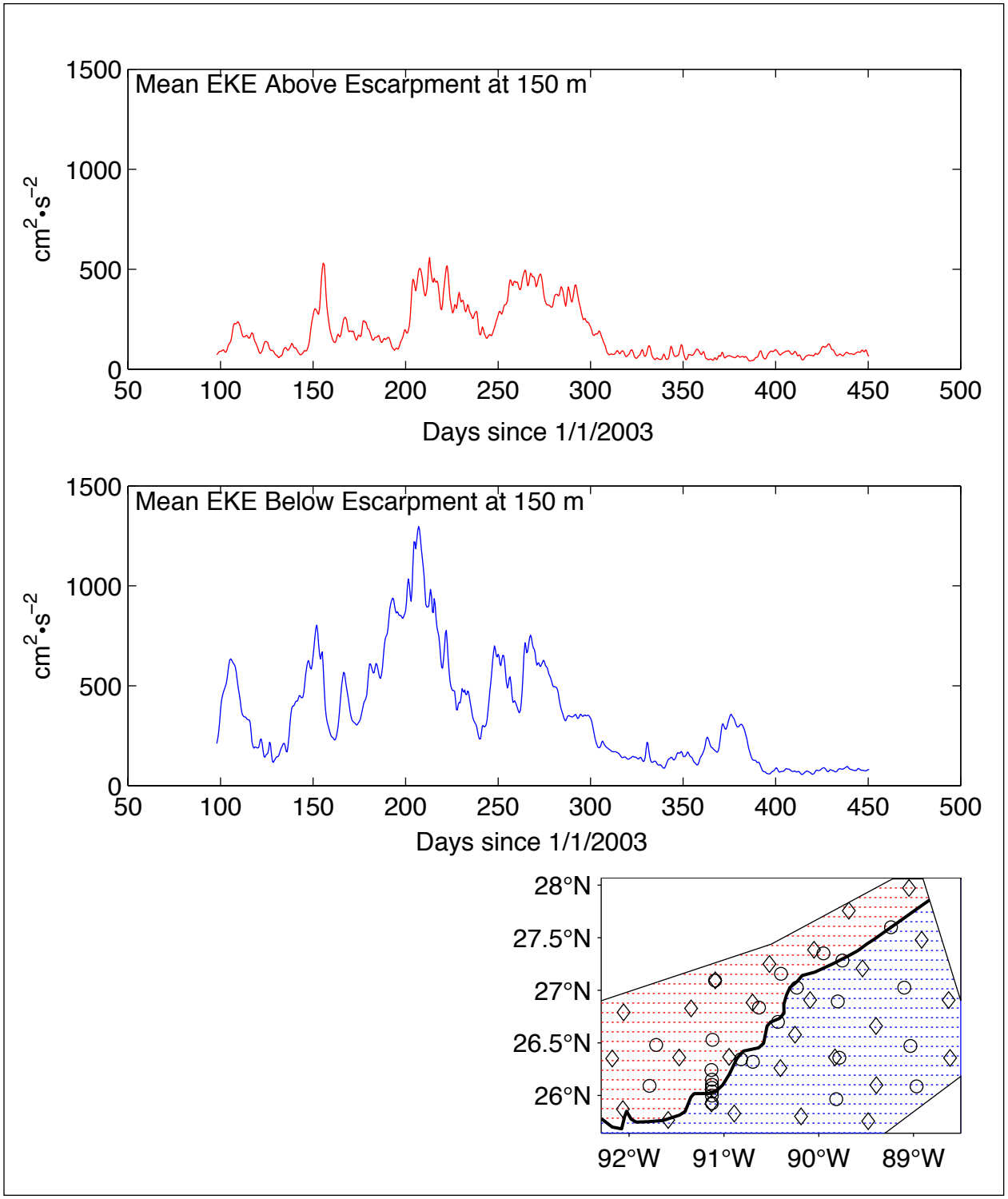

Figure 4.1-46. Mean eddy kinetic energy at 150-m depth spatially averaged above (top panel) and below (middle panel) the Sigsbee Escarpment. The bottom panel shows the spatial area each mean encompasses, red hatching denotes above escarpment; blue hatching indicates below the escarpment.

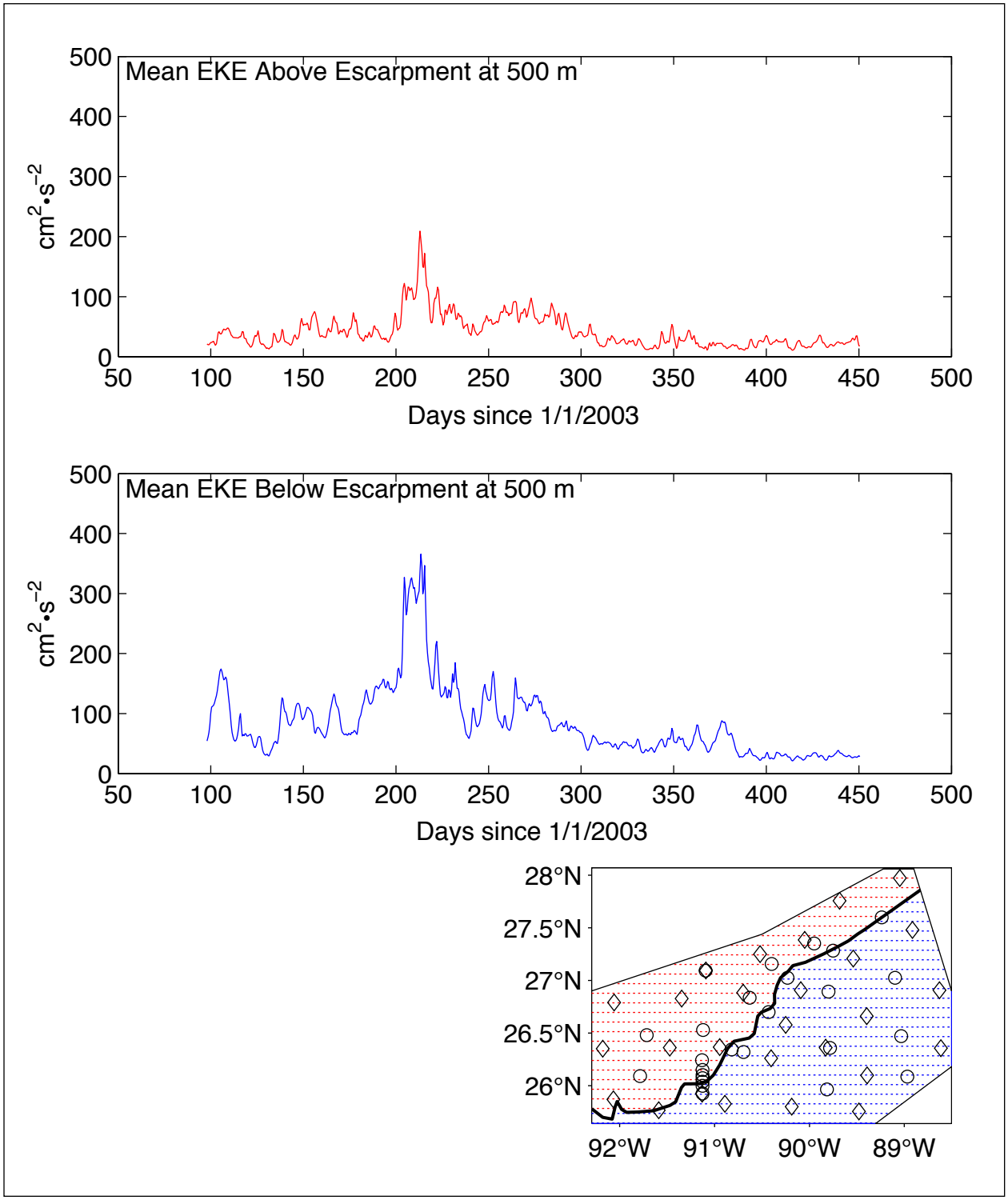

Figure 4.1-47. Top panel: Mean eddy kinetic energy at 500-m depth spatially averaged above (top panel) and below (middle panel) the Sigsbee Escarpment. Bottom panel: Spatial area each mean encompasses, red hatching denotes above escarpment; blue hatching indicates below the escarpment.

border of the PIES observational array and further east. Evidently, those upper-layer eddy processes radiated energetic deep eddies that propagated into the array. This topic will be the subject of further case-studies and process-studies in this report.

Current-speed histograms in Figures 4.1-48, 49, and 4.1-50 show the number of daily observations which had currents in 10 $cm \cdot s^{-1}$ speed-classes centered on 0 to 150 $cm \cdot s^{-1}$ at our mapped points. The observations are grouped for the full study array and for the subregions, N-Sigs and S-Sigs, and they span the measurement year from April 2003 to March 2004. The most probable speed class at 0 m was 20 $cm \cdot s^{-1}$, and values were observed in speed classes up to 120 $cm \cdot s^{-1}$. Correspondingly, at 150 m and 500 m the most probable speed classes were 10 $cm \cdot s^{-1}$, and speed values were observed up to 90 $cm \cdot s^{-1}$ and 50 $cm \cdot s^{-1}$ respectively. Clearly the highest speeds occurred south of the Escarpment, whereas the current histograms for the N-Sig sites fall more quickly with increasing speed: at 0 m, 150 m, and 500 m the highest speed classes that occurred at the N-Sigs sites were respectively 90 $cm \cdot s^{-1}$, 70 $cm \cdot s^{-1}$, and 40 $cm \cdot s^{-1}$.

4.2 Description of Deep-Layer Currents and Events in the Exploratory Study Area

4.2.1 Deep-Layer Eddies and Events in the Study Array

This section provides an overview of deep variability observed in the Exploratory Study, by summarizing deep eddy maps in the study array, and deep current-meter observations. Also, because most floats were ballasted for observations in the lower layer, this section presents float trajectories in the wider region and within the study area.

4.2.1.1 Deep Eddy Maps in the Study Array

The most energetic and persistent currents below 1000 m in the study area were associated with cyclonic and anticyclonic eddies that entered the study area from the east and southeast, on trajectories suggestive of an origin near the LC. While we give an overview here of deep eddies, case studies in Section 6.3 will illustrate their detailed behavior.

Typically, deep eddies were generated near the eastern border of the study area under the LC and associated with its events of strong variability. We now characterize two different patterns of deep eddies entering the array, and depending upon whether an eddy was cyclonic or anticyclonic, we characterize two different outcomes as they approached the Sigsbee Escarpment.

During times when the LC and its peripheral eddies and meanders were southeast of the study array, the deep eddies appear to have originated there also, because they entered the study array near its southeast edges and followed trajectories to the northwest. This pattern typified deep eddy trajectories during April – June 2003, while the main variability of the LC was still to the southeast, and again during October 2003 – January 2004. This latter interval occurred after Eddy Sargassum had separated and the LC had retracted, and while the main variability of the LC was again to the southeast, associated with generating Eddy Titanic. Examples of northwestward trajectories will be shown to illustrate different behavior for deep cyclones and deep anticyclones.

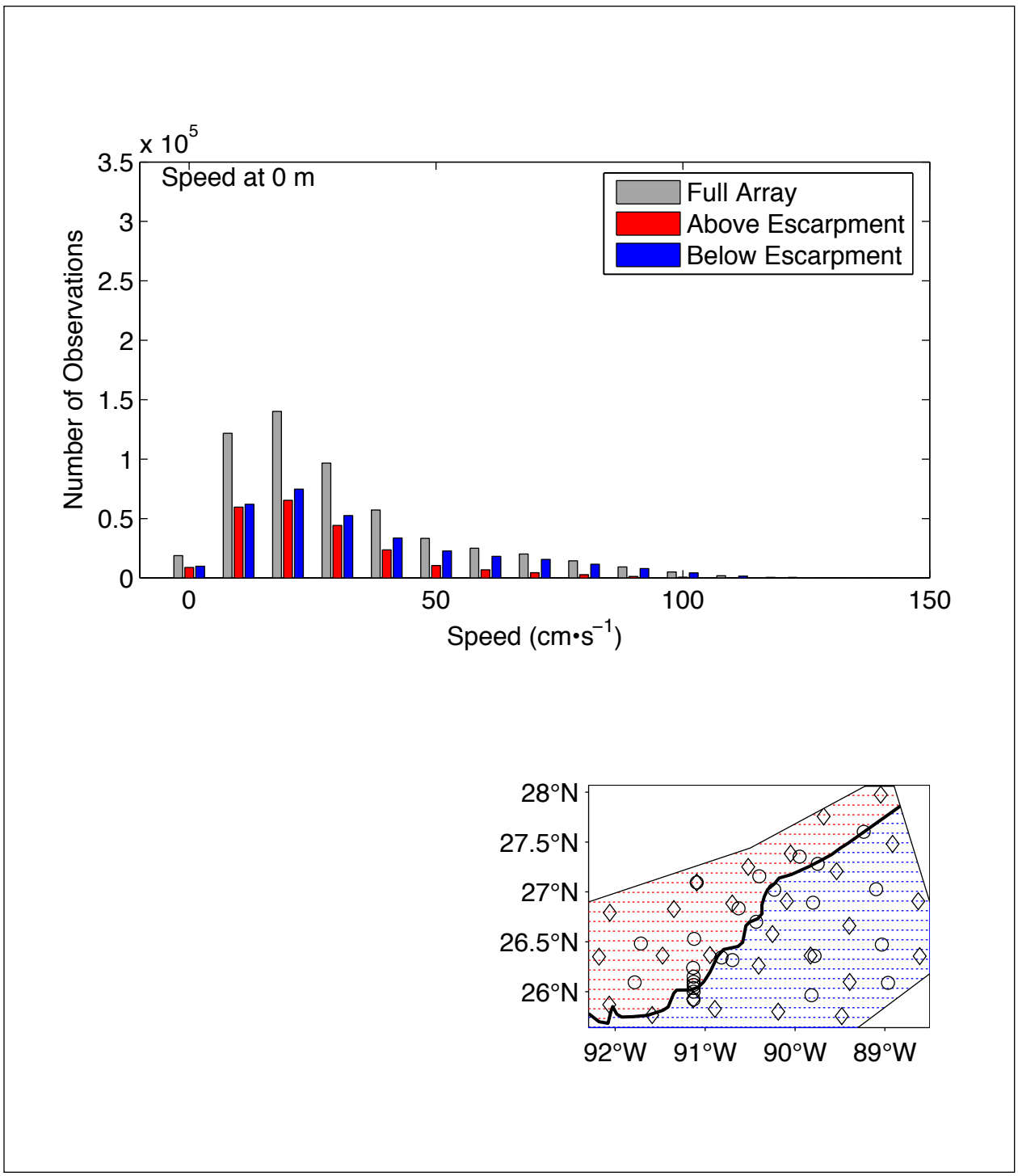

Figure 4.1-48. Top panel: Surface current speed histograms. Currents have been grouped into three categories, the entire array (gray), above (red) and below (blue) the Sigsbee Escarpment. Bottom panel: Map of Exploratory array. Thick black line denotes the midpoint of the Escarpment. Red (blue) hatching indicates that instruments are classified as above (below) Escarpment. Diamonds show PIES locations; circles show current meter mooring locations.

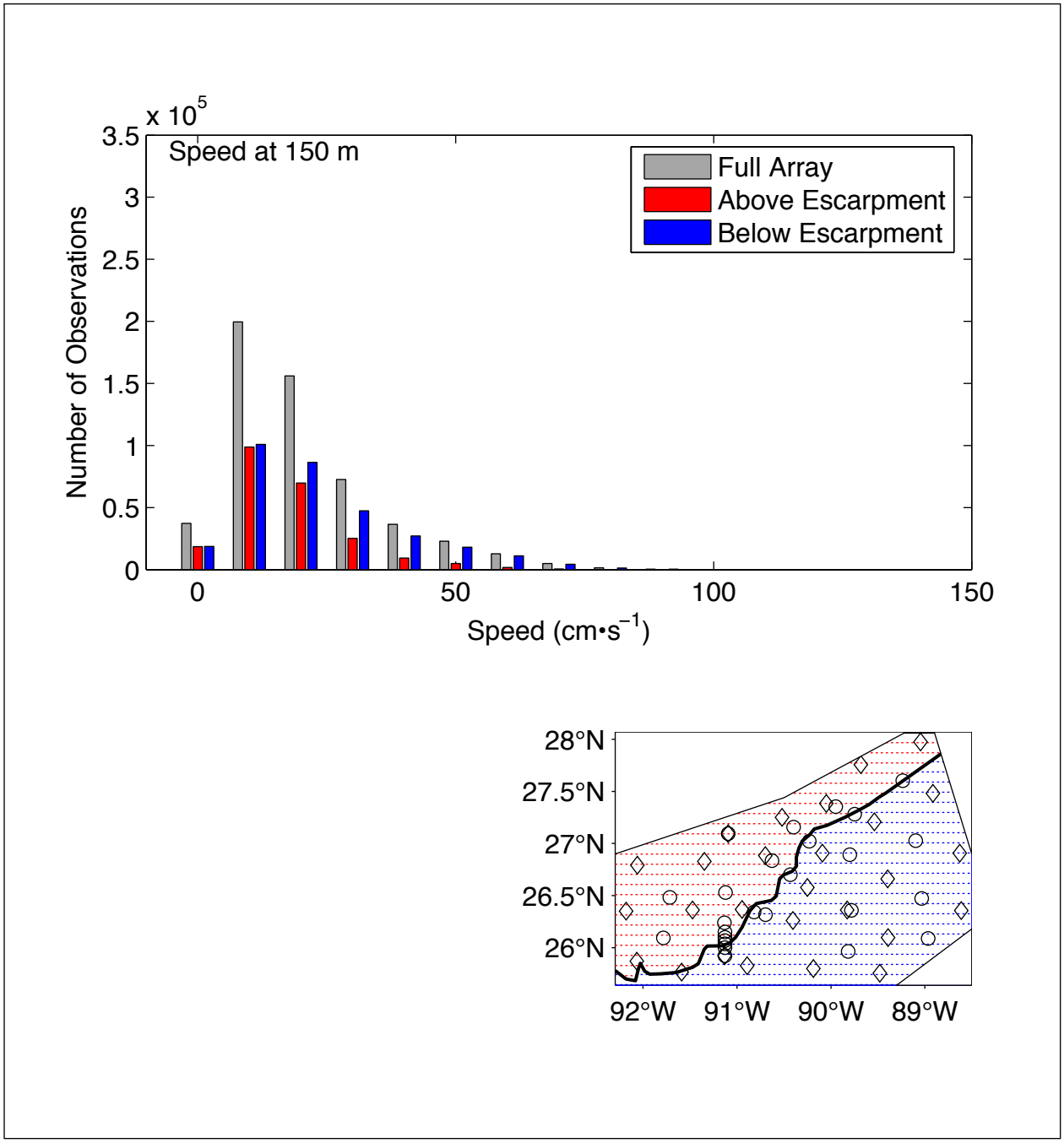

Figure 4.1-49. Top panel: 150-m depth current speed histograms. Currents have been grouped into three categories, the entire array (gray), above (red) and below (blue) the Sigsbee Escarpment. Bottom panel: Map of Exploratory array. Thick black line denotes the midpoint of the Escarpment. Red (blue) hatching indicates that instruments are classified as above (below) Escarpment. Diamonds show PIES locations; circles show current meter mooring locations.

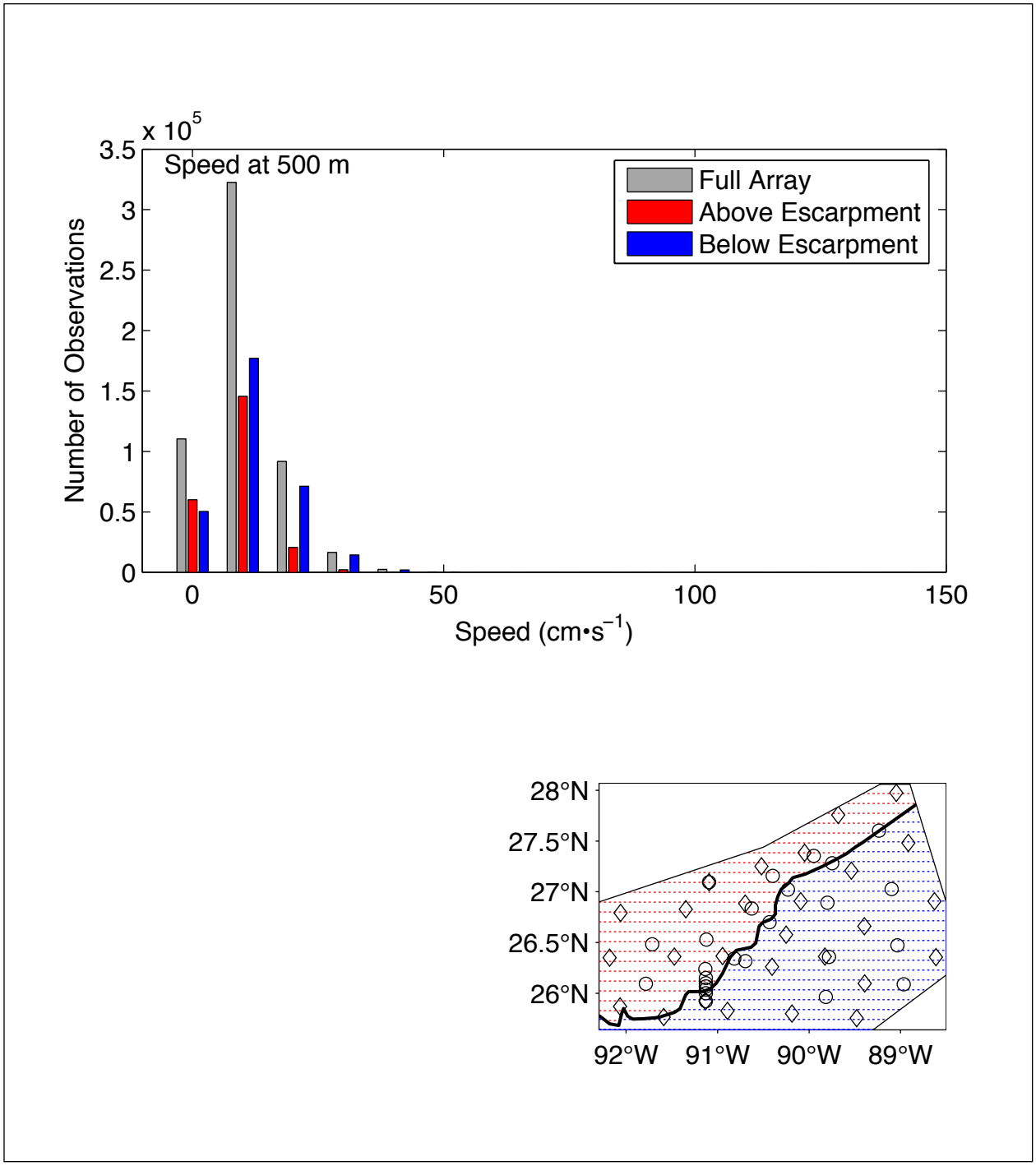

Figure 4.1-50. Top panel: 500-m depth current speed histograms. Currents have been grouped into three categories, the entire array (gray), above (red) and below (blue) the Sigsbee Escarpment. Bottom panel: Map of Exploratory array. Thick black line denotes the midpoint of the Escarpment. Red (blue) hatching indicates that instruments are classified as above (below) Escarpment. Diamonds show PIES locations; circles show current meter mooring locations.

When the LC protruded unusually far north, during July – September 2003, its strong peripheral eddies and meanders occurred due east of the study array. Deep eddies, cyclonic and anticyclonic, were then generated and entered the study array along its eastern border. While north of 26.5°N and east of 89°W, their initial translation was to the southwest and then turned west, typically reemerging into the Study Array near 26°N, 89°W. Thereafter, they typically followed northwestward trajectories as in the preceding paragraph. Figure 4.2-1 (18-23 July 2003) illustrates one such case for a cyclone. Several anticyclones and cyclones followed a similar southward-arced trajectory during July – September 2003.

While we consider deep eddy trajectories that followed this southward arc, note that the bathymetry within the study array has a small rise that extends from the Mississippi River outflow southward along 89°W down to 26°N. Our interpretation is that this bathymetry deflects the deep eddy trajectories. The deep eddies that were generated unusually far north trended generally 'westward' along a path that first curved southwestward around this bathymetric rise and thence arced northwestward into the study array.

Once west of 89°W, deep eddies typically translated northwest until they encountered the Sigsbee Escarpment, whereupon their behavior differed depending upon whether the deep eddy was cyclonic or anticyclonic. Figure 4.2.-2 (15-25 December 2003) illustrates one of several cases in which a strong deep cyclone approached the Sigsbee Escarpment, whereupon its path deflected to the left. Expressed in terms of potential vorticity, this direction corresponds to "topographic westward", because the higher PV created in the deep layer by shoaling topography corresponds to "topographic northward". In strong eddies like this one, their shape also distorted to the left, apparently strained and advected in the same direction as the currents on their northwestward side.

Figure 4.2-3 illustrates the current and temperature structure associated with this deep cyclonic eddy. The upper left and right panels show respectively the surface and deep velocities and streamfunction for 23 December 2003. It illustrates how different the patterns of horizontal currents can be in the upper and deep layers on a given day. This moderately strong deep eddy with currents up to 35 $cm \cdot s^{-1}$ had little expression at the surface. This point is further emphasized in the bottom panel by the temperature section along 90°W which crossed the eddy. The deep currents had little vertical shear, and consequently (being geostrophic) little expression in the temperature structure. Vertical profiles of the currents are shown in the four middle panels for the four sites indicated by stars on the map views. Each current profile shows deep currents circulating counterclockwise around the eddy, while currents in the upper 300 m veered in other directions.

The contrasting character of a strong deep anticyclone approaching the Sigsbee Escarpment is illustrated in Figure 4.2-4 (12-17 August 2003). Its path deflected slightly to the right. Anticyclones encountering the Sigsbee Escarpment typically stalled and decayed rather than propagate away. One may speculate that this behavior reflected a competition between a tendency for southwestward propagation for topographic waves and a tendency for northeastward straining and advection by the currents as the deep anticyclone encountered the Escarpment. Figure 4.2-5 (17 August 2003) illustrates the current and temperature structure associated with this deep anticyclonic eddy. The upper left and right panels show, respectively,

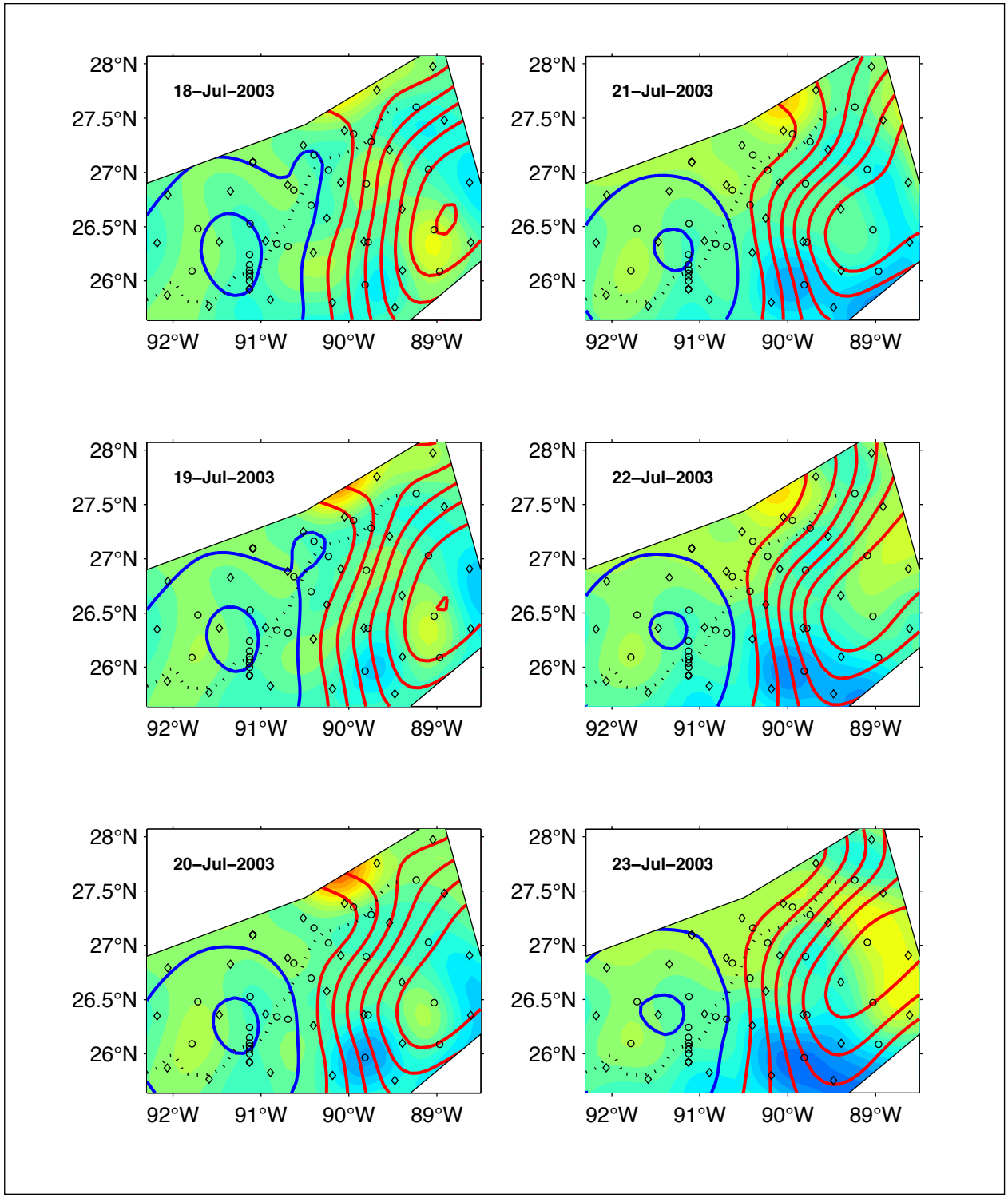

Figure 4.2-1. Case study: Northwest trajectory of a deep cyclone [18-23 July 2003]. Maps of surface streamfunction (bold contour lines) superimposed upon shaded contours of 1500-m depth pressure for 6 separate days. The sequence begins with the top left panel. The dotted line denotes the center of the Sigsbee Escarpment. PIES sites indicated by diamonds; current meters by circles.

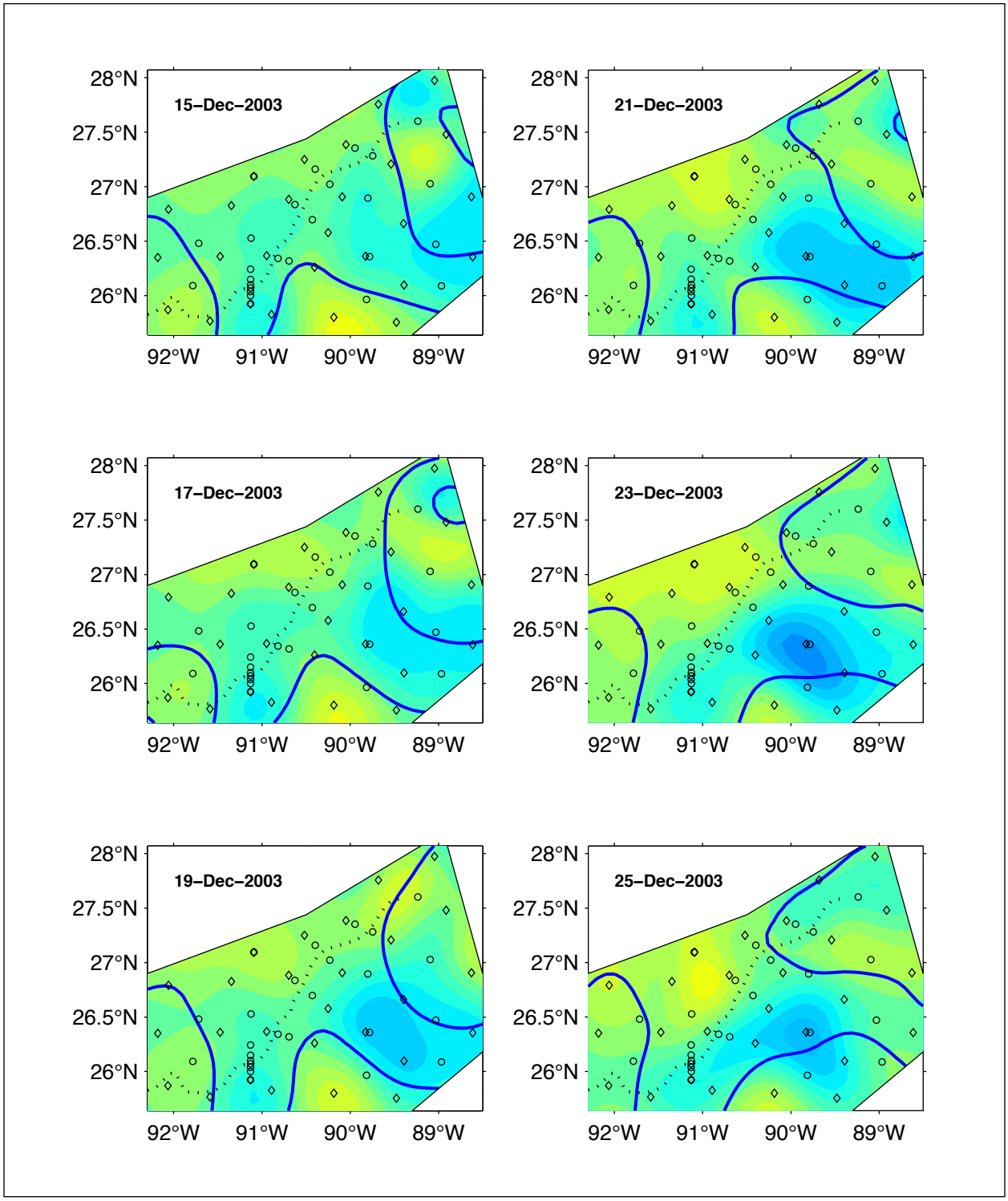

Figure 4.2-2. Case study: A deep cyclone propagates along the Sigsbee Escarpment [15-25 December 2003]. Maps of surface streamfunction (bold contour lines) superimposed upon shaded contours of 1500-m depth pressure for 6 separate days. The sequence begins with the top left panel. The dotted line denotes the center of the Sigsbee Escarpment. PIES sites indicated by diamonds; current meters by circles.

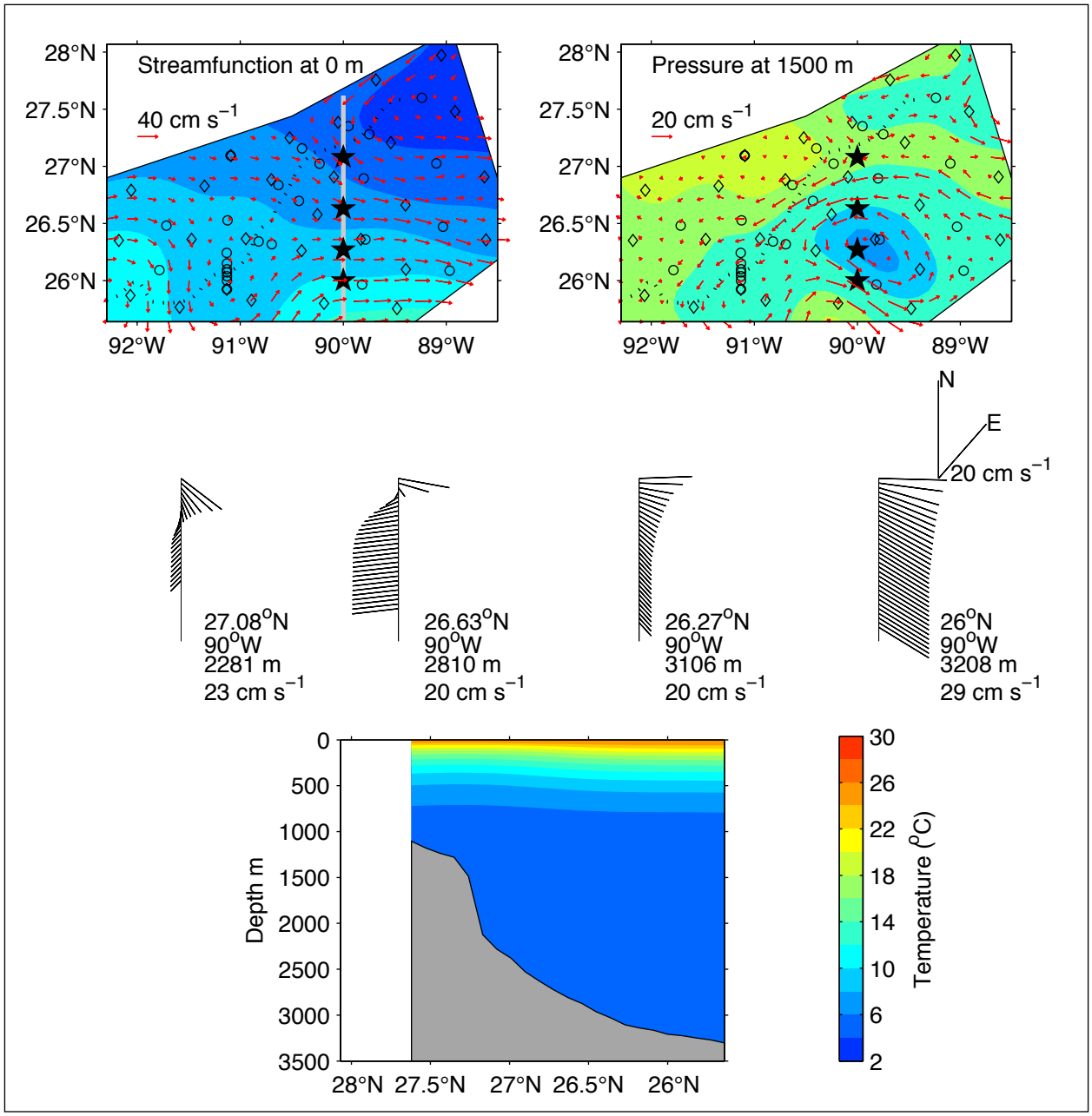

Figure 4.2-3. Several views of current and temperature structure in the region for December 23, 2003 provided by PIES and deep current measurements. Top panels: Streamfunction at the sea surface (left) and pressure at 1500 m (right) in plan view. Contour intervals are 5 km m•s^{-1} and 0.02 dbar, respectively. Anticyclonic circulations are shown by reddish hues; cyclonic circulations by bluish hues. Currents vectors plotted at 20-km spacing. PIES sites denoted by the diamonds; current meter moorings indicated by the circles. A dotted line marks the center of the Sigsbee Escarpment. Middle panels: Vector profiles of absolute velocity every 100 m from the surface to the bottom at 4 locations indicated by the solid black stars in top panels. Latitude, longitude, bottom depth, and surface speed at each location are noted. Bottom panel: Cross-section of temperature in °C along the gray line in the top left panel.

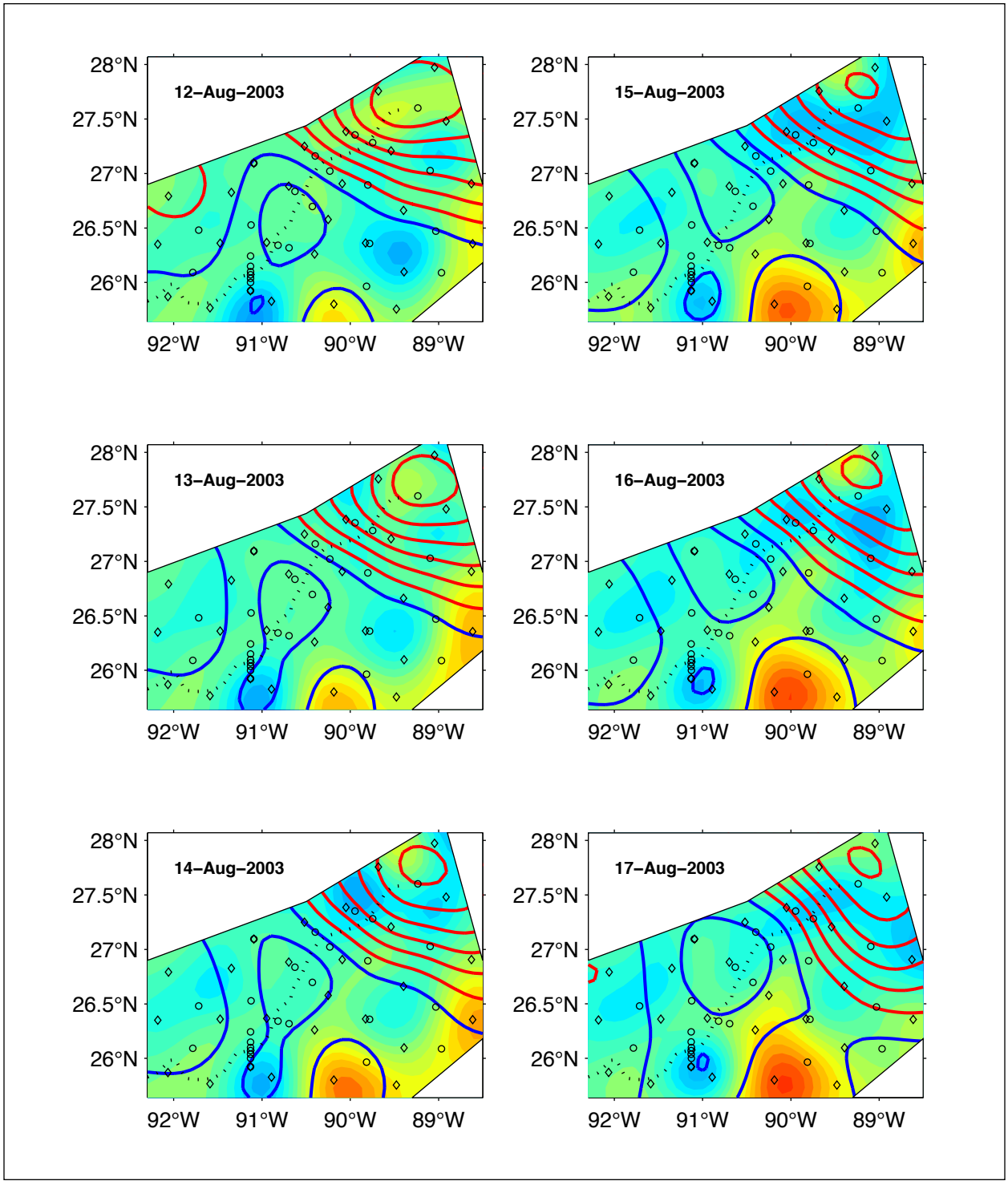

Figure 4.2-4. Case study: A deep anticyclone is deflected to the northeast at the Sigsbee Escarpment [12-17 August 2003]. Maps of surface streamfunction (bold contour lines) superimposed upon shaded contours of 1500-m depth pressure for 6 separate days. The sequence begins with the top left panel. The dotted line denotes the center of the Sigsbee Escarpment. PIES sites indicated by diamonds; current meters by

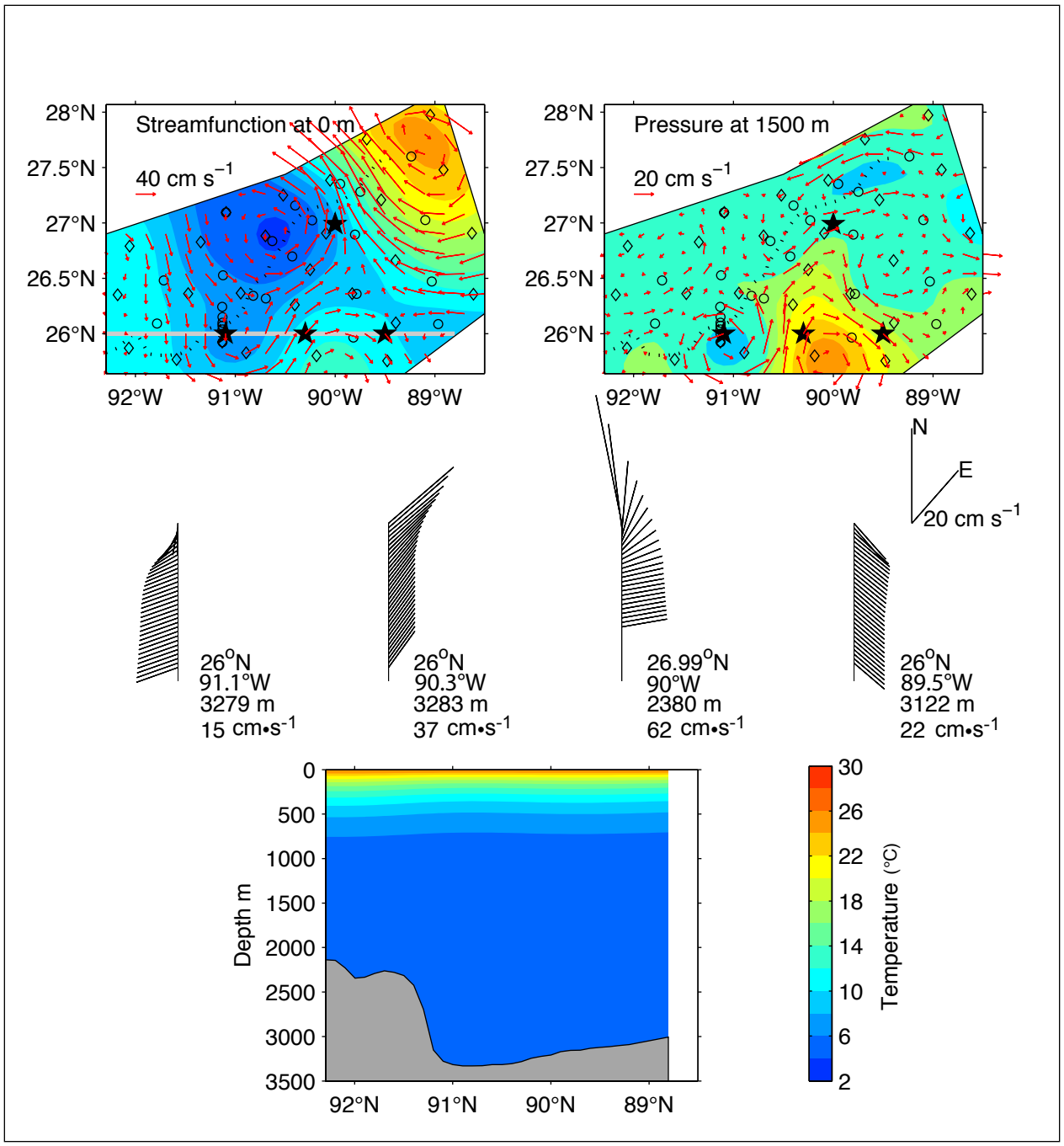

Figure 4.2-5. Several views of current and temperature structure for August 17, 2003 provided by PIES and deep current measurements. Top panels: Streamfunction at the sea surface (left) and pressure at 1500 m (right) in plan view. Contour intervals are 5 km m•s^{-1} and 0.02 dbar, respectively. Anticyclonic circulations are reddish hues; cyclonic circulations bluish hues. Currents vectors plotted at 20-km spacing. PIES sites denoted by the diamonds; current moorings by the circles. A dotted line marks the center of the Sigsbee Escarpment. Middle panels: Vector profiles of absolute velocity every 100 m from the surface to the bottom at 4 locations indicated by the solid black stars in top panels. Latitude, longitude, bottom depth, and surface speed at each location are noted. Bottom panel: Cross-section of temperature in °C along the gray line in the top left panel.

the surface and deep velocities and streamfunction for 17 August 2003. This case again illustrates that upper and deep eddies can produce distinct currents in the upper and deep layers on a given day. This moderately strong anticyclone with deep currents up to 40 $cm \cdot s^{-1}$ had little expression at the surface, and its temperature section that crossed the eddy at 26°N had no obvious temperature structure, because the deep geostrophic currents have little vertical shear. Vertical profiles of the currents are shown in the four middle panels for four sites indicated by stars on the map views. The three locations along 26°N were in a deep cyclone and the western and eastern side of the deep anticyclone, all showing substantial deep currents. The northern site is at the northeast tip of the deep eddy, which still had deep currents exceeding 20 $cm \cdot s^{-1}$ to the northeast, whereas the surface current of 62 $cm \cdot s^{-1}$ was turned to the north in association with the LC.

In addition to deep eddies that propagate into the study array, some cyclonic and anticyclonic features intensified in place. Case studies in Section 6 will illustrate such examples, suggesting examples of baroclinic instability, and other examples of a group of topographic Rossby waves in which crests and troughs propagated through the packet. Section 6 will also discuss cases in which deep eddies advected features in the upper layer.

4.2.1.2 Deep Currents

Deep low-frequency current fluctuations, as measured by instruments 100 and 500 m from the bottom on the short moorings and at various depths below 1000 m on the tall moorings, are extraordinarily inhomogeneous. The Escarpment divides the array approximately in half and flows above and below differ in character and energy. There were also differences in the character of the fluctuations from the eastern and western sides of the array. These deep fluctuations will be interpreted in terms of propagating topographic Rossby waves (TRWs) in the next chapter. In this section, a basic description of the currents is given. In order to illustrate the changes in the nature of the current flows, the 40-HLP current vectors are divided into 4 transects; two across the Escarpment (Figures 4.2-6 and 7), and two along the Escarpment, one below (Figure 4.2-8) and one above (Figure 4.2-9).

From moorings on the L3 to L2 transect (Figure 4.2-6), the current fluctuations had a dramatic change in intensity across the Escarpment from N4 to M3, a distance of 25 km, with a further decrease in the amplitude of the fluctuations at L2, further up the slope. The fluctuations at M3 and L2 had short periods, which contrast with the mixture of periods at N4, O2 and L3. Furthermore, fluctuations at M3 rarely reversed so that there was a mean flow, over the year, along the Escarpment towards the southwest. The major event at M3 occurred in the second half of July 2003 and seems to be followed by a series of short period fluctuations that decayed in amplitude in a similar manner to the short period (~ 10 days) TRW wave trains observed at the I1, I2 and I3 moorings that are discussed in Hamilton (in press) and Hamilton et al. (2003). It is not clear if this event was related to the large southwestward fluctuation at L3 and O2 that occurred earlier in July 2003. The larger, longer period (~30 day) fluctuations that occurred at L3 and O2 in May-September 2003 and N4 in November-December 2003, roughly correspond to the intervals of LC penetration over the southeastern part of the array, and the translation of Eddy Sargassum along the Escarpment, respectively. However, these coincidences may not have

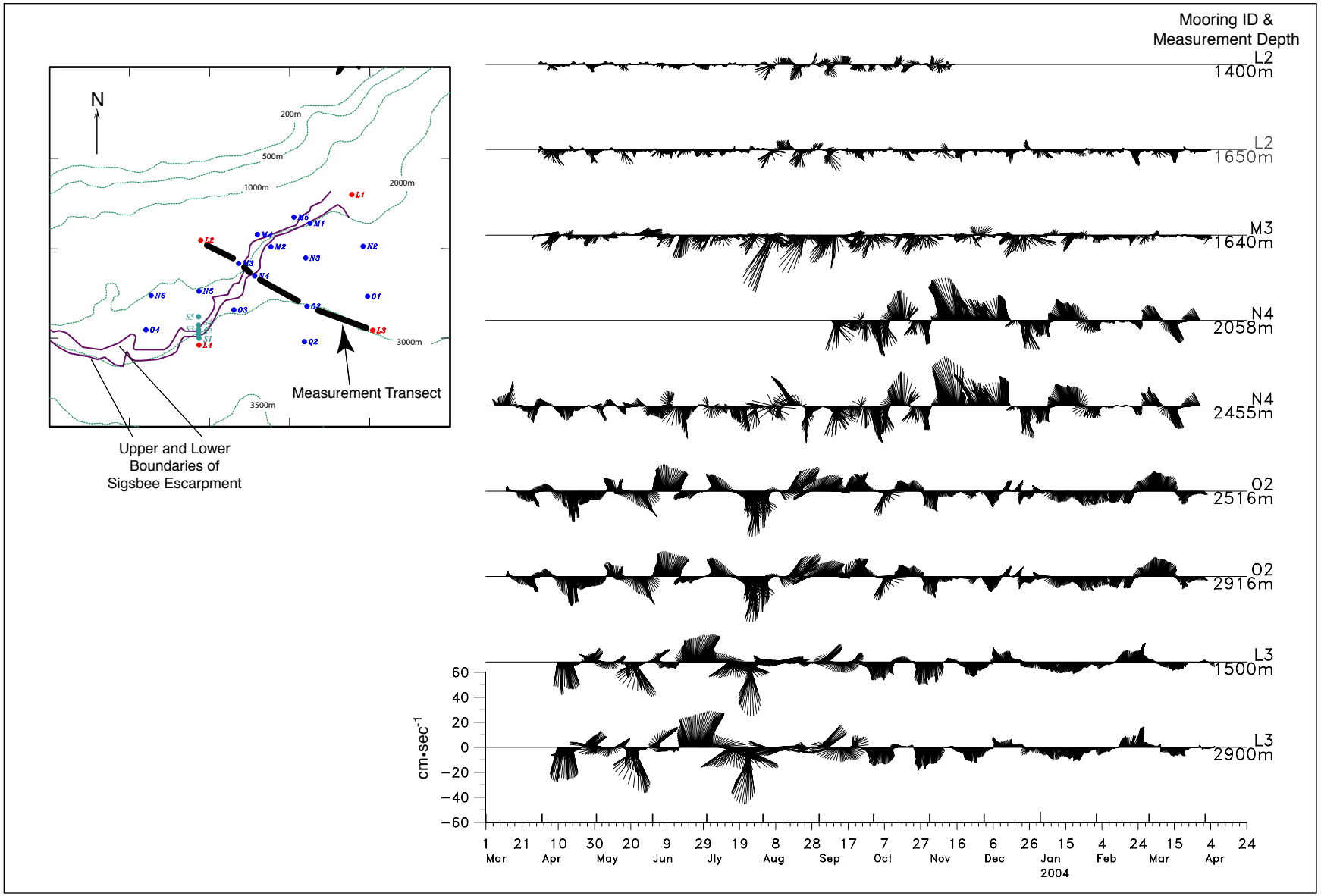

Figure 4.2-6. Near-bottom 40-HLP current vectors from nominally 100 and 500 m above the seabed for the indicated moorings along the transect from L3 to L2 (see inset map). Up is directed along the general trend of the isobaths at each location (i.e. approximately eastward or northeastward).

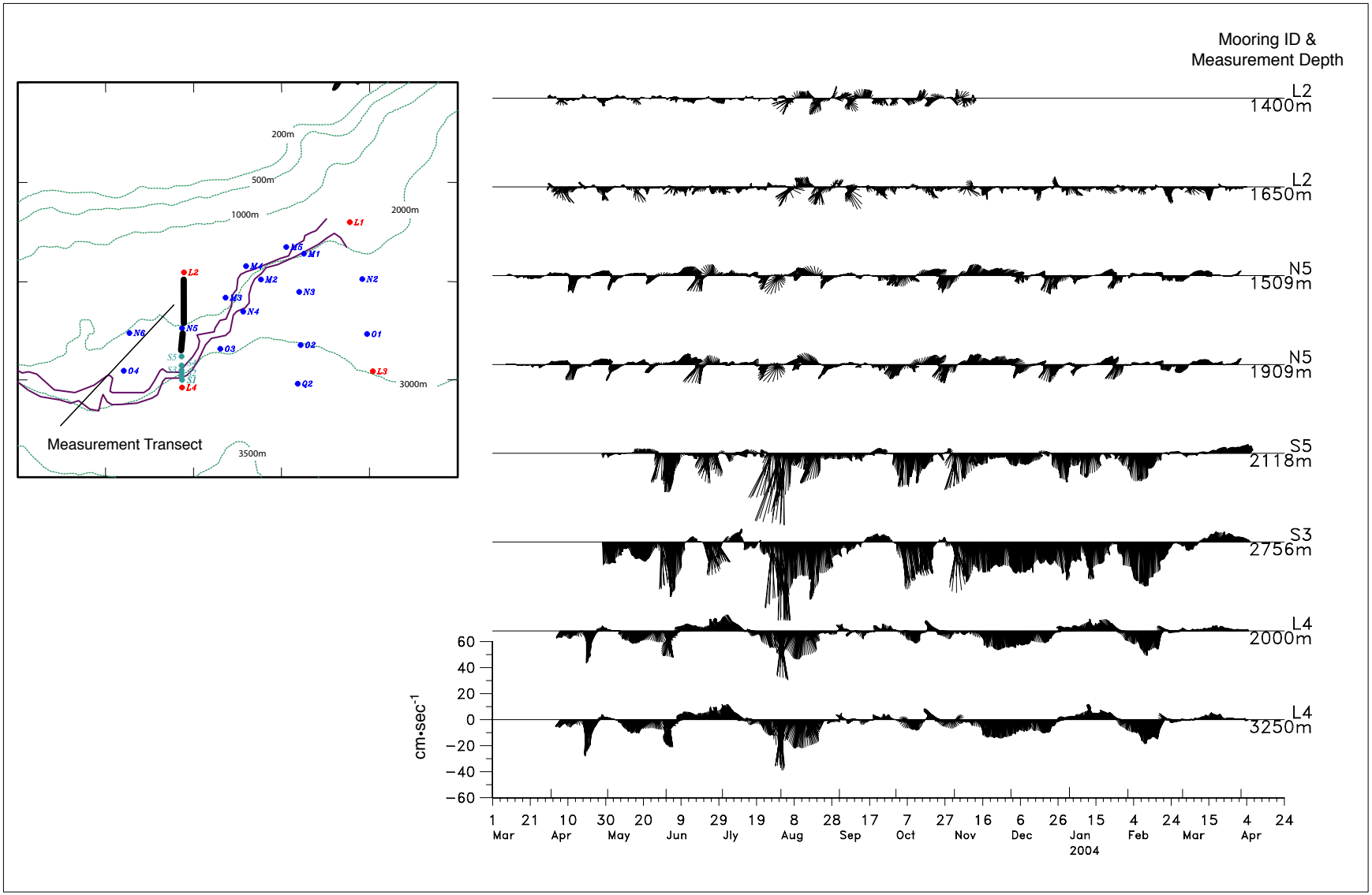

Figure 4.2-7. Near-bottom 40-HLP current vectors from nominally 100 and 500 m above the seabed for the indicated moorings along the transect from L4 to L2 (see inset map). Up is directed along the general trend of the isobaths at each location (i.e. approximately eastward or northeastward).

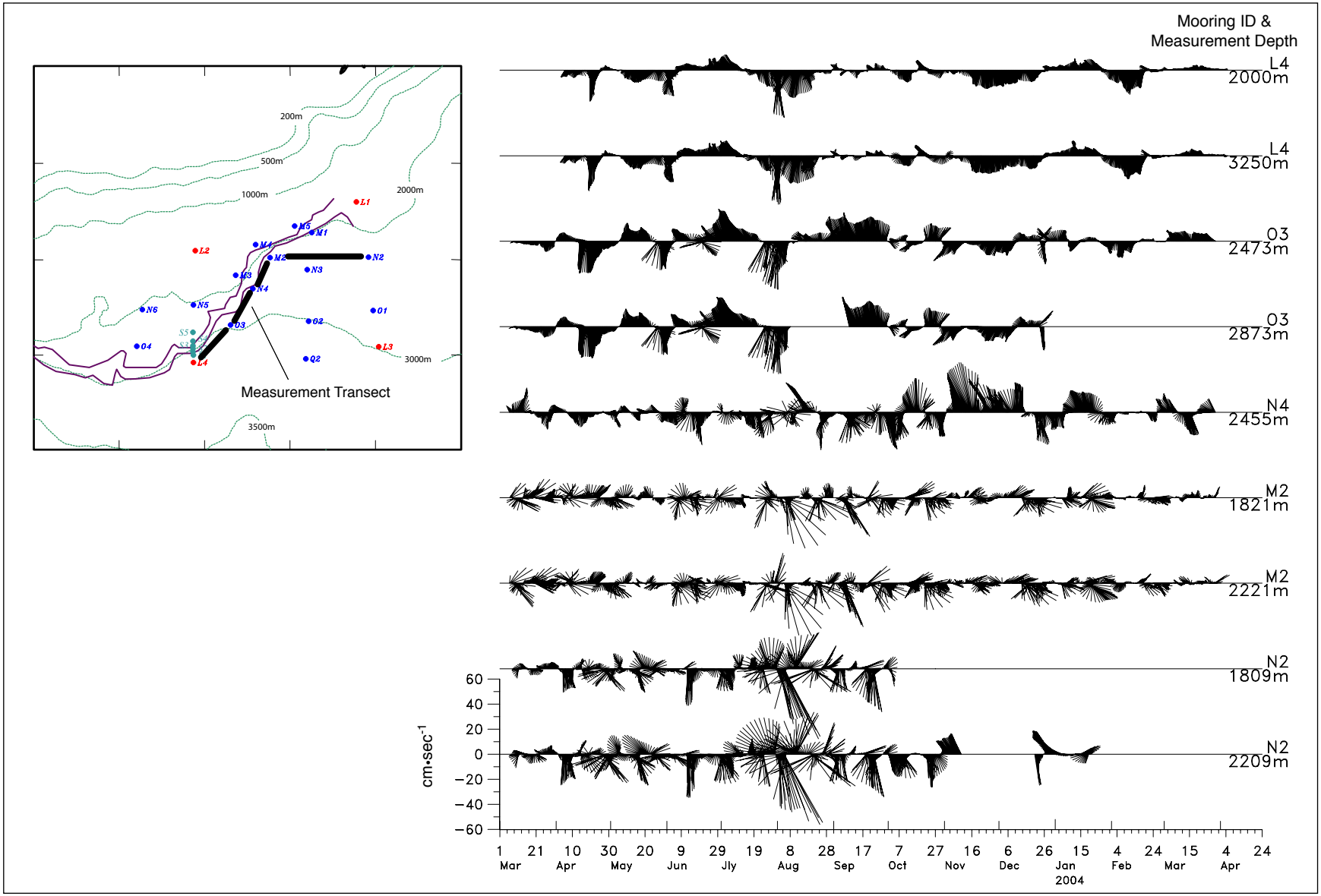

Figure 4.2-8. Near-bottom 40-HLP current vectors from nominally 100 and 500 m above the seabed for the indicated moorings along the transect from N2 to L4 (see inset map). Up is directed along the general trend of the isobaths at each location (i.e. approximately eastward or northeastward).

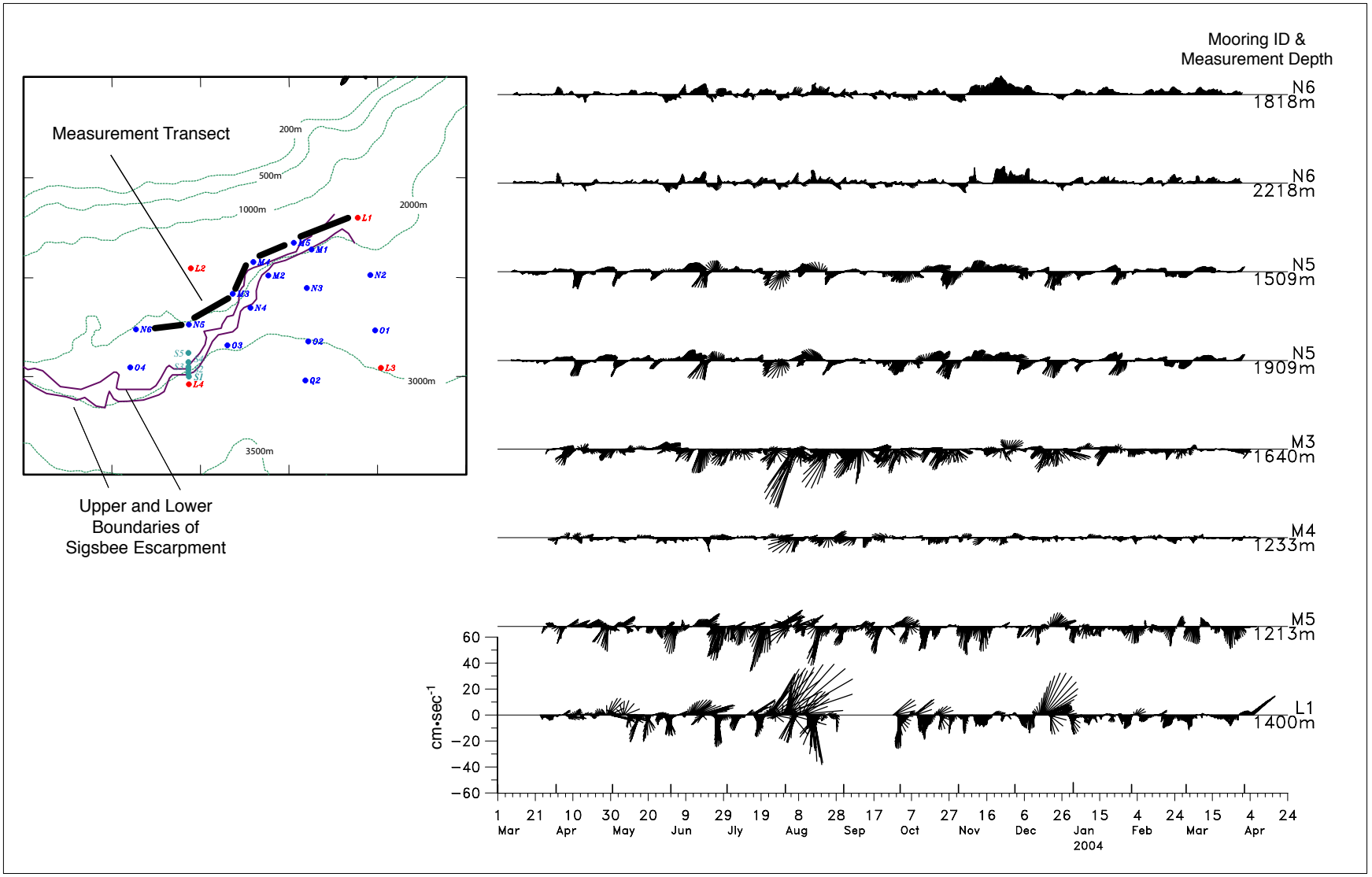

Figure 4.2-9. Near-bottom 40-HLP current vectors from nominally 100 and 500 m above the seabed for the indicated moorings along the transect from L1 to N6 (see inset map). Up is directed along the general trend of the isobaths at each location (i.e. approximately eastward or northeastward).

been significant because energetic deep current fluctuations were observed when the surface layers have been quiescent (Hamilton, In press; Hamilton et al., 2003). Where measurements were made at more than one depth on a mooring, the very high coherences of the fluctuations as well as their barotropic or bottom intensified nature are visually apparent, and are similar to previous deep current observations in the Gulf (Hamilton, 1990; Hamilton, In press). This is one of the characteristic signatures of TRWs.

The transect along the western side of the array also contrasts conditions below and above the Escarpment. This transect contained the SEBECP moorings on the Sigsbee Escarpment. The currents at 200 m above the bottom at S3 and S5 are given in Figure 4.2-7. The mooring in the middle of the Escarpment slope (S3) had the strongest currents, and similar to M3, flows almost never reversed so there was a large residual flow along the Escarpment towards the southwest. The signal at S5, on the top of the Escarpment slope, was similar to that at S3, but with decreased amplitudes. The periods of the fluctuations on and below (S5, S3 and L4) the Escarpment were much longer (~ 1-2 months) than either the fluctuations in the southwest corner of the array (L3; Figure 4.2-6) or above the Escarpment at N5 and L2. The amplitudes of the currents at the latter two moorings were small when compared with the moorings on or below the Escarpment.

The change in character of the fluctuations between east and west, along the Escarpment, is very clearly illustrated by the transect from N2 to L4 that is below the steep slope (Figure 4.2-8). Highly energetic, short-period current fluctuations with rotary components prevailed at N2 and M2 with N2 having the larger events. This is compared with the less energetic, longer period, more rectilinear fluctuations at O3 and L4. N4 had some of the characteristics of both east and west ends of the transect indicating there was a transition between the different types of fluctuations and not necessarily two distinct regions, east and west, that were not dynamically connected. Above the Escarpment (Figure 4.2-9), fluctuations had smaller amplitudes and generally shorter periods. The insulating effect of the steep Escarpment slope is apparently variable as the relatively more energetic records are at L1, M5 and M3. By contrast M4, which is between M3 and M5, has very weak currents.

Some of the highest current speeds in these records occurred at the end of July 2003 and the beginning of August 2003. Not all locations were affected, but large fluctuations were observed at L3, N2, O2, M2, O3, S3 and L4 below, and L1, M3 and S5 above the Escarpment. This time period coincided with the detachment of Eddy Sargassum and its translation northwards up onto the slope around L1. Because both east and west sides of the array below the Escarpment experienced a strong signal at this time, it suggests that broadband radiation (Malanotte-Rizzoli et al., 1987) of TRWs, with propagation speeds of 10 to 20 km·day^{-1}, triggered by the LC-eddy detachment processes, may be an explanation.

4.2.1.3 Float Trajectories in Array

The majority of the RAFOS floats were deployed within the domain of the instrumented array, and in the vicinity of the Sigsbee Escarpment. The trajectories of floats at 1000 and 1500 m within this region are shown in Figure 4.2-10. The average behavior of a float depended on its location within this region. Northwest of the Escarpment, the trajectories indicate that the flow

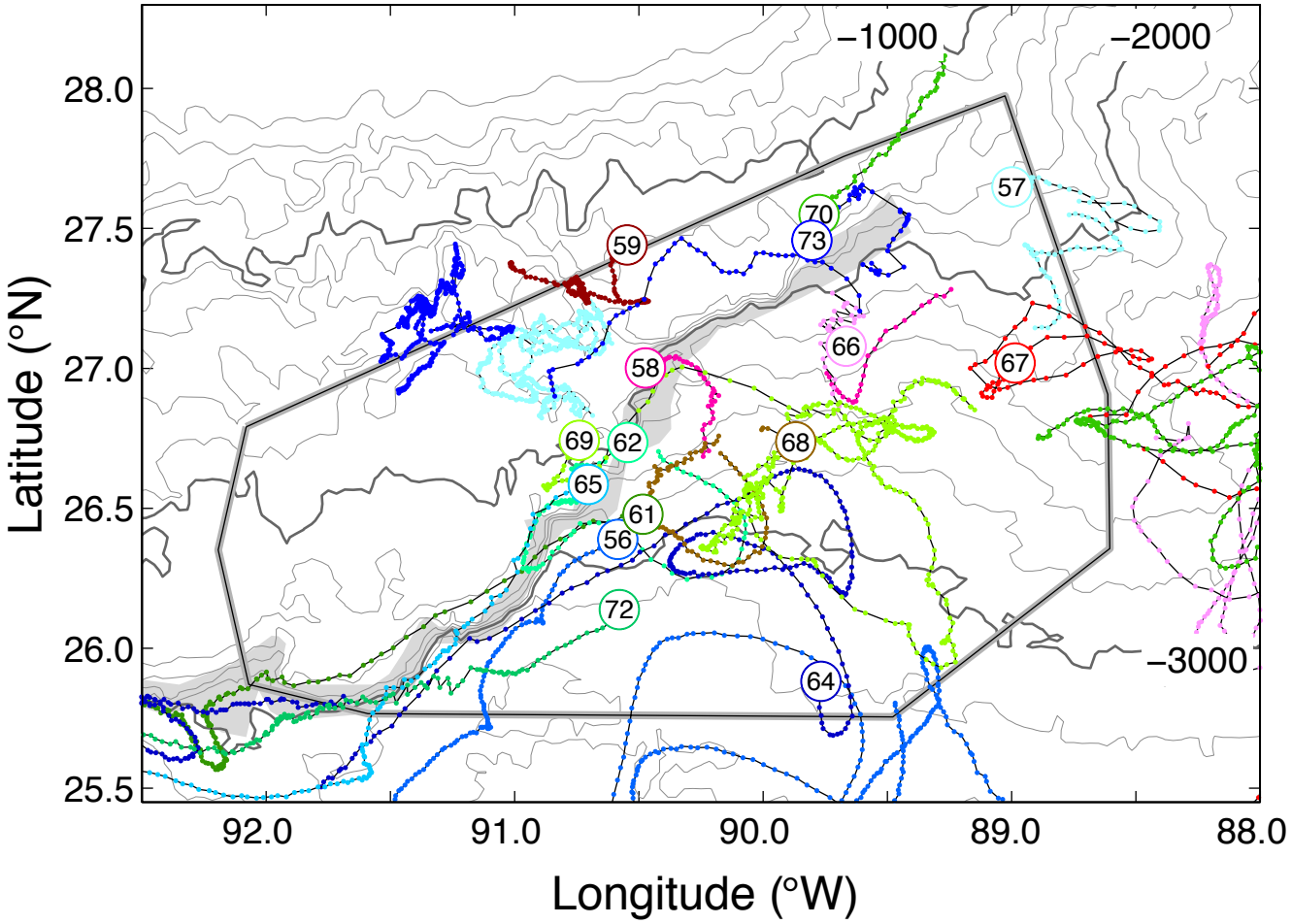

Figure 4.2-10. RAFOS float trajectories at 1000 and 1500 m in the instrument array. Float numbers in the text are 400+NN, where NN is the float identification number in the figure. The numbers mark the first valid position of the float. The large polygon indicates the extent of the current meter and PIES array, while the gray swath denotes the Sigsbee Escarpment.

was slow and unsteady, while to the southeast the flow was more energetic and marked by loops and eddies. Floats in the southwest corner of this region showed steady motion to the southwest, parallel to topography. Only a few floats appear to have crossed the steep topographic gradients of the Escarpment. The character of the float trajectories at 2000 and 2500 m (Figure 4.2-11) is similar to that found in the shallower levels. The Escarpment was an effective barrier for the deeper floats since, out of 19 occasions when floats were at the Escarpment, in only three instances did the float (all at 1500 dbars) cross from one side to the other.

The float trajectories generally followed the dynamical topography of the PIES pressure fields. This is demonstrated in Figure 4.2-12, where RAFOS trajectories were plotted overlaying the pressure anomalies at 1500 dbar as obtained from the PIES array for two specific days (19 April 2003 and 2 January 2004). On both days, well-defined eddies were in the array domain. The floats consistently (and as expected) moved cyclonically around low-pressure anomalies and anticyclonically around high-pressure anomalies. The presence of low-pressure features in the south and southwestern part of the domain caused floats caught between the low and the Escarpment to accelerate westward along the Escarpment and exit the study region.

4.2.1.4 Float Trajectories in the Far Field

As noted above, the Lagrangian nature of these float tracks allows us to observe the overall flow patterns in the GOM over much larger scales than were covered by the more heavily instrumented array. Some general characteristics of the observed float tracks are described here, while a more detailed interpretation is presented in subsequent chapters.

A general east-west asymmetry can be observed in the tracks, with the floats that traveled to the east spreading over the whole eastern basin, while those that went to the west tended to concentrate against steep topography (Figure 3.2-2a). Several westward moving floats followed the bathymetric contours extremely closely and made excursions into and around submarine canyons such as Alaminos Canyon in the vicinity of 26°N, 95°W (float 465 at 1500 meters and float 480 at 1900 m).

The "event" floats launched in October 2003 consisted of floats 456, 465 and 469 at 1500 m and floats 491, 484 and 476 at 2500 m. The deeper floats tended to move to the west or to oscillate in the central part of the basin. However, the shallower floats at 1500 m showed substantially divergent behavior, with floats 456 and 465 moving slowly in the central basin (456) or following bathymetric contours to the west (465), while float 469 moved off to the east. It should be recalled that these floats were launched within a few tens of kilometers of each other over a short time interval.

Floats that made it into the eastern basin (e.g., 458, 462, 466, 467, 470, 482) tended to show a much more eddy-like behavior. This was often, but not always, anticyclonic, and probably reflects accelerations of the lower-layer velocity field under the LC (see discussion of float/SSH comparison).

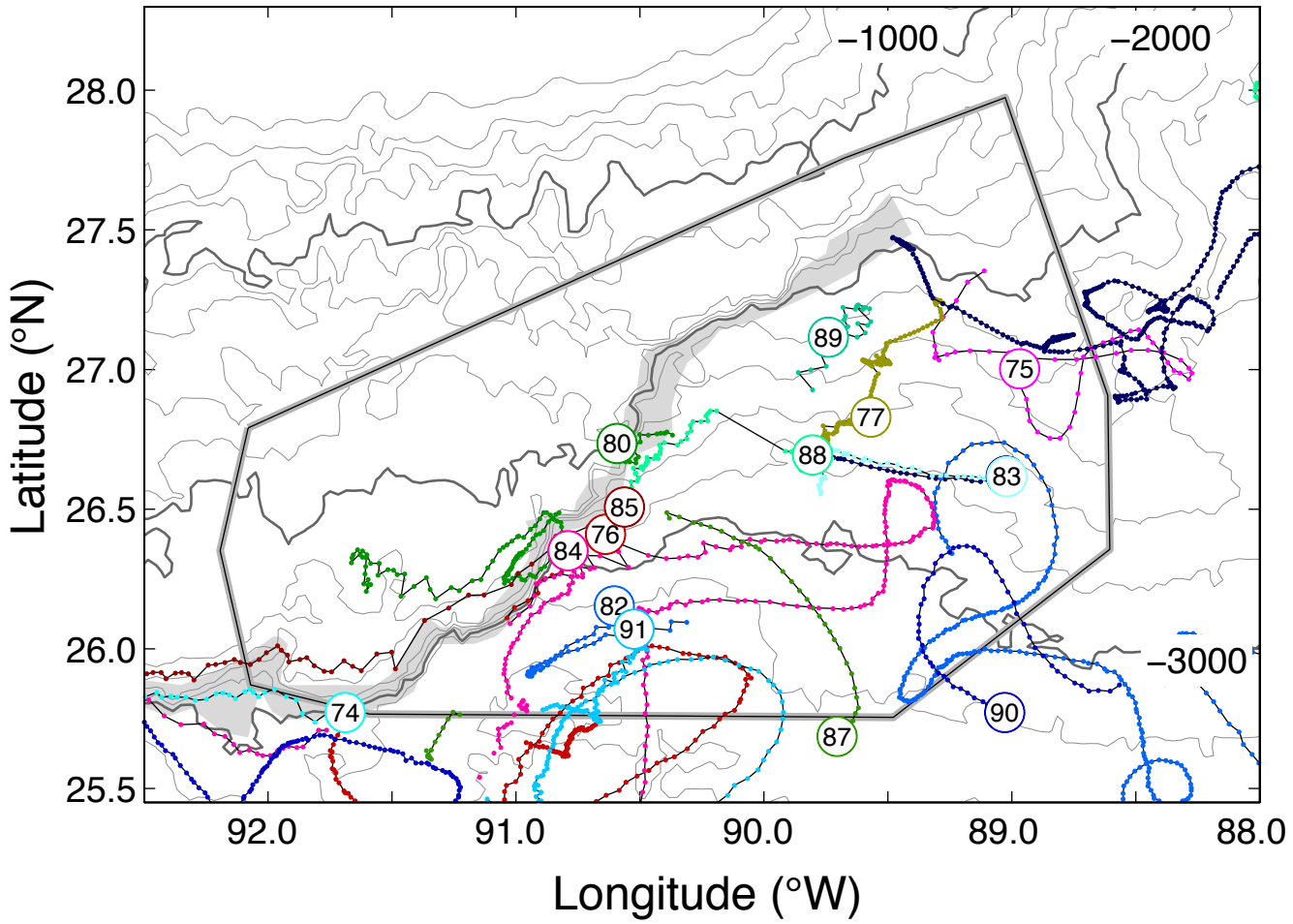

Figure 4.2-11. RAFOS float trajectories at 2000 and 2500 m in the instrument array. Float numbers in the text are 400+NN, where NN is the float identification number in the figure. The numbers mark the first valid position of the float. The large polygon indicates the extent of the current meter and PIES array, while the gray swath denotes the Sigsbee Escarpment.

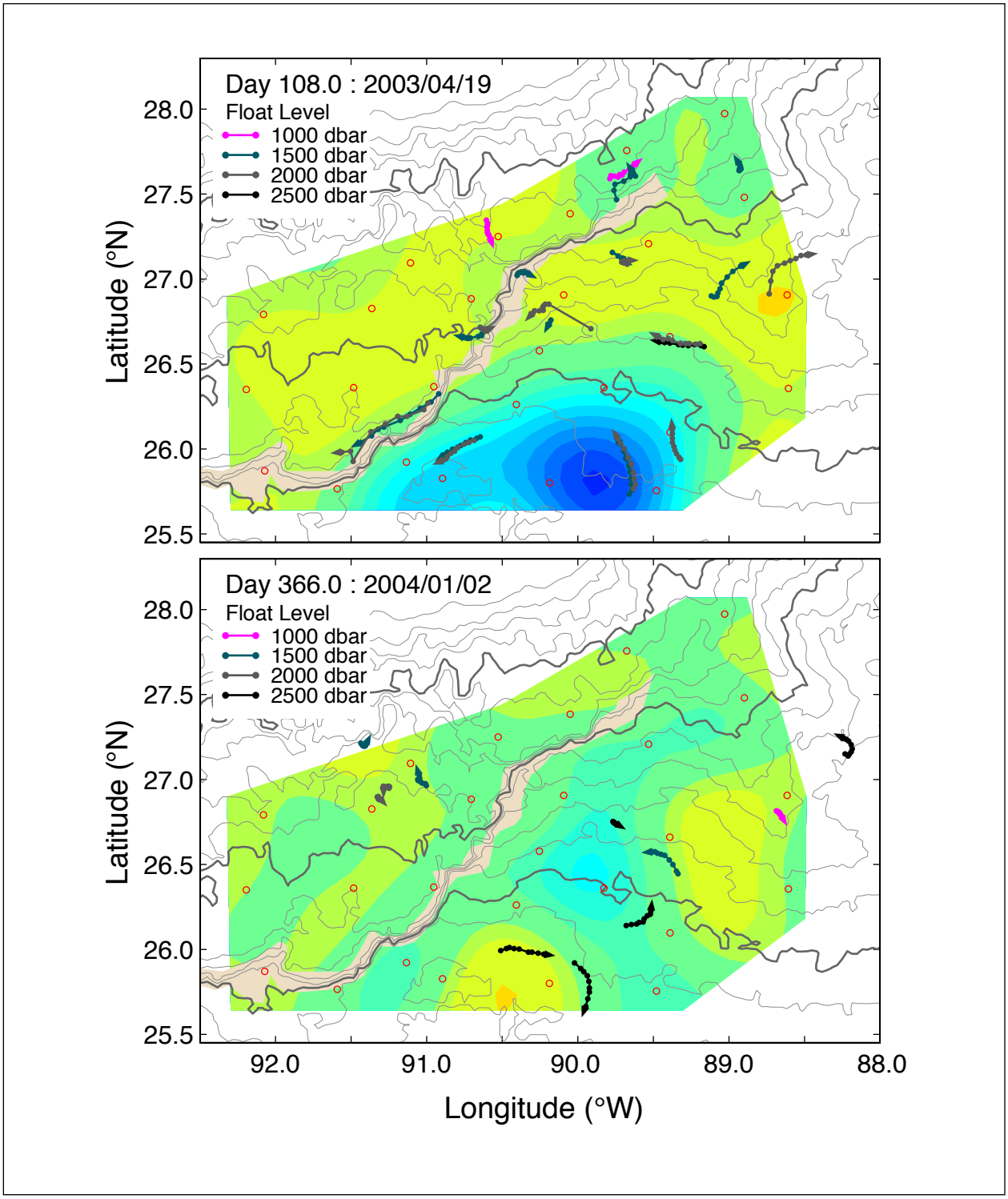

Figure 4.2-12. RAFOS float trajectories superimposed on PIES pressure anomalies at 1500 m for two specific days. Orange and red colors denote high pressure anomalies, while blues denote low anomalies. The Sigsbee Escarpment is shown in beige. The trajectories are 3 days in duration, centered on the time of the pressure field data.

4.2.2 Basic Statistics for Deep-Layer Currents (1000 m and Deeper)

The basic statistics for the lower-layer currents and their variability observed in the Exploratory Study are summarized in this section. Moored current observations are available from five tall moorings at 500 m intervals in the lower water column below 1000 m, and 15 short deep moorings which generally had current meters at 100 m and 500 m above the sea floor.

In addition, the PIES data can map daily absolute currents on any desired depths at a grid of locations in the study area. Just as we presented for the upper layer, we summarize here the mean currents and the EKE at a grid of locations.

For comparison with these mapped currents, the directly measured currents are first reported for the current-meter moored observations at all moorings within the array. We report in this section the deep mean currents (U,V) and the deep eddy kinetic energy $<EKE> = <(1/2)\ [\ (u')^2 + (v')^2\ ]>$, where $< >$ indicates the average over the 1-year observation period, and $u' = (u - U)$, $v' = (v - V)$. We examine not only the time-average EKE distribution, but also how EKE varied with time as packets of deep eddies passed within the study array. We also present current speed histograms for the deep water, and discuss the spatial and temporal correlation scales of deep geostrophic pressure.

4.2.2.1 Lower-Layer Current Statistics from Moorings

Mean current vectors, most of which are from instruments 100 m above the bottom, are shown in Figure 4.2-13. For a few of the short moorings, the 500-m level was used because a full 12-month record was not available at the bottom instrument. Figure 4.2-13 also shows all the available mean currents below 1000-m depth from the five tall moorings. The near-bottom means showed enhanced southwestward flow along the Escarpment. This was particularly strong for the SEBCEP section at S3 and S5. Mean flows above and below the slope, in the southern part of the array also converged towards the Escarpment as if "feeding" the Escarpment mean currents. This is particularly notable at L5, O3 and N4. Measurements on the tall moorings below the Escarpment show almost depth-independent means below 1000 m, whereas above the Escarpment at L1 and L2, means at 1000 m were small compared to near bottom. Enhanced cyclonic deep mean flow along the Escarpment is predicted by some numerical model studies (Oey and Lee, 2002).

The eddy kinetic energy (EKE = 1/2 ($<u'^2> + <v'^2>$), Figure 4.2-14) had a marked decrease above the Escarpment. There were two regions of maximum fluctuations below the Escarpment, one in the northeast corner and the other around 90.5°W. Thus, it appears that the Escarpment (within the resolution of the array) insulated the shallow regions on the slope from the energetic currents in deeper water. It is noted that the station with a very large mean (S5) had similar amplitude fluctuations to its neighbors, which were smaller than those found further east. This suggests that EKE was being converted into mean flows in the vicinity of the Escarpment, particularly where it was steep in the southwestern part of the array. The standard deviation ellipses on the eastern side of the array, in deep water, have major axes that are at a small angle to the isobaths, and because these records have bottom intensification (not shown), this is consistent with westward propagating TRWs (Thompson, 1978). Along the Escarpment, the

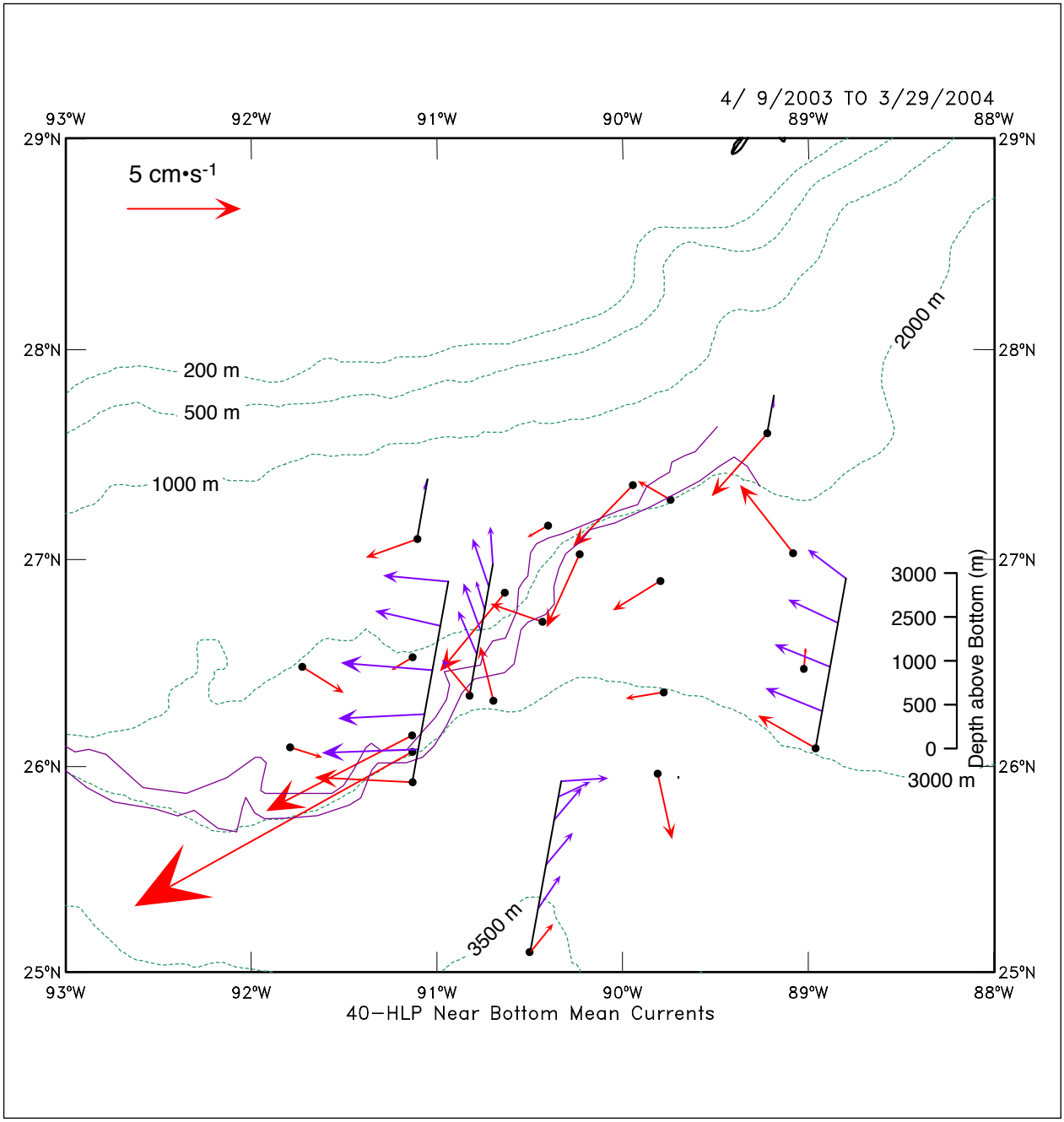

Figure 4.2-13. Mean 40-HLP velocity vectors at nominally 100 m above bottom (red arrows). At the tall moorings (L1 - L6) mean velocities below 1000-m depth (blue arrows) are displayed as pseudo-3D stacks with the depth scale on the right. The top and bottom of the escarpment are indicated by the purple lines.

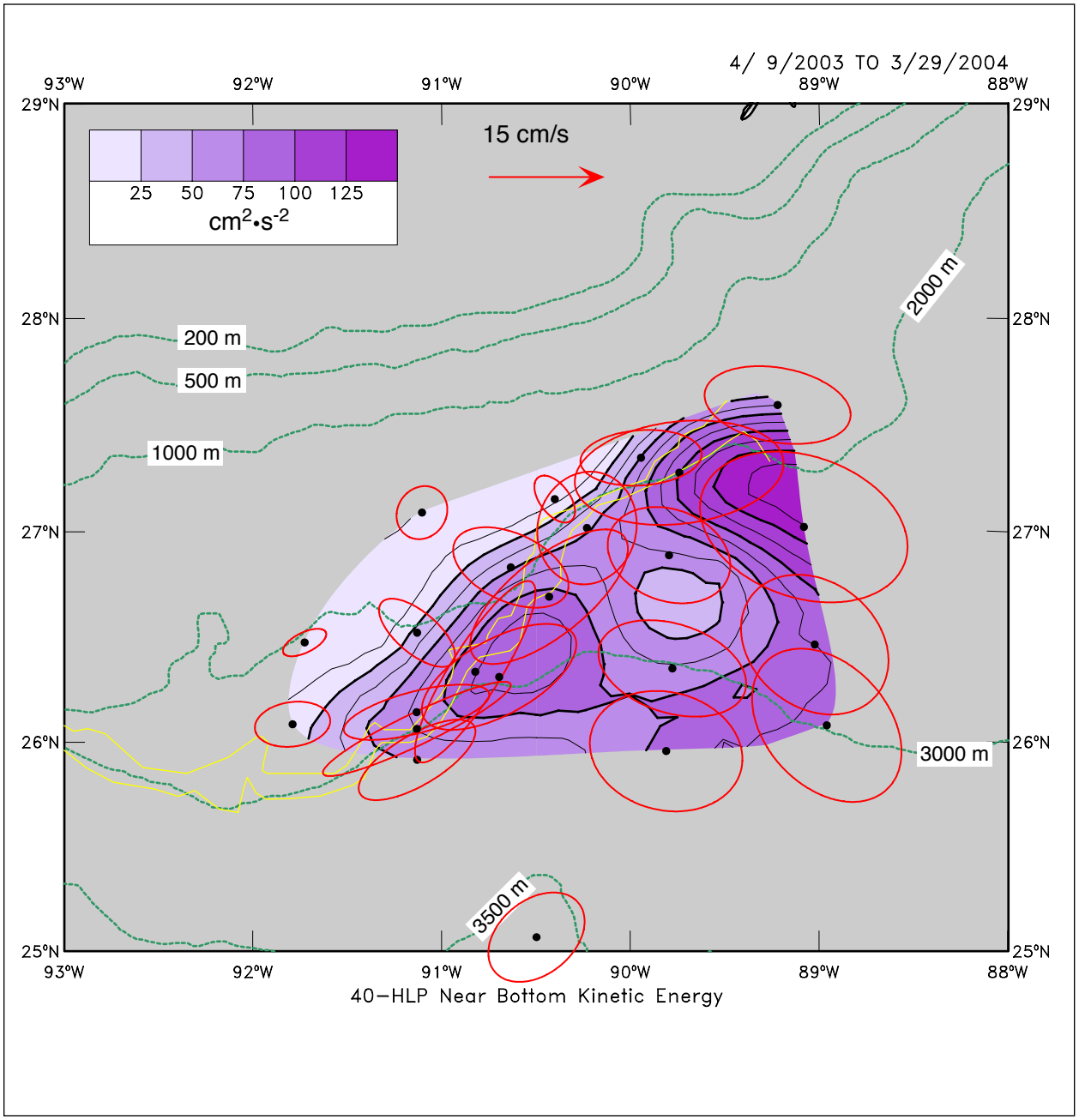

Figure 4.2-14. Standard deviation ellipses from 40-HLP current records at nominally 100 m above bottom (in red), overlaid on a contour map of EKE. Solid yellow line is the upper and lower bound of the Sigsbee Escarpment. The dashed green lines are isobaths.

major axes were aligned with the steep topography, and immediately above the Escarpment (e.g., N5, M3 and M4), the less energetic stations had major axes that were nearly normal to the isobaths. The means and standard deviations of the near-bottom currents showed complex patterns in which the Escarpment played a major role.

To illustrate how closely the high-velocity mean jet was associated with the Escarpment, the bottom along-slope currents from the SEBCEP transect (S1 to S6, plus L4 and N5) are plotted and contoured, with some subjective interpolation, in Figure 4.2-15. Note that the bottom instruments on the S moorings were only 3 m above the bottom and thus well within the bottom frictional boundary layer. The along-slope means over the steepest part of the Escarpment were approximately double those immediately above and below. The highest mean speed observed was 200 m above the bottom at S3. This suggests that the mean jet was centered over the steep part of the slope or possibly the near the base (i.e., S2) and decayed rapidly with distance from the Escarpment. It is not known how far up into the water column these enhanced flows may have occurred. Away from the slope, on the deep side of the Escarpment, the means were largely depth independent below 1000 m (Figure 4.2-13). The standard deviations of the along-slope component show some enhancement on the Escarpment, but more noteworthy was the decrease in amplitude from below (S2) to above (S6) the steep slope.

4.2.2.2 Mapped Current Statistics at 1500-m Depth and 100 MAB

The time-average mapped currents and streamfunction for this one-year observational period at two lower-layer depths are shown in Figure 4.2-16 and 4.2-17. The currents were relatively uniform in the vertical below 1500 m. Because the low frequency currents below the thermocline were only slightly bottom-intensified, we summarize the deep currents in this section by maps and tables for only these two levels, one constant horizon at 1500-m depth, and one bottom-following surface at 100 m above the bottom (MAB). This latter level was chosen to avoid the expected Ekman eddy-frictional turning and decay that would occur closer to the bottom within the bottom boundary layer.

For both levels we illustrate the absolute currents and geostrophic pressure maps, which were generated from the measured deep currents and leveled-bottom pressures. The vertical scale of weak bottom-intensification was fitted as outlined in Section 2.6 (vertical trapping scale details will be discussed in Section 5.2.3). The mean current and EKE maps at 100 m above the bottom are shown to emphasize visually how similar they were to the 1500-m level. It is sufficient to discuss in the following just the 1500-m level.

As discussed in Section 4.2.1, a variety of cyclonic and anticyclonic deep eddies entered the study array, mainly confined south of the Sigsbee Escarpment; the most prevalent and strongest eddies were cyclonic. We can account for the three time-averaged cyclonic regions in the one-year mean map (Figure 4.2-16) as follows. The mean feature near 26°N, 89.5°W arose because strong cyclones entered repeatedly near this location from the southeast. The mean feature near 25.8°N, 91°W arose because several cyclones lingered near this location during their general southwestward transits during the year. The time-average cyclonic feature along the eastern edge arose because numerous weak cyclonic eddies and a few anticyclonic features appeared

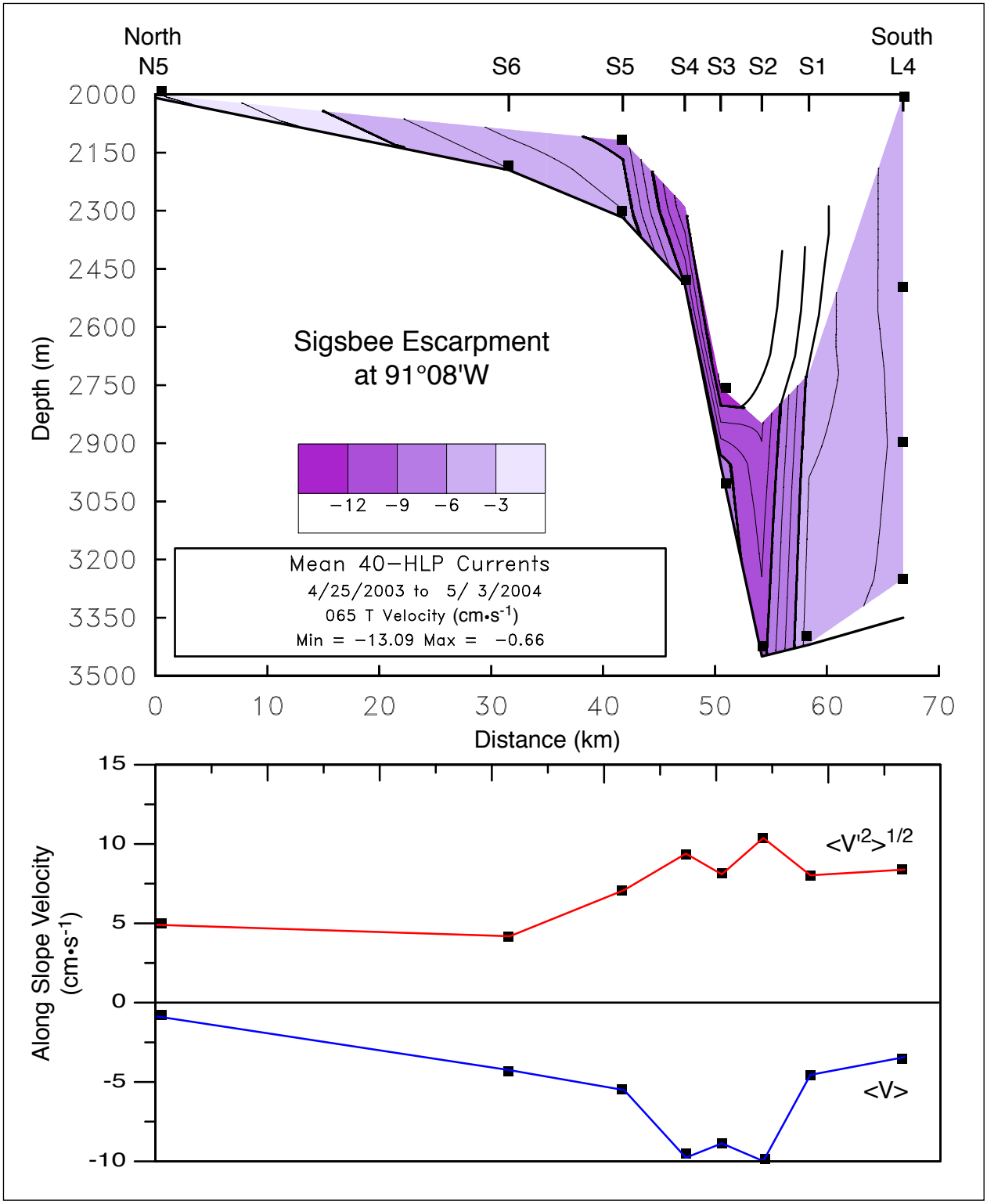

Figure 4.2-15. Upper Panel: Contoured mean along-slope 40-HLP current velocity component (065°T) from the Exploratory and SEBCEP studies. Measurement positions are indicated by the solid squares. Lower Panel: Along-slope mean velocity (blue line) and standard deviation (red line) from the bottom most instrument on each mooring. Negative velocities are towards the southwest.

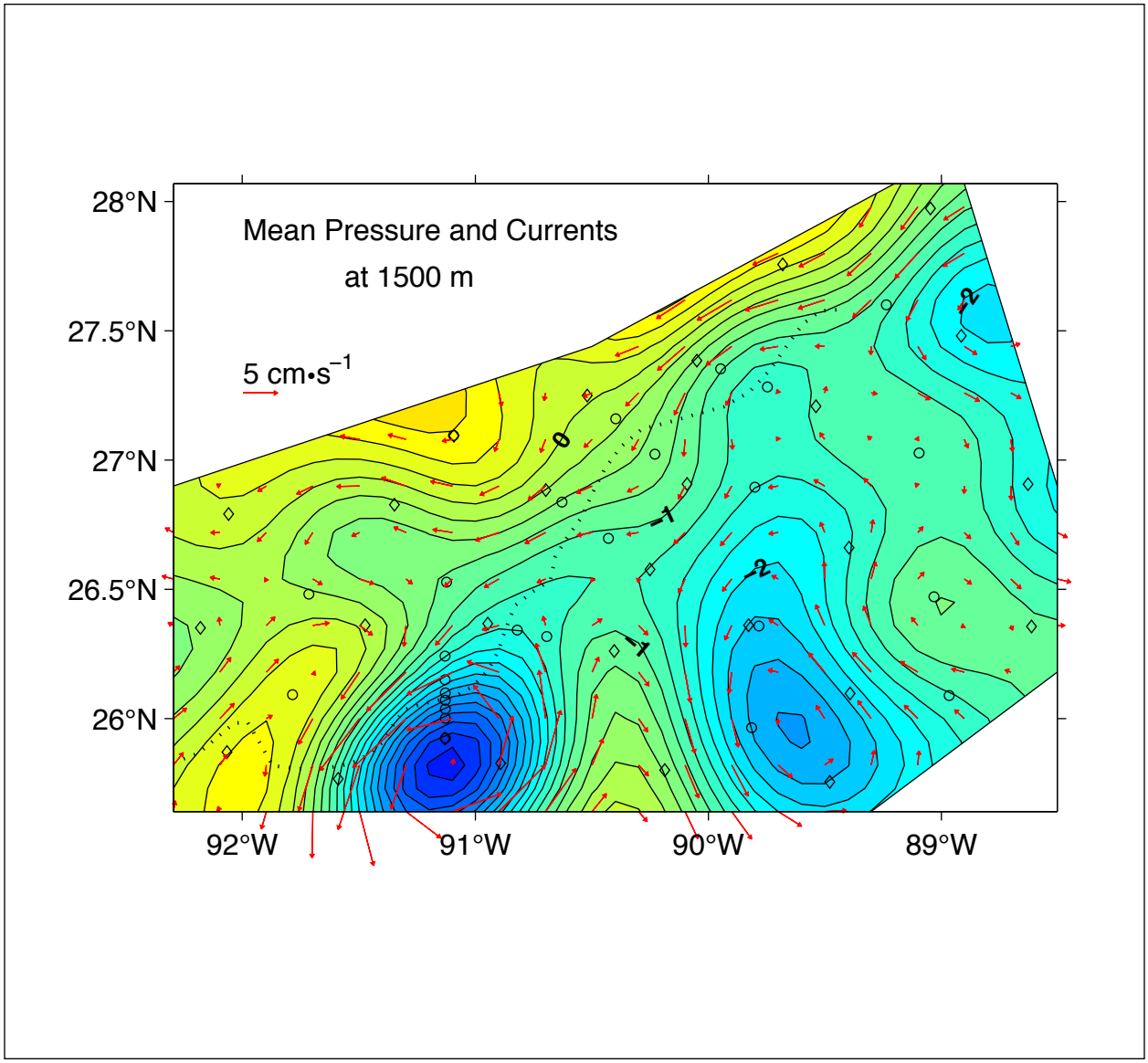

Figure 4.2-16. Time-average mean pressure (contours) and currents (red vectors) at 1500 m. Dotted line denotes the center of the Sigsbee Escarpment. Pressure contoured every 0.25 dbar with low (high) values shown with blue (red) hues. Currents vectors plotted at 20-km spacing. PIES sites indicated by diamonds; current meters by circles.

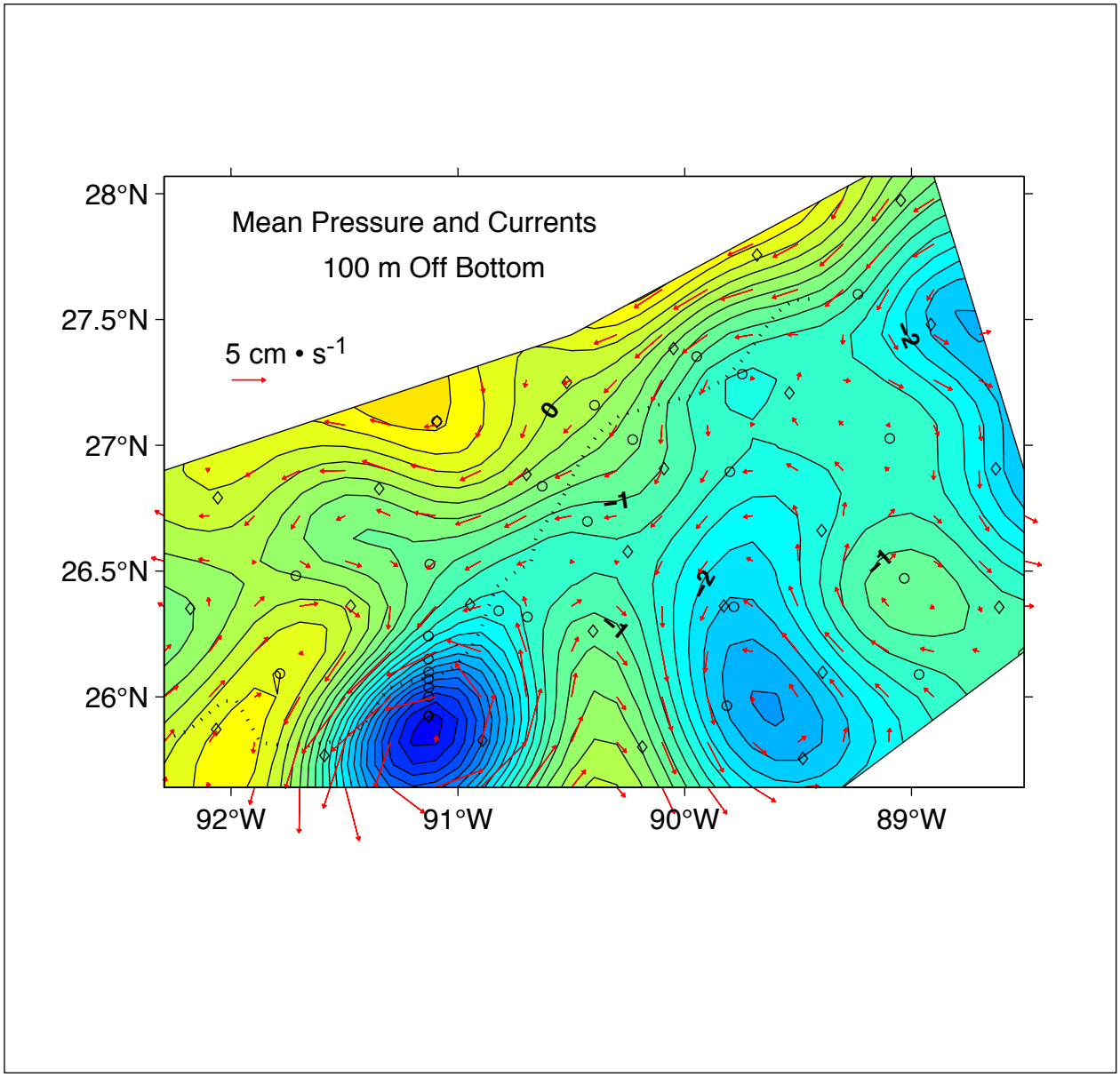

Figure 4.2-17. Time-average mean pressure (contours) and currents (red vectors) 100 m off the bottom. Dotted line denotes the center of the Sigsbee Escarpment. Pressure contoured every 0.25 dbar with low (high) values shown with blue (red) hues. Currents vectors plotted at 20-km spacing. PIES sites indicated by diamonds; current meters by circles.

there. The strongest mean deep currents were about 10 $cm \cdot s^{-1}$ southwestward along the base of the Sigsbee Escarpment near 26°N, 91.5°W.

North of the Sigsbee Escarpment the time-average currents tended to be southwestward at 3-5 $cm \cdot s^{-1}$. These means arose as the sum of the passage of several strong cyclones with their low pressure centers remaining south of Sigsbee, and with their northwestern sector having peripheral currents to the southwest. While the time-average deep current patterns and directions differ greatly from the upper layer, it is again important to recognize that even these one-year mean currents were the average of only a few events. Hence, the deep maps for one year should not be interpreted to represent the long-term mean currents.

As found for the upper layer, the current variability in the deep water is also much greater than the mean currents. Maps of the one-year mean eddy kinetic energy, $\langle EKE \rangle = (1/2) \langle (u')^2 + (v')^2 \rangle$, as defined above, are shown in Figure 4.2-18 and Figure 4.2-19 for the 1500-m level and 100 m above the bottom, respectively. The region south of the Sigsbee Escarpment (S-Sigs) had relatively uniform EKE distributions of 40 to 60 $cm^2 \cdot s^{-2}$, corresponding to mean eddy speeds of 9 to 11 $cm \cdot s^{-1}$ (Figure 4.2-20). Most of the region north of Sigsbee (N-Sigs) had EKE less than 20 $cm^2 \cdot s^{-2}$, and mean eddy speeds lower than 6 $cm \cdot s^{-1}$.

The current speed histogram in Figure 4.2-21 for the 1500-m level shows the most probable deep current speeds in the study array and the S-Sigs region were in the 10 $cm \cdot s^{-1}$ speed class, with values observed up through the 35-45 $cm \cdot s^{-1}$ class. In the N-Sigs region the corresponding values are lower, with the 0-5 $cm \cdot s^{-1}$ speed class being most probable, and values populating the speed classes up through 25-35 $cm \cdot s^{-1}$.

4.2.3 Bottom Pressure Common Mode

An array-wide coherent bottom-pressure signal, the common mode, was removed from the bottom pressures before mapping deep pressure, streamfunction, and velocity in order to enhance and reveal deep mesoscale features. The common mode is the array-wide average of the bottom pressure records (Figure 4.2-22). This signal was coherent across the array and therefore had very weak associated pressure gradients and hence no velocity signal. Retention of the common mode in the deep maps would simply add a daily array-wide constant which has no dynamical significance for the mesoscale circulation.

Spectra of the common mode reveals dominant spectral peaks near 16, 6, and 4 days (Figure 4.2-22). The 6- and 4-day signals are conspicuously similar to the time scale of synoptic-scale weather systems. The 16-day signal remains unexplained. The 16-day signal in the common mode is coherent and in-phase with coastal tide gauges west of Pensacola (west of the broad shallow Floridia continental shelf). The amplitude of the 16-day signal is about 0.05 dbar, equivalent to about 5 cm in sea-surface height. If we assume that the GOM surface area is 1.5×10^6 km^2, the 5 cm height increase or decrease over 4 days equates to 0.2 Sv of mass transport entering the GOM, a small 0.8% fraction of the total 23 Sv of transport through the Yucatan Channel (Sheinbaum et al., 2002). Further progress towards understanding the spectral character of the common mode would include joint analysis of bottom pressure, sea level,

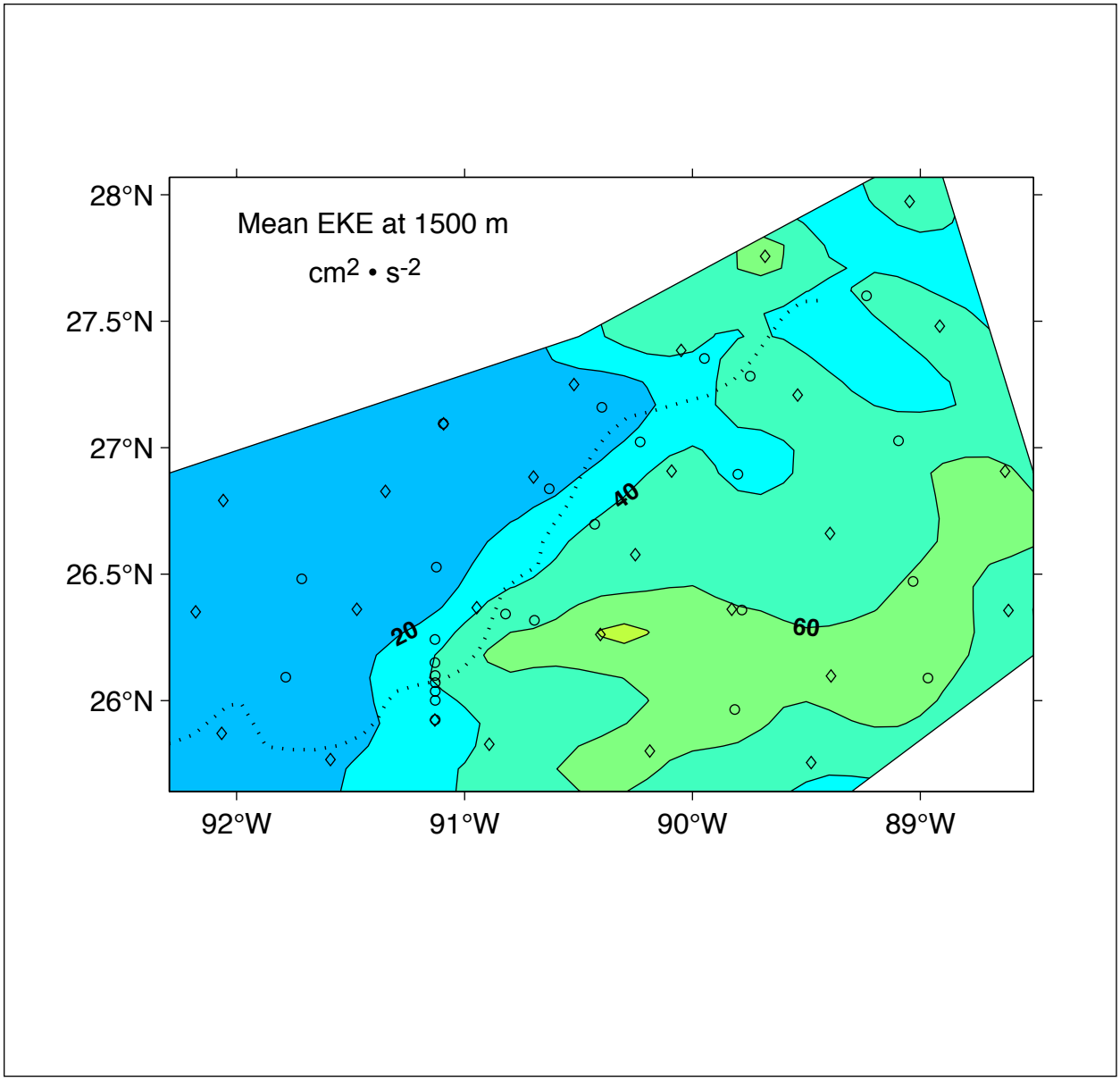

Figure 4.2-18. Map of the 1-year mean eddy kinetic energy at 1500-m depth. Thin dotted black line denotes the midpoint of the Escarpment. Diamonds show PIES locations; circles show current meter mooring locations.

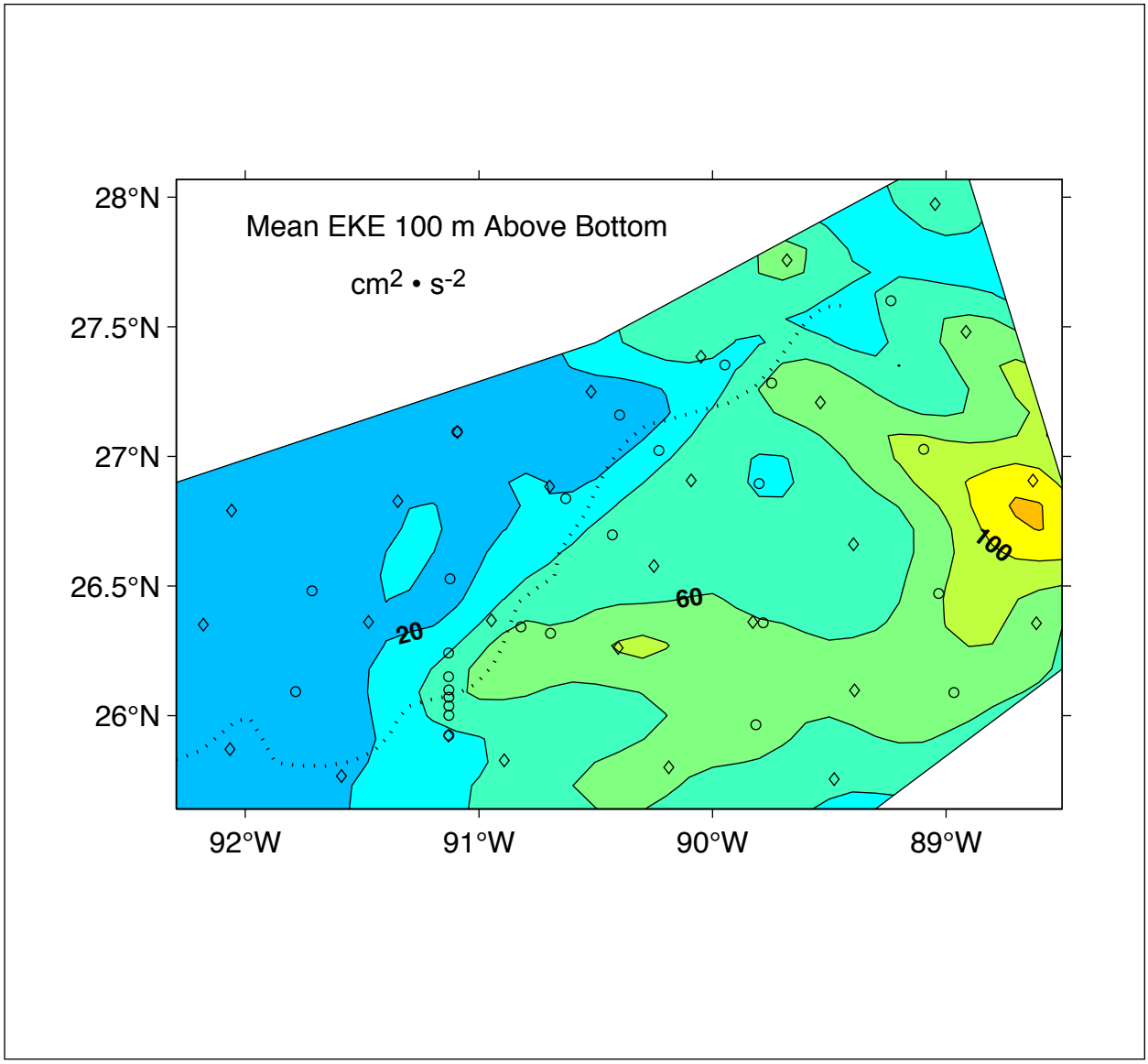

Figure 4.2-19. Map of the 1-year mean eddy kinetic energy 100 m off the bottom. Thin dotted black line denotes the midpoint of the Escarpment. Diamonds show PIES locations; circles show current meter mooring locations.

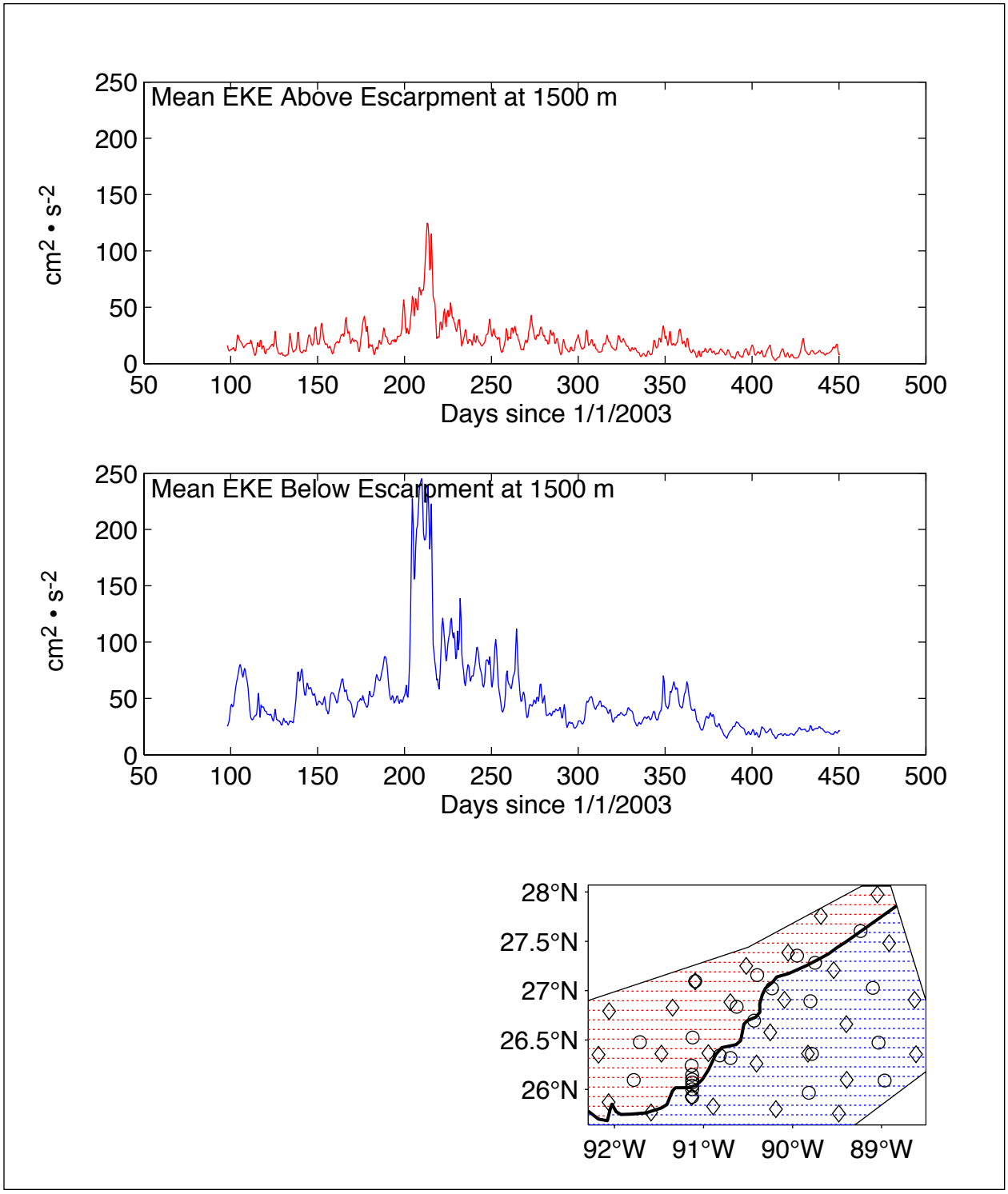

Figure 4.2-20 Top panel: Mean eddy kinetic energy at 1500-m depth spatially averaged above (top panel) and below (middle panel) the Sigsbee Escarpment. Bottom panel: Map of Exploratory array. Thick black line denotes the midpoint of the Escarpment. Red (blue) hatching indicates that instruments are classified as above (below) Escarpment. Diamonds show PIES locations; circles show current meter moorings.

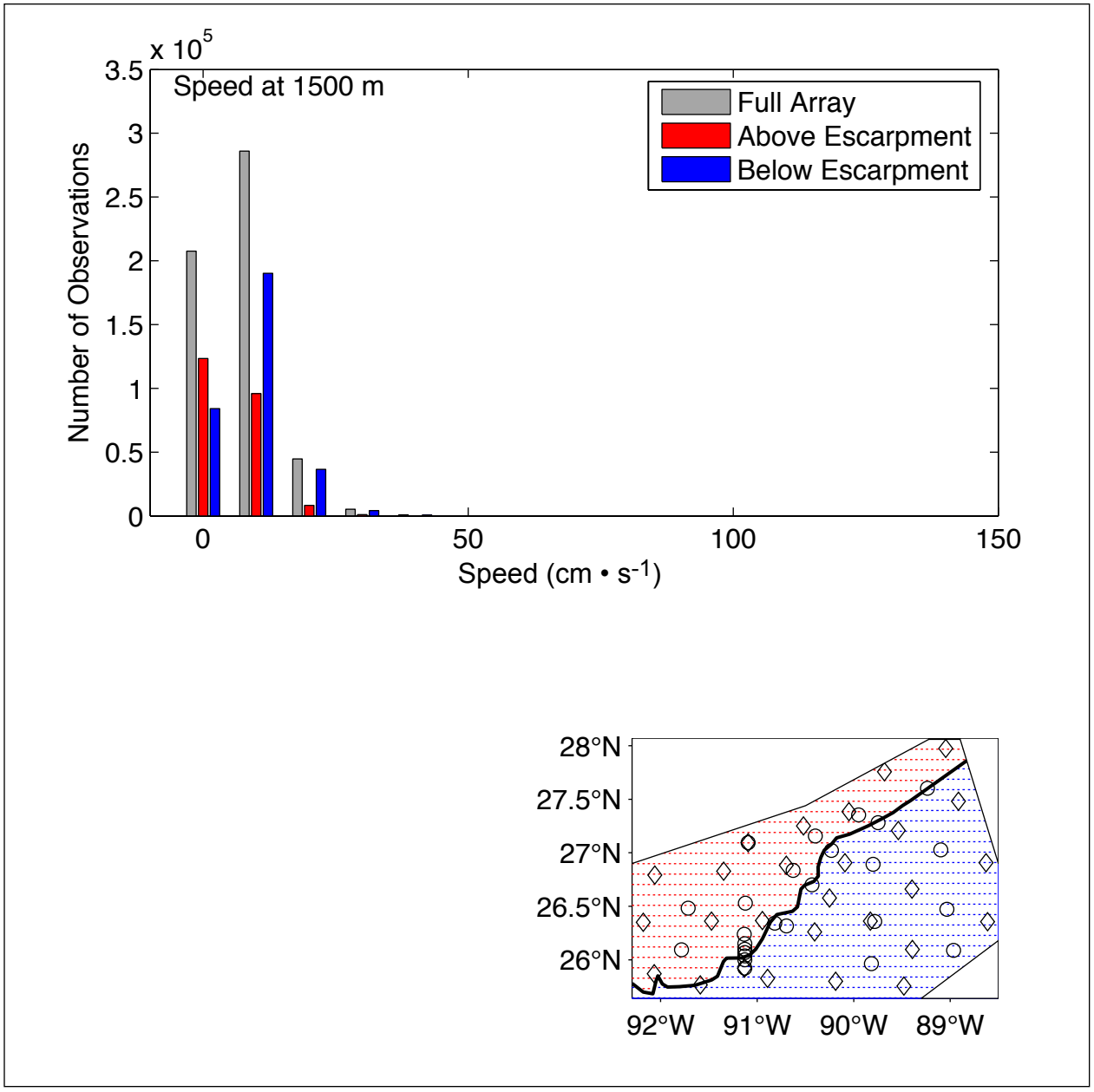

Figure 4.2-21. Top panel: 1500-m depth current speed histograms. Current has been grouped into the entire array (gray), above (red) and below (blue) the Sigsbee Escarpment. Bottom panel: Map of Exploratory array. Thick black line denotes the midpoint of the Escarpment. Red (blue) hatching indicates that instruments are classified as above (below) Escarpment. Diamonds show PIES locations; circles show current meter mooring locations.

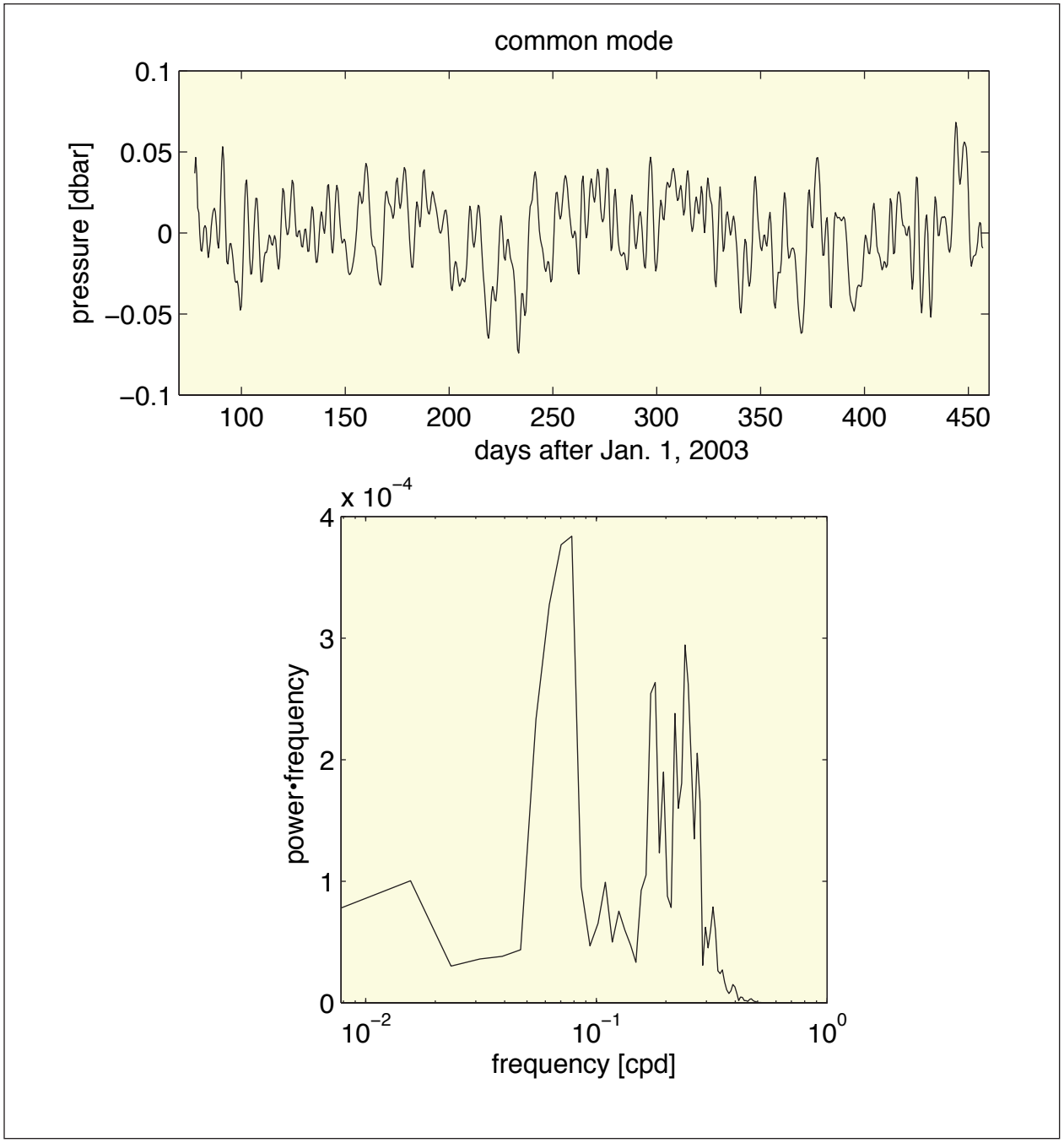

Figure 4.2-22. Top Panel: Common mode subtracted from bottom pressure records before mapping deepwater dynamical properties. Bottom Panel: Spectra of common mode reveals dominant spectral peaks near 16, 6 and 4 days.

atmospheric variables, and possibly current at the Yucatan Channel and Florida Straits. Additionally, analysis of a barotropic model of the GOM forced with realistic forcing would be informative.

4.3 Extreme Events in the Deep Currents

The basic statistics of the 40-HLP near bottom currents have been discussed previously. However, for engineering purposes, it is useful to give the observed maximum speeds as an indication of the strength of extreme currents that might be encountered in the lower layer. Maximum speeds were calculated for the complete current-meter array using the 3-HLP records at 100 m from the bottom, except the 500-m and 200-m levels (S3 and S5 only) were substituted if the lower records were incomplete for the year. The results are given in Table 4.3-1 and Figure 4.3-1. The pattern of extreme velocity magnitudes is very similar to that for the 40-HLP KE with maximums occurring just below or on the Escarpment in two separate regions, one in the northeast and the other in the southwest. The former region has a tongue stretching along the Escarpment towards the westsouthwest. Maximum speeds were observed at M1 (67 $cm \cdot s^{-1}$) and S3 (66 $cm \cdot s^{-1}$). The lowest maximum speeds were west of the Escarpment at N6 (16 $cm \cdot s^{-1}$). The percent time that the currents were in the upper quartile of their speed range were also calculated for each mooring. The results range for about 0.5 to 1.5% of the records, which correspond to between 40 and 120 hours, not necessarily consecutive, out of a year that the currents exceed 75% of the observed maximum speed.

Table 4.3-1

Maximum currents observed near bottom at tall and short moorings during the Exploratory Study.

Mooring	MAB	Date	Time (GMT)	Speed ($cm \cdot s^{-1}$)	Dir. (Deg.)	Comment
L1 (1000m)	500	12/09/03	1700	33.79	242	
L1 (1400m)	100	08/03/03	0100	56.61	111	Depl. 1
L2 (1400m)	350	08/23/03	0700	19.99	277	
L2 (1650m)	100	09/04/03	0200	23.48	193	
L3 (2500m)	500	07/25/03	0700	49.34	308	
L3 (2900m)	100	07/25/03	0800	46.73	305	
L4 (2900m)	450	08/01/03	0900	43.24	250	
L4 (3250m)	100	08/01/03	1000	40.04	251	
L5 (2625m)*	400	08/01/03	0700	39.17	231	
L5 (2925m)*	100	08/01/03	0700	36.66	225	
M1 (1481m)	500	07/29/03	2200	66.49	068	
M1 (1881m)	100	07/30/03	1000	67.65	075	
M2 (1826m)	500	08/04/03	1100	55.74	190	
M2 (2226m)	100	08/04/03	1500	54.58	212	
M3 (1640m)	100	08/05/03	1700	53.12	281	
M4 (1235m)	100	08/05/03	0700	28.42	317	
M5 (1204m)	100	07/20/03	1100	42.37	250	
N2 (1819m)	500	08/04/03	2100	65.33	286	Partial Depl.
N2 (2219m)	100	08/04/03	2000	65.04	283	Partial Depl.
N3 (2080m)	500	09/03/03	0700	45.86	133	
N3 (2480m)	100	09/03/03	0200	38.59	140	Depl. 2
N4 (2038m)	500	11/15/03	0700	41.21	049	Depl. 2
N4 (2438m)	100	11/15/03	0500	46.15	051	
N5 (1520m)	500	07/31/03	0900	19.99	311	
N5 (1920m)	100	06/18/03	1300	22.32	311	
N6 (1832m)	500	11/22/03	2200	15.92	072	
N6 (2232m)	100	11/21/03	2200	16.79	077	
O1 (2330m)	500	08/03/03	0500	40.92	112	
O1 (2730m)	100	08/03/03	0200	44.69	117	
O2 (2518m)	500	07/29/03	0400	39.75	292	
O2 (2918m)	100	07/29/03	0400	38.59	296	
O3 (2460m)	500	07/31/03	1400	39.46	244	
O3 (2860m)	100	07/31/03	1000	40.04	241	Depl. 1
O4 (1722m)	500	08/02/03	0800	21.44	264	
O4 (2122m)	100	08/02/03	0700	21.73	252	
Q2 (2711m)	500	08/20/03	2100	34.23	152	
Q2 (3111m)	100	08/20/03	1000	34.52	147	

MAB = Meters Above Bottom.
* = LSU Data

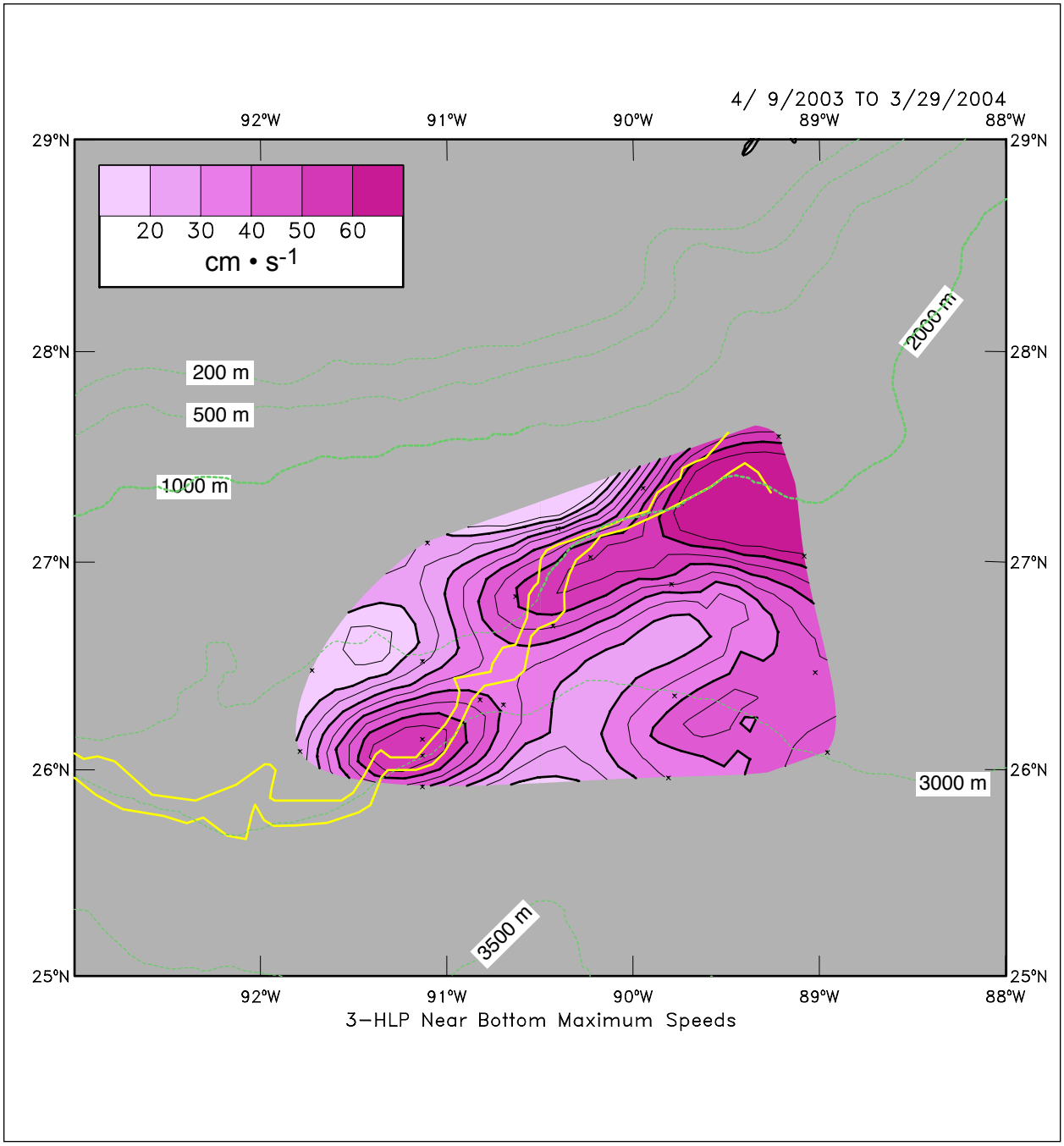

Figure 4.3-1. Maximum current speeds at instruments 100 to 500 m above the bottom. Calculations use 3-HLP records. Yellow lines are the upper and lower bounds of the Sigsbee Escarpment. Dashed green lines are isobaths.

5.0 INTERPRETATION AND ANALYSIS

5.1 Upper Layer

5.1.1 Upper-Ocean Eddy Kinematics and Dynamics

Dynamical interpretation of the upper-ocean circulation can be difficult given the complexity of the eddy interactions in and around the study region during the Exploratory Study – an eddy field that can be best characterized as an energetic nonlinear flow, at least during the first half of the study period. The description of the upper-layer circulation might have been quite different if the LC had exhibited a canonical LCE shedding cycle during the study period, while remaining primarily south of the study region. A canonical LCE shedding cycle, consisting of a modest northern intrusion, eddy separation and retreat, would probably have exhibited a more quiescent surface-eddy field in the study array, much like that observed later in the field program. Instead, as we have noted in the historical perspective presented in Section 3, one of the most northerly and energetic intrusions was observed. This event significantly impacted the upper-ocean circulation in the study region.

In Section 4 the upper-ocean events were presented from a descriptive physical oceanography viewpoint using the available imagery, PIES altimetry, measured currents and drifters. The observed LC intrusion was remarkably complex, consisting of a large northern LC intrusion, LCE detachment, LCE reattachment, another LCE detachment, LCE splitting, another brief LCE reattachment, LCE separation and a modest retreat of the LC (see Table 4.1-1 for a detailed timeline). This scenario is far more complex than the canonical model. Quantitative estimates for event intensity, areal extent and propagation paths were included in the overview in Section 4.1, as well as some qualitative kinematic interpretation of the eddy-eddy and eddy-LC interactions, both cyclonic and anticyclonic. A more thorough investigation of the kinematics should be pursued in future studies and would benefit greatly by the addition of any available surface drifter observations.

Near-field eddy interactions, however, are likely not the controlling dynamics of the observed upper-ocean flow field, which was dominated by the very energetic LC intrusion and LCE shedding cycle. This section will attempt to interpret this complex upper-ocean flow in the dynamical framework of a shielded vortex instability (Flierl, 1988). This type of instability has recently been proposed as an explanation for a portion of the dynamics at play during LCE separation (Chérubim et al., 2005). This is not to say that all of the instabilities observed are of this type. Certainly, baroclinic instabilities that contribute to the twisting and tilting of the LC/LCE vortex system could be and likely are important during this very energetic process. The limited region of full water-column information, however, makes identifying baroclinic instabilities within the LC/LCE system difficult since most of the instability occurs outside the study region. Thus, the interpretation for this initial consideration of the upper-ocean circulation will be confined to upper-ocean observations available that can be related to the conceptual framework of a shielded vortex instability within the upper layer of the LC/LCE vortex system.

5.1.2 Instabilities, Upper-Ocean Cyclones and Eddies/Waves

5.1.2.1 Shielded Vortex Instability

The outer edges of the LC and LCEs are characterized by regions of sharp cyclonic shear that form belts or bands of cyclonic vorticity along the edge of the anticyclonic vorticity within the current or eddy. This cyclonic vorticity acts to "shield" the farfield flow from the induced circulation of the interior rotating current. In the idealized case of an isolated shielded vortex, the shielding completely surrounds the anticyclonic vortex and gives rise to complicated instabilities that control the evolution and ultimate fate of the vortex system (Flierl, 1988).

This cyclonic vorticity, or more properly speaking the positive potential vorticity (PV) anomaly, has been observed in measurements taken in the Yucatan Channel which show strong positive PV on the western side of the Yucatan Current that ultimately feeds the outer sheared band around the LC and its associated eddies (Candela et al., 2002). High-resolution model simulations clearly show these bands and have been used to identify instabilities that give rise to peripheral cyclones that are implicated in the LCE separation process (Chérubim et al., 2005). Candela et al. (2002) also posited a relationship between the vorticity fluxes due to horizontal shear and the behavior of the LC, with periods of cyclonic vorticity influx leading to the shedding of an eddy.

Direct observation of this vorticity is difficult, requiring closely spaced tall moorings as were deployed across the Yucatan Channel by the Deepstar Consortium (Sheinbaum et al., 2002) or sampling of the ocean with a dense PIES array. Neither the Exploratory Study tall moorings/PIES arrays nor the altimeter sampling has sufficient resolution to resolve the fine-scale PV around the LC. Nevertheless, both qualitative and quantitative information can be derived by analysis of the vortex structure within the flow. This can be done using satellite imagery in combination with the array, and altimeter observations in and around the study region to identify the temporal and spatial scales associated with growth of the instabilities along the LC and their associated intensities during the program.

An algorithm to identify vortex instabilities by modal decomposition of the local-layer thickness from numerical experiments has been described by Chérubim et al. (2005). The technique fits the azimuthal modes, which are centered on the LC/LCE in the deepest layer of the intruded LC, to examine the contribution of each mode to the spatial variance of the vortex system through time. The algorithm was validated by a test case on an *f*-plane system where it is known that the mode with the fastest growth rate is mode 4 and the vortex reaches a nonlinear quasi-steady state where the vortex system consists of an anticyclone surrounded by four cyclones. By applying the technique to a realistic simulation of a LC intrusion and LCE shedding cycle in the basin-scale high-resolution North Atlantic Miami Isopycnic Coordinate Ocean Model (MICOM), Chérubim et al. (2005) it was found that vortex rim instabilities contributed to the evolution of the LC and the eventual separation of a LCE (Chérubim et al., 2005). Similar analyses could be applied to PIES data or altimeter-derived SSH, or a combination of the two, however, that will have to be pursued in future work. Instead, for the present data based project, we will use this published model experiment to help us interpret and analyze the upper-ocean observations in this initial investigation of the complex upper-ocean dynamics observed during the Exploratory Study.

The nonlinear growth of the azimuthal modes 3 and 4 observed in the MICOM simulation produced configurations of three or four cyclones surrounding a nearly detached LCE within the intruded LC, early in the separation cycle. An example snapshot from the simulation (day 440 - Figure 10(d) in Chérubim et al. (2005)) is shown in Figure 5.1-1, alongside a similar configuration of the LC observed using altimetry on 1 June 2004. In the model, the peripheral cyclones are clearly observed both in the SSH and the velocity field in the deep LC layer. Thus, we can use remote sensing observations to infer the presence of the more energetic mode 3 and 4 instability modes by the number of LCFE or cyclones, and derive both qualitative and quantitative information on their temporal and spatial evolution.

5.1.2.2 LCFEs and Cyclones

LCFE and cyclones were described previously in Section 4. These features/observations will now be evaluated from an instability perspective. Note that chlorophyll concentration is a good proxy for the shear region and helps with tracking the cyclones on the periphery of the LC, although the signature tends to fade with time. Tracking is easiest in the summer, which was the time of the most energetic events. A cursory examination of the color imagery and SSH maps leading up to separation of Eddy Sargassum finds the intruding LC exhibiting the characteristic triangular or rectangular shape of mode 3 or 4 azimuthal modes, at several times before and during the program's field measurement effort. Most notable is the color image in Figure 4.1-11 showing the brief detachment of Eddy Sargassum in late May 2003, where the eddy took on the characteristic rectangular shape of a mode 4 dominated configuration.

In addition to the LCFEs that mitigated the brief dettachment between the LC and Eddy Sargassum, which are identified in the bottom panel of Figure 4.1-11, several other cyclonic features can be seen along the periphery of the LC in late May. Along the northern flank of Eddy Sargassum (see Figure 4.1-12), we have identified the color signature of the LCFE that passed through the PIES array in late May, and eventually became the strong cyclone that returned through the array and split Eddy Sargassum. This LCFE passed directly over mooring L1 on approximately 20 May 2005 (Figure 4.1-28), which shows that the LCFE had little or no surface thermal signature, yet was quite cold to depths down to 225 meters. The velocity structure of the LCFE was also primarily confined to the upper layer above 800 meters, which is characteristic of a lateral, shear-induced cyclone. Leading up to this time, there were some indications of baroclinic instability that may be seen in the evaluation of the surface stream function over the 1500-m depth pressure surface (as will be discussed in Section 6); however, it appears that the process decays with time along at least the western margin of the LC.

Along the northern margin of the LC, the LCFE gained significant cyclonic circulation. This not only happened to the LCFE in late May, but also to other LCFEs as they squeezed between the LC and the continental slope during this time period when the LC extended far into the northern GOM. These interactions increased the cyclonic circulation of the LCFE either by stretching of the water column advected across the continental slope, by diffusion from the lateral boundary (bottom relative to the slope circulation) and advection into the cyclone as the current interacted with the slope, or by wrapping up additional cyclonic shear along the margin of the LC in the upper layer through the lateral shear instability. Likely, it was a combination of all three. Ultimately, these effects contributed to the instability of the vortex system and the LCFE

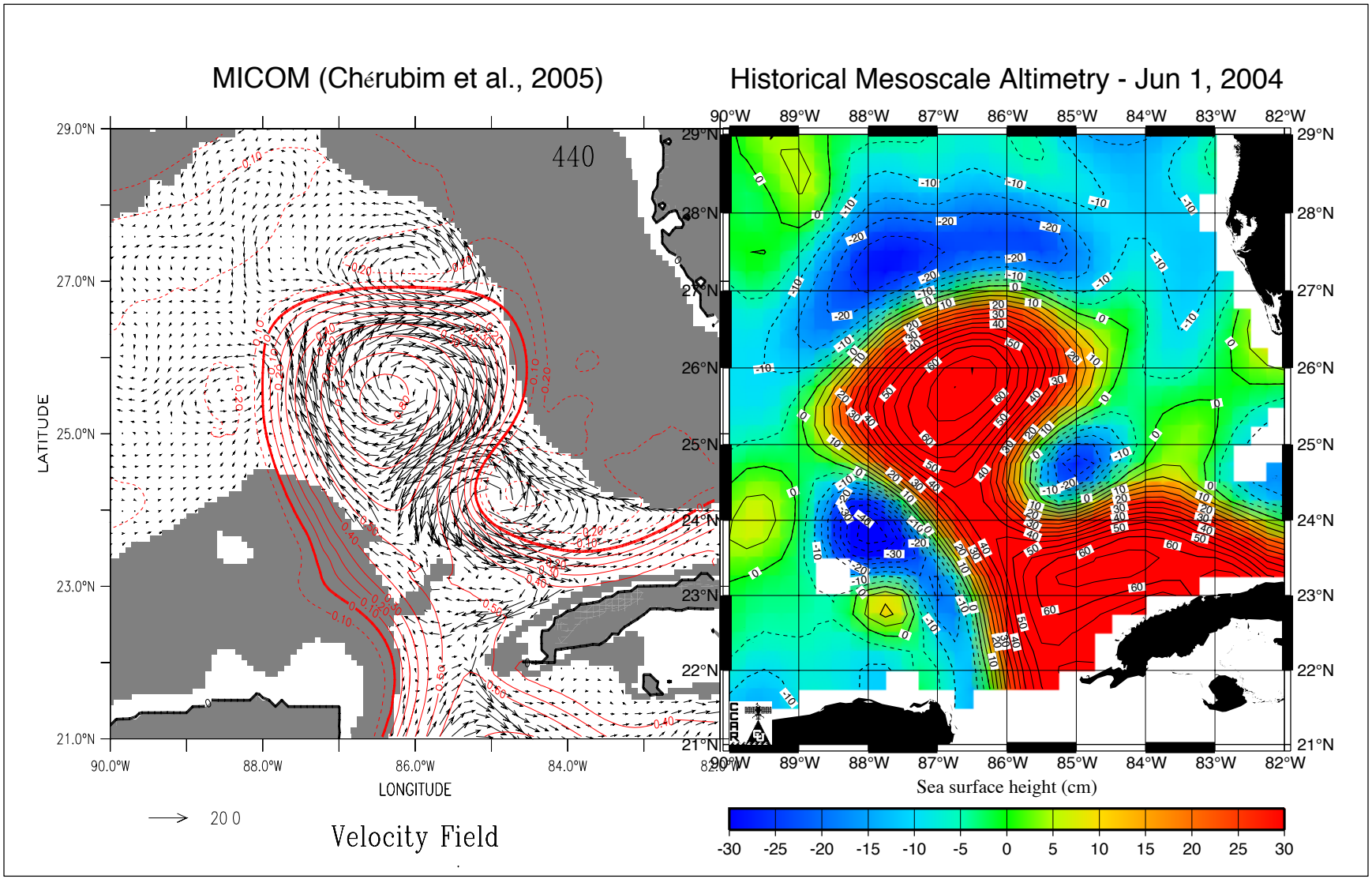

Figure 5.1-1. Example snapshot of the Gulf of Mexico from a the North Atlantic MICOM numerical experiment (Chérubim et al., 2005) alongside a similar configuration of the LC observed using altimetry on June 1, 2004.

increased in both area and intensity to become a large cyclone that interacted with the LC and Eddy Sargassum in a complicated, nonlinear fashion as described in Section 4.

Unlike a model simulation, in which the LC/LCE undergoes more axisymmetric growth and trapping of peripheral cyclones by topography [see the sequence of model snapshots in Chérubim et al. (2005)], the far northern intrusion of the LC during the field program changed the overall evolution and character of the instability. In the observed event, the topographic interactions along the northern margin acted as perturbations to the instability, and after that point the higher-order azimuthal modes were able to propagate freely clockwise around the periphery of the intruded LC front and around the southern periphery of the closed circulation of the embedded LCE. The abrupt topography can also act to block larger LCFEs/cyclones by preventing them from making the northern circuit around the LC. Topographic trapping does not appear to occur in this case. Instead, the cyclonic feature was stripped from the LC/LCE system and evolved independently over the continental slope of the north central Gulf. Zavala-Hidalgo et al. (2003) described this pathway in a study of Campeche Bank cyclones.

In the model, growth of the vortex rim instability leads to a deepening of the LC deep layer and a commensurate increase in the SSH of the LC/LCE. During this project, however, instead of a single deepening event, repeated deepening events were observed. The times associated with these events were identified by looking through the SSH maps for the LC/LCE center maximums associated with the instability-driven deepening scenario. These are shown in Figure 5.1-2. The first was on 2 June 2003 and was located near 26.5°N, 87.5°W. The SSH at the center was about 50 cm. The second occurred on 25 July 2003 and was located near 27°N, 88.5°W. The center maximum SSH reached over 55 cm. The time interval between the two maximums is 52 days, which is the same as the interval between the dates of the two detachments of Eddy Sargussum reported in Table 4.1-1. Recall that the transit time of the strongest cyclone, from exiting and returning back to the study array, was about 70 days. Thus, the time scales that could be involved in this evolving instability event range from periods of 50 to maybe as long as 80 days; and, possibly 12 to 27 days, if we divide by 3 or 4 to account for the peripheral disturbance caused by cyclones associated with the dominant instability modes. These periods are commensurate with the frequency bands of the observed TRWs and potentially provide a surface-layer forcing mechanism for the waves. The location of the deepening under the LC/LCE also agrees reasonably well with the backward ray path of the 61-day period TRW that will be discussed in Section 5.2.5 and is shown in Figure 5.2-11.

Note that this observed instability is not supercritical, which would have brought the vortex system to a new equilibrium state where the nonlinear interaction of the system is quasi-stable. Instead, we observe a nonlinear breakup of the system with the splitting of Eddy Sargassum and the eventual propagation of the cyclone involved in the splitting event directly westward along 26.5°N. A look at the thermal and velocity structure within the cyclone, as its center passes very near the L3 tall mooring on 26 July 2003 (Figure 4.1-30) and L5 on 11 August 2003 (Figure 4.1-31), shows a strong thermal signal and increasingly barotropic flow at depth. The deep pressure signal from the PIES array confirms this (see Figure 6.3-5), showing the deep pressure signature leading the upper ocean signal as the cyclone propagates into the array. This is discussed in more detail in Section 6.3. Interestingly, in animation the surface stream function over the 1500-m depth pressure surface shows that the lower-layer signal is not able to propagate past the Sigsbee

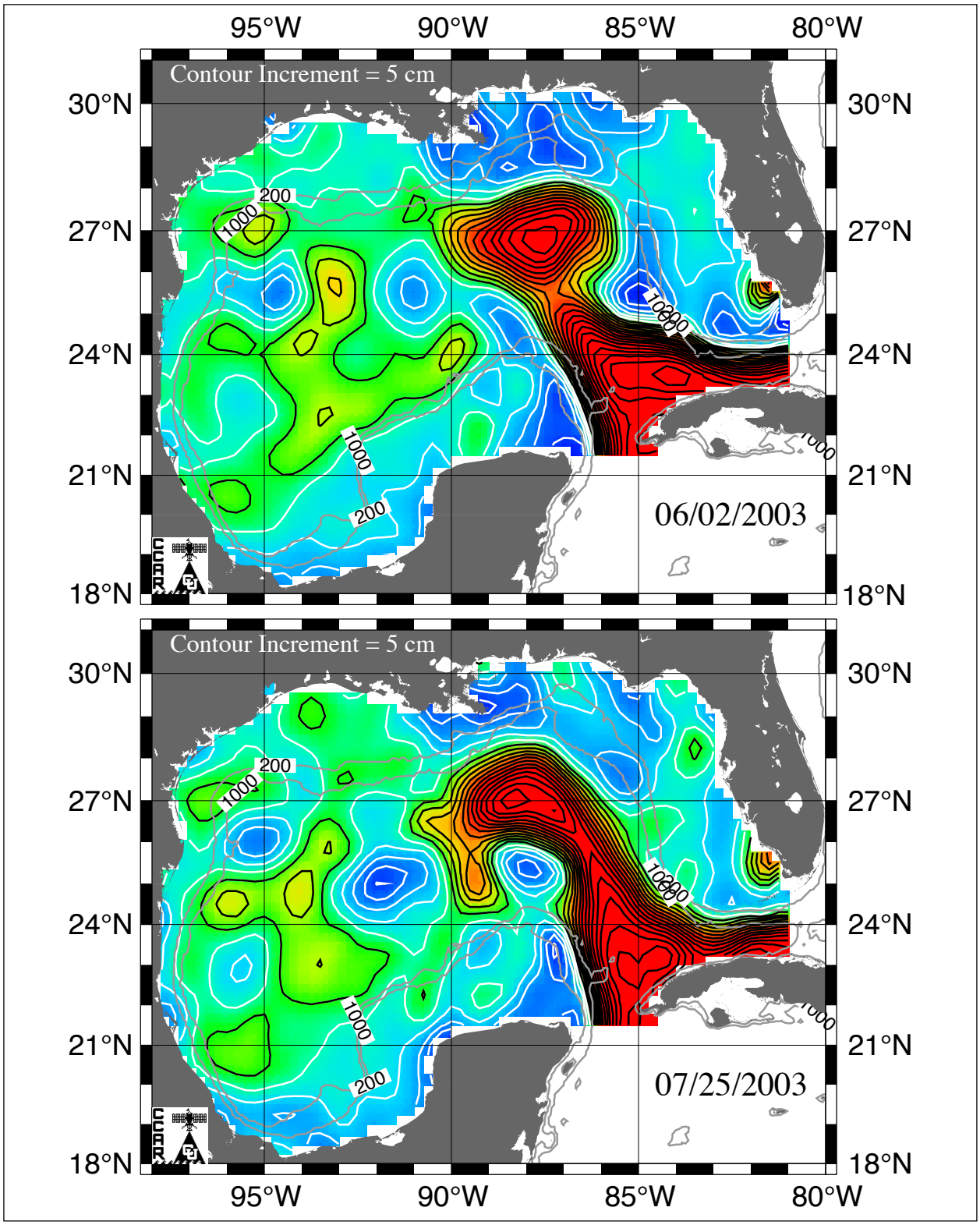

Figure 5.1-2. Altimeter-derived SSH maps from 2 June 2003 and 25 July 2003 at times when the LC/LCE center SSH reached a local maximum value. These values are about 50 cm and over 55 cm, respectively, and are located near 26.5°N 87.5°W and 27°N 88.5°W.

Escarpment as the upper-layer cyclone moves onto the slope. Thus, the cyclone returns to a more baroclinic upper-layer configuration before its propagation westward. When the cyclone center passes between moorings L2 and L4 on 25 August 2003, there is little evidence of any deep circulation associated with the eddy. The direct westward propagation of this baroclinic cyclone is considered further in the next section.

5.1.2.3 Eddies/Waves

Hovmöller plots of the altimeter-derived SSH along 27.5°N and 26.5°N, across the northern Gulf (Figure 5.1-3), show a large-scale perspective of the fate of the baroclinic cyclone after it left the study array. The area within the magenta box identifies the program field study and the PIES array extent. The intrusions along the western margin of the LC front into the eastern side of the array were clearly seen at both latitudes. These were caused by instability-induced perturbations associated with the clockwise rotation and detachment/reattachment and the elliptically shaped LCE within the intruded LC/LCE system. Intrusions not only occurred when there was a closed eddy circulation within the LC/LCE, but also as the LC penetrated northward and westward into the Gulf. The earlier intrusions, however, may have been forced by another mechanism.

The baroclinic cyclone described in the previous section is identified by the thick black line overlaid on the Hovmöller plot along 26.5°N. The westward propagation velocity was approximately 4 $km \cdot day^{-1}$ or about 4.6 $cm \cdot s^{-1}$. Note that there is a clear suggestion of a wave train emanating from the western boundary of the LC front at this latitude. To emphasize this wavelike character of the SSH field, we show lines corresponding to the same wave trough associated wotj the cyclone shifted by two months (60 days) backward in time for several earlier troughs. The distinction between an "eddy" and a "wave" in this case is somewhat artificial, so let us consider the characteristics of the wave field.

The phase speed of long nondispersive baroclinic waves as predicted by conventional Rossby wave theory is given by:

$$c_r = \beta R^2,$$

where R is the baroclinic Rossby radius of deformation. Using a value of R=33.34 km [which was calculated for 26.5°N, 90.5°W by Chelton et al. (1998)] the speed predicted by linear theory is 2.3 $cm \cdot s^{-1}$. In contrast, the observed speed was 4.6 $cm \cdot s^{-1}$, which is twice the predicted speed. Such "faster than predicted" propagation speeds are common at periods from 65-120 days for the nonlinear eddies/waves in the North Pacific (Kobashi and Kawamura, 2001). We can also make a rudimentary estimate of the wavelength using the area of the cyclone observed in the PIES array that we reported in Section 4.1 and by "eyeballing" the wavefield. Four times the cyclone diameter, estimated from the 6000 km^2 area, gives a wavelength of about 3.5 degrees at this latitude, which is in fair agreement with the trough-to-trough estimate made from the Hovmöller plot. Further analysis of these eddy/waves is warranted, but is not relevant to the Exploratory Study and will not be pursued in this report. The main point germane to this study, however, is the close correspondence between the frequency of the observed baroclinic waves and the 60-day TRWs identified in the study array, that suggests a common forcing mechanism which is well explained by the shielded vortex instability mechanism. One other point to consider is that the

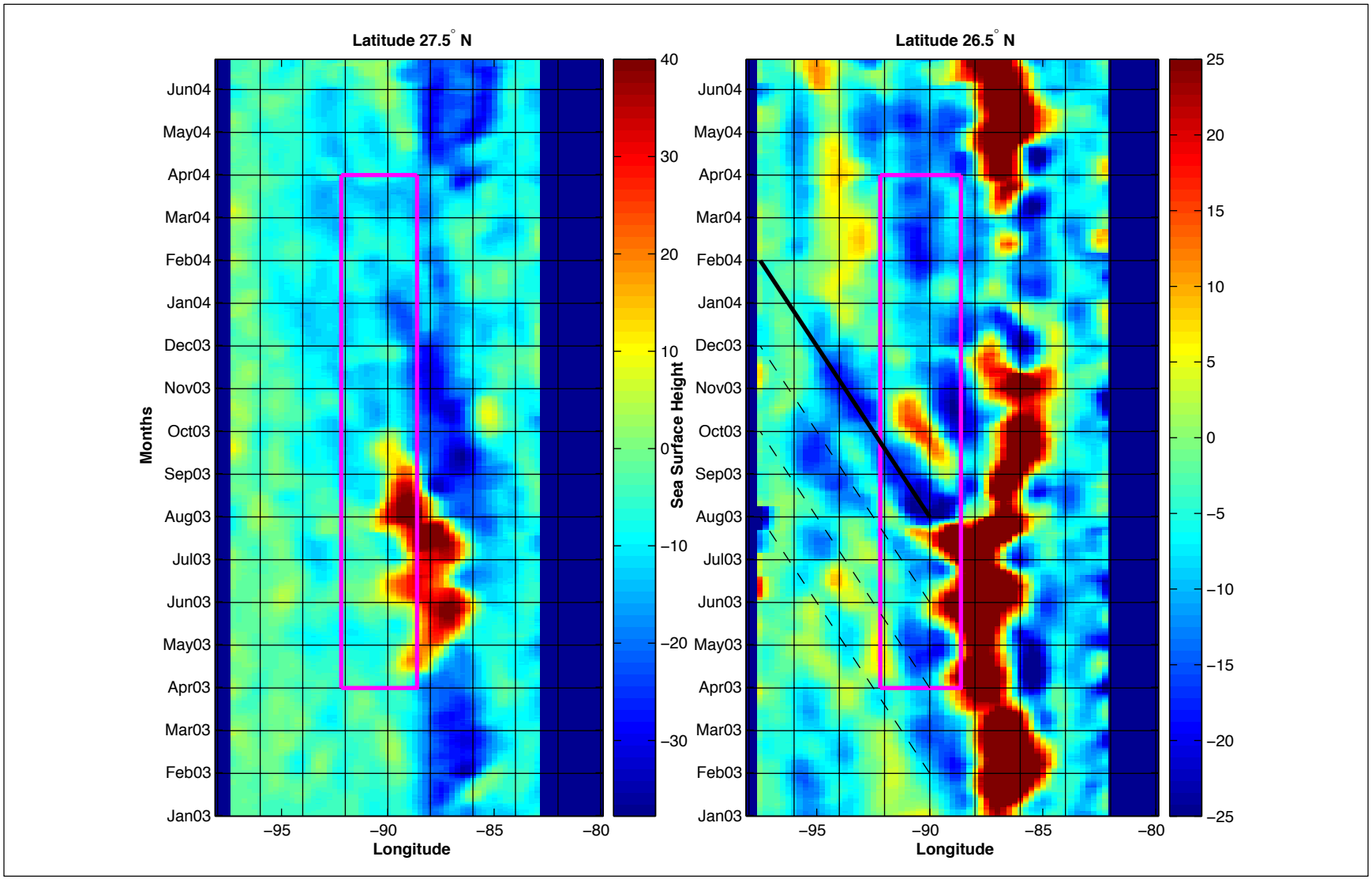

Figure 5.1-3. Hovmöller plots of the altimeter-derived SSH along 27.5°N and 26.5°N across the northern Gulf. The area within box identifies the program time period and PIES array extent. The thick black overlays the SSH trough associated with the westward path of cyclone that leaves the array after splitting Eddy Sargassum and Unknown.

propagating baroclinic eddy/waves along this pathway may have been a possible remote forcing mechanism for the study region occupied by the MMS-funded Survey of Deepwater Currents in the Northwest Gulf of Mexico.

5.1.3 PIES SSH Time and Space

Following the methodology of Hendry et al. (2002), the period corresponding to the frequency at which the cumulative power spectrum reaches 50% of the total variance – the half-power period, $T_{0.5}$ – was determined from the spectral analysis of each of the PIES SSH anomaly time series. $T_{0.5}$ is a more robust measure of time scale than the temporal autocorrelation zero-crossing, T_0, and is the preferred scale to be used to define the effective degrees of freedom of a time series (Fofonoff and Hendry, 1985). This robustness is due in large part to the global and integral nature of the $T_{0.5}$ metric, which is less sensitive to competing time scales within the time series. In contrast, the calculation of T_0 is a less robust measure because the first zero crossing of the temporal autocorrelation function is quite sensitive to the presence of multiple time scales and/or secular trends in the time series. The half-power periods were computed from the yearlong PIES SSH anomaly time series, with no detrending of the time series, so as to provide a realistic measure of the longer time scales of variability in the region that may have been associated with the LC and its eddy variability.

Spatial maps of the half-power, $T_{0.5}$, computed from the PIES barotropic, baroclinic, and combined signal SSH anomaly time series are shown in Figure 5.1-4. Mean values are listed in Table 5.1-1 showing the average time scales at all PIES stations and the averages for stations above and below the Sigsbee Escarpment. The mean values of the half-power period of the component and combined SSH signals were about 30% to 40% longer below the Escarpment than above.

Table 5.1-1

PIES SSH anomaly half-power period.

	Barotropic Signal	**Baroclinic Signal**	**Total SSH Signal**
Location	mean (days)	mean (days)	mean (days)
all stations	19	230	232
above Escarpment	16	188	195
below Escarpment	21	262	260

The barotropic signal half-power period was dominated by high frequency and large spatial scale variations corresponding to the most energetic mode of barotropic variability. This has been referred to as the "Common Mode". The common mode signal is clearly identified with mode 1 in the EOF analysis of the barotropic SSH anomaly that will be discussed in Section 5.1.4. In agreement with the EOF analysis, most of the barotropic half-power periods were in the range from 14 to 16 days, showing clearly that the common mode signal dominated the barotropic signals over the majority of the study region. In the south-central part of the array, below the Escarpment, the half-power periods ranged from 20 to 35 days, commensurate with one of the energetic TRW frequency bands, as will be discussed in Section 5.2.4.

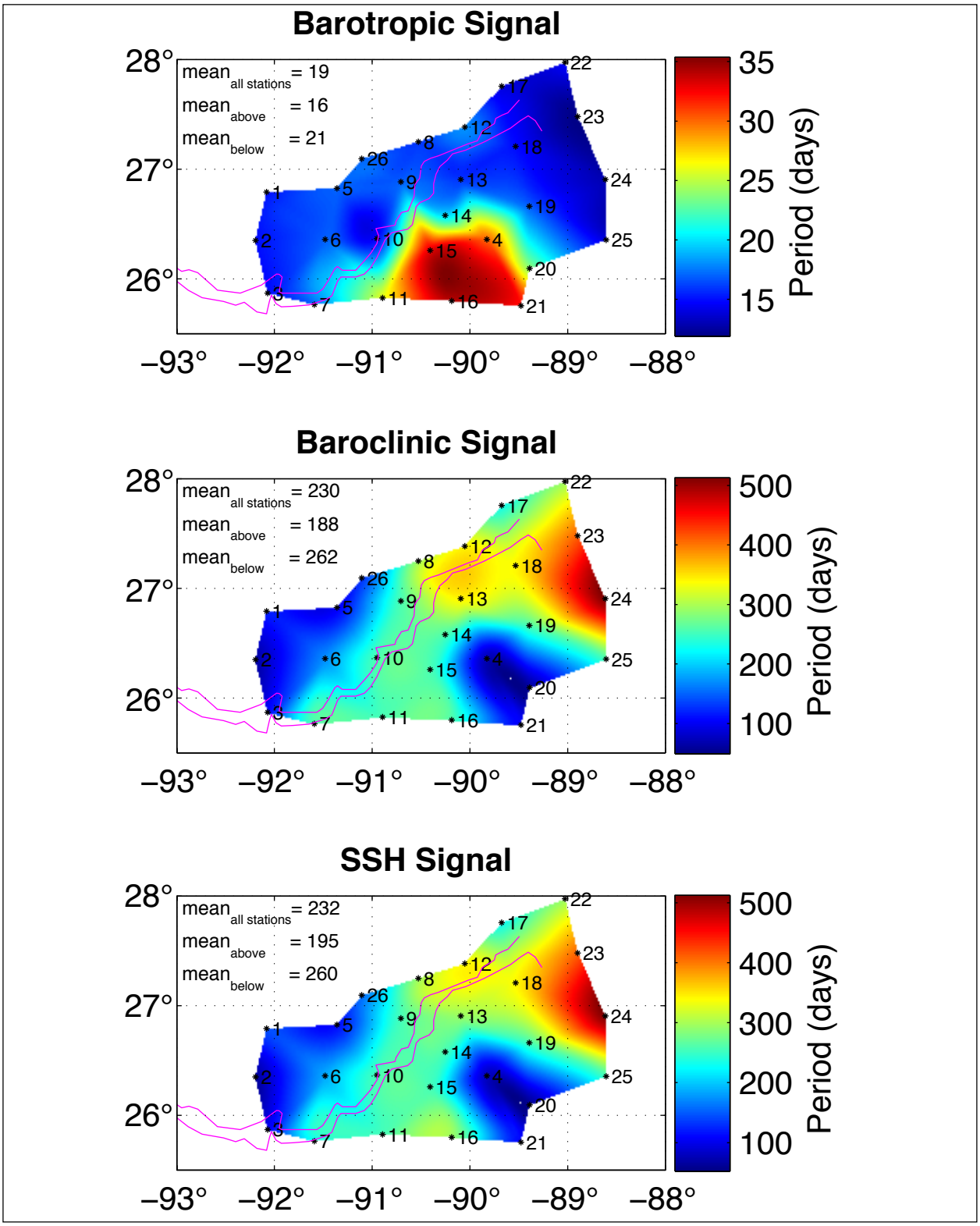

Figure 5.1-4. Spatial maps of the half-power, $T_{0.5}$, computed from the PIES barotropic, baroclinic, and combined signal SSH anomaly time series with means over all stations, and stations above and below the Sigsbee Escarpment.

Time scales of the baroclinic and combined barotropic and baroclinic SSH anomaly signals were very similar because of the small contribution by the barotropic mode to the total signal. The very long half-power periods associated these signals show the dominance of the low-frequency LC and LCE variability in the region during the study. These longer periods, 200 days and greater, were confined to the eastern part of the array and along and near the Escarpment. Regions with the shortest half-power periods, less than 100 days, were found to the northwest of the Escarpment and in southeast part of the array below the Escarpment. This signal likely arose from the higher frequency variability associated with eddies over the continental slope, and frontal eddies along the western margin of the intruded LC.

The spatial scales of the barotropic, baroclinic and the total SSH variability in the study region were examined by estimating the first zero-crossing of the spatial correlation function, L_0, from correlations of the PIES time series between stations as a function of distance between the stations. An array-wide spatial mean was removed from each of the PIES barotropic time series to allow estimation of the dominant scales independent of the common mode observed in the pressure record. Following Hendry et al. (2002), subjective estimates were made by over plotting a model correlation function on the scatterplot of correlation versus spatial lag, using an isotropic spatial correlation curve based on an autoregressive (AR) process (Thiebaux and Pedder, 1987) with the parametric form:

$$R(r) = \frac{1}{1+R_N}\left[\cos(ar) + \frac{c}{a}\sin(ar)\right]e^{-cr}.$$

The spatial lag, r, is the distance between two locations. The parameters, a and c, were selected to match subjectively the zero crossing and the negative correlation lobes observed at the larger lags in the scatter plots shown in the upper left plots in Figures 5.1-5, 5.1-6 and 5.1-7. The barotropic, baroclinic and total signal models were assigned a noise ratio, R_N, of 0.3, 0.09 and 0.09, respectively. To make this procedure more objective, a data adaptive smoothing of the correlation scatterplot was performed using a loess curve fit based on local regression (Cleveland, 1993). Loess parameters were selected to approximate reliably the AR model functions, and were the same for all cases even though the barotropic and baroclinic (and also the barotropic and total SSH signal) L_0 values differed by a factor of two when estimated over all station locations. The loess parameters used were: α=0.5, λ=2 with robust bisquare weighting, which corresponds to a local quadratic fitting within a half-interval smoothing window with bisquare reweighting applied iteratively until convergence. The loess parameters were held fixed and pair-wise correlations between stations were partitioned into those entirely above or below the Escarpment to estimate the dominant spatial scales above and below the Escarpment. The values extracted from the plots shown in Figures 5.1-2, 5.1-3 and 5.1-4 and converted to km are listed in Table 5.1-2.

The length scales were very large, approaching the dimension of the array for all of the signals. In the absence of the common mode, the length scales of the barotropic signal were about 100 km and were slightly larger above the Escarpment than below. The length scales of the baroclinic

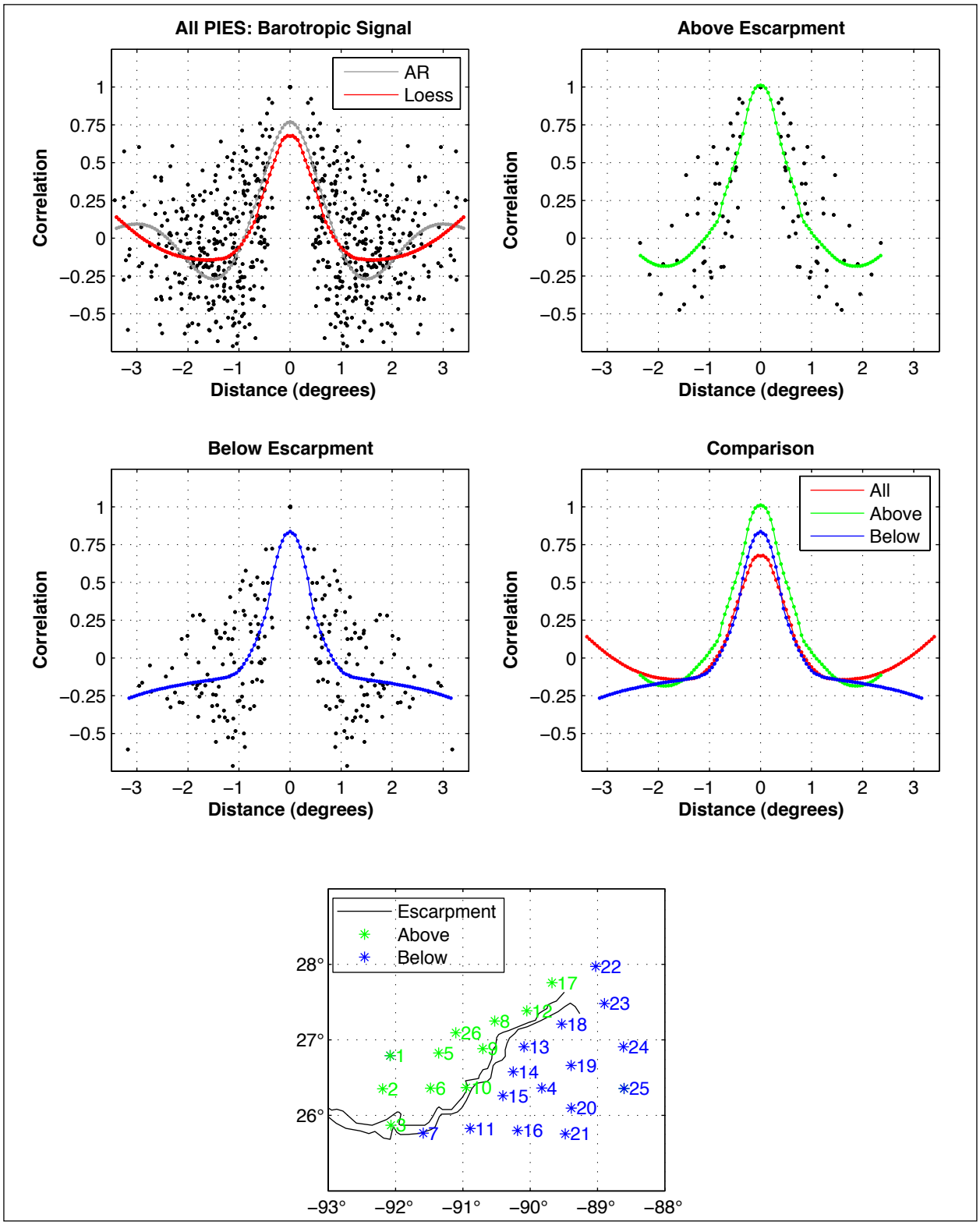

Figure 5.1-5. PIES barotropic SSH spatial-lagged correlation scatterplots and estimated correlation functions for all stations (upper left), station pairs entirely above (upper right) and below the Sigsbee Escarpment (center left), composite of loess-fitted correlation functions (center right), and station locations (bottom panel).

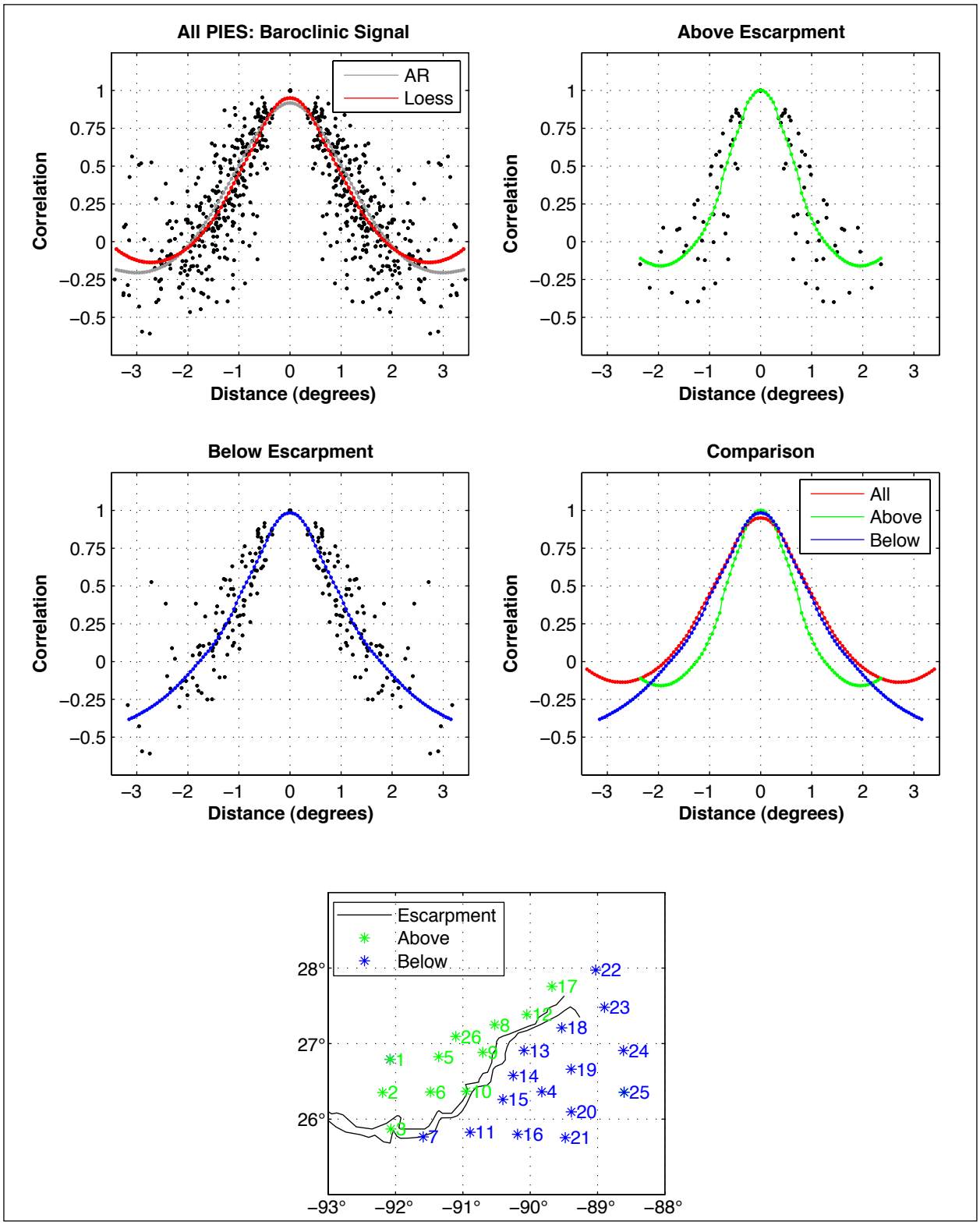

Figure 5.1-6. PIES baroclinic SSH spatial-lagged correlation scatterplots and estimated correlation functions for all stations (upper left), station pairs entirely above (upper right) and below the Sigsbee Escarpment (center left), composite of loess-fitted correlation functions (center right), and station locations (bottom panel).

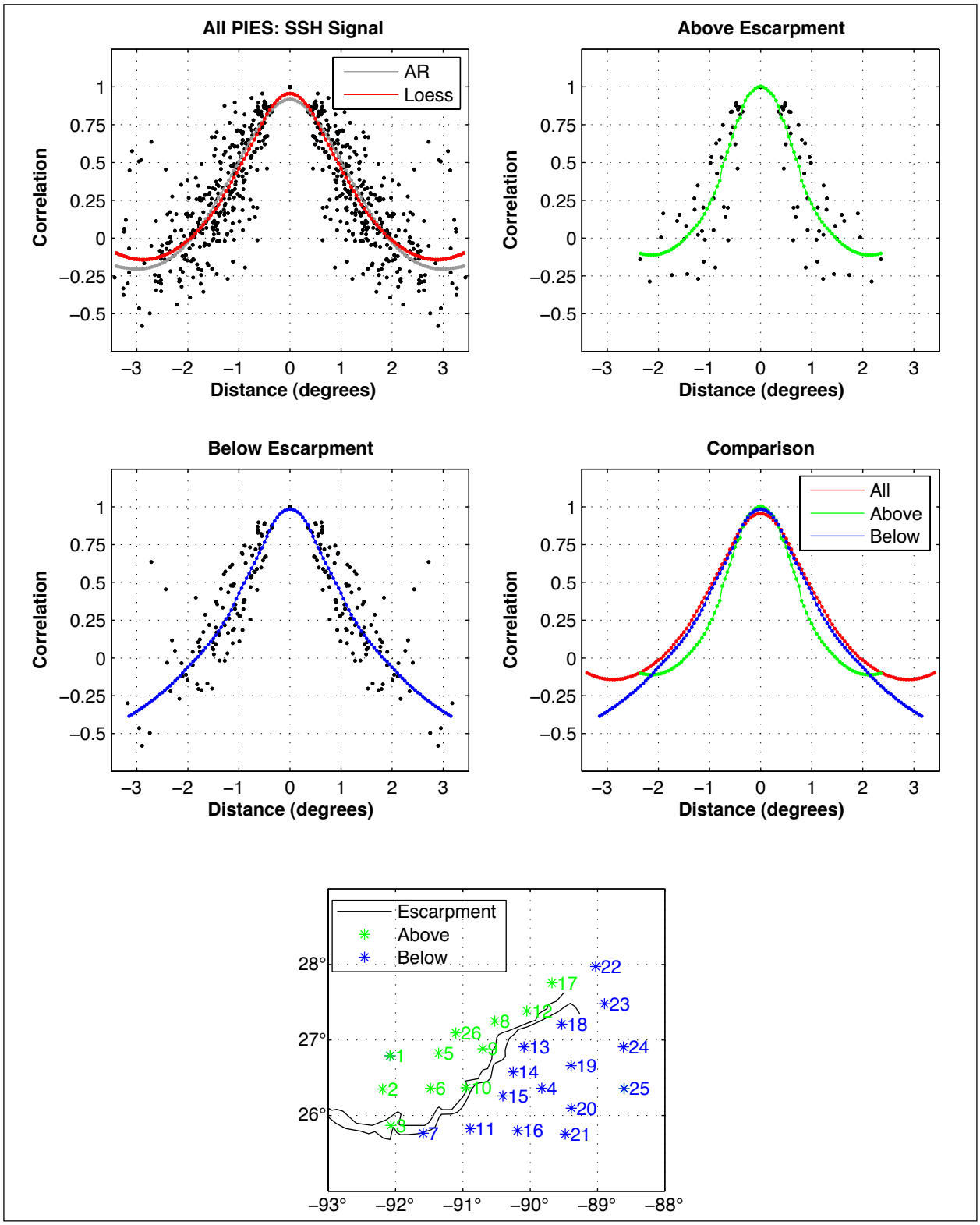

Figure 5.1-7. PIES barotropic plus baroclinic SSH spatial-lagged correlation scatterplots and estimated correlation functions for all stations (upper left), station pairs entirely above (upper right) and below the Sigsbee Escarpment (center left), composite of loess-fitted correlation functions (center right), and station locations (bottom panel).

Table 5.1-2

PIES SSH anomaly dominant spatial scales of motion.

	Barotropic Signal	**Baroclinic Signal**	**Total SSH Signal**
	L_0 (km)	L_0 (km)	L_0 (km)
all stations	95	205	215
above Escarpment	120	140	165
below Escarpment	95	195	200

SSH anomalies and the combined barotropic (including the barotropic common mode) and baroclinic SSH anomalies were about 200 km. These scales were longer below the Escarpment than above. A significant correlation existed for all the signals at the average nearest neighbor distance, which was about 50 km, showing that the PIES array was well designed to capture the dominant modes of variability in the study area.

5.1.4 EOF Analysis of Vertical Current Structure and Dynamic Height

As discussed in Section 4, the upper-layer currents were dominated by fairly slowly evolving eddy events. Therefore it is more appropriate to use time-domain EOF analysis to extract the dominant modes of the variability, rather than the frequency domain methods that are more suitable for wave-like flows. Complex EOF (CEOF) analyses (Munchow and Chant, 2000) of the currents at each mooring, using depth levels with about a 50-m spacing for the ADCPs along with the available currents from meters at deeper levels to 1000 m, were performed. The resulting spatial eigenvectors were rotated into the principal axes of the complex (u,v) amplitude time series following Merrifield and Winant (1989). The results are given in Figure 5.1-8 for the vertical structures, and Figure 5.1-9 for the normalized amplitude time series.

For each of the five tall moorings, the first mode accounted for between 83 and 94% of the total variance, and the vertical structures of the u and v components are similar at each site. The modes were surface intensified, decaying with depth to small amplitudes (< 10 $cm \cdot s^{-1}$) at 1000 m. The most rapid decay took place in the upper 200 to 300 m. The fluctuations were fairly unidirectional with depth, though this was not true for the mean velocity profiles, which were similar to the means discussed in Section 4.1.2 and Figure 4.1-33. The vertical structures at the eastern side of the array, L1 and L3, show that the largest near-surface amplitudes were about 50 $cm \cdot s^{-1}$. The western moorings all had similar near-surface amplitudes even though L2 was more influenced by cyclones than L4 and L5. The dominance of cyclones at L2 is, however, reflected in the more depth-independent mean profiles that have a sub-surface maximum around 200 m. Another noteworthy difference between the east and west moorings is that the principal axis of the fluctuations were approximately aligned with the mean in the east, whereas at L2, L5 and L4, the fluctuations were approximately perpendicular to the average direction of the means. The implications are that upper-layer eddy flows had fluctuations that can be described by a simple surface intensified shape function.

The time-dependent, normalized amplitudes for each of the moorings (Figure 5.1-9) were generally fairly incoherent with each other. This is to be expected since the moorings were

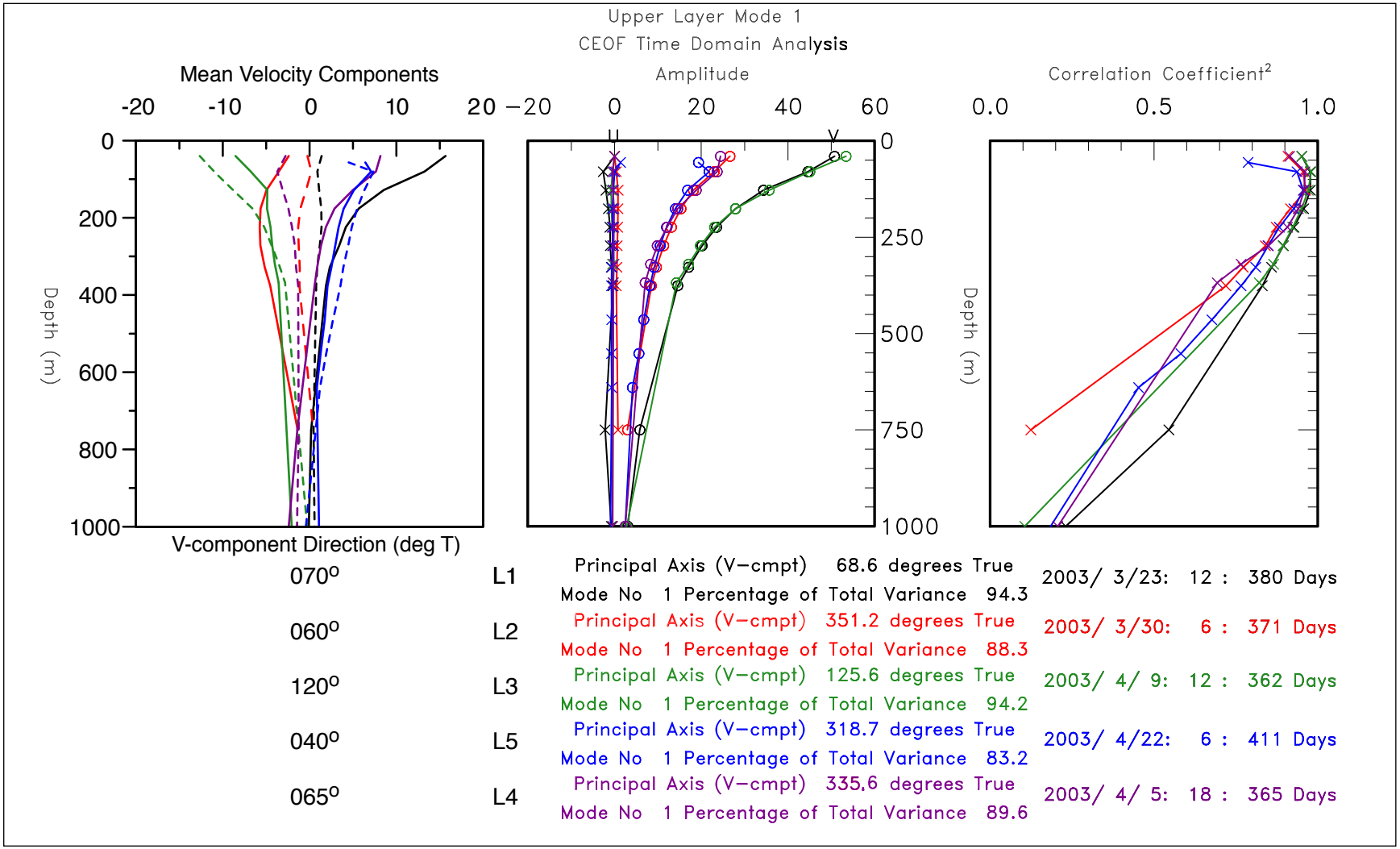

Figure 5.1-8. CEOF analyses of the vertical mode 1 structure of upper-layer 40-HLP currents from the tall moorings L1-L5. Left panel shows mean U (dashed) and V (solid) velocity components (cm•s^{-1}) where the direction of the V-component is indicated. Middle and RH panels show the amplitudes (cm•s^{-1}) of the (U,V) components where the V-component is directed along the major principal axis, and the correlation coefficient squared of the velocity record with the mode, respectively. The results from each mooring are color coded as indicated.

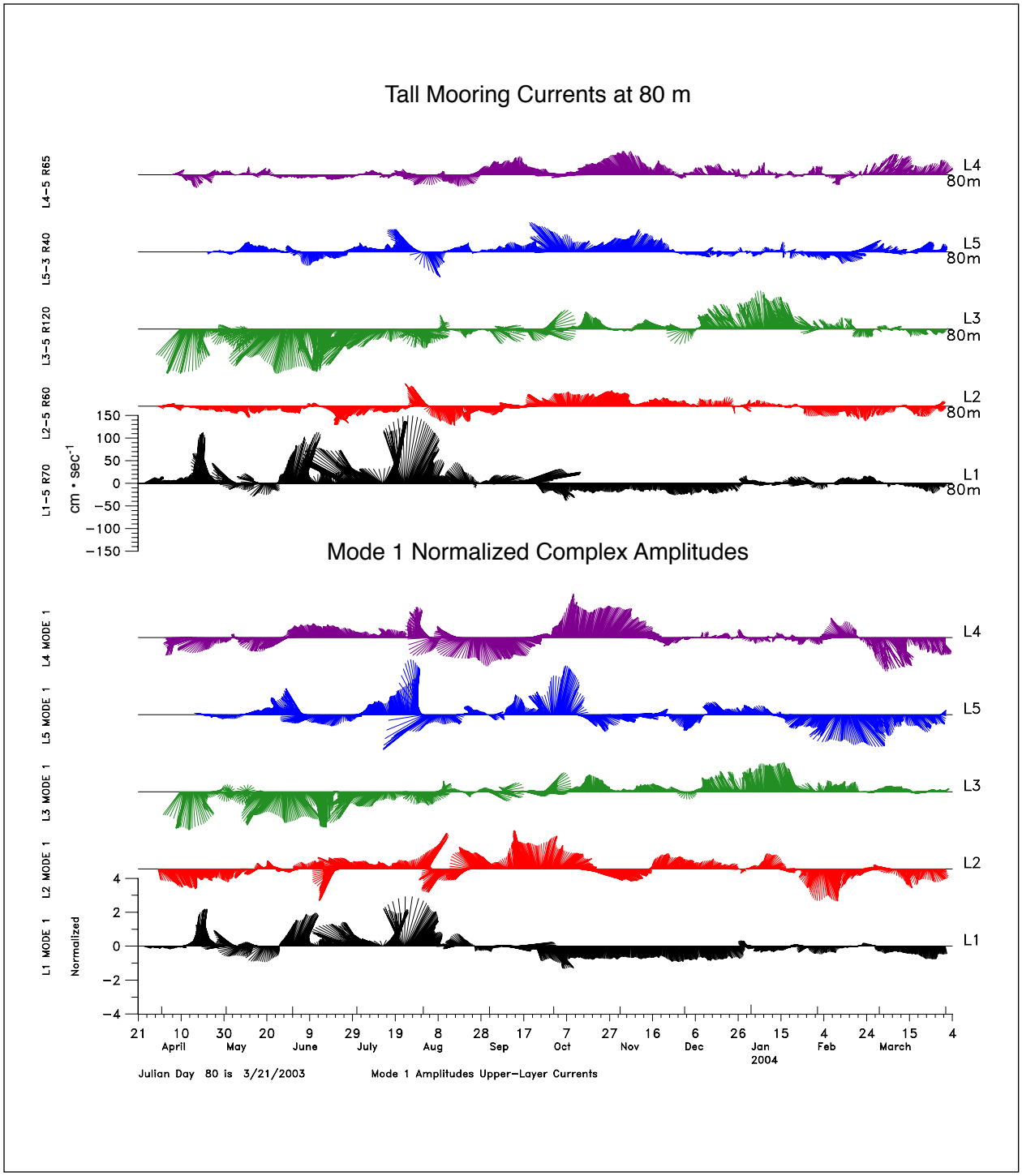

Figure 5.1-9. Time series of complex mode amplitudes from CEOF analyses of 40-HLP upper layer currents from moorings L1-L5. The modes have been normalized and rotated into their principal axis coordinates. Current vectors from the 80-m level records are given in the top panel. Time series are color-coded as in Figure 5.1-8.

further apart than the typical scales of eddies that move through the array. The relationship of each amplitude time series to the observed currents at 80 m is quite clear, even though the principal axes and measurement coordinate directions do not always correspond. Since the vertical current structures in the upper layers can be largely accounted for by one mode, the horizontal structure can be examined using more highly resolved measurements such as SSH. The resulting horizontal patterns can be assumed with some confidence to apply to most of the upper-layer water column.

A time domain EOF analysis was performed using the baroclinic SSH anomaly derived from the PIES array. The purpose was to determine the primary spatial and time scales of the upper-layer eddy circulations that were resolved by the array. The first two modes are significant by the North et al. (1982) criteria, and account for 72 percent of the total variance of the baroclinic SSH signal measured by the PIES. The spatial patterns (Figure 5.1-10) show that the major east-west scales, or wavelengths, were similar to the array's extent for the first mode and slightly larger than the extent for the second mode. The north-south EOFs have scales that were twice the order of the array's dimension, but this still allowed adequate resolution of the major eddy signals. Again, the first mode had slightly smaller scales than the second. The patterns were well resolved by the array spacing.

The first mode had a large amplitude signal on the eastern side of the array, which dominated in the June to September 2003 interval and then fades away in the second six months of the study. This was clearly the major response to the intrusions of the LC and appearance of Eddy Sargassum. During the first part of this mode, from April to July 2003, the second mode was negative and thus represents the cyclonic activity that occurred along the western side of the LC/LCE. Because the modes are orthogonal in time and space, this indicates that the cylones in the center of the array that had large spatial scales were not directly coupled to the mode 1 eddy signal. But they were connected to the subsequent southwest translation of the eddy along the Escarpment that is represented by the positive mode 2 amplitudes after September 2003. Over this later interval, the strong cyclonic circulations appeared on the eastern side of the LCE. Thus, the dominant spatial scales of both the cyclones and anticyclones were large (~ 100 – 200 km) and similar to length scales of the array. Time scales of the signals were also long, ranging from about one to several months.

The barotropic part of the SSH anomaly contains signals that relate to depth-independent current fields over the full depth of the water column. The amplitudes of the barotropic SSH fluctuations were about 10 percent of the baroclinic signals. The space and time-dependant components of the first two significant EOF modes, which account for 76 percent of the total variance of the barotropic SSH anomaly, are given in Figure 5.1-11. The oscillations of the first mode had similar amplitudes over most of the array and consist of a 14- to 16-day signal imposed on a semi-annual, longer-term variation. The shorter-period oscillations appear in the bottom-pressure records. This is being called the “Common Mode” (see Section 4.2.3), and because strong horizontal gradients did not arise, a similar signal was not observed in the currents. The semi-annual signal was most likely related to the steric seasonal heating and cooling cycle. The second mode was confined to the region south of the Escarpment. The spectra and amplitude time series indicate that this mode mainly consisted of long-period oscillations of between ~ 25 and 60 days. This corresponds to longer-period TRWs, that are

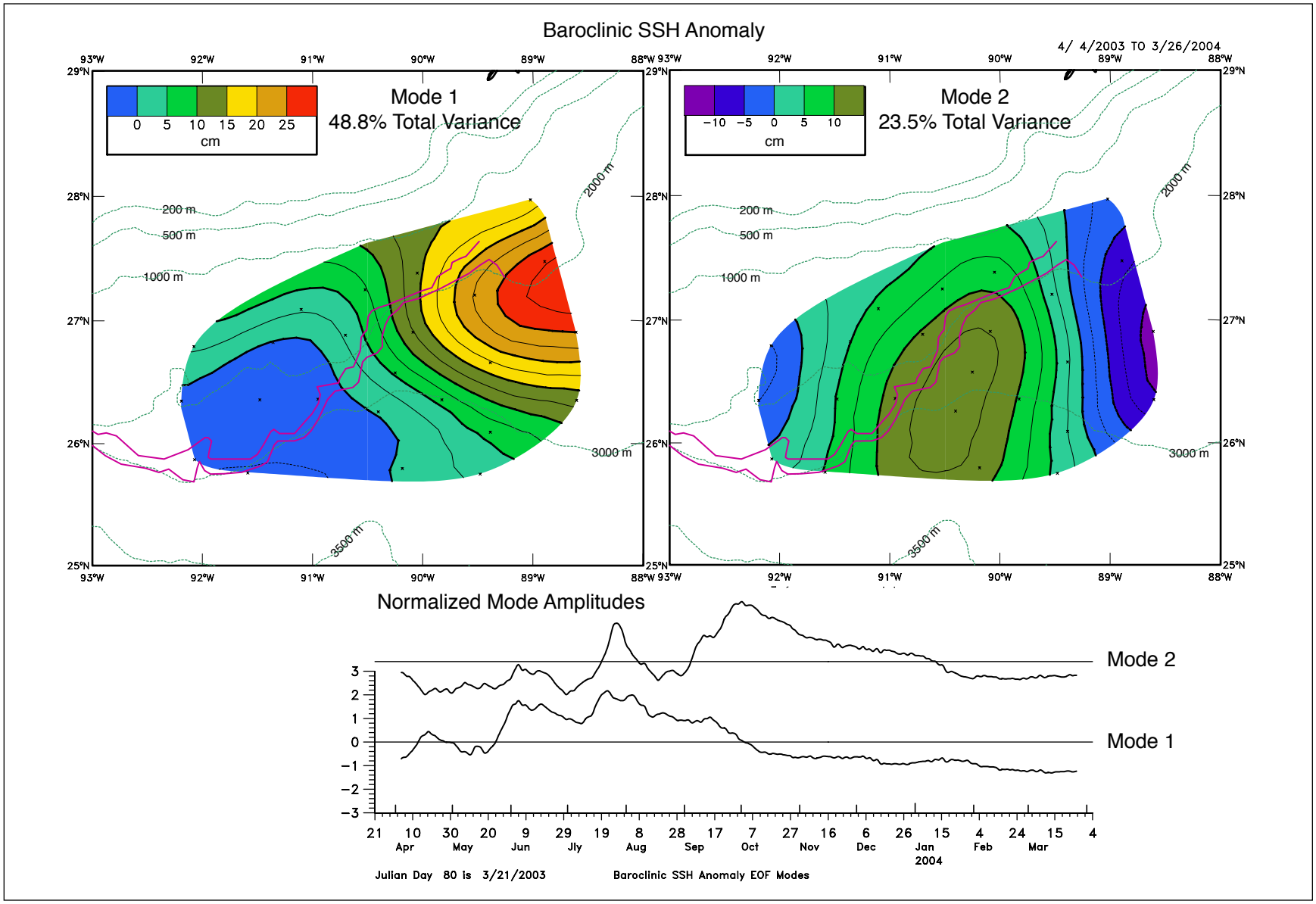

Figure 5.1-10. Modes 1 and 2 spatial eigenvectors (top panels) and time-dependent normalized amplitudes (bottom panel) from a time domain EOF analysis of the baroclinic sea surface height (SSH) anomaly from the PIES array.

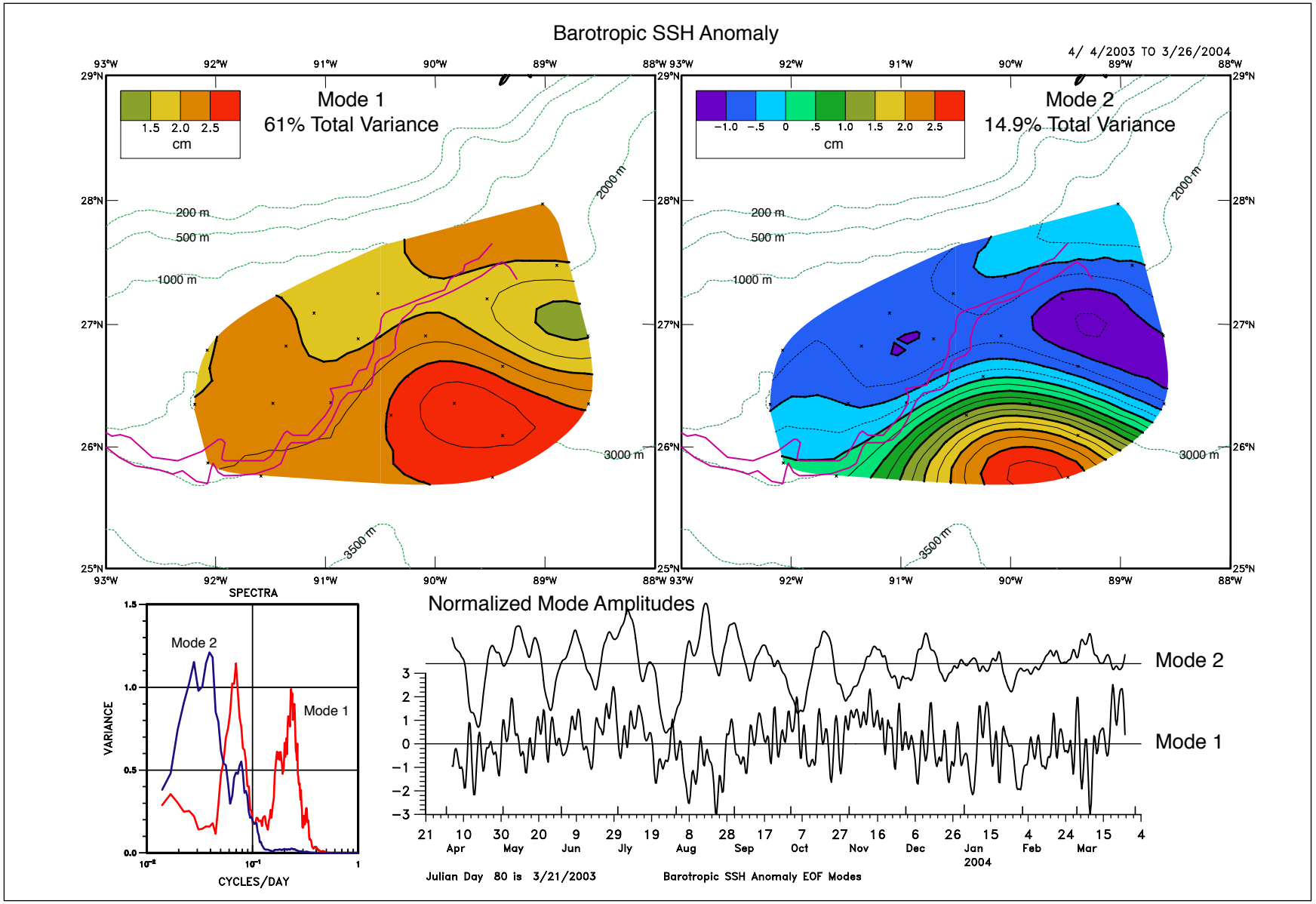

Figure 5.1-11. Modes 1 and 2 spatial eigenvectors (top panels) and time-dependent normalized amplitudes (bottom right panel) from a time domain EOF analysis of the barotropic sea surface height (SSH) anomaly from the PIES array. Spectra of the normalized amplitudes are given in the bottom left panel.

discussed in the next section, which were also confined to the deep water of the southern part of the array. This seems reasonable because longer-period TRWs are less bottom trapped and therefore more barotropic, and thus are present as a small part of the SSH signal. This implies that the longer-period deep TRW motions may have been observable from measurements of SSH.

5.2 Lower Layer

5.2.1 Time Scales of Deep Currents

The description of the lower-layer currents, below 1000 m, in Section 4, emphasized the change in character of the variability from east to west, and the decrease in variance from below to above the Escarpment. Previous deep current measurement studies have interpreted lower-layer fluctuations as TRWs (Hamilton, 1990; Hamilton et al., 2003; Hamilton, In press), and these measurements also have the same characteristics. Thus, motions were highly coherent through different depth levels, were bottom intensified, and the principal major axes of variance were at an angle to the local isobaths. The frequency content of the lower-layer currents are given by the kinetic energy spectra in variance-preserving form, where equal areas under the curve represent equal contributions to the KE (Figure 5.2-1). The spectra were calculated for 12-month long records, and have been grouped such that moorings in the same vicinity are given in a single plot and the plots, are roughly arranged like the array. The groupings are given in Figure 5.2-2. Where more than one depth level was given for a mooring (e.g., O4, M2, M1, N5, O1, G2 and L3), the deeper level always had higher variance at major spectral peaks indicating that the majority of the motions were bottom intensified, as predicted by TRW theory (Rhines 1970). Most of the spectra also show a sharp decrease in energy at higher frequencies. This corresponds to the cut-off frequency, which is a function of bottom slope. TRWs are not dynamically possible at frequencies higher than this cut-off, which ranges from about 7 to 14 days, where the longer periods correspond to the gentler slopes of the abyssal depths below the Escarpment (e.g., O2 and Q2) and the shorter period to the steeper slopes (e.g., M1). A number of spectra show some peaks at periods shorter than 10-days (e.g., M3 and M2), but these are clearly harmonics of the major low-frequency peak. The presence of these harmonics at stations near the Escarpment could indicate that the fluctuations were becoming non-linear in the vicinity of the steep slope.

Energy decreased from east to west and deep to shallow. Therefore, the group 1 moorings (O4 and N6) had the lowest KE, and L4 and O3 are less energetic than L3 and O1 (groups 6 and 7). The spectral content also varied across the array in that different period fluctuations dominated at different positions. M1, which was not far (23 km) from the I2 mooring (Hamilton and Lugo-Fernandez, 2001; Hamilton, In press), deployed from August 1999 to September 2001, also showed high-speed bottom currents and the majority of the energy was at periods of 8 to 10 days. Further south at O1 and L3, the dominant period motions shifted to ~ 12 to14-day periods. However, L3 also had spectral peaks at 16-20 days and ~ 40 days. The 40-day peak was the only one present at L4, and the group 5 spectra plots show a shift in the dominant peak from short to long periods as the locations shifted from the southeast (L3) to the southwest (L4) corners of the array. Similar shifts are seen in group 3 between the deep water at O2 (~ 30 days), N3 (~ 16 days) and M2 (~12-14 days), which was at the base of the Escarpment. Comparing S3, which was in the middle of the Escarpment (group 5), and S5, which was at the top of the Escarpment

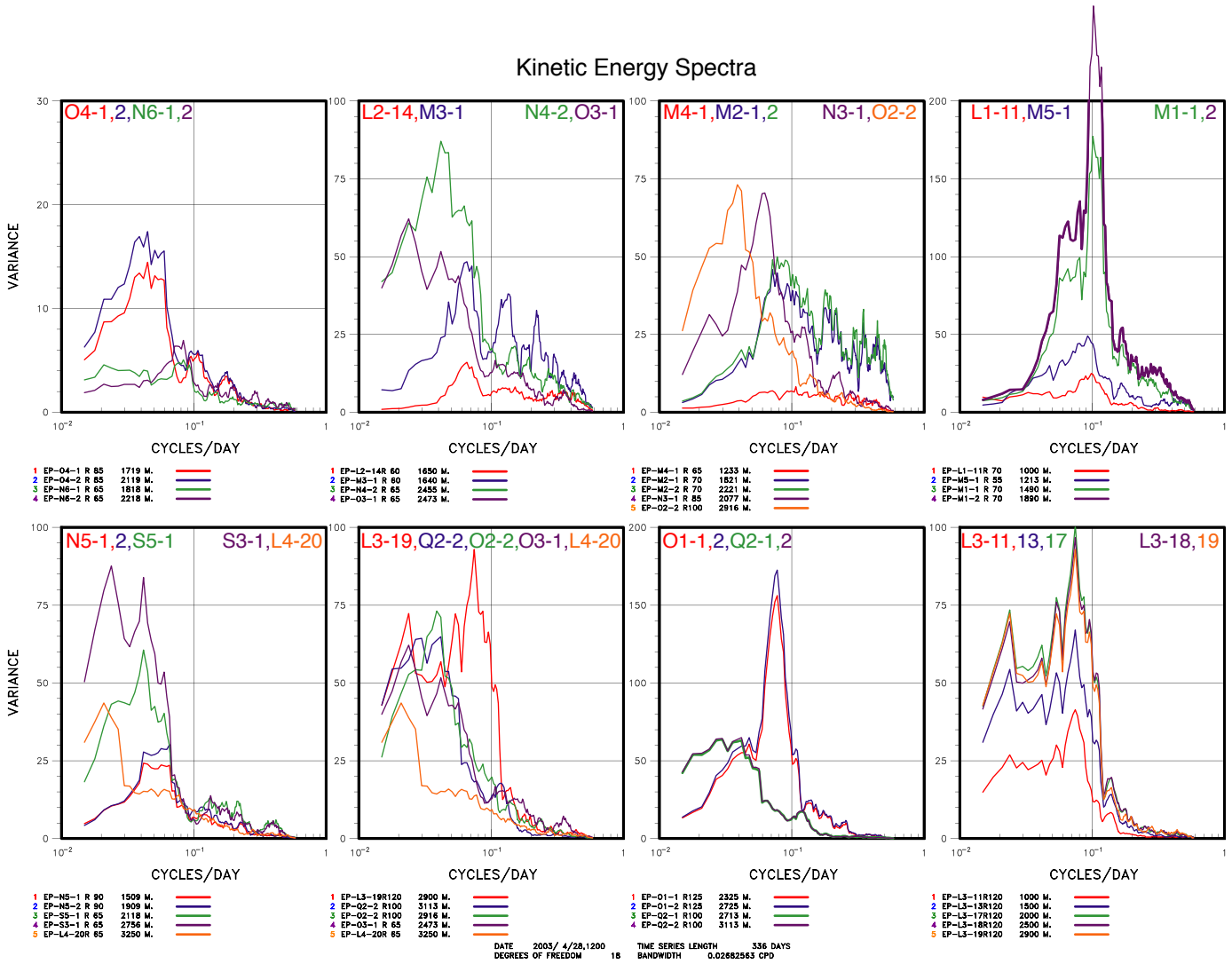

Figure 5.2-1. Kinetic energy spectra in variance preserving form for selected lower-layer 40-HLP current records. The plots group moorings in the same geographical vicinity and are arranged west to east (left to right) and north to south (top to bottom). Plot at bottom right is spectra from lower layer at Mooring L3.

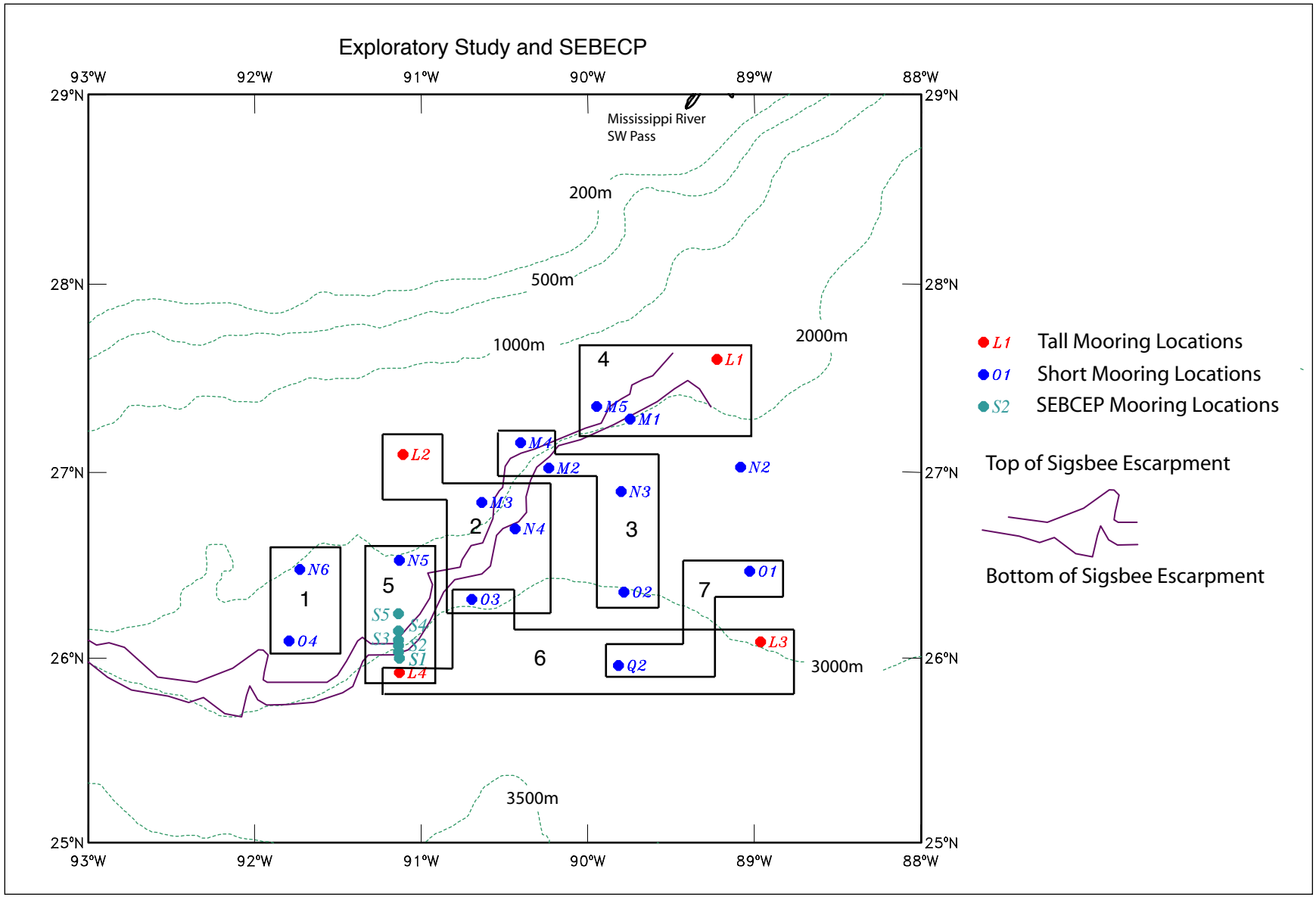

Figure 5.2-2. Groupings of the moorings used for the KE spectra plots in Figure 5.2-1. The number corresponds to the plots going from left to right and top to bottom.

and less than 9 km away, it can be seen that both had a peak around 25 days, but S3 had a lower frequency peak with a period ~ 40 days that was barely present at S5. Thus, the Escarpment appears to have been a filter for longer period motions as well as an impediment to energy transmission into shallower water. As a consequence, periodicities of the fluctuations depended on the location of the records, and both the east-west position and the position relative to the Escarpment were important. This is further illustrated by Figure 5.2-3, where the spectra from all available records from the tall moorings seaward of the Escarpment, are given. All the spectra show bottom intensification (the 2925 m level at L5 was within the frictional bottom boundary layer), however, the intensification was much greater between 1000 and 2000 m than below 2000 m. This is presumably because the Brunt-Väisälä frequency decreased with depth and was very small at great depths. For these three moorings, the highest energy was observed at L5 and had a spectral peak at 25-30 days that was not present at L4 and only weakly present at L3. Moreover the 40-day peak at L5 was also more energetic than at L4. Thus, in the 56 km between L5 and L4, the low-frequency fluctuations had diminished, and the higher frequency fluctuations (including the 12 to 14-day period motions at L3) were absent from the L4 record.

The detided and detrended bottom-pressure anomalies measured by the PIES were directly related to the lower-layer currents through geostrophy. Therefore, the spectral content of the bottom-pressure anomaly should be similar to that of the currents. However, the bottom pressure contains the 14 to 16-day signal of the Gulf common mode that was energetic in the sea-level variability, but did not generate fluctuating currents because amplitudes and phases were similar over the spatial extent of the array. Therefore, to remove this large signal, a spatially averaged bottom-pressure anomaly time series was subtracted from each of the individual PIES pressure anomaly records. This effectively removes this dominant 14-16 day signal (Figure 5.2-4) and the spectra show similar peaks to those of nearby current records (compare Figure 5.2-3 with 5.2-4). These “demoded” spectra can be also used to study spatial coherence patterns (see Section 5.2.4).

The complex spatial distribution of dominant periods argues for bottom motions being controlled by dispersive TRWs of different fundamental frequencies, propagating along different characteristic paths that originate from undetermined LC processes further to the east. A translating eddy model in which cyclones and anticyclones translate southwestward along and adjacent to the Escarpment does not explain the inhomogeneous distribution of spectral peaks, as it would produce similar time series of currents all along the Escarpment and thus similar spectra. Based on this consideration, the spatial analysis of the distribution of coherent fluctuating currents has been divided into four frequency bands:

1. 0 – 0.03 cpd (335 – 33 days); e.g., dominant at L4.
2. 0.03 – 0.058 cpd (33 – 17 days); e.g., dominant at O2.
3. 0.058 – 0.09 cpd (17 – 11 days); e.g., dominant at O1.
4. 0.09 –0.14 cpd (11 – 7 days); e.g., dominant at M1.

The frequency domain EOF analysis for the bottom currents, using these frequency bands, is discussed below.

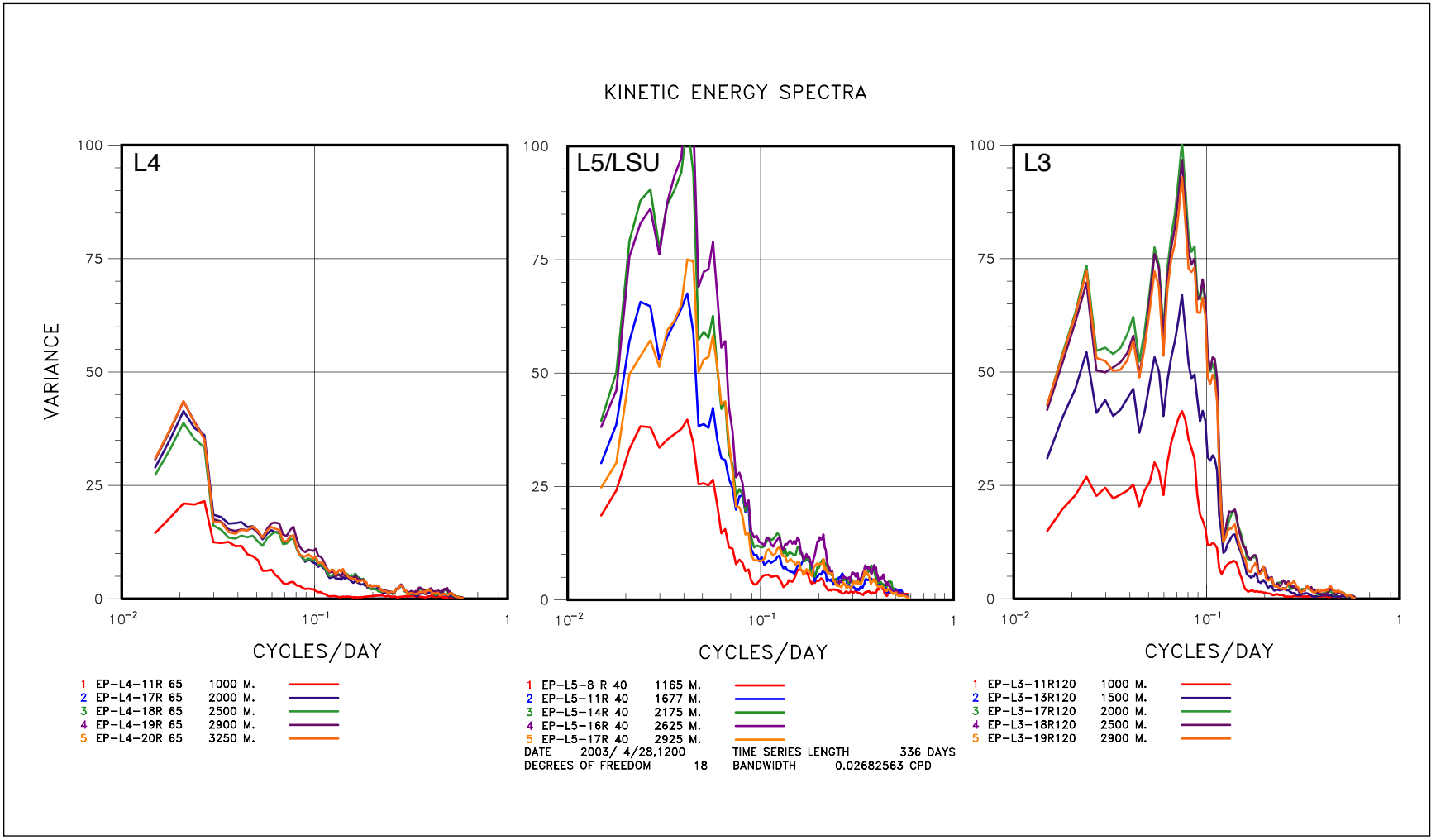

Figure 5.2-3. Kinetic energy spectra of 40-HLP currents at selected depths below 1000 m for the tall moorings L4, L5 (LSU) and L3.

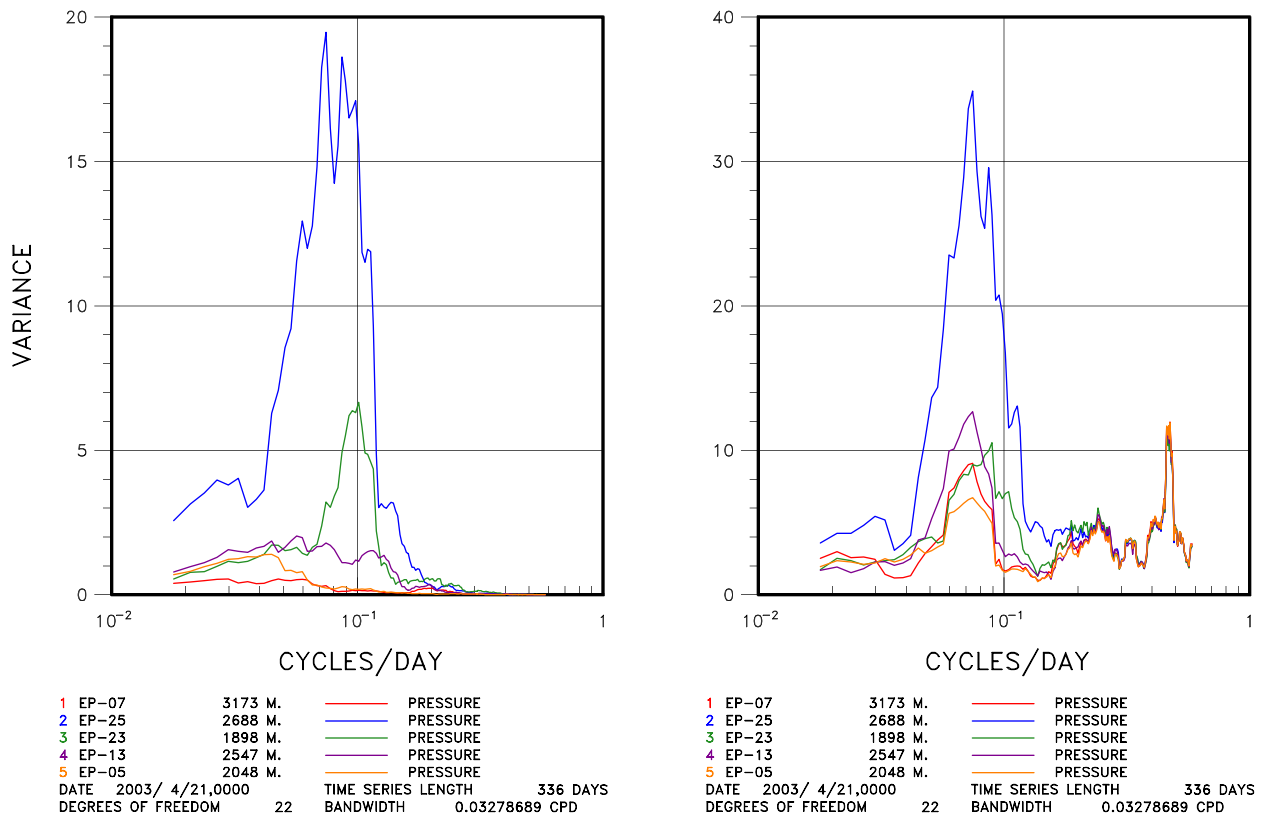

Figure 5.2-4. Spectra of bottom pressure anomaly from selected PIES. Left hand and right hand panels show spectra with and without the spatially averaged common mode removed, respectively. Note the change in scales.

5.2.2 Vertical EOF Analysis of Lower-Layer Currents

The vertical structures of current fluctuations in each of the four frequency bands, identified from the spectral analysis, were obtained for two moorings below the Escarpment. All the instruments with 12-month long records below 750-m depth were included in the EOF analysis. For each of the frequency bands, the first mode accounted for a large fraction (74 to 92%) of the total variance at each mooring. The vertical modes are given as amplitude ellipses in Figure 5.2-5, where the arrowheads show the relative phase of the motions. The similarity both in the direction of the principal axes and relative phase with depth, and the high percentage of the total variance accounted for by a single mode, confirms the high visual coherence of flows through the lower water column. In the southeastern corner of the array, at L3, the major axes turned clockwise as the frequency increases such that highest frequency band was almost at 90° to the lowest frequency band. This is a characteristic signature of TRW motions (Thompson, 1978; Hamilton, 1990). The direction of phase propagation is normal to the fluid particle displacements (i.e., the direction of the major axis) such that the phase vector has a component along the isobaths where the shallower water is on the right. All the ellipses at L3 conform to the TRW model in this respect if the phase vector was directed into deeper water. Because the group velocity vector was ~ 90° to the right of the phase vector (Oey and Lee, 2002), this implies that the source region for the waves was further to the east and in deeper water for all four frequency bands.

In the southwestern corner, at L4, only the two lowest frequency bands had significant amplitudes, as indicated by the spectra in Figure 5.2-3. The lowest frequency band had highly rectilinear fluctuations that were approximately parallel to the steep slope of the Escarpment, and had similar but smaller amplitudes to that at L3 (Figure 5.2-5). However, the much weaker fluctuations in the 33 to 17-day band had major axes that were rotated anticlockwise from those in the lowest frequency band. This indicates that the phase vector had a component directed upslope and therefore, the direction from which the wave groups came, was northeastward along the Escarpment, rather than from offshore. This could be consistent with reflection or partial reflection by the Escarpment of higher frequency TRWs (Hamilton et al., 2003; Hamilton, In press). This will be discussed further in the next sections.

Vertical decay of the amplitudes ocurred at both moorings and for all the frequency bands for depths less than 2000 m. Below 2000 m, fluctuations were essentially depth independent. Decay rates above 2000 m were similar for the four frequency bands at L3 with perhaps slightly greater attenuation at the higher frequencies. The attenuation for constant N was proportional to the horizontal wavenumber which implies that the wavelengths were similar across the TRW spectrum of motions. This has been noted previously for TRWs in the Gulf (Hamilton et al., 2003). This is exploited in the next section where the PIES and bottom-current data are combined to produce current profiles for the complete mapping array. Strongly bottom-trapped motions imply short wavelengths and are usually associated with short-period motions. This does not seem to have been the case for these observations.

The high coherence of current fluctuations through the lower layer are such that a single mode accounts for a majority of the variance in each frequency band, which allows the lower-layer to

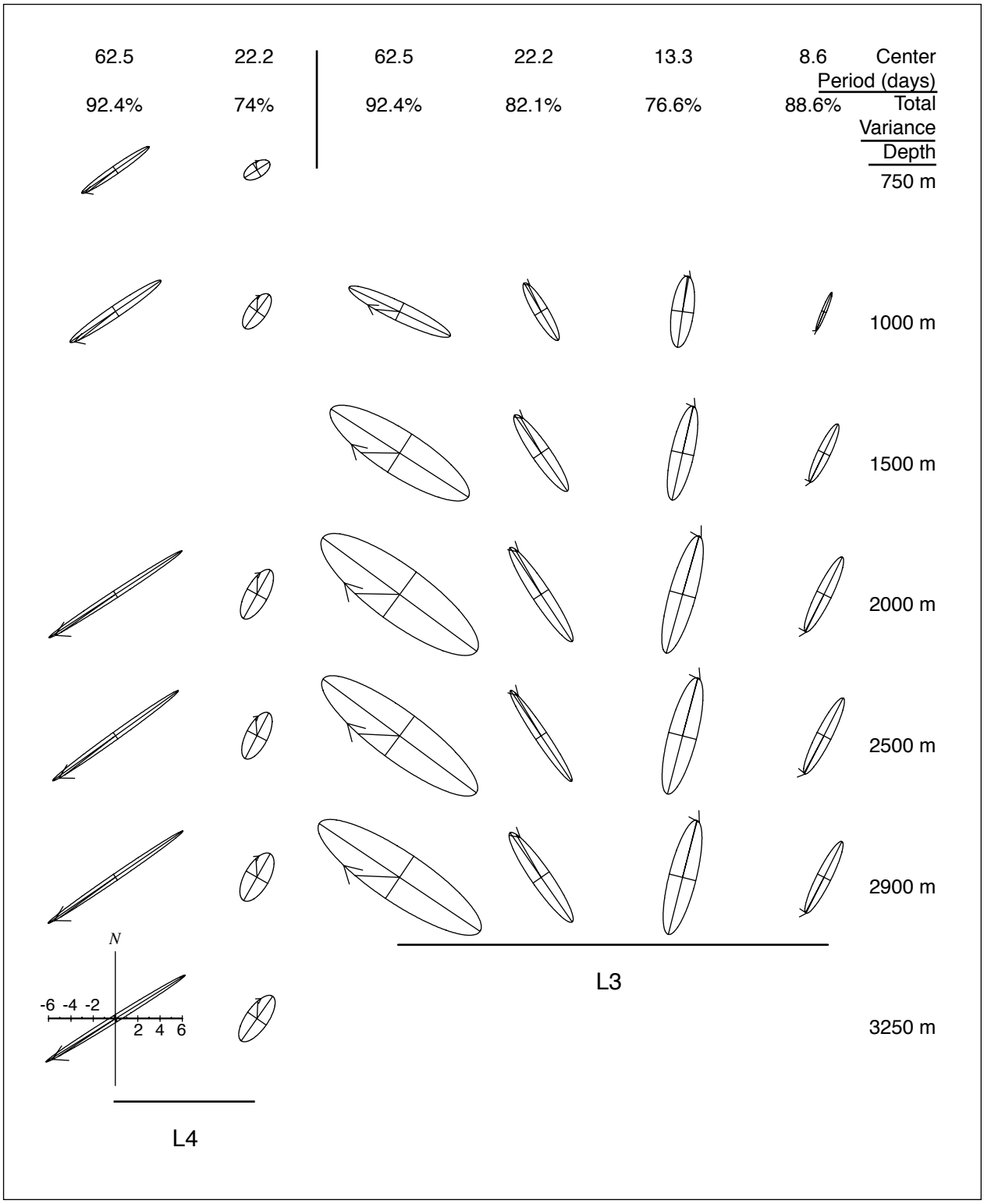

Figure 5.2-5. Vertical distribution of frequency domain EOF amplitudes ($cm \cdot s^{-1}$) for the given instrument depths on moorings L3 and L4. The period of the center of the frequency bands and the percent of the total variances accounted for by the first modes are indicated.

be treated as a single entity. Therefore, the horizontal coherent structures can be investigated using a single record at each mooring.

5.2.3 Vertical Trapping Scale from Cosh Fit

The vertical decay of the current velocity amplitudes with height above the seabed (or more strictly, height above the bottom boundary layer) is characteristic of TRWs, and is a function of the wavelengths of the motions such that shorter wavelengths are more strongly bottom trapped. The dispersion relation also indicates that shorter wavelengths are found at higher frequencies. Thus, an indication of the spatial variability of the waves can be found by calculating the vertical decay scale of the TRW currents as a function of wave period. Trapping depths can be found by least-square fitting the major axis amplitudes of the frequency-dependent modes to the function $A_o \cosh(\lambda z)$, where the depth z is measured upwards from the ocean surface and $(1/\lambda)$ is the trapping depth. The wavelength of the TRWs is then related to λ by the dispersion relation (see equation below) with $\beta = 0$, i.e.,

$$\lambda = NK/f$$

where $K = (k^2 + l^2)^{1/2}$ is the wavenumber magnitude, N is the Brunt-Vaisala frequency and f, the Coriolis parameter. As indicated by the vertical EOF analysis above, most of the change in current amplitudes occurs above 2000 to 2500 m. Fluctuations below these depths are virtually depth independent. The cosh fit assumes a constant N, whereas in the Gulf, N decreases with depth, becoming very small at depths below 2000 m. Therefore, trapping depths were calculated using only the depth levels extracted from the vertical EOF modes between 750 and 2200 m, as these better approximated the exponential decay predicted by the theory. The vertical EOFs were calculated as above for the tall moorings using all depth levels below 750 m for moorings L1, L3, L4 and L5. The mode amplitudes at L2 were too small to produce reliable results. As the discussion above of time scales indicates, not all frequency bands are present at all sites and TRWs are not supported where the frequency exceeds $N\alpha$, where α is the bottom slope. Thus, higher frequency motions are not relevant where the bottom slope is small at the two deepwater moorings, L3 and L4. The resulting trapping depths and wavelengths ($= 2\pi/K$), as a function of period and position, are given in Table 5.2-1. The value of N ($= 10^{-3} \cdot s^{-1}$) approximately corresponds to the average Brunt-Vaisala frequency between 1000 and 2000-m depths.

Table 5.2-1

Trapping depths and TRW wavelengths for the tall moorings.

Moorings / Wave-Periods	L1		L3		L5		L4	
	$1/\lambda$ (km)	$2\pi/K$	$1/\lambda$ (km)	$2\pi/K$	$1/\lambda$ (km)	$2\pi/K$	$1/\lambda$ (km)	$2\pi/K$
335-33 days	N/A		1.878	185	2.575	250	2.063	203
33-17 days	1.362	127	1.901	187	1.974	192	2.229	220
17-11 days	0.775	72	N/A		1.725	168	N/A	
11-7 days	0.484	45	N/A		1.367	133	N/A	

The results show the decrease in trapping depths and wavelengths with increasing frequency, particularly at L1 and L5. The standard deviations of least-square-fit trapping depths (and thus wavelengths) are between 1/4 and 1/2 the calculated magnitudes, so small differences in wavelengths are not relevant. The calculations at L5 are the most accurate because the highest number of depth levels (five) were used to calculate the fit. The other clear result is the general increase in wavelengths from east to west, which may imply that longer waves are more likely to propagate into the western part of the basin.

5.2.4 Horizontal EOF Analysis of the Lower-Layer Currents

Frequency domain EOF analyses were used to determine the distribution of fluctuating current variability as a function of frequency. The four frequency ranges used for the vertical EOFs at the tall moorings were again employed and the input velocity spectra were from the instruments 100 m above the bottom. Occasionally the 500-m record was used if the 100-m record was short or missing. Since the vertical structure at each site is dominated by one nearly barotropic mode, this substitution has little effect on the results. The results are given as amplitude ellipses where the relative phase is indicated by the position of the arrowhead, overlaid on a contour map of the kinetic energy (= $1/2(a^2 + b^2)$, where a and b are the principal axes of the amplitude fluctuations). The ellipses are similar to tidal current hodographs where the velocity vector rotates at the center period of the frequency band and its tip traces out an elliptical path. The results are shown in Figure 5.2-6 through 5.2-9. The first mode, in all cases, accounts for about 50% of the total variance of all the current fluctuations in each frequency band, and represents the dominant coherent motions across the array.

In the lowest frequency band (Figure 5.2-6), the energy is concentrated in the southern part of the array, approximately following the 3000-m isobath. Thus, these motions are only weakly present above the Escarpment and in the northeastern part of the study area. The major axes of the ellipses tend to be aligned with the isobaths, particularly near the steep slope of the Escarpment, and there is generally phase propagation towards deeper water. The 33-17 day band (Figure 5.2-7) is less energetic but has a similar pattern with relatively higher energies above the Escarpment in the southwest. The ellipses major axes are more at an angle to the isobaths, except near the Escarpment. In the next highest frequency band of 17 to 11 days (Figure 5.2-8), the energy is more concentrated on the eastern boundary of the array, and a band of stronger fluctuations extends down along the general direction of the Escarpment that attenuates towards the southwest. The deep area below the Escarpment, between 90 and 91°W, that was energetic for periods longer than 17 days, has almost no response at these shorter periods. For the shortest period band (Figure 5.2-9), the pattern is similar with extreme amplitudes found in the northeast at M1 that show some penetration across the Escarpment to the west. The signal in the southeast is weaker, and there is almost no energy at these 11-7 day periods on the western side of the array, both above and below the Escarpment. Therefore, the EOFs confirm the complex spectral content of the lower-layer flows, and suggest that higher and lower-frequency motions are confined to the east and northeast, and the south and southwest parts of the array, respectively, with the Escarpment acting to deflect energetic flows from the shallower water above the Escarpment in the northwest. There is evidence, however, that some of the deep fluctuations get across the Escarpment, but in a severely attenuated form.

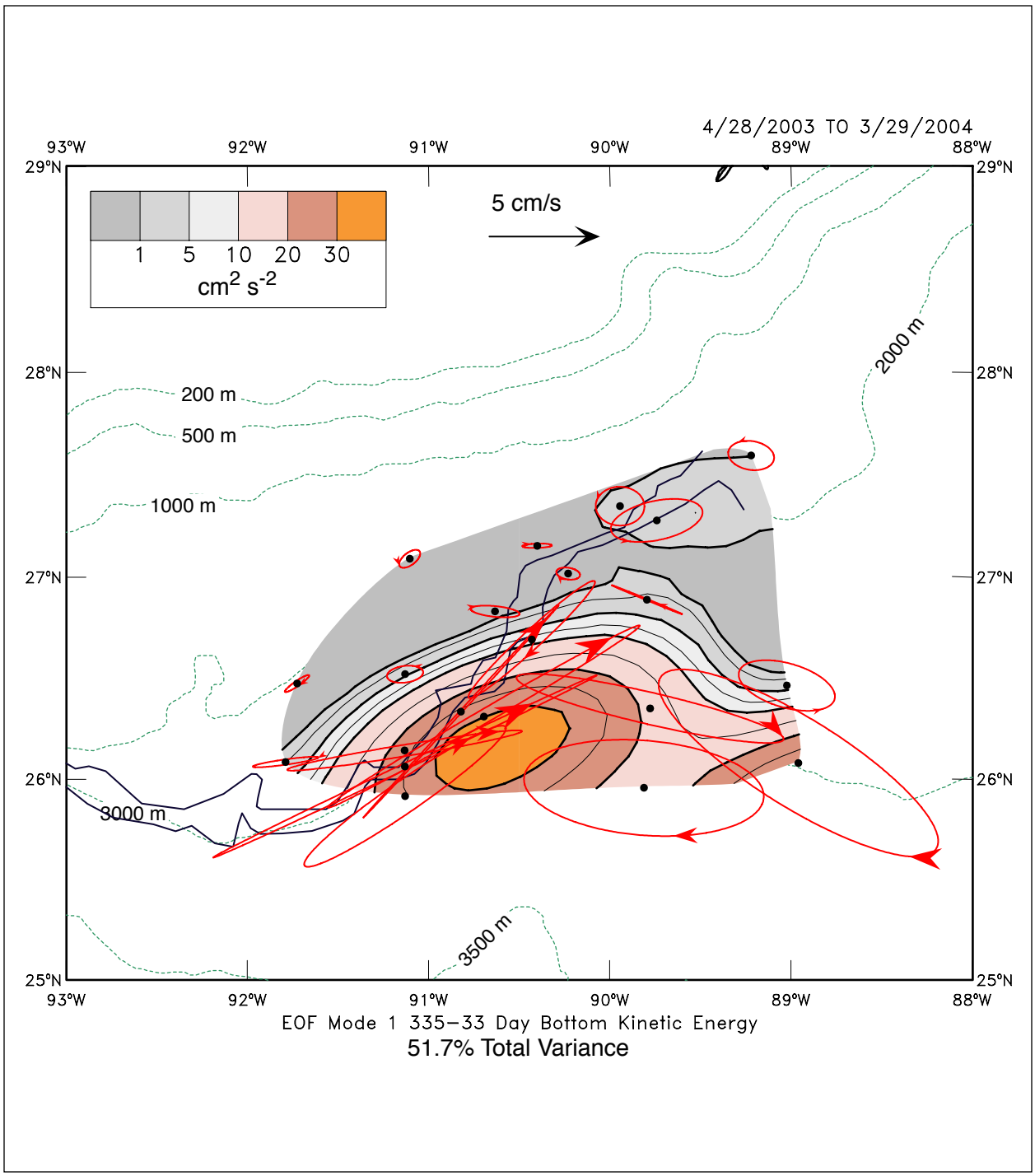

Figure 5.2-6. EOF mode 1 for the 335-33 day frequency band using lower-layer current observations. The EOF is given as an elliptical hodographs overlaid on contoured KE contained in the mode.

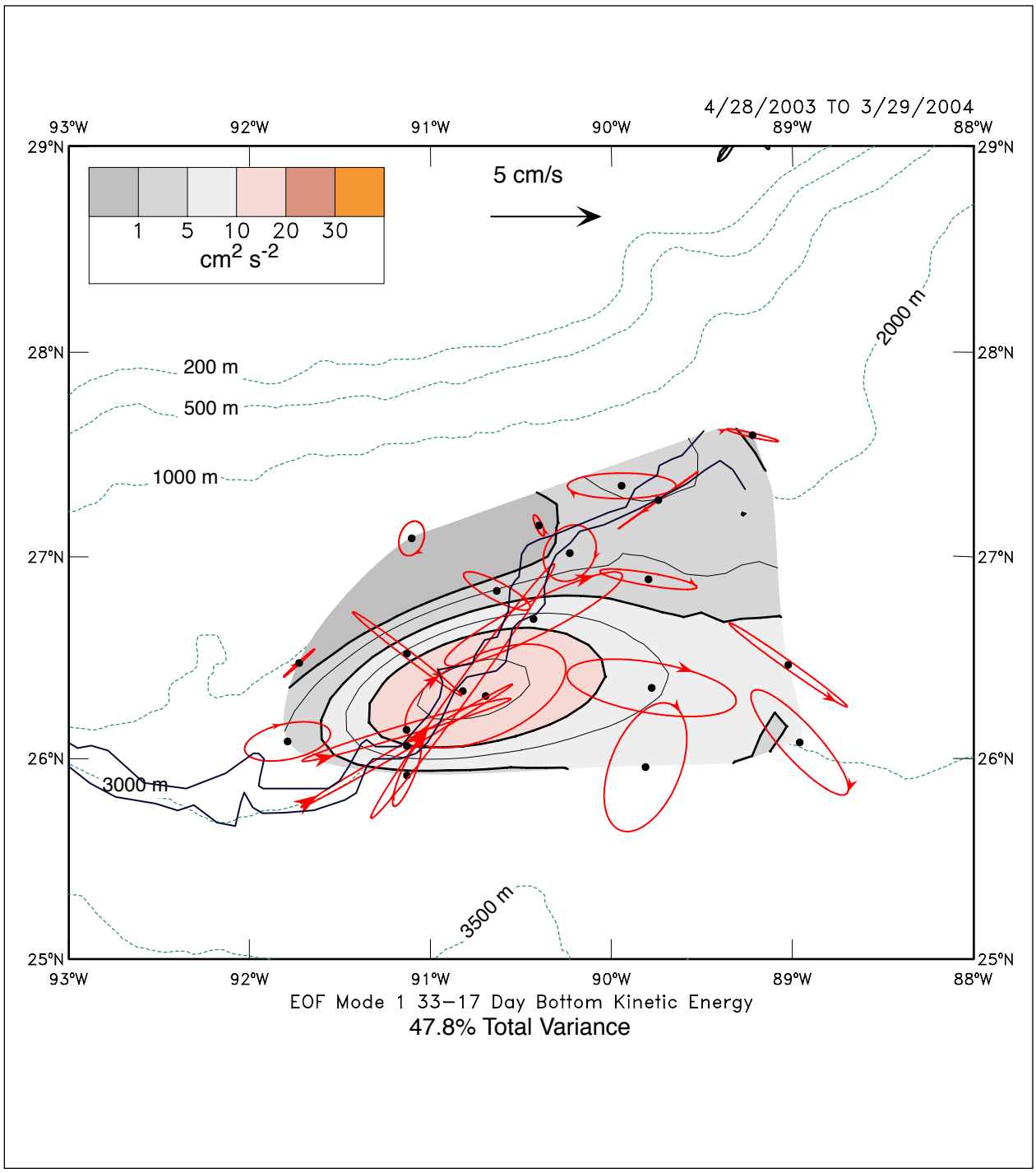

Figure 5.2-7. EOF mode 1 for the 33-17 day frequency band using lower-layer current observations. The EOF is given as an elliptical hodographs overlaid on contoured KE contained in the mode.

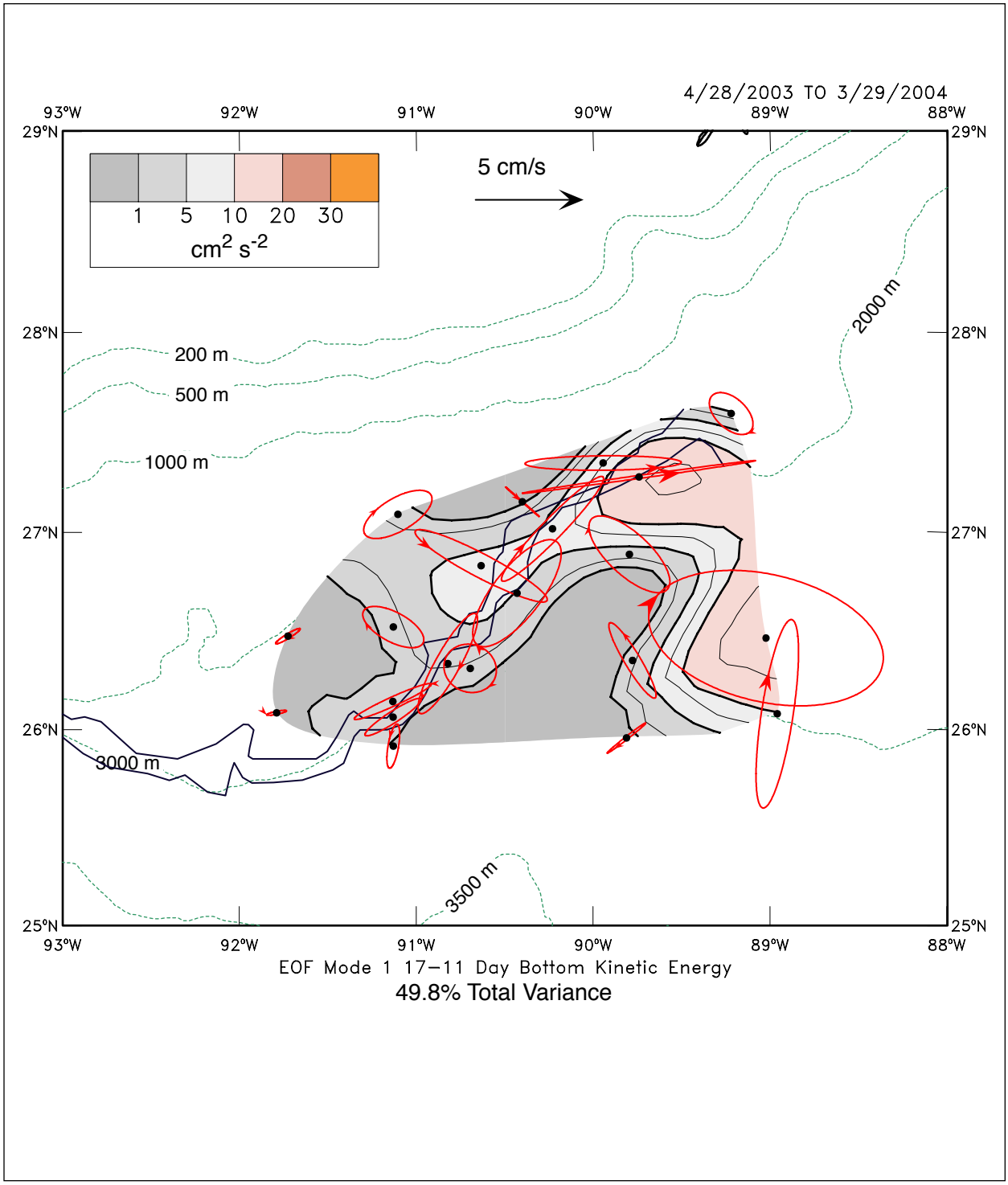

Figure 5.2-8. EOF mode 1 for the 17-11 day frequency band using lower-layer current observations. The EOF is given as an elliptical hodographs overlaid on contoured KE contained in the mode.

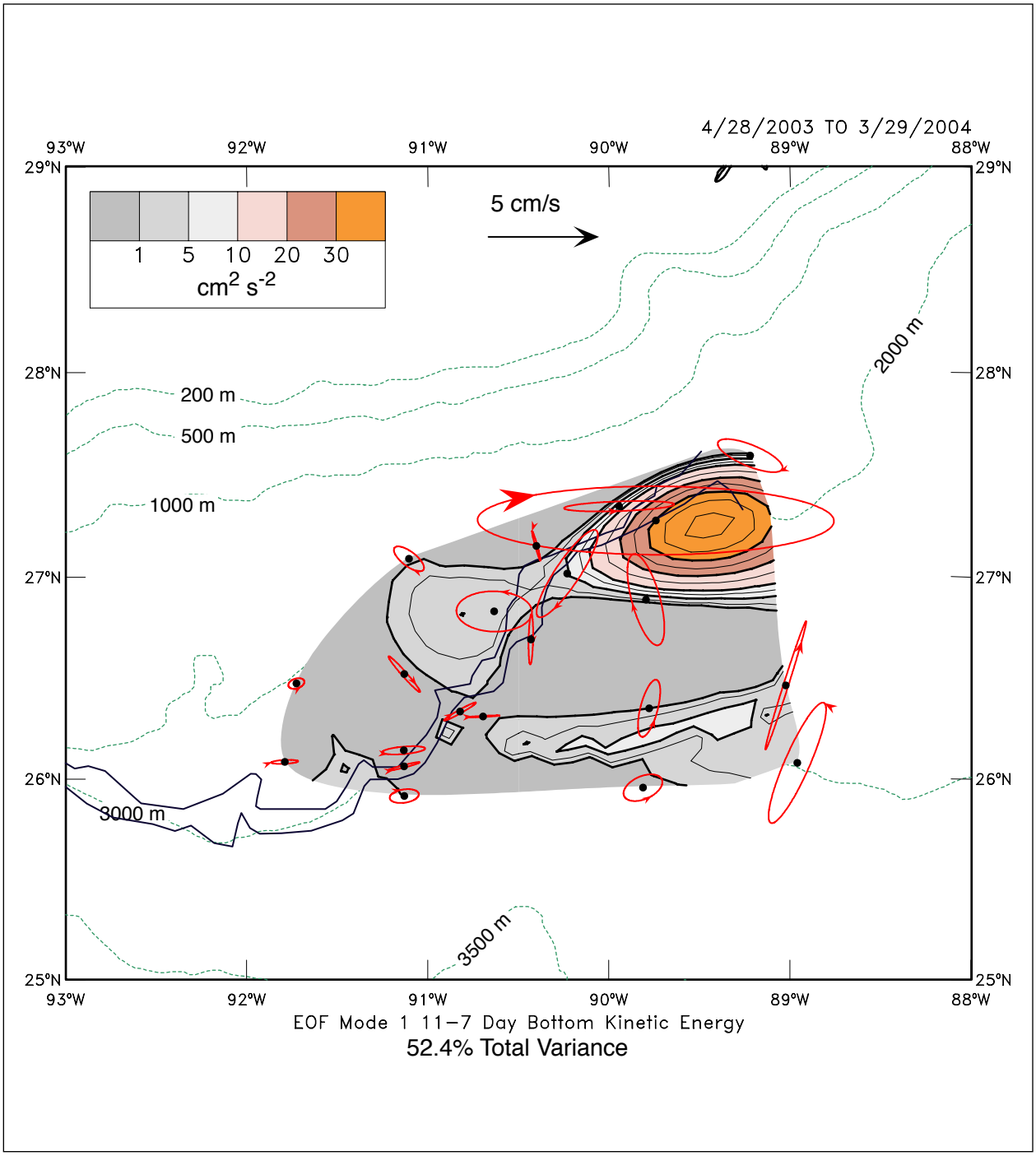

Figure 5.2-9. EOF mode 1 for the 11-7 day frequency band using lower-layer current observations. The EOF is given as an elliptical hodographs overlaid on contoured KE contained in the mode.

The "demoded" bottom-pressure anomalies from the PIES have overall better resolution than the moorings, though the lower-layer current array has better spacing around the Escarpment. The mode 1 EOFs, for each of the four frequency bands (Figure 5.2-10), are similar to their equivalent current analysis. The main differences are that there is a northern and southern band of higher amplitudes that extends westward for all except the 11 to 7-day period fluctuations, whereas the current EOFs either favor the southern or northern part for periods longer or shorter than 17 days, respectively. The higher amplitudes suggest that the fluctuations originate from the southeast or east of the study region, and the higher frequency fluctuations have much less westward penetration than the lower frequency fluctuations. The 11 to 7-day fluctuations differ from their current equivalents in that the large amplitudes at M1 are not present, and thus suggest a local enhancement of the current mode by the steep slope of the Escarpment.

5.2.5 TRW Ray Tracing

TRWs are dispersive waves, and this section examines whether the propagation paths of the different frequency waves can account for the differing spatial distributions of fluctuating energy that were described by the principal EOF modes. TRW paths were calculated using ray tracing, and the model utilized by Pickart (1995) was employed. The principal affect on propagation paths is the "slowly" changing bottom slopes, which were derived from smoothed GTOPO30 bathymetry (Smith and Sandwell, 1997) and were identical to those used in previous analyses by Hamilton et al. (2003) and Hamilton (In press).

TRW ray paths were calculated using the full dispersion relation. The basis of the method is given in Meinen et al. (1993) and used by Pickart (1995) to calculate TRW ray paths generated by the deep Gulf Stream in the Middle Atlantic Bight. The dispersion relation for TRWs is given by the coupled equations (Pickart, 1995):

$$\lambda^2 = (k^2 + l^2 + \beta k/\omega) (N/f)^2 \qquad (5.2\text{-}1)$$

$$\lambda \tanh(\lambda h) = N^2/(\omega f) (k h_y - l h_x) \qquad (5.2\text{-}2)$$

where h is the water depth,
N is the constant Brunt-Väisälä frequency,
f is the Coriolis parameter using the β-plane assumption,
$\mathbf{k} = (k, l)$ is the wavenumber vector in east and north (x, y) coordinates,
ω is the wave frequency, and
$1/\lambda$ is the vertical trapping scale of the wave.

Under the WKB approximation, where changes in wave amplitude and phase caused by the environment are assumed to vary on scales larger than the local wavelength, the equations governing the path of a wave and its wavenumber are (LeBlond and Mysak, 1978):

$$D_t \mathbf{x} = \partial\omega / \partial\mathbf{k} = \mathbf{c}_g \qquad (5.2\text{-}3)$$

$$D_t \mathbf{k} = \sum - \partial\omega / \partial\gamma_i \nabla\gamma_i \qquad (5.2\text{-}4)$$

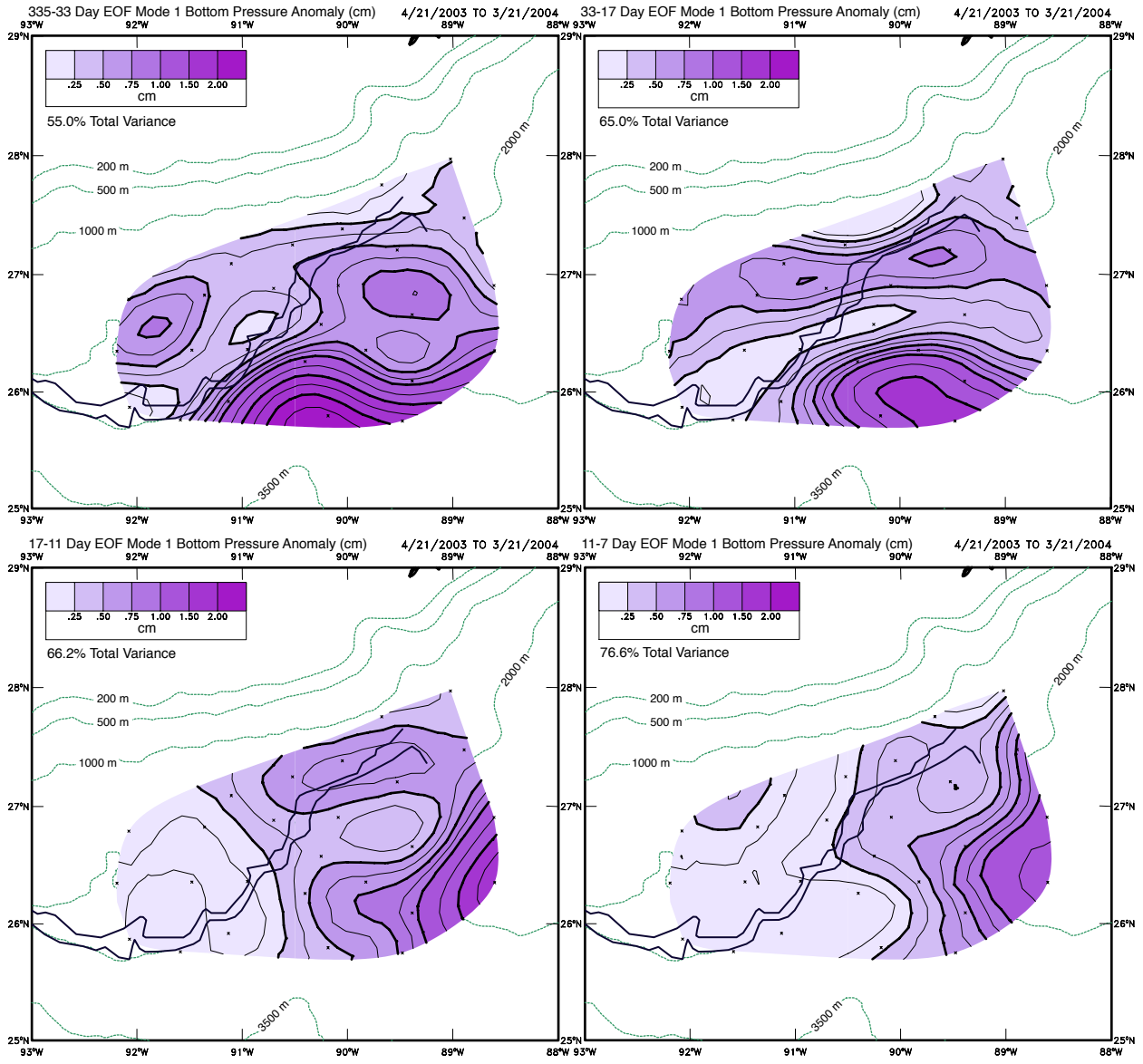

Figure 5.2-10. EOF modes for the four frequency bands from PIES bottom-pressure anomalies.

where $D_t = \partial / \partial t + \mathbf{c_g} \bullet \nabla$

is the derivative following the wavegroup, **x** is the path of the ray, and $\mathbf{c_g}$ is the group velocity. The γ_i are the environmental parameters that cause refraction of the wave. There are three such parameters for TRWs: h (water depth), ∇h (bottom slope), and N (Brunt-Väisälä frequency). N is assumed constant for these calculations. The WKB assumption is marginal though it is often used under conditions that have sharp changes in the environmental parameters. Therefore, the topography must be smoothed over at least the wavelength scale for the method to apply. The ray tracing equations, (3) and (4), were solved using 4th order Runge-Kutta methods to determine ray paths, and the change in the wavenumbers along the rays. Oey and Lee (2002) used essentially the same method for an investigation of TRWs generated by a numerical circulation model of the GOM basin.

Oey and Lee (2002) showed that a background mean current could alter the paths by supplementing the group velocity and changing the relative vorticity along the ray. If westward mean flow with cyclonic shear is present, then the ray has an increased turning towards deep water. This is generally the case along the Escarpment, and the mean flows were substantial enough to make small changes in the paths. However, an alternate viewpoint is given by Mizuka and Hogg (2004), where a model of TRWs over simple shoaling topography indicates that the waves generate a mean flow over steepening slopes through changing vorticity fluxes in the bottom boundary layer. This model indicates that an abrupt change in slope causes reflection of the TRWs back into deeper water. Therefore, whether TRWs propagating towards a steep slope that has a length scale less than typical wavelengths (and thus violate the WKB approximation central to ray tracing) refract, will support a westward mean current, or have a reflected component, is somewhat of an open question. Because incorporating a mean flow field using observations is not straightforward (Oey and Lee (2002) used model results), the ray tracing herein neglects these processes and uses the standard equations given above.

The WKB approximation assumes that the depth, h, and the bottom slope, ∇h, vary smoothly over length scales similar to the wavelength of the TRWs. For this study, the GTOPO30 world ocean bathymetry data set (Smith and Sandwell, 1997) is used as a starting point. Nominal resolution is 2' of latitude and longitude. The northern slope region of the GOM has extremely rough bathymetry, so the challenge is to smooth the topography but keep major features, such as the Escarpment, but not introduce spurious features with surface fitting spline routines (e.g., oscillations where slopes have sharp changes). This was accomplished, after much experimentation, by first using a 50-km square median filter on the GOM subset of the bathymetry, and then fitting bicubic smoothing splines to h and ∇h (Dierckx, 1982). Least-square-smoothing splines compromise between closeness of fit and smoothness of the interpolated surface by varying the number of knots over the grid.

The ray tracing equations were initialized by choosing a period and a wavelength for a given location, before calculating the path both backwards and forwards in time. For these calculations, the initial location was chosen where the largest fluctuations occur southeast of the Escarpment. The wavelength for a given period (taken to be the center frequency of each EOF analysis), was calculated from a least-square fit of the phase differences of the EOF mode 1 of four adjacent moorings arranged roughly in a square (Hamilton, 1990; Hamilton et al., 2003).

The initial wavelength and period are indicated on the plots. Periods longer and shorter than 17 days had initial wavelengths of about 200 and 65 km, respectively, and were very similar to previous estimates for these period waves (Hamilton, 1990; Hamilton et al., 2003). Reflection is not part of the ray tracing theory. Therefore, to reflect the wave, the ray tracing was stopped at the bottom of the Escarpment and the upslope wavenumber reversed before resuming the path.

The calculated ray path for the 61-day period TRW, initialized in the southeast corner of the array is given in Figure 5.2-11. It can be seen that it agrees quite reasonably with the locations where the fluctuations had large amplitudes and were refracted away from the regions with small amplitudes. Moreover, the major principal axes of the fluctuations were approximately aligned with the path direction, which was as expected for long-period TRWs, because the major axis direction was almost parallel to the group velocity, and perpendicular to the phase velocity. At the Escarpment both the transmitted and reflected rays seemed reasonable, with the transmitted ray being more strongly attenuated. The addition of southwestward mean flow along the Escarpment would make the transmitted ray bend towards the reflected ray path and thus reflection may not need to be invoked. The backward ray trace indicates that the origin of the fluctuations may have been under the LC around 25.5°N. The 22-day ray paths (Figure 5.2-12) are similar except that the path penetrates to a more northerly position on the Escarpment, which is consistent with there being relatively larger amplitudes at N4 compared to the southeast corner than occurred for the 62-day fluctuations. Again, both the transmitted and reflected paths were supported by the data if the transmitted path is strongly attenuated after crossing the Escarpment slope. The backward ray path fails or halts near 88.8°W, 25.2°N, suggesting a more local origin to the southeast of the array for these shorter period waves.

The larger amplitude, shorter-period fluctuations were more concentrated in the southeastern part of the array, so the initial location for the ray tracing was moved to between M1 and M2 (Figures 5.2-13 and 5.2-14). In both cases, use of a reflected path, beginning at the initial location, corresponded more closely to the amplitudes of the modes. The 13-day ray paths halt near the southern boundary of the array. The forward path stops near L4 where the amplitudes were very small, and the backward path originates near the 3000-m isobath. This type path, which was towards the Escarpment in the east and then along the Escarpment towards the southwest, corresponds very well to the distribution of amplitudes across the array. The reduction in amplitude as the wave propagated southwestward along the Escarpment either indicates that shorter-period waves were rapidly dissipated or their energy was being converted into the mean flows observed along the Escarpment. Similar but shorter paths were calculated for the 8.6-day wave (Figure 5.2-14). It is interesting that such short period motions were only supported in the immediate vicinity of the northeastern part of the Escarpment, which is where the large amplitudes were observed. This seems to imply that locally generated short-period fluctuations were not able to propagate away, and this may explain the localized high amplitudes at M1 that were also found at I1, I2 and I3 in previous experiments (Hamilton et al., 2003; Hamilton and Lugo-Fernandez, 2001). Therefore, TRW ray paths, originating locally and further east for short and long-period motions, respectively, were consistent with the complex spatial distribution of frequencies and amplitudes over the array.

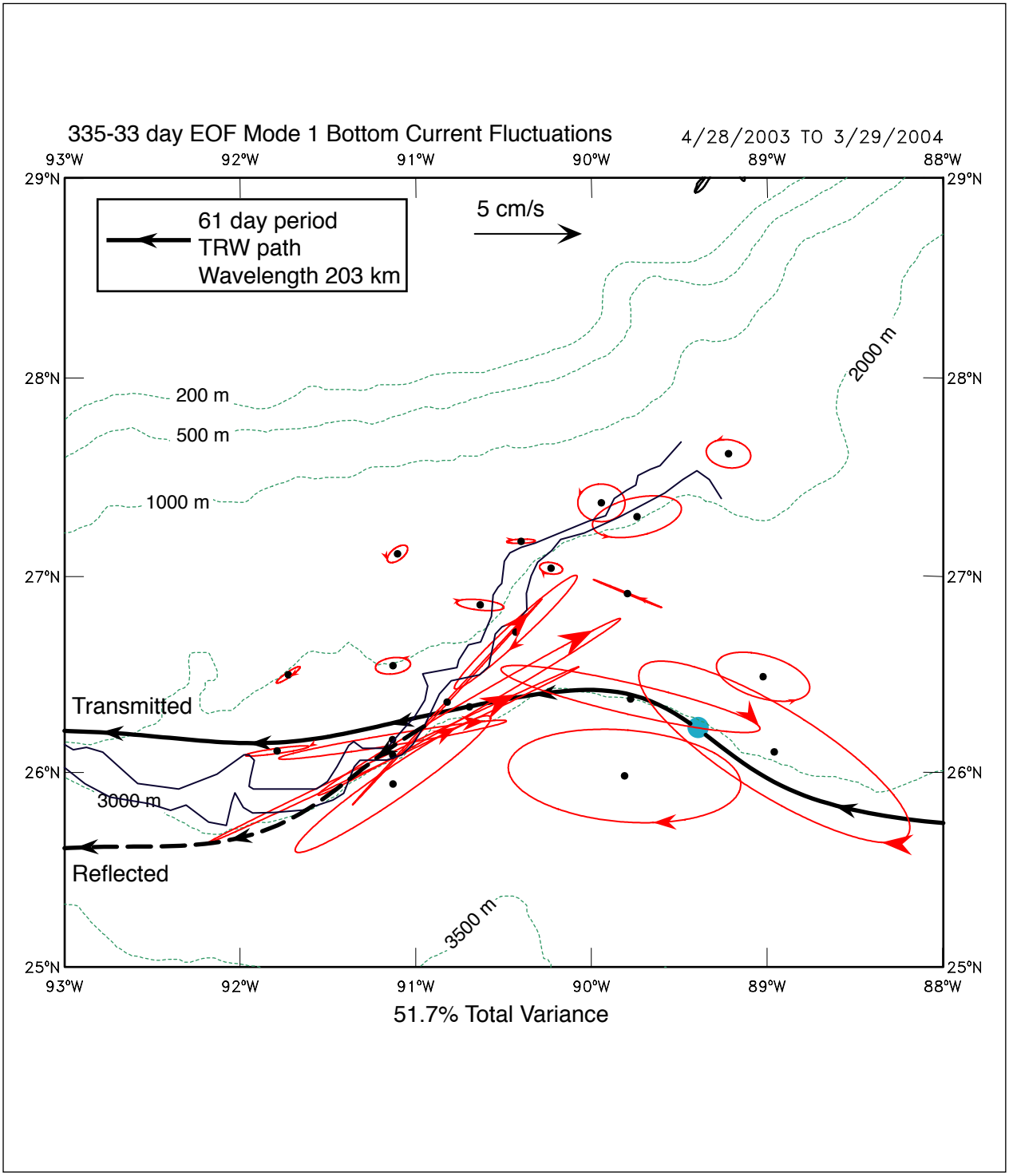

Figure 5.2-11. Path of 61-day period TRW traced backwards and forwards from the inital position given by the blue dot. The initial wavelength is calcualted from the phase differences of the mode 1 EOF at the nearest four moorings to the origin. The dashed line assumes reflection of the wave by the Escarpment. The mode 1 amplitude ellipses are also shown. Arrowheads are at five-day intervals.

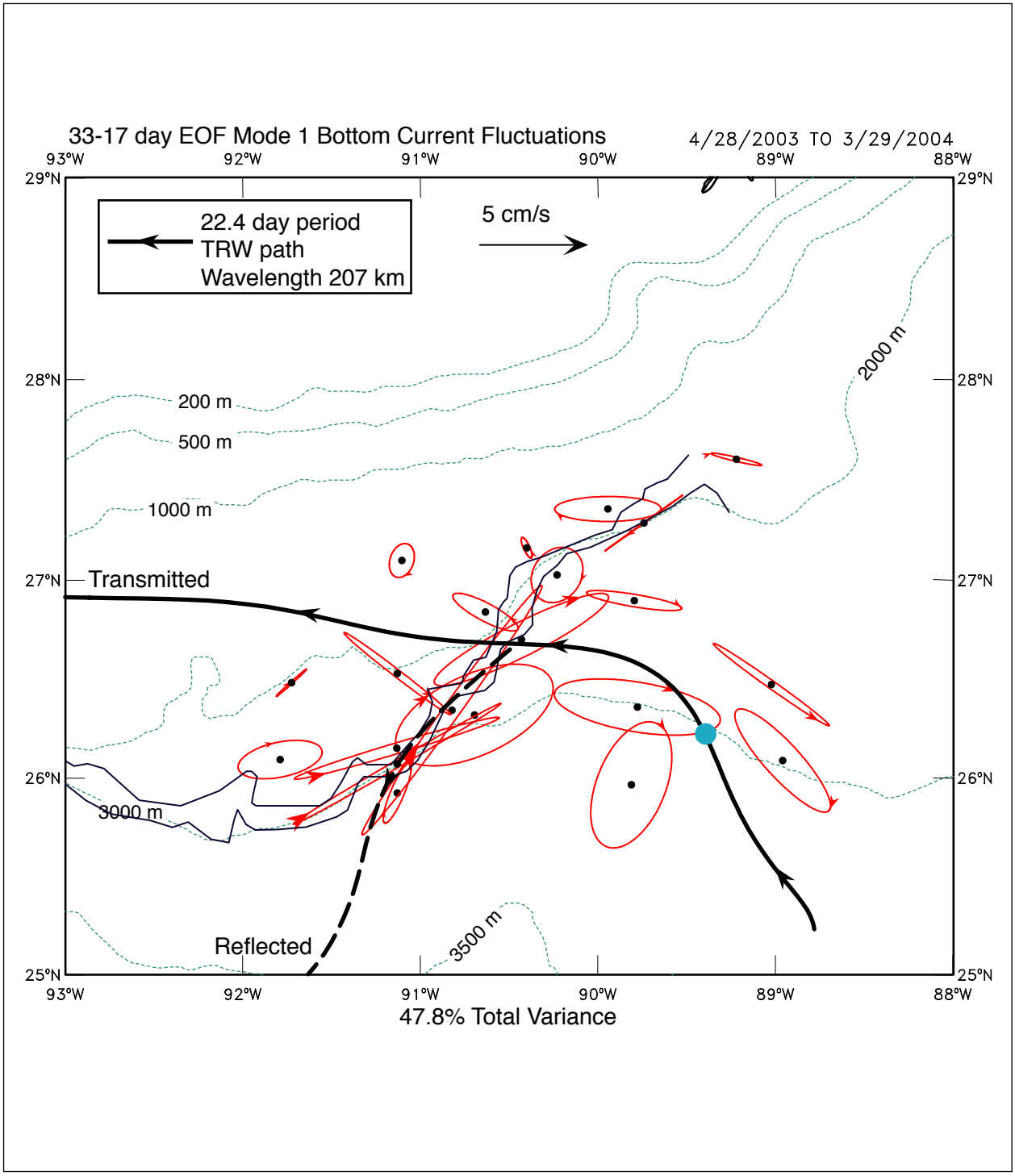

Figure 5.2-12. Path of 22.4-day period TRW traced backwards and forwards from the inital position given by the blue dot. The initial wavelength is calcualted from the phase differences of the mode 1 EOF at the nearest four moorings to the origin. The dashed line assumes reflection of the wave by the Escarpment. The mode 1 amplitude ellipses are also shown. Arrowheads are at five-day intervals.

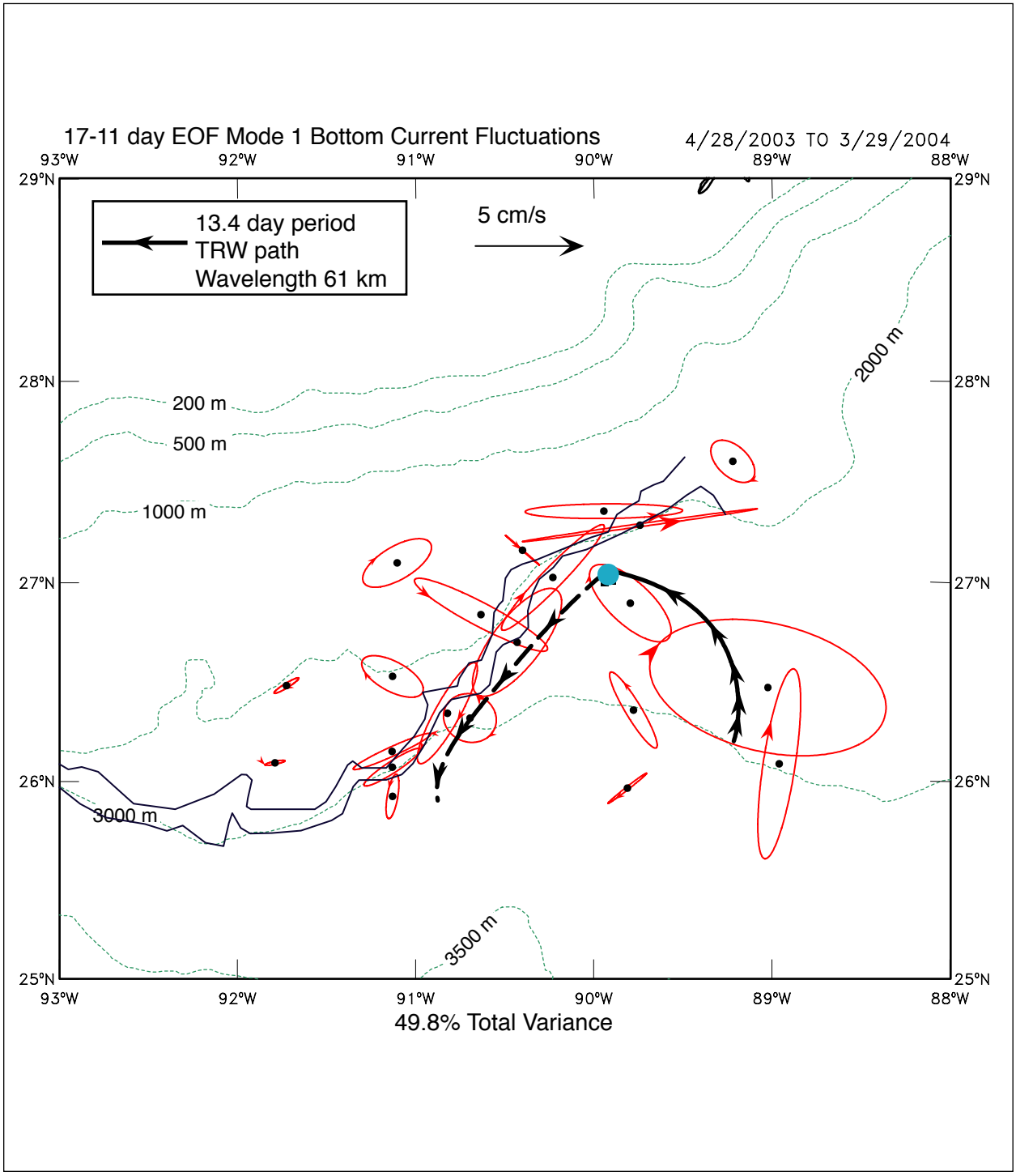

Figure 5.2-13. Path of 13.4-day period TRW traced backwards and forwards from the inital position given by the blue dot. The initial wavelength is calcualted from the phase differences of the mode 1 EOF at the nearest four moorings to the origin. The dashed line assumes reflection of the wave by the Escarpment. The mode 1 amplitude ellipses are also shown. Arrowheads are at five-day intervals.

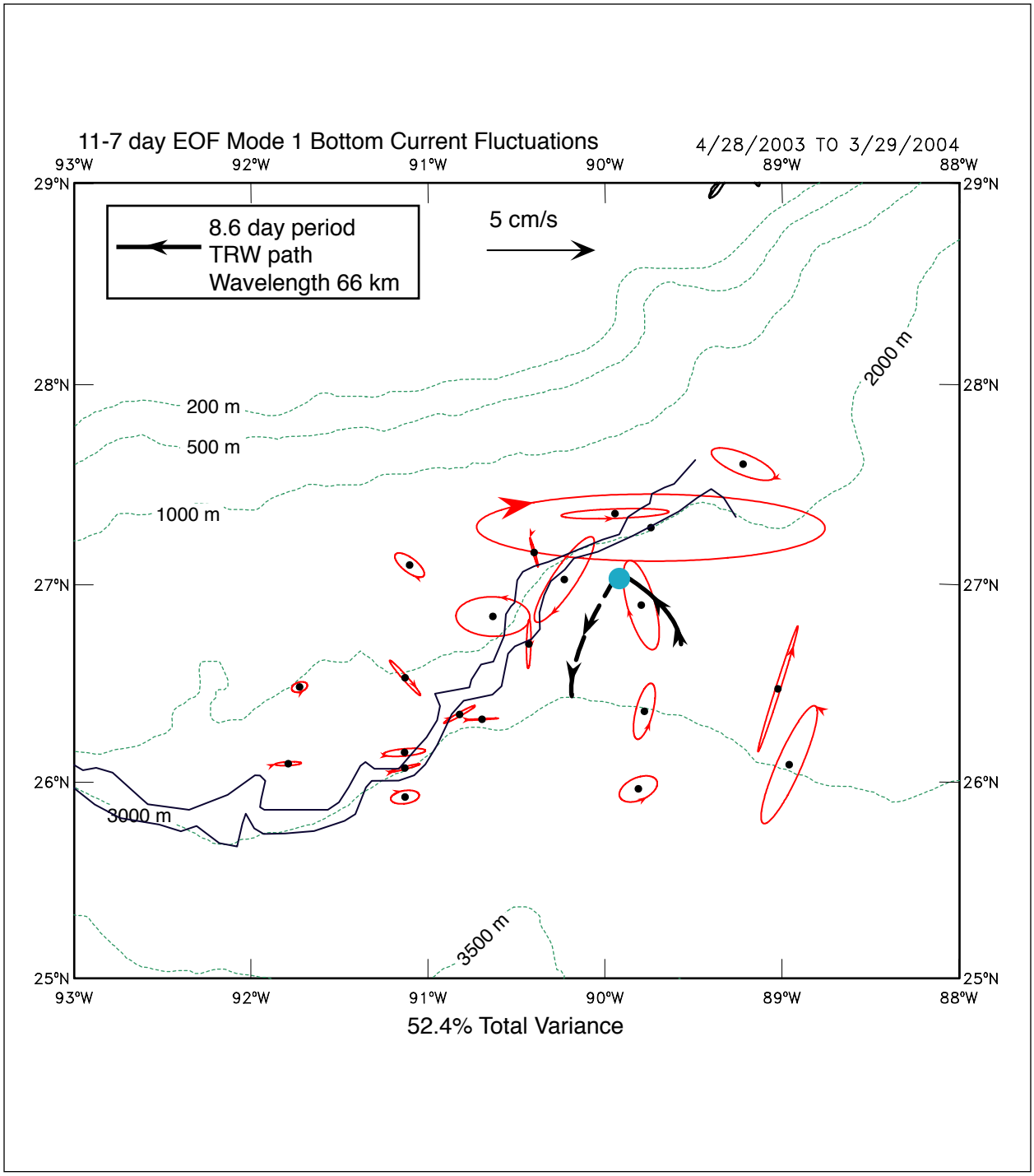

Figure 5.2-14. Path of 8.6-day period TRW traced backwards and forwards from the inital position given by the blue dot. The initial wavelength is calcualted from the phase differences of the mode 1 EOF at the nearest four moorings to the origin. The dashed line assumes reflection of the wave by the Escarpment. The mode 1 amplitude ellipses are also shown. Arrowheads are at five-day intervals.

5.2.6 TRWs and Lagrangian Float Tracks

Particle displacements in linear TRWs are predicted to be rectilinear (Rhines, 1970). Therefore, if deep-water motions are dominated by TRWs, then water particle following devices such as RAFOS floats would be expected to oscillate with little long-term transport and their paths would be similar to the current velocity hodographs given in Figure 5.2-11 and similar plots. It is, of course, more complex than this, as even linear TRWs have a broad range of periods, and in close to the Escarpment, strong mean flows will generate large overall displacements. However, a general description of the RAFOS float trajectories reveals a number of instances where floats stayed in the same vicinity for long intervals (several months), and the virtual float studies, that use the bottom-velocity mapping products, also indicate the dispersive wave-like nature of lower-layer flows (see Section 5.2.9). Therefore, it is an interesting question to what degree the deep-float tracks have similar characteristics to TRWs that have been diagnosed from the moored currents.

There are two good examples of pairs of floats at different depths that remained in the vicinity of the moored array for more than a 5-month interval. Figure 5.2-15 shows the paths of four floats, where the float trajectories have been smoothed and filtered using the methods given in Hamilton et al. (1999). Floats 456 (1500 m) and 476 (2500 m) were found close to the Escarpment when the sound sources were restored, and therefore they moved rapidly to the southwest with the mean flows along the Escarpment. However, after 10 to 20 days, they moved southwards out of the jet and began to oscillate where the displacements along the general trend of the isobaths were much larger than across. Both the 1500-m and 2500-m floats had similar amplitude displacements and their paths overlap with the 1500-m having been about 1° east of the 2500-m float. Floats 470 (1000 m) and 466 (1500 m), during the same time interval, oscillated over the Mississippi fan to the east of the array. The mean positions of these two floats were nearly coincident and it is clear that the deeper 1500-m float had larger amplitude displacements than the 1000-m float. These four float trajectories resemble the rectilinear displacements of TRWs more than those that would result from coherent lower-layer eddies. The presence of the latter would result in trajectories that perform closed circular or elliptical loops familiar from surface drifter tracks in LC eddies (e.g., Hamilton et al., 1999; Glenn and Ebbesmeyer, 1993). The velocities of the floats are given in Figure 5.2-16 along with the currents from the same depths at the nearest moorings (L3 for 470 and 466, and L4 for 456 and 476) to the general locations of the trajectories. The KE spectra for currents from both moorings and floats are also shown. The spectra are quite similar with the longer period ~ 20 to 30-day peaks dominating. The eastern pair of floats had about the same relative amount of intensification between 1000 m and 1500 m as the current meters at L3. It is noted that the energy levels were higher for the floats, which is consistent with the floats being closer to the LC source region. The southern pair of floats had KE similar to L4 currents and the further west trajectory (476) has a lower frequency peak than 0470 or the eastern pair of floats. This is further confirmation that lower frequency TRWs tended to penetrate further to the west in regions below the Escarpment. It is perhaps unsurprising that float velocities resembled those from nearby moorings but, because these velocities result in TRW-like displacements and the floats remain in the same general region for a considerable period, the float trajectories strengthened the supposition that currents in the deep water of eastern and central Gulf slopes are primarily caused by TRWs radiating from the east.

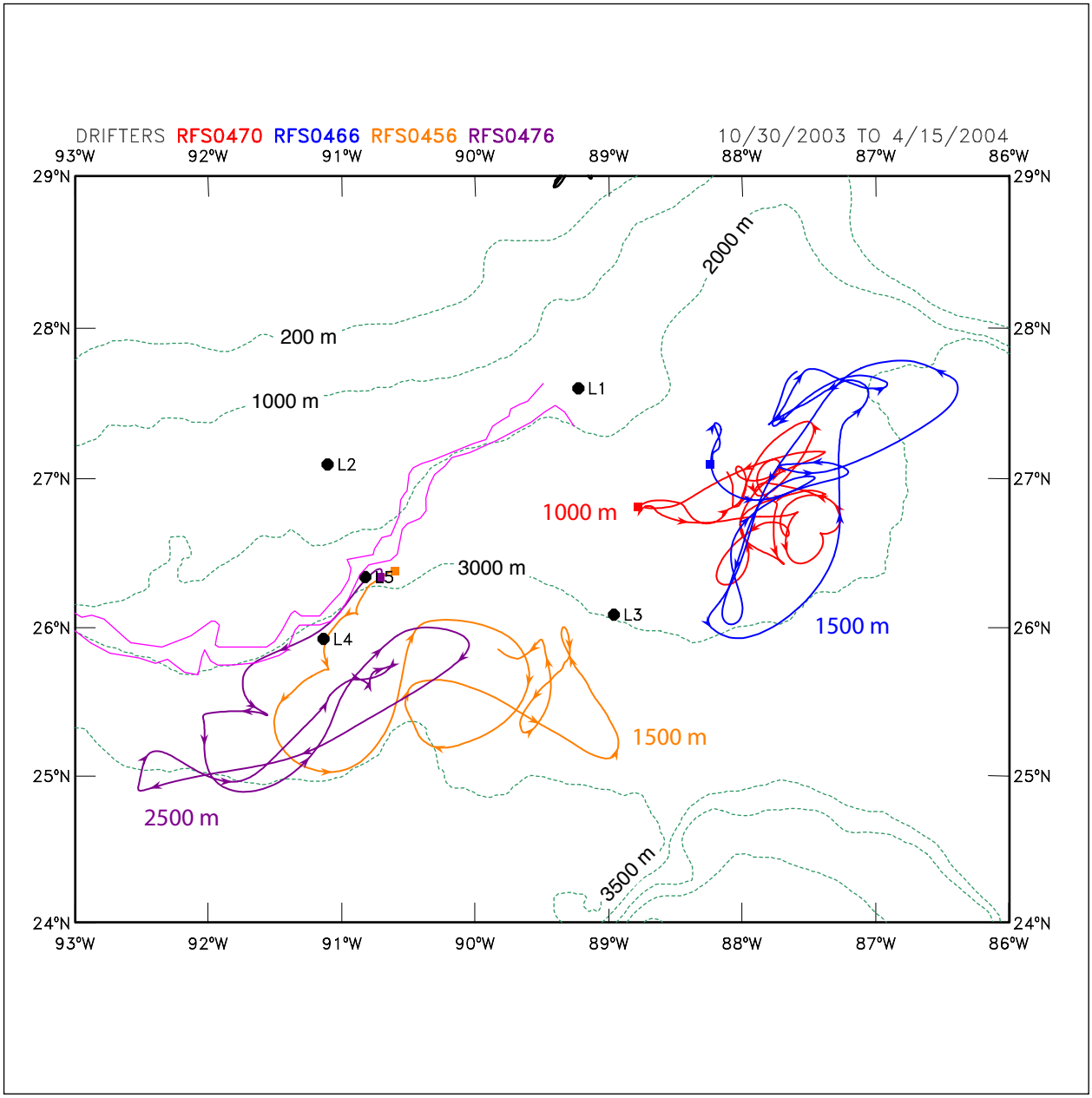

Figure 5.2-15. Smoothed RAFOS float tracks for the indicated periods and depths. Arrowheads are at 10-day intervals.

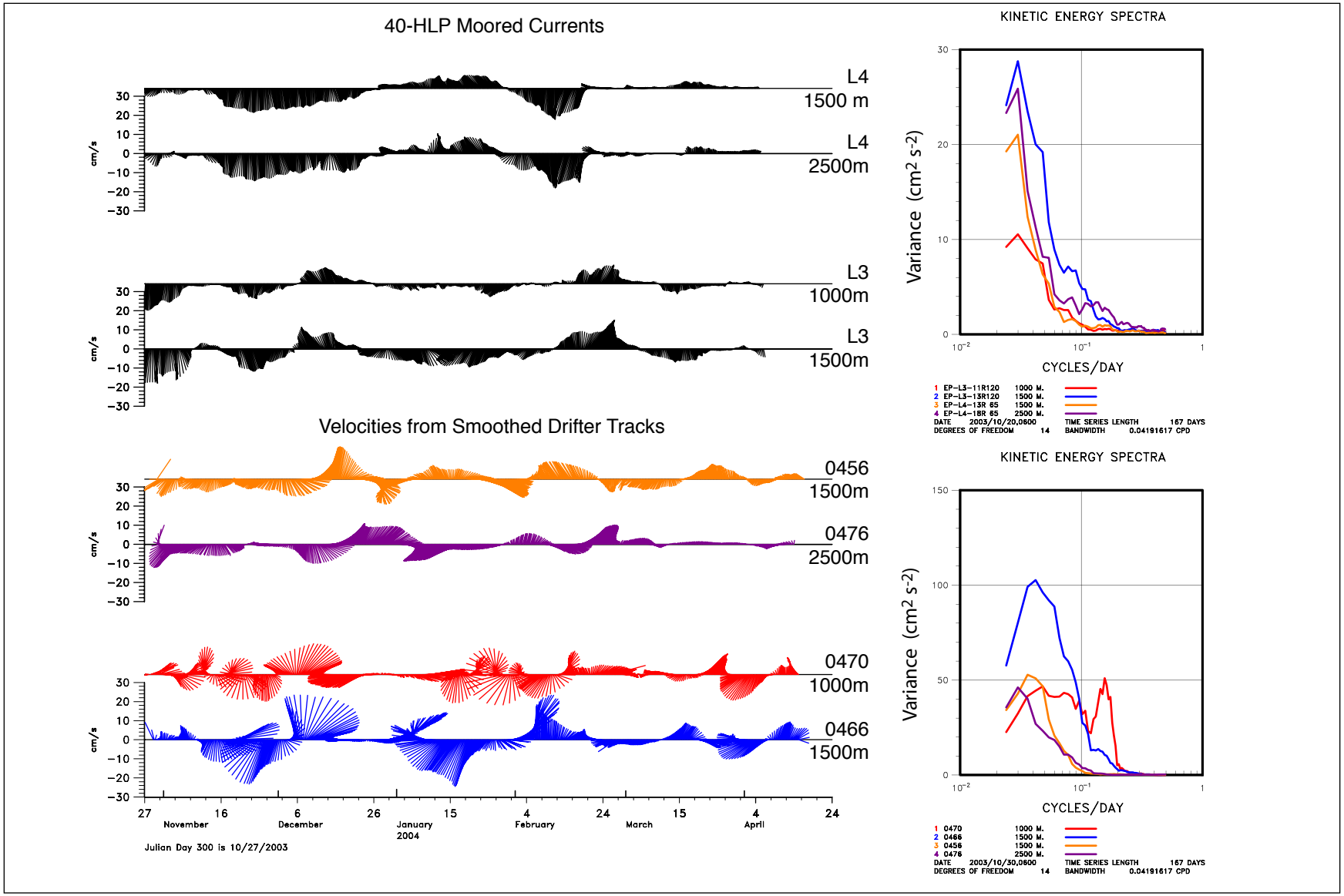

Figure 5.2-16. Current velocities from moorings L3 and L4 (top left), and from smoothed RAFOS-float trajectories (bottom left -colors correspond to the tracks in Figure 5.2-15). Kinetic energy spectra for the moored and float currents are given on the right side of figure.

5.2.7 Hydrographic Conditions - PALFOS Profiles

An examination of Figure 3.2-2c, shows RAFOS drifters 458 and 467 that were ballasted to drift at 1500 m below the ocean surface remained in the eastern GOM and under the expected location of the LC and related features for approximately five months following redeployment of the sound sources. This persistence of the drifters remaining in this eastern portion of the GOM suggested a possible link of the trajectories to LC and LCE influences. The cumulative trajectories for these drifters are shown in Figure 5.2-17, where the arrowheads are placed at five-day intervals. For this presentation and the discussion below, these trajectories have been smoothed which has suppressed motions having periods of less that approximately 2.5 days.

Biweekly images of SSH (Figure 5.2-18) are shown for the interval from 28 October 2003 through 13 April 2004. Overlaid on each image are the trajectories of RAFOS drifters 458 and 467. The trajectories on each image are +/- 7 days from the date shown on an image, hence each trajectory is for 15 days. As discussed previously and seen in these images, it is during this interval that Eddy Titanic separated from the LC. The goal of this presentation was to evaluate whether the movement of these drifters was related to surface dynamic topography associated with the LC and LCE during this protracted event. Visually, there does not appear to be an obvious relationship. The direction of movement of the drifters and the apparent scale of movement differ from what might be associated with these dynamic surface and upper-layer features.

To evaluate further the motion of these two drifters, the cumulative movement during the 15-day intervals are presented for each drifter (Figure 5.2-19). The numbers next to the color-coded trajectory segments indicate the time sequence; comparable numbered segments from the separate drifters are for the same time interval. An examination of these separate trajectories suggests that they often had similar motions at similar sites and times. The rotational sense of the drifters was similar and varied from anticyclonic to cyclonic. The similarity of motion at close but separate locations suggests that the shears were not great and hence movement was at times fairly uniform over spatial separation scales that are yet to be computed.

Displacement of these drifters was used to compute a time series of velocity exhibited by the drifter, and by extension the associated water parcel. These are shown in Figure 5.2-20a. Visually, there is a strong similarity between the velocities of the two drifters. Variance preserving kinetic energy spectra for the two velocity time series were computed and are shown in Figure 5.2-20b. The pronounced spectral peaks are centered on either side of approximately 0.07 Hz. or slightly more than a 14-day period. This is similar to the period of TRWs as measured previously in the region of Green Knoll and Green Canyon (Hamilton et al., 2003). The TRW modeling done by Hamilton et al., (2003) and in this study suggests that the source region for these relatively higher frequency wave motions was south and east of the Green Knoll region (see Section 5.2.6 of this report).

During the November 2003 – April 2004 interval, a fully instrumented mooring (L07 in Figure 5.2-19.) was deployed and maintained by Louisiana State University (LSU). Dr. Masamichi Inoue (LSU) kindly provided some of these data for use in this comparison. A plot of low-pass

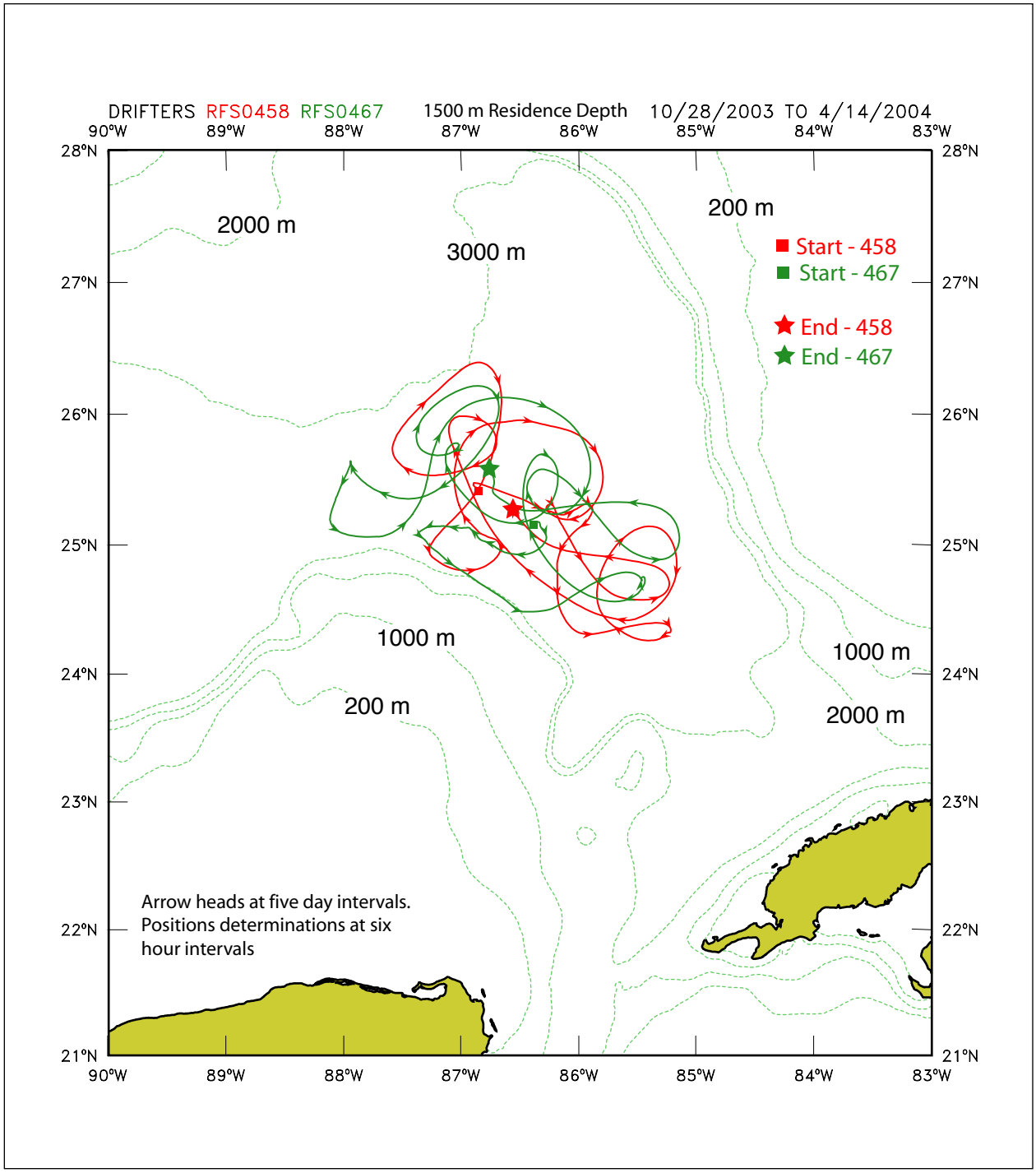

Figure 5.2-17. Trajectories of RAFOS drifters 458 and 467 as they moved underneath and in close proximity to the LC. Arrow heads are placed at five-day intervals. Visually, the reader has the impression that both drifters have somewhat similar motion and features.

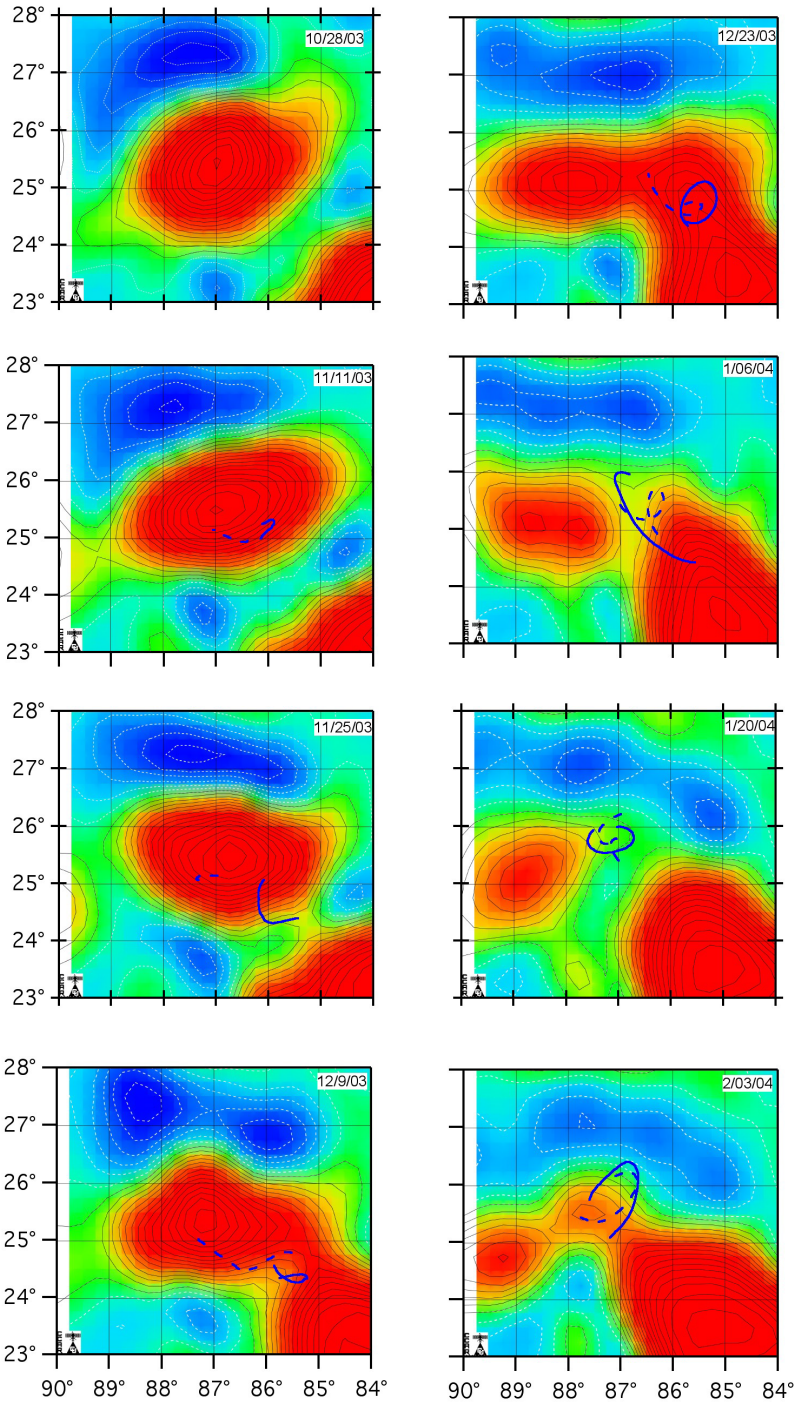

Figure 5.2-18a. SSH images for the indicated dates at two-week intervals. Overlaid on each image are the trajectories for RAFOS drifters 458 (solid line) and 467 (dashed line). On each image, the trajectory for a 15-day interval is plotted; seven days on either side of the image date.

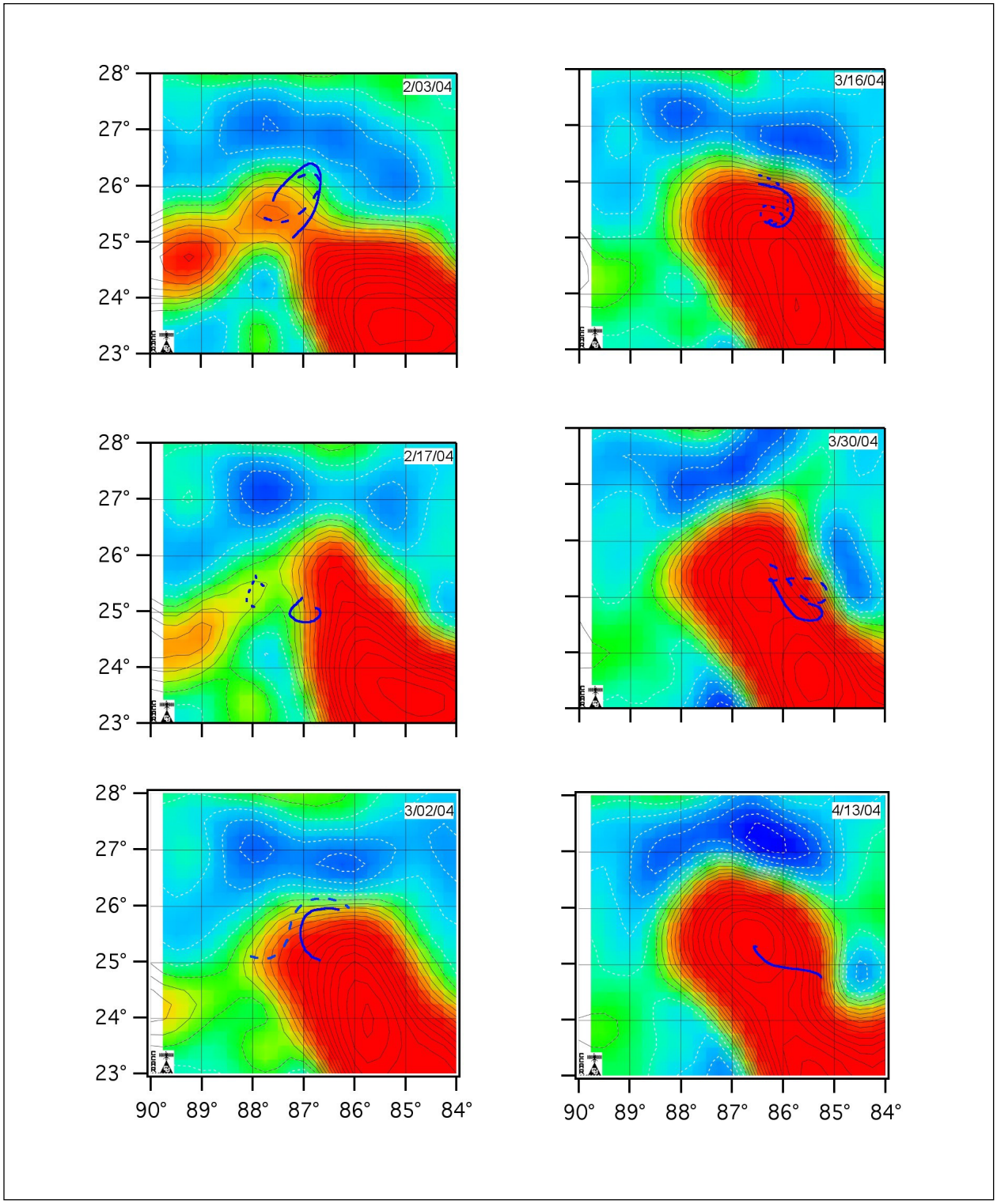

Figure 5.2-18b. SSH images for the indicated dates at two-week intervals. Overlaid on each image are the trajectories for RAFOS drifters 458 (solid line) and 467 (dashed line). On each image, the trajectory for a 15-day interval is plotted; seven days on either side of the image date.

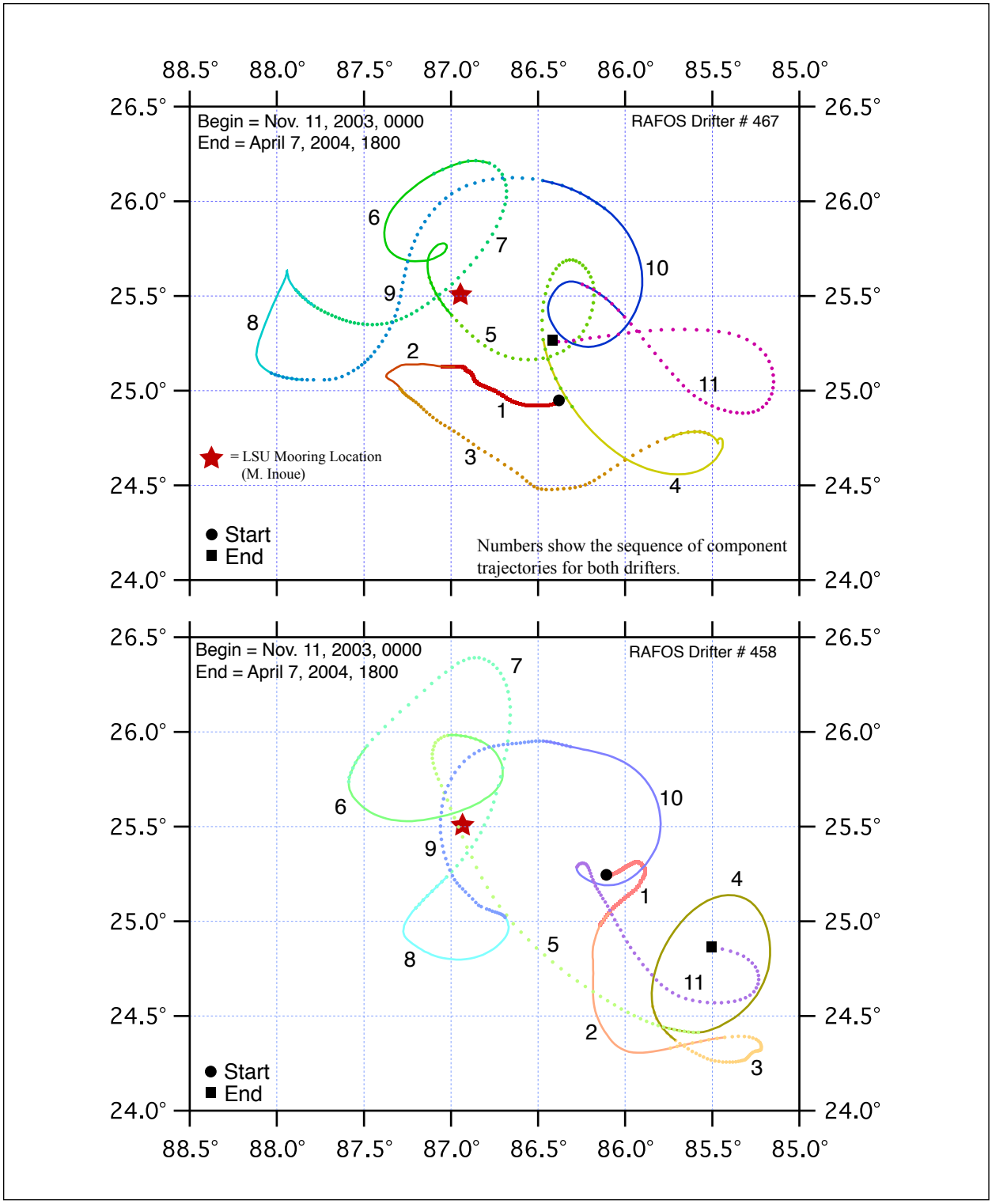

Figure 5.2-19. Concurrent cumulative trajectories for the indicated RAFOS drifters ballasted for 1500-m depth. Each component interval is 15 days (+/- 7 days before and after biweekly images in Figure 5.2-18.) Approximately two days of overlap occur in successive component trajectories. Successive trajectories are different colors and either dots or solid lines to emphasize the displacement and path during the indicated interval. Mooring data provided by Dr. Masamichi Inoue (LSU).

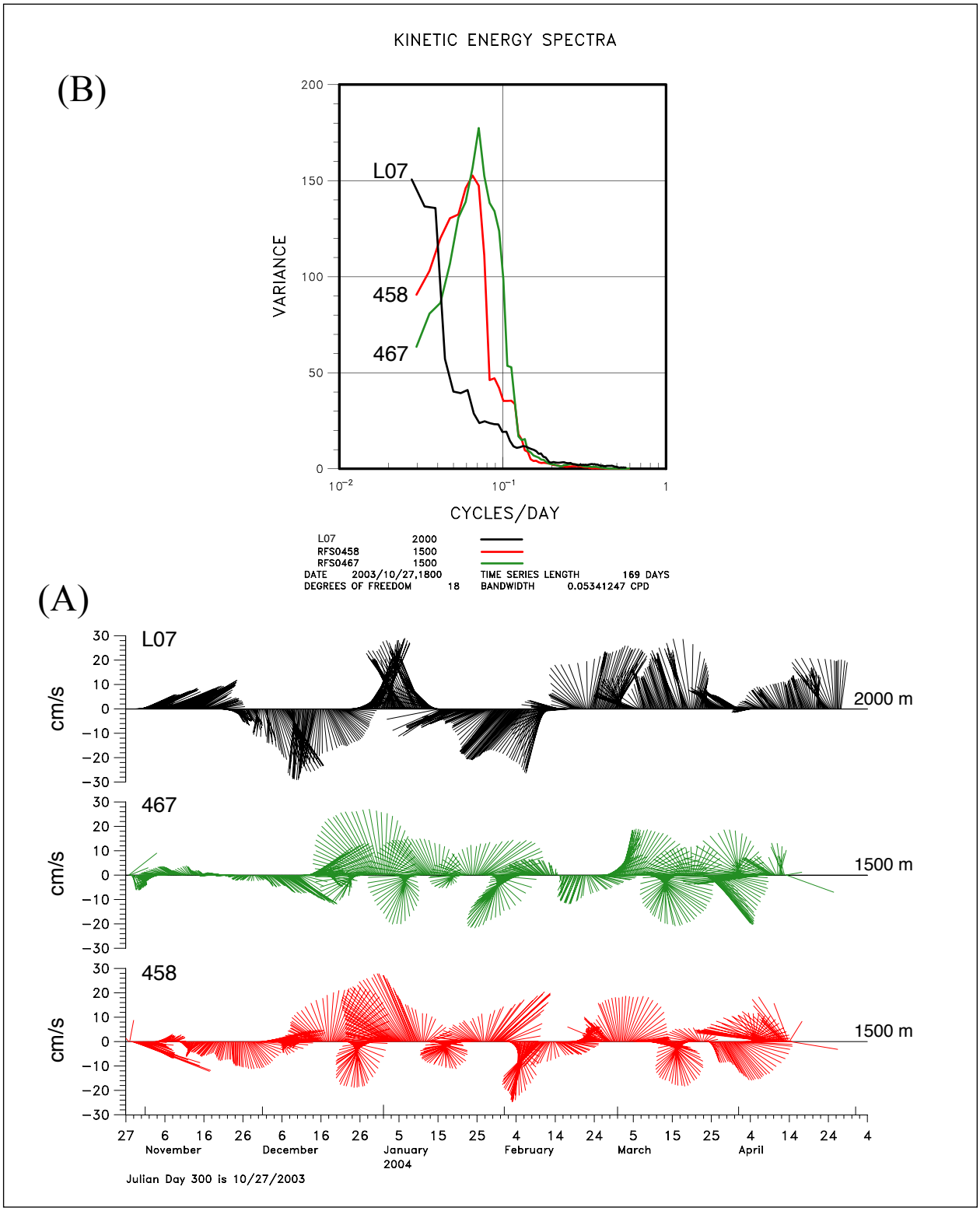

Figure 5.2-20. Lower panel (A) shows the low frequency velocities as measured from the indicated drifters and a comparable level on the LSU mooring in Figure 5.2-19. The dissimilarity points to the inherent problem of comparing Eulerian and Lagrangian current observations. The upper panel (B) shows the respective kinetic energy spectra for the velocities in Panel A.

filtered currents as measured at 2000-m depth is shown in Figure 5.2-20. For drifter trajectory segments 5 (01/06/04) and 7 (02/03/04) which were in close proximity to the mooring, the direction of motion of the drifters and moored current velocity were quite similar.

5.2.8 Eddy/TRW Reconciliation

Two alternate processes are commonly discussed in oceanographic literature regarding how deep currents and their associated pressure fields vary in space and time: as 'waves' and as 'eddies'. The preceding sections of this report also contain this apparent dichotomy of treatment, which could feed a false impression that TRWs and eddies are two distinct processes, respectively characterized by deep current meters and mapped by bottom pressure sensors. Hence, we now pause to reconcile why these observations illustrate complementary rather than conflicting aspects of the same processes in the deep ocean.

The preceding subsections of Section 5.2 developed the interpretation of the deep currents as TRWs, because TRWs are the natural linear response of the deep ocean to perturbations with spatio-temporal scales greater than approximately 10 km and longer than approximately four days. If we are willing to focus upon cases in which deep mean currents are negligible, and to accept the limiting assumption that the perturbation currents and topography are weak enough to be described by linear equations, then the sole unforced modes of variability available to a geostrophic stratified fluid in the presence of bottom topography are TRWs. The great attraction to acquiesce to these limiting assumptions is that under linear theory all deep perturbations – including eddy-like features – can be constructed uniquely as the Fourier sum of wave modes of appropriate amplitudes, phases, and wavenumbers, each exhibiting TRW kinematics. Moreover, waves whose amplitudes are nonlinear usually retain similar dispersion characteristics, structure and kinematics to linear waves. Finally, beyond these theoretical statements, the preceding observational summary has demonstrated great success in attributing a large fraction of the deep current variability to TRWs.

Presented in Figures 5.2-21 and 5.2-22 are two sequences of deep pressure maps to illustrate that the interpretations as waves and eddies are complementary rather than conflicting viewpoints. The geostrophic currents (not shown in these case studies) flow along the mapped isobars with high pressures to their right. Section 6 will consider several additional case studies that include more complicated interactions of deep eddies with the LC or Eddy Sargassum. However, the two cases selected for the present discussion seek to isolate uncoupled 'free modes' of variability, absent of strong upper currents and fronts. During the first six days of the first sequence of maps, 28 October 2003 to 3 November 2003, a trailing portion of Eddy Sargassum departed from the region on its southwest trajectory. The remaining 15 days of the first sequence and all days of the second sequence were free of strong features in the upper layer. Figure 5.2-21 illustrates a 'wave-like' event and Figure 5.2-22 illustrates an 'eddy-like' event.

We interpret the sequence of deep-pressure maps in Figure 5.2-21 as following a group or packet of TRWs. The waves are evident as pressure ridges and troughs throughout the region, excepting the relatively shallow portion northwest of the Sigsbee Escarpment (dotted line, see caption). The ridges and troughs are oriented WNW-to-ESE, approximating plane-waves with wavelengths of approximately 175 km. They propagate slowly SSW, as can be perceived by

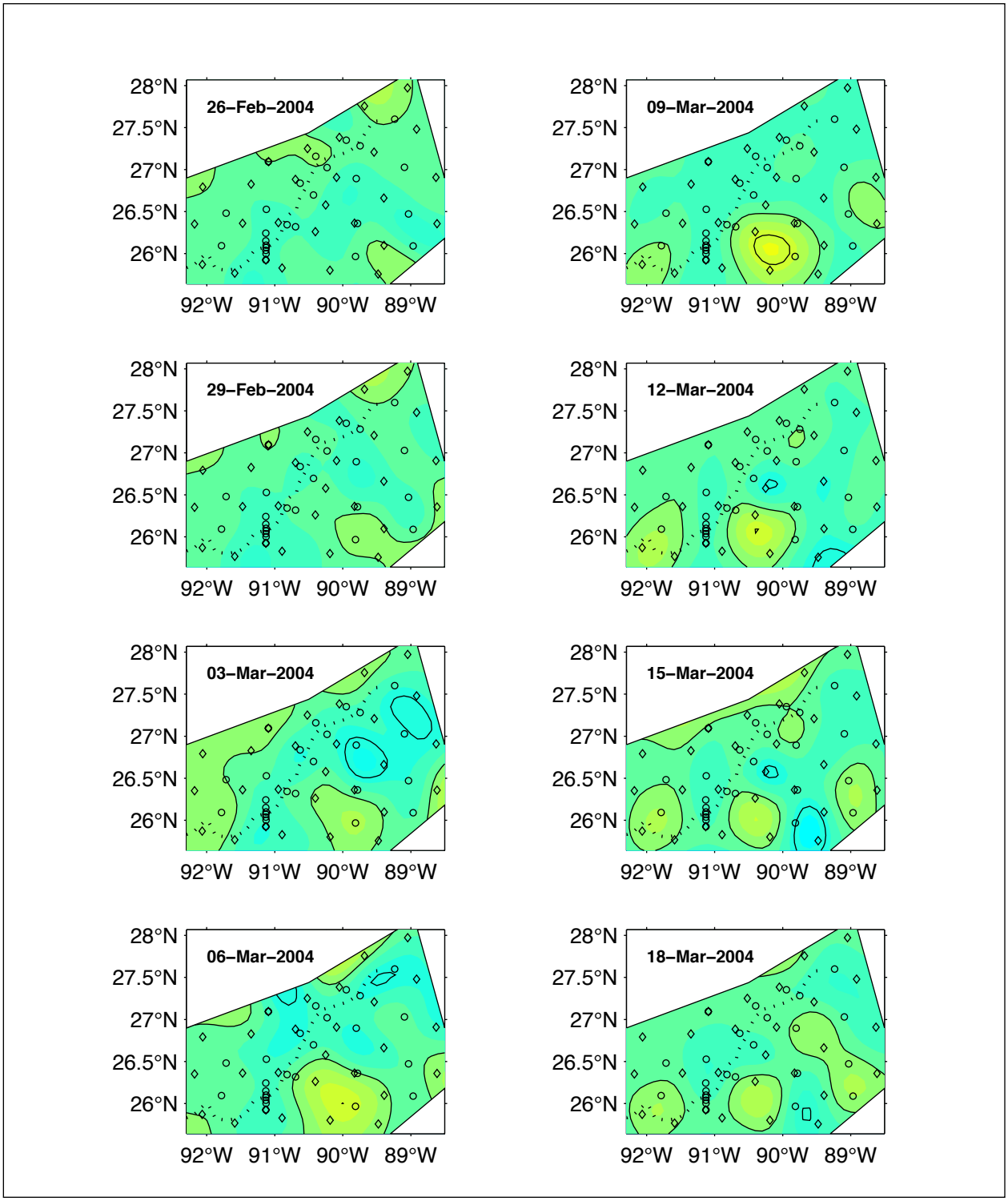

Figure 5.2-21. Topographic Rossby Wave case study. Wave Event (26 February - 18 March 2004). Maps of 1500-m depth pressure for eight separate days. Low (high) values shown with blue (red/yellow) hues. The sequence begins with the top left. The dotted line denotes the center of the Sigsbee Escarpment. PIES sites indicated by diamonds; current meter moorings by circles.

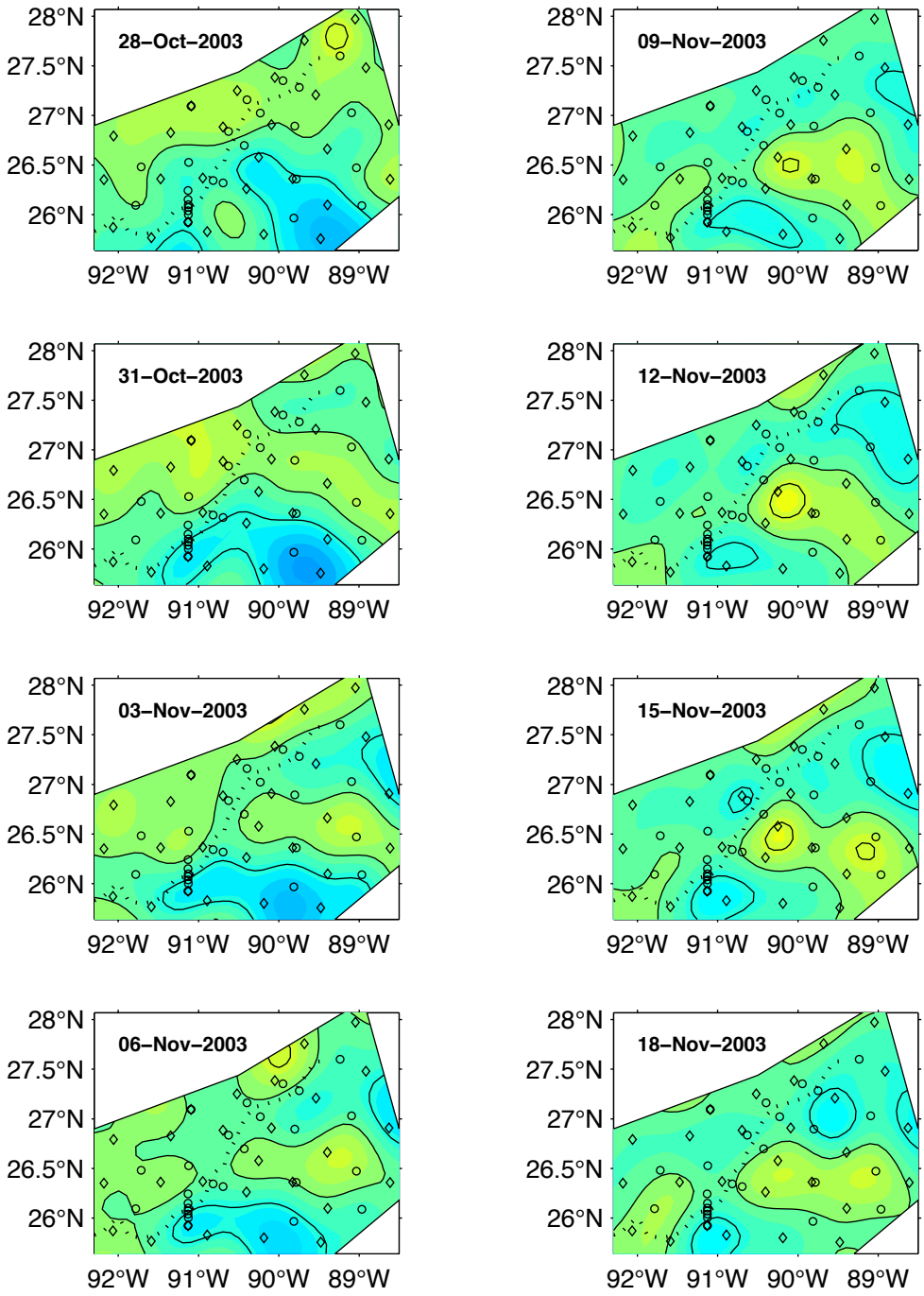

Figure 5.2-22. Topographic Rossby Wave case study: Eddy Event (28 October - 18 November 2003). Maps of 1500-m depth pressure for eight separate days. Low (high) values shown with blue (red/yellow) hues. The sequence begins with the top left panel. The dotted line denotes the center of the Sigsbee Escarpment. PIES sites are indicated by diamonds; current meter moorings by circles.

noting that the central trough in the first panel of Figure 5.2-22 (28 October 2003) has translated nearly out of the region by the last panel (18 November 2003) and has been replaced by the central ridge that followed behind it. The waves in this event are consistent with the TRW dispersion relation, insomuch as wave energy arriving from the ESE (as discussed in Section 4) is associated with phase speed and wave vectors pointing approximately SSW.

The above sequence of maps, chosen to illustrate unforced nearly-plane waves, are in fact exceptional insomuch as they are sufficiently dominated by a single wave vector as to produce clearly identifiable long parallel ridges and troughs. More commonly, the deep pressure maps exhibited a collection of approximately elliptical eddies. Eddy-like features require the sum of at least two plane waves with wave vectors crossed in different directions, so that the pressure field oscillates in both x and y directions.

A commonly cited example arises from the sum of two wavenumbers, (-*k*, -l) and (-*k*, +l),

$$\mathrm{Re}[\, \exp(\mathrm{i}(k\mathrm{x}+l\mathrm{y})) + \exp(\mathrm{i}(k\mathrm{x}-l\mathrm{y}))] \;= 2\cos(k\mathrm{x})\cos(l\mathrm{y})$$

which is a field of closed high and low pressure eddies. It is also common knowledge that isolated eddies can be composed as the Fourier sum of contributions over a finite bandwidth of (*k*, l) wave numbers.

Figure 5.2-22 illustrates a sequence of deep pressure maps filled with cyclonic and anticyclonic low and high-pressure centers during 26 February – 18 March 2004. We interpret these eddy features as unforced 'free modes', because only insignificant vertical stretching could be imposed on the lower layer by such weak, nearly invariant, upper baroclinic features in the region during this time.

The panels in this case study are at 3-day intervals, and the weak quasi-elliptical eddies translated westward approximately 90 km in the 21 days shown. The corresponding near-bottom currents in these features were generally less than 12 $\mathrm{cm \cdot s^{-1}}$, in most places less than 5 $\mathrm{cm \cdot s^{-1}}$. A ridge trough pair is present in the eastern portion of the last panel (18 March), and propagates SW at approximately 20 km / 3 d = 7 $\mathrm{km \cdot d^{-1}}$ (subsequent panels are not shown). It is particularly informative to note that features intensified and decayed during this example – i.e., this occurs even in the absence of forcing. For example, the anticyclone attained greatest amplitude on 9 March; two different cyclones attained greatest amplitude on 3 March and 12 March. Recall in linear theory, TRWs are dispersive, with different wave numbers propagating at different speeds. Thus, we interpret such intensifications as the superposition of different propagating wave components, which causes the amplitude to increase or decrease when their phases add or cancel, respectively.

The two case-studies of this section were chosen to argue qualitatively that TRWs and the eddies can be the same physical process. The deep pressure maps are visually dominated by eddies, cyclonic and anticyclonic. The quantitative demonstration that these deep fluctuations are TRWs was provided by the analyses in the preceding subsections of Section 5.2, which showed the currents of this same collection of features projected well onto TRW kinematics. Hence, it is

appropriate to also view the eddies as constructed from a superposition of waves of different crossed wave vectors.

5.2.9 Actual Float Dispersion

It is clear that the central GOM is one of active east-west exchange. Although the predominant circulation in the deeper layers of the western basin (Sigsbee Plain, Mexico Basin) is cyclonic, the picture in the intermediate layers (1500 m, for example) is less clear. There is a tendency in the eastern basin to observe anticyclonic flow in the intermediate layer; however, the fact that the LC extended far to the north during much of the experiment may contribute to this. Also, there is not an even distribution of the floats, so statistics can be deceiving. For this reason, we have chosen not to try to present figures for quantities such as mean flows.

Another clear feature of the large-scale flow pattern was the tendency for westward moving floats often to follow bathymetric contours and even converge towards the boundary. Recent work with the University of Miami MICOM numerical model shows the presence of an energetic, rectified mean flow concentrated along the northwestern and western deep boundary (Jaimes, 2005). It is interesting to note that the model flow pattern would be expected to produce a pattern of float drifts similar to those observed. On the other hand, at 1500 m the mean flow is still anticyclonic in the model (that is, the mean cyclonic flow does not appear in the model until somewhat greater depths).

5.2.10 Virtual Float Dispersion within the PIES Array

Numerical (or "virtual") floats were used to examine the characteristics of the circulation and eddies that move water properties and momentum across the study area, as well as to determine the dominant pathways of transport. These numerical particles were advected not by a numerical model, but instead by horizontal velocity fields obtained every 12 hours from the PIES analysis (Section 2.4) at the 1500 dbar pressure level. The virtual floats were advected for up to six months with a 4th-order Runge-Kutta scheme (Press et al., 1992) using horizontal bilinear interpolation, resulting in daily positions. Virtual floats that were transported beyond the coverage of the PIES were removed from consideration and no longer advected. The virtual floats were deployed on a 10-km grid every three months, resulting in nearly 3000 virtual deployments. Sensitivity tests (not shown) indicate that the virtual and RAFOS float trajectories tend to follow one another closely, especially in areas of well-developed eddies.

Three-day virtual float trajectories for two specific times (19 April 2003 and 2 January 2004) are presented in Figure 5.2-23, superimposed on the pressure anomalies at 1500 m from the PIES array. The virtual floats mimic the RAFOS float trajectories and characteristics, and show the same acceleration westward along the Escarpment in the presence of cyclones. Flows tend to be parallel to topography, except in the vicinity of eddies. The majority of the virtual floats are expelled from the domain within three months after deployment, primarily due to the effect of structured circulation around eddies.

Another view of the pathways in the study area used the concept of directional stability. The directional stability of the flow (Dickson et al., 1985) indicates the persistence of the flow, and is

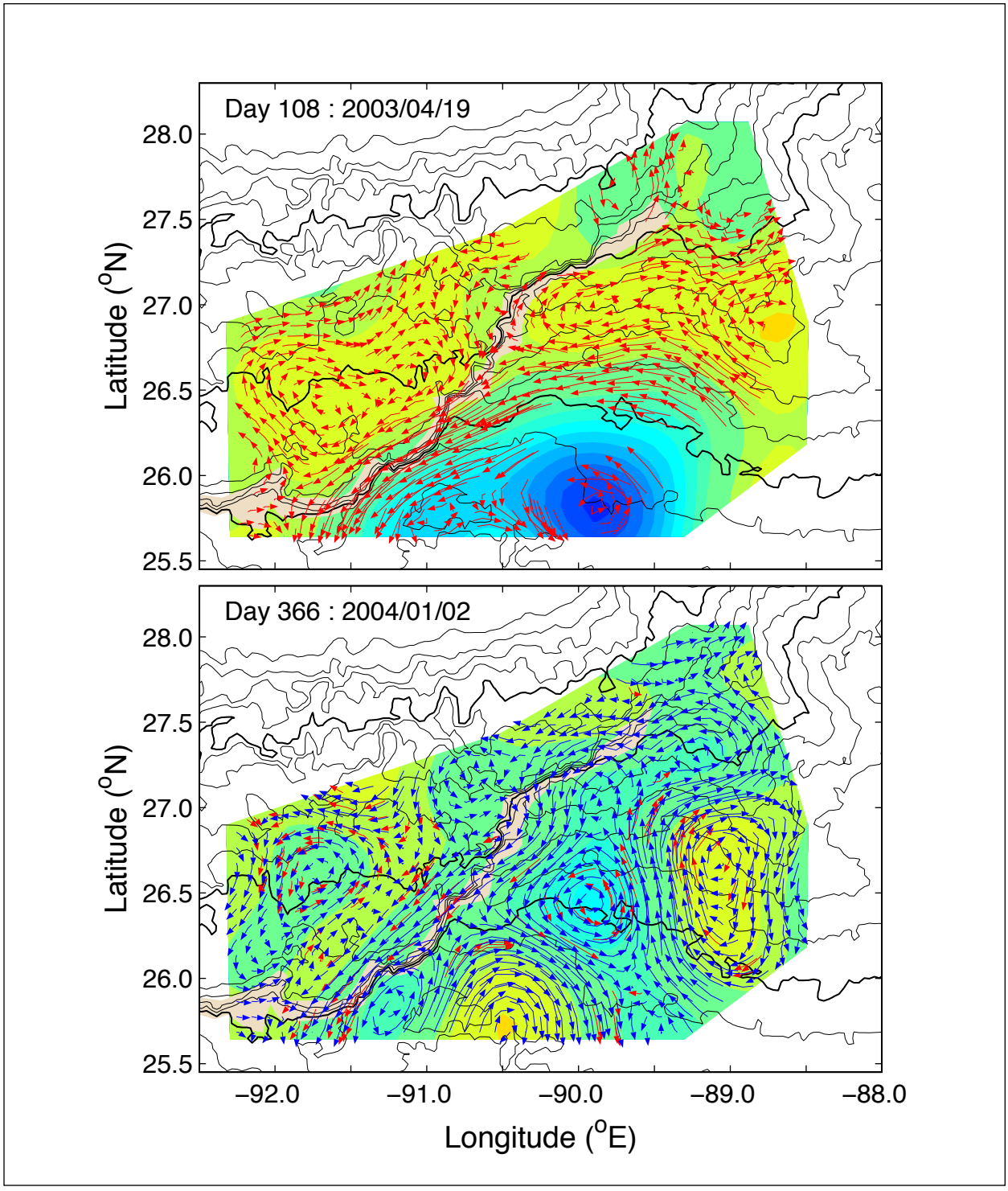

Figure 5.2-23. Three-day trajectories of virtual (numerical) floats superimposed on PIES pressure anomalies at 1500 m for two specific days. The floats were advected by horizontal velocities derived from the PIES pressure anomalies. Floats deployed in 3-month intervals, with the arrow color alternating between deployments. Orange and red colors denote high pressure anomalies. Blues denotes low pressures. Sigsbee Escarpment is shown in beige.

defined as the ratio of the magnitude of the mean velocity vector and the average speed. The ratio varies between 100% for constant, unidirectional flow and 0% for completely random currents. The velocity vectors at each of the PIES-mapped grid points was analyzed, and the directional stability ratio was computed (Figure 5.2-24). Each box was shaded according to its value of directional stability, and those boxes with values greater than 60% were overlaid with unit vectors that show the heading of the mean velocity. The analysis shows that much of the eastern half of the study area had nearly random flow orientation, while a persistent cyclone is found in the southwest corner. The region of consistent vectors to the southwest is the same area where the RAFOS and virtual floats were caught between cyclones and the Escarpment, and were advected out of the study area.

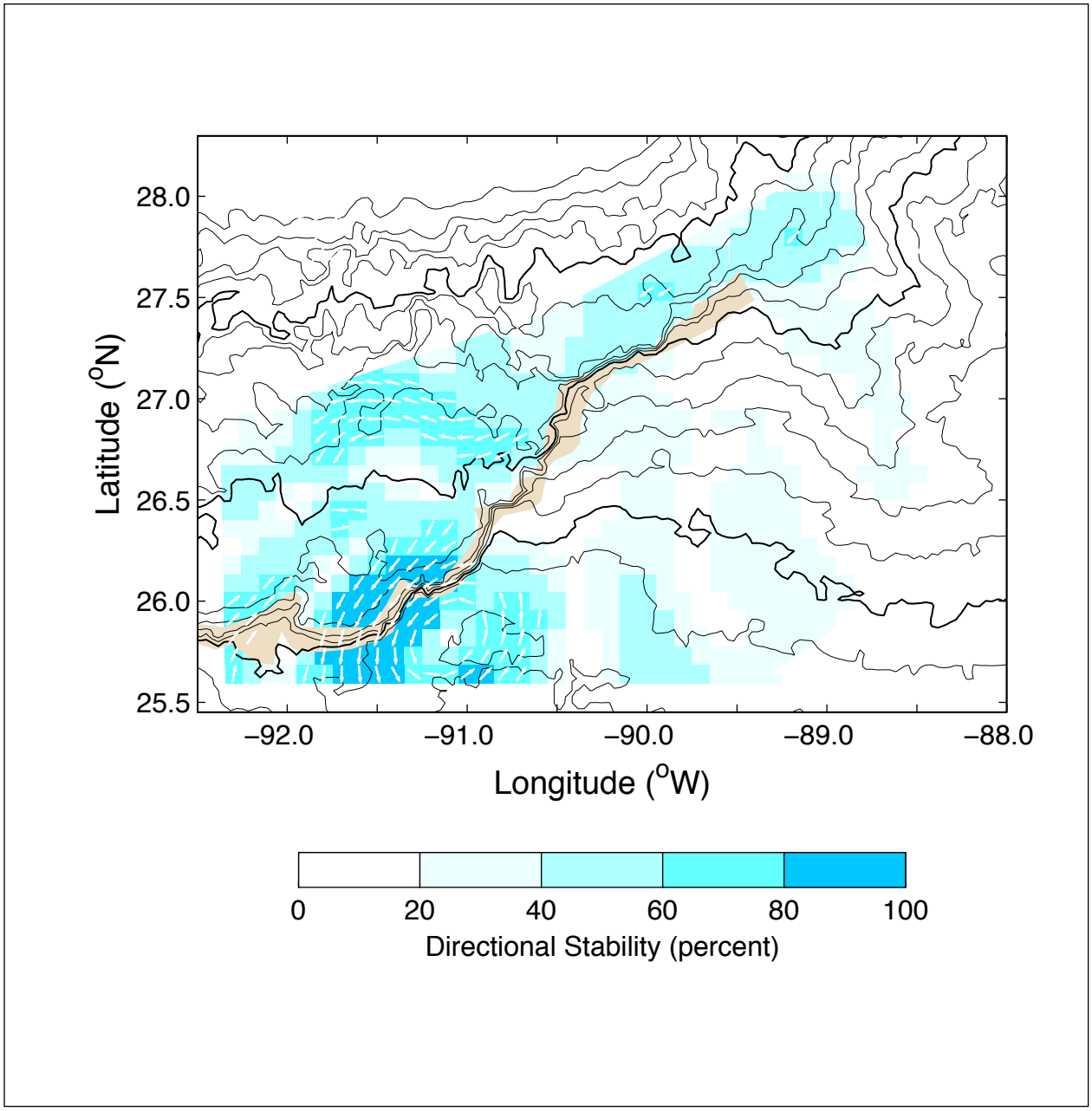

Figure 5.2-24. Directional stability from PIES-derived horizontal velocities, with directional vectors of the most stable flows.

6.0 UPPER– AND LOWER–LAYER INTERACTIONS

Measurements of ocean currents in the GOM that span both upper and lower layers of the water column can provide some insight to linkages that may exist between two dynamically different environments. In Section 4, a fairly detailed description of the measured currents in these two layers was presented and discussed. The reader is referenced to that material for information on actual velocity characteristics within the differing layers. As mentioned several times previously in this report, a basic characteristic of the physical oceanography of the GOM is that the circulation and currents can generally be divided into two layers – the upper layer that extends from the surface to a nominal depth of 1000 m, and the lower layer that extends from a nominal depth of 1000 m to the local bottom. Current patterns in the upper and lower layers are generally quite dissimilar, reflecting differing processes controlling the observed circulation. The present section attempts to identify situations in these upper and lower layers when patterns may be related.

6.1 Full Water Column EOFs on Currents

In the previous sections, analyses of current fluctuations were divided into upper and lower layers, dominated by LCEs and their associated circulations and TRWs, respectively. This was justified by weak direct correlations between near-bottom and near-surface currents. However, it is reasonable that TRWs had a weak manifestation in the surface layers, as has been observed previously at I1 (Hamilton et al., 2005; Hamilton et al., 2003) for a specific wave train that occurred when surface eddy activity was low, and vice versa for the surface-layer eddy currents. The TRW frequency-domain EOFs over the one-year records reasonably resolved the 10 to 60-day fluctuations, characteristic of the near-bottom currents. However, in the eddy-dominated upper layer, the events were not frequent enough to use spectral techniques. Therefore, these analyses used time domain CEOFs. For an analysis of currents through the full water column at each tall mooring (LI through L4), the disparity of time scales between upper and lower layers favors this time domain approach. Therefore, separate CEOF analyses of the 40-HLP currents for each tall mooring were performed using the available year-long records from 750 m and below, and four depth levels as measured by the ADCP at 400 m. The latter depths were 56, 136, 216, and 368 m. This allowed reasonable resolution of the depth profile without unduly biasing the upper versus the lower layer by using the full depth resolution of the ADCP. However, because the records in the upper 400 m of the water column had higher variances than typical records below 1000 m, each current time series was normalized to unit variance. Therefore, the utilized records were equally weighted through the water column. The mode eigenvectors were denormalized to return them to measurement units before plotting. Apart from the difference in weighting, the CEOF analysis for each mooring current record was exactly as in Section 5.1.4, including the rotation of the eigenvectors and amplitudes into the principal axis coordinate system of the amplitude time series.

The depth profiles of the U and V components of the EOFs are given in Figure 6.1-1. Note that the modes for each mooring had different principal axis directions. Only modes that were significant are displayed and they account for more than 80 percent of the total variance of the normalized current records at each mooring used in the analysis. Modes 1 at the moorings, L3 and L4, below the Escarpment, were bottom-trapped and can be associated with TRWs discussed

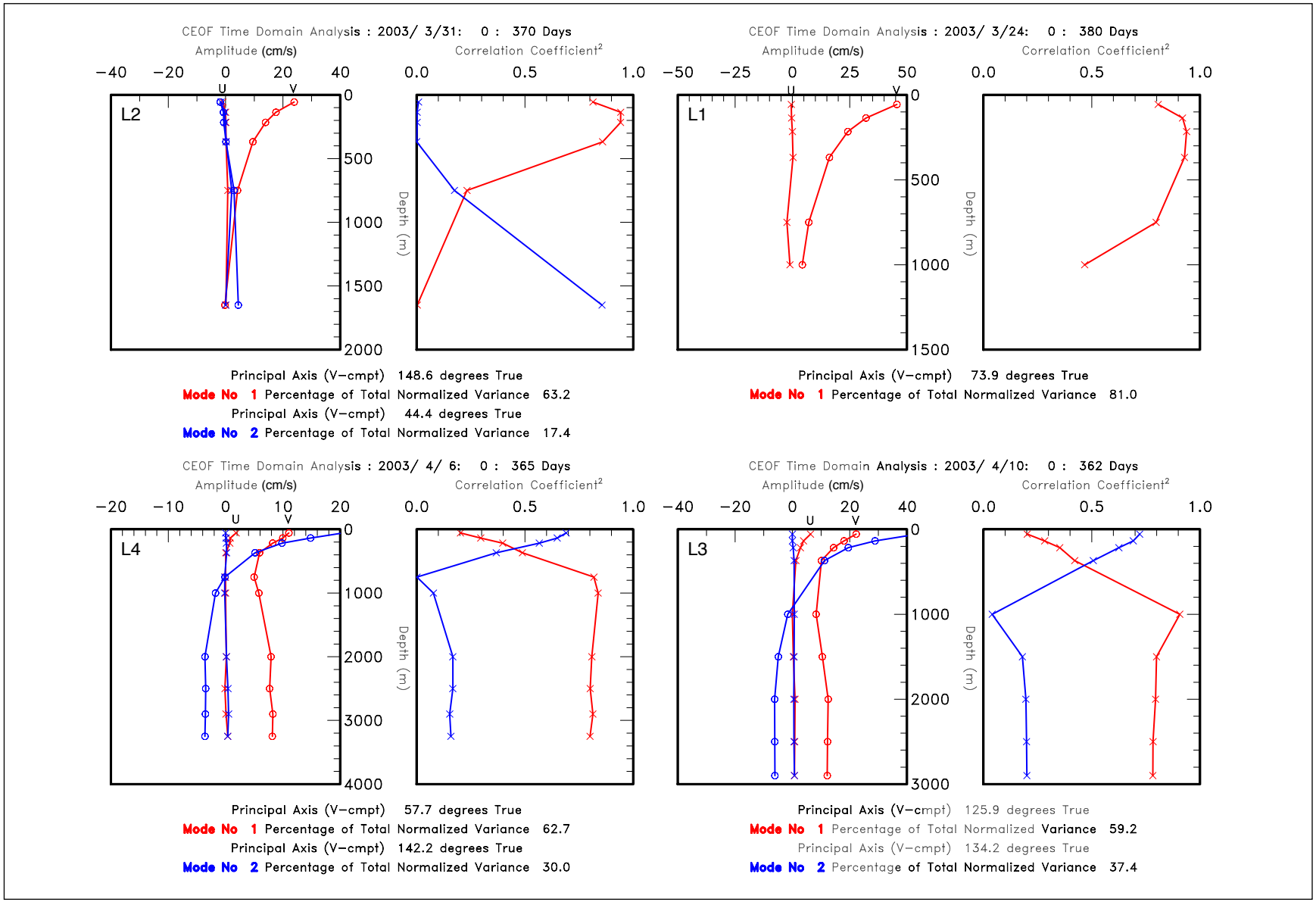

Figure 6.1-1. Vertical modes from CEOF analyses of 40-HLP currents using selected records from the full water column at the four tall moorings. In each case modes 1 and 2 are in red and blue, respectively.

previously. Similarly, mode 2 at L2 had the same characteristics with the correlations (right hand panels in Figure 6.1-1) of the records below 1000 m with those modes being high, whereas the correlations in the upper layer were low, and in some cases, not significant. The opposite situation occurred for modes 2 at L3 and L4 and modes 1 at L1 and L2. The modes were surface intensified and account for large fractions of the variances of the current in the upper 400 m of the water column. The clearest separation of upper and lower-layer signals, which can be denoted as being characteristics of eddies and TRWs, occurred at L2, where the weak bottom-trapped mode profile had no surface expression and the surface-intensified eddy profile had no contribution from the bottom currents. However, at the two deep moorings, L3 and L4, there was a near-surface signal present for the TRW modes, and a weak lower-layer signal in the opposite direction to surface fluctuations in the eddy modes. Modes 1 and 2 in these two cases were very similar to the barotropic and first baroclinic dynamic modes calculated for a flat-bottomed ocean. At L3 and L4, the zero crossing of the eddy mode was around 1000 and 750 m, respectively. This, along with the lower magnitude upper-layer currents at L4, compared to L1 and L3, may have been an indication of the westward decay of eddy circulations. Thus, below the Escarpment, the gently sloping bottom seems to have allowed stronger connections between upper and lower layers than in regions with steep or rough topography.

The time series of normalized mode amplitudes are given in Figure 6.1-2. They have been grouped by mode characteristics (primarily bottom trapped TRW) and surface intensified (eddy), respectively), rather than by mode number. The two modes at each mooring are by definition uncorrelated at zero lag. The TRW modes were very similar to the near-bottom currents discussed in previous sections. Longer periods dominated at L3 and L4 and short-period motions at L1. There was more high frequency content at L3 than at L4 consistent with the lack of penetration of high frequency (~ 10 day periods) TRWs into the west. The eddy time series had quite similar characteristics and were also similar to the surface-layer EOFs discussed previously. Lagged correlations between moorings were calculated for these full depth modes and the only significant (at the 99% level) relations were found between L3 and L4 for the TRW modes and between L3 and L1 for the eddy modes. The L3 versus L4 (V component) correlation was 0.57 (99 percent significance level = 0.19) at a lag of 6.75 days (L3 leading L4). This corresponds to the westward propagation of low-frequency current fluctuations along the Escarpment described previously. The L3 versus the L1 correlation was –0.48 (99 percent significance level = 0.45) with L3 leading by 18 days. This was probably a result of LC activity on the eastern side of the array. The long lag time and barely significant correlation are a reflection of the relatively slow translations of large eddies compared to the higher group velocities of the TRWs.

6.2 Comparison of Upper and Lower Layers as Observed by Floats and Satellite SSH

Evaluating a time sequence of overlaid images of float trajectories and satellite SSH data shows that in most cases and areas very little correlation existed between what is seen in the surface elevation fields and in the float tracks. The only significant exception appears to be late in the record (March-May 2004) under the LC as it extended into the GOM. In this case, several floats at 1500 m (poor coverage was available from the shallow floats at 1000 m) were seen to retreat northward into the Gulf as the LC extended. Several floats can also be observed to become

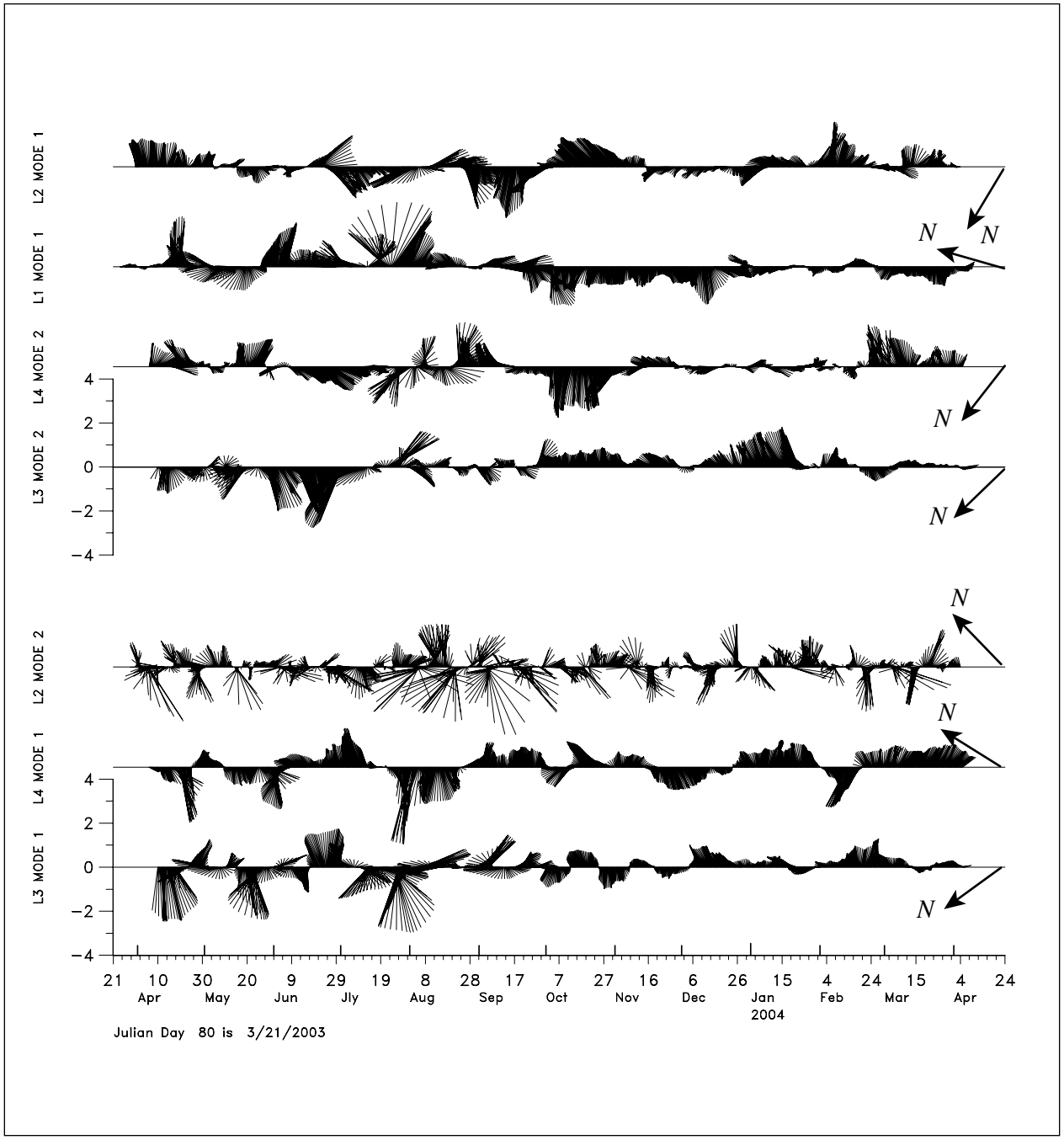

Figure 6.1-2. Time series of normalized amplitudes for modes from the CEOF analyses at each tall mooring. The north direction relative to the principal axis (vertically up) of each mode is indicated by the arrows at the ends of the time axes. The lower three time series are the "TRW" signal, and the upper four, the "eddy" signal.

trapped at a "saddle point" between the main part of the LC and an eddy that separated to the north. Several of these floats also were observed to follow along the SSH contours of the LC for fairly short time intervals, but then diverged from them and crossed contours. During this time, there is little relation between the float tracks in the western GOM and what was in the SSH fields.

6.3 Mapping Case Studies

Interactions between upper and lower layers in the GOM can be visualized by sequences of maps that superpose the upper and lower stream functions and pressure maps. The upper and lower stream-function fields are presented in these several case studies by the PIES generated SSH and by the P1500 (1500 m) pressure maps, respectively (see Section 2.6 for methodology). First, a simple case is presented in which the propagation of a deep cyclone was temporarily halted when it encountered Eddy Sargassum. Following presentation of this simpler case, are two examples of joint propagation in the upper and lower layers of a cyclone pair and an anticyclone pair. In each of these latter two cases, the lower-layer eddy led the upper-layer eddy in a vertically tilted fashion characteristic of coupled propagation. Finally, a baroclinic instability is illustrated in which the phase of this vertical tilt and the wavelength led to a joint growth of the upper- and lower-layer perturbations.

6.3.1 Upper-Layer Circulation Halts Deep-Eddy Propagation

The first case study of upper- and lower-layer interactions illustrates the intuitive and straightforward concept that strong upper-ocean flow can influence the propagation of deep eddies. The dynamics are straightforward; the upper-layer flow distorts the background flow field. In this example, Eddy Sargassum's deep thermocline presented an obstacle in the path of a deep cyclone; Eddy Sargassum temporarily halted the westward propagation of a deep cyclone.

In the absence of strong upper-ocean flows, lower-layer cyclones tended to propagate through the array in two patterns (see Section 4.2.1). In one pattern, deep cyclones that entered the array along its eastern boundary translated northwest until they encountered the Sigsbee Escarpment where they were deflected to the southwest (topographic westward). See for example, Figure 4.2-2.

Deep cyclone propagation is quite different in the presence of strong upper-ocean circulation, however (Figure 6.3-1). During 22 September to 2 October 2003, Eddy Sargassum dominated the upper-layer circulation. A deep cyclone entered the array around 15 September, propagated west until 21 September, and then stalled when it encountered Eddy Sargassum's deep-reaching thermocline and the associated flow which opposed its propagation. Note that this figure begins after the initial westward propagation of the deep cyclone and illustates its nearly stationary position from 22 to 26 September. The deep cyclone remained locked to Eddy Sargassum's southeastern edge until Sargassum's major axis rotated from a northwest-southeast orientation to a north-south orientation. During this clockwise rotation, the deep cyclone again moved westward until it encountered the Escarpment. After 28 September, Eddy Sargassum no longer flowed counter to the 'natural' path of the deep cyclone, and the deep cyclone propagated along the Escarpment and out of the array.

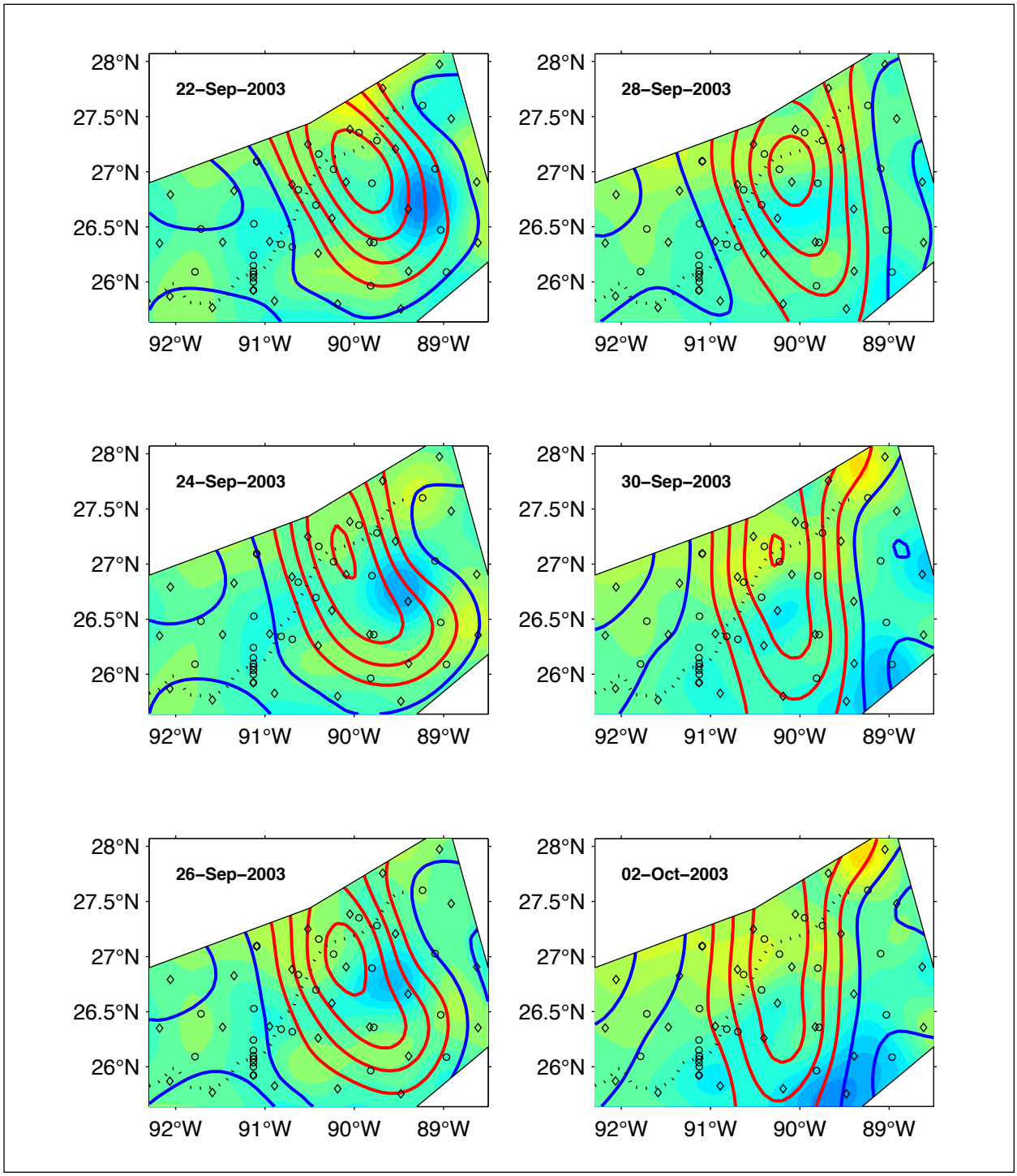

Figure 6.3-1. Case study: Upper-layer circulation halts deep-eddy propagation [22 Sept - 02 Oct. 2003]. Maps of surface streamfunction (bold contour lines) superimposed upon shaded contours of 1500-m depth pressure for six separate days. The sequence begins with the top left panel. The dotted line denotes the center of the Sigsbee Escarpment. PIES sites indicated by diamonds; current meter moorings by circles.

6.3.2 Lower-Layer Eddies Lead Upper-Layer Features

The second category of upper- and lower-layer interaction represents the more dynamic vertical coupling that results when propagating upper-ocean features stretch or squeeze the lower layer. The lower-layer response to vortex stretching/squeezing requires the acquisition of respectively positive/negative relative vorticity to balance the changes in thickness in order to conserve total potential vorticity. Consider the idealized case of a propagating upper-ocean anticyclone (Figure 6.3-2). As the upper-ocean anticyclone propagates it alters the lower-layer vorticity. The lower layer shrinks ahead of the eddy and stretches behind the eddy. To conserve potential vorticity, shrinking must be accompanied by a decrease in relative vorticity. Hence, a lower-layer anticyclone advances ahead of the upper-ocean anticyclone. Behind the upper-ocean anticyclone, the stretching and increase in relative vorticity results in a lower-layer cyclone. Note that this scenario is highly idealized: we have neglected the effects of topography, a spherical earth or a lower-layer background flow field. The reader is referred to Cushman-Roisin et al. (1990) for a more in-depth discussion. Note that Welsh and Inoue's (2000) modeling study reveals the joint spin-up of lower layer eddies beneath strong translating upper-ocean features.

An example of a lower-layer anticylone leading an upper-ocean anticylone is shown in Figure 6.3-3, 11-16 April 2003. In early April 2003, the LC intruded into the eastern side of the PIES array. As the LC propagated westward and slightly northward, a lower layer anticyclone resided ahead of the LC center and its direction of propagation.

The counterpart to the propagating upper-ocean anticylone is a propagating cyclone. First we begin with the schematic, then the case study from the Exploratory Array (Figure 6.3-4). As the upper-ocean cyclone propagates it alters the lower-layer vorticity. The lower layer stretches ahead of the eddy and shrinks behind the eddy. To conserve potential vorticity, stretching must be accompanied by an increase in relative vorticity. Hence, a lower-layer cyclone advances ahead of the upper-ocean cyclone. Behind the upper-ocean cyclone, squashing and a decrease in relative vorticity results in a lower-layer anticyclone.

An example of a lower-layer cyclone leading an upper-ocean cyclone is shown in Figure 6.3-5 for 21 July 2003 to 31 July 2003. This energetic time period encompassed the detachment of Eddy Sargassum and the separation of Unnamed Eddy (See discussion in Section 4.1.1). Recall that an intense LCFE associated with the detachment of Eddy Sargassum propagated into the study area, interacted with Sargassum and split Unnamed Eddy from the southwest flank of Sargassum. The sequence shown in Figure 6.3-5 reveals that a strong lower-layer cyclone preceded the upper-ocean cyclone.

6.3.3 Baroclinic Instability

Often perturbations develop along the edge of the LC as it enters the GOM from the Yucatan Channel. They typically start as small meanders that propagate downstream around the LC and grow into frontal eddies. This growth is called an instability process, because it is capable of drawing upon the kinetic and potential energy of the basic LC to feed the growth of perturbations. In the classic theory of baroclinic instability, these perturbations can grow if they

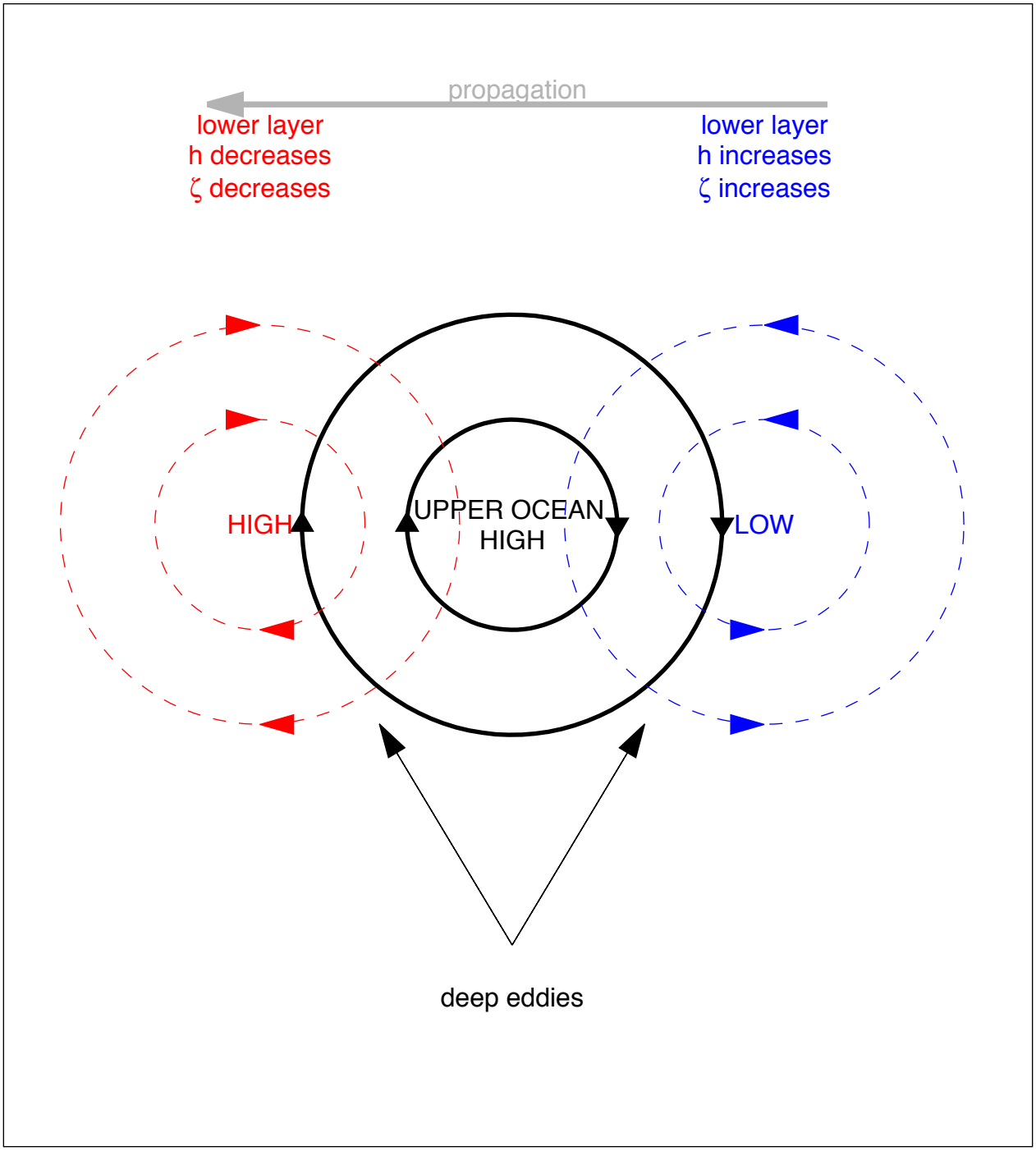

Figure 6.3-2. Schematic representation of propagating upper-ocean anticyclone (solid black) and leading lower-layer anticyclone (dashed red) and trailing lower-layer cyclone (dashed blue).

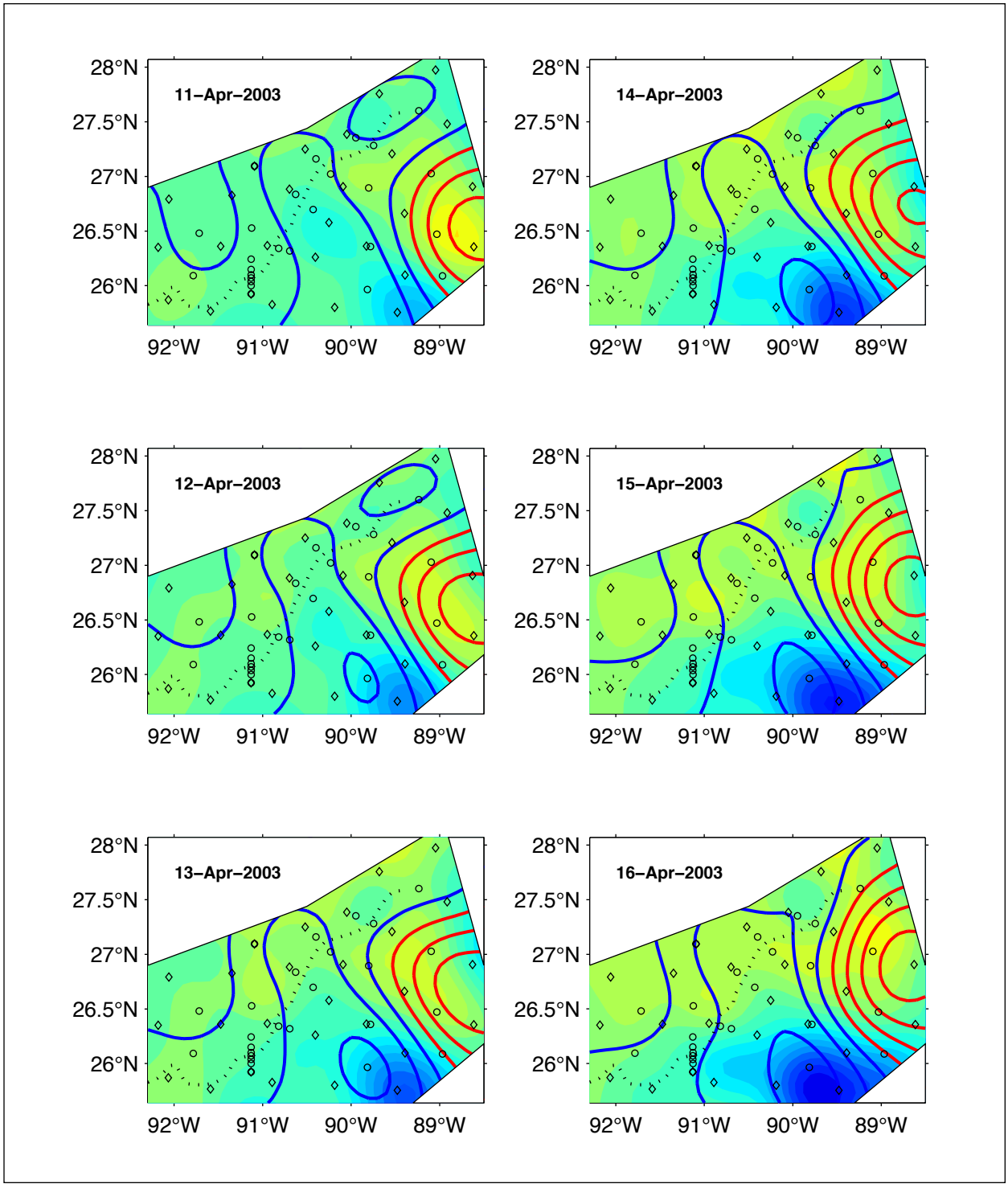

Figure 6.3-3. Case study: Lower-layer anticyclone leading an upper-ocean anticyclone [11-16 April 2003]. Maps of surface streamflunction (bold contour lines) superimposed upon shaded contours of 1500-m depth pressure for six separate days. The sequence begins with the top left panel. The dotted line denotes the center of the Sigsbee Escarpment. PIES sites are indicated by diamonds; current meter moorings by circles.

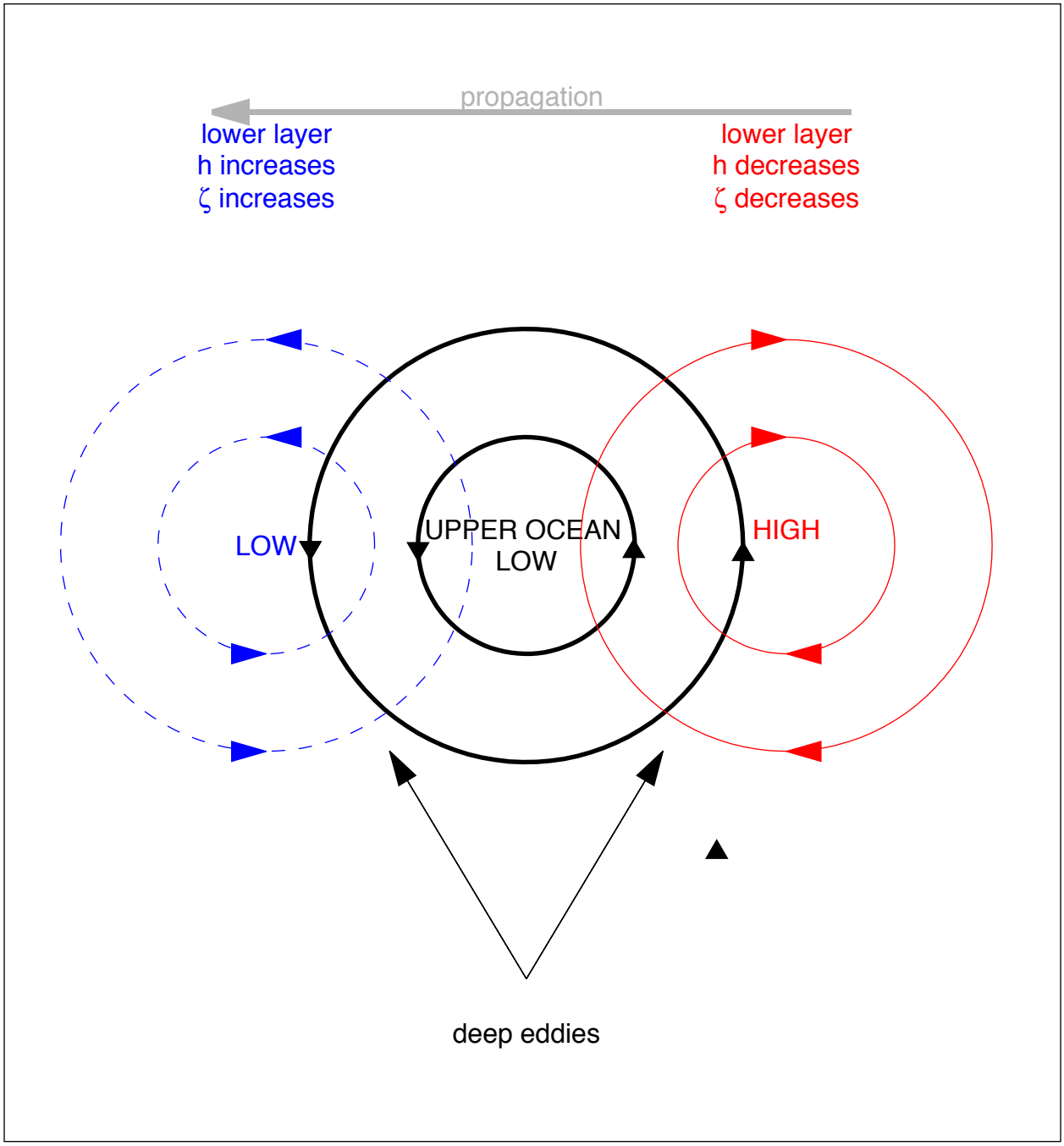

Figure 6.3-4. Schematic representation of propagating upper-ocean cyclone (solid black) and leading lower-layer cyclone (dashed blue) and trailing lower-layer anticyclone (dashed red).

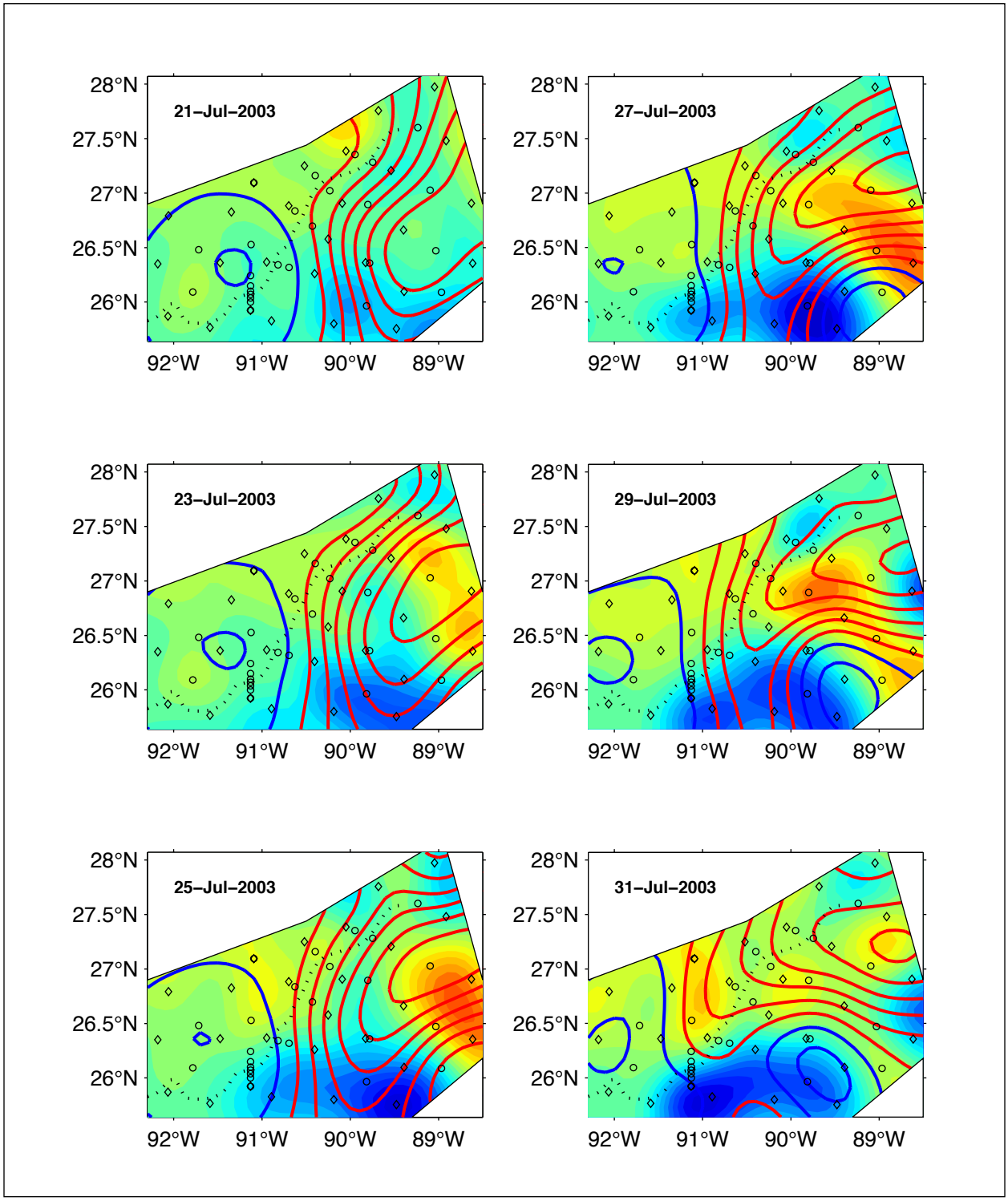

Figure 6.3-5. Case study: Lower-layer cyclone leading an upper-ocean cyclone [21-31 July 2003]. Maps of surface streamfunction (bold contour lines) superimposed upon shaded contours of 1500-m depth pressure for six separate days. The sequence begins with the top left panel. The dotted line denotes the center of the Sigsbee Escarpment. PIES sites are indicated by diamonds; current meter moorings are indicated by circles.

have the right structure and long enough wavelength – eddies vertically coupled in the upper and lower layer and tilted as discussed below.

Figure 6.3-6 schematically illustrates cyclonic and anticyclonic perturbations, each coupling eddies in the upper and lower layers; they exhibit the characteristic phase-offset that is necessary, according to the theory of baroclinic instability [see for example Cushman-Roisin (1994)]. For simplicity, this illustration ignores effects of bottom topography, so would apply to a flat-bottom ocean. The orientation shown resembles a portion of the LC, with a meander crest and trough propagating to the north along the upper baroclinic jet. A deep anticyclone leads the upper anticyclonic crest. Similarly, a deep cyclone leads the upper cyclonic trough. Hence, these low- and high-pressure centers are each vertically tilted; the phase offset sketched here is approximately one-eighth of the wavelength which, according to baroclinic instability theory, would favor growth of features of wavelength longer than about 3 to 4 times the radius of deformation.

A simple vorticity argument helps to understand how the coupling between upper and lower eddies allows them to both grow (meteorologists call the analogous behavior "self-development" as applied to meanders of the atmospheric jet stream and associated pressure centers). The lateral shift of the upper baroclinic front associated with a crest/trough respectively squash/stretch the lower water column, tending to add anticyclonic/cyclonic vorticity in deep eddies. Importantly, the deep eddies also act upon the upper flow. Consider in this schematic a water parcel in the upper level en route from the crest to the trough; the circulation around the deep high- and low-pressure centers draws the parcel across the baroclinic front deeper into the trough. This stretches the upper water column and adds cyclonic vorticity, tending to grow the trough. Correspondingly, an upper water parcel enroute from trough to crest is pushed by the deep eddies higher into the crest; this squashes the upper column and adds anticyclonic vorticity and grows the crest. In this configuration the upper meanders and deep eddies act upon each other to make the perturbation vorticities grow in both layers.

Figure 6.3-7 presents a case study from our observations which is consistent with baroclinic instability. The LC had protruded relatively far north along the east portion of the study area. On 17 May 2003, a meander crest and accompanying deep high-pressure center entered from the south. For the next 2 –3 days they developed together, with the deep anticyclone center offset to the west and slightly north of the developing upper crest. A more thorough analysis of this event would require, at least, consideration of the sloping bottom that alters how the lower water column is stretched, and may account for why, after 20 May, the feature decays rather than grows.

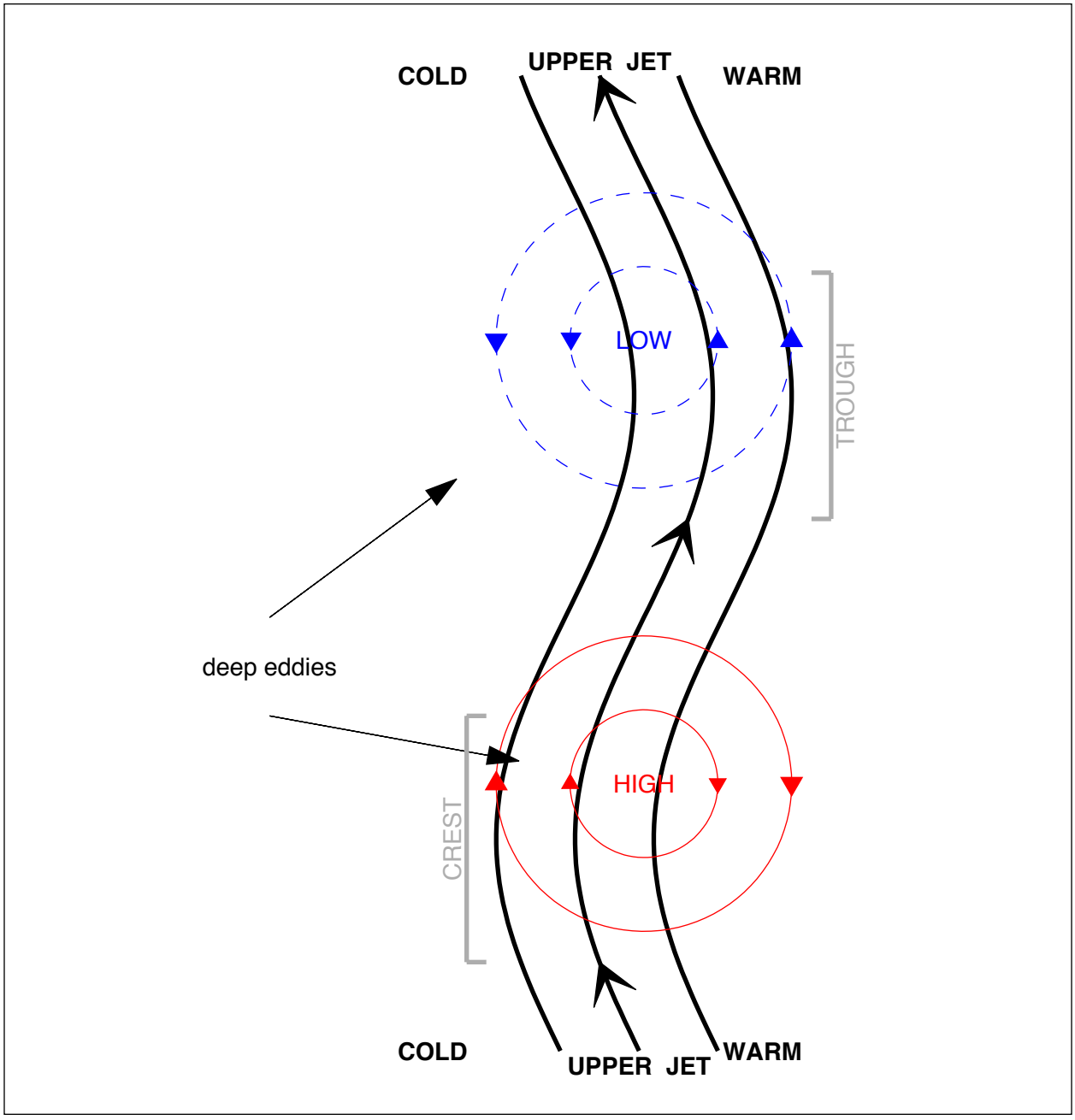

Figure 6.3-6. Schematic representation of the characteristic phase offset between upper and lower-layer cyclonic or anticyclonic perturbations that favors baroclinic instability. The orientation shown resembles a portion of the LC, with a meander crest and trough propagating to the north along the upper baroclinic jet (bold black contours). The thermocline is shallow with relatively cold waters to its left, and deeper with relatively warm waters to its right. Leading the upper crest is a deep anticyclone (thin red contours); leading the upper trough is a deep cyclone (thin dashed blue contours). The phase offset (vertical tilt of the low pressure centers and respectively the high pressure centers) is approximately one-eighth wavelength in this schematic, which according to baroclinic instability theory would favor growth of features longer than about three to four times the radius of deformation.

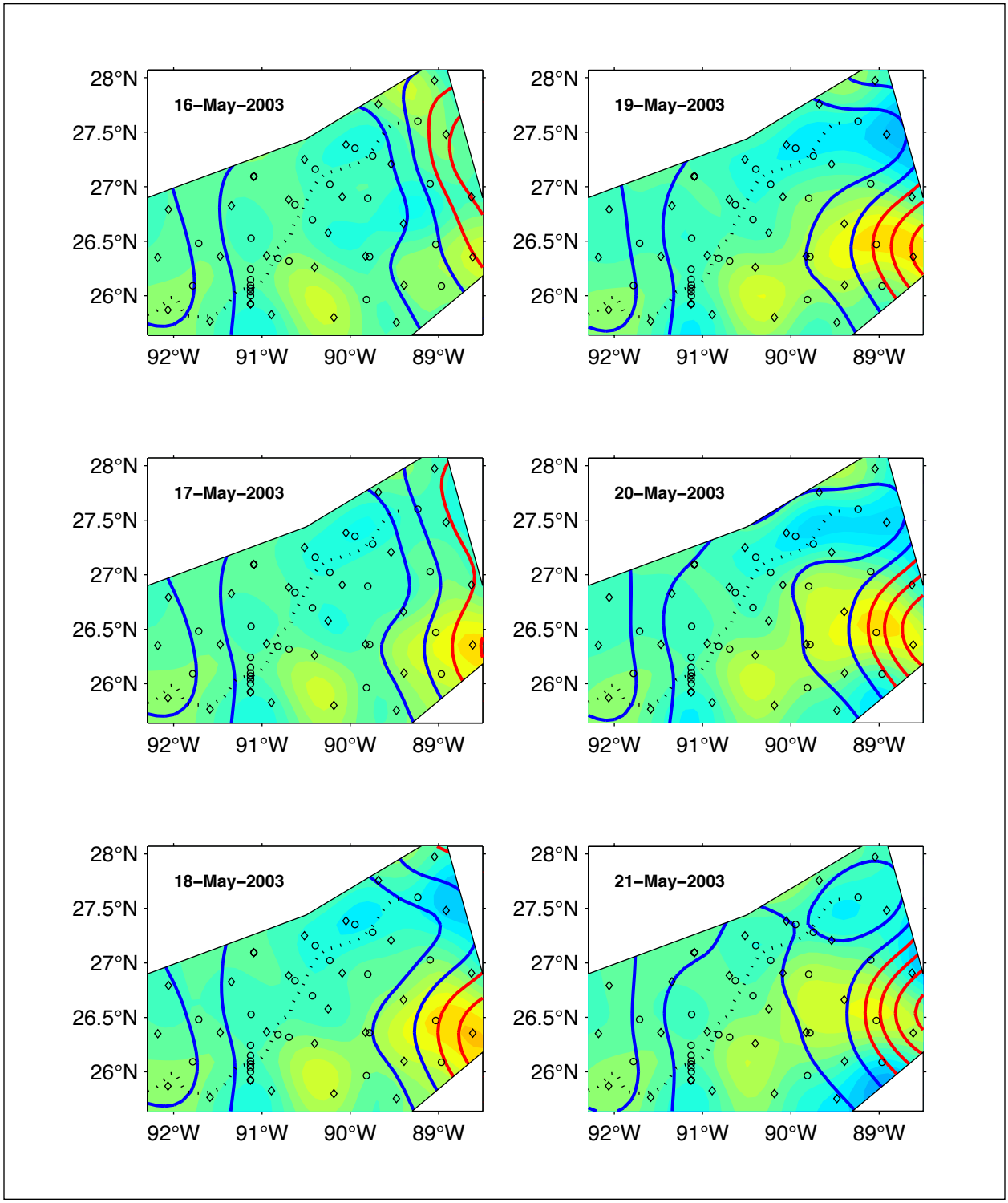

Figure 6.3-7. Case study: Baroclinic instability [16-21 May 2003]. Maps of surface streamfunction (bold contour lines) superimposed on shaded contours of 1500-m depth pressure for six separate days. The sequence begins with the top left panel. The dotted line denotes the center of the Sigsbee Escarpment. PIES sites are indicated by diamonds; current meter mooring sites indicated by circles

7.0 HIGH-FREQUENCY VARIABILITY

Previous studies of high-frequency currents in the deep GOM have shown them to be dominated by inertial oscillations. Near-inertial currents are internal waves with periods near $2\pi/f$, where f is the Coriolis parameter. Motions are characterized by a clockwise rotating vector (viewed from above), and the internal wave has upward phase propagation and a downward component of group velocity. Near-inertial currents are usually generated by changing surface winds that often occur in conjunction with storms. Rapidly moving hurricanes can generate large inertial wakes in deep water that can persist for many days to as long as several weeks after the tropical storm has passed (Brooks, 1984a; Shay and Elsberry, 1987; Hamilton et al., 2000). Though surface winds are thought to be the major source of inertial energy, inertial oscillations can also be generated by processes of geostrophic adjustment, and thus may be generated by large-scale flow interactions such as eddy – eddy and eddy – topography interactions. Direct evidence for this is difficult to discern in current data. However, there are many observations of energetic inertial oscillations at considerable depths below the wind-forced surface layer.

The longest period that inertial waves can freely propagate is given by $2\pi/f_e$,, where f_e is defined by (Mooers, 1975):

$$f_e^2 = f\,(f + \varsigma)$$

and ς is the relative vorticity of the background current field. Thus, a region with negative relative vorticity, such as an anticyclonic eddy, can support inertial oscillations at longer periods than regions of positive ς, that surround an anticyclonic eddy as an annulus (Kunze, 1985; 1986). In this situation, the longer period inertial energy becomes trapped and can lead to enhanced inertial currents where there are strong relative vorticity gradients in both the horizontal and vertical directions. Relative vorticity magnitudes decrease with increasing depth in anticyclones (Kunze, 1986; Hamilton et al., 2003).

Local inertial periods ($2\pi/f$) in the study region range from 25.9 hours at L1 (NE tall mooring) to 27.4 hours at L4 (SW tall mooring). These periods overlap those of the dominant diurnal tide in the GOM. As a consequence, it is almost impossible to separate diurnal tidal notions from inertial motions. However, the barotropic diurnal tidal current in water depths greater than 1000 m has small amplitudes of a few $mm \cdot s^{-1}$ and therefore can be safely neglected.

7.1 Eddy Sargassum Inertial Currents

An initial investigation of high-frequency current oscillations in the upper layer, above 400 m, showed that L1 had unusually large currents when Eddy Sargassum was over the site. The inertial oscillations during this event are shown in Figure 7.1-1, where the velocity components have been high-passed filtered with a filter having a cut-off period of 50 hours. This removed motions with periods longer than about two days without suppressing the longer period (but much less than two-day) inertial oscillations. The north or V-component leads the east or U-component by 1/4 (90°) period and has a similar magnitude. This is the signature of a clockwise, almost circular, rotating current. The event emerged from similar shorter period, lower-amplitude oscillations, grew and then decayed over a period of about 25 days. Maximum amplitudes occurred at ~168 to 200-m depth, around 25 August 2003, with lesser currents above

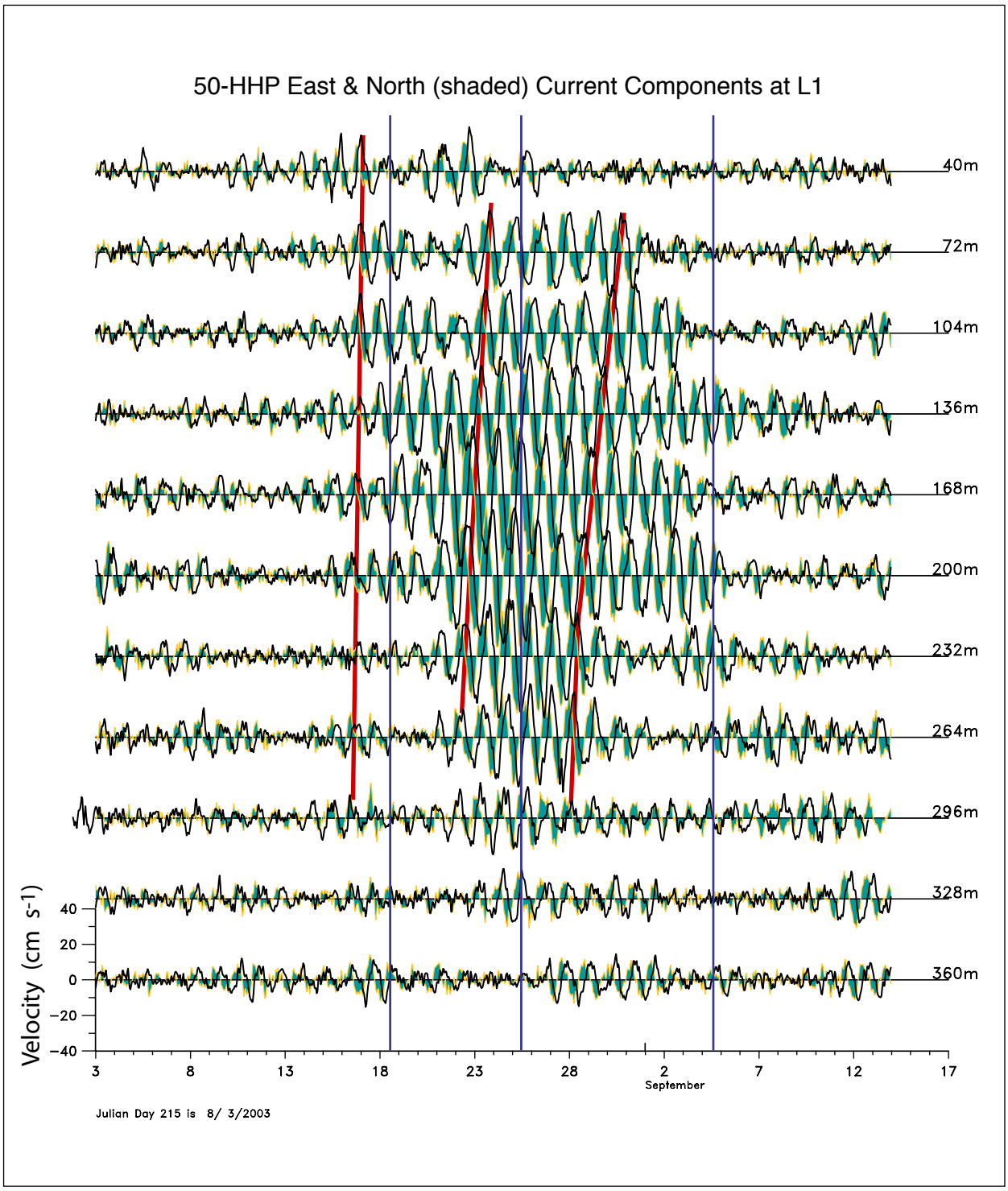

Figure 7.1-1. Inertial currents from the upper-most ADCP at L1 during the passage of Eddy Sargassum. Current records have been 50-HHP filtered. East (U) component is solid, and north (V) component is blue shaded. Red lines show approximate propagation of V-component peaks. Blue lines mark times discussed in the text.

and below. Upward phase propagation is evident from tracing the velocity peaks through the depth levels (Figure 7.1-1), but the rates are not constant with time. The phase differences between depth levels increased with time as the event progressed, and in the later part of the event, phase differences were slightly larger above the depth of maximum amplitudes (~200 m) than below. The vertical component of the group velocity is proportional to the vertical component of phase velocity and in the opposite direction for inertial-internal waves. Therefore, a build up of energy around 200 m could be related to a change in the downward energy flux below this depth.

The inertial peaks in the spectra, for a 36-day period centered on 25 August 2003, are shown in Figure 7.1-2. The center frequency was about 0.8 cpd or 13% less than the local inertial period. This corresponds to a period of about 30 hours and thus a latitude of ~24°N if the waves were generated in a quiescent ocean. The spectra also show the increase in variance at 200-m depth compared with near-surface (40 m) and deeper (300 m) depths. Figure 7.1-2 also shows 36-day spectra from a more typical interval at L1. This was a relatively energetic interval from the winter of 2003-2004. In this case, the spectra peaks were higher than f and the energy decreased with increasing depth, as would be expected for locally wind generated inertial-internal waves. In the latter period, maximum amplitudes of the inertial-internal waves were ~ 20 $cm \cdot s^{-1}$ at 40 m compared to ~ 40 $cm \cdot s^{-1}$ at 200 m in the August Eddy Sargassum event.

A frequency-domain EOF analysis of the inertial oscillations in both periods is given in Figure 7.1-3. In both cases, two modes were significant and accounted for greater than 75% of the total variance in the bands centered about the peak frequencies of 0.8 and 1.0 cpd, for the eddy and winter, respectively. In Eddy Sargassum, the first mode had a maximum at about 180-m depth and was confined between 100 and 350-m depth levels. The phase differences showed upward propagation (positive phase differences lead) with vertical wavelengths of ~100 m and 200 m above and below the maximum. Note that the V-component led U by about 90° at all depths and because the U and V amplitudes were almost identical, circular clockwise rotating current vectors were observed at all depths in the upper 400 m of the water column. The second mode had a subsurface maximum at about 100 m, which was associated with a slightly shorter vertical wavelength of ~70 m. It appears that the eddy contained two wave trains of similar period that had different trapping depths. This could be because the vertical shapes of the modes resulted from waves generated at different times in the past or they could have had slightly different frequencies not resolved by the band averaging of the analysis. The vertical group velocity is very sensitive to the difference between the wave frequency and f_e (Phillips, 1969), and thus the spatial distribution of the background relative vorticity.

The vertical distribution of inertial amplitudes and phases in the winter case also requires two modes. RMS amplitudes were considerably less than in the eddy, and maximum oscillations were found in the surface mixed layer above ~ 60 to 70 m. Phases were confused above 150 m, but below this depth the usual 90° phase difference between V and U and upward phase propagation was evident. The vertical change in phase indicates that the vertical wavelengths of the inertial-internal waves were much greater (estimated ~600 to 800 m) than in the eddy case. Previous analyses of inertial currents at mooring I1 in the deep GOM (Hamilton et al., 2003) during wind-forced periods when LC eddies were not present, were very similar to this winter

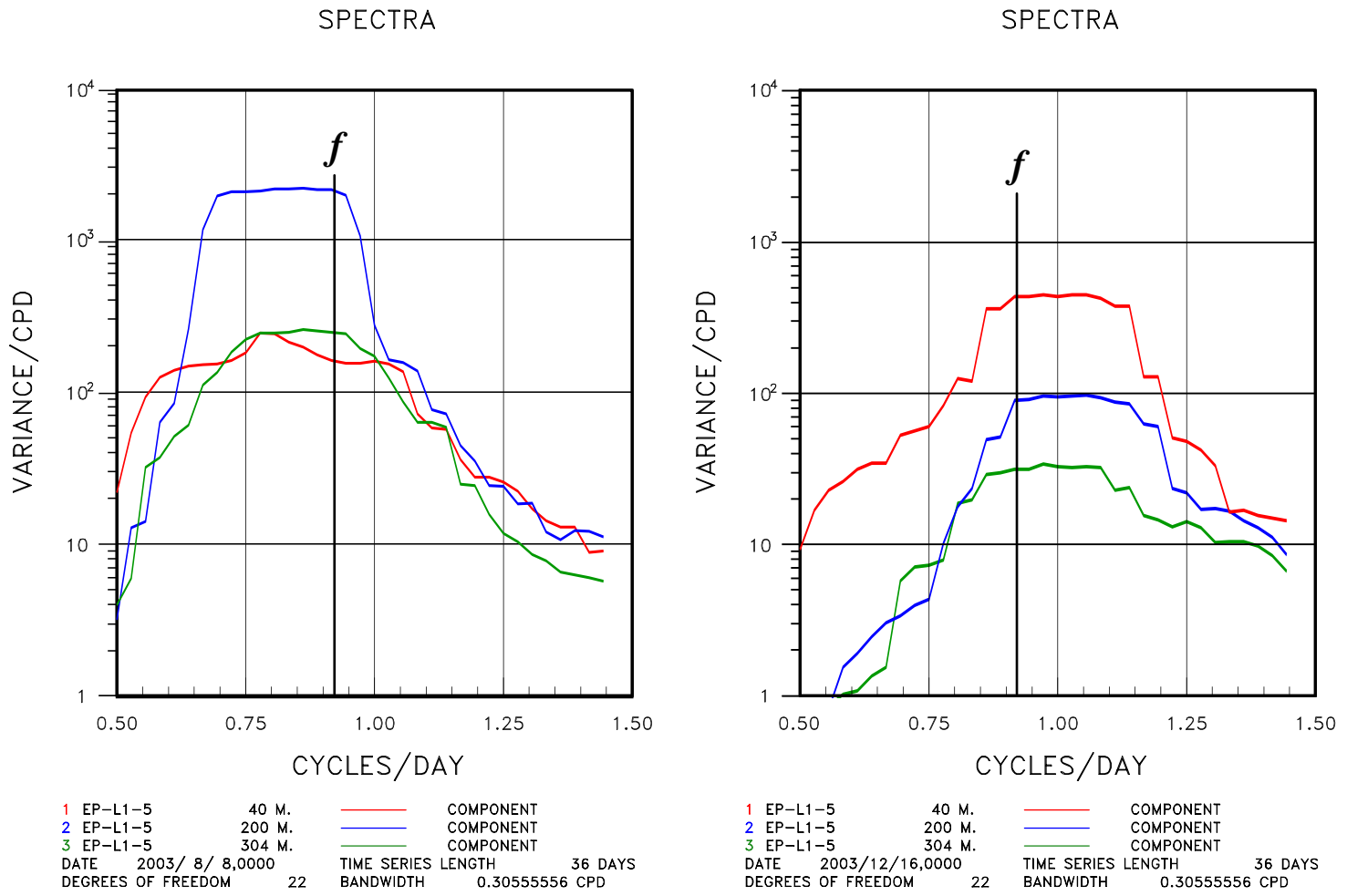

Figure 7.1-2. Clockwise component of rotary spectra at the indicated depths at L1 for 36-day intervals. Left panel: August 2003 eddy Sargassum event. Right panel: Winter storm event. Local inertial frequency (*f*) is indicated.

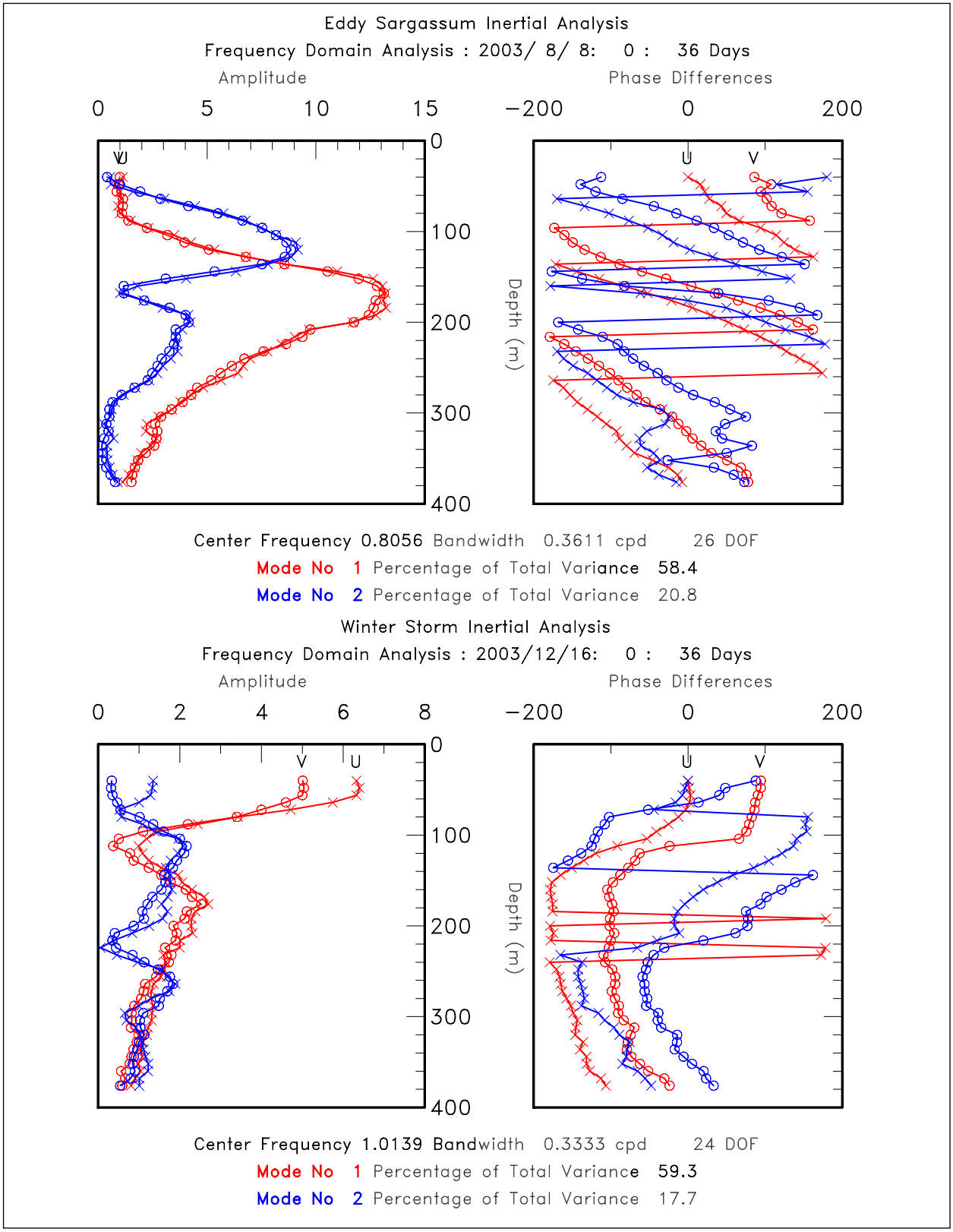

Figure 7.1-3. Frequency domain EOF modes for the August (top panel) and December (bottom panel) 2003 inertial currents in the upper 400 m at L1. Amplitude units are cm•s^{-1}. Straight lines occur in phase because it is a rotary value.

case. Again the implications are that the vertical distribution of wind-generated inertial currents at any given time may have had more than one source.

The inertial oscillations at L1, during August, had different characteristics than normal high frequency currents. Peak frequencies were less than local f, and amplitudes were larger and strongly confined to the 100 to 250-m depth range with short vertical wavelengths. More than one significant EOF mode was required to account for the majority of the variance. The low-frequency currents and temperatures during this interval are given in Figure 7.1-4. The vertically sheared anticyclonic eddy currents appeared at the beginning of August as the eddy moved over the site from the east. Magnitudes declined until about 12 August, which was about the time of the maximum depression of the deeper isotherms. The energetic longer period oscillations were not evident except for a short burst near the surface at 40 m. This could be attributed to the wind event at this time that also rotated clockwise after 15 August. The winds were from Hurricane Erika (see Section 7.2), which tracked east to west with its center near L3 and L4, over this time interval. It is noted that this wind-forced event propagated downwards and seems to have merged with major inertial oscillations at depth that appeared after 18 August. This could be an interpretation of a mode 2 signal being separate from mode 1 and effecting shallower depths. Eddy currents increased as the isotherms shoaled as the eddy axes rotated through the site. The time of the lowest currents (around 25 August) contained the most energetic inertial oscillations. The eddy mapping products place L1 at this time on the eastern side of the center, which accounts for the shallower isotherm depths. The eddy moved off to the southwest and elongated in this direction. The strong inertial currents were gone by early September and the eddy had moved away from L1 by the middle of the month.

The most energetic oscillations were above the depth of the 20°C isotherm (Figures 7.1-1 and 7.1-4) and thus above the main thermocline in the part of a LC eddy that best approximates solid body rotation (Hamilton et al., 2003). Figure 7.1-5 maps the depth of the 20°C isotherm, and the surface geostrophic velocities, calculated from the SSH anomaly. Both quantities were derived from the PIES array. These maps correspond to the beginning, the time of maximum amplitude, and the end of the inertial event (see blue lines on Figure 7.1-1). On 18 August (Figure 7.1-5a) the site (L1) was on the north side of the eddy center, the center having earlier moved across the site from the east. The eddy was interacting with a vigorous cyclone to its west and the warm water of a filament was being wrapped around the north side of this cold-core eddy. Note that cyclones do not show up in maps of surface-layer temperatures. Eddy Sargassum's major axis rotated towards the northwest and by the time of maximum inertial activity (25 August; Figure 7.1-5b) the site was on the east side of the center. The eddy was moving west or southwest and its translation was reducing the magnitude of the eastward swirl currents at L1 so the net effect was the small, low-frequency currents observed at this time. The cyclone appears to have been becoming unstable with complex secondary flows developing, including a small anticyclone on its western edge. The center of Eddy Sargassum then moved to the southwest, and became stretched along its major axis in this direction. The isotherms in the center of Eddy Sargassum also shoaled about 25 m by 4 September (Figure 7.1-5c). The site was then in stronger swirl currents and the inertial currents had dropped down to background level. The small anticyclone in Figure 7.1-5b had grown and rotated eastward around the cyclone producing a cyclone-anticyclone pair to the west of Eddy Sargassum. Thus, it appears that the anomalous inertial event between 18 August and 4 September was confined to the northern and eastern side, or

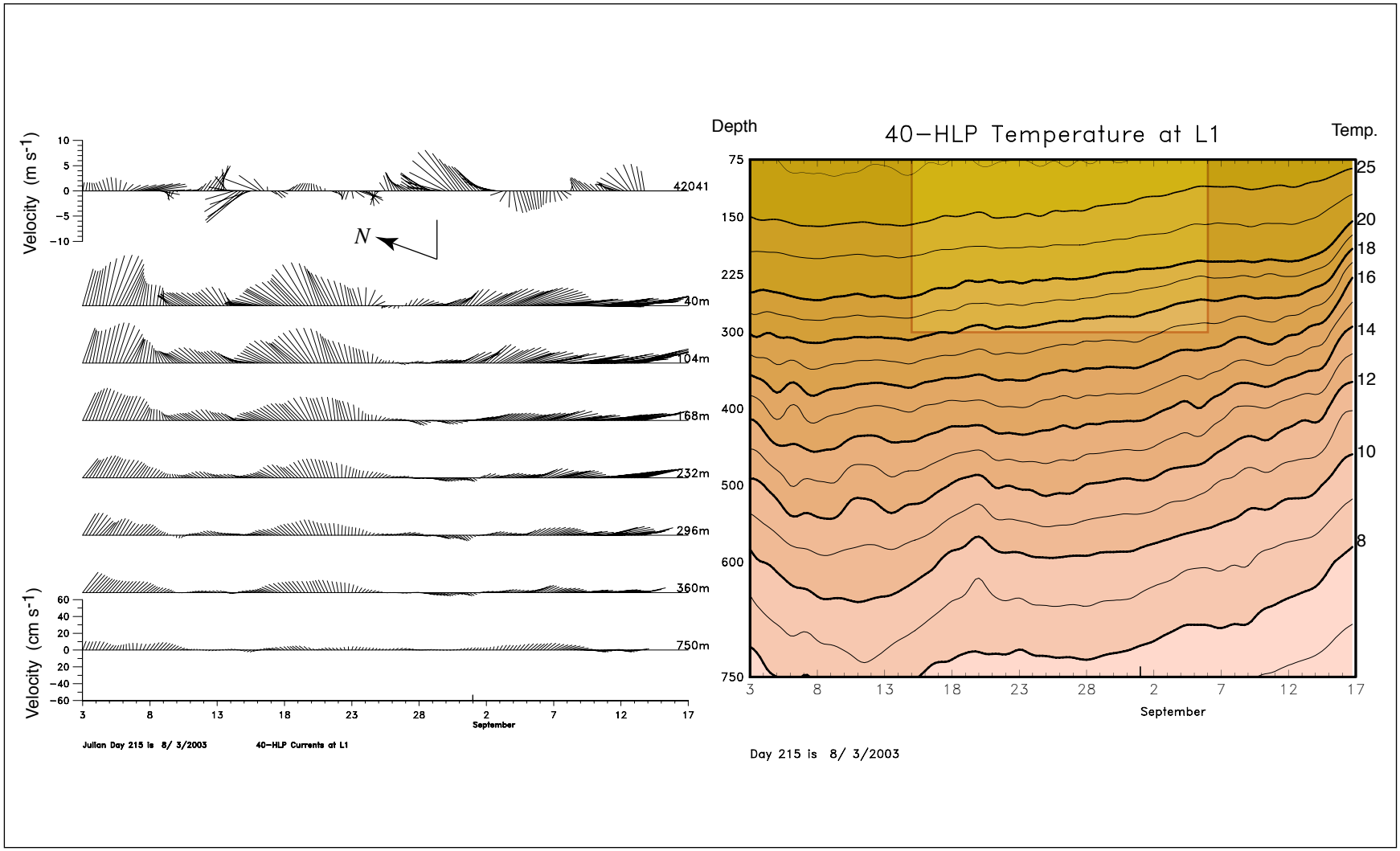

Figure 7.1-4. 40-HLP currents (left panel) and temperatures (right panel) at L1 during the passage of Eddy Sargassum. The period and depth range of the inertial event shown in Figure 7.1-1 is indicated by the lighter shading on the temperature contour plot.

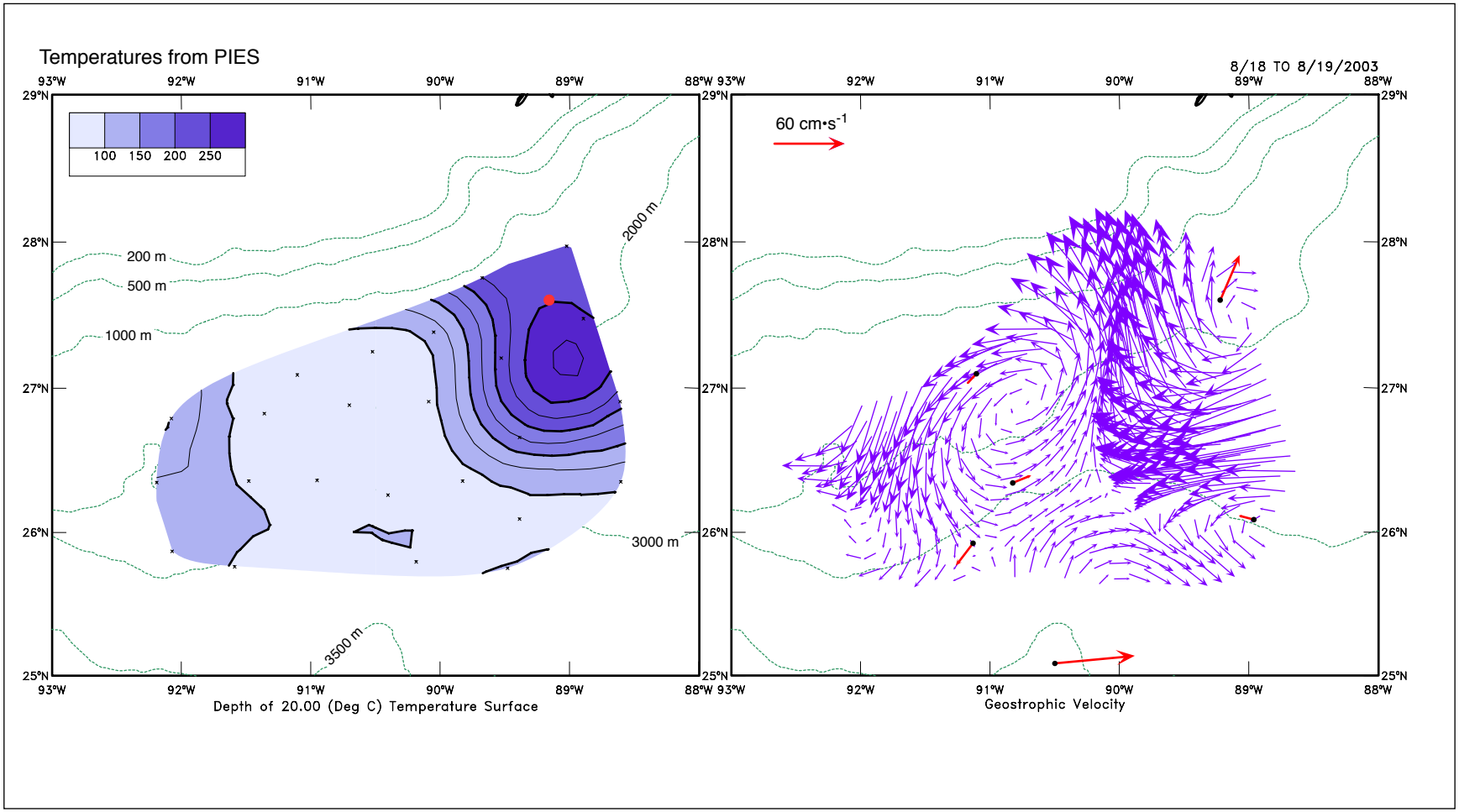

Figure 7.1-5a. Depth of the 20°C isotherm (left panel) from PIES temperature profiles, and surface geostrophic velocity from PIES SSH anomaly (right panel) for August 18, 2003 at 1200 GMT. The L1 site is shown as a red dot on the left panel and daily averaged 40-HLP current vectors at 40-m depth as red arrows on the right panel.

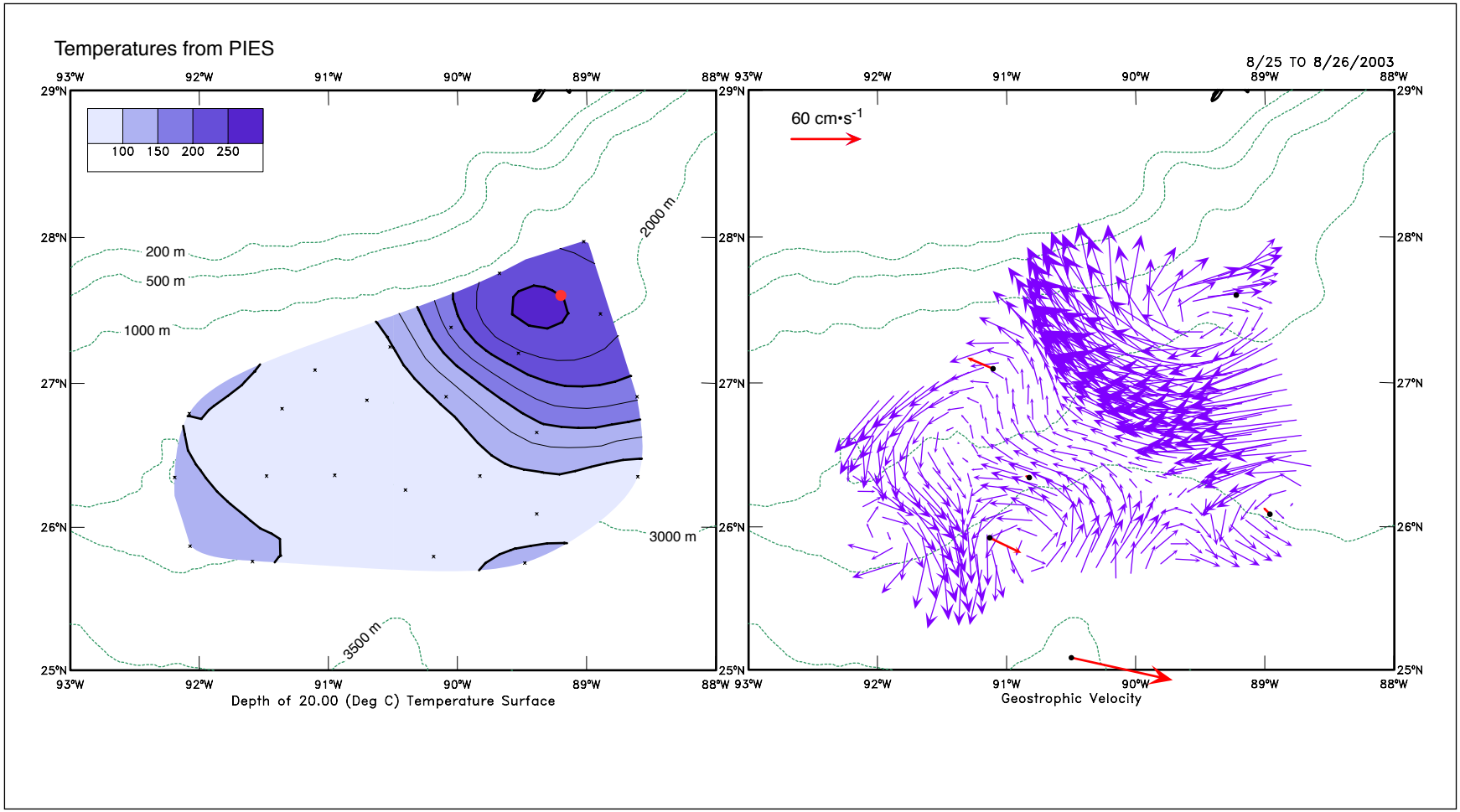

Figure 7.1-5b. Depth of the 20°C isotherm (left panel) from PIES temperature profiles, and surface geostrophic velocity from PIES SSH anomaly (right panel) for August 25, 2003 at 1200 GMT. The L1 site is shown as a red dot on the left panel and daily averaged 40-HLP current vectors at 40-m depth as red arrows on the right panel.

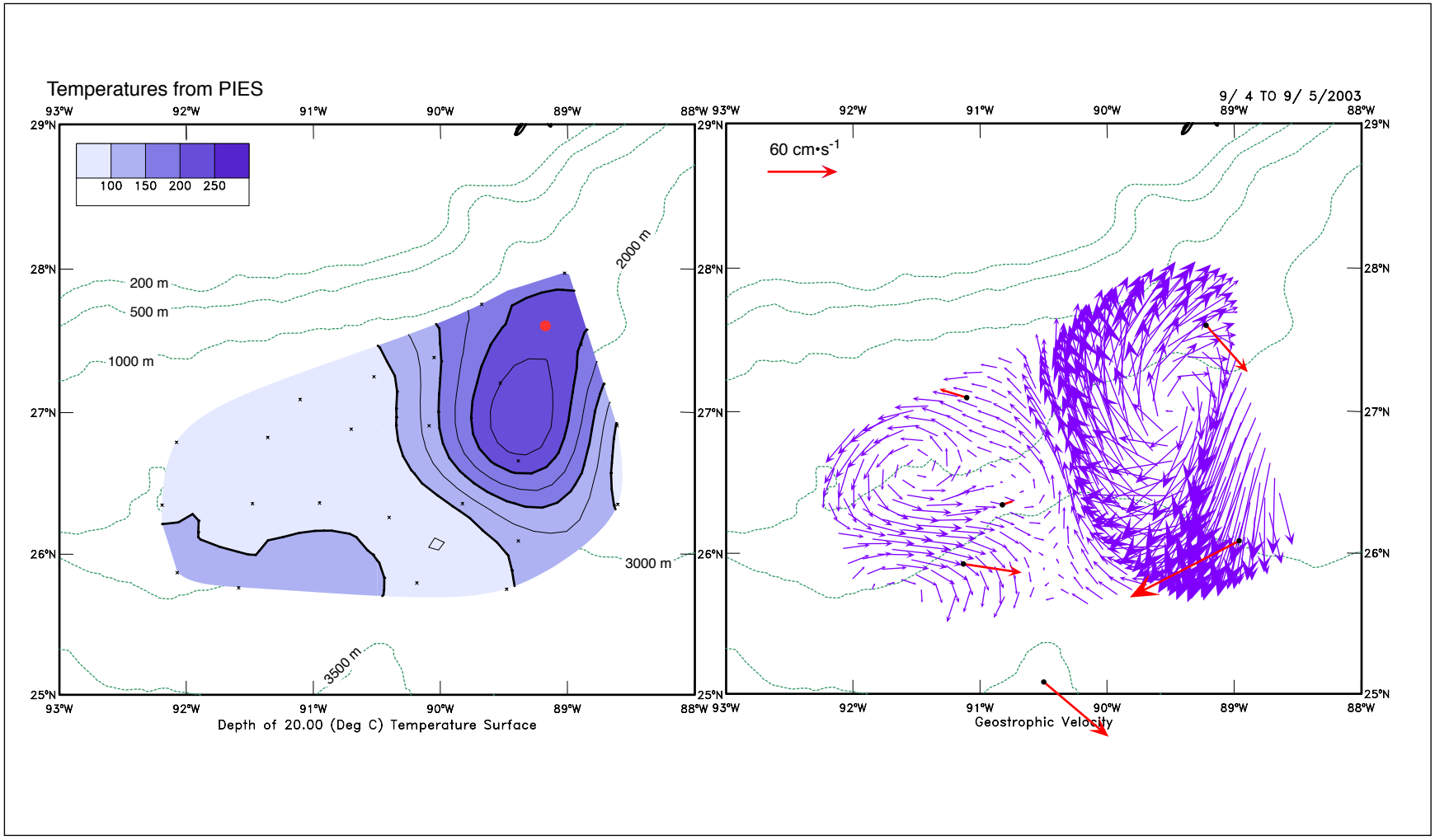

Figure 7.1-5c. Depth of the 20°C isotherm (left panel) from PIES temperature profiles, and surface geostrophic velocity from PIES SSH anomaly (right panel) for September 4, 2003 at 1200 GMT. The L1 site is shown as a red dot on the left panel and daily averaged 40-HLP current vectors at 40-m depth as red arrows on the right panel.

alternatively the trailing part of the eddy center with most of the energetic fluctuations occurring at depth above the main thermocline. Calculations of relative vorticity, using the geostrophic velocity fields in Figure 7.1-5, give a value of ~ -25×10^{-6} s^{-1} in the center of Eddy Sargassum, which is about 0.37f and implies $f_e \approx 0.75$ cpd. This is lower than the diagnosed inertial frequency of 0.8 cpd and slightly above the low frequency edge of the peak in Figure 7.1-2. Therefore, the observed inertial oscillations could propagate as inertial-internal waves but were trapped in the center of the eddy as the negative relative vorticity decreased in magnitude away from the center and below the thermocline. This is consistent with previous observations of inertial currents in warm-core rings by Kunze (1986).

Between August and October 2003, Eddy Sargassum translated southwestward, with the center moving across L5. If the center had continued on this path, approximately along the Escarpment, then it would have also moved over L4. However, on reaching L5, the eddy turned southward, and began to weaken so that the western side of the swirl currents only affected L4 in October and November. Therefore, if strong inertial oscillations at frequencies below f observed at L1 persisted, then the best chance of observing their consequent evolution was at L5. The LSU mooring (L5) was differently configured from four Exploratory tall moorings, with the upper layer ADCP spanning a deeper depth range of about 56 to 640 m. The upper bins, above 100 m, have sometimes have noisy signals because they are approaching the range limit of the instrument. The 50-HHP velocity components for October are given in Figure 7.1-6. Relative to L5, the center of the eddy on 11 October had a similar configuration to the eddy, relative to L1, on 25 August. The October inertial currents at L5 (Figure 7.1-6) were more similar to average upper-ocean activity that was observed at all the tall moorings, with 5 to 10-day bursts of coherent signals rising above the background at apparently almost random intervals at different depths. The exception was a longer, more energetic signal that had maximum amplitudes of about 20 $cm \cdot s^{-1}$ that was centered at about 600-m depth between 5 and 29 October, whilst the center of the eddy was in the vicinity of the site.

As the eddy translated southwestward from L1 to L5, the effective inertial frequency, f, decreased, without taking into account the relative vorticity contribution, because of a change in latitude. Local f at L5 and L1 are 0.89 (27-hour period) and 0.93 (25.9-hour period) cpd, respectively. Therefore, this reduction in f over time could allow sub-inertial internal waves to escape the center of the eddy. Figure 7.1-7a shows the clockwise rotary power spectra for selected depth levels at L5. The same length time series (36 days) were used for these calculations as for the L1 spectra (Figure 7.1-2). Unlike at L1, the displacement of the peak to sub-inertial frequencies decreased with depth, so that at 600 m, which had the largest power except for the 100-m level, the peak was approximately centered slightly below local f. The 600-m center frequency of the peak was about 0.05 cpd higher than that observed at 200 m at L1 in August. An EOF analysis of the frequency band centered on this 600-m inertial peak (Figure 7.1-7b) shows the enhanced energy (mode 1) was restricted to a narrow depth range around 600 m, and this mode decays toward the surface. However, this signal had much less amplitude than the 200-m peak at L1 (Figure 7.1-3). The vertical wavelength at 600 m, estimated from the phase differences, was ~ 400 m or more than twice that observed at L1 in August. Both modes showed the upward phase propagation characteristic of inertial-internal waves.

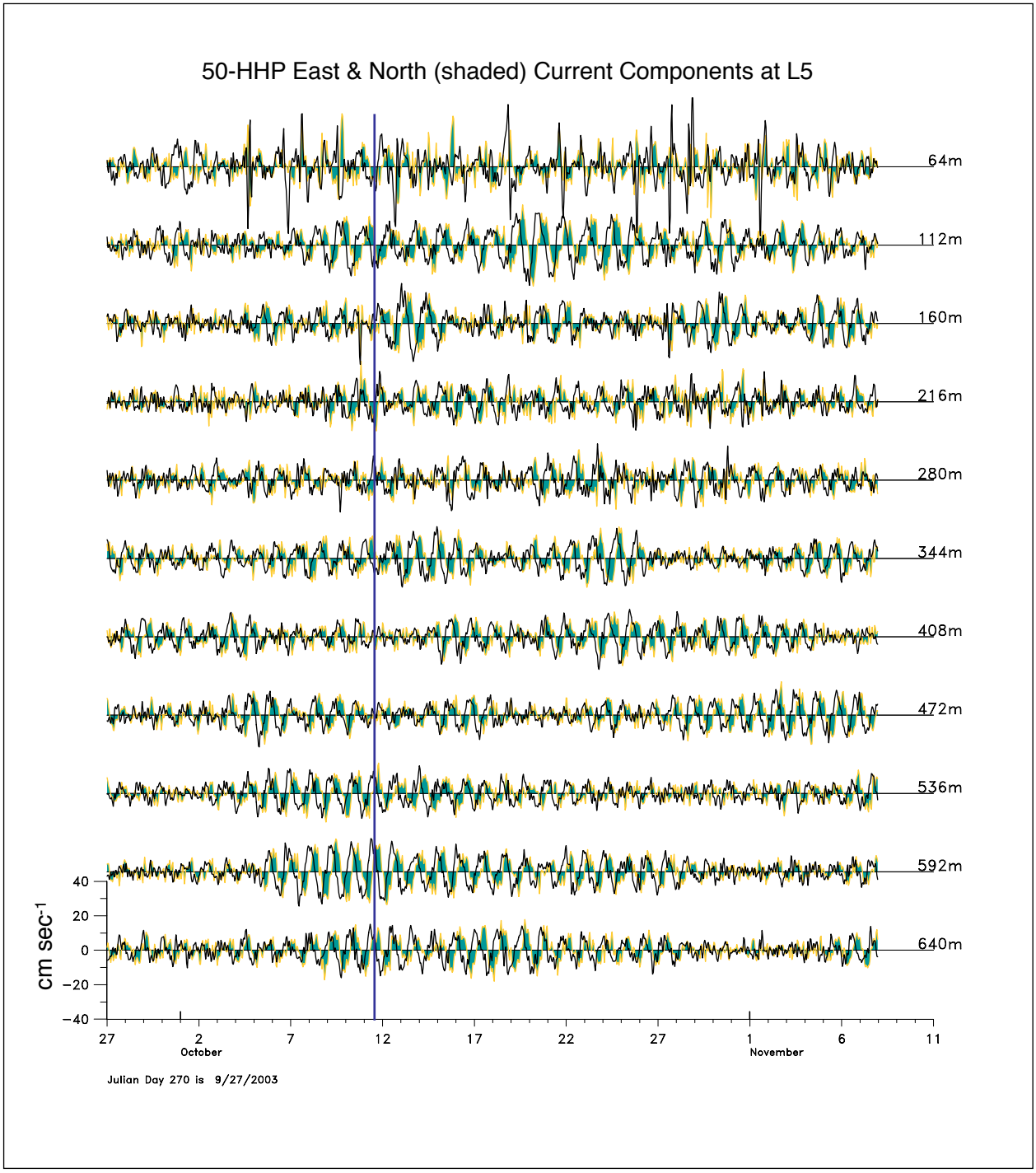

Figure 7.1-6. Inertial currents from the upper most ADCP at L5 during the passage of Eddy Sargassum. Current records have been 50-HHP filtered. East (U) component is solid, and north (V) component is blue shaded. The blue line marks the time the eddy center is close to the mooring.

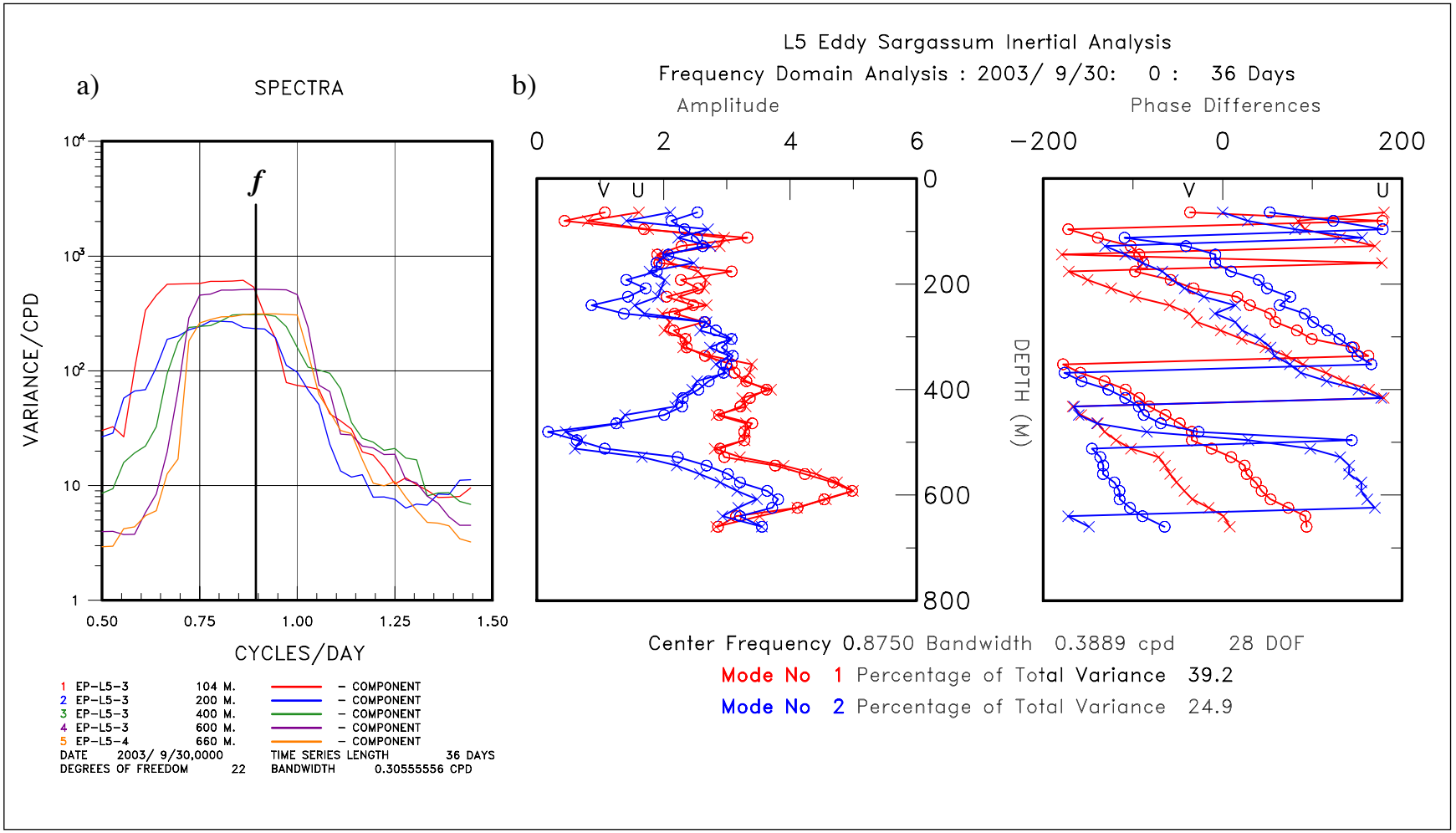

Figure 7.1-7. (a) Clockwise rotary power spectra of the inertial peak at selected depth levels at L5. Local diurnal frequency, f, is marked. (b) The amplitude ($cm \cdot s^{-1}$) and phase differences of the 1st and 2nd mode from a frequency domain EOF analysis of the upper-layer inertial currents at L5 during the passage of Eddy Sargassum.

The low-frequency currents at L5 during the eddy's passage are given in Figure 7.1-8. Currents were north or eastwards indicating that L5 remained slightly west and north of the center before the eddy moved off to the south. The temperature signal at 660 and 167 m clearly showed the warm water moving over the site. Salinity at 167-m depth, which is a little below the depth of the subtropical underwater (SUW) maximum, had high values of 36.5 indicating that the core still had the characteristic SUW signal that was derived from the LC. The wind record showed more storm activity than in August, including some clockwise rotating events around 11 October. Clockwise rotating wind vectors tend to favor the generation of clockwise inertial currents. The substantial inertial event at 100 m (Figure 7.1-6), which began on about 7 October and peaked around 21 October, had a spectral peak that is displaced below f by about the same amount as the peaks at L1 in August (Figure 7.1-2). The relative vorticity at the surface was about the same (~ $-25\ 10^{-6}\ s^{-1}$) for the center of the eddy in October as in August. Thus, the wind event beginning on 7 October appears to have been generating inertial oscillations with a frequency below local f, which is consistent with f_e having a substantial component due to ζ, the relative vorticity. These oscillations would be expected to remain trapped in the upper part of the eddy's core. Figure 7.1-9 shows the eddy on 11 October. The 8°C surface shows that the eddy still had a deep expression, though the currents were weak at that level (600 m). There was a large cyclone interacting with Eddy Sargassum on its eastern side, which enhanced the southward flow between them and probably contributed to Eddy Sargassum's subsequent southward move through self-advection.

Contrasting the results for L1 and L5 when the eddy was similarly situated relative to the moorings, indicates that the exceptionally large amplitude (~ 40 $cm \cdot s^{-1}$) inertial oscillations, with a frequency substantially lower than local f, short vertical wavelengths and confined to the upper 300 m, had essentially disappeared during the month-long passage from L1 to L5. There is a possibility that the amplitude maximum at 600 m in October was a remnant of this activity with some of the inertial waves escaping confinement by the eddy's vorticity, and propagating down into the water column as the eddy translated southwestward along the Escarpment. However, this deep event at L5 could have propagated vertically and horizontally from outside the eddy to the lower part of the eddy where the low-frequency currents and relative vorticity were small. Thus, its occurrence could be coincidence and just part of the complex fields of inertial oscillations that are ubiquitous in the upper layers of the GOM. The source of the exceptional inertial currents at L1 is unknown, but it is speculated that during the long period when the eddy was still attached to the LC and was relatively stationary (see Section 4) inertial energy could have accumulated from frequent favorable wind events. Another possibility is that the detachment process or other eddy-eddy interaction, converted some of the ring's low-frequency energy to inertial oscillations through geostrophic adjustment processes. It seems fairly clear that these trapped inertial currents dissipated fairly rapidly after their occurrence at L1.

7.2 General Characterization of Inertial Oscillations

Inertial oscillations are intermittent, narrow-band, clockwise rotary current fluctuations. The main source is surface wind fluctuations, though eddy instability processes involving geostrophic adjustment may also be a source in certain circumstances. The use of ADCP current profilers in the upper part of the water column on the tall moorings allows the characterization of inertial oscillation velocities in both space and time. The statistical tool that gives the amplitude of

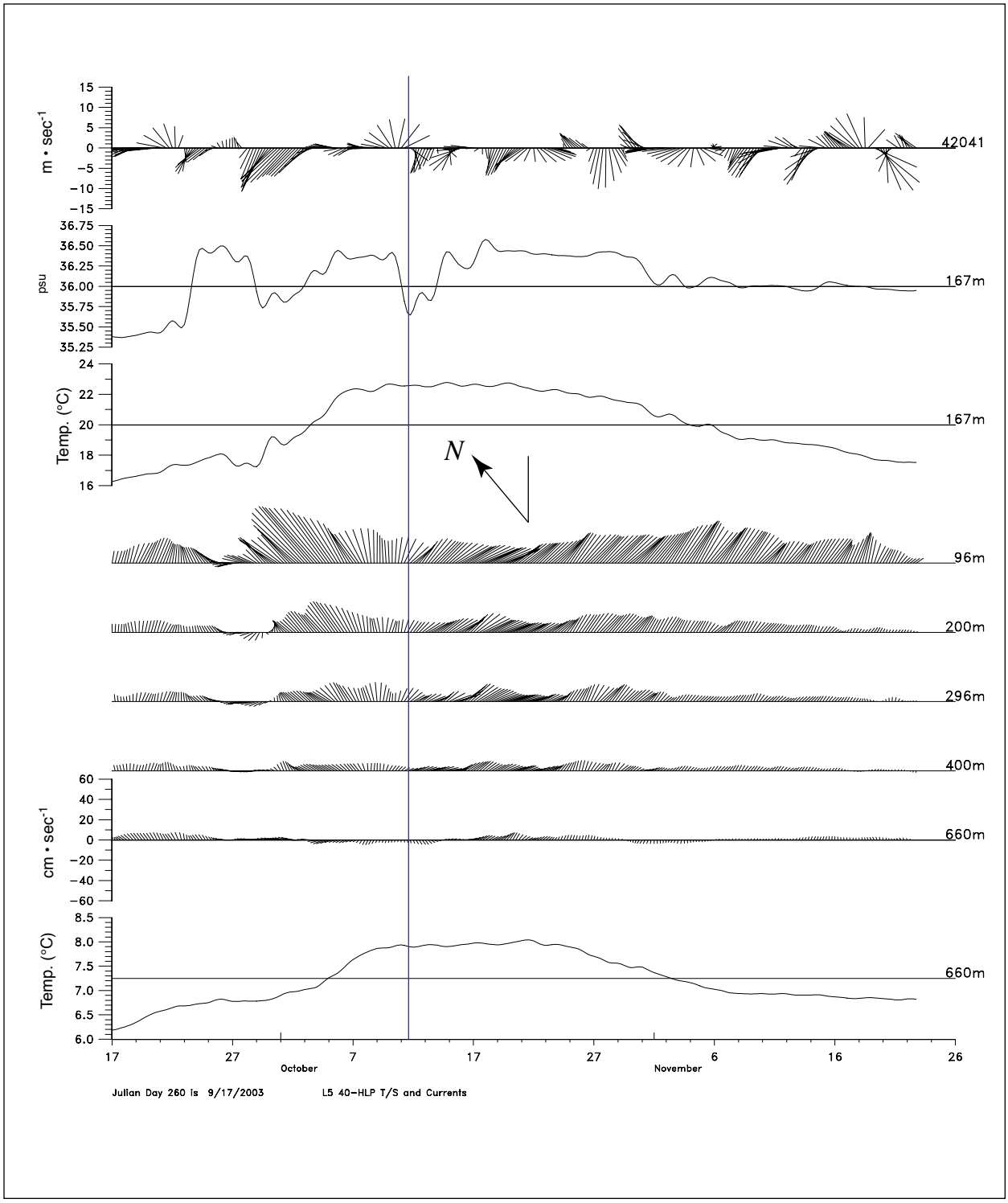

Figure 7.1-8. 40-HLP currents, temperature and salinity during the passage of Eddy Sargassum through L5.

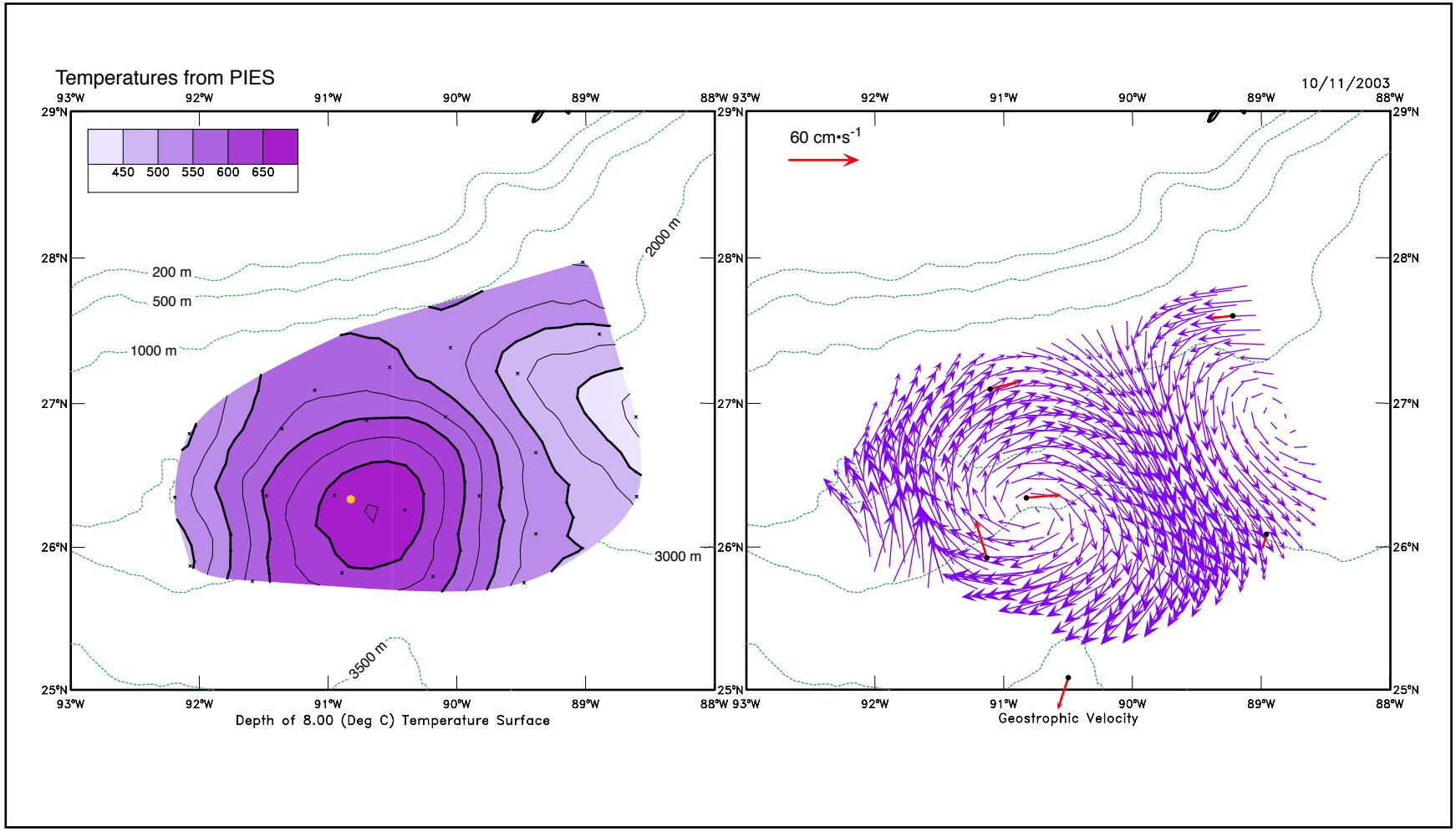

Figure 7.1-9. Depth of the 8°C isotherm (left panel) from PIES temperature profiles, and surface geostrophic velocity from PIES SSH anomaly (right panel) for October 11, 2003 at 1200 GMT. The L5 site is shown as a yellow dot on the left panel and daily averaged 40-HLP current vectors at 40-m depth as red arrows on the right panel.

narrow-band fluctuations as a function of time is complex demodulation (Priestley, 1981). For the calculations discussed below, a modulation period was chosen close to $2\pi/f$ such that twice the period was an integral number of time steps. The input series was the 3-HLP east (U) component of current velocity for each depth level of the current profile. The series had a running mean, also averaged over twice the period, removed. This effectively removes any low-frequency contributions to the spectrum. Finally, the amplitudes were filtered with a 4-day low pass Lanzcos kernel and decimated to 6-hour intervals. The contours of the amplitudes for the ADCPs on moorings L1 through L5 are given in Figures 7.2-1 to 7.2-5, respectively. These figures also include the 40-HLP current velocities from the upper-most level (40 m), the wind from the NDBC buoy 42041, and the temperature from the depth of the instrument (400 m for L1 to L4, and 660 m for L5). The current vectors and temperature help show when the moorings were affected by warm and cold eddies. The frequency discrimination of complex demodulation is not very precise, so frequencies close to the demodulation period are resolved by the analysis and frequency shifts caused by changes in the effective f, discussed above, are accommodated by the analysis (Priestley, 1981). For example, calculation of amplitudes at L1 using a period of 30 hours, corresponding to the August event, instead of 27 hours ($\sim 2\pi/f$) made only small differences to the amplitude results in Figure 7.2-1.

At L1 (Figure 7.2-1), the exceptional amplitudes centered at about 200-m depth, that occurred during August, are well captured by the complex demodulation analysis. Prior to this event, strong eddy or LC flows dominated the surface layer, and it is noteworthy that higher amplitudes were observed deeper in the water column than later in the year when Eddy Sargassum had departed from the site. However, July and August experienced a number of tropical storms and hurricanes which would also be expected to increase near-surface inertial amplitudes. Near-surface (40 m) amplitudes are similar in the April-June and October-March intervals and had some correspondence with the strength of the winds. Spring winds during 2003 had similar magnitudes, but with longer period events to the storms of the 2003-2004 winter. In the latter half of the record, the amplitudes generally decayed down from the near surface, and sloping of the isolines with depth (e.g., around the middle of October and the middle of February) show that the inertial energy propagated down into the water column at a rate of about 400 m in 25 days (16 $m \cdot day^{-1}$).

Two hurricanes and two tropical storms passed over or close to the array in the summer of 2003. 40-HLP winds and hourly wind speeds are given in Figures 7.2-1 and 7.2-2, respectively, for station 42041 north of the array, and Figures 7.2-3 and 7.2-4, for station 42001 south of the array. The storm tracks, obtained from the National Hurricane Center's analysis, are given in Figure 7.2-6 and are also identified in the wind records. The storm summaries are given in Table 7.2-1. Tropical storms Henri (3-8 September) and Larry (1-6 October) also occurred over the eastern Gulf and the Bay of Campeche, respectively, but had little or no influence on winds over the array.

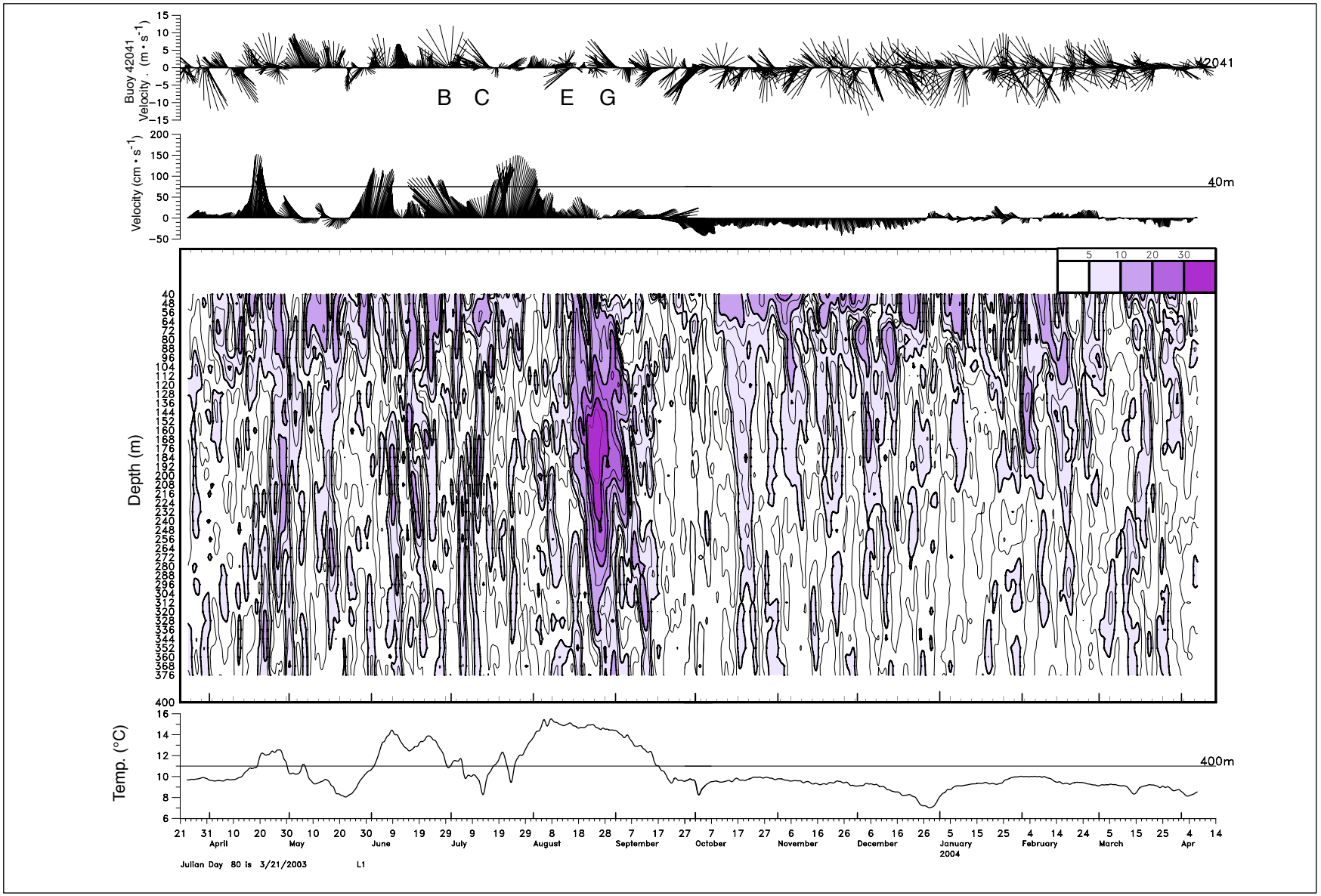

Figure 7.2-1. Contours of inertial amplitudes (cm•s^{-1}) for the upper 400 m of the water column at L1, from complex demodulation using a period of 26 hours, along with 40-HLP temperature at 400 m, current velocity at 40 m (up is directed toward 070^{o}T), and wind from NDBC buoy 42041 (up is north). Temperature was measured at an ADCP located at 400 m.

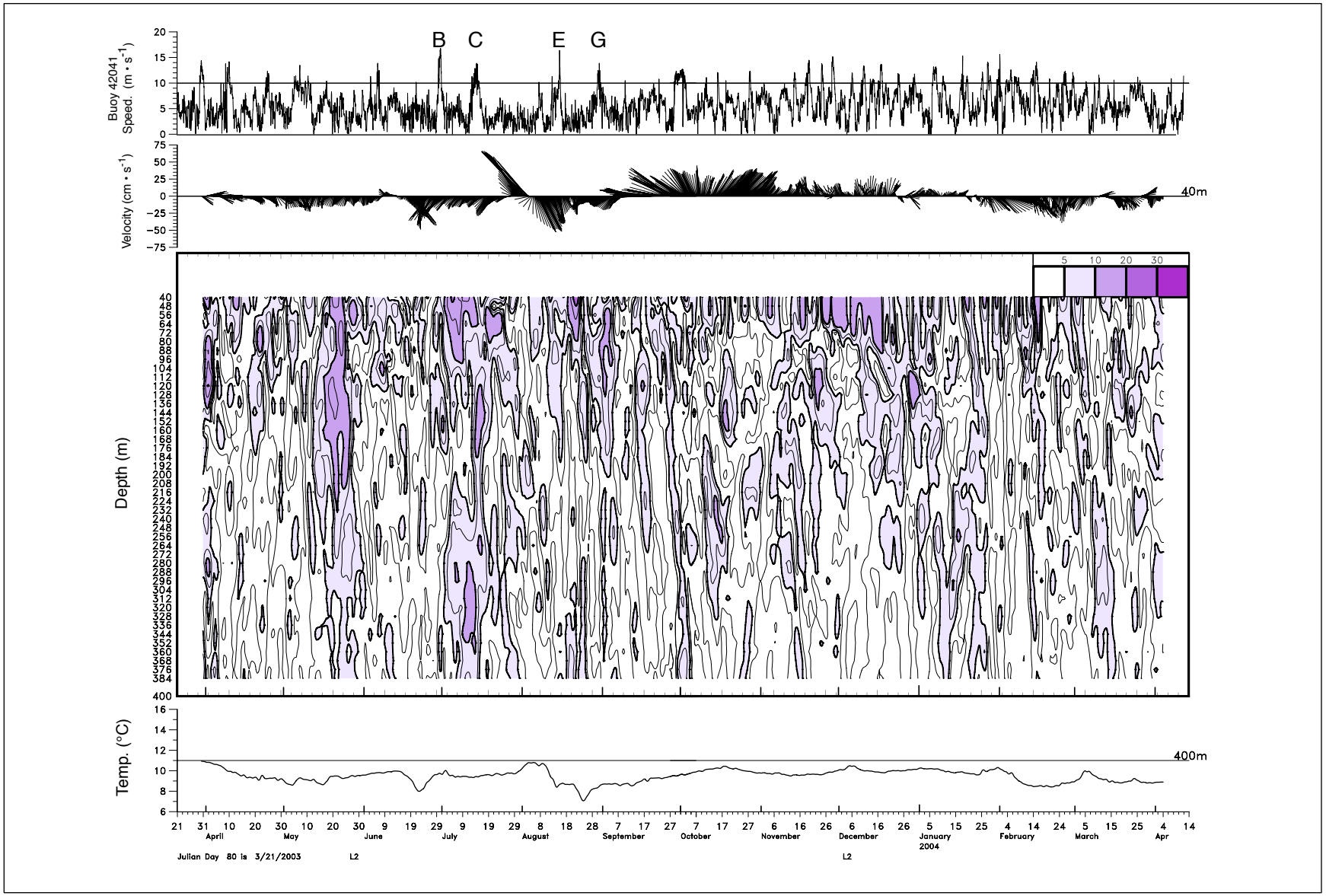

Figure 7.2-2. Contours of inertial amplitudes ($cm \cdot s^{-1}$) for the upper 400 m of the water column at L2, from complex demodulation using a period of 26 hours, along with 40-HLP temperature at 400 m, current velocity at 40 m (up is directed toward 060°T), and wind speed (unfiltered) from NDBC buoy 42041. Temperature was measured at an ADCP located at 400 m.

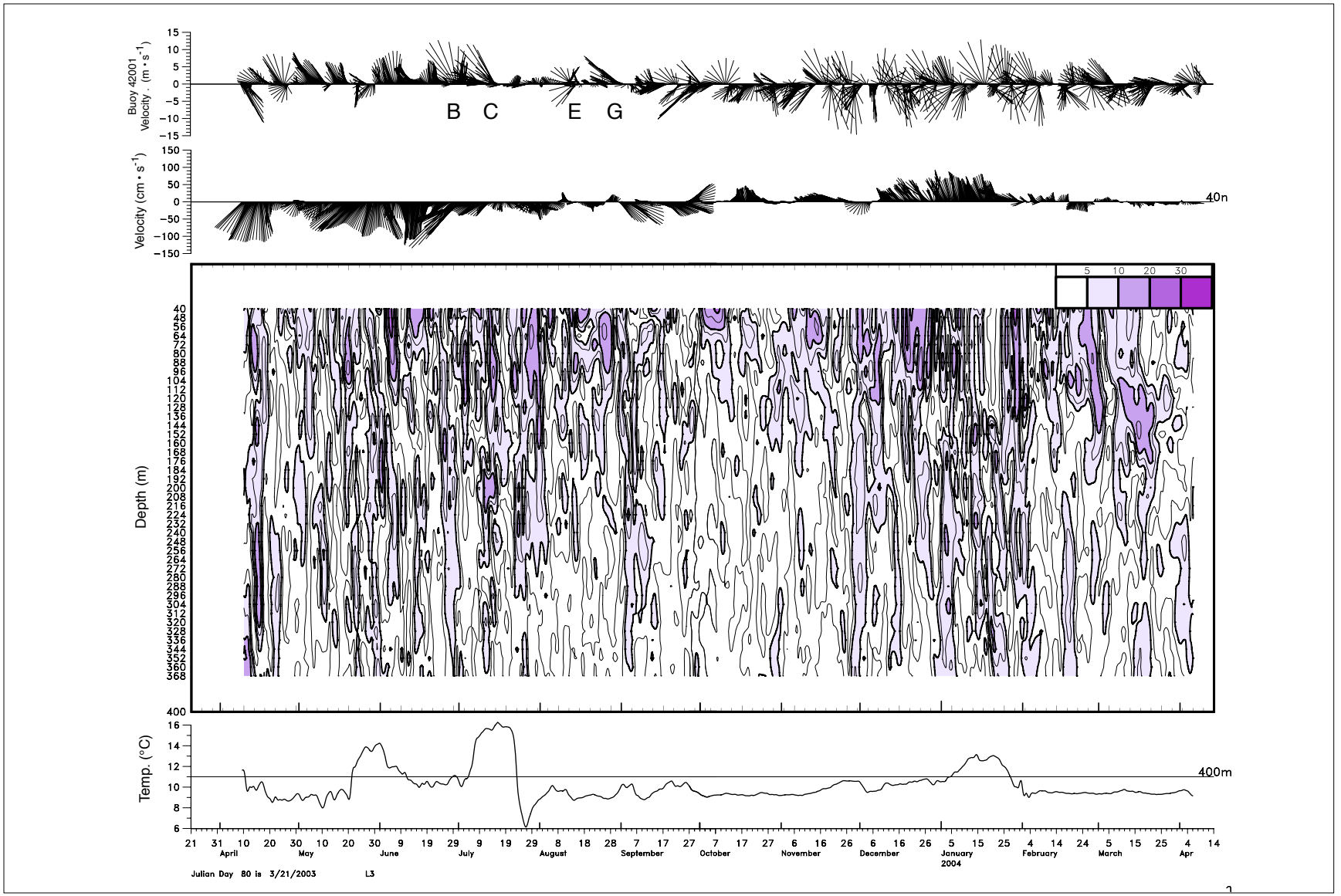

Figure 7.2-3. Contours of inertial amplitudes ($cm \cdot s^{-1}$) for the upper 400 m of the water column at L3, from complex demodulation using a period of 27.5 hours, along with 40-HLP temperature at 400 m, current velocity at 40 m (up is directed toward 120°T), and wind from NDBC buoy 42001 (up is north). Temperature was measured at an ADCP located at 400 m.

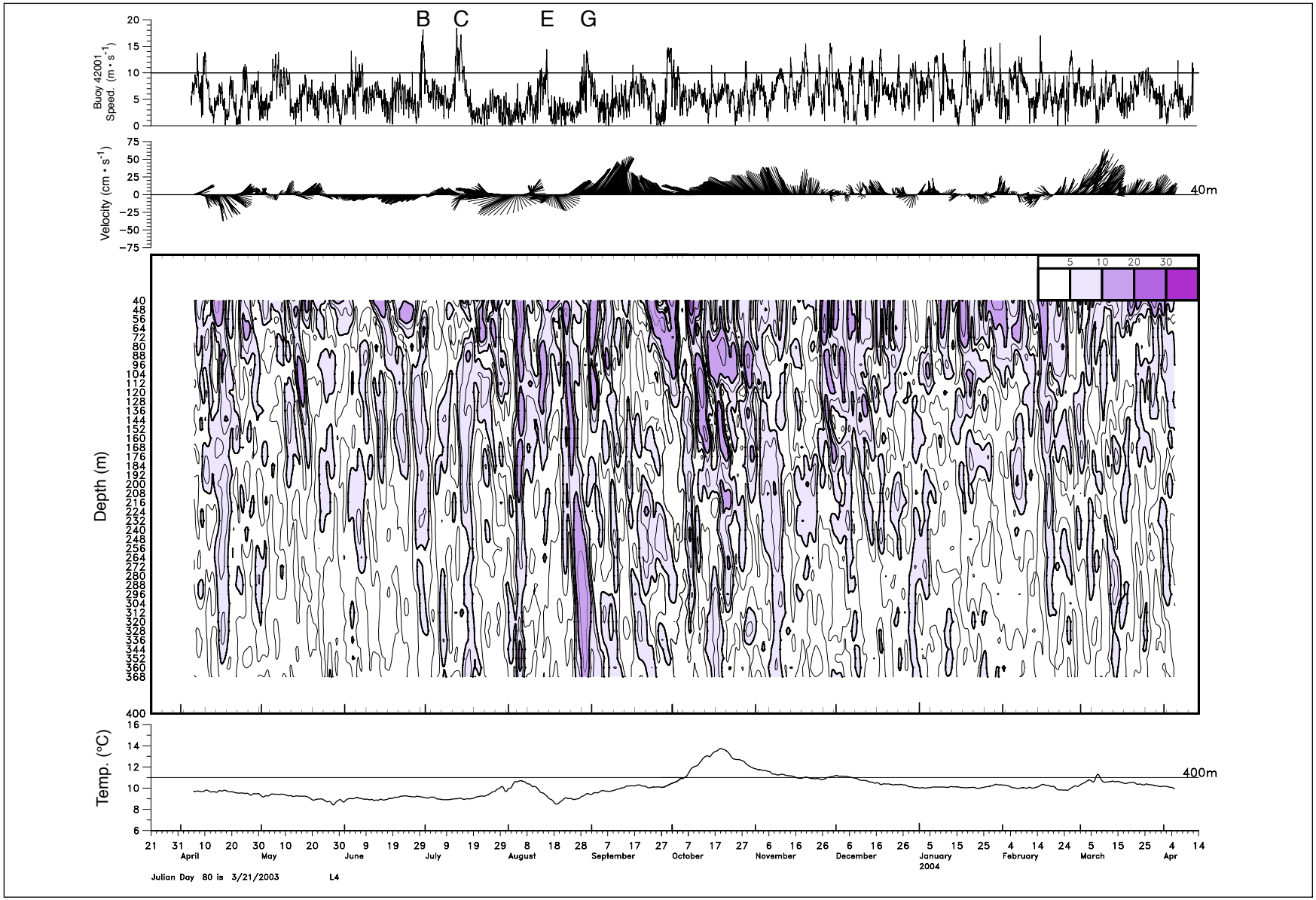

Figure 7.2-4. Contours of inertial amplitudes ($cm \cdot s^{-1}$) for the upper 400 m of the water column at L4, from complex demodulation using a period of 27.5 hours, along with 40-HLP temperature at 400 m, current velocity at 40 m (up is directed toward 065°T), and wind speed (unfiltered) from NDBC buoy 42001. Temperature was measured at an ADCP located at 400 m.

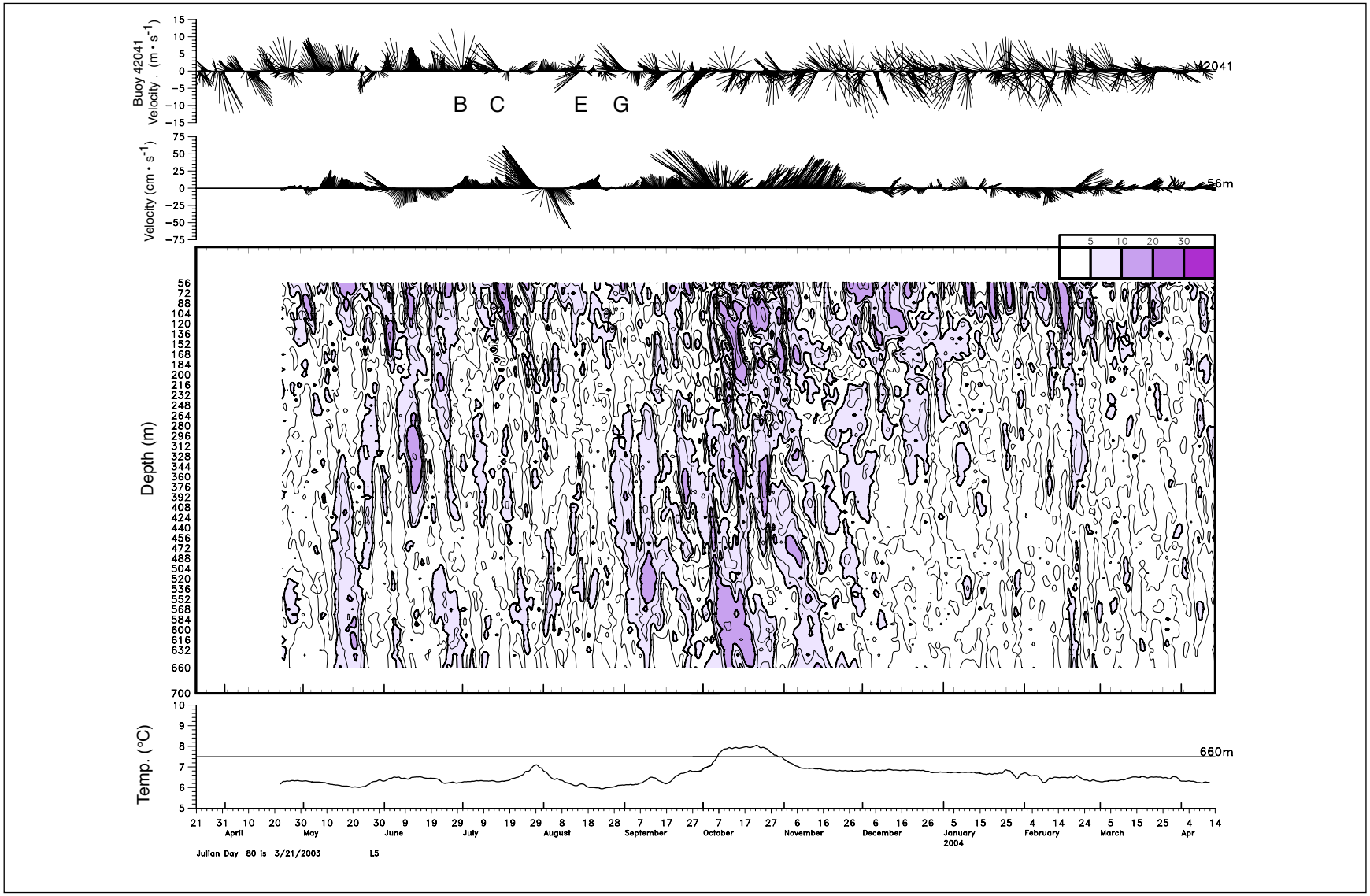

Figure 7.2-5. Contours of inertial amplitudes ($cm \cdot s^{-1}$) for the upper 660 m of the water column at L5, from complex demodulation using a period of 27 hours, along with 40-HLP temperature at 660 m, current velocity at 56 m (up is directed toward 040°T), and wind from NDBC buoy 42041 (up is north). Temperature was measured at an ADCP located at 660 m.

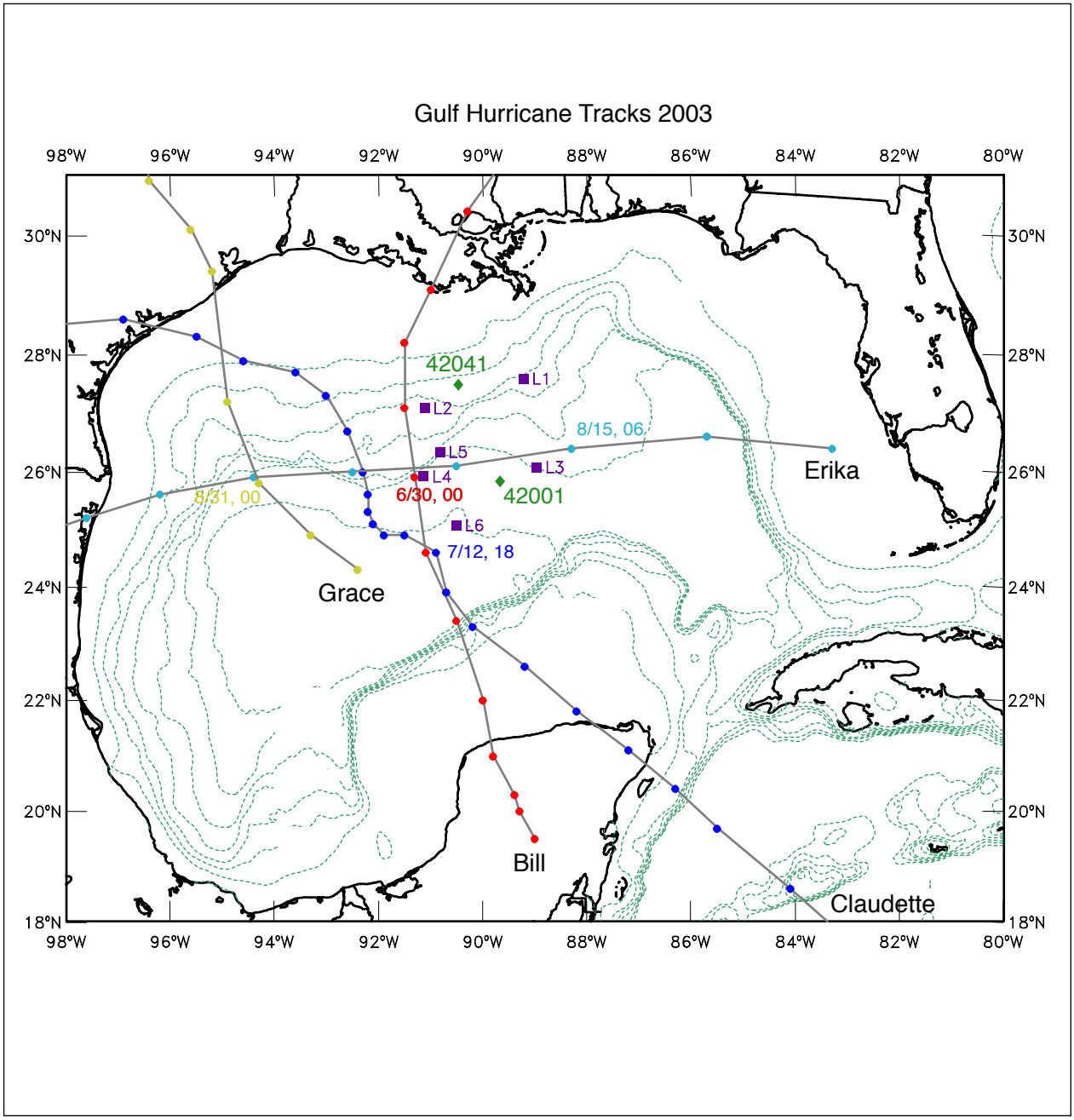

Figure 7.2-6. Tropical storm and hurricane tracks for the Gulf of Mexico in 2003. The center low pressure positions are given by the dots at 6-hour intervals. Date and time (GMT) of a close approach to the array is noted for each track, and the positions of the tall moorings (squares) and NDBC buoys (diamonds) are also shown.

Table 7.2-1

Gulf of Mexico hurricanes.

Name	Dates	Maximum Sustained Winds ($m \cdot s^{-1}$)
Tropical Storm Bill	29 June to 2 July 2003	25
Hurricane Claudette	8-17 July 2003	37
Hurricane Erika	14-17 August 2003	32
Tropical Storm Grace	30 August - 2 September 2003	17

Strong inertial oscillations are usually observed on the right hand side of the track of the central low pressure of a rapidly moving tropical depression. All the tracks, except Erika, passed to the west of the measurement array (Figure 7.2-6), and Erika's east-to-west track passed almost directly over L3 and L4. It is, however, difficult to see a consistent response of large-amplitude oscillations at the various moorings to the passage of these storms. For example, there was a burst of large amplitudes at L4 immediately following Erika (Figure 7.2-4), which propagated down through the upper 400 m of the water column. However, L5, which was a similar distance north of the track that L4 was south, shows only a relatively weak signal. L5 was closer to the center of a vigorous cyclone (Figure 7.1.5a) than L4, which was on the periphery, and thus, f_e was about 10% higher at L5. This may have been just enough to make the water column have less resonance with the overlying changing winds.

Similarly, Tropical Storm Bill passed close to both L2 and L4 and a direct response was measured at each site. However, at L2, there was a large amplitude signal that propagated down into the water column after the storm had passed that was not observed at L4. Both stations were on the peripheries of cold cyclones at this time, so there was no significant difference caused by relative vorticity contributions to f. Some of this signal at L2 probably had propagated in from further north as the storm strengthened before it made landfall in Louisiana. Inertial-internal wave signals are difficult to interpret in terms of wind forcing at a site because of influences from more distance sources. Horizontal wave paths are influenced by time and space varying horizontal density and velocity structures such as eddies and fronts that can cause refraction and reflection. It is noted that L2 (Figure 7.2-2), which was the least influenced by Eddy Sargassum and some of the larger cyclones, had a much more uniform distribution of energy over the year when compared with L1 (Figure 7.2-1). There were similar amplitudes, near surface and at depth, for the both the hurricane season and winter.

The increase in amplitudes when the site is strongly influenced by a major anticyclone has been noted for L1 and L5 in the previous section. The increase in inertial-internal wave activity at L5, particularly at depth, during October is clear in Figure 7.2-5, but it can also be seen at L4 (Figure 7.2-4) in October and at L3 in July (Figure 7.2-3). In these latter two cases, the moorings did not pass through the center of the eddy, but nevertheless, the relatively low currents and high temperatures at these times show that they were within the core of Eddy Sargassum when the higher levels of activity were indicated. At L3, the July episodes could also be the result of

Tropical Storm Bill and Hurricane Claudette which supports the idea that wind forcing and trapping within the eddy accumulated inertial energy that resulted in the exceptional amplitudes observed at L1 in August (Figure 7.2-1). It is also noteworthy that when the northern part of the unnamed LC eddy was over L3 in January 2004, as shown by the warm temperatures and eastward currents in Figure 7.2-3, there was also an increase in amplitudes. However, again this could be attributed to winter storm activity which was at a maximum at this time.

Despite the great complexity of the inertial-internal wave field, there is some evidence that activity was greater when a site was within a warm-core eddy and this increase was probably caused by trapping of the energy by the negative relative vorticity field. The observed energy is then the result of the cumulative effects of wind forcing and trapping.

7.3 Float Bursts

Based on a suggestion by one of the Exploratory investigators, an attempt was made to detect inertial oscillations in the RAFOS float tracks. For this purpose, float x- and y-positions (i.e., East, North) over a 20-day moving window were fit to a low-order time polynomial, and a wave with a period appropriate to the local inertial frequency. In only a limited number of cases, and for short time intervals, were any signals detected in the inertial frequency band that rose above the level of background noise as determined from the fitting procedure. This is perhaps not surprising since an inertial circle at 26.5ºN latitude would have a radius of roughly 1.5 km for a 10 $cm \cdot s^{-1}$ current. As noted in Appendix E, the radial distance resolution of a float from a given sound source is only about 500 m, and positions are determined only three times per day. It therefore might be difficult to resolve such inertial motions with these data unless they were extremely energetic.

8.0 SUMMARY AND RECOMMENDATIONS

8.1 Summary of Study Results

8.1.1 Upper Layer

The LC and associated eddies, both anticyclonic and cyclonic, dominated the upper-layer circulation in and around the study region during the field measurements. Dynamical interpretation of this upper-layer circulation was difficult because of the complexity the eddy interactions – an eddy field that can be best characterized as an energetic nonlinear flow, at least during the first half of the program time period. A shielded vortex instability was proposed as a strawman framework for dynamically interpreting the Eddy Sargassum LC/LCE vortex system that impacted the study region early in the measurements. The deepening of the upper layer and the peripheral LC cyclones associated with this instability process provide physical forcing mechanisms at frequencies and wavelengths commensurate with the time and space scales associated with the forcing of the most energetic TRWs and upper-layer baroclinic eddies/waves observed. Upper-lower layer coupling through baroclinic instabilities likely contributed to the twisting and tilting of the Sargassum LC/LCE vortex system. The limited region of full water column information, however, makes identifying baroclinic instabilities within the LC/LCE system difficult since most of the instability likely occurred outside the study region.

Highly energetic (amplitude ~30 to 40 $cm \cdot s^{-1}$) inertial oscillations were observed at L1, at thermocline depths (150 to 250 m), in the core of Eddy Sargassum. The peak period was longer than local f, the Coriolis parameter, and therefore, it was surmised that the inertial energy was trapped by the negative relative vorticity of the eddy and was possibly the result of energetic wind events (some from tropical storms) that occurred earlier while the eddy was further south and still attached to the LC. Eddy Sargassum translated southwestward through mooring L5, but the trapped inertial oscillations were less apparent at this time and may have escaped the core and propagated down to deeper depths. The summer of 2003 had a quite active hurricane season with two tropical storms and two hurricanes passing close to or through the array. The inertial response to these events was observed at most of the tall moorings, with more energetic fluctuations propagating down from the surface. In general, the distribution of inertial energy in the upper part of the water column was complex both in time and with depth and was sometimes difficult to relate to local wind events.

8.1.2 Lower Layer

Deep energetic currents below 1000 m were typically associated with eddies observed in the deep pressure fields. Deep eddies may be interpreted as resulting from a field of dispersive TRWs. Thus, the frequency domain EOF analysis of TRWs in Section 5 can be regarded as analogous to a frequency and wavenumber decomposition of an eddy field. The dispersive nature of the bottom circulations, as shown by the model float calculations (Section 5.2), and the relatively continuous character of the current fluctuations confirm the fundamentally wave-like behavior of the deep flows in the study region. Once west of 89°W, deep eddies typically translated northwest until they encountered the Sigsbee Escarpment, where their behavior depended upon the sense of eddy rotation. Strong cyclones approached the Escarpment and

deflected left in the direction corresponding to topographic westward. In contrast, anticyclones encountering the Escarpment typically stalled and decayed rather than propagate away.

Mean and fluctuating flows had distributions that were inhomogeneous in both magnitude and frequency content, from deep to shallow and east to west along the slope. The strongest fluctuations (~60 $cm \cdot s^{-1}$) were found below the Escarpment in the east and have the characteristics of TRWs, presumably generated by the LC, that propagate westward towards the steep slope. The Sigsbee Escarpment effectively barred these energetic currents from penetrating into shallower water, and also trapped short period (~10 days) waves in the east of the study area. Longer period waves (30 to 60-day) were refracted and propagated back southwest towards deeper water. Closely spaced measurements across the Escarpment at ~91°W showed a strong mean jet-like flow centered over the steepest slope, with a maximum mean velocity over 12 months of 13 $cm \cdot s^{-1}$ directed towards the southwest. A number of deep-float tracks also had the characteristics of TRWs in that they oscillated with an across-isobath component, over a limited area of the abyssal plain for periods of several months. Near the Escarpment, float tracks tended to rapidly translate along the steep bathymetry into the western Gulf.

Bottom pressure measurements revealed a ~ 16-day oscillation that was essentially uniform in amplitude and phase across the array. This was denoted the "Gulf common mode". The cause of this apparently Gulf-wide, sea-level oscillation is presently unknown.

8.1.3 Upper-Lower Layer Coupling

Strong upper-ocean circulation features were found to be coupled with the deep circulation. These interactions between upper and lower layers were illustrated through map sequences, here referred to as "case studies." Each map superposed upper- and lower-layer circulation. Three classes of dynamical coupling were presented. In the simplest case, the upper-layer flow distorted the background flow field. Eddy Sargassum's deep thermocline presented an obstacle in the path of a deep cyclone and temporarily halted its westward propagation. The second category highlighted the more dynamical vertical coupling that results when propagating upper-ocean features stretch or squeeze the lower layer. The lower-layer response to vortex stretching/squeezing requires the acquisition of positive/negative relative vorticity to balance the changes in thickness in order to conserve total potential vorticity. Two cases revealed the joint propagation in the upper and lower layers of a cyclone pair and anticyclone pair. In each case, the lower-layer eddy led the upper-layer eddy in a vertically-tilted fashion characteristic of coupled propagation. Finally, a case study presented observations consistent with baroclinic instability, in which the phase of this vertical tilt and the wavelength led to joint growth of the upper- and lower-layer perturbations. A meander crest within the LC jointly spun up with a deep anticyclone, which was offset to the west and slightly north of the growing crest.

8.1.4 PIES – Altimeter Comparison

The study of the altimeter sampling using the PIES SSH data showed that 87% to 99% of the subinertial period SSH variability in the Exploratory Study region is unaliased by the approximately 10-day TOP/POS repeat-period sampling; however, there can be significant

aliasing of the GOM SSH signal in satellite altimetry even with the dominance of the longer-period baroclinic signals in the deep water of the Gulf. This is especially true for 35-day sampling. The degree to which this affected the space/time interpolated maps of SSH needs to be investigated in more detail. It also is unclear whether the weak surface signature of TRWs can be mapped effectively using satellite altimetry, given the presence of the strong baroclinic SSH and the difficulties associated with aliasing of the signal. More useful for the evaluation of altimeter-derived estimates of SSH is the ratio of the unaliased variance to the aliased variance of the SSH signal, which was an estimate of the signal-to-noise ratio (SNR) of a perfect on-orbit measurement system. The SNR in the study region was very good for 10-day and 17-day altimetric sampling. The 35-day sampling was more problematic showing SNRs consistently as low as 2 over much of the array, which made it difficult to distinguish between signal and aliased signals at that sampling frequency.

The CCAR mesoscale SSH gridded-altimeter data product that was distributed and used for data synthesis activities in this report was evaluated by comparison with the coincident PIES SSH. The CCAR/PIES SSH correlations were good with an overall mean correlation of 82%. Lowest correlations were found above the Escarpment and along the western edge of the study array. SSH slopes between PIES stations were also compared to the coincident slopes calculated from the CCAR mesoscale product. The overall mean correlation was 80%. We also compared the along-track detrended SSH data for the altimeters to the coincident PIES SSH collected along the respective groundtracks. The correlations ranged from 56% (TOP/POS) to 81% (GFO), with four satellites in the range of correlation values from 72% to 81%.

8.1.5 Gulfwide Circulations from Deep Floats and Remote Sensing

The Gulfwide, upper-ocean circulation during the Exploratory Study was dominated by two strong LC events, Eddies Sargassum and Titanic, that resulted in strong LC and LCE circulation in and around the study region throughout the program. Cyclonic circulation that is typically associated with strong LC intrusions and eddy-separation events was also present. The summary of the historical record of remote sensing observations of LC intrusion and LCE detachment and separation events described in Section 3 was used to place the program field interval into an historical context. While it may be simplistic to characterize the Gulfwide oceanographic conditions impacting the study region as unique during the Exploratory Study, the observed LC variability resulted in a range and duration of oceanographic conditions that may not typically be observed over a one-year time set of measurement. This was confirmed quantitatively using the historical record of altimeter derived LC and LCE metrics. The Eddy Sargassum intrusion is the most northerly intrusion event observed in the altimetric record to date and shed a LCE that passed directly through the Exploratory array, interacting with the Sigsbee Escarpment along its entire trajectory. The two LCEs observed during the program time period, Sargassum and Titanic, both momentarily detached from the LC. If these eddies had not reattached to the LC they would have ranked near the top of all LCEs in terms of eddy size and intensity. While we had the good fortune to observe a great range of energetic LC activity during the yearlong program, the conditions were not so atypical that the average LC behavior over the one-year time period, as measured by the mean LC metric statistics, differed remarkable from the long-term average.

Floats launched in the central northern GOM at 500m intervals from 1000 m to 3000 m+ depth showed evidence of strong east-west exchange in the central Gulf. However, their behavior once they exited this region was distinctively different depending on whether floats moved to the west or to the east (a small majority moved to the west, while a very few remained in the central part of the GOM; all these were deeper floats). Most floats that moved to the east tended to display eddy-like motions in the "Eastern Basin" (i.e., east of the topographic constriction at about 90°W) and tended to "wander" into the central part of this basin. These floats in general did not show a strong correlation with motions inferred closer to the surface from other (e.g. altimetric) data, with some significant exceptions. In particular, floats that were present in the eastern Gulf during times when the LC was present at shallower depths showed brief (several week) intervals when the deep flows of the LC penetrated far enough downward to influence the float behavior at deep (2000-m) levels. These are the only times when deeper currents seem to have been significantly correlated with upper-layer currents based on the float data.

Floats that moved to the west toward the Sigsbee Basin behaved quite differently. The majority of these floats converged and moved closer to the slope, accelerated, and followed narrow paths westward and then southward along the boundary, giving the appearance of a "Deep Western Boundary Current" along the western Gulf. A few of these floats eventually were caught up in deep eddies along the western boundary and moved into deeper parts of the basin. The tendency of these floats to follow topographic contours was quite striking, such as one float that entered Alaminos Canyon and cyclonically followed the wall of the Canyon, eventually exiting to the southwest. As with the eastern floats, the western floats showed little visual correlation with flows nearer the surface as inferred by altimetric data.

8.2 Hypotheses

As one part of the overall objectives for this study, the MMS defined eight hypotheses to be examined using the results and insights developed in this study. Presented below are those hypotheses with an associated response.

H1: Currents shallower than 800 m are dynamically uncoupled from currents at depths greater than about 1,000 m.

Although some dynamical linkage of upper and lower layers have been postulated based on a diverse evidence set in this report, there was not conclusive evidence of the importance and nature of this linkage. In a visual inspection of the upper- and lower-layer kinematics, the linkage is not generally well supported. If, as suggested, the vertical offset of linked upper- and lower-layer eddies may make such a visual comparison more difficult. Note that the argument still remains that lower-layer dynamics need to be driven by some source and the most likely is a linkage to the upper layer such as the LC or LCEs. This linkage may not be easily deciphered, but measurements similar to those in this study, but underneath and to the west of the LC may provide more information on linkages that affected the present study area.

H2: Rare mid-water jets occur in areas of eddy-eddy interactions.

There was no substantial evidence of mid-water jets at the various full depth moorings, so this hypotheses can not be resolved.

H3: Currents in water depths greater than 1,000 m never show a large vertical gradient of velocity.

Generally, currents in the lower layer are strongly barotropic and hence have weak vertical gradients. This pattern was consistently seen in this study. That is not to say that gradients do not occur in the lower layer; they do. Generally, the depth having the lowest velocity occurs in the transition region where upper-layer dynamics diminish in importance to local circulation patterns and the lower-layer patterns begin to dominate. From this transition zone to the local bottom, the relative magnitude of currents tends to increase.

H4: Deep-water parameters measured in areas dominated by cyclones/anticyclones of scales of 50-100 km are not different from areas not dominated by cyclones/anticyclones of 50-100 km.

A definitive response to this hypothesis is not presently possible. In the present study the presence and path of 50-100 km cyclonic/anticylonic eddies was greatly affected by the position of the LC and the path of LCEs. Clearly, these locations and positions were major factors affecting eddy development and movement.

H5: There are no differences in the occurrence and/or intensity of near-bottom currents near steep bathymetric gradients and areas of small bathymetric gradients**.**

Results of this study have shown that near-bottom currents tend to be greater in the vicinity of steeper bathymetry in the study area. The presence of the Sigsbee Escarpment is a major influence on local dynamics and resulting current patterns. With the more limited, but horizontally well- resolved measurements made in the western portion of the study area, there appeared to be a local current maximum approximately mid-way up the Escarpment. In the eastern portion of the study area, stronger currents tended to be more concerntrated at the base of the Escarpment, although the presence of TRWs over the lower sloping portion of the eastern study area also produced substantial near-bottom currents.

H6: The characteristics of topographic Rossby waves change from east to west in the Gulf of Mexico because of changes in bottom slopes and frictional dissipation that causes the TRWs to reflect, trap and dissipate by wave breaking**.**

Results indicated that the previously postulated transition from short to longer period TRWs in going from east-to-west over the GOM basin was true over the measurement domain of this study. A factor in this could have been the role of bottom slope in governing the characteristics of TRWs supported by regional bathymetric conditions.

H7: Circulation below 1,000 m in the Gulf of Mexico is dominated by cyclone/anticyclone pairs and is fundamentally cyclonic.

The role or presence of lower-layer cyclones/anticyclone pairs is not well resolved. The reader is also refered to the discussion of the resolving of eddies vs. wave motions and that they can be different forms of the same thing. See Section 8.1.2 where it is stated that “deep eddies may be interpreted as resulting from a field of dispersive TRWs. Thus, the frequency domain EOF analysis of TRWs in Section 5 can be regarded as analogous to a frequency and wavenumber decomposition of an eddy field.” There did appear to be

a persistent cyclonic flow along the Sigsbee Escarpment that seemed to intensify toward the west.

H8: Storm generated inertial oscillations trigger resonant phenomena that propagate into deepwater.

At the tall moorings, inertial oscillations were observed and related to tropical storms. These periodic current patterns propagated vertically into deeper water, although given the separation of tall moorings there was no clear evidence of the same but evolved wave field arriving at two moorings. It was difficult to specifically relate all inertial oscillations to meteorological events. It is possible that some inertial patterns may have resulted from geostrophic adjustment (this is when the pressure field and the velocity field are changing to maintain a balance of forces) due to eddies interacting with bathymetry.

8.3 Assessment of Measurement Program

8.3.1 Introduction

The Exploratory Study was designed with three complimentary components: the mapping array of PIES and current meter moorings, the deep Lagrangian drifters, and remote sensing by altimeters and SST/Ocean color. Principal aims of the design were to observe, map, and track the four-dimensional (x,y,z,t) dynamical structure of the circulation in both the upper and deep layers throughout a substantial region of the northern Gulf slope. This information is needed to reveal and understand the important vertical coupling by which deep and upper eddies affect circulation and eddies in the opposite layer. This goal was achievable at much less cost than by deploying a similar array of full-depth current meter moorings. By necessity, the mapping is restricted to subinertial-period geostrophic motions associated with eddies and topographic Rossby waves. The choice of the lateral separation between measurement sites took advantage of previous observations which had demonstrated that the predominant large scale low-frequency currents are geostrophic, both in the upper eddies and in the deep topographic Rossby waves and eddies. Finer spaced observations were required in the deep layer near steep topography such as the Sigsbee Escarpment. Also, finer spaced upper observations would be appropriate in the future to resolve smaller scale, upper-layer motions, such as rapidly translating peripheral cyclones on the LC or LCE fronts. A limited number of full-depth moorings (including moorings deployed by LSU (Nan Walker) and CICESE (Antoine Badan)) were included in the array so that some aspects of higher-frequency motions (principally inertial oscillations) and ageostrophic flows could be examined. The PIES/mooring array was highly successful in resolving the temperature, salinity, current and dynamic height structures of upper-layer eddies and also the smaller length scales of the currents and pressure fields of the deep TRWs and eddies.

A unique aspect of the array design was placement of PIES on or near altimeter ground tracks so that the satellite measured SSH could be directly compared with PIES derived dynamic heights and bottom pressure. Thus, the contribution of lower-layer eddies and TRWs to SSH could be assessed. The barotropic component of SSH was 5 to 10% of the total signal, in rms average, with peak displacements of 20 cm, compared to about 80 cm total SSH range across a LCE. It is noted that most numerical models assimilate SSH from altimeters purely as a baroclinic signal;

however, PIES measurements could provide useful information to develop techniques for assimilating both the baroclinic and barotropic components of SSH derived from altimeter observations. The SSH maps, from the altimeters, also provided a Gulfwide perspective within which the more highly-resolved and smaller-scale PIES array was placed. Thus, the LC and eddies were tracked before and after they directly affected the array.

Drifters provided the other Gulf-wide perspective for the lower layer. The use of RAFOS floats tracked by sound sources, during the Exploratory Study, was a first for the GOM. The RAFOS tracks provided new results for the deep water in that large displacements, that imply strong mean flows, tended to occur in the vicinity of steep slopes such as the Sigsbee Escarpment. However, in many cases the floats oscillated around the same relatively small region for several months at a time. The latter behavior is consistent with deep motions being dominated by TRWs, rather than translating eddies. TRWs, at small linear amplitudes, do not transport mass or relative vorticity. There also appears to be weak exchange between the eastern and western basins as a result yet unseen in some modeling results. It also raises questions on the flushing times for renewal of deep water in the western basin that have not yet been explored. There is also almost no relationship between the deep-float tracks and the upper-layer eddy circulations given by the altimeter SSH, except for a few occasions under the LC. Within the mapping array, the float tracks were consistent with geostrophic currents derived from the PIES and current meters, as well as with the wave-like dispersive nature of the lower-layer flow field.

8.3.2 Resolution

A PIES array with mean nominal spacing of 60 km resolved the temperature, density, and velocity structure of the LC, LCE (Sargassum and Titanic) and several cyclonic features. Mapping accuracy was consistent with the correlation properties of the observed mesoscale features. Closer horizontal resolution would be required to resolve more fully the strong cyclonic frontal cyclones that exist along the periphery of the LC, typically between 89° W and 86°W.

The deep circulation, TRWs, and eddies were observed by deep current meters and bottom pressure recorders, which are needed in combination to resolve the somewhat smaller lateral scales associated with these deep processes. The horizontal resolution was effective in the moderately-sloped topography away from the Sigsbee Escarpment. The SEBSEP array of current meters spanned the Sigsbee Escarpment near 91°W, with very close spacing (5 sites spaced ~4 km) across the steep bathymetry, and revealed deep jet-like flows narrowly-focused along the steep isobaths. The location for the SEBCEP was well chosen to observe strong currents, because deep eddies commonly paused nearby contributing their strong currents to the S-Array records. The question naturally arises, how typical the 91°W location is of other locations along the Sigsbee Escarpment? Measurements in this and earlier programs near 90°W were at the base of the Escarpment. High currents were observed at 90°W but it is not known whether current fluctuations or mean flows increased over the middle of the slope, as were observed at the S-section (91°W). The Sigsbee Escarpment zigzags WSW, alternating between segments that trend nearly-westward and others that trend SSW; an important clue to understand the deep jet dynamics may be offered by closely-resolved observations like the S-Array, but with better vertical coverage, on approximately four short transects between about 90°W and 91°W.

8.3.3 Duration

The Exploratory Study was fortunate to capture the effects of Eddy Sargassum, through a duration spanning most of its influence upon the study area, from its formation and the radiation of numerous energetic deep eddies, through its complete passage and associated events of vertical-coupling. Eddy Titanic formed and passed mainly to the south, producing less influence upon currents in the Study Array, followed by ~3 months of relatively weak upper and deep currents.

If the objective was to estimate the temporal-mean currents with statistical significance in the upper or deep regions of the Exploratory Study, the duration of the study would have to be 2-3 times longer. A bigger question for future study is, how typical were the currents associated with Eddy Sargassum, and how similar or different the currents would be during the passage of another event like Eddy Sargassum? To address this question will require more observations of at least a similar duration.

8.3.4 Spatial Extent

A future experiment of larger spatial extent in all directions would help in understanding the propagation and impact of LCEs. It would be particularly valuable for observations to simultaneously span further east across the LC to study the forcing and radiation of deep eddies and to understand and predict the pinch-off process of a LCE. In evaluating this program, it is pertinent to bear in mind that Eddy Sargassum was the farthest-north LCE to form and pass through this region in the past several years of observations; so it is unusual that a LCE would extend north beyond the Exploratory Study array.

8.3.5 Type of Observations

The mix of observations was valuable – PIES, current meters, satellite altimeter, and both profiling (PALFOS) and RAFOS floats. This enabled both a 4D mapping of dynamical structures and Lagrangian tracking of water-parcel trajectories. It was valuable to have two or more deep levels of current meter observations at several sites, especially over sloping topography, to quantify the vertical scale of bottom intensification of the currents. Now that these mean vertical scales have been mapped, it may be sufficient in future to measure deep currents at just one level at locations away from steep topography. At the mid-point of the Exploratory Study, the PIES data were collected by acoustic telemetry aboard ship while the CTD profiles were taken. The daily-processed records of variability agreed well between the telemetered data and the records recovered at the end of the observational period. In the future, the PIES or CPIES data could be acoustically telemetered to shore in real time (twice daily), or by other schemes at intervals of several days.

8.4 Further Analyses

The success of the Exploratory Study observational program opens a new opportunity to analyze and understand important dynamical processes in the GOM. The measurements captured, with

unique 4-dimensional space-time resolution, the coupled behavior in the upper and deep ocean associated with LCEs and strong deep eddies. Moreover, the observations demonstrate important vertical coupling: upper-eddy developments generate deep eddies which can feed back to steer and grow and split the upper eddies. It is now understood that a numerical model that does not generate realistic deep eddies cannot hope to chart and predict the development of upper-ocean currents and eddies. It is essential to the success of any numerical model to produce simulations of realistic deep eddies.

A first-order question is whether a model shows the correct deep EKE distribution relative to bathymetry and the LC. Even if one's objective is focused on just the upper ocean and accurate eddy forecasting, a model must also get the deep eddies right – whether for operational purposes or for process modeling.

Based on analyses and evaluations described in this report, some additional "exploration" of this Exploratory Study data set could include:

- diagnostic studies of vertical motions, vertical stretching, vorticity tendency, effects of bottom topography, baroclinic/barotropic coupling;
- calculate in stream coordinates, the mean potential vorticity structure of the Loop Current and Loop Current Eddies – this tests the necessary conditions for baroclinic / barotropic instability and is useful for dynamically balanced initialization of process models;
- examine operational model(s) regarding the dynamical origin of surface features that are developed; in particular, examine deep EKE values and spatial distribution; if these levels are approximately right, diagnose the associated vertical coupling processes in the presence of topography;
- examine process model(s) with these same questions regarding the deep EKE spatial distribution and dynamical diagnosis of vertical coupling processes over variable topography;
- examine near-inertial oscillations in the IES acoustic travel time data, particularly seeking to map its distribution in Eddy Sargassum, where current meters have noted a peak;
- seek to understand what process is associated with the energetic 16-day band of oscillations discovered as a common mode amongst all the bottom pressure records;
- perform a kinematic study to quantify eddy-eddy and eddy-LC interactions, both cyclonic and anticyclonic, using the available program observations in concert with coincident surface drifting-buoy observations;
- develop altimeter- and PIES/altimeter-derived SSH products using optimal interpolation techniques and space/time correlation functions tuned to the SSH variability in the GOM, with the ultimate goal of combining altimeter and PIES SSH in a single data product, exploiting the full sampling capabilities of the combined systems.

8.5 Recommendations for Future Deepwater Studies

The Exploratory Study improved our dynamical understanding of deep-water circulation in the GOM and allows us to refine a list of outstanding research questions.

- What regulates the northward intrusion and southward retreat of the LC and the detachment and ultimate separation of LCEs?
- What processes generate and/or radiate deep energy in the GOM near and away from steep topography?
- What determines how steep topography steers, dissipates or focuses deep energy?
- Is there a feedback between deep eddies and the upper ocean; can deep eddies modulate the stability of the LC?

These questions and insights gained from the Exploratory Study motivate the design elements of future observational programs.

- Event-based or process-oriented studies that diagnose key dynamics.
- Simultaneous maps of upper and deep circulation.
- Fine horizontal resolution above steep topography.
- Current measurements at several vertical levels.
- Remote sensing for a large-scale and historical perspective.
- International cooperation for observing the GOM in a basin-wide context.
- Multi-year observational program that captures multiple LCE shedding events.
- Targeted surveys within a core array. Surveys could include glider-based high horizontal resolution surveys of a developing LCE or the interaction between the LC and a frontal eddy.

9.0 REFERENCES

Berger, T. 1993. Loop Current eddy shedding cycle. LATEX Program Newsletter. 2(24) College of Geosciences, Texas A&M University. [Available from Dept. of Oceanography, Texas A&M University, College Station, TX.]

Biggs, D.C., G.S. Fargion, P. Hamilton, and R.R. Leben. 1996. Cleavage of a Gulf of Mexico Loop Current eddy by a deep water cyclone. J. Geophys. Res. 101(20):20,629-20,642.

Bretherton, F.P., R.E. Davis, and C.B. Fandry. 1976. A technique for objective analysis and design of oceanographic experiments applied to MODE-73. Deep Sea Res. 23:559-582.

Briggs, W. L. 1987. A multigrid tutorial. Philadelphia, PA. Soc. For Ind. and Appl. Math. 88 pp.

Brooks, D.A. 1984a. The wake of Hurricane Allen in the western Gulf of Mexico. Deep-Sea Res. 13:117-129.

Candela, J., J. Sheinbaum, J. Ochoa, A. Bedan, and R. Leben. 2002. The potential vorticity flux through the Yucatan Channel and the Loop Current in the Gulf of Mexico. Geophys. Res. Lett., 29(22):2059. doi:0.1029/2001JC001256.

Chelton, D.B., R.A. deSzoeke, M.G. Schlax, K. El Naggar, and N. Siwertz. 1998. Geographical variability of the first-baroclinic Rossby radius of deformation. J. Phys. Oceanogr. 28:433-460.

Chérubim, L.M., W. Sturges, and E.P. Chassignet. 2005. Deep flow variability in the vicinity of the Yucatan Straits from a high-resolution numerical simulation. J. Geophys. Res. 110:C04009. doi:0.1029/2004JC002280.

Cleveland, W.S. 1993. Visualizing data. Summit, NJ: Hobart Press. 360 pp.

Cressman, G.P. 1959. An operational objective analysis system. Mon. Weather Rev. 87:367-374.

Curry, R.G., B. Dickson, and I. Yashayaev. 2004. A change in the freshwater balance of the Atlantic Ocean over the past four decades. Nature 426:826-890.

Cushman-Roisin, B. 1994. Introduction to geophysical fluid dynamics. Prentice-Hall. 320 pp.

Cushman-Roisin, B., E.P. Chassignet, and B. Tang. 1990. Westward motion of mesoscale eddies. J. Phys. Oceanogr. 20:758-768.

Davis, R.E., J.T. Sherman, and J. Dufour. 2001. Profiling ALACEs and other advances in autonomous subsurface floats. J. Atmos. Oceanic Tech. 18(6):982-993.

Dickson, R.R., W.J. Gould, T.L. Müller, and C. Maillard. 1985. Estimates of the mean circulation in the deep (>2000 m) layer of the eastern North Atlantic. Progress in Oceanography. 14:103-127.

Dierckx, P. 1982. A fast algorithm for smoothing data on a rectangular grid while using spline functions. SIAM J. Numer. Anal. 19:1286-1304.

Flierl, G.R. 1988. On the instability of geostrophic vortices. J. Fluid Mech. 197:349-388.

Fofonoff, N.P. and R.M. Hendry. 1985. Current variability near the southeast Newfoundland Ridge. J. Phys. Oceanogr. 15:963-984.

Fratantoni, P.S., T.N. Lee, G. Podesta, and F. Muller-Karger. 1998. The influence of Loop Current perturbations on the formation and evolution of Tortugas eddies in the southern Straits of Florida. J. Geophys. Res. 103: 24,759-24,779.

Fu, L.-L., D. Stammer, R.R. Leben, and D.B. Chelton. 2003. Improved spatial resolution of ocean surface topography from the T/P–Jason-1 altimeter mission. EOS, Transactions, American Geophysical Union. 84:241,247-249.

Gille, S.T. and C.W. Hughes. 2001. Aliasing of high-frequency variability by altimetry: evaluation from bottom pressure records. Geophys. Res. Lett. 28:1755-1758.

Glenn, S.M. and C.B. Ebbesmeyre. 1993. Drifting buoy observations of a Loop Current anticyclonic eddy. J. Geophys. Res. 98:20105-20,119.

Greenslade, D.J.M., D.B. Chelton, and M.G. Schlax. 1997. The midlatitude resolution capability of sea level fields constructed from single and multiple altimeter datasets. J. Atmos. Oceanic Technol. 14:849-870.

Hamilton, P. 1990. Deep currents in the Gulf of Mexico. J. Phys. Oceanogr. 20:1087-1104.

Hamilton, P. In press. Deep current variability near the Sigsbee Escarpment in the Gulf of Mexico. J. Phys. Oceanogr.

Hamilton, P. and A. Lugo-Fernandez. 2001. Observations of high speed deep currents in the northern Gulf of Mexico. Geophys. Res. Lett. 28:2867-2870.

Hamilton, P., G.S. Fargion, and D.C. Biggs. 1999. Loop Current eddy paths in the western Gulf of Mexico. J. Phys. Oceanogr. 29:1180-1207.

Hamilton P., T.J. Berger, J.H. Churchill, R.R. Leben, T.N. Lee, J.J. Singer, W. Sturges, and E. Waddell. 2000. DeSoto Canyon eddy intrusion study: Final report. Volume II: Technical report. U.S. Dept. of the Interior, Minerals Management Service, Gulf of Mexico OCS Region, New Orleans, LA. OCS Study MMS 2000-080. 269 pp.

Hamilton, P., T.J. Berger, and W. Johnson. 2002. On the structure and motions of cyclones in the northern Gulf of Mexico. J. Geophys. Res. 107:3208 doi:10.1029, 1-18.

Hamilton, P., J.J. Singer, E. Waddell, and K. Donohue. 2003. Deepwater observations in the northern Gulf of Mexico from in-situ current meters and PIES: Final report. Volume II: Technical report. U.S. Dept. of the Interior, Minerals Management Service, Gulf of Mexico OCS Region, New Orleans, LA. OCS Study MMS 2003-049. 95 pp.

Hendricks, J.R., G.H. Born, C. Koblinsky, and R.R. Leben. 1996. EOF analysis of global TOPEX/POSEIDON data and implications for detection of global sea level rise. J. Geophys. Res. 101:14,131-14,146.

Hendry, R.M., D.R. Watts, and C.S. Meinen. 2002. Newfoundland Basin sea-level variability from TOPEX/POSEIDON altimetry and inverted echo sounder - bottom pressure measurements. Can. J. Remote Sensing. 28:544-555.

Jaimes, B. 2005. A look at the energetics of the wind and Loop Current-driven circulation in the Gulf of Mexico. M.S. Thesis, University of Miami, Rosenstiel School of Marine and Atmospheric Science, Miami. FL. 129 pp.

Kantha, L., J.-K. Choi, K.J. Schaudt, and C.K. Cooper. 2005. A regional data assimilation model for operational use in the Gulf of Mexico. In: Sturges, W. and A. Lugo-Fernandez, eds. Circulation in the Gulf of Mexico: Observations and models. Geophysical Monograph 161. American Geophysical Union, Washington DC. pp. 165-180.

Kobashi, F. and H. Kawamura. 2001. Variation of sea surface height at periods of 65-220 days in the subtropical gyre of the North Pacific. J. Geophys. Res. 106:26,817-26,831.

Koblinsky, C.J., B.D. Beckley, R.D. Ray, Y.-M. Wang, and A. Brenner. 1999. NASA Ocean altimeter pathfinder project. Report 1: Data processing handbook. NASA/TM-1998-208605.

Kunze, E. 1985. Near-inertial wave propagation in geostrophic shear. J. Phys. Oceanogr. 15:544-565.

Kunze, E. 1986. The mean and near-inertial velocity fields in a warm-core ring. J. Phys. Oceanogr. 16:1444-1461.

LeBlond, P.H. and L.A. Mysack. 1978. Waves in the ocean. Elsevier, Amsterdam.

Leben, R.R. 2005. Altimeter-derived Loop Current metrics. In: Sturges, W. and A. Lugo-Fermandez, eds. Circulation in the Gulf of Mexico: Observations and models. Geophysical Monograph 161. American Geophysical Union, Washington DC. pp.181-202.

Leben R.R., G.H. Born, and B.R. Engebreth. 2002. Operational altimeter data processing for mesoscale monitoring. Marine Geodesy 25:3-18.

Lee, T.N., K. Leaman, E. Williams, T. Berger, and L. Atkinson. 1995. Florida Current meanders and gyre formation in the southern Straits of Florida. J. Geophys. Res. 100:8607-8620.

Malanotte-Rizzoli, P., D.B. Haidvogel, and R.E. Young. 1987. Numerical simulation of transient boundary-forced radiation. Part I: The linear regime. J. Phys. Oceanogr. 17:1439-1457.

Meinen, C.E., E.Fields, R.S. Pickart, and D.R. Watts. 1993. Ray tracing on topographic Rossby waves. Technical Report 93-1. Graduate School of Oceanography, University of Rhode Island. 43 pp.

Meinen, C.S. and D.R. Watts. 2000. Vertical structure and transport on a transect across the North Atlantic Current near 42N: Time series and mean. J. Geophys. Res. 105:21,869-21,891.

Merrifield, M.A. and C.D. Winaut. 1989. Shelf circulation in the Gulf of California: A description of the variability. J.Geophys.Res. 94:18,133-18,160.

Mizuta, G. and N.G. Hogg. 2004. Structure of the circulation induced by a shoaling topographic wave. J. Phys. Oceanogr. 34:1793-1810.

Mooers, C.N.K. 1975. Several effects of a baroclinic current on the cross-stream propagation of inertial-internal waves. Geophys. Fluid Dyn. 6:245-275.

Munchow, A., Chant, R.J., 2000. Kinematics of inner shelf motions during the summer stratified season off New Jersey, J. Physical Oceanography 30:247-268.

Munk, W.H. and D.E. Cartwright. 1966. Tidal spectroscopy and prediction. Philosophical Transactions of the Royal Society of London 259(A):533-581.

North, G.R., T.L. Bell, R.F. Calahan, and F.J. Moeng. 1982. Sampling errors in the estimation of empirical orthogonal functions. Mon. Wealth. Rev. 110:699-706.

Nowlin, W.D., Jr., A.E. Jochens, S.F. DiMarco, R.O. Reid, and M.K. Howard. 2001. Deepwater physical oceanography reanalysis and synthesis of historical data, synthesis report. U.S. Dept. of the Interior, Minerals Management Service, Gulf of Mexico OCS Region, New Orleans, LA. OCS Study MMS 2001-064. 530 pp.

Oey L.Y. and H.C. Lee. 2002. Deep eddy and topographic Rossby waves in the Gulf of Mexico. J. Phys. Oceanogr. 32: 3499-3527.

O'Reilly, J.E., S. Maritorena, B.G. Mitchell, D. Siegel, K. Carder, S. Garver, M. Kahru, and C. McClain. 1998. Ocean color chlorophyll algorithms for SeaWiFS. J. Geophys. Res. 103:24,937-24,953.

Parke, M.E., R.H. Stewart, D.L. Farless, and D.E. Cartwright. 1987. On the choice of orbits for an altimetric satellite to study ocean circulation and tides. J. Geophys. Res. 92:11693-11707.

Phillips, O.M. 1969. The dynamics of the upper ocean. New York, NY: Cambridge University Press, 261 pp.

Pickart, R.S. 1995. Gulf Stream-generated topographic Rossby waves. J. Phys. Oceanogr. 25:574-584.

Press, W.H., S.A. Teukolsky, W.T. Vettering, and B.P. Flannery. 1992. Numerical recipes in FORTRAN, the art of scientific computing. New York, NY: Cambridge University Press. 963 pp.

Priestley, M.B. 1981. Spectral analysis and time series. London: Academic Press. 890 pp.

Rhines, P.B. 1970. Edge-, bottom-, and Rossby waves in a rotating stratified fluid. Geophys Fluid Dyn. 1:273-302.

Rossby, H.T., D. Dorson, and J. Fontaine. 1986. The RAFOS system. J. Atmos. Oceanic Tech. 3:672-679.

SAIC, 1986. Gulf of Mexico Physical Oceanography Program: Final report: Years 1 and 2: Volume II: Technical report. U.S. Dept. of the Interior, Minerals Management Service, Gulf of Mexico OCS Region, New Orleans, LA. OCS Study MMS 85-0094. 377 pp.

Schmitz, W.J., D.C. Biggs, A. Lugo-Fernandez, L.-Y. Oey, and W. Sturges. 2005. A synopsis of the circulation in the Gulf of Mexico and on its continental margins. In: Sturges, W. and A. Lugo-Fernandez, eds. Circulation in the Gulf of Mexico: Observations and Models, Geophysical Monograph 161. American Geophysical Union, Washington DC. pp. 11-30.

Shay, L.K. and R.L. Elsberry. 1987. Near-inertial ocean current response to Hurricane "Frederic." J. Phys. Oceanogr. 17:1249-1269.

Sheinbaum, J., J. Candela, A. Badan, and J. Ochoa. 2002. Flow structure and transport in the Yucatan Channel. Geophys. Res. Lett., 29(3):1040. doi:10.1029/2001GL013990.

Smith, W.H.F. and D.T. Sandwell. 1997. Global sea floor topography from satellite altimetry and ship depth soundings. Science. 277:1956-1962.

Sturges, W. 1994. The frequency of ring separations from the Loop Current. J. Geophys. Oceanogr. 24:1647-1651.

Sturges, W. and R. Leben. 2000. Frequency of ring separations from the Loop Current in the Gulf of Mexico: A revised estimate. J. Phys. Oceanogr. 30:1814-1819.

Thiebaux, H.J. and M.A. Pedder. 1987. Spatial objective analysis. London: Academic Press. 299 pp.

Thompson, R.O.R.Y. 1978. Observations of Rossby waves near site D. Prog. Oceanogr. 7:135-162.

Tierney, C.C., M.E. Parke, and G.H. Born. 1998. An investigation of ocean tides derived from along-track altimetry. J. Geophys. Res. 103:10,273-10,287.

Vukovich, F.M. 1988. On the formation of elongated cold perturbations off the Dry Tortugas. J. Phys. Oceanogr. 18:1051-1059.

Vukovich, F.M., and G.A. Maul. 1985. Cyclonic eddies in the eastern Gulf of Mexico. J. Phys. Oceanogr. 15:105-117.

Walker, N., S. Myint, A. Babin, and A. Haag 2003. Advances in satellite radiometry for the surveillance of surface temperatures, ocean eddies and upwelling processes in the Gulf of Mexico using GOES-8 during summer. Geophys. Res. Lett. 30(16):1854. doi:10.1029/2003GL017555.

Wang, Y.M. 2001. GSFC00 mean sea surface, gravity anomaly and vertical gravity gradient from satellite altimeter data. J. Geophys. Res. 106:31167-31174.

Watts, D.R. and H. Kontoyiannis. 1990. Deep-ocean bottom pressure measurement: Drift removal and performance. J. Atmos. Ocean. Tech. 7:296-306.

Watts, D.R., X. Qian, and K.L. Tracey. 2001. Mapping abyssal current and pressure fields under the meandering Gulf Stream. J. Atmos. Ocean. Tech. 18:1052-1067.

Watts, D.R., K.L. Tracey, and A.I. Friedlander. 1989. Producing accurate maps of the Gulf Stream thermal front using objective analysis. J. Geophys. Res. 94(C6):8040-8052.

Weatherly, G. 2004. Intermediate depth circulation in the Gulf of Mexico: PALACE float results for the Gulf of Mexico between April 1998 and March 2002. U.S. Dept of the Interior, Minerals Management Service, Gulf of Mexico OCS Region, New Orleans, LA. OCS Study MMS 2004-013. 51 pp.

Weatherly, G.L., N.Wienders, and A. Romanou. 2005. Intermediate-depth circulation in the Gulf of Mexico estimated from direct measurements. In: Sturges, W. and A. Lugo-Fernandez, eds. Circulation in the Gulf of Mexico: Observations and Models. Geophysical Monograph 161. American Geophysical Union, Washington, DC. pp. 315-324.

Welsh, S.E. and M. Inoue. 2000. Loop Current rings and deep circulation in the Gulf of Mexico. J. Geophys. Res. 105(C7):16,951-16,959.

Zavala-Hidalgo, J., S.L. Morey, and J.J. O'Brien. 2003. Cyclonic eddies northeast of the Campeche Bank from altimetry data. J. Phys. Oceanog. 33:623-629.

Appendix A

Supplemental Information Relating to Field Operations, Cruises, and Logistics

This appendix presents assorted information concerning field operations, moorings locations and deployment intervals.

A listing of the included tables is provided below:

Table A-1. Listing of cruises during the MMS Exploratory Study.

Provides the dates, vessel, vessel cruise ID number and the activities conducted on that cruise leg.

Table A-2. Hydrographic data collected during the MMS Exploratory Study Cruises.

A listing of cruise ID, cruise dates, profiling data taken, where taken and underway hydrographic and ADCP observations.

Table A-3. Mooring deployment periods for the Exploratory Study.

Moored arrays were rotated at approximately the six month interval, i.e. two deployments.

Table A-4. Moored instrument data return (by good record count) during the Exploratory Study..

Listing of data return by deployment interval and instrument type.

Table A-5. PIES deployment periods for the Exploratory Study.

PIES were deployed only once for the entire measurement program. The beginning and ending dates for each PIES (instrument) is provided.

Table A-6. Triangulated mooring locations and depth by department.

Table provides mooring ID, deployment site for first and second deployments and the water depth at each site. Also given is the estimated distance between the deployment sites for intervals one and two.

Table A-7. PIES deployment locations for the Exploratory Study.

Table A-8. PALFOS and RAFOS Drifter deployment sites in March/April 2003 during the Exploratory Study.

Table lists the drifter type, ballasted depth, drifter ID, deployment date and deployment location.

Table A-9. RAFOS drifter deployment sites in October 2003 during Exploratory Study.

Six of the 36 available RAFOS were not deployed with the original group presented in Table A-9. These six were to be placed in a special event. The buoy type, ID, deployment date and location for these drifter is presented.

Table A-1. Listing of Cruises During the Exploratory Study.

Dates (CTU)	Vessel	Cruise Number	Purpose
27 February – 8 March 2003	R/V LONGHORN	LH845-03	Short Mooring deployments.
11 – 15 March 2003	R/V LONGHORN	LH846-03	Three Sound Source and one PALFOS deployment.
16 March – 6 April 2003	R/V LONGHORN	LH847-03	Tall Mooring and PIES deployments.
12 – 15 April 2003	M/V EPIC ENDEAVOR	---	Five PALFOS and 30 RAFOS deployments.
31 August – 7 September 2003	R/V PELICAN	PE04-10	Short Mooring rotations.
10 – 24 September 2003	R/V PELICAN	PE04-12	Tall Mooring rotations and PIES telemetry.
26 – 30 October 2003	R/V PELICAN	PE04-17	Two Sound Source and Six RAFOS deployments.
26 March – 3 April 2004	R/V TOMMY MUNRO	TM080-04	PIES recoveries.
1 – 6 April 2004	R/V PELICAN	PE04-34	Short Mooring recoveries.
7 – 12 April 2004	R/V PELICAN	PE04-35	Tall Mooring recoveries.
25 – 27 May 2004	R/V TOMMY MUNRO	TM084-04	Two Sound Source recoveries.

Table A-2. Hydrographic data collected during the Exploratory Study cruises.

.

Cruise	Dates (CTU)	CTDs	T5 XBTs	CTD/XBT Location	Underway	
					Temp/ Salinity	75 KHz ADCP
LH847-03	03/16/03 – 04/06/03	0	48*	PIES 1-27 + 15 Stations	Yes	No
		6	0	PIES 12 Site		
PE04-10	08/31/03 – 09/07/03	4	0	PIES 4, 6, 13, 15	Yes	Yes
PE04-12	09/10/03 – 09/24/03	27	0	PIES 1-27	Yes	Yes
PE04-34	04/01/04 – 04/06/04	0	0	N/A	Yes	Yes
PE04-35	04/07/04 – 04/12/04	0	7	Moorings L1, L2, L3, L4, M3, M4, M5	Yes	Yes

*Some casts repeated due to short record or bad drop.

Table A-3. Mooring deployment periods for the Exploratory Study.

Mooring	Deployment Number	Deployment Periods (CTU)
L1	1	03/18/03 – 09/21/03
	2	09/22/03 – 04/11/04
L2	1	03/23/03 – 09/11/03
	2	09/12/03 – 04/08/04
L3	1	04/04/03 – 09/17/03
	2	09/19/03 – 04/10/04
L4	1	03/31/03 – 09/13/03
	2	09/15/03 – 04/09/04
M1	1	02/28/03 – 09/01/03
	2	09/01/03 – 04/02/04
M2	1	03/01/03 – 09/02/03
	2	09/02/03 – 04/02/04
M3	1	03/23/03 – 09/20/03
	2	09/20/03 – 04/08/04
M4	1	03/28/03 – 09/20/03
	2	09/21/03 – 04/11/04
M5	1	03/20/03 – 09/23/03
	2	09/23/03 – 04/11/04
N2	1	03/06/03 – 09/06/03
	2	09/06/03 – 04/05/04
N3	1	03/01/03 – 09/01/03
	2	09/02/03 – 04/04/04
N4	1	03/01/03 – 09/02/03
	2	09/02/03 – 04/02/04
N5	1	03/03/03 – 09/04/03
	2	09/04/03 – 04/03/04
N6	1	03/04/03 – 09/03/03
	2	09/03/03 – 04/03/04
O1	1	03/07/03 – 09/06/03
	2	09/06/03 – 04/05/04
O2	1	03/07/03 – 09/05/03
	2	09/05/03 – 04/04/04
O3	1	03/04/03 – 09/04/03
	2	09/04/03 – 04/02/04
O4	1	03/04/03 – 09/03/03
	2	09/03/03 – 04/03/04
Q2	1	03/07/03 – 09/05/03
	2	09/05/03 – 04/04/04

Table A-4. Moored instrument data return (by good record count) during the Exploratory Study.

Deployment	Aanderaa RCM-7/8 (CUR&T)	General Oceanics MK2 (CUR&T)	Hugrún Seamon Mini (T)
1	363,651 / 383,472 (45)	Not Deployed	98,994 / 98,994 (12)
2	408,427 / 421,824 (42)	14691 / 19698 (2)	118,182 / 118,182 (12)
TOTALS	772,078 / 805,296 (87)	14691 / 19698 (2)	217,176 / 217,176 (24)
Percent Good	95.9%	74.6%	100.0%
Deployment	InterOcean S4 (CUR&T)	RD Instruments ADCP* (CUR&T)	Sea-Bird MicroCat/SeaCat (T&S)
1	17,110 / 17,110 (2)	32,982 / 32,982 (4)	180,858 / 180,858 (12)
2	39,394 / 39,394 (4)	39,388 / 39,388 (4)	235,016 / 236,364 (12)
TOTALS	56,504 / 56,504 (6)	72,370 / 72,370 (8)	415,874 / 417,222 (24)
Percent Good	100.0%	100.0%	99.7%

GRAND TOTAL: 1,548,693 / 1,588,266 (151) = 97.5%
*All ADCP levels for each instrument counted as one (1) time series record.
(#) = Number of Instrument Deployments.

Table A-5. PIES deployment periods for the Exploratory Study.

PIES (SN)	Deployment Number	Deployment Periods (CTU)
P1 (094)	1	03/25/03 – 03/27/04
P2 (095)	1	03/24/03 – 03/29/04
P3 (084)	1	03/24/03 – 03/29/04
P4 (101)	1	03/28/03 – 04/02/04
P5 (090)	1	03/23/03 – 03/28/04
P6 (080)	1	03/25/03 – 03/29/04
P7 (088)	1	03/24/03 – 03/29/04
P8 (085)	1	03/22/03 – 03/28/04
P9 (078)	1	03/22/03 – 03/30/04
P10 (100)	1	03/25/03 – 03/30/04
P11 (106)	2*	09/15/03 – 03/30/04
P12 (087)	1	03/22/03 – 03/29/04
P13 (077)	1	03/26/03 – 03/31/04
P14 (103)	1	04/01/03 – 03/31/04
P15 (079)	1	04/01/03 – 03/31/04
P16 (097)	1	04/01/03 – 03/30/04
P17 (086)	1	03/17/03 – 03/29/04
P18 (082)	1	03/20/03 – 03/31/04
P19 (091)	1	03/20/03 – 04/01/04
P20 (083)	1	03/20/03 – 04/02/04
P21 (076)	1	03/21/03 – 04/02/04
P22 (099)	1	03/18/03 – 03/28/04
P23 (096)	1	03/18/03 – 04/03/04
P24 (081)	1	03/19/03 – 04/02/04
P25 (089)	1	03/19/03 – 04/02/04
P26 (093)	1	03/23/03 – 03/28/04
P27 (098)	1	03/31/03 – 03/30/04

*Original PIES lost at this site (no data).

Table A-6. Triangulated mooring locations and depths by deployment.

Mooring	Deployment 1	Depth (m)	Deployment 2	Depth (m)	Distance Between (km)
L1	27°36.065'N 89°13.369'W	1512	27°35.999'N 89°13.520'W	1503	0.277
L2	27°05.708'N 91°06.395'W	1762	27°05.534'N 91°06.268'W	1780	0.385
L3	26°05.304'N 88°57.770'W	2998	26°04.979'N 88°57.822'W	3002	0.609
L4	25°55.431'N 91°07.932'W	3350	25°55.423'N 91°07.958'W	3352	0.046
M1	27°16.991'N 89°44.620'W	1981	27°17.136'N 89°44.712'W	1973	0.309
M2	27°01.392'N 90°13.958'W	2326	27°01.524'N 90°13.976'W	2314	0.247
M3	26°50.197'N* 90°38.123'W*	1740*	26°50.267'N 90°38.171'W	1734	0.152
M4	27°09.572'N 90°24.182'W	1335	27°09.709'N 90°24.269'W	1335	0.292
M5	27°21.186'N 89°56.817'W	1304	27°21.147'N 89°56.788'W	1302	0.087
N2	27°01.636'N 89°05.081'W	2319	27°01.523'N 89°05.151'W	2317	0.239
N3	26°53.703'N 89°47.911'W	2580	26°53.747'N 89°47.910'W	2571	0.082
N4	26°41.877'N 90°25.996'W	2538	26°41.905'N 90°26.030'W	2535	0.077
N5	26°31.636'N 91°07.942'W	2020	26°31.650'N 91°07.891'W	2018	0.089
N6	26°28.871'N 91°43.647'W	2332	26°28.811'N 91°43.590'W	2332	0.146
O1	26°28.247'N 89°01.583'W	2830	26°28.132'N 89°01.769'W	2830	0.375
O2	26°21.523'N 89°46.885'W	3018	26°21.562'N 89°46.949'W	3018	0.129
O3	26°19.070'N 90°41.855'W	2960	26°19.111'N 90°41.770'W	2970	0.161
O4	26°05.579'N 91°47.492'W	2222	26°05.615'N 91°47.471'W	2219	0.075
Q2	25°57.879'N 89°48.854'W	3211	25°57.837'N 89°48.927'W	3210	0.145

*Triangulation data bad; used anchor drop coordinates and depth.

Table A-7. PIES deployment locations for the Exploratory Study.

PIES (SN)	Location	Water Depth (m)	Top (m)
1 (094)	26°47.4862'N 92°04.7671'W	1691	1690
2 (095)	26°21.0692'N 92°11.5560'W	1920	1919
3 (084)	25°52.2408'N 92°04.1873'W	2816	2815
4 (101)	26°21.6831'N 89°49.6071'W	3015	3014
5 (090)	26°49.6246'N 91°21.6642'W	2049	2048
6 (080)	26°21.6533'N 91°28.9134'W	2169	2168
7 (088)	25°45.9855'N 91°35.4169'W	3174	3173
8 (085)	27°15.0040'N 90°31.6150'W	1367	1366
9 (078)	26°53.0441'N 90°42.2887'W	1806	1805
10 (100)	26° 22.0488'N 90° 57.1260'W	2151	2150
11 (106)	25° 49.655'N 90° 53.602'W	3410	3409
12 (087)	27° 23.0787'N 90° 03.0382'W	1310	1309
13 (077)	26°54.4347'N 90°05.5328'W	2548	2547
14 (103)	26° 34.6419'N 90° 15.1708'W	2800	2799
15 (079)	26° 15.6624'N 90° 24.3875'W	3130	3129
16 (097)	25° 48.0554'N 90° 11.2595'W	3300	3299
17 (086)	27° 45.4195'N 89° 40.5344'W	1150	1149
18 (082)	27° 12.4747'N 89° 31.9270'W	2252	2251
19 (091)	26° 39.6708'N 89° 23.4760'W	2812	2811
20 (083)	26° 05.8294'N 89° 23.3885'W	3105	3104
21 (076)	25° 45.2827'N 89° 28.7109'W	3282	3281
22 (099)	27° 58.4256'N 89° 01.6292'W	1346	1345
23 (096)	27° 28.8516'N 88° 53.8236'W	1899	1898
24 (081)	26° 54.4277'N 88° 36.8181'W	2340	2339
25 (089)	26° 21.3770'N 88° 36.3263'W	2689	2688
26 (093)	27° 05.6756'N 91° 06.3775'W	1750	1749
27 (098)	25° 55.3903'N 91° 07.9835'W	3350	3349

Table A-8. PALFOS and RAFOS Drifter deployment sites in March/April 2003 during the Exploratory Study.

Site	Drifter/Depth (m)	ARGOS ID/SN	Date	Location
A	PALFOS/1000	28447/pf3	03/14/03	27°15.10'N 89°25.54'W
B	RAFOS/1000	40240/460	04/12/03	28°15.07'N 89°00.12'W
C	RAFOS/1500	40211/457	04/13/03	27°37.85'N 88°59.59'W
D	PALFOS/1000	28445/pf1	04/13/03	27°23.12'N 88°59.83'W
E	RAFOS/1500	40221/467	04/13/03	27°03.61'N 88°59.06'W
	RAFOS/2000	40229/475		
F	RAFOS/1500	40225/471	04/13/03	26°35.00'N 89°00.57'W
	RAFOS/2000	40237/483		
	RAFOS/2500	40235/481		
G	PALFOS/1000	28446/pf2	04/13/03	26°10.58'N 88°59.83'W
H	RAFOS/1500	40217/463	04/13/03	25°45.00'N 89°00.00'W
	RAFOS/2000	40244/490		
	RAFOS/3000	40232/478		
I	PALFOS/1000	28448/pf4	04/14/03	25°51.01'N 89°45.01'W
	RAFOS/1500	40218/464		
	RAFOS/2000	40241/487		
	RAFOS/3000	40233/479		
J	RAFOS/1500	40222/468	04/14/03	26°40.00'N 89°45.00'W
	RAFOS/2000	40242/488		
	RAFOS/2500	40212/486		
K	RAFOS/1000	40213/459	04/14/03	27°27.69'N 90°30.16'W
L	RAFOS/1500	40214/458	04/14/03	27°02.86'N 90°28.93'W
M	PALFOS/1000	28449/pf2	04/14/03	26°46.83'N 90°30.33'W
	RAFOS/1500	40216/462		
	RAFOS/2000	40234/480		
N	RAFOS/1500	40215/461	04/14/03	26°29.75'N 90°30.01'W
	RAFOS/2000	40239/485		
	RAFOS/2500	40210/474		
O	PALFOS/1000	28450/pf6	04/14/03	26°06.79'N 90°30.04'W
	RAFOS/1500	40226/472		
	RAFOS/2000	40236/482		
	RAFOS/3000	40231/477		
P	RAFOS/1500	40220/466	04/15/03	27°06.42'N 89°44.90'W
	RAFOS/2000	40243/489		
Q	RAFOS/1500	40227/473	04/15/03	27°22.58'N 89°45.17'W
R	RAFOS/1000	40224/470	04/15/03	27°30.17'N 89°45.15'W

Depth = Ballast Depth.

Table A-9. RAFOS Drifter deployment sites in October 2003 during the Exploratory Study.

Site	Drifter/Depth (m)	ARGOS ID/SN	Date	Location
S	RAFOS/2500	40245/491	10/28/03	26°05.04'N 90°31.94'W
T	RAFOS/2500	40238/484	10/28/03	26°13.96'N 90°31.89'W
U	RAFOS/1500	40228/456	10/29/03	26°25.94'N 90°31.85'W
	RAFOS/2500	40230/476		
V	RAFOS/1500	40219/465	10/29/03	26°38.99'N 90°31.98'W
W	RAFOS/1500	40223/469	10/29/03	26°46.98'N 90°32.00'W

Depth = Ballast Depth.

Appendix B

Salinity and Specific Volume Anomaly GEM Fields

This appendix provides plots of the salinity and specific-volume anomaly GEM fields used in the analysis and interpretation of the Exploratory PIES. Section 2.4 details the GEM methodology. Similar to the temperature fields, a functional relationship exists between the integrated variable, $\tau(150\text{-}1000)$ and vertical profiles of salinity and specific volume anomaly. The rms values for salinity and specific volume anomaly are small, ~.02 psu and $.02 \times 10^{-6}$ $m^3 kg^{-1}$, respectively, within the thermocline and decrease with increasing pressure.

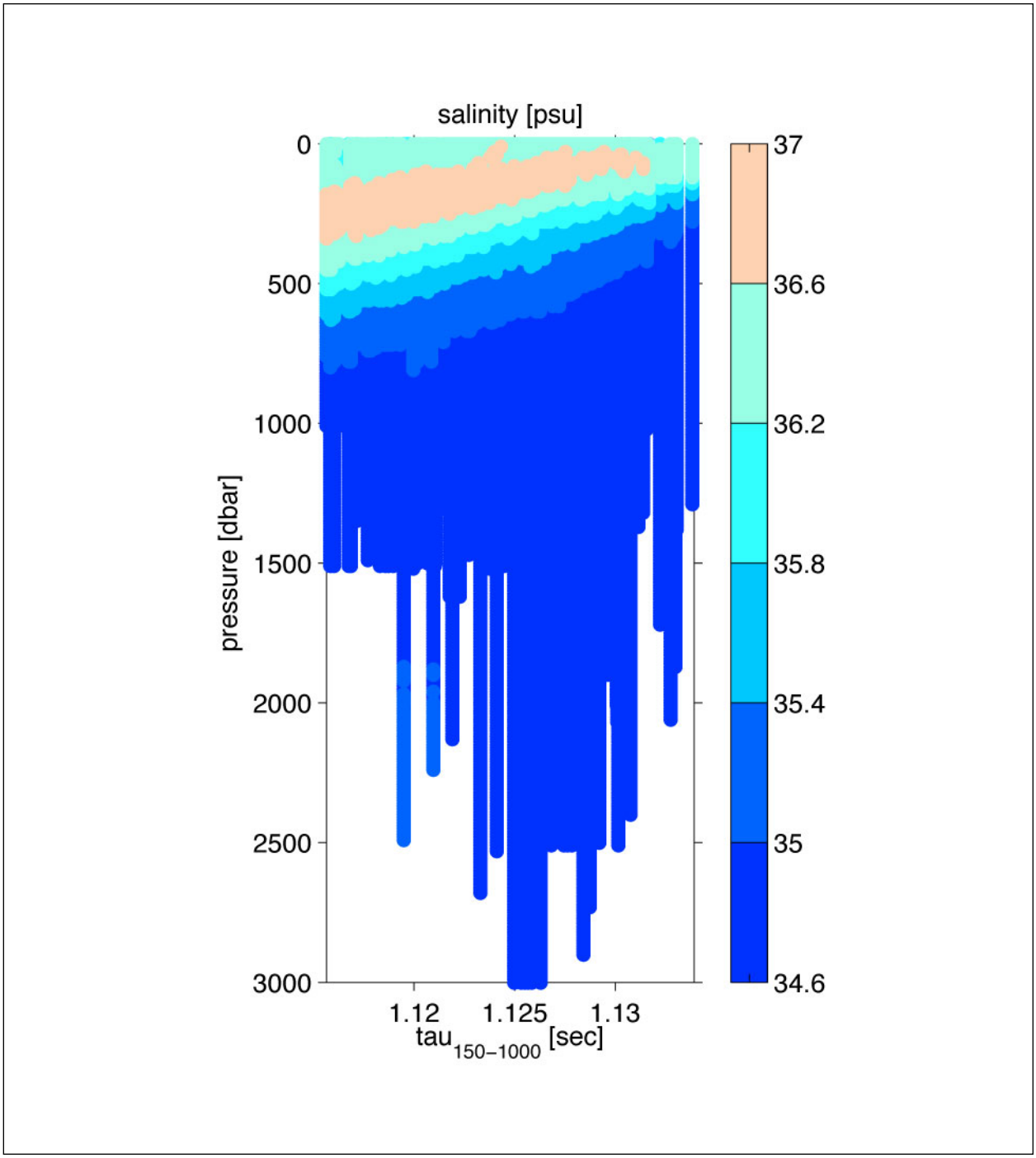

Figure B-1. Salinity profiles interpolated every 10 dbar and sorted by ?(150-1000).

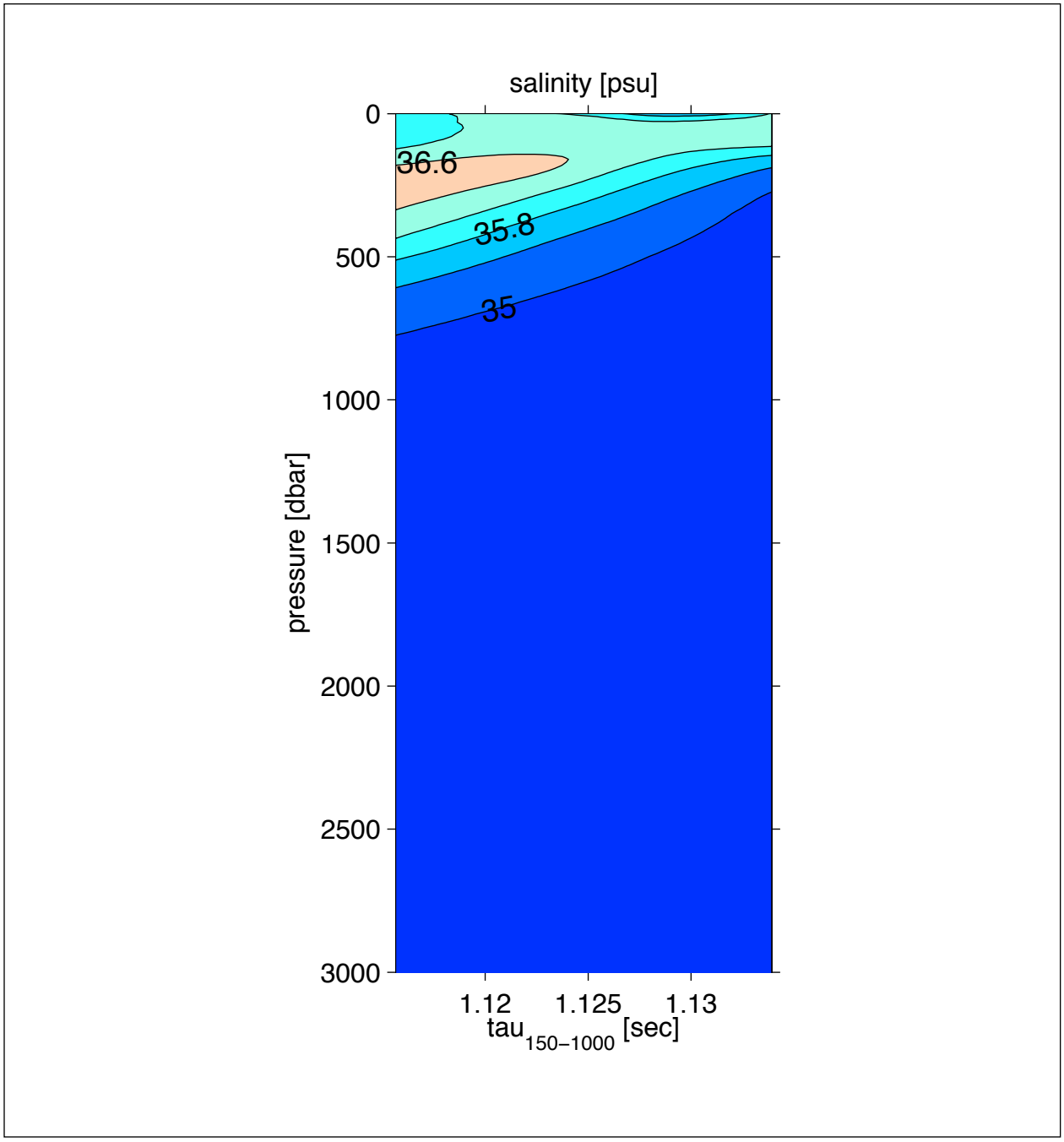

Figure B-2. Contour plot of the cubic smoothing spline fits for the salinity GEM field.

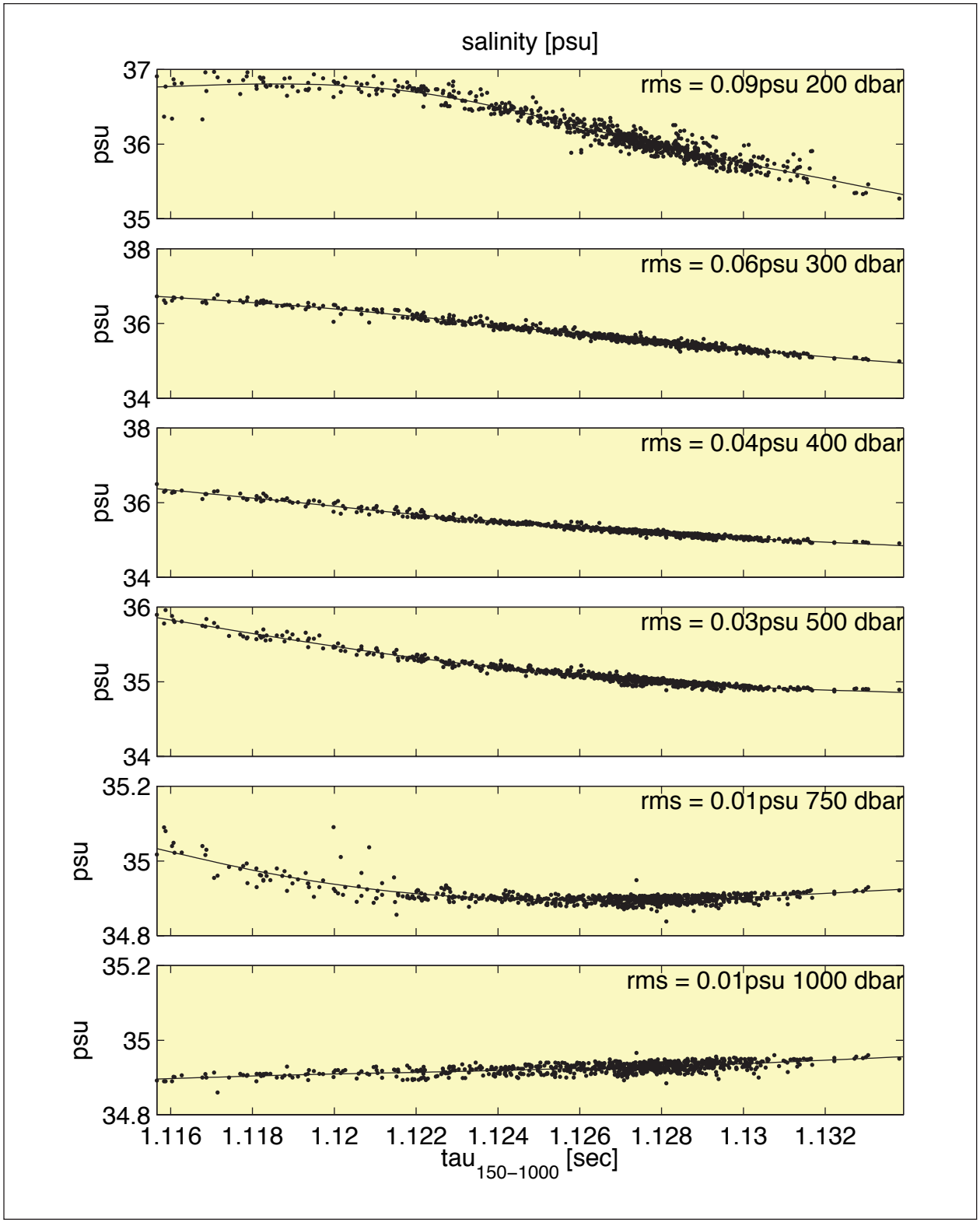

Figure B-3. Scatter plots of salinity versus tau(150-1000) for six representative pressure levels. At each pressure, the salinity versus tau(150-1000) data were fit by a cubic smoothing spline (solid curve).

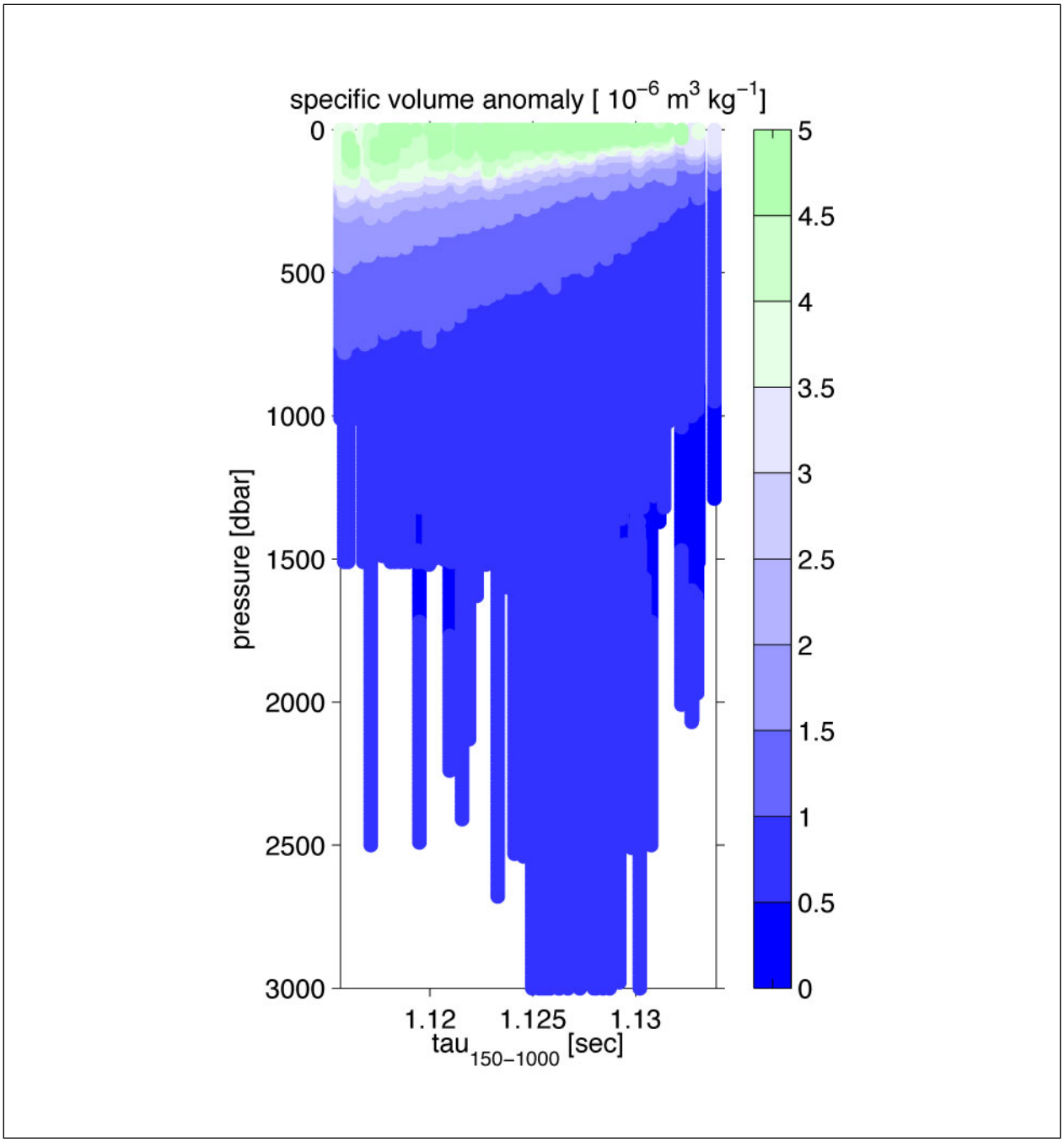

Figure B-4. Specific volume anomaly profiles interpolated every 10 dbar and sorted by tau(150-1000).

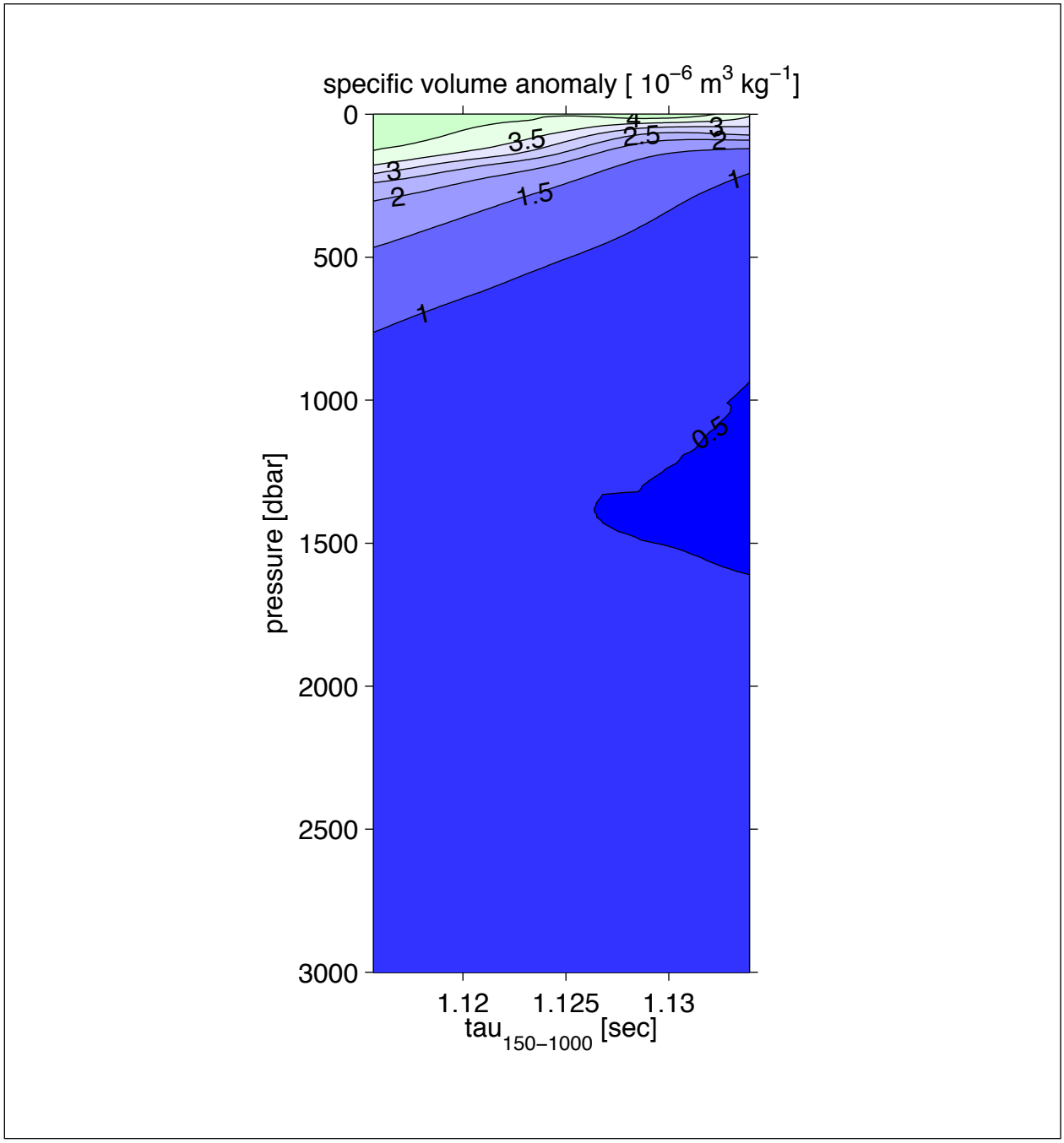

Figure B-5. Contour plot of the cubic smoothing spline fits for the specific volume anomaly GEM field.

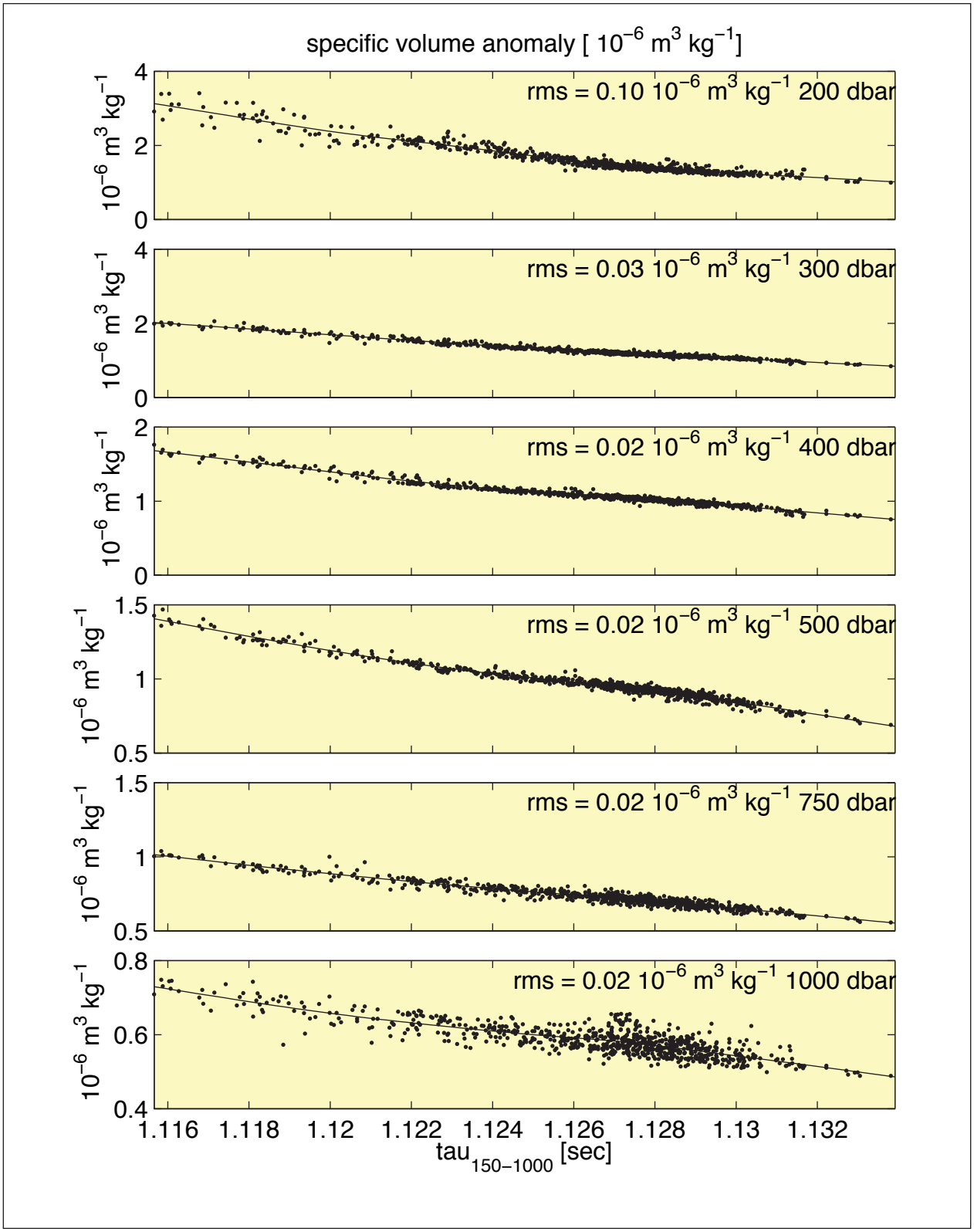

Figure B-6. Scatter plots of specific volume anomaly versus τ(150-1000) for six representative pressure levels. At each pressure, the specific volume anomaly versus τ(150-1000) data were fit by a cubic smoothing spline (solid curve).

Appendix C

Validation of PIES/GEM - Methodology

This appendix documents the statistics of various comparisons between PIES-derived and direct measurements. Here we provide plots of comparisons between mooring and PIES-derived time series of temperature, salinity, and velocity (Figures C-?-C-??) and detailed statistics of the comparisons Tables (C-1,C-2,C-3).

Note that the tall moorings experienced some vertical motion when ocean currents caused the moorings to 'blow over.' The proper comparison was thus between measured and estimated T(t,p(t)), S(t,p(t)), u(t,p(t)),v(t,p(t)). PIES and tall moorings were collocated only at PIES26 so we compared moored time series against mapped time series. A more stringent test of the GEM/PIES/mapping methodology is the comparison with measured velocities since the PIES velocities are 2^{nd}-order quantities determined via differentiation. Note that four of the tall moorings are located at the periphery of our mapping grid which means that the most direct comparison is not necessary between zonal or meridional velocity but between cross-PIES velocities. We term this 'meridional rotated velocity.'

Comparisons are excellent. Note that for all comparisons PIES-derived series track the measured series. Typically the statistics are slightly more favorable below the influence of the seasonal mixed layer. Small differences arose from instrument errors (both mooring and PIES), the GEM parameterization, and from mapping.

Table C-1

Statistics for the comparison between measured and PIES-estimated temperature time series. Nominal depths (first column), root-mean-squared of the difference between mooring and PIES estimated series (second column), correlation coeffiecient squared (third column), standard deviation of the mooring (third column) and PIES estimated (fourth column) time series and length of series (sixth column) are provided.

Temperature					
	rms (°C)	r^2	std mooring (°C)	std PIES (°C)	Length (days)
L1					
75 m	1.24	0.82	2.76	2.12	360
150 m	1.29	0.92	3.32	2.95	287
225 m	1.00	0.94	2.73	2.57	233
400 m	0.70	0.95	1.98	1.93	360
1000 m	0.11	0.86	0.27	0.23	360
L2					
75 m	1.14	0.40	1.29	1.37	360
150 m	0.51	0.80	1.14	1.02	282
225 m	0.57	0.74	0.87	0.95	342
402 m	0.36	0.77	0.61	0.69	360
1000 m	0.09	0.63	0.14	0.08	360
L3					
75 m	1.29	0.76	2.45	1.67	354
150 m	1.28	0.83	2.92	2.32	286
225 m	1.09	0.83	2.52	2.00	354
402 m	0.66	0.88	1.63	1.33	354
1000 m	0.15	0.73	0.24	0.16	354
1500 m	0.03	0.42	0.03	0.01	354
L4					
75 m	1.14	0.94	2.41	1.72	193
150 m	0.81	0.91	2.07	1.60	193
402 m	0.58	0.93	0.89	0.88	193
1000 m	0.08	0.63	0.10	0.08	193
1500 m	0.02	0.22	0.02	0.01	190
LSU/L5					
210 m	0.40	0.96	1.85	1.76	340
170 m	0.55	0.96	2.14	1.93	340
660 m	0.16	0.95	0.45	0.52	340
680 m	0.21	0.95	0.45	0.47	340
670 m	0.12	0.95	0.44	0.50	340
940 m	0.13	0.80	0.20	0.18	340
1020 m	0.09	0.72	0.16	0.13	340
1160 m	0.10	0.63	0.10	0.07	340
1320 m	0.04	0.50	0.05	0.03	340
1400 m	0.06	0.43	0.03	0.02	340

Table C-2

Statistics for the comparison between measured and PIES-stimated temperature time series. Nominal depths (first column), root-mean-squared of the difference between mooring and PIES estimated series (second column), correlation coeffiecient squared (third column), standard deviation of the mooring (third column) and PIES estimated (fourth column) time series and length of series (sixth column) are provided.

Salinity					
	rms (psu)	r^2	std mooring (psu)	std PIES (psu)	Length (days)
L1					
75 m	0.13	0.38	0.13	0.06	360
150 m	0.13	0.86	0.29	0.19	287
225 m	0.14	0.93	0.42	0.36	233
L2					
75 m	0.11	0.01	0.09	0.01	339
150 m	0.08	0.78	0.17	0.14	282
225 m	0.11	0.64	0.15	0.15	342
L3					
75 m	0.15	0.47	0.14	0.06	354
150 m	0.17	0.71	0.28	0.19	286
225 m	0.15	0.80	0.33	0.26	354
L4					
75 m	0.10	0.05	0.08	0.01	193
150 m	0.12	0.78	0.17	0.09	193
LSU/L5					
170 m	0.00	0.26	1.02	0.23	340
670 m	1.44	0.94	0.02	0.02	340
1020 m	0.00	0.72	0.01	0.01	340
1320 m	0.00	0.49	0.00	0.00	340

Table C-3

Statistics for the comparison between measured and PIES-estimated velocity time series. Nominal depths (first column), root-mean-squared of the difference between mooring and PIES estimated series (second column), correlation coeffiecient squared (third column), standard deviation of the mooring (third column) and PIES estimated (fourth column) time series and length of series (sixth column) are provided.

Velocity					
	rms (cms^{-1})	r^2	std mooring (cms^{-1})	std PIES (cms^{-1})	length (days)
Meridional Velocity Rotated (60°)					
L1					
75 m	19.6	0.72	33.1	23.9	354
150 m	14.1	0.71	24.8	18.2	354
225 m	12.1	0.74	21.3	14.8	354
Meridional Velocity Rotated (30°)					
L2					
75 m	7.1	0.81	15.0	12.9	151
150 m	7.0	0.72	11.2	9.8	151
225 m	6.4	0.65	9.5	8.0	151
Meridional Velocity Rotated (37°)					
L3					
75 m	18.3	0.79	36.8	31.7	354
150 m	16.0	0.71	27.5	25.0	354
225 m	12.6	0.66	19.5	18.9	354
Meridional Velocity Rotated (25°)					
L4					
75 m	14.0	0.84	19.2	17.2	354
150 m	10.5	0.84	13.1	12.1	354
Meridional Velocity Rotated (0°)					
LSU/L5					
210 m	5.4	0.73	10.3	9.6	340
170 m	6.0	0.73	11.4	11.0	340
680 m	4.0	0.24	4.5	2.8	340

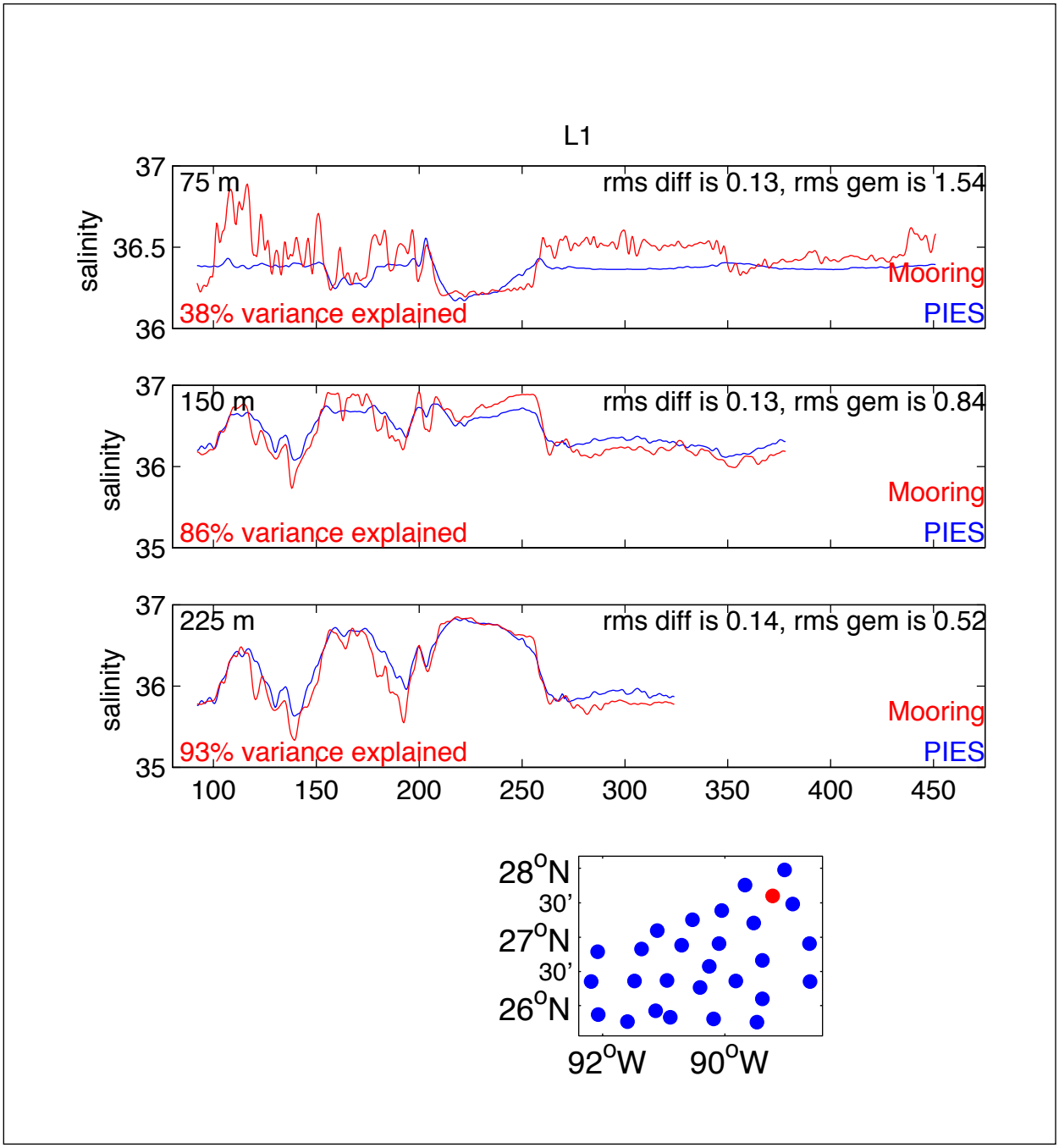

Figure C-1. Comparison between L1 mooring (red) and PIES-derived (blue) salinity. The variance explained is noted in red in the bottom left corner of each panel. The rms difference between the series and the rms in the GEM is noted in the upper right corner. The bottom panel shows the location of the PIES (blue) and the mooring (red).

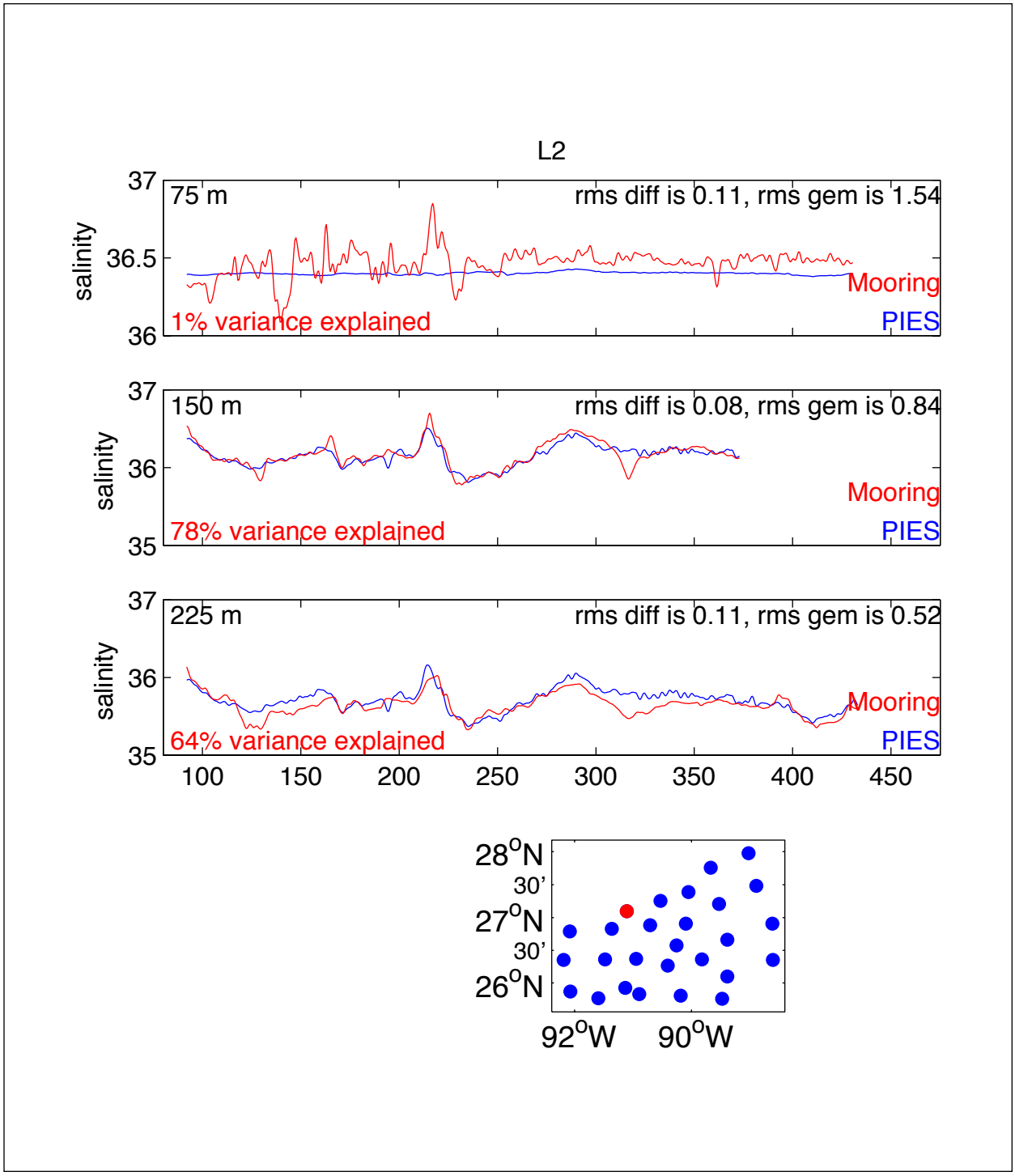

Figure C-2. Comparison between L2 mooring (red) and PIES-derived (blue) salinity. The variance explained is noted in red in the bottom left corner of each panel. The rms difference between the series and the rms in the GEM is noted in the upper right corner. The bottom panel shows the location of the PIES (blue) and the mooring (red).

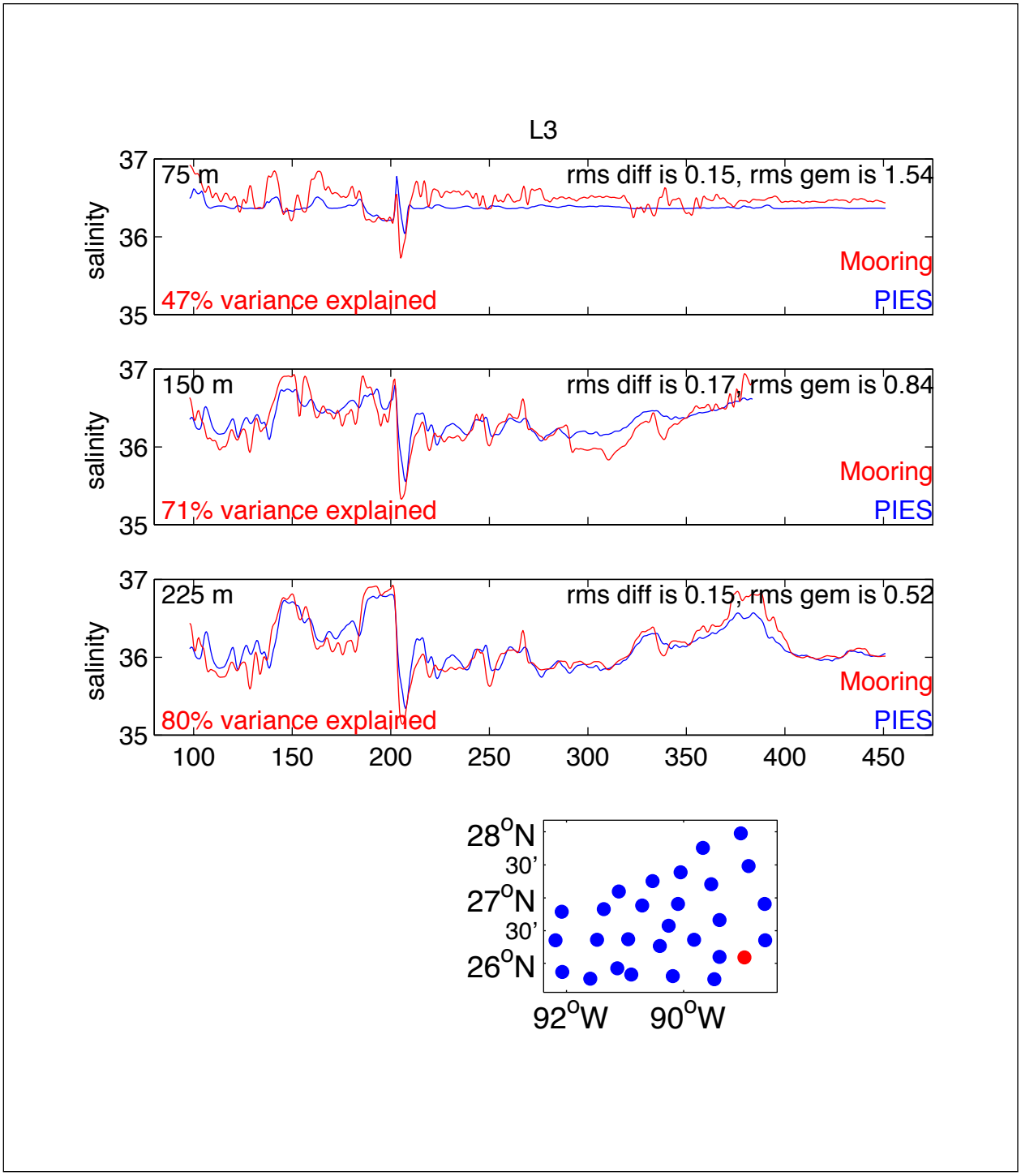

Figure C-3. Comparison between L3 mooring (red) and PIES-derived (blue) salinity. The variance explained is noted in red in the bottom left corner of each panel. The rms difference between the series and the rms in the GEM is noted in the upper right corner. The bottom panel shows the location of the PIES (blue) and the mooring (red).

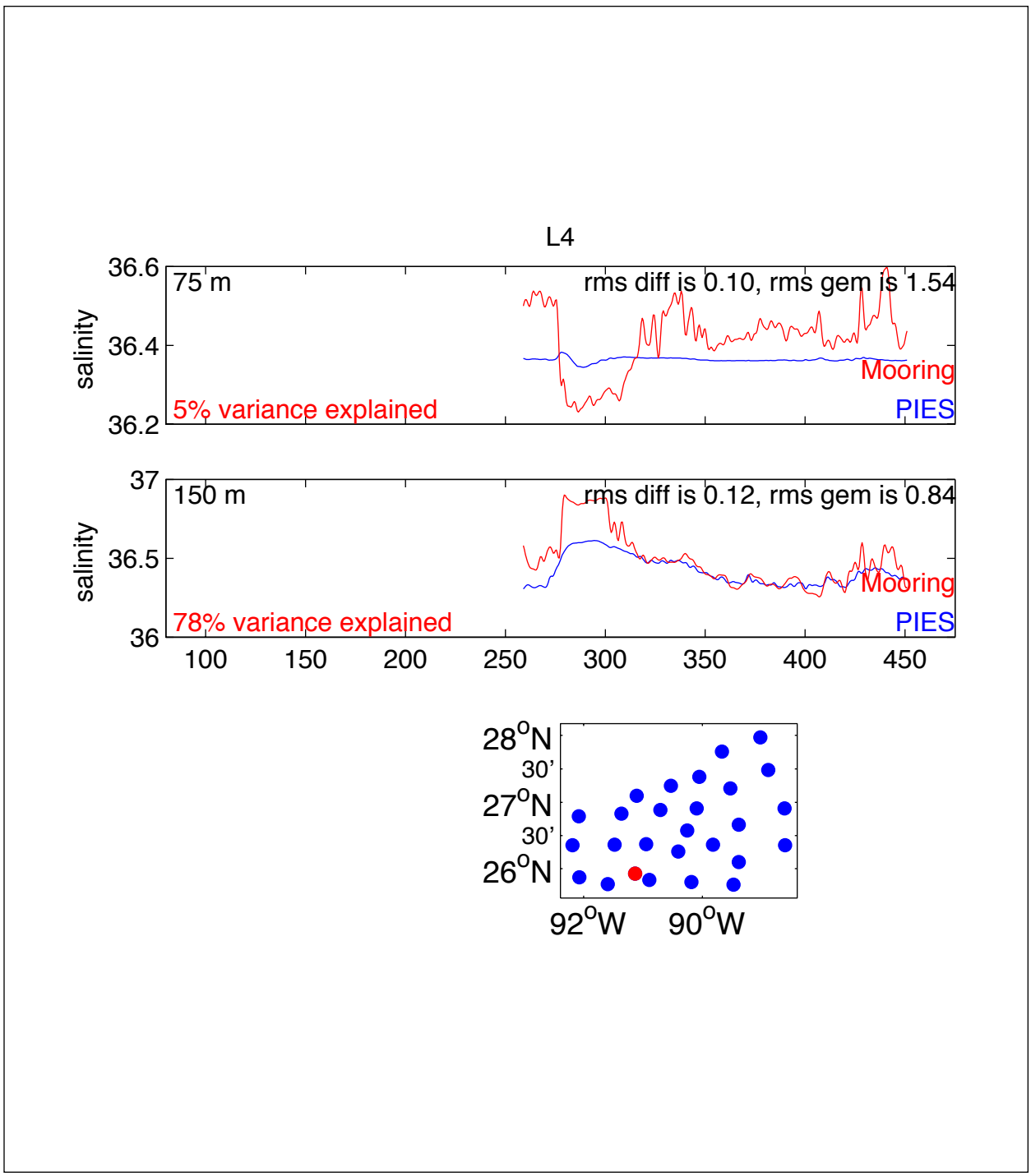

Figure C-4. Comparison between L4 mooring (red) and PIES-derived (blue) salinity. The variance explained is noted in red in the bottom left corner of each panel. The rms difference between the series and the rms in the GEM is noted in the upper right corner. The bottom panel shows the location of the PIES (blue) and the mooring (red).

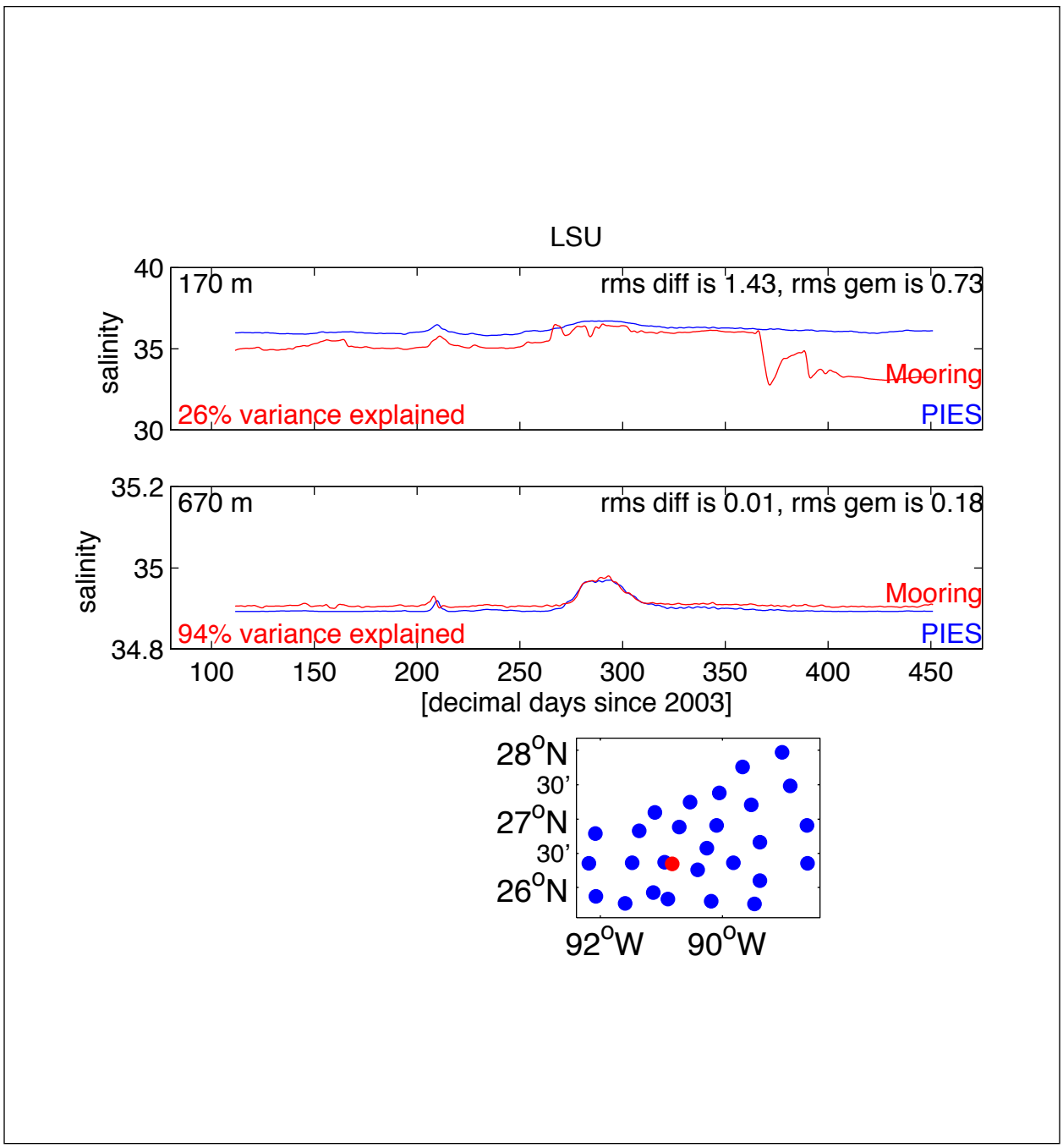

Figure C-5. Comparison between LSU/L5 mooring (red) and PIES-derived (blue) salinity. The variance explained is noted in red in the bottom left corner of each panel. The rms difference between the series and the rms in the GEM is noted in the upper right corner. The bottom panel shows the location of the PIES (blue) and the mooring (red).

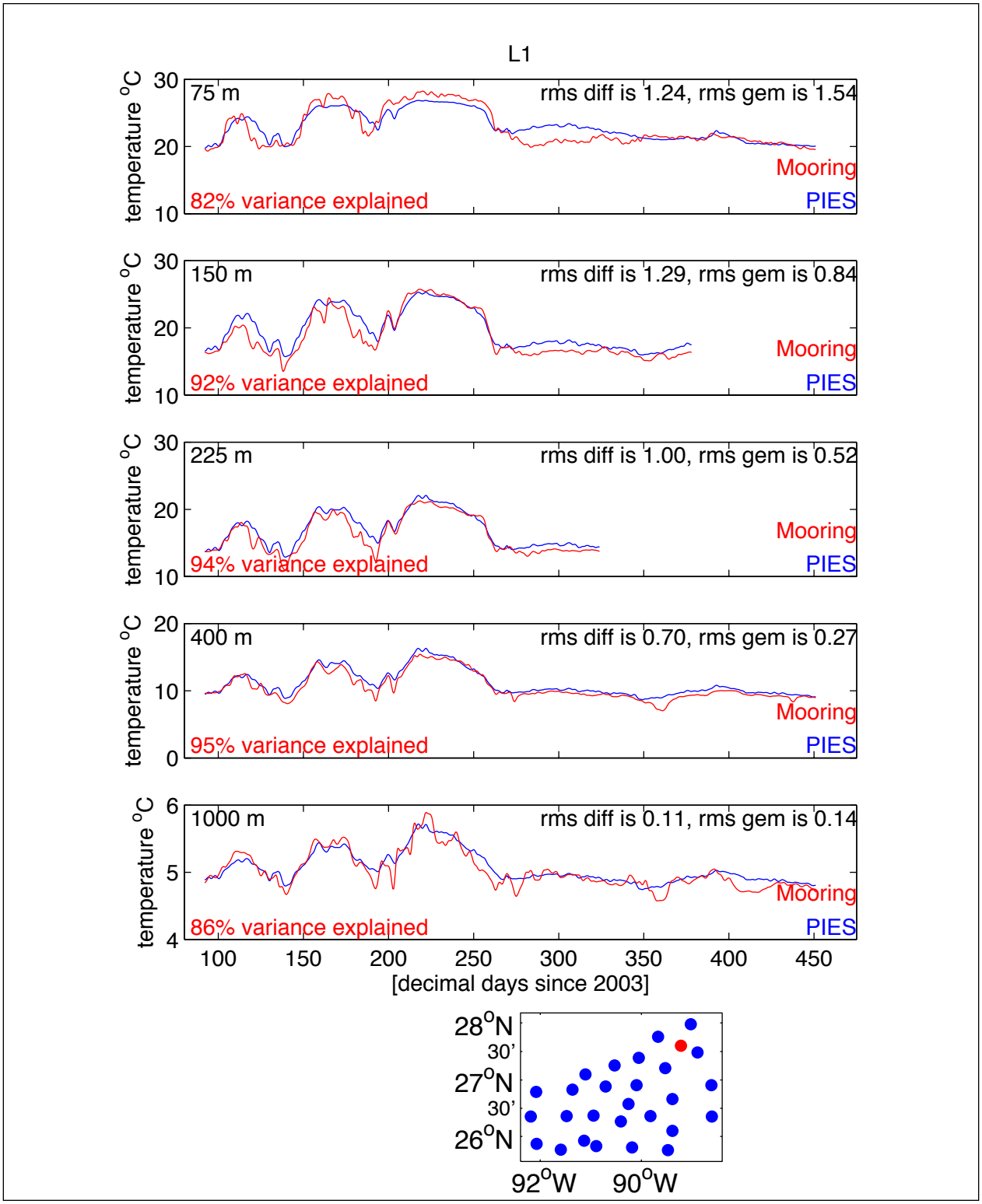

Figure C-6. Comparison between L1 mooring (red) and PIES-derived (blue) temperature. The variance explained is noted in red in the bottom left corner of each panel. The rms difference between the series and the rms in the GEM is noted in the upper right corner. The bottom panel shows the location of the PIES (blue) and the mooring (red).

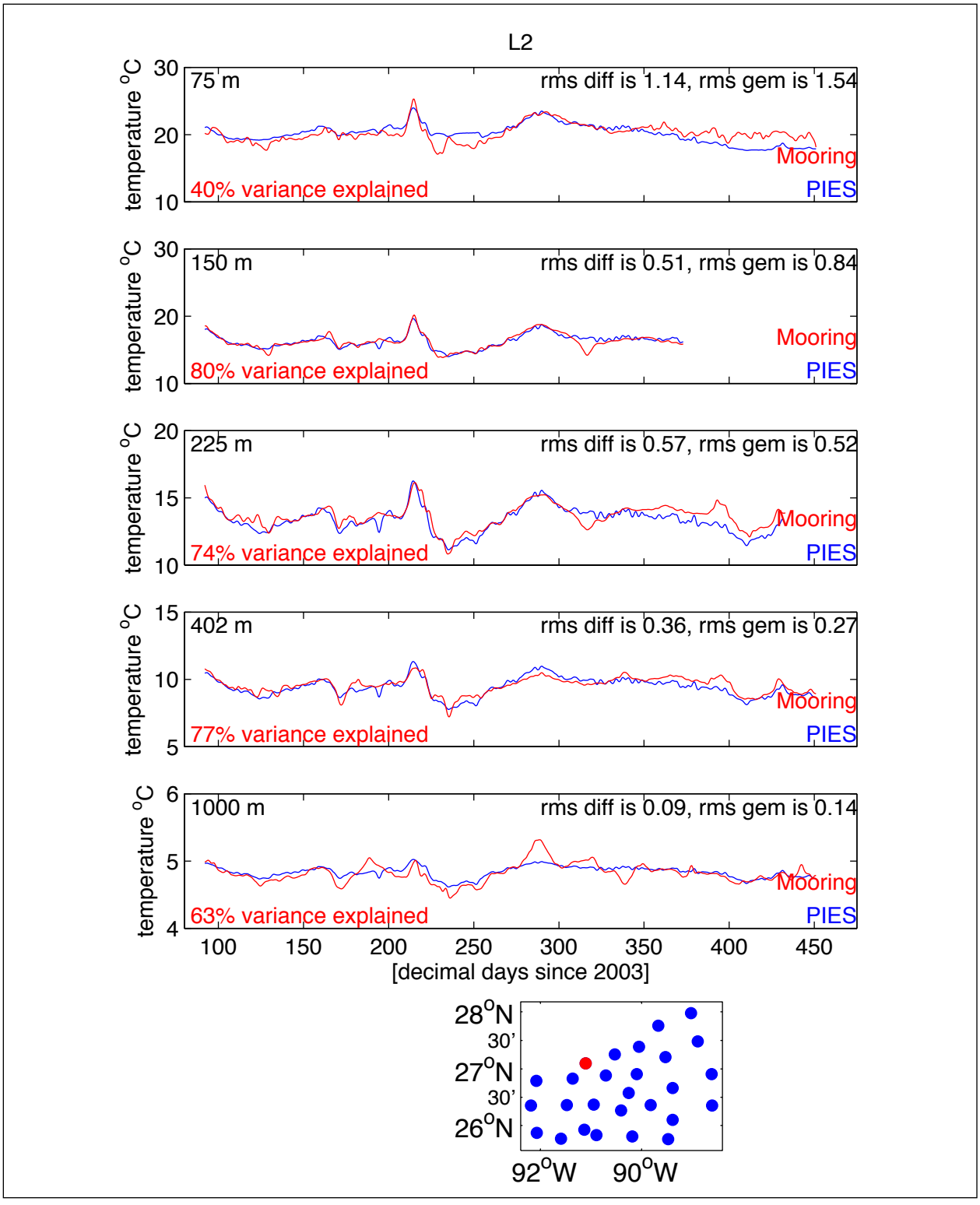

Figure C-7. Comparison between L2 mooring (red) and PIES-derived (blue) temperature. The variance explained is noted in red in the bottom left corner of each panel. The rms difference between the series and the rms in the GEM is noted in the upper right corner. The bottom panel shows the location of the PIES (blue) and the mooring (red).

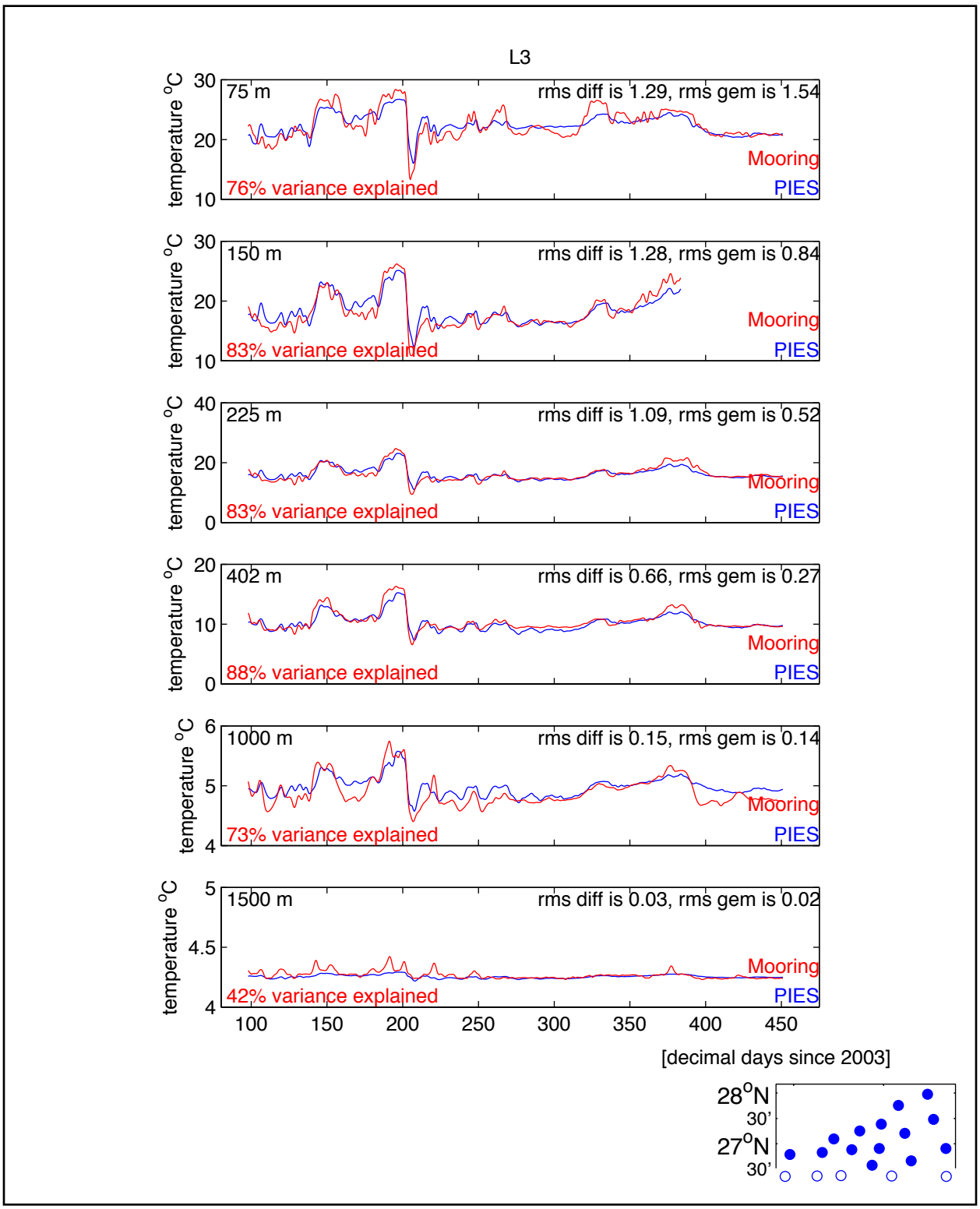

Figure C-8. Comparison between L3 mooring (red) and PIES-derived (blue) temperature. The variance explained is noted in red in the bottom left corner of each panel. The rms difference between the series and the rms in the GEM is noted in the upper right corner. The bottom panel shows the location of the PIES (blue) and the mooring (red).

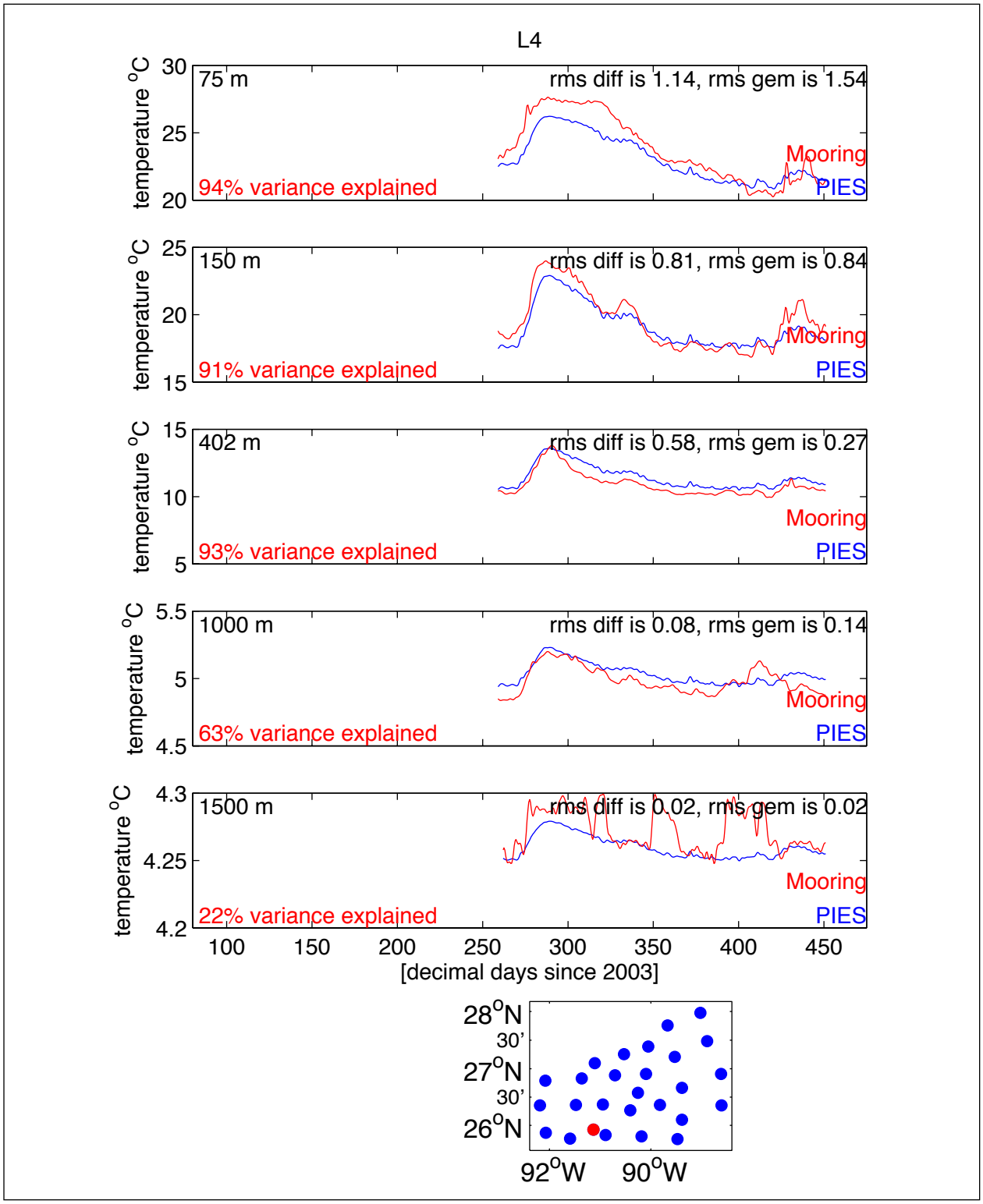

Figure C-9. Comparison between L4 mooring (red) and PIES-derived (blue) temperature. The variance explained is noted in red in the bottom left corner of each panel. The rms difference between the series and the rms in the GEM is noted in the upper right corner. The bottom panel shows the location of the PIES (blue) and the mooring (red).

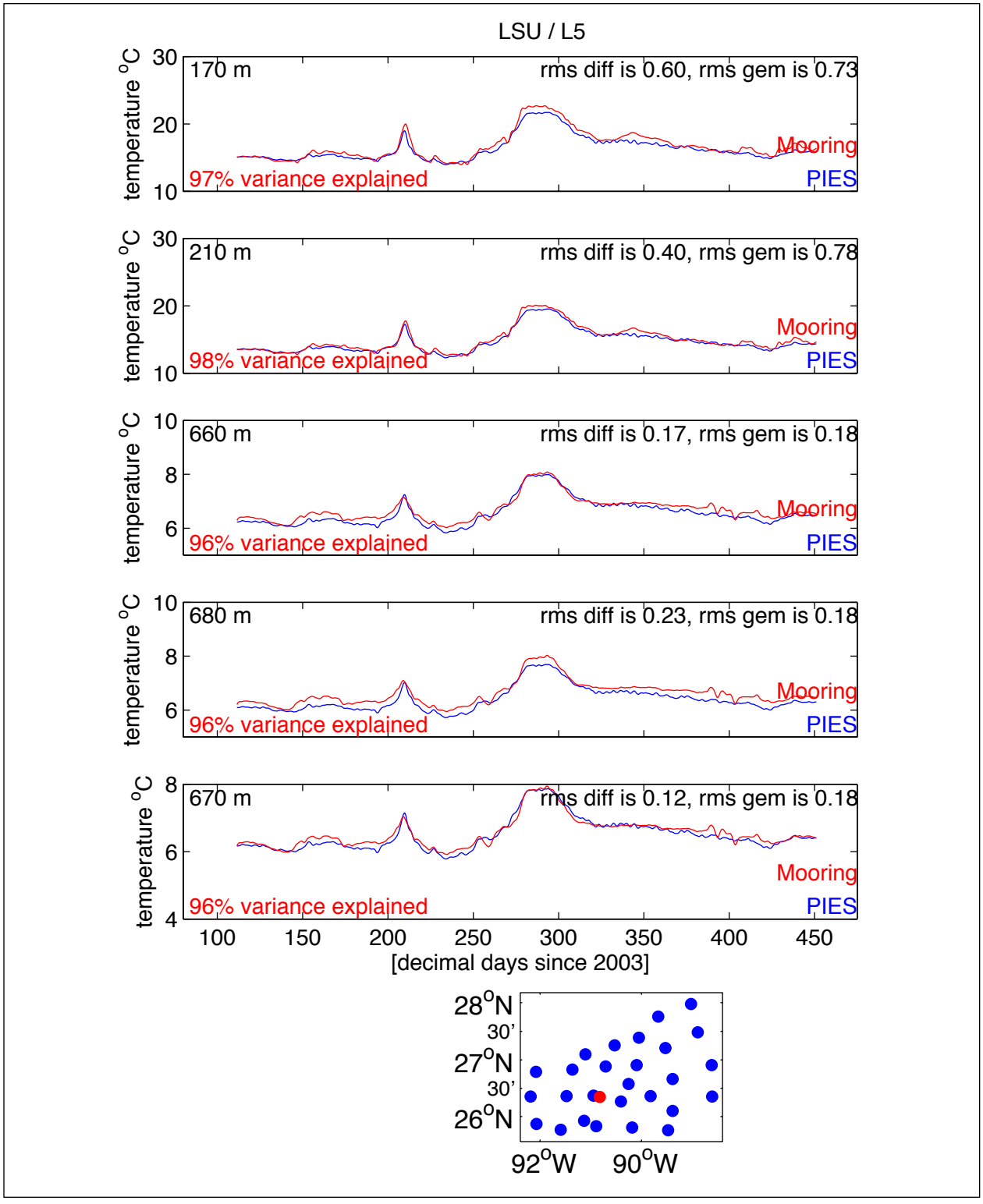

Figure C-10. Comparison between L5 mooring (red) and PIES-derived (blue) temperature. The variance explained is noted in red in the bottom left corner of each panel. The rms difference between the series and the rms in the GEM is noted in the upper right corner. The bottom panel shows the location of the PIES (blue) and the mooring (red).

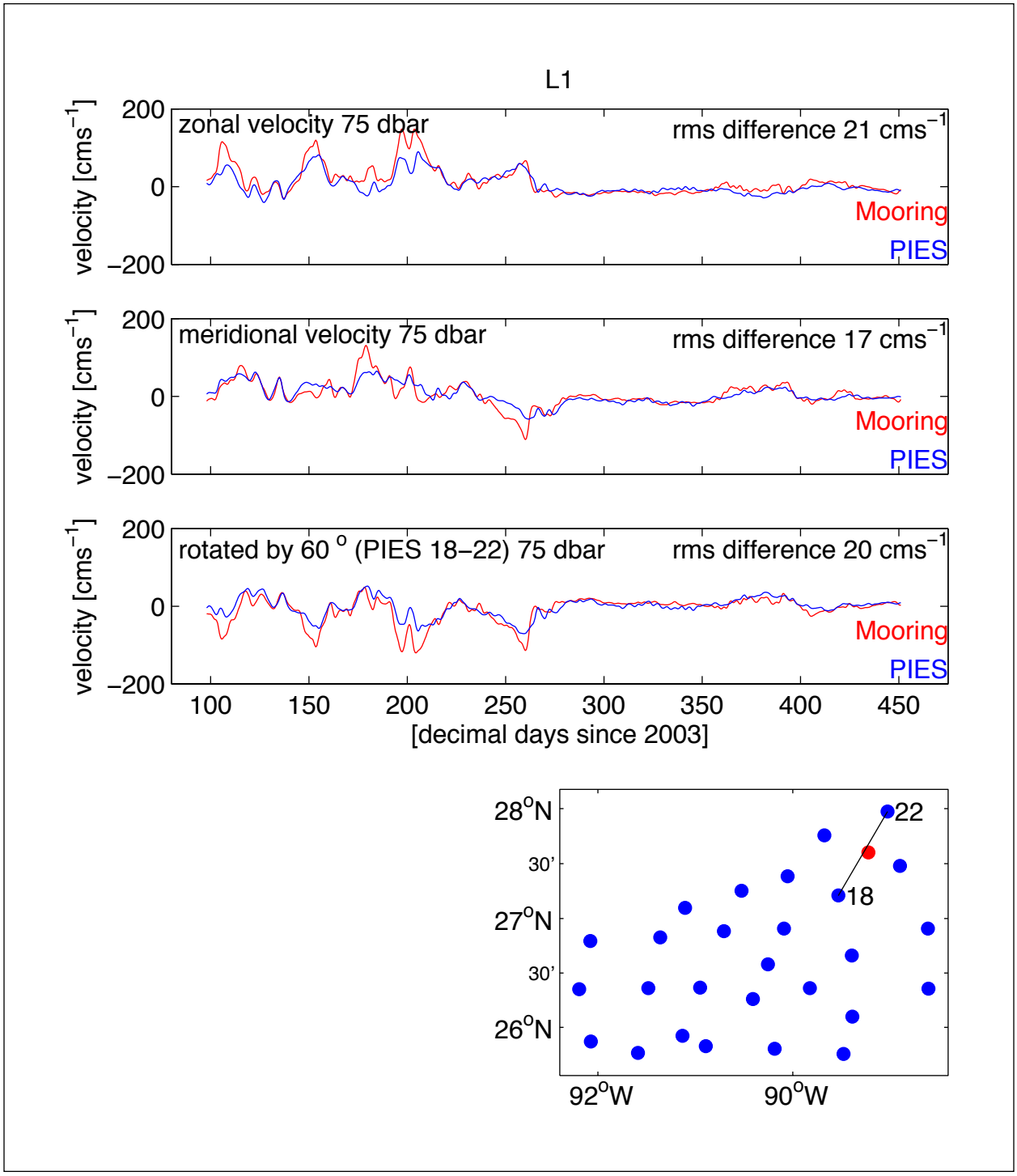

Figure C-11. Comparison between L1 mooring (red) and PIES-derived (blue) velocity for zonal, meridional, and rotated meridional velocity components for the indicated level. The rms difference between the two series is noted in the upper right corner. The bottom panel shows the location of the PIES (blue) and the mooring (red).

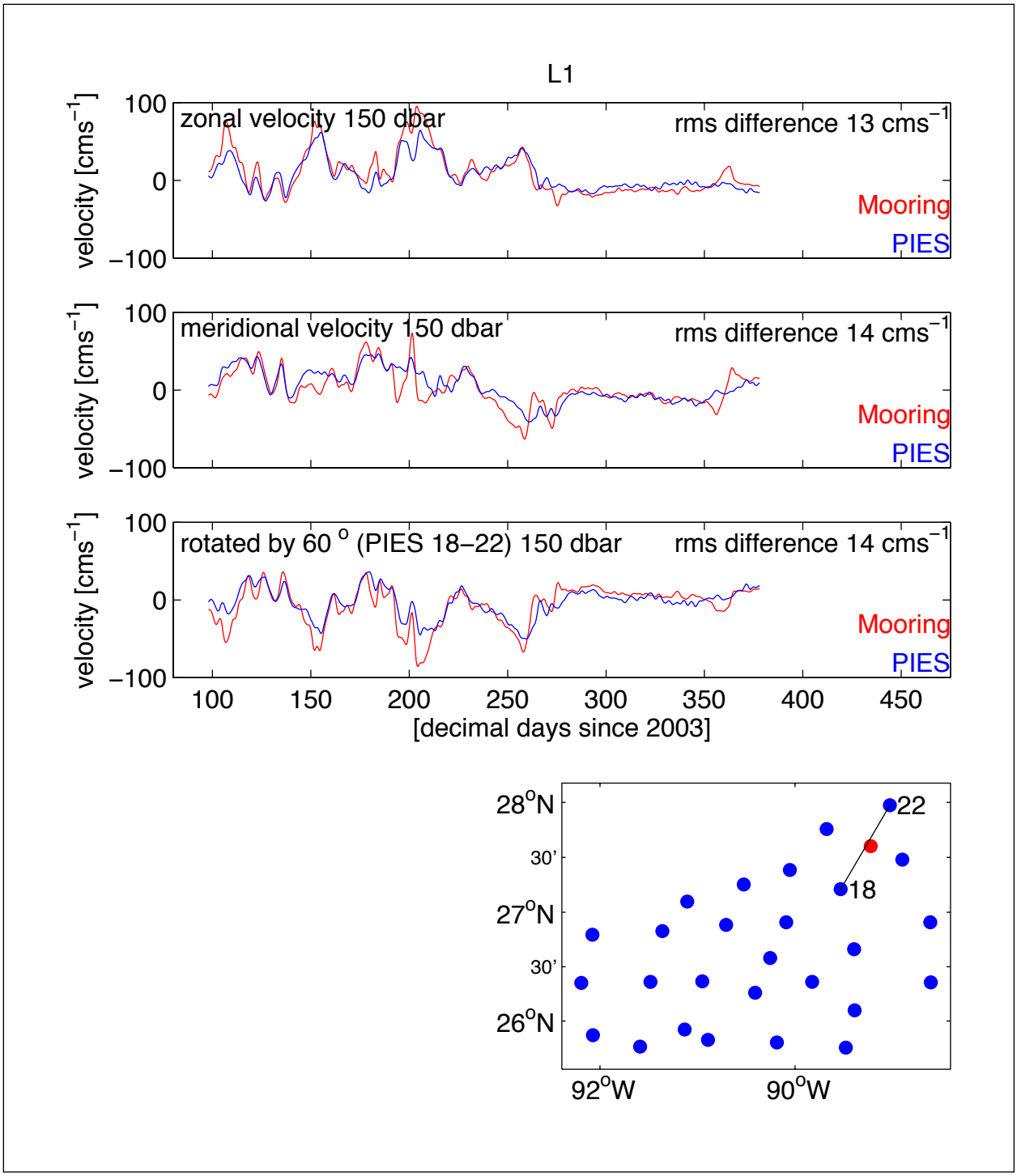

Figure C-12. Comparison between L1 mooring (red) and PIES-derived (blue) velocity for zonal, meridional, and rotated meridional velocity components for the indicated level. The rms difference between the two series is noted in the upper right corner. The bottom panel shows the location of the PIES (blue) and the mooring (red).

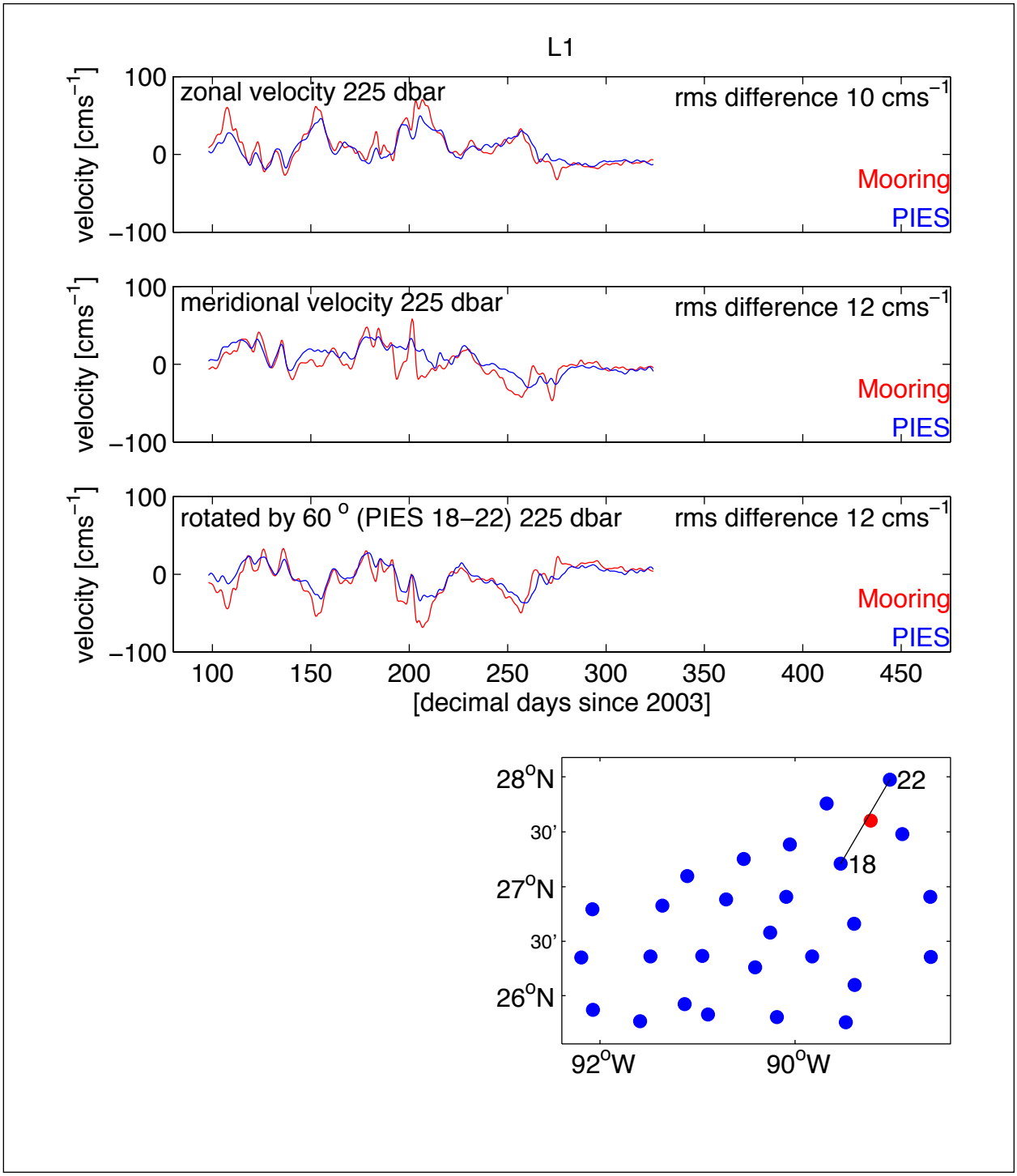

Figure C-13. Comparison between L1 mooring (red) and PIES-derived (blue) velocity for zonal, meridional, and rotated meridional velocity components for the indicated level. The rms difference between the two series is noted in the upper right corner. The bottom panel shows the location of the PIES (blue) and the mooring (red).

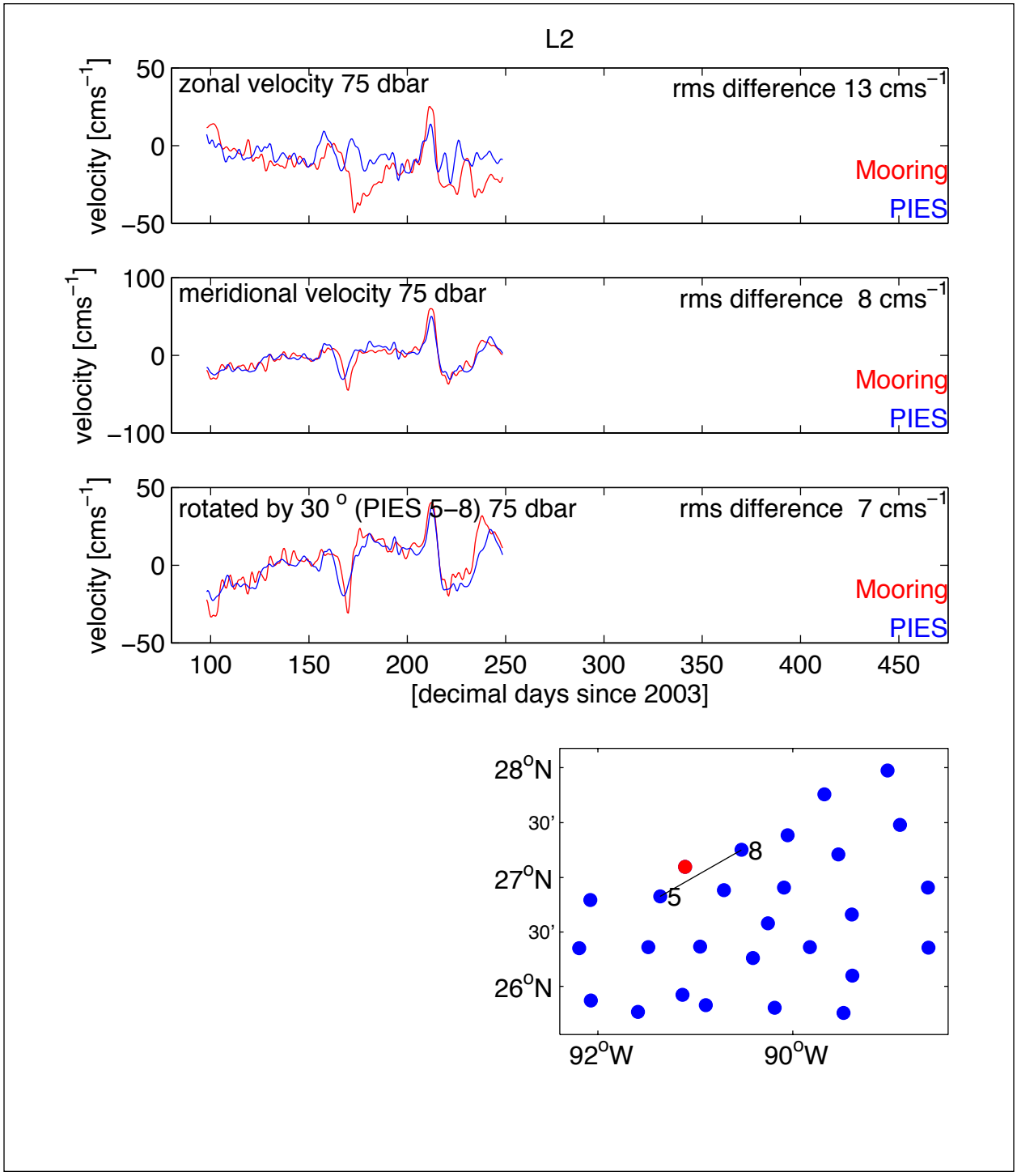

Figure C-14. Comparison between L2 mooring (red) and PIES-derived (blue) velocity for zonal, meridional, and rotated meridional velocity components for the indicated level. The rms difference between the two series is noted in the upper right corner. The bottom panel shows the location of the PIES (blue) and the mooring (red).

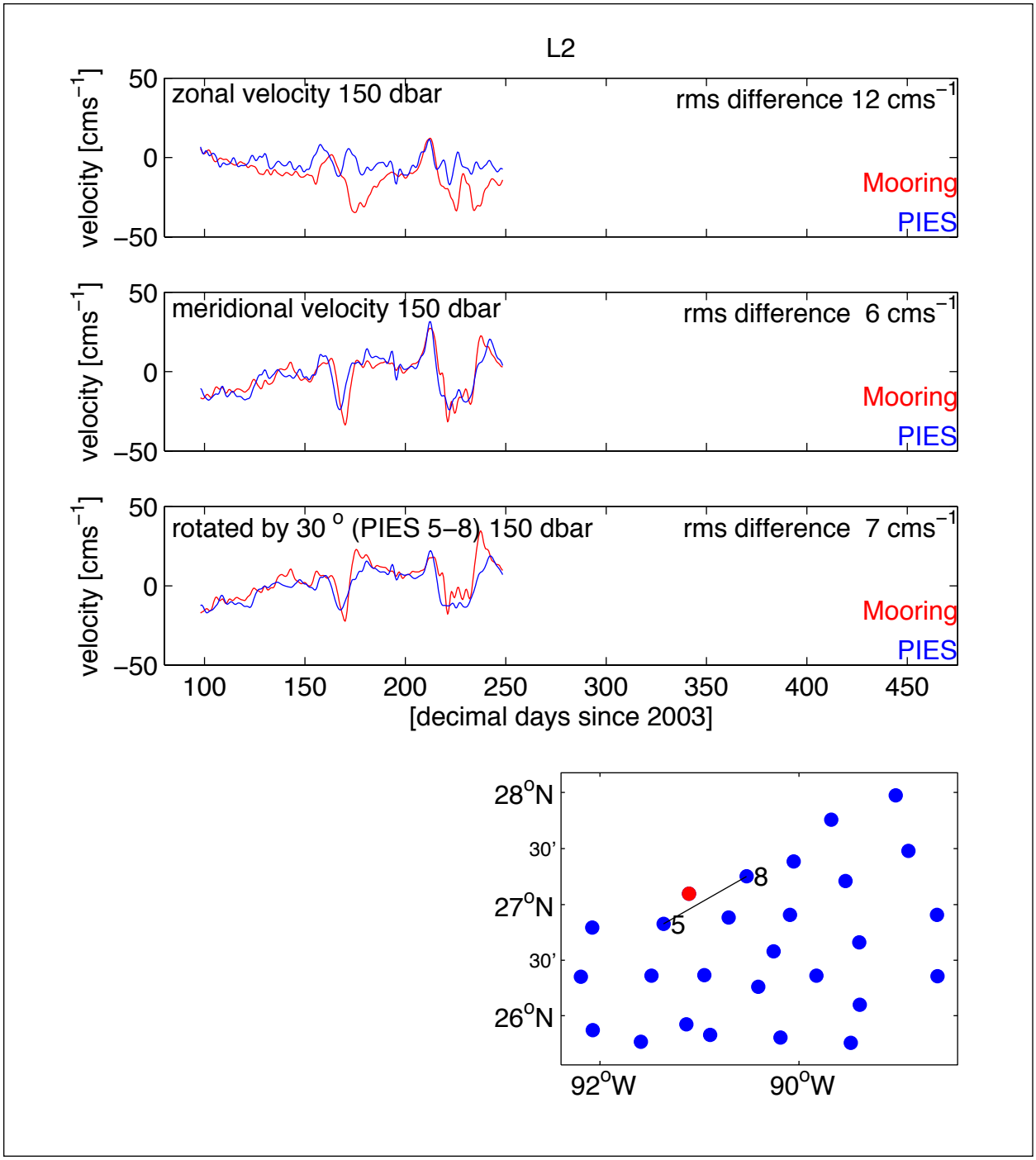

Figure C-15. Comparison between L2 mooring (red) and PIES-derived (blue) velocity for zonal, meridional, and rotated meridional velocity components for the indicated level. The rms difference between the two series is noted in the upper right corner. The bottom panel shows the location of the PIES (blue) and the mooring (red).

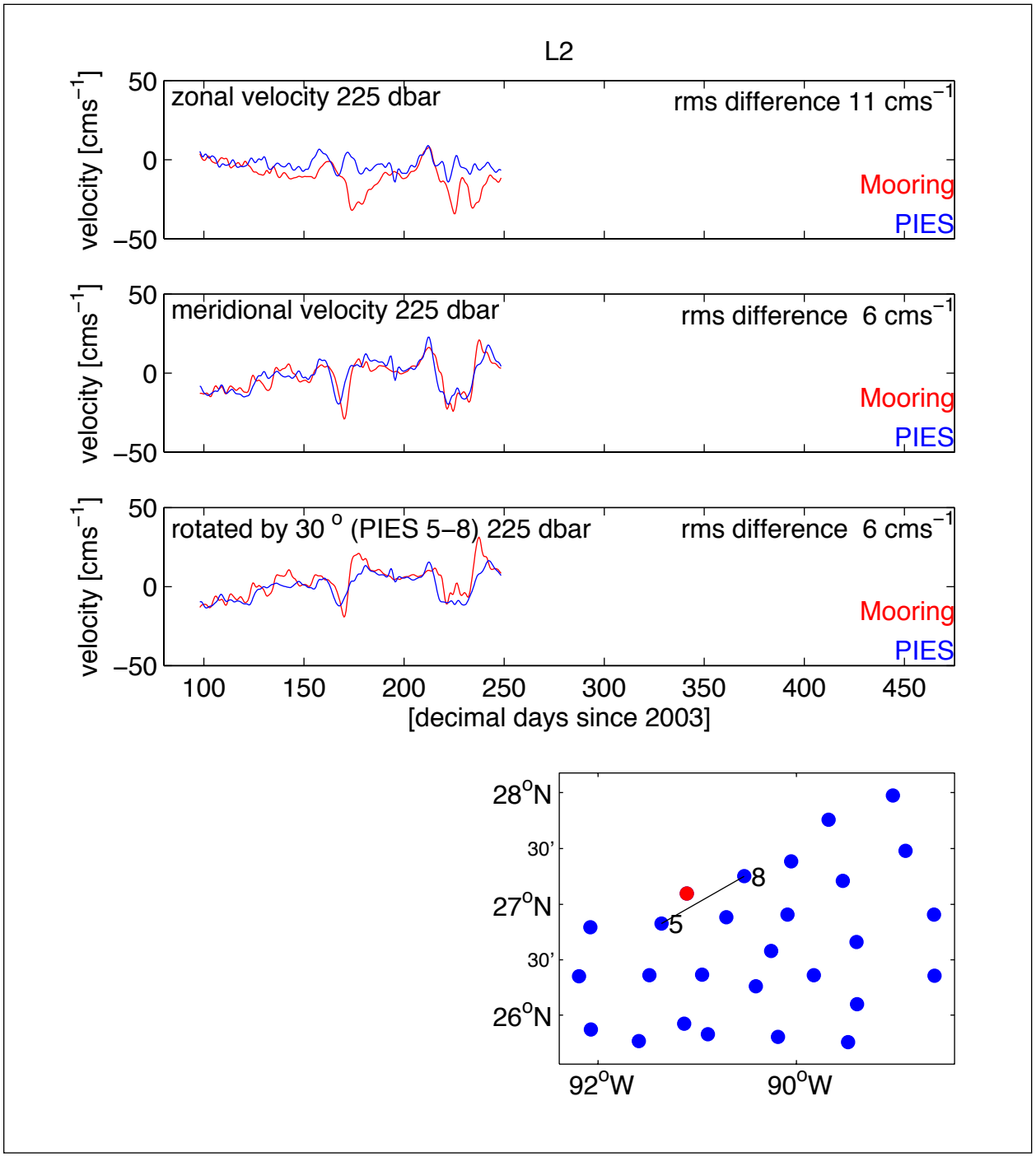

Figure C-16. Comparison between L2 mooring (red) and PIES-derived (blue) velocity for zonal, meridional, and rotated meridional velocity components for the indicated level. The rms difference between the two series is noted in the upper right corner. The bottom panel shows the location of the PIES (blue) and the mooring (red).

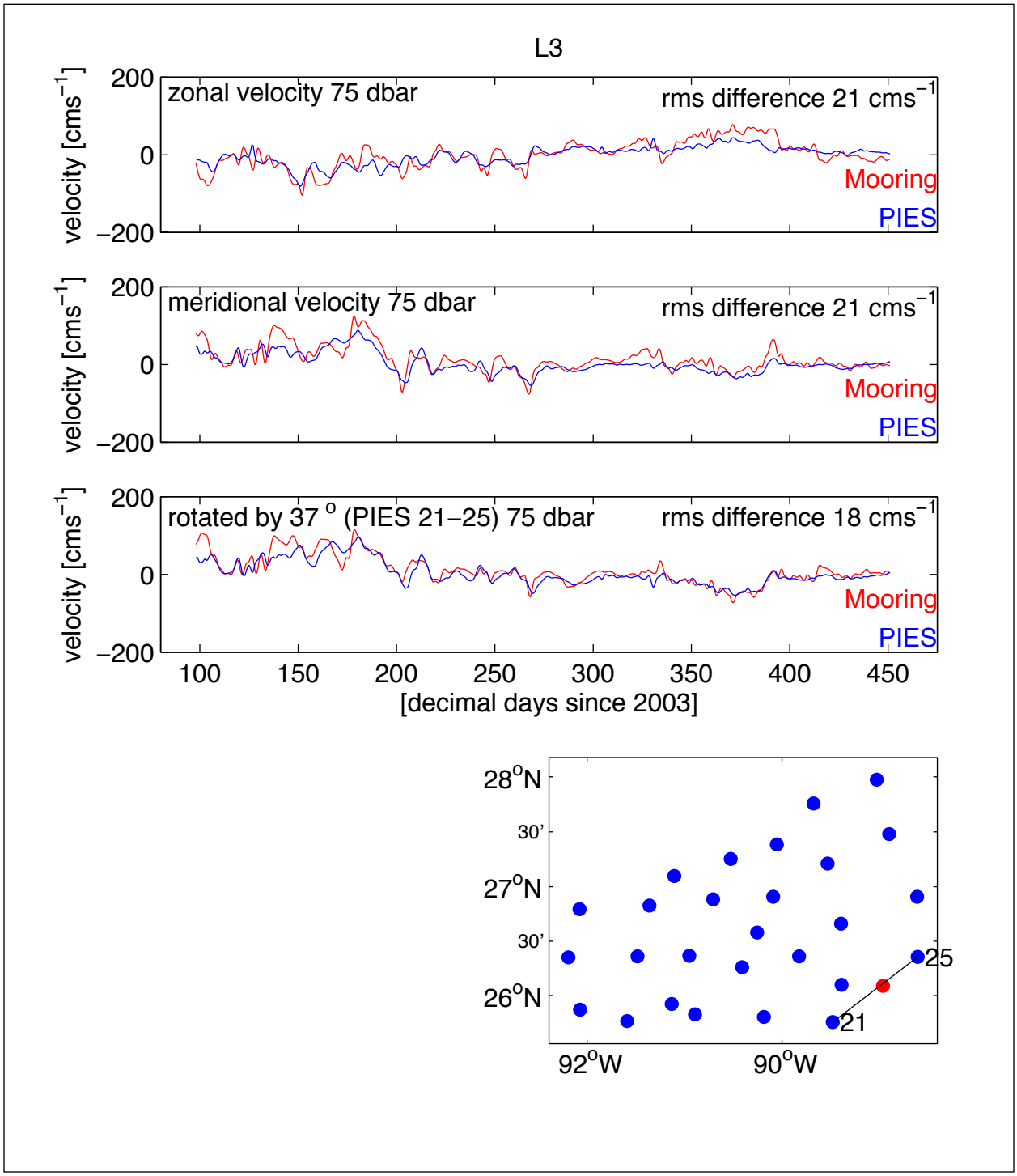

Figure C-17. Comparison between L3 mooring (red) and PIES-derived (blue) velocity for zonal, meridional, and rotated meridional velocity components for the indicated level. The rms difference between the two series is noted in the upper right corner. The bottom panel shows the location of the PIES (blue) and the mooring (red).

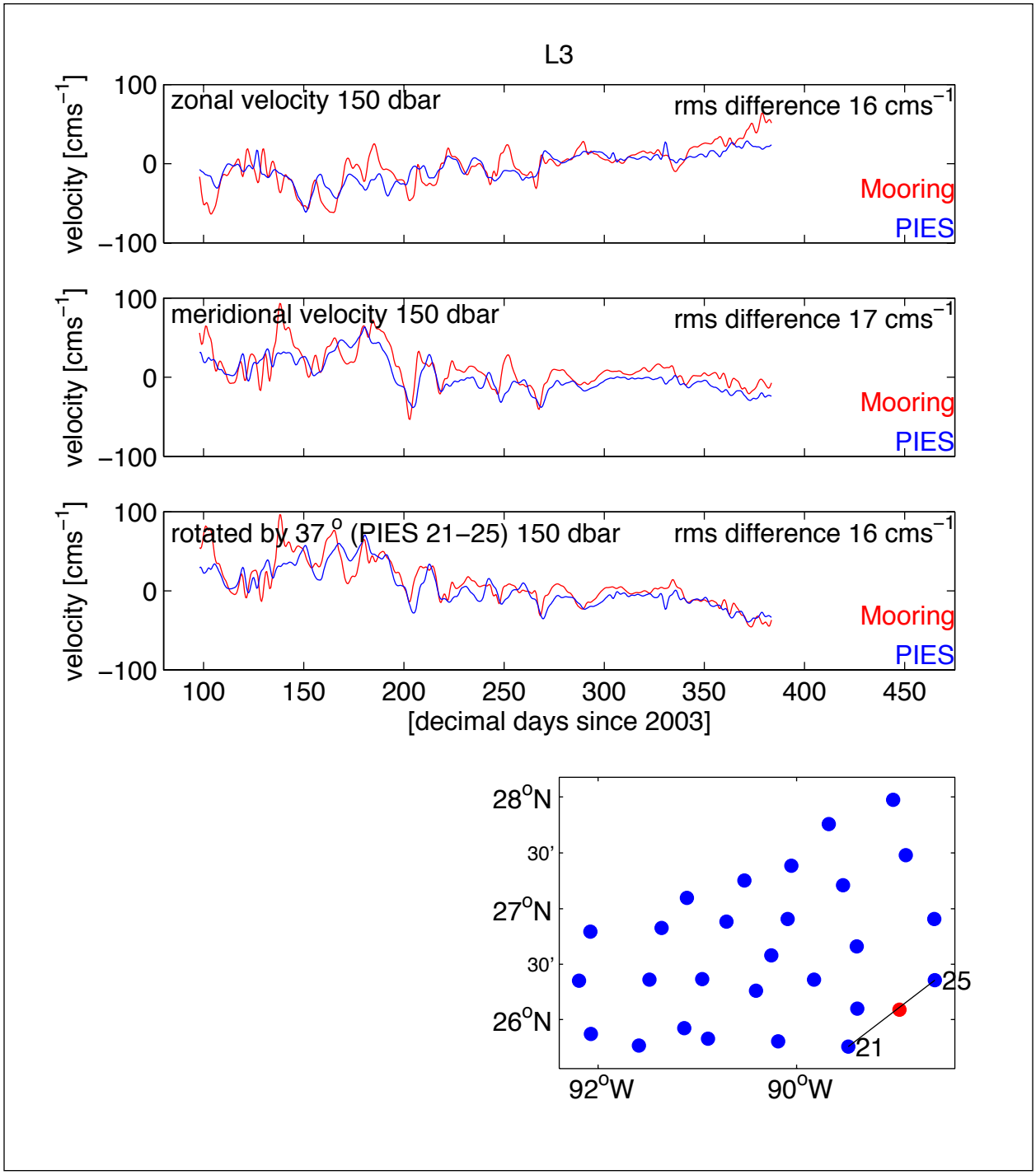

Figure C-18. Comparison between L3 mooring (red) and PIES-derived (blue) velocity for zonal, meridional, and rotated meridional velocity components for the indicated level. The rms difference between the two series is noted in the upper right corner. The bottom panel shows the location of the PIES (blue) and the mooring (red).

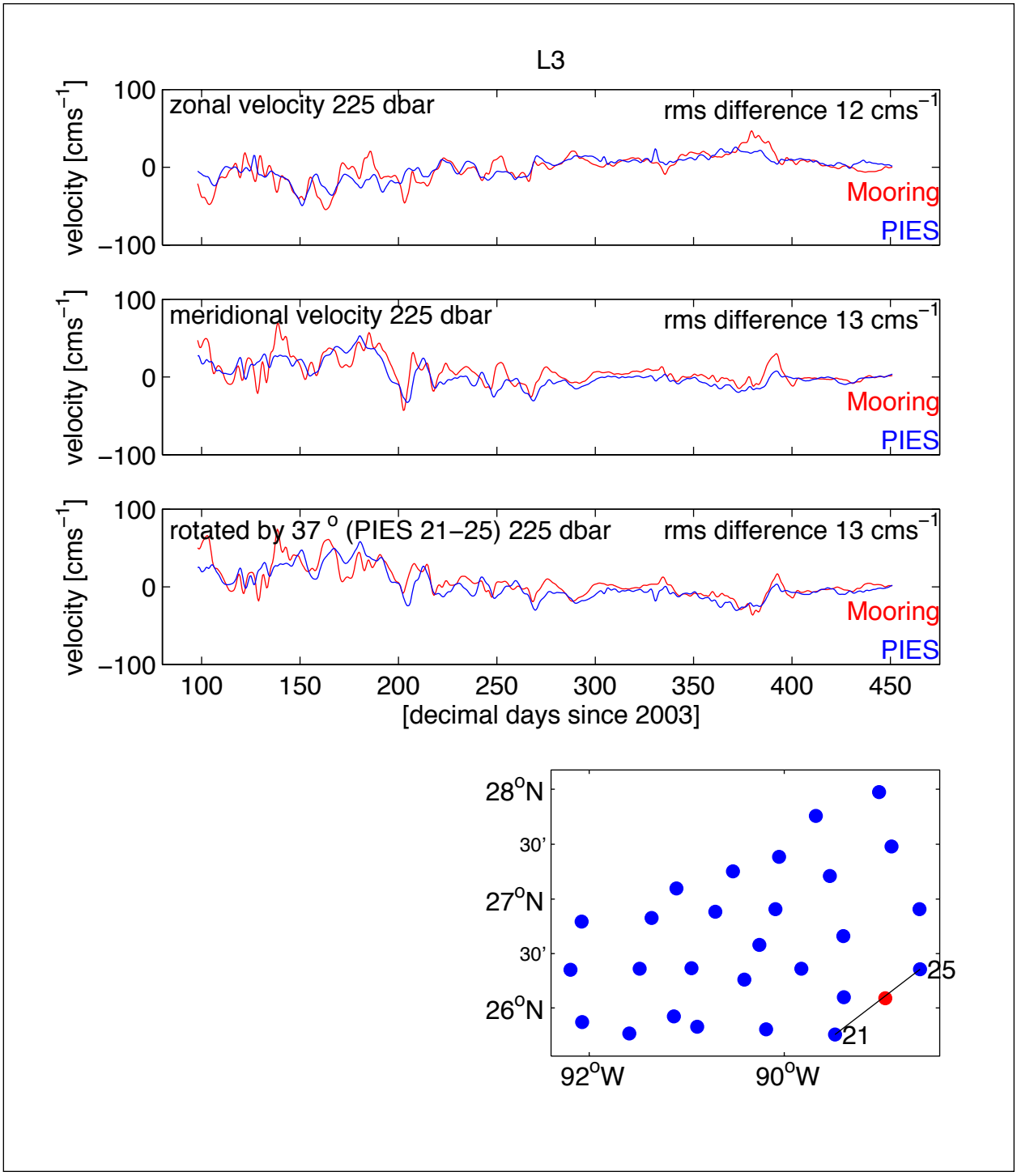

Figure C-19. Comparison between L3 mooring (red) and PIES-derived (blue) velocity for zonal, meridional, and rotated meridional velocity components for the indicated level. The rms difference between the two series is noted in the upper right corner. The bottom panel shows the location of the PIES (blue) and the mooring (red).

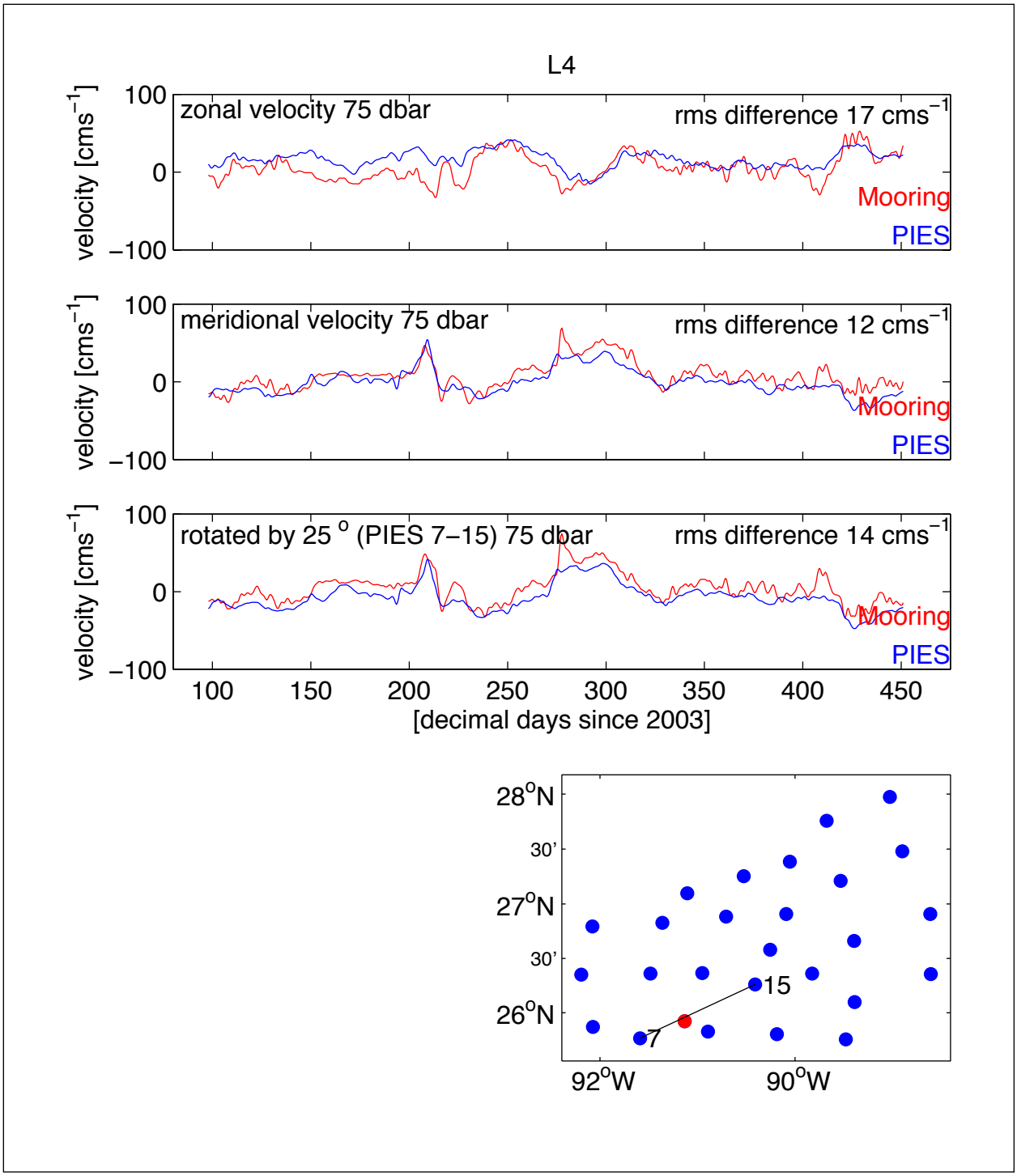

Figure C-20. Comparison between L4 mooring (red) and PIES-derived (blue) velocity for zonal, meridional, and rotated meridional velocity components for the indicated level. The rms difference between the two series is noted in the upper right corner. The bottom panel shows the location of the PIES (blue) and the mooring (red).

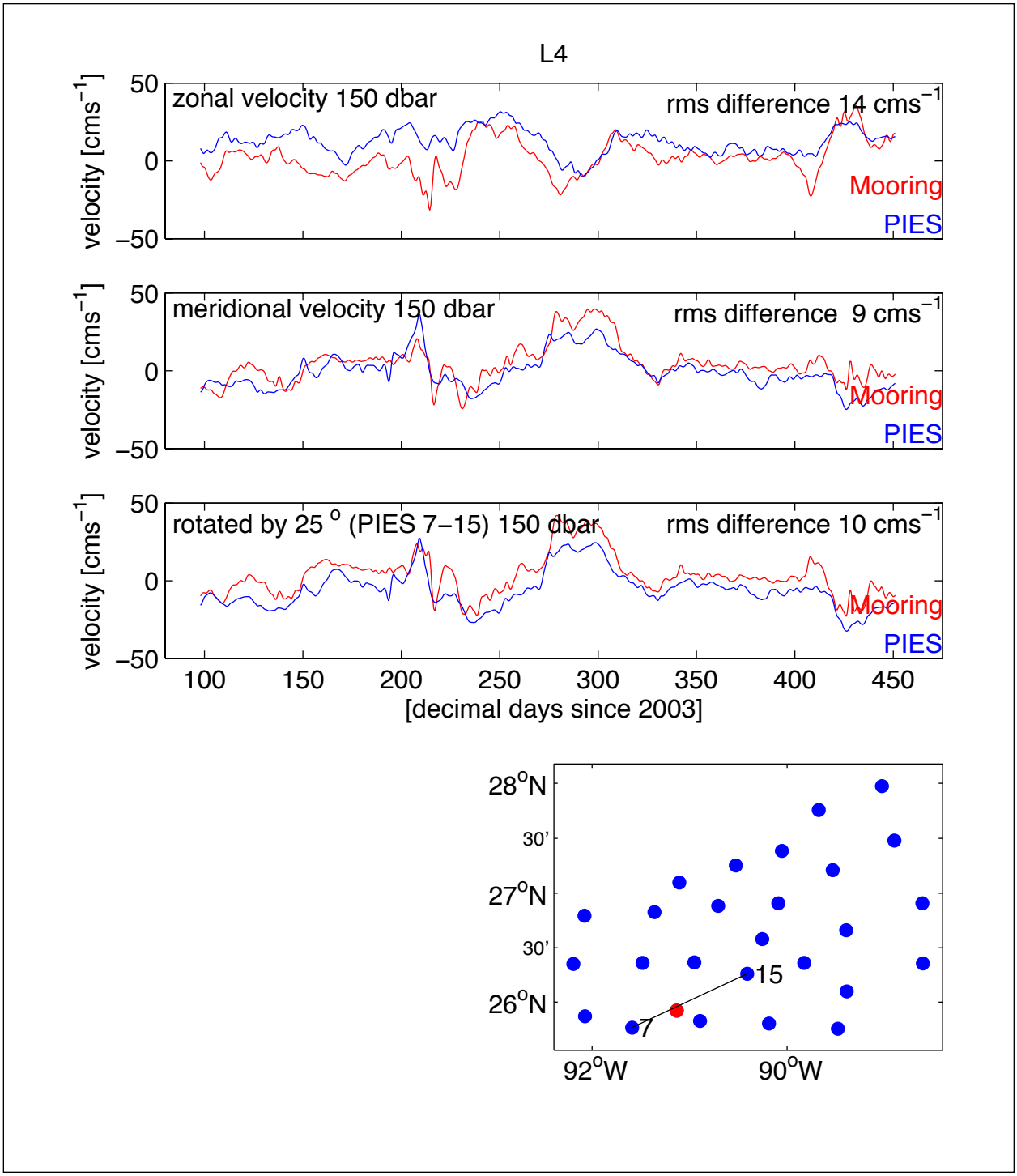

Figure C-21. Comparison between L4 mooring (red) and PIES-derived (blue) velocity for zonal, meridional, and rotated meridional velocity components for the indicated level. The rms difference between the two series is noted in the upper right corner. The bottom panel shows the location of the PIES (blue) and the mooring (red).

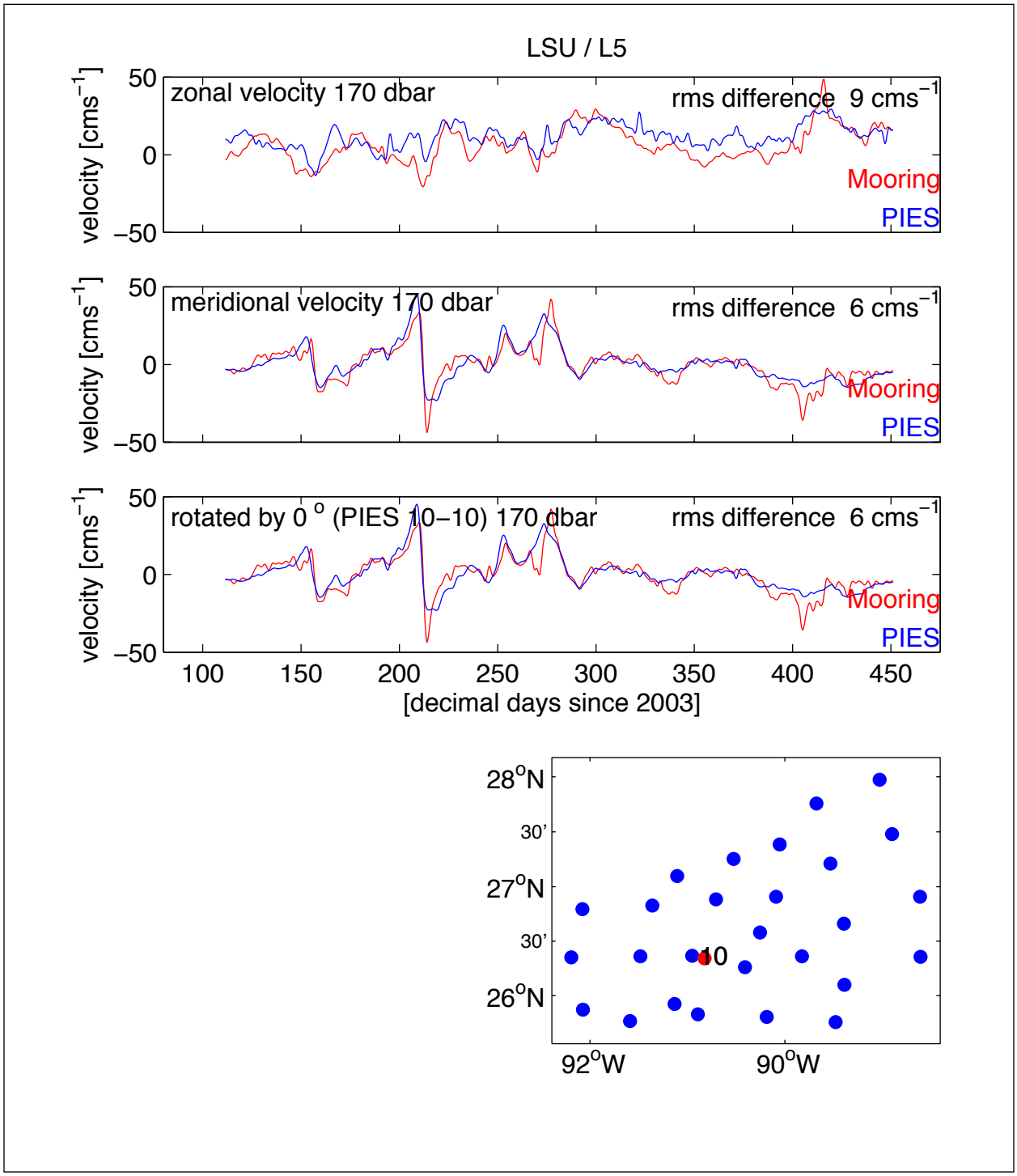

Figure C-22. Comparison between L5 mooring (red) and PIES-derived (blue) velocity for zonal, meridional, and rotated meridional velocity components for the indicated level. The rms difference between the two series is noted in the upper right corner. The bottom panel shows the location of the PIES (blue) and the mooring (red).

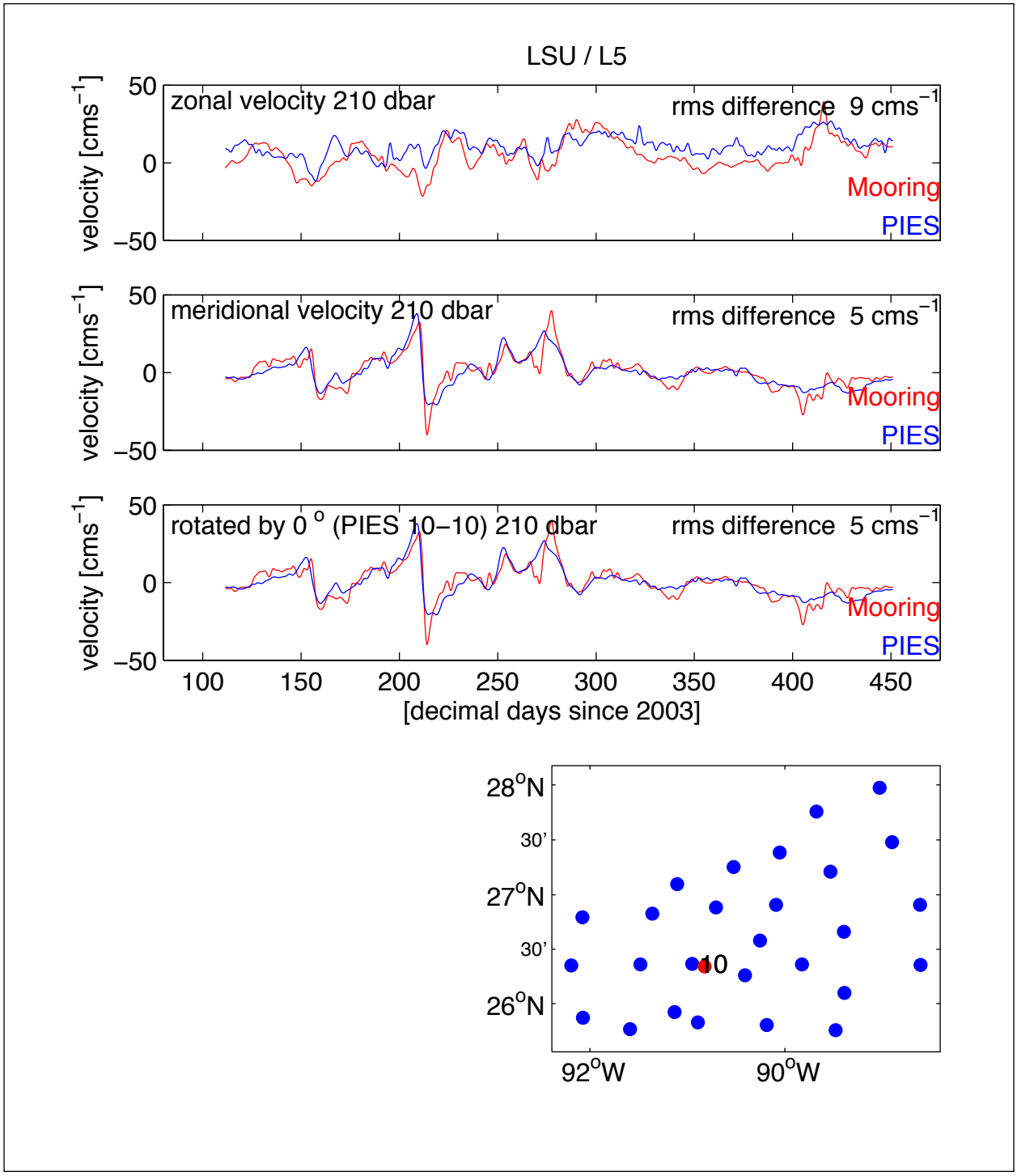

Figure C-23. Comparison between L5 mooring (red) and PIES-derived (blue) velocity for zonal, meridional, and rotated meridional velocity components for the indicated level. The rms difference between the two series is noted in the upper right corner. The bottom panel shows the location of the PIES (blue) and the mooring (red).

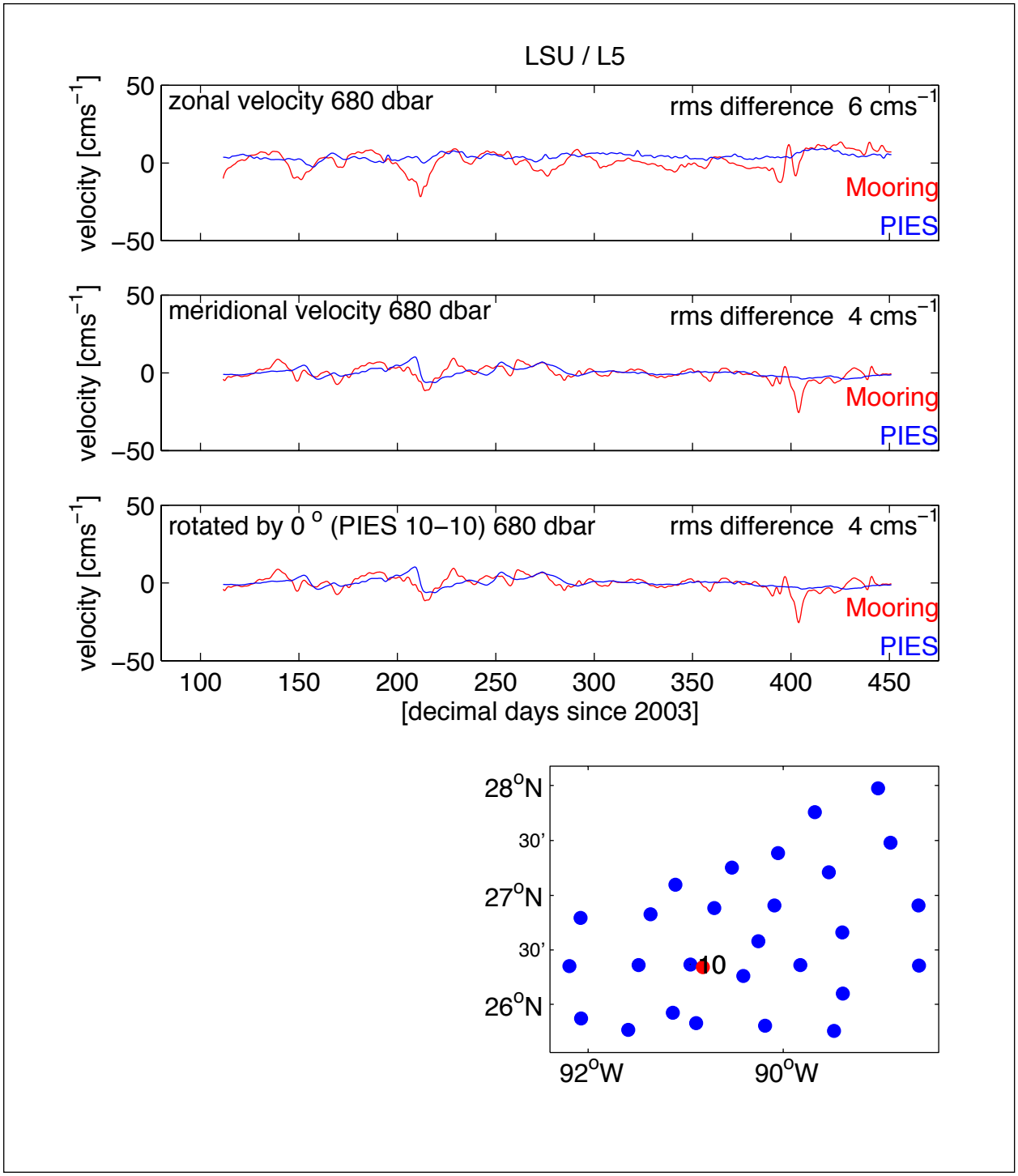

Figure C-24. Comparison between L5 mooring (red) and PIES-derived (blue) velocity for zonal, meridional, and rotated meridional velocity components for the indicated level. The rms difference between the two series is noted in the upper right corner. The bottom panel shows the location of the PIES (blue) and the mooring (red).

Appendix D

Barotropic Tides

Tidal response analysis (Munk and Cartwright, 1966) determined the amplitude and phase for eight major tidal constituents (O1, K1, Q1, P1, M2, K2, N2, S2) from the twenty-seven bottom pressure records within the array (Figures D-1, D-2, and Table D-1). Estimated phase and amplitude vary smoothly across the array as expected. Tidal amplitudes are generally small. The largest tidal amplitudes are near 15 cm for O1 and K1, near 5 cm for P1, and less than 5 cm for the remaining five constituents. Amplitudes have been converted to meters by dividing pressure by density times gravity, $\rho g = 1.02$.

Table D-1a

Amplitude in cm and phase in degrees for the 4 major tidal constituents (O1, K1, Q1, P1) constituents determined with the tidal response method (Munk and Cartwright, 1966) from the twenty-seven bottom pressure records.

	O1		K1		Q1		P1	
SITE	Amplitude (cm)	Phase (degrees)	Amplitude (cm)	Phase (degrees)	Amplitude (cm)	Phase (degrees)	Amplitude (cm)	Phase (degrees)
1	14.81	13.86	15.32	21.93	3.32	3.42	5.18	22.51
2	14.79	14.48	15.30	22.66	3.32	4.09	5.17	23.22
3	14.83	14.83	15.31	22.86	3.33	4.50	5.18	23.43
4	14.17	14.05	14.57	21.71	3.19	3.83	4.93	22.31
5	14.65	13.59	15.17	21.57	3.29	3.19	5.13	22.15
6	14.63	14.24	15.14	22.28	3.28	3.96	5.12	22.84
7	14.72	14.90	15.20	22.73	3.31	4.71	5.14	23.31
8	14.35	12.94	14.81	20.73	3.21	2.63	5.01	21.32
9	14.38	13.45	14.86	21.30	3.23	3.48	5.02	21.84
10	14.53	14.12	15.02	21.95	3.26	3.99	5.08	22.51
11	14.73	14.42	14.38	22.88	3.38	5.11	4.88	23.33
12	14.20	12.68	14.61	20.45	3.19	2.46	4.94	21.04
13	14.25	13.33	14.68	21.10	3.20	3.13	4.96	21.69
14	14.31	13.70	14.74	21.61	3.21	3.71	4.99	22.14
15	14.39	14.14	14.82	21.98	3.23	4.12	5.01	22.52
16	14.36	14.74	14.75	22.50	3.23	4.77	4.99	23.06
17	14.07	12.04	14.50	19.67	3.18	1.76	4.90	20.29
18	14.11	12.57	14.50	20.33	3.18	2.24	4.90	20.95
19	14.03	13.32	14.39	21.06	3.16	2.99	4.87	21.67
20	14.04	14.21	14.39	21.90	3.17	3.97	4.87	22.51
21	14.02	14.80	14.39	22.43	3.17	4.64	4.86	23.04
22	13.85	11.58	14.27	19.25	3.12	1.65	4.82	19.81
23	13.86	12.31	14.26	19.94	3.11	2.29	4.82	20.52
24	13.68	12.72	14.07	20.43	3.08	2.64	4.76	21.01
25	13.72	13.52	14.06	21.20	3.10	3.47	4.75	21.79
26	14.57	13.17	15.07	21.10	3.27	2.78	5.09	21.69
27	14.63	14.97	15.06	22.98	3.28	4.91	5.10	23.51

Table D-1b

Amplitude in cm and phase in degrees for the 4 major tidal constituents (M2, K2, N2, S2) constituents determined with the tidal response method (Munk and Cartwright, 1966) from the twenty-seven bottom pressure records.

	M2		K2		N2		S2	
SITE	Amplitude (cm)	Phase (degrees)	Amplitude (cm)	Phase (degrees)	Amplitude (cm)	Phase (degrees)	Amplitude (cm)	Phase (degrees)
1	3.30	236.74	0.29	156.18	0.95	217.53	0.90	163.59
2	3.47	239.03	0.29	160.34	0.98	219.79	0.90	168.47
3	3.46	239.30	0.29	158.89	0.98	220.51	0.91	166.68
4	1.12	194.22	0.41	121.11	0.48	194.67	1.33	120.78
5	2.53	229.68	0.32	141.87	0.79	211.99	0.99	145.79
6	2.74	233.42	0.31	145.69	0.84	215.31	0.95	150.32
7	2.99	236.47	0.30	150.32	0.90	218.44	0.94	155.77
8	1.63	208.37	0.37	127.34	0.60	198.12	1.19	128.31
9	1.82	218.23	0.35	131.28	0.63	203.78	1.12	132.92
10	2.15	226.41	0.34	136.80	0.72	210.39	1.05	139.15
11	2.28	228.86	0.33	135.62	0.76	212.51	1.03	138.01
12	1.25	186.14	0.41	120.55	0.49	185.50	1.34	120.76
13	1.27	197.36	0.40	122.59	0.51	194.44	1.30	122.65
14	1.44	209.21	0.38	125.18	0.56	200.90	1.23	125.56
15	1.62	217.67	0.37	128.24	0.61	205.49	1.17	128.95
16	1.51	217.28	0.37	127.37	0.59	206.44	1.19	127.72
17	1.23	154.90	0.45	115.26	0.44	171.30	1.52	114.80
18	1.11	157.88	0.45	115.15	0.42	174.28	1.49	114.63
19	1.00	159.11	0.45	115.04	0.41	179.42	1.49	114.27
20	0.90	170.87	0.43	116.67	0.41	188.02	1.44	115.74
21	0.91	187.07	0.42	118.50	0.44	194.12	1.38	117.62
22	1.55	122.42	0.50	109.18	0.40	144.78	1.72	108.49
23	1.49	122.22	0.50	109.58	0.38	149.12	1.72	108.68
24	1.51	114.52	0.51	107.67	0.34	143.89	1.76	106.67
25	1.35	115.90	0.51	109.07	0.32	152.21	1.74	107.83
26	2.25	223.86	0.34	137.35	0.74	207.13	1.05	140.15
27	2.45	232.64	0.32	142.00	0.78	215.18	0.99	145.32

Munk, W.H. and D.E. Cartwright. 1966. Tidal spectroscopy and prediction. Philosophical Transactions of the Royal Society of London 259(A):533-581.

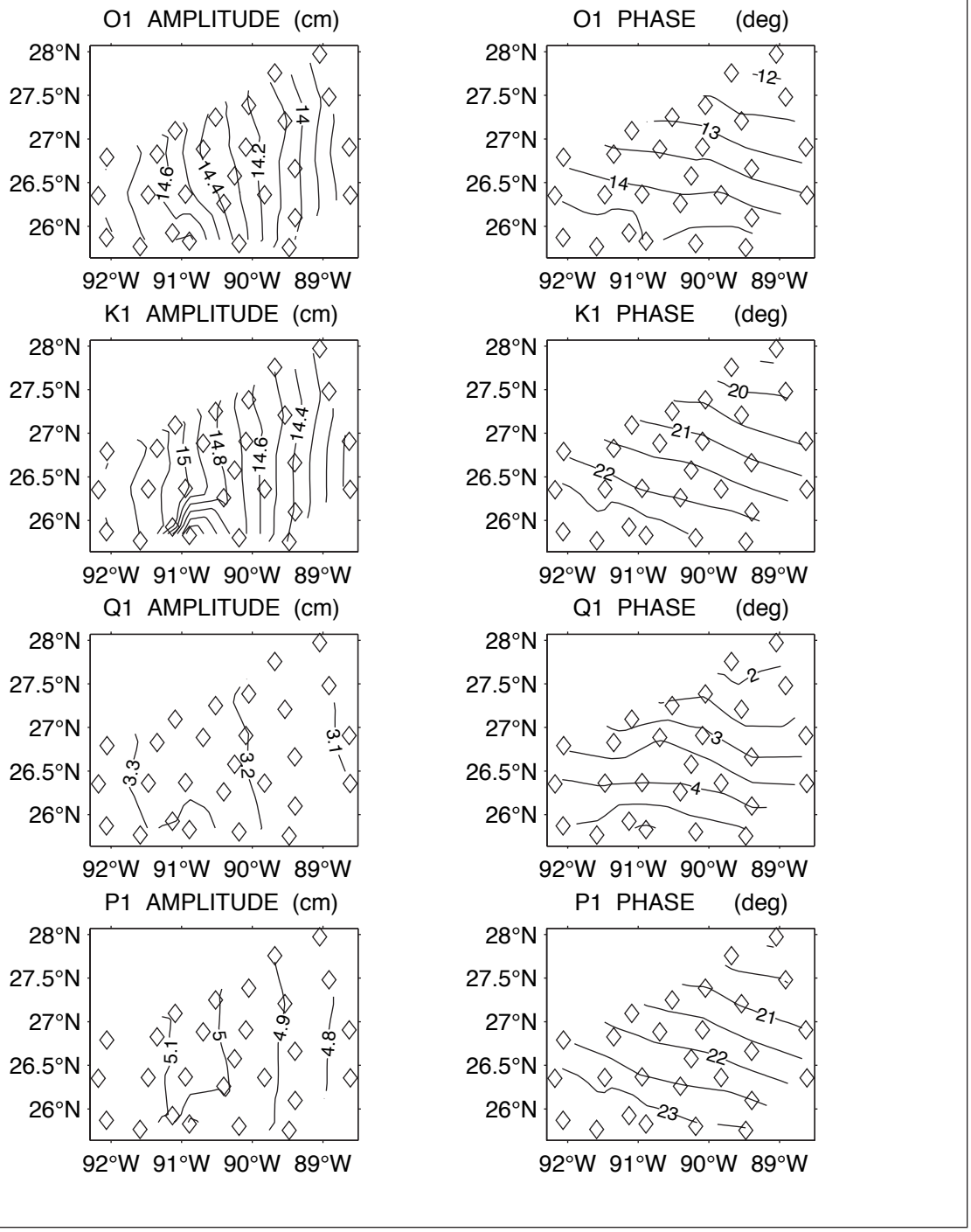

Figure D-1. Amplitude (left column) and phase (right column) of the O1, K1, Q1, and P1 constituents determined with the tidal response method (Munk and Cartwright, 1966) from the twenty-seven bottom pressure records.

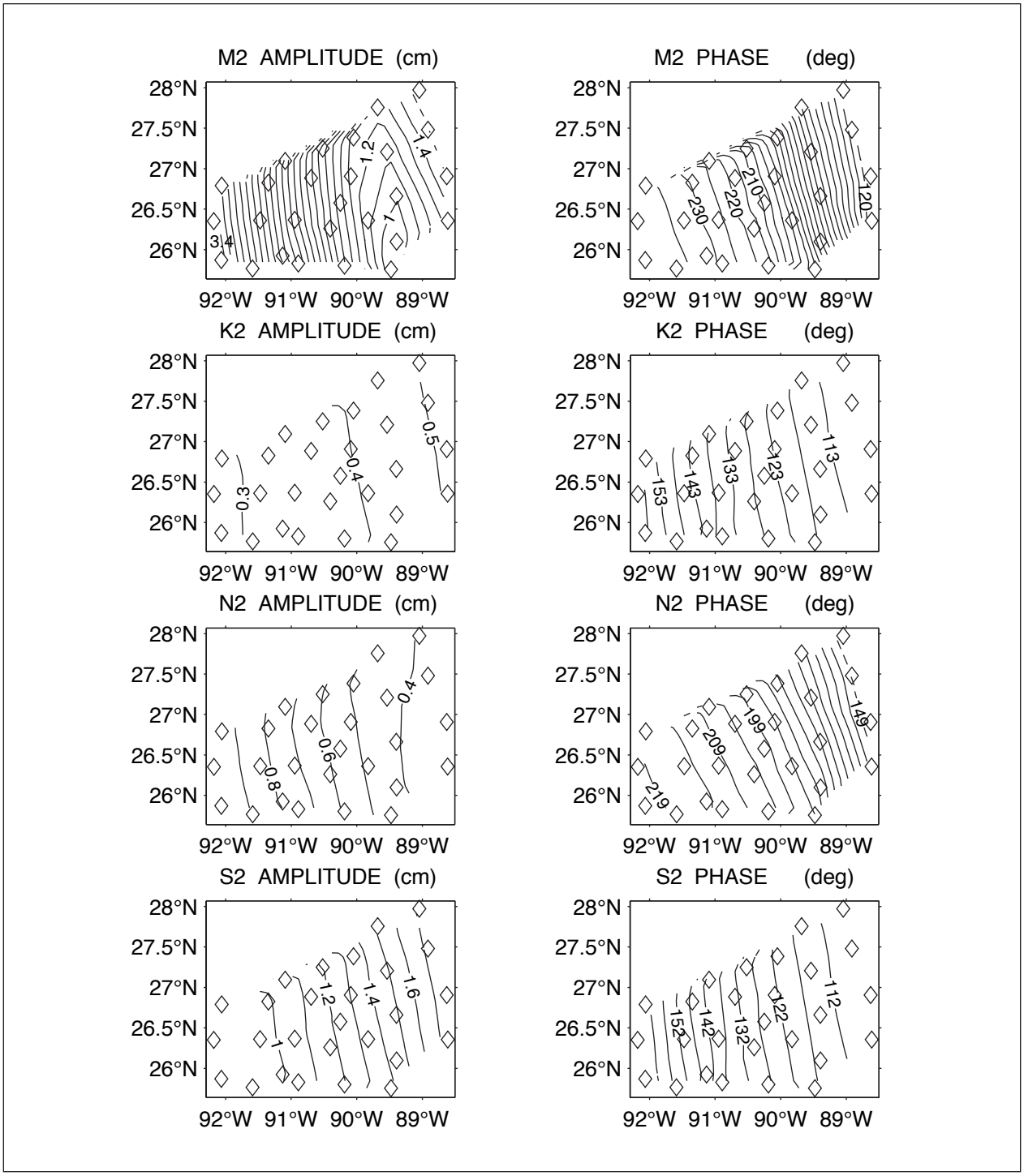

Figure D-2. Amplitude (left panels) and phase (right panels) of the M2, K2, N2, and S2 constituents determined with the tidal response method (Munk and Cartwright, 1966) from the twenty-seven bottom pressure records.

Appendix E

Float Tracking and Sound Source Replacement

As noted in this report, RAFOS and PALFOS floats listen for, and record the time of arrival of, signals generated by sound sources moored in the ocean. For maximum range, these sources are located near the depth of the sound channel axis, in this case slightly less than 1000m. Each sound source transmits a swept frequency signal centered on a frequency of 260 Hz, for a duration of 80 sec. Sources were set in this experiment to transmit every 8 hours. In order to avoid conflicts, source transmissions were offset by 30 min; thus, for example, SoSo1 might transmit at 1200 hrs, SoSo2 at 1230 hrs, and SoSo3 at 1300 hrs.

On each float, a correlator compares arriving signals with an internally generated comparison signal. Because of the time step of this correlator, the horizontal resolution is about 300 msec, or a radial distance of about 500m between each source and a float. Of course, the actual accuracy of the determined float position is much more complicated as it depends on the relative geometry of the three sources and the float.

To check the accuracy of the source clocks, an ALS (Autonomous Listening Station) was deployed on one of the tall moorings. This was essentially a RAFOS float configured in a cage that could be mounted to the mooring wire. By comparing the ALS clock at the beginning and end of the deployment it was determined that the ALS itself drifted less than one second during the one year deployment. Relative to that drift, it was impossible to detect any noticeable clock drift in SoSo1, the source that continued functioning for the whole experiment (and is still functioning). The obvious conclusion is that timing errors were not a major source of navigation errors in this experiment.

Unfortunately, two of the three sound sources (SoSo2, SoSo3) failed within a couple of months of deployment. These sources were replaced by two others (of an earlier design) kindly loaned to us by the German Institut fur Meereskunde, in late October 2003.

On two occasions attempts were made to recover these sources, without success. These were part of a batch of 9 sources of a new design that were found to have failed in several experiments. Woods Hole scientists were finally able to recover one of the failed sources off Newfoundland. A "post mortem" showed that the source failed due to a manufacturing problem in a switch that was designed to turn the source to full power once the source was submerged. The earlier sources borrowed from the Institut fur Meereskunde did not use these switches.

The Department of the Interior Mission

As the Nation's principal conservation agency, the Department of the Interior has responsibility for most of our nationally owned public lands and natural resources. This includes fostering sound use of our land and water resources; protecting our fish, wildlife, and biological diversity; preserving the environmental and cultural values of our national parks and historical places; and providing for the enjoyment of life through outdoor recreation. The Department assesses our energy and mineral resources and works to ensure that their development is in the best interests of all our people by encouraging stewardship and citizen participation in their care. The Department also has a major responsibility for American Indian reservation communities and for people who live in island territories under U.S. administration.

The Minerals Management Service Mission

As a bureau of the Department of the Interior, the Minerals Management Service's (MMS) primary responsibilities are to manage the mineral resources located on the Nation's Outer Continental Shelf (OCS), collect revenue from the Federal OCS and onshore Federal and Indian lands, and distribute those revenues.

Moreover, in working to meet its responsibilities, the **Offshore Minerals Management Program** administers the OCS competitive leasing program and oversees the safe and environmentally sound exploration and production of our Nation's offshore natural gas, oil and other mineral resources. The MMS **Minerals Revenue Management** meets its responsibilities by ensuring the efficient, timely and accurate collection and disbursement of revenue from mineral leasing and production due to Indian tribes and allottees, States and the U.S. Treasury.

The MMS strives to fulfill its responsibilities through the general guiding principles of: (1) being responsive to the public's concerns and interests by maintaining a dialogue with all potentially affected parties and (2) carrying out its programs with an emphasis on working to enhance the quality of life for all Americans by lending MMS assistance and expertise to economic development and environmental protection.